PHOTOMETRIC INVESTIGATIONS OF SEVERAL EARLY-TYPE VARIABLE STARS USING THE STEREO SATELLITE

by

Dogus Ozuyar

A thesis submitted to
The University of Birmingham
for the degree of
DOCTOR OF PHILOSOPHY

Astrophysics and Space Research Group
School of Physics and Astronomy
The University of Birmingham
May, 2015

Abstract

We present results from high-precision photometric monitoring of a significant number of bright early-type stars. The data cover five years (2007–2011) and are collected by the *STEREO* satellite. Stellar types covered are a sample of CP stars, Be-stars and δ Scuti stars. We describe the *STEREO* data and the data pipeline developed to produce the final light curves.

We studied long-term variations in the rotational periods of 14 CP stars. With our pipeline, we were able to accurately determine their periods (typical precision $\sim 10^{-6}$ days), and hence we investigated any period changes.

The second study concerned Be-stars and looked at the connection between disk structures and their non-radial pulsations. *STEREO* photometric data were supported by spectroscopic information on the Hα line. As a result, we found that, in some cases, variations in emission line properties were connected with changes in pulsation characteristics, and we discussed the consequences of this situation.

In the final study, which involved a sample of δ Scuti stars, *STEREO* data were used to investigate the stars' pulsational properties and to look for any possible changes in their pulsations. Pulsation constants and modes of the main frequencies for these stars were identified, and regular spacings in the frequencies were examined. Several cases in which pulsational characteristics changed were also determined, and their consequences were interpreted.

Acknowledgements

This thesis shall not be considered my piece of work only, but that of a number of people who never ceased in helping until this work took its final form. I would like to extend my sincere gratitude to:

my supervisor **Prof. Dr. Ian R. Stevens**, without whom this thesis might not have been written. He has not only broadened my horizons by guiding me into fields different from my background, but has also done his utmost to improve my academic skills by sharing his advanced knowledge on subjects as frequency analysis, statistics, and computer programming. He and his family generously offered their help whenever I was in need of housing, assistance, or just company. For all of this, he is an immensely valuable person to me both in my personal and academic life.

to **the Republic of Turkey's Ministry of National Education** and **its caring employees**. Without their financial and motivational support, it would not have been possible to receive such a good education or live abroad for such an extended period.

Also, to **Sakir Sengul** and **Cem Vural**, who sponsored me and my education by taking on a massive repayment risk. They always stand next to me, and never leave me alone. I am deeply grateful for their spiritual support.

to my dear colleagues **Dr. Gemma Whittaker** and **Dr. Vinothini Shankar**, who helped me with computer coding and provided data from the *STEREO* satellite. I also would like to thank them for facilitating whenever I needed.

to **David Stops**, for doing me the favour of providing me with a license for the Interactive Data Language program and for allowing me comfortably to ask an excessive amount of questions about computers and coding.

Additionally, to **Dr. Ben Aylott**, **Dogan Kaya**, and **Saadet Ozcan**, for welcoming me into their home and allowing me to stay for a long period.

to **Ergun Tamer**, my room-mate, for assisting me in my studies and creating such a peaceful work environment in the house.

to my best friend and astronomer, **Sedat Altintop**, for enlightening me in multiple areas of my work by sharing his worthy ideas.

to, **Gokce Yorukoglu** and **Lisel Hintz**, for proofreading my entire thesis from beginning to end and helping me to improve it.

to, my beloved, **Dr. Sevilay Ece Gumus**, for reading all my work, caring for me more than I care myself, and providing her endless support.

to, my biggest supporter, **my family**. They always believed in me, even during the times that I lost faith in myself. As is very well known, chasing rainbows is slightly different from making them come true. My family taught me how to chase rainbows without losing myself in the river of dreams. Hence, they deserve to be more appreciated than anyone else does. I will always remain grateful to them.

Statement of Originality

Variable stars have been one of the most popular and most rapidly developing areas of astronomy since their discovery. Due to their spectroscopic and photometric changes, these types of stars have great importance in gaining a better understanding of stellar structure and evolution. Unlike non-variable stars, precisely because of their variabilities, they assist in calculating physical parameters by providing valuable information such as period and amplitude. The purpose of this study is therefore to analyse light curves of several early-type variables using data obtained from the *STEREO* satellite, and to acquire detailed information about the structure of target stars with the help of frequency analyses. This study, which consists of eight sections, was conducted under the guidance of **Dr. Ian R. STEVENS** at the University of Birmingham between the years of 2010 and 2015. The full implementation of all the work completed in this study belongs only to the author. In the thesis:

Chapter 1 introduces variable stars by providing basic information about them. It starts by categorizing these stars and continues with examples regarding sub-groups, in order to comply with the purpose of the study. In particular, Be- and δ Scuti type variables, as well as chemically peculiar stars are presented as samples of intrinsic and extrinsic variables, respectively.

Chapter 2 discusses the *STEREO* satellite and its properties as related to the study. The primary objective of this satellite is to detect Coronal Mass Ejections of the Sun, but it has another asteroseismologically important mission. Instrumental characteristics of the *STEREO* allow us to obtain high-precision measurements of background stars. Thus, it has the ability to capture the smallest variations in stars, irrespective of their types. In this section, observation instruments and targets of the *STEREO* are explained.

Chapter 3 compares four data analysis techniques that are suitable for examining non-uniformly spaced astronomical data. The chapter focuses particularly on the two widely-used methods of the Lomb-Scargle and the Phase Dispersion Minimization. It describes the advan-

tages and disadvantages of these techniques.

Chapter 4 is a preparation for frequency analyses of real light curves. In this chapter, various synthetic light curves that are similar to real data have been produced. In order to increase the authenticities of the curves, the cadence (40 min) and the duration (20 days) of observations that are unique to the *HI-1* instrument, as well as different noise levels affecting data quality, have been used. Subsequently, these curves are analysed with the Lomb-Scargle, the Phase Dispersion Minimization, and Period04 techniques to test which method generates more accurate results under different circumstances.

Chapter 5 presents a semi-automated pipeline to refine *STEREO* light curves of 14 chemically peculiar stars. The purpose in this chapter is to acquire the most accurate rotation periods with the smallest possible errors. Thus, long-term variations in periods have been investigated with great precision and mechanisms causing these changes are discussed.

Chapter 6 contributes to studies concerning the phenomenon observed in classical Be-stars. Photometric and spectroscopic data of nine Be-samples derived from the *STEREO* satellite and the *BeSS* Database are analysed. The relation between non-radial pulsations and their amplitudes, as well as equivalent widths and component ratios of the Hα lines are probed.

Chapter 7 sheds light on the stellar structures of six known δ Scuti stars. With the help of *STEREO* light curves, multi-periodicities in these variables are displayed. On the basis of this, the pulsation characteristics of these stars, such as pulsation constants and frequency spacings, are calculated. Among these frequencies, the ones displaying a long-time continuity have been identified and their variations have been monitored. Also, by employing the period-luminosity-colour relation, an attempt is made to derive the physical parameters of the sample stars.

Chapter 8 provides a concise overview of the thesis and suggests future work related to the variable stars discussed therein.

Contents

List of Figures

List of Tables

Chapter 1

Introduction

1.1 Variable Stars

As is very well known, when the twinkling of the atmosphere is not considered, stars appear to be fixed and steady. Detailed investigations, however, reveal that the luminosity of most stars changes over time, and some of them exhibit periodic fluctuations in brightness. These variations can continue to occur over years or last only milliseconds, and may show dramatic changes from one-thousandth of a magnitude up to dozens of magnitudes. These facts illustrate the variable star concept in general terms. Briefly, a variable star can be described as a star whose apparent brightness changes over time with respect to an observer's point of view. Although this definition is a common way for understanding whether a star is variable or not, sometimes changes may take place in chemical structure that provides variety in a spectrum. The reasons that cause photometric and spectroscopic variations in stars can be listed roughly as:

- Presence of a third light affecting overall radiation,
- A non-circular orbit,
- Component(s) with extended atmosphere,
- Variable star(s) in the system,
- Mass-transfer between components or mass-loss from the system,
- Disk, ring or cloud structure around components,
- Non-uniform luminosity distribution on stellar surfaces,

- Presence of a magnetic field.

With the help of these properties, a large number of stellar parameters that are difficult to obtain for non-variable stars such as types (e.g., regular, irregular); periods (e.g., short term, long term); shapes of light curves (e.g., symmetrical, asymmetrical); stellar characteristics (e.g., temperature, luminosity); element abundances (in atmosphere and surroundings); orbital features (multiple or single); and magnetic properties can all be illuminated. This facilitates the generation of or improvement upon theoretical models, and provides an opportunity for understanding physical processes, including the internal formation and structure of stars.

It is known that there are more than 100,000 variable stars in the sky; thousands more are also believed to be variable. Mira is the first known variable star, characterized as a nova by David Fabricius in 1596. Its regular periodic cycles were discovered by Holwards in 1638 (Hoffleit, 1997). Since this discovery refuted the belief that stars were invariable, it has been quite important in terms of scientific progress.

In 1784, Goodricke identified the second variable star, whose variability originated from temporary light decrease (Batten, 1989). He also detected the prototype of the Cepheid variables. Thus, variable stars gained another level of meaning and importance in astronomy, as there has been a strong relation between pulsation periods and luminosities for these stars. This means that period and then luminosity can be calculated by observing a Cepheid. Period value can therefore be used to determine the distance of a star by means of the distance module. Also, since these stars are relatively luminous, they can be detected in very distant galaxies. Indeed, by monitoring these variables, Hubble (1929) proved that the Andromeda Galaxy was not within the Milky Way, but much further away from it. In the following years, discoveries accelerated, and a vast number of variable stars was observed. As a result of this progress, around 50,000 stars in our galaxy were listed in the General Catalogue of Variable Stars (GCVS).

For a better understanding of variable stars' nature and their contribution to the universe, they are classified under two main categories according to factors mentioned above. This classification is primarily formed upon whether the change in a star is extrinsic or intrinsic. Intrinsic variables are stars showing light and brightness variations caused by changes within star. Pulsating variables such as β Cephei and δ Scuti stars are the examples of this group. The brightness values of extrinsic variables, in contrast, vary due to external reasons. One of the best examples is rotating variable stars that display periodicities because of chemically non-uniform surface

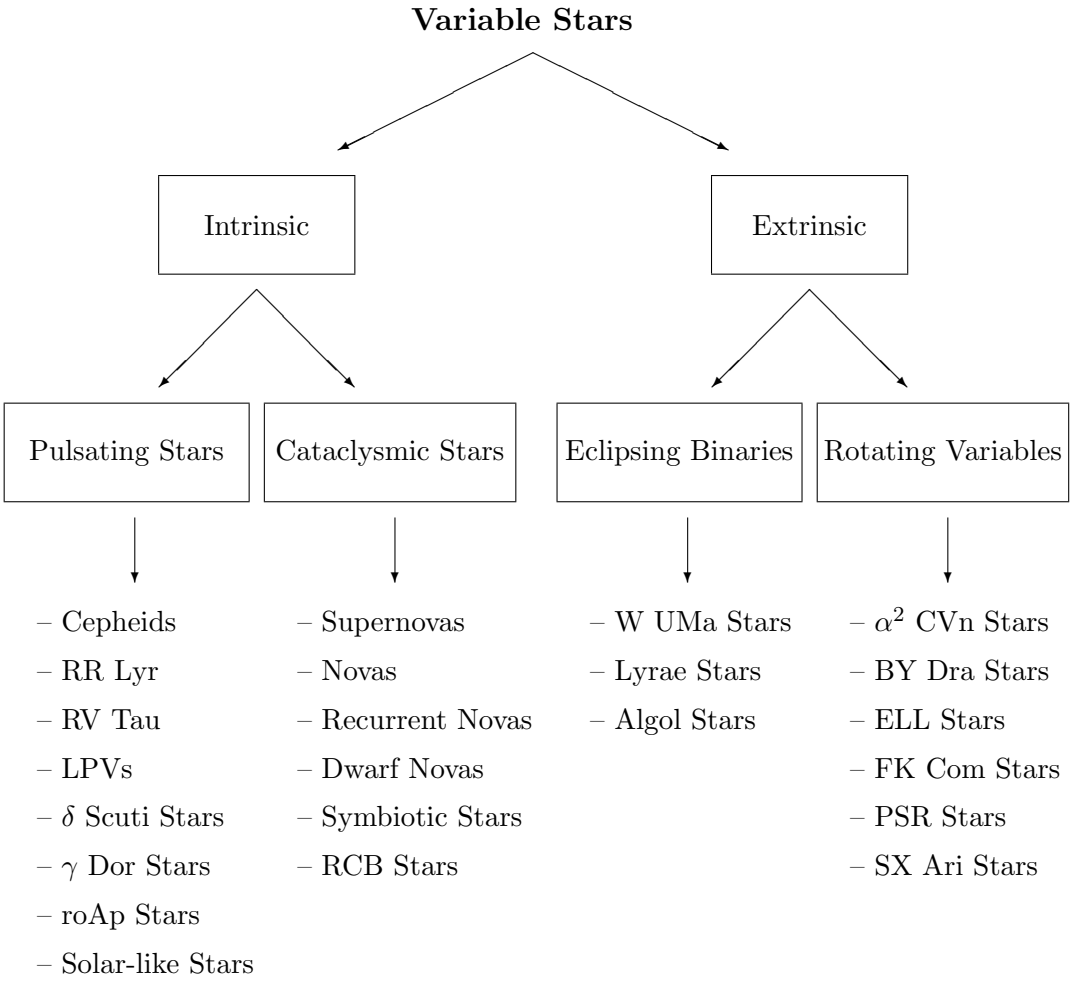

Figure 1.1: Classification diagram for variable stars.

distribution. Since the content of our study is related to pulsation properties of δ Scuti stars, emissions of B-type stars and period determination of CP stars, only some particular variable stars will be discussed in the thesis.

1.2 Intrinsic Variable Stars

Intrinsic variables are single stars whose brightness values change as a consequence of physical processes within a star. The study of this group of variables is crucial for gaining new perspectives on stellar evolution and inner structures. Intrinsic variable stars can be arranged in subgroups, one of which is pulsating stars. Another type of intrinsic variables is eruptive stars, such as novae and supernovae, which will not be discussed in this study.

1.2.1 Pulsating Variable Stars

Stars with periodical or irregular large-scale dynamic movements in their inner layers are called *pulsating variable stars*. Pulsation occurs in stars with different temperatures and luminosities, as well as stars at different evolutionary stages, which means that pulsation takes place all over the H-R diagram. Important questions arise from the phenomenon of pulsation: How does a star pulsate? Why does a star (not) pulsate? What is the type of pulsation? What is the driving mechanism behind pulsation?

Since the light variability of a pulsating star could not be explained by the uniform rotation of a single spotted star or a double/binary star assumption, Shapley (1914) suggested that light variation could be caused by periodic or semi-periodic expansion or contraction. The first theories regarding pulsations were basically simple calculations assuming that the physical parameters of a star were dependent on their distance from the stellar centre. However, models gradually evolved with the development of computers. In the initial years of this investigation, a linear and adiabatic model was formulated and used by Eddington (1918). According to that study, there was no energy transfer between layers within a star. Later, a linear and non-adiabatic theory replaced this model; this time, layers losing or gaining energy were considered. In other words, it was assumed that pulsation amplitudes could increase or decrease over time. Finally, a non-linear and non-adiabatic theory, which was also a time-dependent and hydrodynamic model, was implemented. Unlike other models, it included movements and forces on these layers (Percy, 2007). Since this theory could explain some variations in stars, the pulsation hypothesis was widely accepted in the astrophysics community.

The most common definition of a variable star is that the physical and geometrical features of a star change over time. According to this description, every star can be regarded as a variable star. However, the primary characteristic in identifying a variable star is its observed brightness. Indeed, most of these stars have been discovered because of their brightness variations. Other physical changes such as pulsations in size and matter ejection as well as variations in spectral type, colour, and temperature are usually correlated with fluctuations in brightness. Stars are gaseous spheres in hydrostatic equilibrium, and pulsations are directly related to equilibrium features given by Tayler (1970) as:

$$\frac{dp}{dr} = \frac{-GM(r)\rho(r)}{r^2} \ , \tag{1.1}$$

where G is the gravitational constant, $M(r)$ and $p(r)$ are the mass and pressure enclosed within a radius r, and $\rho(r)$ is the density. Here, it is assumed that forces on any mass element in a star stabilize each other. However, this equation is not completely satisfactory in capturing all of the factors at work. It means that stars do not strictly obey hydrostatic equilibrium conditions. In a broad sense, internal forces cannot be balanced and local accelerations enforce star material to move. As gas pressure outwards is greater than gravity on outer layers, the star begins to expand. While expansion carries on, gas pressure and gravitational force are balanced because pressure becomes weaker as stellar volume increases. Yet, outward moving materials still have momentum. This momentum extends layers beyond equilibrium position. Now, outward gas and radiation pressure are weaker than gravitational force, and the star contracts. During the contraction, gravitational force decreases and gas pressure becomes dominant. Thus, the second expansion phase starts.

These natural oscillations are in fact the observable results of the sound waves travelling inside a star. Different types of waves not only cause periodic changes in a star's brightness but also lead to periodic surface motions such as moving up and down, and back and forth. The forms of these pulsations can be basically arranged into two classes: radial and non-radial pulsations (NRPs), outlined below.

1.2.1.1 Radial Pulsations

Actually a special subset of NRPs or non-radial p-modes, radial pulsations are the simplest and most obvious mode of pulsations. In a radial oscillation, a star preserves its spherical shape but changes its volume. During the pulsation, the star matter moves radially. To describe such variations, the motions associated with breathing can be given as an example. A radially pulsating star can be considered as an organ pipe that is open at one end as an illustration (Fig. 1.2b). In this case, there is a displacement node at the closed end of the pipe that refers to the centre of star where there is no movement. The open end has an anti-node that represents maximum movement at the stellar surface. The number of modes for radial pulsation is unlimited and characterized by the radial wave-number 'n'. The simplest modes are known as the fundamental, the first overtone, the second overtone, etc. (Jones and Percy, 2007). In the fundamental mode, the movement of stellar material is in the same direction at every point in the star. The next simplest mode is the first overtone. In this type, there is a nodal sphere in the star, and material moves in opposite directions on either side of the node. In the second

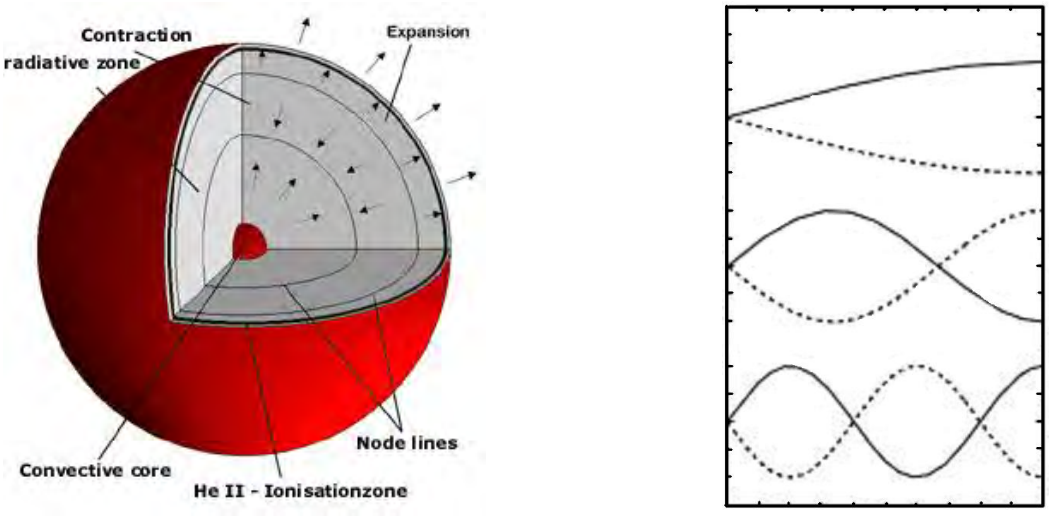

(a) (b)

Figure 1.2: (a) Illustration of the node lines for a radial pulsation with $n = 2$ (from Kilkenny (2013)); (b) the first three oscillation modes for an open-at-one-end organ pipe. From top to bottom: the fundamental mode, the first and second overtones are presented (Aerts et al., 2010).

overtone, two nodal spheres exist in the star, and material moves in opposite directions on either side of these nodes (AAVSO, 2010). Whereas pulsating variables such as δ Scuti stars mainly oscillate in the fundamental mode and/or the first overtone, all of these modes can be excited at the same time (Aerts et al., 2010).

During the radial expansion and contraction phases, the luminosity, brightness, temperature, colour, and radial velocity of a star considerably change. Thanks to the effects of these pulsations, observable through the Baade-Wesselink method (Percy, 2007), the radius of a star can be calculated. This method is only used for radial pulsators. In accordance with this method, minimum and maximum stellar parameters during a pulsation cycle are assumed to be $L_1, L_2, T_1, T_2, R_1, R_2$, and are linked through the luminosity relation ($L = 4\pi R^2 \sigma T^4$). If the luminosity ratio is used in Pogson's equation below, a new relation that is independent from the luminosity parameter is found.

$$\begin{aligned} m_{bol1} - m_{bol2} &= -2.5\ log\frac{L_1}{L_2} \\ &= -2.5\ log\frac{R_1^2\ T_1^4}{R_2^2\ T_2^4} \\ &= 5\ log\frac{R_2}{R_1} + 10\ log\frac{T_2}{T_1}\ . \end{aligned} \tag{1.2}$$

Also, variation in the radius is $\Delta R = R_2 - R_1$. To calculate ΔR, the radial velocity curve

between t_1 and t_2 is integrated. In this way, we get rid of another unknown parameter (R_2) and the equation becomes:

$$m_{bol1} - m_{bol2} = 5\ log\frac{R_1 + \Delta R}{R_1} + 10\ log\frac{T_2}{T_1}\ . \tag{1.3}$$

Here, bolometric brightness values in expansion and contraction phases can be found from photometric observations. T_1 and T_2 can be derived from the $B-V$ diagram or can be cancelled by choosing same colour indices at given times t_1 and t_2. Finally, R_1 value, and thus R_2 value, can be obtained.

1.2.1.2 Non-Radial Pulsations (NRPs)

According to a study conducted by Kholopov et al. (1998), most of the pulsating stars likely exhibit radial pulsations, and some exceptions such as V649 Per show NRPs. Unlike radial oscillations, a case in which spherical symmetry is not preserved is known as an NRP. In non-radial type pulsations, spherical shape changes but volume remains constant. To describe such oscillations, there are two types of modes that have infinite numbers on the star surface, and they are characterized by 'l' and 'm'. While the number of surface nodal lines is represented by the degree 'l', the number of surface lines running through the rotation axis is shown by the azimuthal number 'm' (Aerts et al., 2010).

The axisymmetric dipole mode is the most basic mode having $l = 1$ and $m = 0$. In this type, the southern hemisphere expands while the northern hemisphere contracts, and then the motion switches. Non-radial modes are observed if $n \geq 1$. In the case $l = 1$, there is at least one radial node. On the other hand, if a star has two surface lines with $l = 2$, it displays quadrupole modes. For $l = 2$ and $m = 0$, the poles expand while the equator contracts, or vice versa (Aerts et al., 2010). It is possible to increase the number of nodes and thereby to create oscillation diversity. In solar-type stars, which typically are slow rotators, the modes up to $l = 3$ can be observed in some cases, whilst in hotter classical (more rapidly rotating) pulsators even higher degrees can be detected.

A wide variety of stars such as white dwarf pulsators, the slowly pulsating B-stars (SPB), γ Dor stars, as well as many β Cephei and δ Scuti stars (the latter two show both radial and non-radial pulsations) pulsate with non-radial modes. Compared to radial pulsations, NRPs typically generate smaller amplitudes in brightness and colour variation. Their relative amplitudes and periods can be used to make a precise mode determination. For instance, there can be NRPs

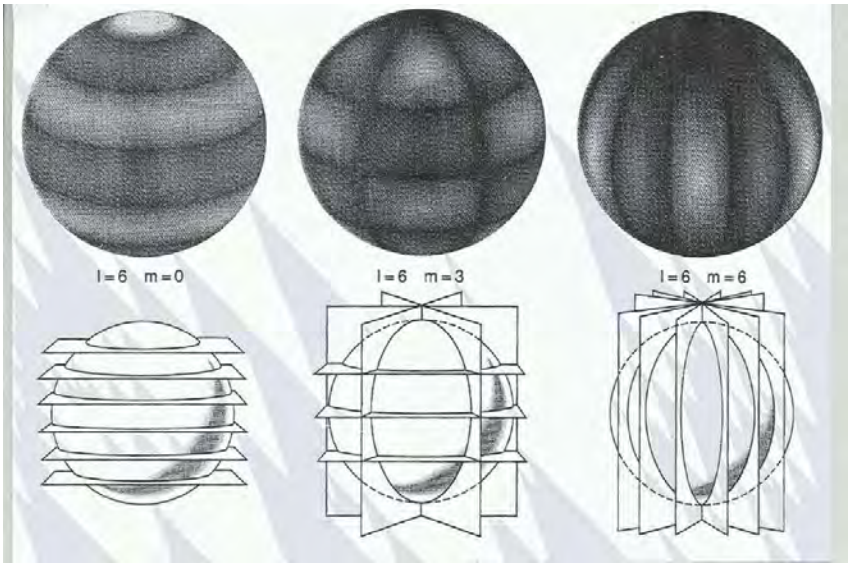

Figure 1.3: Non-radial pulsation modes and combinations of wave numbers are illustrated. While dark regions contract, light-coloured parts expand outwards, although all surface moves together in radial pulsations (taken from National Solar Observatory[1]).

that are quite close to each other within star, and their differences give some hints about mode identification. These close modes are nearly similar to each other in non-rotating stars. Mode differences change depending on rotation velocity in rotating stars. In addition, NRPs not only cause photometric variabilities, but also produce characteristic absorption line profile variations (LPVs) in the spectra (Percy, 2007).

There are two primary restoring forces, pressure and gravity, to bring the star back to its equilibrium state. For a radial motion, the gravitational force in a star increases during a contraction phase, which means that it does not restore the oscillation but rather accelerates. For this reason, the restoring force should be pressure. On the other hand, for a mainly transverse motion, gravity restores the motion through the help of buoyancy. Therefore, NRPs are divided into p- and g-modes in addition to their identifications with pulsational quantum numbers (n, l and m). These two types of modes differ by their frequencies and the direction of the motion (Handler, 2013).

1.2.1.3 Pressure modes (p-modes)

The p-modes are known as acoustic modes. In this type of pulsation, stellar material moves radially and the convective zone is responsible for these motions. The restoring force is pressure that causes material to move from high-density to low-density regions. To produce standing

[1] http://www.pnas.org

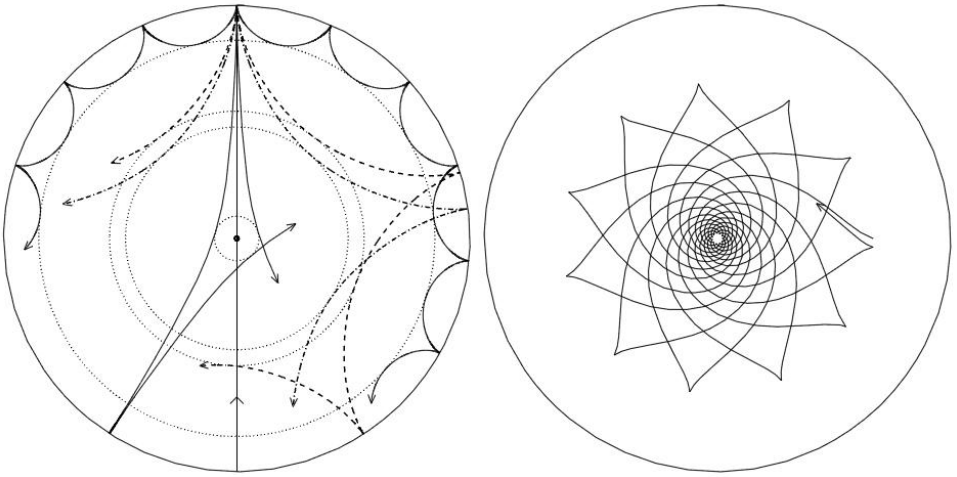

Figure 1.4: Propagations of p- (left) and g-modes (right) in different depths of a star are illustrated. On the left figure, the dotted circles indicate the inner turning points where the p-modes are bent by the increase in sound speed and reflected. Also, these acoustic waves are reflected by the rapid decrease in density at the surface. The line intersecting with the centre represents the radial mode, and others are p-modes of frequency 3000 μHz and l = 75, 25, 20 and 2 (according to increasing depth). On the right, a g-mode with a frequency of 190 μHz and l = 5 is shown. It is trapped underneath the convective region, and therefore contains information about the core and the radiative region (Aerts et al., 2010).

acoustic waves, a cavity is required. The waves are reflected at its boundaries, which vary between the top and the bottom. There is an intensive decrease in density at the top of the convective zone, and the acoustic cut-off frequency is quite high. Thus, almost all modes are reflected toward the interior (Tarrant, 2010). In other words, these modes are trapped between an inner turning point and surface. The interior reflection of the pressure modes can be better understood with *the ray theory* (Gough, 1984, 1986). A mode can be considered as a superposition of propagating sound waves. While they propagate in the star, the deeper parts of the wave fronts are exposed to higher sound speed, and move faster. As a result, the direction of the propagation bends away from the radial direction, and the wave moves horizontally at the reflection point. The position of this trough in the cavity differs from one mode to another.

The formation of pressure modes is dependent on degree of mode, and its interpretation is extremely important in understanding the interior of a star. For small l, the turning point is quite close to the centre, whereas it approaches to the surface for higher degrees. As an example, the modes with $l \leq 20$ can access the radiative zone while the modes having $l \geq 40$ are trapped in the convective zone in the Sun (Christensen-Dalsgaard, 2003).

1.2.1.4 Gravity modes (g-modes)

The g-modes are internal gravity modes having gravity and buoyancy that attempt to re-establish the equilibrium. Gravity modes are produced in regions where the energy is mainly conveyed by radiation. In particular, they arise from the upward adiabatic displacement of a fluid blob. This displacement causes a density differential between the fluid element and its surrounding. If the square of the buoyancy (*Brunt-Väisälä frequency*) is greater than zero, then the element is heavier than the displaced fluid, and the buoyancy pushes the blob toward its original position. Thus, the element executes an oscillation around the equilibrium position. Otherwise, the buoyancy forces the element away from the equilibrium, which is correspondent to convective instability. In the convective zone, the displacement of the blob is continuous. Thus, standing waves cannot propagate and eventually vanish in this region (Christensen-Dalsgaard, 2003). In solar-like stars, the radiative zone is underneath the convective envelope. Therefore, the g-modes are trapped inside the stellar interior, and only low amplitudes can reach the surface. On the other side, in more massive main-sequence (MS) stars, these modes are confined outside the convective core (Tarrant, 2010).

In brief, there are important properties of both p- and g-modes. Depending on the increase in radial node number, the frequencies of the gravity modes decrease, whereas the frequencies of the pressure modes increase. The g-modes contain important information regarding the deep interior, but the p-modes provide information about conditions in the outer part of the star. If n is much greater than l, there is an asymptotic relation for both p- and g-modes. Accordingly, pressure modes are approximately equally spaced in frequency, and g-modes are approximately equally spaced in period (Aerts et al., 2010). Apart from these, g-modes generally have longer pulsation periods than those of radial fundamental mode, whereas p-modes are equal to or shorter than it. Also, radial pulsations are always in p-mode (Handler, 2013).

1.2.2 Driving Mechanisms

During a pulsation cycle, a star expands, contracts, heats, cools, and so on. This process leads to energy loss, and also causes a damping in oscillation. However, stellar pulsation is somewhat of a constant feature in many stars, which means that there must be some excitation mechanisms within the star to cope with such a damping.

1.2.2.1 ϵ-Mechanism

The ϵ-mechanism is known as *the energy mechanism* and is based on a variation in the rate of stellar nuclear reactions. It is proposed as a possible driving mechanism for variable stars such as Cepheids.

The reasons for the existence of such a mechanism are particularly cyclic enhancement and decrement of nuclear reactions in the core based on temperature dependence of the nuclear reaction rate. In this process, heating of the core region causes an increase in the rate of nuclear reactions. This leads to additional heating and an expansion of stellar material in and around the core. As the material expands, it cools and slows the energy production rate. The lower rate of energy production results in further cooling as well as contraction of the material in the core. Consequently, the material heats and initiates the process once again (Tarrant, 2010).

It is suggested that this energy mechanism, which is similar to the working principle of a diesel engine, is present in different pulsators. However, mathematical models indicate that it most likely occurs in completely convective stars (e.g., coolest M dwarfs) and in massive stars with $M > 60$ $M_\odot$ (Kilkenny, 2013). Also, it is believed that such a mechanism is ineffective in the vast majority of pulsating stars, but that it may be the excitation force for g-mode oscillations in δ Scuti variables (Lenain et al., 2006).

1.2.2.2 Stochastic Mechanism

This mechanism is due to the stochastic noise generated by convection near the surface, and occurs in the Sun, solar-like stars, and some pulsating red giants. Convection cells are located in the region starting from approximately 0.7 $R_\odot$ and extending close to the surface. While the material approaches the top of the convective zone, the temperature gradient becomes steeper than that occurring in adiabatic conditions. As a result, the material reaches speeds close to that of sound and moves upward very quickly. Following this, a large number of convective elements randomly appears at the surface and excites acoustic waves in a broad frequency range. Due to the destruction of self-excited modes, only those excited waves that can become standing waves within the cavity exhibit adequate amplitudes on the surface. However, these amplitudes are temporary and highly variable.

The convective excitation is observed in MS stars having mass values less than 2 $M_\odot$ because larger stars have outer radiative layers. Nevertheless, the existence of convective cells may be detected in all giant stars cooler than the instability strip. To make sense of the observational

distinction between a normal mode and a stochastic mode, their power spectra can be compared. Accordingly, the modes of a constant amplitude and frequency produce a single peak in a periodogram, whereas stochastically excited modes display a wide structure. By analysing the time-evolution of mode amplitudes and phases, stochastic excitation can also be identified in a time-domain (Tarrant, 2010).

1.2.2.3 κ- and γ-Mechanisms

The κ-mechanism is connected with opacity. Opacity is known as a process of electron scattering or free-free absorption at a given frequency. It is generally a function of density (ρ) and temperature (T), which is given as:

$$\kappa = \kappa_2 \ \frac{\rho}{T^{3.5}} \ , \tag{1.4}$$

where κ_2 is a constant depending on stellar chemical composition (Baker and Kippenhahn, 1962).

This equation, also known as *the Kramer law*, is an analytical approximation since opacity value changes by temperature. The variations connected to both density and temperature are shown in Fig. 1.5. As seen in the figure, opacity is low at both low and high temperature values of gas. For gas at low temperatures, photons do not have enough energy to ionize atoms, and there are few electrons to scatter radiation. Thereby, gas density and opacity values remain low. On the other hand, opacity is due primarily to the pressure ionization and collision effects of atoms at high temperatures. Since photons have high energy at high temperatures, their absorptions are less easy than those with lower energy. As a result of this, opacity decreases once again by increasing temperature values.

To have a better understanding of the pulsation phenomenon, the ionization of material should be completely understood. There are some regions, below which stellar matter is ionized and above which it is neutral, located at different depths within stars. These regions are known as *partial ionization zones*, which are composed of different elements depending on the type of stars (δ Cephei, RR Lyrae, δ Scuti star HeII ionization; roAp stars HI and HeI ionizations; β Cephei and SPB stars Fe ionization (Handler, 2013)). In these regions, some of the atoms are ionized whereas others are neutral, and any change in the temperature varies the balance between atoms.

Opacity acts in different ways inside and outside the partial ionization regions. During a

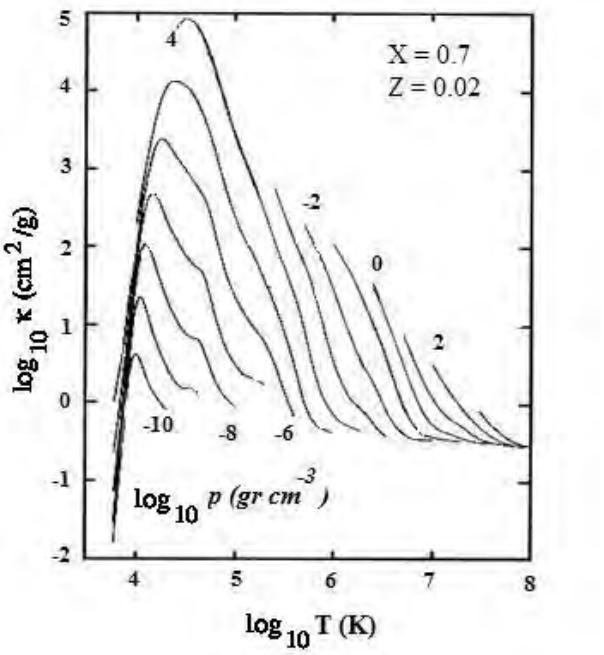

Figure 1.5: Opacity, as a function of density and temperature. Each curve represents a different density value and is denoted by $\log \rho$ [g/cm^3] (Tayler, 1970).

compression, temperature and radiation flow increase outside the zone. However, due to the Kramer law, opacity decreases. Therefore, energy gained at the lower level is less than energy lost at the upper for a given section of material, and this process very quickly suppresses the pulsation.

Inside the partial ionization zone, while the star contracts, the energy mostly increases ionization instead of heating the zone. This results in enhancing the opacity of the zone. Hence the radiation is more effectively trapped, which causes outward pressure on the zone. The decrement of the radiation is known as *the γ-mechanism*. The zone moving outward cools while it rises and also prompts changes in opacity and outward pressure. However, the ionized material is recombined due to further cooling. Thus, a sudden decrease in opacity as well as in outward pressure occurs, and the zone falls to the original position. Through a cycle, any pulsation movement stimulates the partial ionization zone. In this case, the star is not stable, and any small variation is reinforced. This process makes pulsations continue without fading. It is the best mechanism that explains pulsations of stars, and is known as *the κ-mechanism* (Kilkenny, 2013).

The pulsation characteristic of a star is mainly dependent on the depths of the partial ionization zones. Their locations within the star are determined by temperature. If a star is

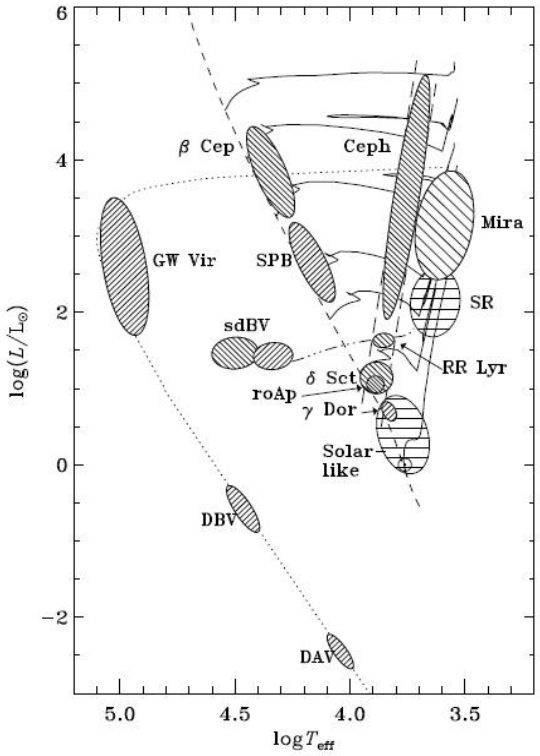

Figure 1.6: Positions of variable stars on the H-R diagram. The parallel lines show the type of modes and excitation mechanisms: up-left for opacity driven p-modes, up-right for opacity driven internal g-modes, and horizontal for stochastically excited modes (Christensen-Dalsgaard, 2004).

hotter than 7,500 K, then these regions are quite close to the surface. Since there is not enough mass above the regions, the mechanism cannot initiate the acceleration needed for pulsations. For stars cooler than 5,500 K, in contrast, the partial ionization zones are too deep in the star. As a result, the mechanism becomes insufficient for maintaining pulsations.

Obviously, the location of the zone is highly important in determining whether any pulsation movement occurs in stars. Indeed, accumulation of pulsating stars in a particular region on the H-R diagram, known as *the instability strip* and shown with two slanted dashed lines in Fig. 1.6, indicates that the driving zone is well situated in some variables. The oscillations observed in this strip are caused by the heat mechanism that specifies the cool and hot edges. For example, Cepheids, RR Lyrae, δ Scuti and roAp stars, which have an HeII partial ionization zone, are located in the hot part of the strip, whereas cool red giants and supergiants such as the Mira stars and semi-regular variables, which have HI and HeII partial ionization zones combined with strong and efficient convection, are seen in the cool side of the strip (Aerts et al., 2010). The different types of pulsating stars are presented in Fig. 1.6, and their pulsation periods are given

Table 1.1: Some pulsating stars and their characteristics.

Variable Type	**Pulsation Period (days)**	**Spectral Type**
α Cygni	2 - 6 (weeks)	O - B - A
β Cephei	0.1 - 0.3	Early B (B0 - B3)
Be Stars	0.4 - 3	O6 - B9
53 Per, SPB Stars	0.5 - 3	O8 - B5
δ Scuti	0.02 - 0.25	A2 - F5
γ Dor	0.5 - 3	F
RR Lyrae	0.2 - 3	A - F
Cepheid	1 - 70	F - G - K
Type II Cepheids	0.75 - 40	–
RV Tauri	30 - 150	G - K
Semi-regular and Slow-Irregular	20 - 2000	F - G - K - M
Mira	80 - 1000	M
ZZ Ceti	30 seconds - 25 minutes	DA - DB

in Table 1.1.

There are various techniques used to study stars, but the most common one is to probe their outer layers. However, oscillations also provide valuable information about internal structures. Therefore, pulsating stars are quite important in testing evolution and structure models. In the next section, different types of variable stars will be presented.

1.2.3 B-Type Variable Stars

B-type variables are hot and massive stars distinguished by hydrogen and neutral helium lines in their spectra. Even though they have relatively simple structures that can provide some fundamental clues, the process of understanding their interiors is highly complicated.

Since their luminosity range is quite wide, several sub-types of B-stars are observed. Similar to other stars, information about their atmospheres and internal structures can be derived through the calculation of physical parameters (rotational velocity, mass and luminosity, etc.). B-stars are divided into three sub-groups based on these parameters.

1.2.3.1 β Cephei Stars

β Cephei stars are population I objects, located slightly above the MS, and having a spectral type of O9 to B3 (Schoeller et al., 2013). The luminosity of these bright stars (luminosity class of II-IV) varies from 1% up to 30%, and generally reaches the maximum level in the minimum contraction phase. They are 10 to 20 times more massive than the Sun (De Ridder, 2001). Due to their evolutionary states (located near the centre of the MS, having mixed p/g-modes),

these stars provide valuable information about the convective core, convective overshooting, and differential inner rotation (Pamyatnykh et al., 2004).

This type of stars exhibits periodic light variations on the time scale of 0.1 to 0.3 days. Their light curves (LCs) are well described by *sine* or superposition of many *sine* waves with the amplitude of 0.01 to 0.3 mag (typically smaller than 0.1 mag in V-filter). The amplitudes are also larger at blue wavelengths than at red (De Ridder, 2001), and display phase difference of around 0.25 with radial velocity changes. Such a phase lag is the outcome of adiabatic oscillations (Aerts et al., 2010). The majority of these stars shows multi-periodicities (one radial and one or more non-radial periods) and is known as β *Canis Majoris* variables (Percy, 2007). These stars' pulsation schema is mostly composed of low-degree, low-order p- and g-modes. However, some samples such as ν Eri and 12 Lac have high order g-modes in addition to these pulsations (Daszyńska-Daszkiewicz et al., 2013). Periods of oscillations are generally close to each other, and fluctuations in pulsation amplitudes are their typical characteristics. Differing from non-rotating stars, which have degenerate non-radial periods (i.e., have the same period values), the rotations of β Cephei Stars remove this degeneration. As a result, the periods are slightly different, and their combinations or interceptions generate a phenomenon called as *the beat effect* (Diago et al., 2010). The oscillations of these variables are defined by the κ-mechanism associated with the ionisation of iron-peak elements.

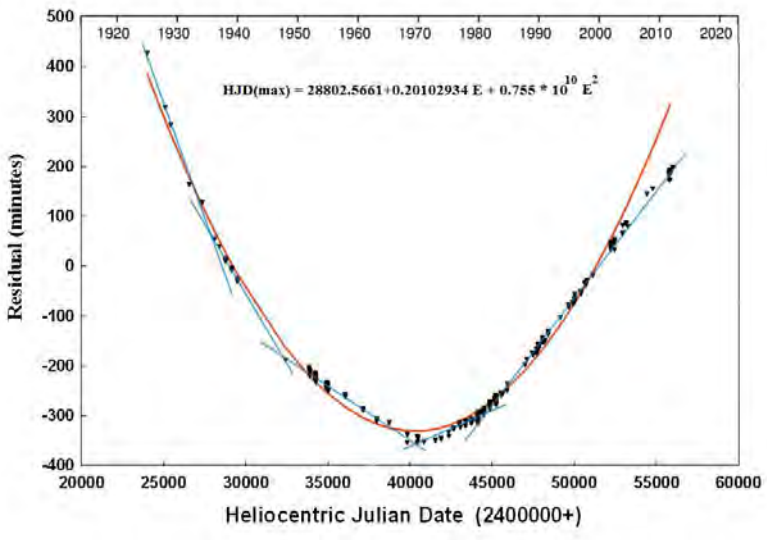

Figure 1.7: O-C diagram of the largest amplitude β Cephei star, BW Vulpeculae, is shown in the figure. The variation is well represented by a parabola (solid red line). Also, the subsets of the data are fitted by five piecewise-linear fits (blue lines) (Odell, 2012).

Even though their pulsation periods are generally stable, it is possible to observe long-term changes around 1.0 second per century (s/cent) or less in some cases. This corresponds to the late core-burning stage on the H-R diagram. Beside the linear pulsations of these stars, there is an extraordinary example, BW Vul, which has a period of around 0.20 days. In the last 30 years, its period has undergone tremendous changes, and the rate of this variation is calculated as approximately 2.4 s/cent in the O-C diagram (Fig. 1.7). This is the largest amplitude among the β Cephei stars, but it indicates that the star must be in the shell hydrogen-burning phase, which conflicts with the concept that β Cephei stars are in the late core-burning stage (Odell, 2012). Despite ongoing observations and analysis, the origin of this unusual change is still not clear. It is believed to be a combined effect of the increase of the pulsation period and the light-time effect of a companion star.

An O-C diagram is a special plot generally used to determine period changes that are difficult to detect by direct measurements. On this plot, the x-axis is epoch (number of cycles), and the y-axis is the difference of observed and calculated extremum time values of a LC. The variation is basically given as:

$$O - C = JD - JD_0 - P \cdot E \quad ,$$

where JD is the minimum time, JD_0 is the initial time, E is the corrected epoch and P is the period. If there is not any measurable change in period, then the O-C difference generates a straight line. If any variation in period is detected, however, the O-C data generate a structure that displays the characteristic of the mechanism causing this variation. According to Mikulášek et al. (2012), these mechanisms can be arranged as: mass transfer between components or mass loss from the system, spin-orbital interactions, angular momentum loss through stellar winds, gravitational waves, oscillations in rotation, differential rotation, apsidal motion, presence of a third light, and magnetic activity.

In terms of binarity, orbital period change is quite an important subject since it is related to the formation, structure, and evolution of binary stars. These variables gain and lose mass and angular momentum as specified by Roche geometry. These events are the first proposed mechanisms to explain observed period changes. Both of these mechanisms can increase or decrease the period of the system and generate parabolic structures in the O-C diagram (upward parabola if material flows from the primary to the secondary, downward parabola if material flows from the secondary to the primary star). The effect of the mass transfer depends on the

direction of flow within the binary, whereas the mass loss is dependent on the direction of speed of the escaping material. The mass transfer between components is more effective in changing the orbital period than the mass loss from the system. The most basic case to be considered for exchanging material between components is conservative mass transfer. In this case, the mass lost by one component is gained by the companion star, so the total mass of the system and thus the total orbital angular momentum is preserved. Accordingly, the period change is proportional to the mass transfer and is given as:

$$\frac{\dot{P}}{P} = 3\ \frac{1-q^2}{qM_{tot}}\dot{m}_1\ , \tag{1.5}$$

where q is the mass ratio, $M_{tot} = M_1 + M_2$, and $\dot{m}$ is the mass transfer rate (Rovithis-Livaniou, 2006). Lanza and Rodonò (1999) estimate the median modulation period observed in O-C diagrams as 40-50 yr for Algol and RS CVn systems, from years to decades for cataclysmic variables. They also give the amplitudes of these variations to be $\Delta P/P = 10^{-7} - 10^{-6}$ for cataclysmic variables, 10^{-6} for W UMa binaries, and 10^{-5} for Algols and RS CVn systems.

Also, the components in a contact binary state are not in a thermal equilibrium and can freely transfer mass between themselves. If the total mass and the angular momentum are conserved, the system undergoes cycles around the marginal contact stage (thermal relaxation oscillation) in which the mass is transferred from the secondary to the primary star. On the other hand, angular momentum loss through magnetic braking is also important in the evolution of these stars. Accordingly, a contact binary evolves into a low mass ratio and hotter components due to magnetic torque. This is indicative of decreasing efficiency and of angular momentum loss through magnetic braking (Qian, 2001).

Additionally, mass loss rates triggered by stellar winds in binaries depend on spectral types of the components and their evolution states. To obtain a simple relation between orbital period changes and mass loss due to stellar winds, spherical symmetry is taken into account, and the relation is given differentiating Kepler's third law:

$$\frac{\dot{P}}{P} = \frac{-2\dot{m}_1}{m_1 + m_2}\ . \tag{1.6}$$

If the increasing stellar winds are considered for a binary system with a circular orbit, change in the period associated with the rates of mass transfer and loss is as follows:

$$\frac{\dot{P}}{P} = \frac{-2\dot{m}}{m_1 + m_2} - \frac{3\dot{m}_2(m_1 - m_2)}{m_1 m_2} + 3K \ , \tag{1.7}$$

where $\dot{m}_1$ and $\dot{m}_2$ are the mass loss rate of the donor and the rate of mass gained by the companion star, respectively. Here, K represents an additional mechanism, such as magnetic braking or gravitational wave radiation, for angular momentum loss, which also decreases the orbital period of the binary.

Apart from these, another mechanism to cause period variation in binary stars is magnetic activity cycles. In the systems having late-type components, if the shape of the companion star is distorted by tidal and centrifugal forces, changes in the internal rotation associated with a magnetic activity cycle vary the gravitational quadrupole moment. As the quadrupole moment increases, the gravitational field increases leading to a decrease in the period. Otherwise, if the quadrupole moment decreases, the orbital period increases (Applegate, 1992). Magnetic activity produces cyclic modulations in the O-C diagram, and their periods are from years to decades.

Among the common mechanisms given above, apsidal motion involves a change in the orientation of the system's major axis, since the potential energy between the components does not exactly obey Newton's gravitational law. In the O-C diagram, the times for secondary and primary minima shift in opposite directions. However, as this mechanism requires large eccentricities, it is rarely observed (Zavala et al., 2002). Alternatively, it is assumed that the cyclic pattern is caused by the presence of a third body in the system. Based on this assumption, the primary and secondary eclipse times are produced by the motion of the binary around the common centre of mass of a triple system. In this case, the periodic pattern arises from the light-time effect (Borkovits and Hegedues, 1996).

There is also a possibility that a binary system contains a pulsating star. Such a case is very important in identifying the nature of the pulsator. Even if some of its parameters such as brightness, effective temperature, and surface gravity are affected by the companion, this is a unique opportunity to directly calculate the mass of the pulsating star. The binarity can be determined through radial velocity measurements. However, it is not possible to obtain precise measurements for systems with long orbital periods. On the other hand, the binarity can be detected in the period changes of a pulsating star, and also discovered by light-time effect under certain circumstances. Still, the interpretation of the O-C diagram is sometimes problematic,

since temperature and brightness of the pulsator change as a result of evolution. Consequently, this affects the pulsation period and causes changes given as (Breger and Pamyatnykh, 1998b):

$$\frac{dP}{Pdt} = -0.69 \ \frac{dM_{bol}}{dt} - \frac{3}{T_{eff}} \ \frac{dT_{eff}}{dt} \ . \tag{1.8}$$

If the light-time effect is the only reason for apparent changes, the variability ranges in the O-C diagram for different pulsating stars are estimated to be (Szeidl, 2005):

- RR Lyrae stars; $M_1 + M_2 = 1.2$ $M_\odot$; range $\sim 0.01 \ P_B^{2/3} Dsini$; periods ~ 4 yr,
- Cepheids; $M_1 + M_2 = 8$ $M_\odot$; range $\sim 0.002 \ P_B^{2/3} Dsini$; periods ~ 20 yr,
- HADS; $M_1 + M_2 = 3$ $M_\odot$; range $\sim 0.08 \ P_B^{2/3} Dsini$; periods ~ 0.5 yr.

In these estimations, $D = \sqrt{1 - e^2 cos^2 w}$ where e is the eccentricity and ω is the longitude of periastron passage, P_B is the orbital period. Period values are the least observable values if it is assumed that $i \sim 90°$, $e \sim 0$ or $\omega \sim 90°$ and the relative accuracy of the O-C values $\delta(O - C/P_0) \sim 0.01$.

During the passage of a pulsating star through the instability strip in which it burns core helium, the observed rate of period changes is much larger than that of theoretical models. Due to this notable discrepancy and the complex structure of some O-C diagrams, it is suggested that some kind of noise, a so-called *period change noise*, is superimposed on the period variations (Szeidl, 1975). This is believed to be a result of evolutionary change in the mean stellar radius. Particularly, it is related to random mixing movements associated with the semi convective zone of the stellar core. There are two factors changing the inner structure of a variable star: gradual changes in the core composition (caused by nuclear burning) and composition redistribution in the deep interior (caused by convective overshooting), and the formation of a semi-convective zone. Among them, nuclear burning produces a slow rate of period change, and it is almost stable during a lifetime. On the other hand, if mixing events quickly occur, they can produce abrupt period changes. However, the period variation rate seems constant on longer time-scales (Zhou, 1999).

1.2.3.2 Slowly Pulsating B-Stars (SPB)

The pulsation schema of the β Cephei stars is mostly formed of low-degree, low-order pressure and gravity modes. For instance, the beat effect has been explained by the existence of both radial pulsations and NRPs. However, there are some other stars that display typical photometric

variabilities having only NRPs among B-type pulsators. Their periods vary between 0.5 and 3 days with the amplitude of a few mmag. Therefore, these stars are called *Slowly Pulsating B-Stars (SPB)* (Percy, 2007). Due to their pulsation type, they are also known as *Non-Radially Pulsating B-Stars*. These variables are population I objects with the spectral type of B3–B9. Even though they share the same asteroseismic characteristics with γ Dor stars, mass (3–7 $M_\odot$) and effective temperature (10,000–20,000 K) are distinctive properties for SPBs (Aerts et al., 2010). Their LC amplitudes decrease with increasing wavelength, and there is no phase lag between variations in different colours. The source of their pulsations is the excitation of high-order, low-degree g-modes caused by the κ-mechanism acting on the iron opacity bump around 200,000 K. As g-modes can penetrate into the deep stellar interior, these stars are quite important in terms of asteroseismology (Sódor et al., 2014).

Most of the g-mode pulsators are multi-periodic. As a result, the observed variabilities show long beat periods and are notably complex. To obtain a sufficient number of pulsation modes, to understand the oscillation pattern, and to define their l and m values, large observational efforts are needed (Sódor et al., 2014). Yet, it is not enough to identify individual peaks in a frequency spectrum. Therefore, some researchers use a method in which equidistant spacing in period is sought. The CoRoT target HD 50230, which has eight modes with a significantly constant spacing, can be given as the best sample (Degroote et al., 2010). However, not every star follows such a pattern, as is the case with the CoRoT object HD 43317, whose frequency spectrum does not display a specific equidistant spacing (Savonije, 2013).

The oscillation and the rotation periods of many SPB stars are comparable. For this reason, rotation should be taken into account more than the perturbation theory for theoretical studies (Handler, 2013). The effects of rotation are also explained by Ushomirsky and Bildsten (1998). Accordingly, rotation affects the g-mode properties when $2P_{mode} \geq P_{spin}$ where P_{mode} is the mode period in the co-rotation frame and P_{spin} is the spin period. Although rotation should be close to the break-up velocity to affect p-modes in β Cephei stars, rotational velocities of:

$$V_{rot} \geq 75 \text{ kms}^{-1} \left(\frac{1 \text{ day}}{P_{mode}}\right)\left(\frac{R}{3 \text{ R}_\odot}\right) , \tag{1.9}$$

substantially affect the g-modes in typical SPB variables ($M = 4$ $M_\odot$ and $R = 4$ $R_\odot$), since they have high radial order g-mode pulsations of day-like periods. If it is considered that the mean rotational velocity for a B-type star is around 200 km s^{-1}, rotation should not be ignored

in pulsation calculations.

Among B-stars, another subgroup is Be-variables. Similar to other stars discussed above, they are also hot and massive non-supergiant stars located on the MS. Due to their rapid rotations, they attract the special attention of astrophysicists for studying pulsation properties. Recently launched satellites such as the *STEREO* enable scientists to discern the role of NRPs produced in Be-stars. In order to understand the Be-phenomenon, these stars will broadly be examined in the next sections.

1.2.3.3 Be-Stars

The general definition of a Be-star is given by Collins (1987) as "a non-supergiant B-star whose spectrum has, or at some time had, one or more Balmer lines in emission". However, this definition is clearly quite broad and contains all B-type stars with emission lines due to circumstellar material above densities of about 10^{-13} g cm^{-3}. Based on the description, stars that have a luminosity class of V to III with emission should be classified as Be-stars regardless of their physical differences. Yet, there are some distinctions that separate objects commonly termed *classical Be-stars* from those emission line objects of other provenance such as Herbig stars or mass transferring systems (Rivinius et al., 2013).

Classical Be-stars are population I type, MS, or slightly evolved B-stars with a spectral range of late-O to early-A (Neiner et al., 2009) and a luminosity class of V to III (Zorec and Briot, 1997). Their surface temperatures are between 10,000 K and 30,000 K. Unlike normal B-stars, unusual Balmer emission lines, singly-ionized metals, and neutral He are seen in their spectra. Approximately 20% of B-stars are classified as Be-stars (Percy, 2007), and most of these are between B1 and B2 spectral types (Porter and Rivinius, 2003).

Despite sharing the same region with β Cephei and SPB stars on the H-R diagram, Be-stars are quite different in a number of ways, such as their rapid rotation velocities. The average rotational velocity of these extremely fast rotators is around 88% of their critical break-up velocity (Frémat et al., 2005), which corresponds to an equatorial velocity between 250 and 500 km s^{-1} (Kogure and Leung, 2007). Cooler samples are also known to rotate faster than earlier type Be-stars (Cranmer, 2005). Furthermore, it is believed that the rapid rotation of a Be-star assists radiation pressure and pulsational driving by reducing effective gravity around the equator. This reduction potentially results in the formation of a disk-like equatorial structure expanding outward, which means that they are surrounded by a decretion disk (Rivinius et al., 2013).

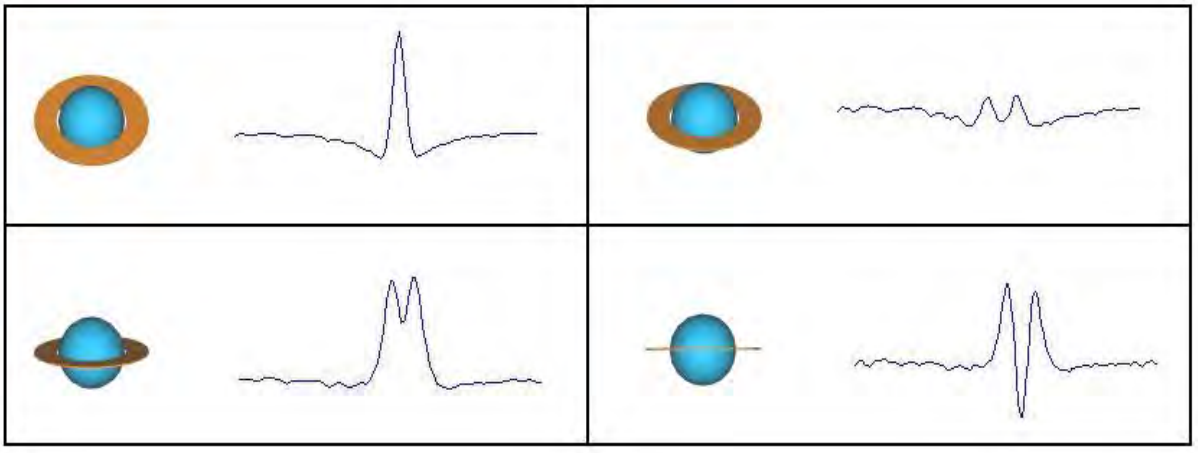

Figure 1.8: The figure presents an illustration of line profiles produced according to different inclination angles (The French amateur astronomers[2]).

Although such a structure is one of the defining characteristics of Be-stars, its size is unstable and varies from star to star (e.g., the diameter of the Hα emitting region is $R_d = 16.36$ R$_\star$ for ψ Per and 3.24 R$_\star$ for β CMi; Rivinius et al. (2013)).

The emission lines of Be-stars are produced by the disk structure. This circumstellar material is not as hot as the central star. Therefore, the electrons in the atoms contained in the disk absorb high-energy photons coming from the star. As a result, they move to a higher energy orbit. Afterwards, they generate emission lines in the spectrum by de-exciting emitted photons. On this basis, the Balmer emission lines are caused by the de-excitation of the hydrogen electrons to the first excited state ($n = 2$ orbit). According to disk inclination with respect to the observer's line of sight, it is possible to detect different sorts of line profiles. These are basically *single- or double-peaked, wine bottle, and shell profiles* (Hanuschik et al., 1996).

When inclination (i) is defined, $i = 0°$ matches up to the disk at pole-on positions while $i = 90°$ corresponds to equator-on (Slettebak, 1988). Pole-on stars are characterized by narrow and single-peaked emission lines superimposed on a photospheric absorption line (Fig. 1.8 upper left). Wine bottle profiles are observed when a star is viewed close to pole-on ($i \sim 0°$) as seen in Fig. 1.8 (upper right). The most dominant line profile type is the double-peaked emission line, which occurs in the spectrum of ordinary Be-stars and generally forms when the star is observed at mid-inclination angles (Fig. 1.8, lower left). Moreover, shell profiles are also identified by a deep and sharp absorption in the centre of a double-peaked emission line (Hanuschik, 1996), and the profiles can only be observed if the disk is close to edge-on position ($i \sim 90°$) (Fig. 1.8,

[2]http://www.astrosurf.com/buil/us/bestar.htm

lower right). Examples of these types of line profiles will be presented in the relevant section.

Line profiles can be either symmetric or asymmetric. Approximately one-third of all double-peaked line profiles shows variable asymmetries. Sometimes, the violet-to-red component ratio (V/R) of double-peaked profiles can exhibit long-term cyclic variations, and there can be phase lags between different lines. It is known that the origin of these variations is not related to photospheric components but is rather associated with structures in the circumstellar disk (Porter and Rivinius, 2003). Okazaki (1991) was the first to propose the existence of a slowly precessing, one-armed spiral structure within the equatorial disk to explain the cyclic variations. Also, McDavid et al. (2000) suggested a model required a spiral wave structure to explain phase lags in 48 Lib between Hα observations. Moreover, Meilland et al. (2007) provided some evidence from the spectroscopy of α Arae that the disk has a Keplerian rotation.

In addition to these, line profiles can sometimes show transformations in shape, depending on expansion and contraction phases of the disk (Tanaka et al., 2007). For instance, the CoRoT field object NW Ser goes between B- and Be-phases by changing its spectrum from photospheric absorption to double-peaked emission and fading back toward photospheric absorption (Grundstrom et al., 2011). Furthermore, Hα profiles of a classic Be-star γ Cas transform from a single-peaked to a double-peaked structure (Cramer et al., 1995). There can sometimes be transitions from a shell profile to emission lines or vice versa, as in the spectrum of 59 Cyg (Barker, 1982). Be-stars also display variations on multiple time-scales:

1. Days to weeks – connected with binarity (Percy, 2007),
2. Weeks to decades – related to disk formation (Wisniewski et al., 2010),
3. Months to years – quasi-cyclic variations arising from wave structure in disk (Okazaki, 1997).

Apart from these longer term variations, several Be-stars exhibit photometric and line profile variabilities with periods from 0.1 to a few days (dominantly from 0.5 to 2 days). Balona (1990) pointed that the periods of these variations were quite close to rotational periods, and therefore their sources were rotation modulations. This type of stars is called λ *Eri* variables. The amplitude of their LCs is a few tens of mmag, and there is an obvious correlation between their photometric and rotation periods (Aerts et al., 2010). It is also known that Be-stars pulsate, and that the formation of LPVs is associated with NRPs (Rivinius et al. (2003); Gutiérrez-Soto

et al. (2007)).

According to Rivinius et al. (2003), the observed variability in most early type Be-stars is due to high-degree, low-order non-radial g-modes, with grouped multi-periodicity including modes with higher mode number l. As evidence for these multi-periodicities, the MOST targets ζ Oph (Walker et al., 2005), HD 127756 and HD 217543 (Cameron et al., 2008) can be given. Moreover, Saio et al. (2007) are the first to detect low amplitude, non-radial g-mode pulsations ($\sim$ 1 mmag) in a late-type Be-star β CMi.

Gravity and pressure modes can be automatically excited based on the temperature and the depth of the iron opacity bump within the star. In the Milky-Way, p-modes are seen in the hot Be-stars down to B3 spectral type, whereas g-modes are observed in cooler Be-stars from B2 spectral type to early-A. Therefore, B2-3 types are most likely hybrid stars. In this context, Huat et al. (2009) revealed that HD 49330 had pulsation modes typical of β Cep stars (p-modes) and SPB stars (g-modes). In contrast, Neiner et al. (2012) discovered stochastic gravito-inertial modes that are not in the domain of those excited by the κ-mechanism in the hot CoRoT star HD 51452. A similar characteristic was also detected in HD 43317 (Pápics et al., 2012).

Due to their rotation nature, the LCs of Be-stars sometimes produce double or triple waves. The LCs of the CoRoT stars HD 50209 (Diago et al., 2009) and HD 181231 (Neiner et al., 2009) are good examples to display frequency groupings of multi-periods. Also, Semaan et al. (2011) analysed 18 Be-stars in the first CoRoT exoplanet field and demonstrated that the power spectra of the samples consisted of frequency accumulation around one or two main frequencies as well as several isolated frequencies. This is a quite common configuration for both SPB and β Cephei stars.

As previously mentioned, Be-stars are characterized by high rotation and believed to rotate close to their critical velocities. However, the actual velocities can be difficult to estimate due to gravity darkening. Also, most of the sample stars rotate below the critical limits (Cranmer, 2005), and hence were insufficient in reducing gravity to eject material from the star. Since NRPs are excited even in late-type Be-stars as in β CMi, it is believed that they most probably play a critical role in mass ejection and are the additional mechanism required for disk formation. To confirm such a suggestion, several spectroscopic and photometric investigations have been conducted. For instance, Rivinius et al. (1998b) found that the beating of pulsating modes could be the cause of the mass-loss episodes in the star μ Cen in a spectroscopic study. Moreover, Goss et al. (2011) reported that α Eri, one of the most famous and important samples due to its

close proximity to the Earth and its brightness (0.46 mag), showed correlation between pulsation amplitude and disk activity. CoRoT 102719279 and HD 49330 can be also given as photometric studies regarding this correlation. Among them, a strong amplitude increase is observed with the brightness fading caused by newly ejected matter in CoRoT 102719279 (Gutiérrez-Soto et al., 2010), whereas the observed strength of short-period p-modes decreases and additional longer, transient periods arise during outburst in the latter star (Huat et al., 2009).

The fact remains that the existence of the magnetic field in some Be-stars also turns a new page in the study of disk generation mechanisms. According to Schoeller et al. (2013), angular momentum transfer as well as the transportation and accumulation of stellar material in the equatorial disk are more easily explained if magnetic fields can be considered. Recently, Hubrig et al. (2009) reported results related to magnetic fields in a sample of Be-stars in the cluster NGC3766, and revealed that their targets showed magnetic fields of the order of 100 G or less. Of these samples, HD 62367 had the strongest field (117 ± 38 G). Based on the weak fields, they speculated that a non-detection of the magnetic field might be a temporal variability of their magnetic fields, since Brown et al. (2008) considered that weak magnetic fields can provide a mechanism for triggering and maintaining circumstellar disks in Be-stars.

On the other hand, the indirect detection sources of a magnetic field are X-ray emissions and transient features in absorption line profiles. However, an alternative explanation for these structures is offered by Sterken and Manfroid (1996). Accordingly, Be-stars are close binaries consisting of massive components with elliptical orbits. The primary component evolves as a compact object (mostly neutron star) by losing most of its mass, and the other component is a Be-star that has dominant radiation in the optical region. In this case, the disk is formed of the material ejected from the evolved star and is hence an accretion disc. While the compact object is moving in elliptic orbit, it periodically passes through the dense disk around periastron point of the Be-star. Therefore, it gathers disk material and emits radiation in X-ray region. These systems are called *Transient X-Ray Sources*. However, they are not considered within the classical Be-group, since no classical Be-star has yet been found to have a Roche lobe filling companion (Rivinius et al., 2013).

Among the given disk formation mechanisms detailed above, the presence of pulsational variability and disk structure are highly likely to be strongly entwined. Therefore, we expect that changes in the pulsational characteristics of a star might result in consistent changes in disk structure (as measured by Hα line profile changes). To investigate such a relation, we will

present photometric LCs covering a five-year time interval for a number of Be-stars in Chapter 6. These LCs are generated by *STEREO* satellites, which are capable of detecting photometric pulsations with mmag amplitudes. Many Be-stars discussed here have extremely complicated photometric power spectra, and show substantial changes over the course of five years; they will be scrutinized in the relevant chapter. In addition, spectroscopic changes (in Hα) seen in these stars over the same period will also be discussed in the search for any correspondence between photometric (i.e. pulsational) changes and disk evolution.

1.2.4 δ Scuti Type Variable Stars

Another type of intrinsic variable stars is δ Scuties, which are located at the intersection of the classical Cepheid instability strip and the MS (Fig.1.6). Their luminosity classes vary between V and III, since some massive samples evolve towards the giant region and across the strip at higher luminosities. Hence, they are generally referred as dwarf or sub-giant stars (Alcock et al., 2000). Spectral types of these stars range from A2 to F0 in the MS and from A3 to F5 in the giant region (Kurtz, 2000). Also, the mass values are between 1.5 and 2.5 $M_{\odot}$ for δ Scuties with solar metal abundance and 1.0–2.0 $M_{\odot}$ for metal-poor samples (Silva, 2011). Therefore, it is known that these stars are either at the core or shell hydrogen-burning stages.

δ Scuti stars display small and regular multi-periodic LC variabilities with periods ranging from 0.02 to 0.25 days. The typical amplitude is around 0.02 mag, but the brightness variations in the V-band are between 0.003 and 0.9 mag (Breger, 1979). Although most δ Scuti stars pulsate in several non-radial p-modes, some of them have radial oscillations. As stated by Breger (2000), the excitation in the HeII ionization zone with temperatures around 48,000 K is enough to counterbalance the damping in the underlying layers. For this reason, the origin of the oscillations is believed to be the κ-mechanism excited by the HeII partial ionization zones. Based on multi-periodic pulsation behaviours, they have been specified as transition objects between the NRPs observed in the hot part of the H-R diagram and radial pulsations with large amplitudes detected in the classical instability strip.

As seen in Fig.1.6, δ Scuti stars share same location with other pulsating variables such as RR Lyrae, roAp, and γ Dor stars in the instability strip. To distinguish them from the star types mentioned above, physical and chemical parameters such as period, age, luminosity, and chemical composition can be considered. For example, RR Lyrae stars are less massive (between 0.4 $M_{\odot}$ and 0.6 $M_{\odot}$), more evolved, and brighter than δ Scuties even though their periods

overlap. On the other hand, the period values of δ Scuties provide a unique differentiation from γ Dor stars (0.5 days $< P_{\gamma Dor} <$ 3.0 days; Oldershaw (2006)). Also, there are many chemically peculiar (CP) stars situated in the δ Scuti instability domain. Among them, evolved Am stars (known as δ Del or ρ Pup stars) pulsate within the same frequency interval with δ Scuties, yet they differ by their chemical peculiarities due to over-abundance of some metals (Aerts et al., 2010). Similar to δ Scuti stars, roAp stars are core-hydrogen burning, multi-periodic pulsators and are in the same mass interval. However, they are separated from δ Scuti stars by their short periods (between 0.003–0.013 days) in addition to their chemical peculiarities (De Ridder, 2001).

Furthermore, δ Scuti stars can be divided into two well-defined subgroups. The classification is generally made based on pulsation amplitude and metal abundance, since some samples show low-metallicity and high space velocity. The stars that have pulsation with an amplitude < 0.3 mag are called as *Low-Amplitude δ Scuti (LADS)* or *SX Phe* stars. These are metal-weak, population II type old pulsators located between pre-main and post-main sequences. They show multi-periodic LCs with periods shorter than δ Scuti stars (-1.47 days $< logP < -0.90$ days), and pulsations are mainly in non-radial p-modes. They are also smaller-mass stars (1.0–1.3 $M_{\odot}$) (McNamara, 2011).

In contrast, stars with an amplitude greater than 0.3 mag are named *High-Amplitude δ Scuti (HADS)* or *AI Vel* stars. *HADS* tend to be more evolved. Their LCs are mono-periodic, simple, and asymmetric with a rapid rise to maximum and a slower decline, similar to those of RRab stars. They generally display radial fundamental or first overtone mode oscillations (Silva, 2011), and the majority have beat effects caused by two or more interfering periods as in double-mode Cepheids (Percy, 2007). Their period evolution is not well understood, because stellar evolution theories suggest period increases, although the reverse situation is observed during short phases (Breger and Pamyatnykh, 1998a). These stars were regarded as asteroseismologically less interested objects due to their mono-periodic behaviours. However, Walraven et al. (1992) showed that AI Vel pulsated in several radial modes and in a non-radial mode. Afterwards, the existence of non-radial modes in *HADS* was confirmed for many other stars such as V974 Oph (Poretti, 2003) and CoRoT 101155310 (Poretti et al., 2011). Thus, these objects have recently begun to attract more attention. Moreover, *HADS* rotate with the rotational velocities $Vsini \leq 30$ km s^{-1}. Their fast-rotating samples have small amplitudes, a characteristic that has been attempted to be explained in terms of the rotational turbulence and deformation,

which support the excitation of non-radial modes and dampen radial oscillation (Breger, 2000). *HADS* are also the second distance indicators after Cepheid variables because of a clear relation between period, luminosity, and colour (McNamara, 2000). This relation shows the dependency of the radial pulsation period on stellar radius and mass.

The most common way to study δ Scuti stars is through frequency analysis and mode identification. From photometric observations, it is known that low-degree ($l \leq 3$) and low-order ($n = 0$ to 7) p-modes are the characteristics of non-radial pulsators. On the other hand, it was thought before missions to space that the power spectra of δ Scuties might be very dense as the detection limit was lowered. Hence, it was not possible to detect higher degree modes from the Earth because of cancellation effects. However, these modes should be easily seen in the precision photometry of these space missions. After the spectroscopic discovery of the existence of high-degree NRPs in τ Peg (with l up to 20 and frequencies below 35 cycles per day (cd^{-1}); Kennelly et al. (1998)), the presence of these modes was photometrically proved in the first δ Scuti star, HD 50844, and monitored with CoRoT. Poretti et al. (2009) presented a uniformly dense periodogram with typical amplitudes of 0.10 mmag for frequencies less than 25 cd^{-1}, and reported at least 1,000 observable frequencies with modes as high as $l = 14$ in this star .

Moreover, the detection of regularities in the periodogram is one of the typical methods used for stars whose modes are in the asymptotic regime, as in the case of the Sun and solar-like pulsators. δ Scuti modes are generally observed near the fundamental radial mode and outside the asymptotic regime, so regularities in their frequency sets are not expected (García Hernández et al., 2013). However, ground-based observations of several δ Scuti stars have already revealed that their photometric frequencies are not distributed at random. Breger et al. (2009) explained this uniformity by pointing to the higher probability of certain $l = 1$ modes, so-called trapped modes in the stellar envelope, but this explanation did not illuminate the exact equidistance seen in some periodograms.

During the analyses of Kepler data for δ Scuti stars, Breger et al. (2011) reported that several samples showed exactly equally-spaced frequencies, and stated that harmonics as well as non-linear combinations were the reason for such patterns. They calculated an absolutely regular frequency spacing (2.7763 cd^{-1}) produced by combinations in KIC 9700322. In another sample, García Hernández et al. (2013) extracted 185 frequencies from the data of the CoRoT object HD 174966, and found a quasi-periodic pattern of around $\Delta\nu = 5.53$ cd^{-1} in its frequency spectrum.

Along with some problems in identifying the modes due to the complex structures in the frequency spectrum of δ Scuti stars, another difficulty in mode identification is the occurrence of mixed modes, especially in more evolved samples. MS stars with a mass around 2 $M_\odot$ are transition objects as far as the occurrence of a convective ($M < 2$ $M_\odot$) versus radiative ($M > 2$ $M_\odot$) outer zone is concerned. Also, a convective core is seen in the stars between 1 and 2 $M_\odot$. Therefore, δ Scuties contain these transition objects. In this context, CoRoT 101155310 ($M = 1.6$ $M_\odot$, $T = 7{,}300$ K) can be given as an example to illustrate different mode types in δ Scuties (Poretti et al., 2011). In its frequency spectrum, 12 mixed-nature modes have been detected.

Like β Cephei variables, it is known that some δ Scuti stars have period and amplitude variations. The period variation is approximately given as 10^{-7} yr^{-1} and can be both increasing and decreasing (Breger and Pamyatnykh, 1998a). Instead of evolutionary effects, other mechanisms such as a light-time effect due to binary motions or mode interactions are considered as leading to these changes (Kim et al., 2010). V1162 Orion ($P = 0.078686$ days, $A \sim 0.10$ mag) is one of the most interesting samples to present such variabilities. The O-C diagram of the star showed that there was a period decrease in f_1 with the period change rate of $dP/Pdt = -1.60(4) \times 10^{-5}$ yr^{-1} (Arentoft et al., 2001). Subtraction of the constant period variation from the overall data also revealed a secular sinusoidal variation with the period of around 277 days, which corresponded with the period of amplitude change of f_1. However, Khokhuntod et al. (2011) could not confirm such a period decrease by using recent data.

With the advent of the space missions MOST, CoRoT, and Kepler, new opportunities have been created to understand the seismic behaviour of δ Scuti type pulsators. These missions provide determination of long-period oscillations and resolution of beat frequencies with the help of long-term continuous monitoring. Also, their high photometric precision from mmag to μmag enables obtaining more complete frequency spectra and detecting low-amplitude variations that are not easy to observe from the ground. In line with these examples, we used high-precision and long-period photometric data of another space mission, the *STEREO* satellites, to investigate and characterize the pulsational behaviour of a sample of δ Scuti stars. The details of this study will be given in Chapter 7.

1.3 Extrinsic Variable Stars

Extrinsic variables are those in which light output varies due to geometrical effects, the position of object relative to the observer, or stellar rotation. Extrinsic stars are classified in two groups. Eclipsing binaries, which are formed of two or more stars, show light variations because of transits, occultations, or eclipses, while rotating stars exhibit variabilities due to rotational modulation of chemically inhomogeneous regions. In the next section, only some types of rotating stars will be discussed in terms of their contributions to stellar structure studies.

1.3.1 Rotating Variable Stars

Rotating variable stars exhibit light variations as a cause of non-homogeneous surface brightness or ellipsoidal stellar shape. Non-homogeneity of a star can occur due to spots that produce either thermal or chemical peculiarities. Observed variation in luminosity is not a consequence of a physical change within a star, but an event caused by axial rotation with respect to the observer. The period of variation is the period of rotation (Percy, 2007). It is thus related to the equatorial rotation velocity V, which can be spectroscopically derived from line broadening measurements, and the stellar radius R by:

$$V(\mathrm{kms}^{-1}) = \frac{50.6\ R_{\star}/\mathrm{R}_{\odot}}{P\ (\mathrm{days})}\ . \tag{1.10}$$

One of the most exciting groups of this type is *the chemically peculiar stars*. Ap stars (the CoRoT target HD 50773; Lüftinger et al. (2010)), HgMn stars such as the CoRoT star HD 45975 (Morel et al., 2014), and A-stars with metallic lines (Am) (KIC 11402951 and KIC 11445913; Balona et al. (2011b)) are some of the sub-classes.

1.3.2 Chemically Peculiar (CP) Stars

CP stars, which are present both at the core hydrogen-burning phase and at the end of it, are located from the zero age MS to the terminal age MS. They have masses that range from 1.5 to about 7 $\mathrm{M}_{\odot}$ (Netopil et al., 2014). Their spectral types spread from early-B to late-F (Smith, 1996); they therefore contain various stars with effective temperatures greater than 6,500 K (Hubrig et al., 2005). They generally consist of Ap- and Bp-type variables that are significantly separated from normal stars with the same effective temperature due to abnormal chemical compositions in their spectra and low rotational velocities (typically $Vsini < 100\ \mathrm{km\,s}^{-1}$) (LeBlanc, 2010). The reason for this peculiarity is the under-abundance of solar-like elements

as well as over-abundant metal and rare-earth elements across their surfaces (Mikulášek et al., 2009).

Based on their chemical peculiarity, CP variables are divided into four main subgroups (Preston, 1974). CP1 stars (A0m–F4m, $T_{eff} \sim$ 7,000–10,000 K) are metallic line variables that show an over-abundance of metals in their spectra. CP2 stars are known as Ap type stars with abnormal abundance of Si, Cr, and Sr-Cr-Eu. Their spectral types are between B6 and F4 ($T_{eff} \sim$ 7,000–16,000 K). In addition, those stars having an excessive abundance of Hg or/and Mn are called HgMn or CP3 variables. They are between B6 and A0 spectral types ($T_{eff} \sim$ 10,500–16,000 K). In contrast, CP4 stars are B-type objects (B2–B8) with abnormally weak lines of HeI ($T_{eff} \sim$ 14,000–20,000 K). Even though the groups are quite well-characterized, the classification is not fully adequate to identify the diversity of abundance anomalies in the CP temperature interval. Therefore, λ Boo (weak MgII and metals) and He-rich (enhanced HeI) stars are also included with these variables. In this way, the temperature intervals between 7,500–9,000 K and 20,000–25,000 K are better covered. The CP episode is over around 25,000 K with the onset of significant mass loss events (Smith, 1996).

In addition, CP stars are clearly split up into two main groups by the fact that CP2 and some of the CP4 stars show organised magnetic fields with a large-scale structure (typical from 300 G to about 30 kG), whereas CP1 and CP3 stars do not have such fields (Preston, 1974). However, the production mechanism of this magnetic field is still a matter of debate. The mechanism varies depending on whether or not there is an extensive convective layer under the surface of the star. For example, subsurface layers of cool stars with $T_{eff} \leq$ 7,000 K are convective, and the convective motions generate magnetic fields by combining with the differential rotation. The fields are ubiquitous, quite variable, and complex in configuration. Also, they are concentrated in cool spot areas, which evolve in short time periods. These properties are very similar to solar magnetic fields and are thought to be produced by *the solar-type dynamo* (Mikulášek et al., 2009).

However, the thickness of the convective zone substantially decreases in MS stars with 7,000 K $\leq T_{eff} \leq$ 8,500 K while the hotter stars ($T_{eff} \geq$ 8,500 K) have fully radiative subsurface layers and transport heat by radiation (Smalley, 2004). This radiative subsurface is quite stable and magnetic fields cannot be produced here. Two different origins for the field formation have been considered for these stars. In the first theory, it is proposed that the fields originate in the core and then diffuse through the radiative layer to produce the observed fields (*the*

dynamo hypothesis). However, this proposal is not sufficient to explain several observational inconsistencies such as high field strengths, as discussed by Alecian (2014). Another mechanism, which is widely accepted, is *the fossil field theory*. Accordingly, the observed fields in the upper MS magnetic star are the remnants of a parental interstellar cloud. The star sweeps up the galactic magnetic fluxes during the protostar phase. As a result of contraction, the field lines are intensified in the protostar, become large-scale, and gradually decrease with the evolution of the star (LeBlanc, 2010). This theory successfully explains the mechanism in Ap and Bp stars. On the other hand, it is also speculated that these fields are produced during the fully convective phase of the protostar (Alecian, 2014).

Furthermore, the formation of anomalous chemical compositions is another controversial issue. Concerning these, several hypotheses such as the interior nucleo-synthesis resulting from evolution (Fowler et al., 1965), surface contamination of a normal star by a supernova companion (Guthrie, 1967), radiative diffusion by gravity and radiation pressure (Michaud, 1970), and the selective accretion of interstellar matter via the stellar magnetic field (Havnes and Conti, 1971) have been suggested. However, none of these theories, except for radiative diffusion, can successfully account for the CP phenomenon, as discussed by LeBlanc (2010).

Diffusion is an atomic process that effectively occurs in hydro-dynamically stable stellar regions in which large-scale mixing processes like convection or turbulence are absent (Groth et al., 1985). Different elements have different photon absorption abilities from the radiation field. Thus, they are separated at different depths within the star. When an atom absorbs a photon, it gains the momentum of the photon. This situation produces a radiative force on the atom. Since there is a positive radiative flux in the outgoing direction in the star, the atoms are pulled towards the centre while the momentum transfer pushes them to the surface. If gravity is dominant, then the atom sinks. Otherwise, they diffuse towards the surface. This leads to the accumulation or depreciation of the atoms at certain depths. Consequently, some of the elements become excessive at the surface while others are under-abundant (Michaud (2004); LeBlanc (2010)).

Magnetic fields play an important role in the distributions of elements at the stellar surface by directly affecting radiative acceleration and atomic diffusion. This effect manifests itself in two ways. Radiative acceleration of some elements can be strengthened by Zeeman splitting, since the magnetic field stretches the atomic lines and allows for more photon absorption. The saturation of these lines is therefore decreased. Also, the Lorentz force changes the trajectory

of the diffusing elements. As a result, diffusions that take place in the presence of horizontal and vertical magnetic fields differ from each other, since the spherical symmetry of the diffusive segregation of chemical elements is broken. This situation is believed to lead to the formation of spots and rings of enhanced element abundance (Michaud et al. (1981); LeBlanc (2010)).

With the combination of the stellar rotation, these non-uniformly distributed spot regions on the surface cause periodic variations in the average magnetic field characteristics, line profiles, spectral energy distribution, and brightness in different photometric bands (Kochukhov, 2011). All of these variabilities can most successfully be explained using *the oblique–rotator model* (Stibbs, 1950). According to this model, magnetic variations depend highly on the angle between rotation and magnetic axis. Obliquity between these axes forms a magnetic configuration as the star rotates. Photometric, spectral, and radial variabilities can also be understood based on chemical abundance concentrations at the magnetic poles (Kupka et al., 2003).

From several observations, it is known that the phases of these periodic modulations are directly correlated (Catalano et al., 1992). For some CP stars, the phase extrema of the variations coincide with each other (53 Cam; Jarzębowski (1960)), while some of the extrema occur in the anti-phase for some other stars (HD 125248; Mikulášek et al. (2004)). On the other hand, in some cases such as HD 83368 (Polosukhina et al., 1999), the extrema do not take place at the same time even though the periods of all these variations are same.

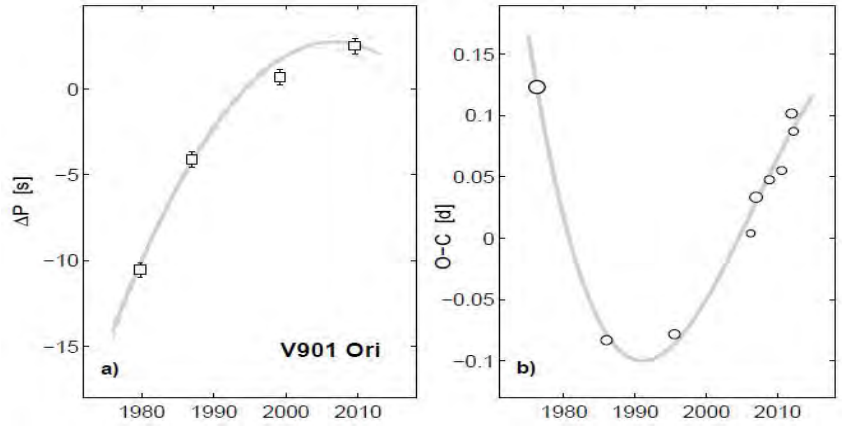

Figure 1.9: Variation in rotation period and O-C values of V901 Ori is shown in the figure. The variation rate of the period is found as $\dot{P} = 0.356\ \mathrm{s\,yr^{-1}}$ from the O-C diagram (Mikulášek et al., 2014).

Most of the CP stars are slow rotators with periods roughly between a day and a week. Long-term observations have revealed that the geometry of the spots can remain stable on the surface for decades as a consequence of slow rotation. Thereupon, surface distribution,

rotational periods, and even rotational braking of some of these stars can be calculated with unprecedented accuracies (Mikulášek et al. (2008); Kochukhov (2011)) .

In fact, 90% of the CP stars discovered both in our galaxy and others thus far do not exhibit an LC or a period variation, although many members such as 33 Lib, α Cir, and HI Lib are located just under the δ Scuti instability strip on the H-R diagram. Yet, it is reported that there is a small number of CP stars such as SX Ari ($\dot{P} = 0.02$ s yr^{-1}; Adelman et al. (2001)), V901 Ori ($\dot{P} = 0.356$ s yr^{-1}; Mikulášek et al. (2014)), and CU Vir ($\dot{P} = 0.165$ s yr^{-1}; Pyper et al. (2013)) whose rotation periods slightly or excessively change over decades. Even though these variations and their origins differ from one star to another, it is believed that magnetic braking is the major cause.

The changes in period can be easily obtained through long-term monitoring of seasonal LCs, and they are generally seen as parabola in O-C diagrams. However, peculiarities of only a small CP fraction have been investigated, and approximately one-tenth has been observed to calculate rotation or photometric periods. To determine these parameters, high-precision instruments and long-term observations are needed (accuracy > 0.005 mag; Mikulášek et al. (2009)). Taking advantage of five-year observations of the space mission, the *STEREO*, we introduce several CP stars presenting periodic light variations in this thesis. Also, we investigate long-term period changes by calculating their extremum times and make a connection between periods and light variations in the relevant section.

Chapter 2

Solar TErrestrial RElations Observatory (STEREO)

Coronal Mass Ejections (CMEs) are one of the most attractive and energetic phenomena in the solar system. During these eruptions, approximately 10^{13} kg of material is spewed out at speeds of around 350 $\mathrm{km\,s^{-1}}$ (Eyles et al., 2009). Understanding such an event is the principle goal of developing solar and heliospheric physics, as it is an indicator of solar coronal evolution. Many spacecraft, such as SOHO, SMEI, and TRACE as well as the *STEREO* were therefore launched into space to observe these bursts.

The *STEREO* is the third Solar Terrestrial Probes program of the National Aeronautics and Space Administration (NASA). It consists of two identically designed spacecraft positioned in a heliocentric orbit at radii of around 1 AU, similar to that of the Earth. The *STEREO-A* orbits ahead of the Earth, while the *STEREO-B* lags behind it: they are not fixed with respect to the planet, but rather drift by 44° per year.

The main task of the *STEREO* is to monitor photospheric activities of the Sun as well as the development and propagation of CMEs. The satellites carry several instrument packages for fulfilling these missions, one of which is the Sun Earth Connection Coronal and Heliospheric Investigation (*SECCHI*). *SECCHI* is comprised of several imaging and coronagraphy tools, such as an Extreme Ultra-Violet Imager (*EUVI*), two white-light Lyot Coronagraphs (*COR-1, COR-2)*, and a Heliospheric Imager (*HI*), to investigate CMEs and create their stereoscopic images (Eyles et al., 2009).

Photometric data are produced by the *HI* instruments on-board the *STEREO* satellites. These imagers contain two visible-light cameras (*HI-1* and *HI-2*), referred to as *HI-1A*, *HI-1B*,

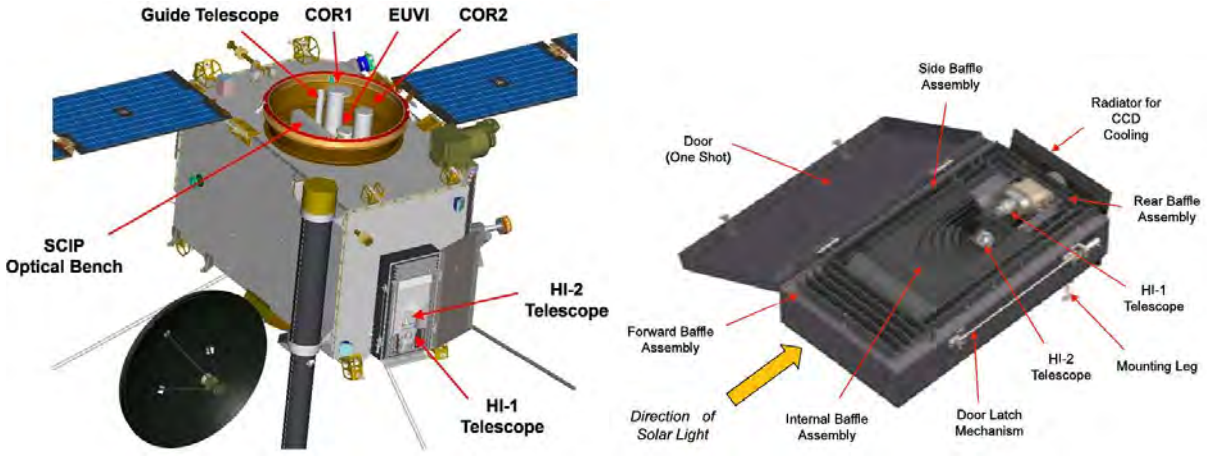

(a) (b)

Figure 2.1: (a) Configuration of the *HI* telescopes and the *SECCHI* instrument package. (b) Internal design of the Heliospheric Imager (from Eyles et al. (2009)).

HI-2A, and *HI-2B*, depending on the satellite on which they are located. *HI-1* instruments have $20° \times 20°$ fields of view (FOV) with an elongation angle of $4° - 24°$, and *HI-2* imagers have $70° \times 70°$ FOV with an elongation between 18.7° and 88.7°. Such a wide view angle from 4° to 88° offers an advantage for observing the Sun–Earth line, and hence provides an excellent opportunity to investigate CME propagations in the direction of the Earth (Eyles et al., 2009).

The *HI* instruments observe the regions that are quite close to the solar disc. Specifically, *HI-1* and *HI-2* focus 14° and 53.7° away from the Sun, and take CME images with a resolution of $70.3''$/pixel and $4.01'$/pixel, respectively. Their detectors are CCDs consisting of 2048×2048 pixels, and the size of each pixel is $13.5\ \mu\text{m} \times 13.5\ \mu\text{m}$. The nominal exposure times of these cameras are 40 and 50 seconds. Putting 30 exposures together on-board, a 40-minute integrated cadence becomes ready to transmit to the ground for each *HI-1* image. Unlike this process, 99 exposures are combined to obtain an integrated image cadence of 120 minutes for each *HI-2* image (Eyles et al., 2009).

The *HI* cameras scan a large portion of the sky during each orbital motion, and they are exposed to a significant amount of background light due to their large pixel size. However, a reasonable signal-to-noise ratio (SNR) and exposures cleansed of the effects of cosmic radiation are needed to create high-quality images. For this reason, a baffle system consisting of a forward, side, rear (perimeter), and internal baffle is used to block stray light coming from the Sun, stars, planets, and zodiacal light as well as from reflections of satellite components. Thus, not only is unwanted light discarded, but SNR is also increased and, in this way, the *HI* instruments

Table 2.1: Camera and imaging properties of the Heliospheric Imagers.

STEREO	*HI-1*	*HI-2*
Angular FOV	20°	70°
Centre of FOV	14°	53.7°
Angular Range	4° – 24°	18.7° – 88.7°
CCD	2048 × 2048 × 13.5μm	2048 × 2048 × 13.5μm
CCD size	35.15″/pixel	2.05′/pixel
Image bin size	70.3″	4.01′
Telescope Aperture	16 mm	7 mm
Focal Length	78.4 mm	19.74 mm
F-ratio	f/4.9	f/2.8
Passbands	4500 Å – 7500 Å	4000 Å – 10000 Å
Nominal exposure time	40 sec	50 sec
Exposure per image	30	99
Total cadence	40 min	120 min

become much more sensitive to even the faintest solar outbursts.

The spectral response of the *HI* instruments is very broad (essentially an unfiltered CCD response). The effective spectral range of the *HI*'s CCDs is between 4,500 Å and 7,500 Å since a standard anti-reflection coating, which is used to achieve maximum efficiency in this interval, is applied. However, although the *HI-1* instrument is sensitive in this wavelength range, *HI-2* has a larger passband (from 4,000 Å to 10,000 Å). Hence, these instruments can observe a wide spectral range from infra-red up to the blue part of the spectrum. The best quantum efficiency (93%) for the instruments is at approximately 5,500 Å, but this is not stable, dropping to around 30% at 3,000 Å and 9,000 Å.

Apart from monitoring CMEs, the *STEREO* has secondary scientific duties that are equally important as the main mission, due to its unique observation equipment (Bewsher et al., 2010). Some of these duties are:

- Scanning co-rotating interaction regions (Sheeley et al., 2008),
- Observing variability of background stars and searching for exoplanets (Eyles et al., 2009),
- Following comets and 3D imaging of cometary tails (Fulle et al., 2007),
- Investigating interactions of comets with CMEs (Vourlidas et al., 2007),
- Tracing asteroids (Davis and Harrison, 2005).

Over the course of a year, these instruments observe the brightness of many hundreds of thousands of background stars with magnitudes up to 12 mag or brighter. They also serve as useful stellar photometers covering the region around the ecliptic. The durations of observation vary for each imager due to their positions in the orbit. Although the semi-major axis of the *STEREO-A* is around 0.96 AU and follows targets for 20 days, the distance of the *STEREO-B* (1.08 AU) provides a slightly longer observation period (22 days).

On the other hand, even though the *HI* instruments have many advantages, the large pixel size causes some problems during background star observations within the Galactic Plane crossings. In other words, some stars are not adequately tracked due to the existence of numerous objects in this region (Sangaralingam et al., 2010). Moreover, data for traceable stars can sometimes be affected by solar activities, since the satellites are centred quite close to the solar disk (Fig. 2.2). In order to dissociate the data from unwanted signals and make them re-usable, various processes are performed (Sangaralingam and Stevens, 2011). This allow us to acquire good photometric data for stars having brightness values up to 10 mag. (Sangaralingam et al. (2010); Whittaker et al. (2012); Bewsher et al. (2010)).

In this thesis, we will only use the data obtained from the *HI-1A* instrument, as the data quality and pointing information of *HI-1B* are of poorer quality as compared to *HI-1A*. Similarly, the data taken from *HI-2* instruments are also not photometrically as good, since different apertures are used on each imager (Bewsher et al., 2010).

2.1 STEREO Data and Reduction Procedures

There are three different levels of processed data that can be downloaded from the UK Solar System Data Centre (UKSSDC[3]). L0 is uncalibrated data consisting of raw summed images; L1 is semi-processed images that have undergone basic processes, and L2 is pre-processed images that have had an additional background applied. As previously mentioned, the exposure time of the *HI-1* is 40 seconds, and each image consists of 30 exposures. This not only prevents saturation but also produces the required SNR in the observations. Before summing these images on-board the spacecraft, each image is cleansed of cosmic rays whose estimated impact rate is 45 pixels per second (Eyles et al., 2009). To remove these rays, each exposure is compared pixel by pixel. If the pixel value is $> 5\sigma$, where σ is the noise standard deviation predicted according to the photoelectrons number, it is replaced with the pixel value of the previous image.

[3]http://www.ukssdc.rl.ac.uk

These images are known as the raw summed images (Fig. 2.2a). The cadence of the total image is 40 minutes (due to the telemetry restrictions and time-scales of CME propagation), which means that only half of the total observation duration is efficiently used. The L0 data does not have basic reduction procedures; hence, they are not suitable for scientific usage. These reduction procedures can be performed by the *secchi_prep* routine in the *Interactive Data Language* (IDL) with the following pipeline:

2.1.1 Secchi_prep Pipeline

1. **Missing data:** Due to the overflow integer problem, the data is compressed and coded using either the word 'low' or 'high' before transmission to the ground. Any communication loss during telemetry causes a series of data being lost at random times. These lost chunks are eliminated and replaced with appropriate values if the lost parts are small or repairable. Otherwise the image is tagged as a bad file (Eyles et al., 2009).

2. **Bad files:** Some images are tagged as bad for various reasons such as corrupted data or files, and high or low word matching problems. Beside these, files with split star fields due to shaken frames and unidentified point sources, integer overflow, mathematical corruptions occurring during image transmissions, composite images from multiple cameras, and many other unclassified problems are also considered as bad files. The complete list of bad files is provided by the UKSSDC for their removal from further analysis.

3. **Blooming:** The *HI-1A* instrument has a full pixel capacity of around 200,000 electrons. If this limit is exceeded (for stars brighter than 4 mag), the CCD pixels are saturated (Fig. 2.2c). In this case, the pixels bleed vertically and affect the adjacent pixels in the same column. Physical barriers in the CCD prevent this leakage from reaching the next rows unless extremely bright objects are observed. Since these saturated pixels affect the shutter-less readout correction, the entire column is identified and replaced with 'NAN' values (Eyles et al., 2009).

4. **Shutter-less readout:** The imagers do not have a shutter due to mechanical constraints. For this reason, CCD pixels are exposed to additional incoming radiation between the readout ($T_r \sim 2.3$ ms) and cleaning ($T_c \sim 0.1$ ms) times (Fig. 2.2b). For each exposure, each CCD row is read out, pixel counts are recorded (during the readout process, the photo-electrons are converted to a digital number (DN), whereby 15 photoelectrons give

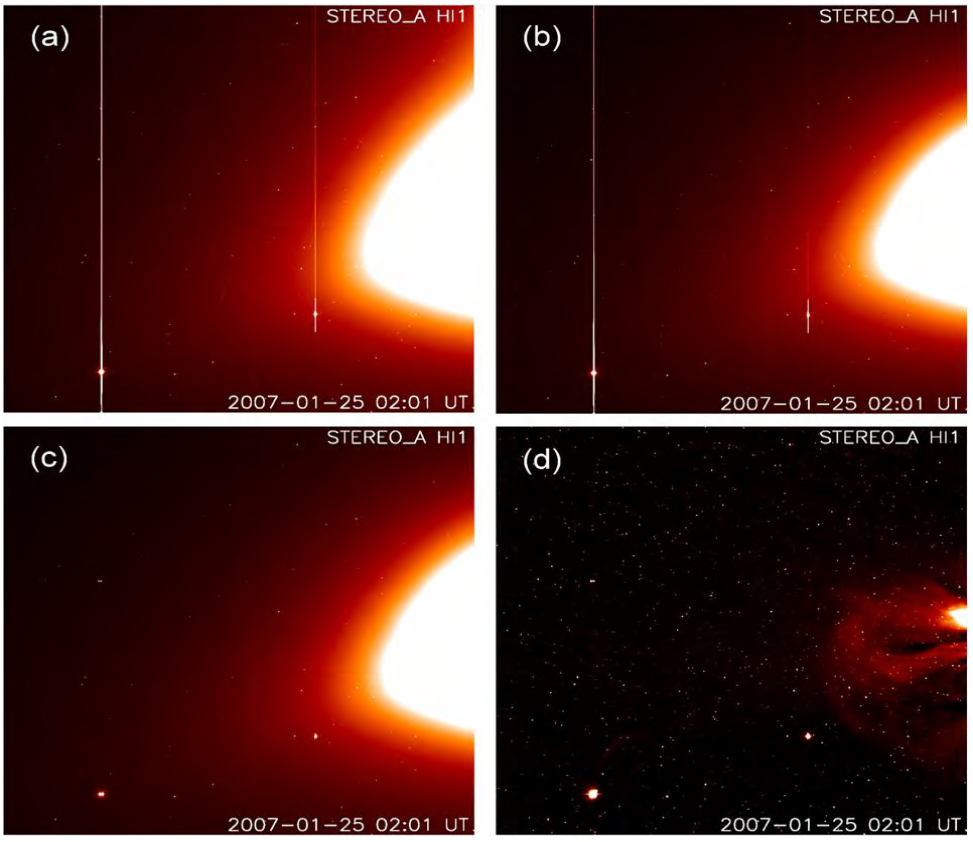

Figure 2.2: Some stages of the Secchi_prep pipeline and F-corona subtraction from an image taken by HI-1A are illustrated in the figure: a) the raw image, b) the shutter-less and flat-field corrections, c) the removal of saturation around the planets Venus and Mercury, and d) the background subtraction and the effect of a CME (Eyles et al., 2009).

1 DN), and the CCD is prepared for the next observation by being cleaned in a vertical direction. However, an additional time of $m \times T_r$, where m are pixel rows ($0 < m < 2048$), occurs at every turn. This results in vertically smeared images in the readout direction. For subsequent analyses, a mathematical correction is applied to remove this effect from the images (Eyles et al., 2009). As a consequence of this procedure, a total signal in DN is converted to the units of count rate (DN s^{-1}) since the total readout time for the CCD ($\sim$ 4.8 seconds) is a considerable fraction of the observation time (Whittaker, 2013).

5. **Flat field:** The quantum efficiency and the response of pixels in the corners and centre in a CCD are different. For this reason, it is necessary to correct the differential gain effect in a CCD reduction. This correction procedure is known as *the flat field* (Fig. 2.2b). For the imagers, a flat field map was prepared on the ground during the calibrations of the instrument. Since there were some constraints in measurements, a flat field was only measured in the centre line, and an initial flat field for the entire CCD was obtained

through extrapolation of these centre line values (Sangaralingam, 2011). However, the procedure failed to correct for the vignetting effects and caused observational problems in the final LCs. This was overcome by deriving the ratio between measured and predicted intensity across the CCD from a star-field observed between 2007–2008 and by updating the correction with the equation of $f = 1/R$ (Brown et al., 2009).

6. **Update pointing parameters:** Pre-flight pointing information and camera optics of the instrument turned out to be incorrect after the observation of a drifting star field. Therefore, the average radial error in pixels between the positions of stars in the image and the catalogue was calculated image by image. An error value of < 1 pixel is considered as good, while a value of < 5 pixels is acceptable (Brown et al., 2009). Sangaralingam (2011) gives the median of the error residuals to be 0.157 pixels with a scatter of 0.012 pixels, which shows the tracking accuracy of the objects in terms of position in *STEREO* LCs.

After these corrections, there is still the possibility of finding a few corrupted frames due to other reasons such as untagged data containing certain spikes or black-outs. Even though the number of such frames is small, they must be taken out to obtain an accurate F-corona map. These bad frames are removed by using a 5σ clipping of the image pixel values. The data obtained at the end of all these processes is known as L1 data.

2.1.2 Background Subtraction

F-corona is the sunlight scattered from dust particles in the inner heliosphere. This light reaches up to the Earth's orbit and merges with zodiacal light. The brightness of the F-corona changes from 10^{-12} to 10^{-14} times the solar disk brightness (B_0), and its presence is quite dominant in L1 data (Fig. 2.2d). Therefore, the removal of this effect from the data is crucial for studies of CME evolution ($B_{CME}/B_0 = 10^{-13} - 10^{-14}$) and for carrying out stellar photometry ($B_{star}/B_0 = 10^{-17} - 10^{-18}$) (Sangaralingam and Stevens, 2011).

To reduce the F-corona effect, a minimum map is derived from the minimum value of each pixel over a sequence of 36 images (a day's worth of images), and is subtracted from each image. This method is quite effective, since F-corona evolves more slowly than drifting stars in the FOV (~ 2.5 arcmin/hour). However, other background variations such as CMEs are not distinct and occur in different time-scales. Hence, they cannot be cleaned by this process (Whittaker, 2013). Therefore, a new method that uses a running window with the length of either one day or eleven

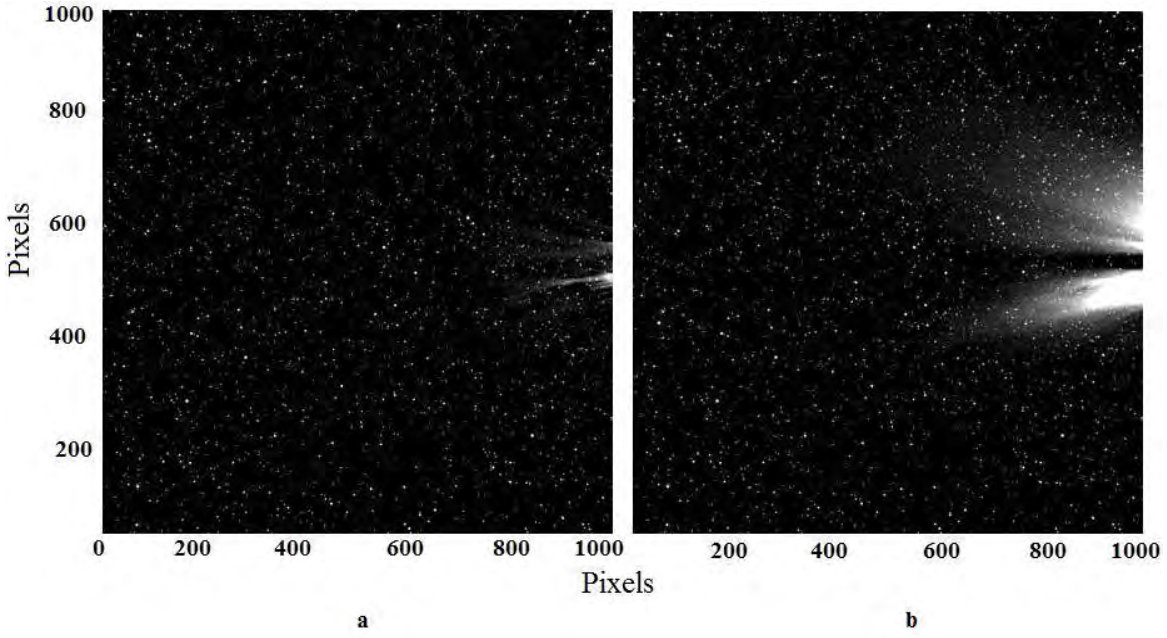

Figure 2.3: This plot is an illustration of the two different types of running window method formulated for the F-coronal subtraction: a) one-day running window background map cleans most of the F-corona and makes the stars visible for photometry, b) eleven-day running window reduces the F-corona, but its various streamers are still observable and the background stars are contaminated (Sangaralingam, 2011).

days is applied. In this method, the lowest 25 per cent of the data is picked by the window, and an average of this data is formed on a pixel-by-pixel basis. This average is then subtracted from the images. These final images are known as L2 data (Sangaralingam and Stevens, 2011). Even though the one-day window is appropriate for stellar photometry, the final images still retain some residuals as seen in Fig. 2.3a. To study any stellar variability, even the smallest effects in LCs should be cleaned. Therefore, we will introduce a freshly coded pipeline in Section 5.

2.1.3 Light Curve Derivation

LCs are produced by using L2 data. The coordinates of the target stars are derived from the Naval Observatory Merged Astrometric Dataset (NOMAD[4]), which contains ∼600,000 stars with $4^m < R < 12^m$, and are converted into pixel locations on the CCD. These positions are then matched with the peaks that have an intensity greater than 1.5 times the surrounding in an area of 5×5 pixels. If the source is located within 1 image pixel of the catalogue position, the match is completed, and the target is identified. This identification is restricted to the brightest stars by an area with a radius of 6 pixels centred on the target (a factor of 1.5 in the

[4]http://www.nofs.navy.mil/data/fchpix/

surrounding). Thus, the blending risk of two LCs is reduced. In brief, if there are two stars within 6 pixels on the CCD and their brightness difference is less than a factor of 1.5, then neither is selected. On the other hand, the brighter star is picked if the brightness difference is greater (Whittaker, 2013).

The measurements of stellar and background flux values are obtained by aperture photometry. In this method, a centroid is used to pinpoint star position, and star flux is measured by summing the photon counts in a user-specified region in the image. However, flux values are affected by background noise and possible light contamination, since *HI-1A* covers a large angular area (3.3 square arcmin). As a result, the most suitable measurements are required to provide a maximum benefit from *HI-1A* LCs. Accordingly, aperture photometry is performed with an aperture radius of 2.5 pixels for target stars. Sky background is also calculated in an annulus between 6 and 10 pixels around targets and subtracted from the aperture measurement to obtain a final flux value (Whittaker, 2013). However, it should be noted that the background values measured are affected by sky variance, uncertainty in average sky brightness, and random photon noise. The flux value discussed here is in the unit of DN/s and can be converted to the actual value (photon/s) by multiplication with the photon-electron conversion gain (1 DN = 15 photoelectrons; Bewsher et al. (2010)). The time stamp marks the start of the observation and is in Coordinated Universal Time (UTC). It is also converted to Julian Date (JD) and then to Sun-centred time (HJD) for subsequent analyses (Sangaralingam, 2011).

As a result of aperture photometry, target stars are observed for 20 days. Since observations are repeated in every 40 minutes, around 720 data points are obtained for each star. Such a data set provides the opportunity to perform analysis in a wide frequency range with the Nyquist frequency of around 18 cd^{-1} ($\approx$ 1.5 h). However, this data generally shows systematic trends that occur due to basic instrumental design, pipeline procedures, observed star regions, or changes in the basic conditions of the images. Among them, the most common reasons are CME effects, flare-like events, end-of-frame and flat-field effects. Although all of these are time-dependent and related only to *STEREO* observations, there are some basic noise sources in any observation. Even in an ideal case, LCs have a photon-shot noise, which exhibits a Poisson distribution. The amount of shot noise is inherent in the signal and is also a function of the amount of signal (shot noise = $\sqrt{signal}$). Thus, if the number of observed particles is small, shot noise contributes to the signal more, and uncertainties in the distribution increase (Sangaralingam and Stevens, 2011).

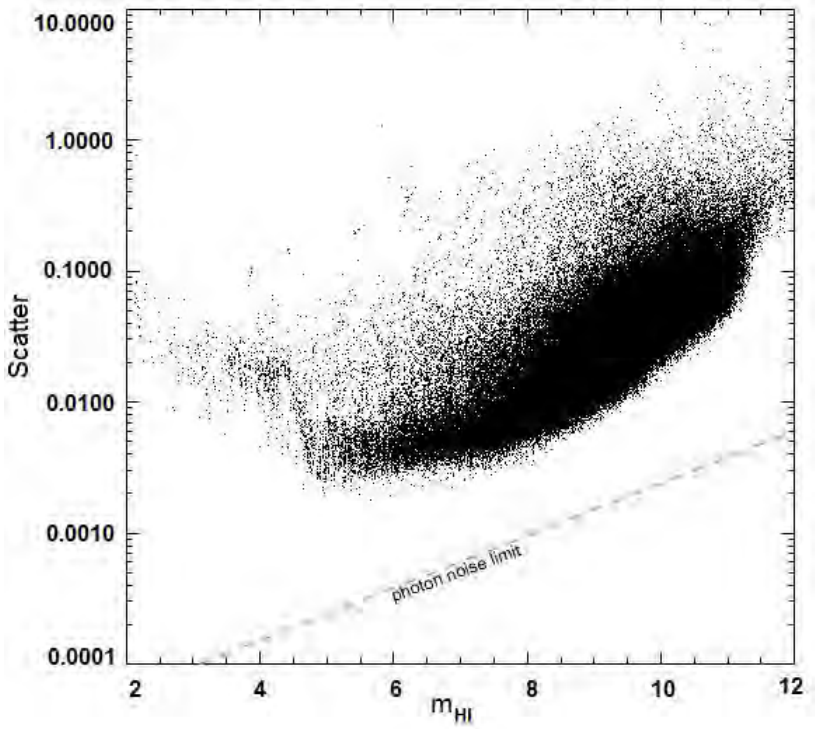

Figure 2.4: Photon-shot noise for the raw light curves is given in the figure. It is a function of m_{HI} (calculated directly from the measured flux) and plotted on a logarithmic scale. The green dashed line is the lower level to the observable precision of stellar variability for the Heliospheric Imagers (Whittaker, 2013).

In stellar photometry, the electron number is directly proportional to the brightness of an observed object. Therefore, shot noise changes with brightness (Fig. 2.4). This noise also sets a base level to the observable precision of stellar variability (Whittaker, 2013). Hence, systematic noise removal procedures are used to reach this lower level in every project. In this sense, space missions are quite advantageous because they are independent of atmospheric effects. Yet, the *STEREO* has some negative factors such as pixel size, CMEs, and planets in the studies on stellar variability, since its main purpose is to monitor solar phenomena. Thence, *STEREO* data have some unexplained sources that produce much higher scatter than the photon-shot noise limit for stars fainter 10^m. However, it is still possible to reach a precision of $< 1\%$ for stars brighter than 8^m and a few per cent for fainter objects (Sangaralingam and Stevens, 2011). The scatter values of *STEREO* raw LCs are shown as a function of m_{HI} in Fig. 2.4. Also, the photon noise level of the *HI* instrument is given by the green dashed line.

As a result, it can be said that sufficient amounts of data as well as high-precision measurements of *HI-1A* are considerable enough to model stellar variations. Apart from the CME detection duty, instrumental characteristics of the *STEREO* also allow us to obtain detailed

Table 2.2: Comparison of the *STEREO* satellites and other space projects.

Project	**CCD FOV**	**Sky Area Observed**	**Cadence**
TrES	$6^\circ \times 6^\circ$	0.2% (STARE & PSST)	9 min
MOA/OGLE	$6' \times 6'$	All sky	–
HATnet	$10.5^\circ \times 10.5^\circ$	10% of sky	3.5 min
SuperWASP	$7.8^\circ \times 7.8^\circ$	All sky	30 sec
CoRoT	$2.8^\circ \times 2.8^\circ$	0.03% of sky	512 sec and 32 sec
KEPLER	5 $\deg^2$	0.2% of sky	30 min and 1 min
XO	$7.2^\circ \times 7.2^\circ$	55% of sky	10 min
N2K	–	2000 stars	4 ms^{-1}
MOST	4.3°	individual	< 1 min
STEREO HI-1	$20^\circ \times 20^\circ$	each 20% of sky	40 min
STEREO HI-2	$70^\circ \times 70^\circ$	each 60% of sky	120 min

information about internal structures of stars. Therefore, almost all types of variables from pulsating to rotating stars can be investigated. In addition, due to covering 20% of the sky, the *HI-1* plays quite an important role among the space missions given in Table 2.2 in terms of the identification of new candidates and their analyses. For these reasons, the *STEREO* satellite will be focused on in this study, and numerous *STEREO* stars belonging to various variable types will be introduced as examples in forthcoming sections.

Chapter 3

Analysis Techniques of Numerical Data

3.1 Introduction

The best way of understanding the characteristics of physical systems is to analyse their behaviours over time. Therefore, time series analyses have always been at the centre of astronomers' attention. The main goal of these analyses is to detect hidden signals within a time series in the presence of noise; Fourier techniques are generally performed to determine these signals. In applying Fourier transforms, a signal is decomposed into *sine* waves, and is basically specified via continuous or discrete Fourier transforms. However, astronomical time series include gaps and non-uniformly spaced data, which can occur due to the Earth's orbital motion, telescope scheduling based on moon phases, or daily interruptions of single-site measurements by the Sun (Aerts et al., 2010). In the case of such interrupted measurements, existing classical theories are not appropriate for analyses. Therefore, various software, languages, and effective procedures have been written to carry out reliable analyses. IDL is one of these breakthroughs. In principle, IDL is a flexible scripting language that uses functions and procedures to perform a wide range of data and image-processing tasks. To analyse different data sequences with IDL, several frequency detection methods are used, through which a period of a variation can be accurately calculated. In the following sections, some of the methods used such as Lomb-Scargle (LS), Phase Dispersion Minimization (PDM), Period04, and Wavelet Transformations are briefly described. Among them, the advantages and disadvantages of two widely-used techniques, LS and PDM, are highlighted.

3.2 Lomb-Scargle Periodogram (LS)

If the intent is to derive complete information about a time series, there must be equally spaced data sets. However, due to the reasons mentioned in the previous section, such data sets cannot be obtained. The best method for examining these non-uniform data is LS periodogram analysis. In this method, a normal Fourier power spectrum is calculated as if data is equally spaced, and weak periodicities in the spectrum are detected by this powerful and effective technique.

In order to avoid spurious signals and detect the most accurate period, Lomb (1976) initially derived statistics by implementing least-squares fits to sinusoidal waves, and then aimed to find the probability distribution of the maximum point of the highest frequency in a periodogram. Scargle (1982) carried this study a step forward by including a false alarm probability (FAP) to determine the significance of a peak given its height. Scargle (1982) also showed that if the periodogram is properly normalized, peak heights in the periodogram give an exponential probability distribution, and this normalization is achieved by dividing by the total variance of the data (Horne and Baliunas, 1986). The FAP feature has great importance, since the origin of a signal may not be only stellar, but may also be due to instrumental or atmospheric turbulence effects. To uncover the real cause, a requisite criterion is thus to identify whether a peak is generated by stellar activity or noise. Accordingly, the probability of producing a high amplitude peak by noise is lower than producing a low amplitude frequency. This means that FAP will be lower for a real signal with higher amplitudes in a spectrum. When considering that the highest amplitude peak is selected for analysis, this definition is quite reasonable. In this respect, FAP is a reliable criterion for detecting real signals in given data sets.

To mathematically explain the working principles of the LS method, a time series consisting of N elements $t_1, t_2, \ldots, t_N$ and corresponding data points $h_1, h_2, \ldots, h_N$ are assumed. Initially, the mean ($\overline{h}$) and the variance (σ^2) of the data are obtained:

$$\overline{h} = \frac{h_1 + h_2 + h_3 + \ldots + h_N}{N} = \frac{1}{N}\sum_{i=1}^{N} h_i \qquad and \qquad \sigma^2 = \frac{1}{N-1}\sum_{i=1}^{N}(h_i - \overline{h})^2 \ . \tag{3.1}$$

Unlike Fourier analysis, M frequencies $f_1, f_2, \ldots, f_k, \ldots, f_M$ are taken into account for LS, and their corresponding angular frequencies (w_k) are derived by:

$$w_k = 2\pi f_k \ . \tag{3.2}$$

As a function of angular frequency $w_k > 0$, the Lomb normalized periodogram is given by the equation:

$$P_N(w) = \frac{1}{2\sigma^2}\left[\frac{\left[\sum_{i=1}^{N}(h_i - \overline{h})cos[w_k(t_i - \tau)]\right]^2}{\sum_{i=1}^{N} cos^2[w_k(t_i - \tau)]} + \frac{\left[\sum_{i=1}^{N}(h_i - \overline{h})sin[w_k(t_i - \tau)]\right]^2}{\sum_{i=1}^{N} sin^2[w_k(t_i - \tau)]}\right], \tag{3.3}$$

where the coefficient $1/2\sigma^2$ is a normalization constant and changes the vertical scaling of the periodogram. As a result of this normalisation, the mean power in white noise will be 1.0 in the frequency domain, meaning that the data is pre-whitened (Tarrant, 2010). Besides, τ, which is an offset that makes the Eqn. 3.3 completely invariant to shifts in the origin of time, is defined by:

$$tan(2w_k\tau) = \frac{\sum_{i=1}^{N} sin(2w_k t_i)}{\sum_{i=1}^{N} cos(2w_k t_i)} \ . \tag{3.4}$$

Through this offset, the periodogram remains the same if all the data are simultaneously shifted in time (Sangaralingam, 2011). This τ definition also contains another contribution: its specific selection makes the Eqn. 3.3 identical to the equation for obtaining frequency harmonics by a linear least-squares fitting of *sine* waves to the data ($h(t) = Acos\omega t + Bsin\omega t$).

The observed data points (h_i) generally consist of a combination of a periodic signal and independent Gaussian noise. To determine the significance of these data, a null hypothesis, in which the data values are independent Gaussian random values, is considered. In the case of this hypothesis, $P_N(w)$ has an exponential probability distribution for a specific w in the periodogram normalized by variance of the data (Scargle, 1982). In brief, the probability that $P_N(w)$ varies between some positive z and $z + dz$ will be $e^{-z}dz$, where z is the power threshold. Accordingly, the probability that no other values greater than z becomes: $p = [1 - e^{-z}]^{N_{id}}$. Thus, the FAP of the null hypothesis can be found by:

$$P_0(> z) \equiv 1 - [1 - e^{-z}]^{N_{id}} \ , \tag{3.5}$$

where N_{id} is the number of independent frequencies that can be derived from a simple least-

squares formula, suggested by Horne and Baliunas (1986) as:

$$N_{id} \approx -6.362 + 1.193N + 0.00098N^2 \ . \tag{3.6}$$

Finally, if the Eqn. (3.5) is solved for z, the horizontal significance level is determined to be:

$$z = -ln[1 - (1 - P_0)^{1/N_{id}}] \ . \tag{3.7}$$

Scargle (1982) points out that FAP is a constant and small number. For example, if the probability P_0 is picked as 0.01, the threshold will be $z \approx ln(N/P_0) = 4.6 + ln(N)$. Assuming the number of data points is $N = 30$, z will be greater than 8, corresponding to a signal with a 99% confidence.

In the case of *HI-1A* instrument, the observation duration is around 20 days, and the maximum number of collected data during this period is around 720. Since the data is equally spaced due to 40-min cadence, N_{id} should be calculated from $N/2$. This provides 360 independent frequencies. Thus, if there are frequencies having 95% significance ($P_0 = 0.05$) within these data, their amplitudes should be higher than $z = 8.86$ in the power spectrum. If the significance level is decreased to $P_0 = 0.01$, then the threshold becomes 10.5. In a sense, a small value for FAP indicates a highly significant signal.

Although strong signals can be detected successfully, there is a possibility that power can go down under the threshold level. In this case, probability depends not only on the number of independent frequencies, but also on peak intensity (P). This is known as *the Detection Efficiency* of the LS method and is given as:

$$DE = 1 - p^*(N, P) \ . \tag{3.8}$$

The calculation details of this detection procedure can be found in Scargle (1982). Since the LS method implies four calls to trigonometric functions, it has N^2 operations to analyse N data points, which makes it a slow algorithm (Kay and Marple, 1981). On the other hand, with a new method called *the Fast Fourier Transformation*, Press and Rybicki (1989) accelerated the process to an order of $NlogN$ operations, replacing trigonometric calls with recurrences. Thus, the duration of analysis is decreased by a factor of four. However, the results of both methods are nearly similar.

3.3 Phase Dispersion Minimization (PDM)

The traditional way of searching for and detecting a signal in time series is to apply numerical techniques based on Fourier transformations. To obtain efficient results in these methods, there should be a simply sinusoidal signal whose parameters, such as phase and frequency, should remain constant over the observation period. However, real LCs can be a composition of various periodic signals occurring in different time-scales, and can also consist of structures that are not described with simple sinusoidal functions in a time domain. Additionally, other reasons, such as uneven gaps in the observed data, render the Fourier methods unusable by negatively affecting the results (Lu et al., 2012).

In contrast, PDM is a non-parametric method in which there is no need to assume any chosen model function to express the data. Even though it is a least-squares fitting technique, it fits the mean curve produced by means of each bin, rather than fitting only a given curve. PDM is, therefore, a unique algorithm for period analysis of data displaying non-sinusoidal variations and irregular samplings (Stellingwerf, 1978). Moreover, this method is quite effective in identifying a signal in just a few observations obtained over a limited time (as few data points as 10; Sangaralingam (2011)). Unlike Fourier-based algorithms, statistical reliability, computation duration, application efficiency, and the ability to separate real signals from noise are some of PDM's advantages (Lu et al., 2012).

PDM is a different data-folding technique. Initially, a series of trial period values is determined, and the data are folded according to these values. The full phase interval from zero to one is split into a user-specified number of bins for each trial period. The width of each bin is also specified by the user. After grouping the data in separate bins, the variance of each bin is computed. Thereby, a distribution around the mean LC, defined by the means of the data in each bin, is obtained. The PDM statistic, (θ), is then calculated: the overall variance of all bins is divided by the variance of the unbinned dataset. This process is repeated for the next trial frequency until a period that produces minimum dispersed observations with respect to mean LC is found (Lu et al., 2012). If the trial period is true, then $\theta \sim 0$. Otherwise, the PDM statistic becomes close to unity, and all these processes are repeated for the next period (Starlink[5]).

To explain PDM numerically, N points ($i = 1, 2, 3, \ldots, N$) with the vectors x (observations)

[5]http://www.starlink.ac.uk/star/help/period/period_pdm.hlp

and t (corresponding time values) are initially defined. If the coordinates of i-th data point are assumed to be "x_i, t_i", the mean ($\overline{x}$) and the variance (σ^2) of the data set can be found with:

$$\overline{x} = \sum_{i=1}^{N} \frac{x_i}{N} \qquad and \qquad \sigma^2 = \frac{\sum_{i=1}^{N}(x_i - \overline{x})^2}{N-1} \ . \tag{3.9}$$

Also, let M be the number of the phase bins. If a proper M is picked by considering the trial period, the data points in each bin have similar phases for a given trial period, i.e., the phase of i-th point becomes $\phi_i = t_i P - int(t_i P)$, where P is the trial period, and $int(t_i P)$ represents the integer part of $t_i P$. Supposing that there are M different sample s, they will contain n_j data ($j = 1, 2, 3, \ldots, M$) with the variance of s_j^2. In this case, the total variance of all samples can be found by:

$$s^2 = \frac{\sum_{j=1}^{M}(n_j - 1){s_j}^2}{\sum_{j=1}^{M}(n_j - M)} \ . \tag{3.10}$$

In order to produce a mean LC that will be used as a reference, PDM selects the mean value of each bin ($\overline{x}_j$) and calculates distributions of data points according to this curve (Fig. 3.1a, b). The goal here is to minimize the variance of data based on the mean curve. To be able to assess this scatter numerically, a statistic ($\theta = s^2/\sigma^2$) is described (Stellingwerf, 1978) and given as:

$$\theta = \frac{\frac{\sum_{j=1}^{M}\sum_{i=1}^{N}(x_{ij} - \overline{x}_j)^2}{\sum_{j=1}^{M} N_j - M}}{\frac{\sum_{i=1}^{N}(x_i - \overline{x})^2}{N-1}} \ , \tag{3.11}$$

where x_{ij} is x_i-th data point in j-th bin. For the actual period value, θ will be small; in fact, it will even be close to a value of zero. For all other instances, $s^2 \approx \sigma^2$ and statistical quantity will be $\theta \approx 1$.

However, an equal number of bins can contain a disadvantage, as there is a possibility that some bins can be empty if the width of the bin is incorrect or if there is only a few data points

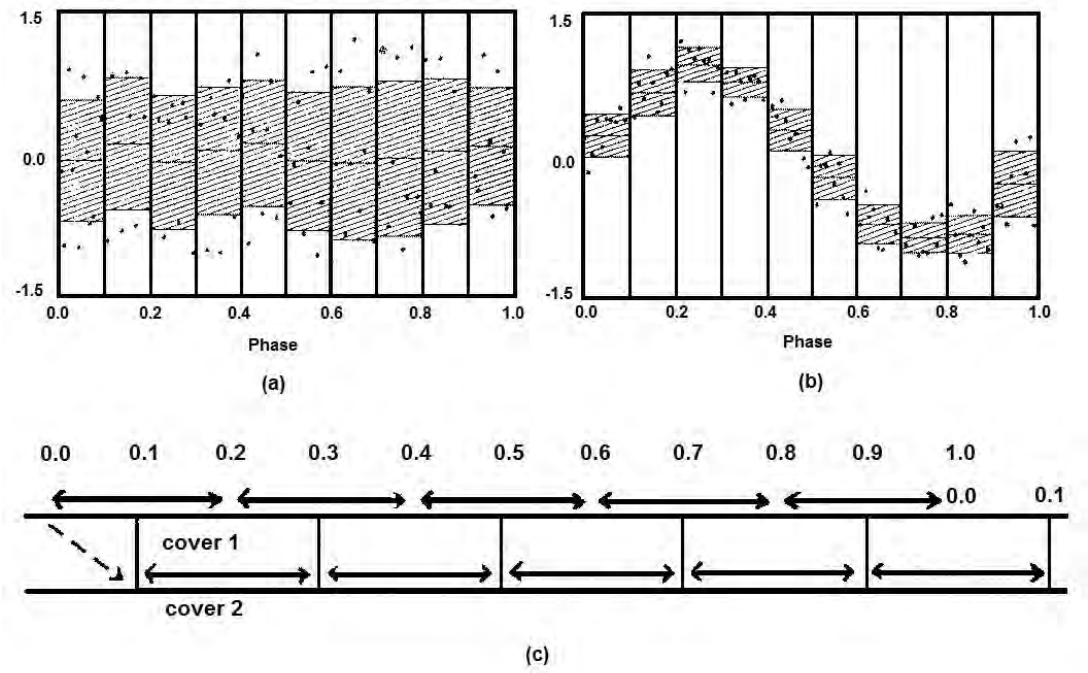

Figure 3.1: The mean light curves produced with a bad (a) and a good (b) trial period are represented in the figures above. Bin and cover numbers are chosen as 10 and 1, respectively. The working principle of the bin/cover ($B = 5, C = 2$) structure is shown in the Figure c (taken from De Cat (2001)).

with a particular time spread. For this reason, a bin (B)/cover (C) structure is used (Fig. 3.1c). In this case, the phase diagram is divided into B bins with the length of $1/B$. This partition is applied C times, and each partition is shifted in phase by $1/(B \times C)$. Finally, the incomplete bin near $\phi = 1$ is combined with the data near $\phi = 0$. Thus, the phase diagram is covered C times, and each observation definitely goes into at least one bin (Stellingwerf, 1978). To obtain the best results, B and C should be between 5-20 and 1-10, respectively. To increase detection probability, more covers can be used, but the computation time takes longer (Radiman et al., 1998).

3.4 Period04

Period04 is specifically developed for statistical analysis of astronomical time series that include gaps (Lenz and Breger, 2005). It can easily determine a singular frequency within multi-periods of a time series. In addition, multi-frequency fitting can be performed with the help of user-friendly interfaces.

The software consists of three main modules, which are divided into many sub-units to simplify frequency analyses. The "time string module" allows users to manipulate the data. It

is possible to cut a set of data into small groups or put different sets together in this module. The "fit module" is the interface in which several frequencies are fitted by the least-squares method. Their amplitude and phase variations can also be calculated. In addition, noise levels at given frequencies and analytic uncertainties for the peaks obtained are other parameters provided in the module. To determine new frequencies, Fourier transforms are performed in the "Fourier module". A time-domain signal of infinite duration is converted into a continuous spectrum using an infinite number of sinusoids. However, discretely sampled signals (usually sampled at constant intervals) and finite duration or periodic signals are in question for astronomical observations. In this case, only a limited number of sinusoidal functions is required. Therefore, Period04 uses Discrete Fourier transform algorithm for signal detection (Lenz and Breger, 2005).

Data are imported to the "time string" section on the main window to start analysis. If the data are in the unit of magnitude, the related box is ticked and the "Fourier" section is clicked. There are two boxes that allow for inserting the related frequency interval on the left of the main window; the Nyquist frequency of the data is also shown there. The Fourier transformation is applied to the original data set in this section, and the most dominant frequency can be seen in a periodogram under the "display graph" button. Further, the obtained frequency and corresponding amplitude as well as phase value can be found on the "fit" section. Marking the box on the left side of the values, the frequency calculated from the transformation is fitted to data. As there may be many other frequencies hidden in time series, the most dominant frequency is extracted from data, and new periodicities are searched. This process can be carried on until the last significant frequency is determined. Apart from these, in order to identify whether a peak represents a real stellar activity or noise, the "calculate noise at frequency" option under the "special" section is chosen. A noise value for each frequency and an SNR can be derived in this part.

Additionally, the uncertainties of obtained values can be seen in the "show analytic uncertainties" option in the same section. For a detailed derivation, LS uncertainties and Monte-Carlo simulations are also available in the "goodness of fit" option in the program. Further information about the details of and tools for analysis can be found in Lenz and Breger (2005).

3.5 Wavelet Transforms

Wavelet is a new frequency analysis technique and an improved version of Fourier transforms. For a particular signal or image, it provides more accurate information about data than other

methods. These transforms are performed to find a signal frequency varying over time within a time series. Application of the Fourier technique to an entire time axis does not detect a frequency variation with respect to time if a signal is a non-stationary signal. In such a case, short-time Fourier transforms can be experimented with. In doing so, a frequency can be searched for via a sliding window. However, window sizes affect frequency resolutions. In spite of this, Wavelet uses small wavelets in restricted time intervals, which means that function is represented by a wavelet instead of a series of numbers in this method.

Furthermore, unlike the Fourier technique, wavelets are localized in both time and frequency domains, and so time information is also preserved. Compared to the Fast Fourier transform, it uses a Fast Wavelet transformation, and thus computation duration becomes much shorter. Moreover, small and large wavelets are very effective for individually storing fine and coarse details (Sifuzzaman et al., 2009). Beside these properties, there are many other advantages that can be considered. In these respects, Wavelet transforms are good options to supplement deficiencies of the other methods (Liu, 2010).

The wavelet technique has a very wide range of applications from mathematics and physics to engineering, communications, and biomedical studies. Matlab and Wavelet toolbox are two of the programs that allow the calculation of wavelet transformation coefficients. The toolbox contains several wavelet transforms using wavelet frames such as continuous, discrete, and stationary wavelet transformations[6]. There are also several Wavelet functions such as Haar, Meyer, Morlet, Daubechies, and Mexican Hat Wavelets. Among these, we will only use the Morlet Wavelet transformation for frequency comparison in the following chapter. In brief, Morlet Wavelet is a type of original Continuous Wavelet transformation and is widely accepted as a complex wavelet. It pretends to be a periodic wave-train in which a Gaussian envelope covers a combination of many *sine* waves, and it shifts through the data for analysis. This mother function is defined as:

$$\psi(t) = \frac{1}{\sqrt[4]{\pi}} \Big\{ e^{jw_0 t} - e^{\frac{w_0^2}{2}} \Big\} e^{\frac{t^2}{2}} \ , \tag{3.12}$$

where the term $e^{\frac{w_0^2}{2}}$ represents the correction of the non-zero mean of the complex sinusoid. If w_0 is greater than 5, this term can be ignored. For more detailed information about Wavelet transforms, on-line tutorials can be accessed.

[6] http://www.mathworks.com/discovery/wavelet-transforms.html/

3.6 Discussion

Among the period analysis methods whose working principles are briefly discussed in previous sections, only LS, PDM, and Period04 are usually applied for period detection in this thesis. Wavelet transform is, similar to other methods, a widely-used technique in time variability analysis. Apart from its fast computation ability due to Fast Wavelet transformation and individual storage of fine or coarse signal details, it has interesting features such as localizing in both time and frequency domains. It therefore preserves time information of the data. However, this localization allows the wavelet functions to have limited durations. For this reason, this method is predominantly used in capturing transient flares or short-term periodic signals (Lu et al., 2012). Also, it provides quite consistent results with other analysis techniques such as LS and PDM. For these reasons, wavelet transformations are ignored during the analyses, but the comparison of all methods mentioned is given in Fig. 3.2.

On the other hand, LS, which uses Discrete Fourier transform, converts time series into a linear combination of sinusoidal functions. The algorithm used is based on the transformation of the data from time domain to frequency domain with the help of a linear least-squares fitting of *sine* waves. Thus, LS is more sensitive to sinusoidal variations, and is suitable for analyses of rotating variables such as CP stars. During the Discrete Fourier transformation, it is not important whether or not the data is equally or unevenly spaced, as LS ignores the uneven spacing of the data. Therefore, it prevents spurious or shifted peaks relative to the true frequencies. Moreover, it eliminates the aliasing problem caused by non-uniformly spaced data. Time shifts also do not affect the calculation of transform coefficients. The normalized power in the periodogram provides an exponential probability distribution, and thus the most probable period is compatible with the one with the maximum power. Additionally, LS allows for predicting FAP on the basis of peak intensities in the power spectrum. If this feature is not considered, random fluctuations generated by noise may lead to a false period detection.

Similar to LS, Period04 is a computer program for performing statistical analyses of large astronomic data sets containing gaps. It has a flexible interface that enables multi-frequency detection with a combination of least-squares fitting and the Discrete Fourier transform algorithm. Period04 also provides several tools for extracting individual frequencies from complex time series. Furthermore, it allows for examining amplitude and phase variations as well as for calculating LS and Monte-Carlo uncertainties. Based on these advantages, it can be suitable for

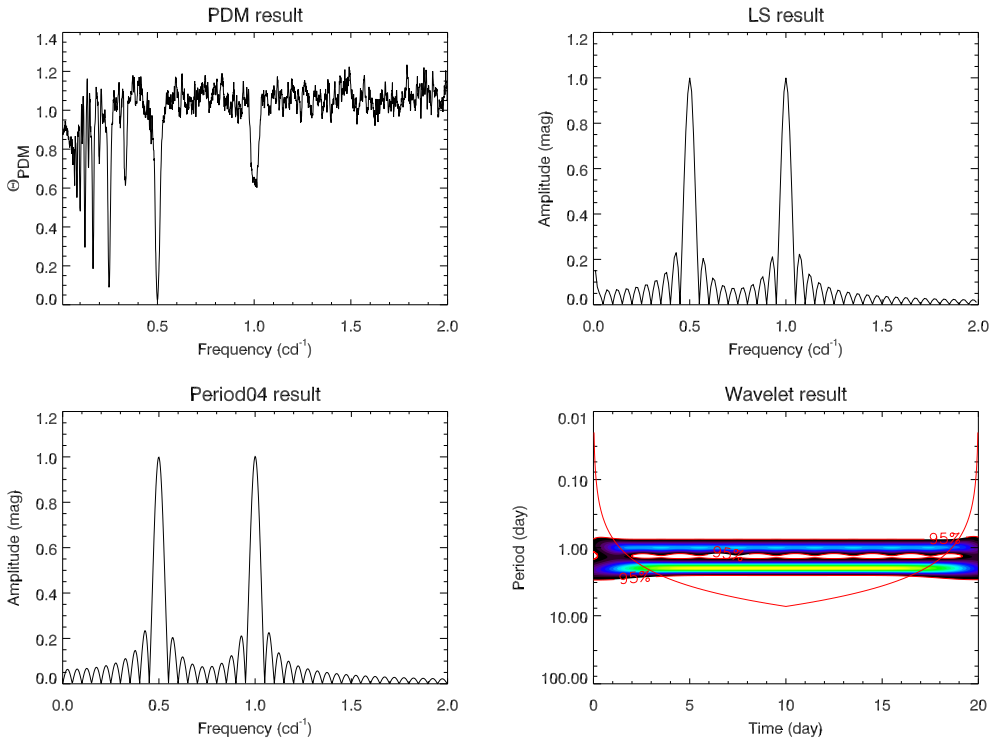

Figure 3.2: A periodogram comparison of four frequency analysis techniques. These power spectra are the analysis results of a synthetic LC with unequal minimum depths, which is produced by the equation of $F(t) = \sum_{i=1}^{n} \left\{ \alpha_i \cos\left(2\pi(t - t_i)/P_{rot}\right) + \beta_i \sin\left(2\pi(t - t_i)/P_{rot}\right) \right\}$, where the variation period is 2 days.

the analyses of stars such as β Cephei, SPB, and δ Scuti types that have complex periodograms.

Last but not least, PDM is principally a data-folding technique. The data is folded according to a series of trial periods, and the variance values of each bin are calculated. The trial period that gives the minimum variance is identified as a possible period of the time series. PDM is a non-parametric method, and does not require any specific trigonometric function for the trial period. Although PDM is a least-squares fit of the data to the mean LC, the LC can have any shape, i.e, a sinusoidal shape is not necessary. It can extract the periodic components from time series having irregular time intervals, poor time coverages, non-sinusoidal variations, or data with high noise (Wang et al., 2014). Therefore, this method can be applied to data of any stellar type.

Chapter 4

Frequency Analyses of Synthetic Light Curves

4.1 Introduction

The most important problem in observational astrophysics is to uncover periodic or nearly periodic signals in noisy time series. This detection is not so difficult for high amplitude frequencies. However, the frequency number increases with decreasing amplitude. It is therefore necessary to distinguish whether a peak is produced due to random fluctuations in the noise spectrum or due to a periodic component (Vaughan, 2010).

A complete analysis of these structures is also quite important in terms of determining the physical and geometrical parameters of the target stars. To analyse such noisy data sets and to find accurate parameters, methods of analysis based on quick, reliable, and rational physical models are needed. This chapter is specially organized toward understanding the effects of noise structures on the true period. For this reason, several synthetic LCs with and without noise are generated. Thus, the period determination abilities of the most effective techniques – PDM, LS, and Period04 – are investigated.

In this chapter, noise types that are common in time series, their basic properties, and the autocorrelation function, which is a method for measuring the strength of these noise structures, are discussed; procedures for the production of synthetic LCs are described; period analysis results are illustrated; and the positive and negative features of the methods discussed are highlighted.

4.2 Noise Types

If the time series comprises a random fluctuation ($f_R(t)$) and a periodic signal ($f_P(t)$), it can be represented with the sum of these components: $f(t) = f_R(t) + f_P(t)$. Since these two components are independent, the power spectrum of $f(t)$ can also be defined as $S_f(t) = S_R(t) + S_P(t)$. In this periodogram, the periodic time series generates narrow lines in which all power is concentrated in only some specific frequencies, whereas the stochastic one displays power spread over many frequencies. As the periodogram of these random fluctuations affects large regions, it is sometimes difficult to separate the real spectrum (Vaughan, 2010).

The most common noise types in astronomy are white (uncorrelated) and red (correlated) noise structures. Uncorrelated noise, $\epsilon(t)$, is comprised of independent random values that show normal Gaussian distribution, and has equal power in every part of the periodogram ($S(t) \propto f^0$). The integration of this power from some finite frequencies to zero frequency leads the power spectrum to be convergent at low frequencies. Conversely, integration towards infinity causes a divergent periodogram at high frequencies. As a result of these two situations, the mean value of the noise converges when it is averaged over longer time intervals (Press, 1978). In order to clean up this type of noise, several well-established statistical procedures – particularly those using the least-squares method, such as the IDL functions *savgol, convol* or *poly_fit* – are frequently used (details can be found in Section 5.2).

Correlated noise can be expressed as:

$$x(t) = a\ x(t - \Delta t) + b\ \epsilon(t) \qquad ; \qquad b = \sqrt{1 - a^2}\ , \tag{4.1}$$

where x is a standardized variable, a is the one-lag autocorrelation of x ($0 < a < 1$), and Δt is the time interval between data points. This noise type exhibits a characteristic slope that diminishes with increasing frequency in power spectrum. This variation is consistent with the power law, given as $S(t) \propto f^{-2}$, even though periodogram of white noise is flat. In other words, correlated noise is the integral of white noise. However, when it is integrated towards infinity, the power spectrum is convergent, and there is no well-defined mean value over long time intervals for this type of noise (Press, 1978). The effects of red noise on LCs can be reduced with filters that use lower-order polynomials (e.g. *savgol* or *poly_fit* with a degree of 2; details can be found in Section 5.2).

4.3 The Auto-correlation Function

The auto-correlation function, expressed as $\rho(L)$, is one of the methods for measuring the mean relation existing between the pairs of points in a time series. Basically, it calculates the covariance of a variable data point at two different times that are separated with a lag L. The auto-covariance function is given as:

$$\gamma(L) = \frac{1}{N-L} \sum_{i=0}^{N-L} (x_i - \overline{x})(x_{i+L} - \overline{x}) \ , \tag{4.2}$$

where N is the number of data points x_i $(i = 0, \ldots, N)$ for a discrete time series, and L is the integer number of data points $(L = 0, 1, \ldots, N)$. If the time series in question is continuous, then L values can be equal to the time difference between two data points (40 minutes for the *HI-1A* data). The normalization of $\gamma(L)$ with the variance of the sample values makes the coefficients of $\rho(L)$ vary between -1 and 1. In this case, a value of or close to 1 indicates that there is a perfect correlation between two points. For the correlation of the first data point with itself, $\rho(0) = 1$ at $L = 0$ (Whittaker, 2013).

For uncorrelated data (white noise), $\rho(0)$ is also 1 at $L = 0$, yet it rapidly decreases. If N is large enough, other coefficients exhibit a normal distribution with the scatter of $1/\sqrt{N}$ around a mean of zero. This type of distribution implies that there is no specific trend in the data. Another important issue is the half-life of the auto-correlation ($\rho(L) = 0.5$). In the case that white noise is dominant in the data, the correlation reaches the half-life within couple of points. Otherwise, it takes longer. An example of such a data set, one that is produced with 720 data points, is given on the first row of Fig. 4.1. The LC, in the form of normalized flux, represents full white noise with $\sigma \sim 0.03$ mmag, which is the average scatter of the raw LCs of the sample stars used in this thesis. In the auto-correlation plot, the red straight line is the mean of zero, the blue dotted line is the half-life, and the region between the blue dash-dotted lines, which are calculated using confidence levels in a normal distribution ($0 \pm 1.96\sqrt{N}$)[7], are the 95% confidence intervals (± 0.07 for this sample) for concluding the significance of the correlations with respect to white noise. If the fluctuations take place within the confidence boundaries, this means that there is no strong correlation between the points (Whittaker, 2013).

On the other hand, the auto-correlation function oscillates at the signal's period for a correlated noise. In Fig. 4.1 (the second row), an exaggerated red noise component with the periodic

[7] http://www.jgsee.kmutt.ac.th/exell/PracMath/Estimat.htm/

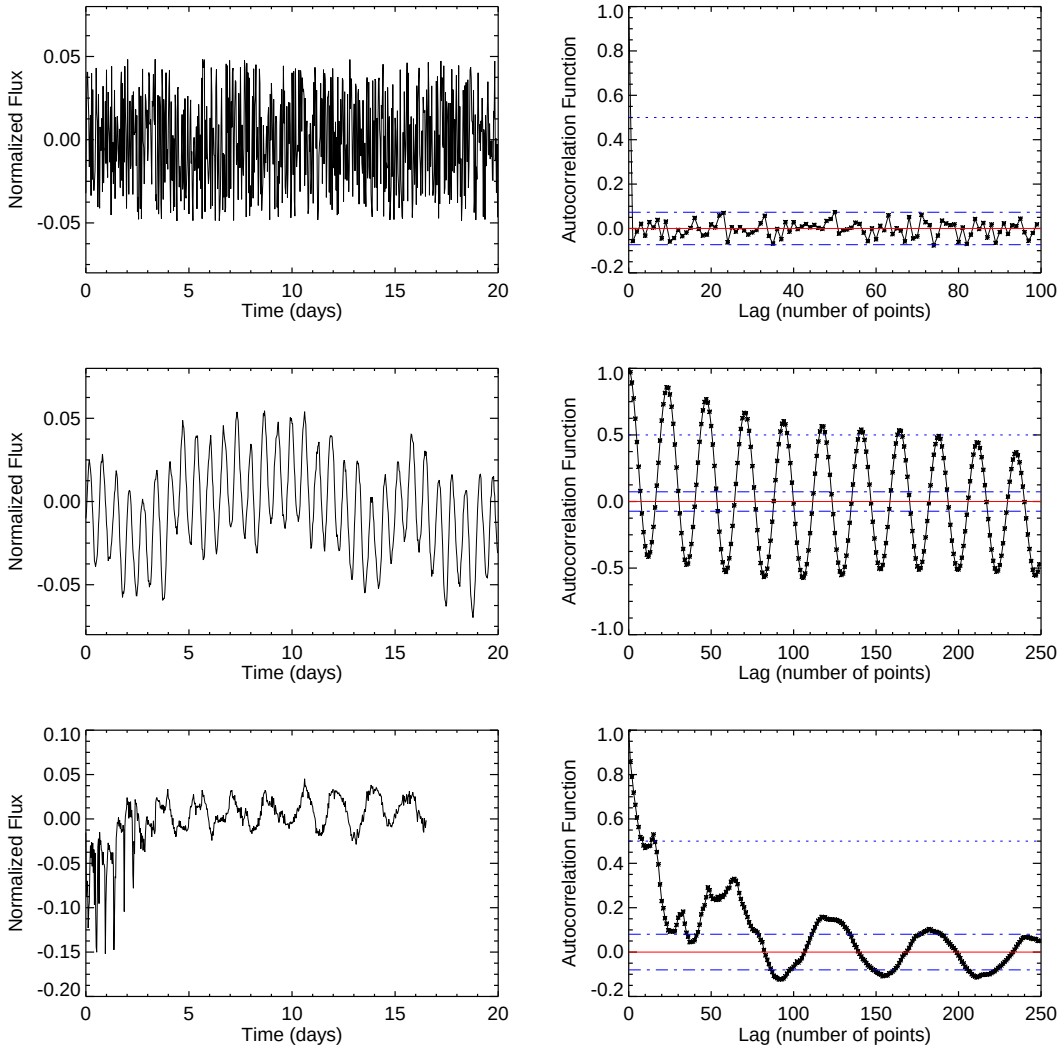

Figure 4.1: The figure presents different types of noise and their auto-correlation functions. A time series for pure white noise (with $N = 720$ and $\sigma = 0.03$ mmag) and its corresponding correlation function is shown in the first row. Due to the dominance of uncorrelated noise, the correlogram rapidly reaches the mean of zero. The fluctuations stay within the 95% confidence boundaries ($\sim \pm 0.07$), which indicate uncorrelated data points. In the second row, an instance of red noise and its corresponding correlogram are illustrated. The explicit sinusoidal variations display a strong correlation between data points separated by 24 points. In the last row, both white and red noise components are seen in the LC of HD 34547, taken in 2008. Its correlogram shows that there is a strong correlation between data points over 5 days ($\sim$ 189 points).

signal of around 0.65 days (around 24 points in the auto-correlation graph) is presented ($\sigma \sim 0.03$ mmag, $N = 720$). The half-life of the function is determined according to the imaginary line that connects consecutive peak points in the plot. This line generally produces an exponential slope. For instance, the function slowly decreases and reaches its half-life at $L = 189$. If white noise is more dominant than the correlated noise in the data, then the slope of this imaginary

line becomes steeper (Whittaker, 2013).

Additionally, white and red noise may affect data at the same time as in the LC of the *STEREO* object HD 34547 (Fig. 4.1, bottom row). The LC is formed of 596 data points with a scatter of around 0.03 mmag. The combination of both noise types can clearly be seen on the auto-correlation graph on the right. Even though the dominance of the uncorrelated noise is observed up to $L = 30$, the existence of the exponential variation shows itself after this lag. The long-scale trend becomes insignificant at $L \sim 185$ (significance level = 0.08). The period of the star of around 1.70 days, corresponding to 61 points, is explicit in figure. In addition, another periodic pattern with a period of 0.55 days is also indicated, but its strength is suppressed by the white noise in time.

4.4 Synthetic Light Curves

The sample stars chosen for subsequent investigations exhibit a wide range of LCs. For a better understanding of the working principles of LS and PDM for different curve types, and for avoiding any mistakes during real data analyses, several synthetic LCs similar to real ones were produced. The effects of noise on periodic modulations were analysed by employing these in this experiment. In addition to these methods, Period04 was also utilized to compare results.

The simplest LC of a variable star shows a perfect sinusoidal variation. For this reason, a basic synthetic LC was, initially, produced by the following equation:

$$m(t) = \sum_{i=1}^{n} A_i cos\big\{2\pi[f_i(t - t_i) - \phi_i]\big\} \ , \tag{4.3}$$

where $m(t)$ is the theoretical flux, A_i is the amplitude of i-th sinusoidal, f_i is the frequency, ϕ_i is the phase, and $(t - t_i)$ is the time variable. A noise component (white noise), which was derived from a Gaussian distribution with a mean of zero and a standard deviation multiplied by the sigma value of the most noisy raw LC observed in the sample stars ($\sigma = 0.3$ mmag), was added to the equation to obtain more realistic results. A set of simulated curves was also generated by twice the original sigma value, $\sigma = 0.6$ mmag, for comparison. In extreme cases, the red noise component, which was produced based on Eqn. 4.1, was used. Therefore, the effects of varying noise level on a frequency were investigated. For the convenience of further representations, the lowest and the highest error values were referred to as 0.3 and 0.6 in figures, respectively.

Furthermore, there must be a carefully chosen observation strategy related to the purpose of

analysis. In this thesis, the intention is to observe many oscillation cycles in order to perform a reasonable and accurate frequency analysis. Therefore, each observation interval (cadence), as well as other observational parameters, is crucial. For instance, the *STEREO* uses a 40-minute cadence to be able to detect the smallest variabilities. Considering this, time sampling the same as that of the real *STEREO* data was used in simulations.

Another important issue for creating a synthetic LC is observation durations that are directly proportional to photon statistics. It is the essential limitation in frequency measurement, since the travel time and detection of photons are scattered processes. If the number of detected photons is N, standard deviation will statistically be $\sqrt{N}$. Thus, the SNR will be $N/\sqrt{N} = \sqrt{N}$, which indicates that longer observation durations lower the error rate. Since all data were obtained from the *STEREO* satellite that has observed target stars for nearly 20 days in a year, observation duration was adjusted to 20 days for obtaining realistic results.

As discussed in Section 4.1, the number of frequencies increases with decreasing amplitude, and a real signal may be confused with noise, or vice versa. Hence, the estimation of the FAP is also an important point for such an investigation. The significance level can easily be calculated for evenly spaced data with the help of LS. However, this calculation is not as simple for non-uniform data sets, and the four-sigma limit is generally used for the approximation of the significance level (Breger et al., 1993). Even though this method is quite useful and reasonable for many observations, in particular for ground-based data sets, it is unfortunately an empirical rule and must be questioned for space-based data. For instance, Koen (2010) shows that data characteristics such as the number, cadence, and total duration of observations as well as the frequency interval that is searched have some influence on the significance level. Koen (2010) also suggests that the four-sigma rule tends to underestimate the significance of a single frequency, meaning that lower amplitude peaks are not considered as significant by this rule.

Therefore, a separate significance level, z, for a synthetic LC having $N = 720$, was calculated with a 99% confidence by using:

$$z = -\sigma_0^2 \; ln\Big(1 - (1 - P(z))^{1/N_{id}}\Big) \; . \tag{4.4}$$

In this equation, $\sigma_0 = A_m\sqrt{N}/2$; where A_m is the mean amplitude of the amplitude spectrum where there is no significant signal (pure white noise). Since an LS method, in which power was not normalized by noise variance, was used during the analyses, the σ_0 value was added

to Eqn. 3.7. The N_{id} was also found from $N/2$. In Eqn. 4.4, z is in the unit of power, and hence the corresponding amplitude was derived from $A_z = 2\sqrt{z/N}$ (Balona, 2014). Since the fundamental parameters of the synthetic LCs were same, the z values were estimated to be approximately 0.07 and 0.13 mmag for noise levels of 0.3 and 0.6, respectively. In addition, the four-sigma value was computed based on the amplitude A_m. This value was multiplied by 4.0 to specify the significance level. The four-sigma levels were roughly calculated as 0.08 and 0.16 mmag for noise levels of 0.3 and 0.6, respectively.

Taking all key points into consideration, frequency analyses of synthetic LCs were performed in six different cases. The power spectra of PDM, LS, and Period04 methods are given for these cases in the corresponding figures. Each figure consists of 4 rows and 3 columns. In the first row, synthetic LCs produced based on different functions are plotted. The second, third, and fourth rows display Period04, PDM, and LS periodograms, respectively. Each column shows LCs with different noise levels and their analyses. In the first column, clean curves (noise = 0.0) and their analysis results are presented. Noise level increases in the second and third columns. Additionally, the four-sigma and z significance levels are respectively represented by blue and red straight lines on the figures.

4.5 Results

4.5.1 Case 1

A simple sinusoidal LC was generated by the following function:

$$m(t) = \sum_{i=1}^{n} A_i \cdot \cos\left\{2\pi\big((t - t_i)/P\big)\right\} + \epsilon(t) \ , \tag{4.5}$$

where P was the variation period with an amplitude of A. These were assumed to be 1.0 day and 1.2 mmag for all simulated LCs, and $\epsilon(t)$ was the noise component.

All methods gave rather good results for the noiseless curve. However, PDM produced

Table 4.1: Analysis results of the period determination methods for Case 1.

LC	**Noise Level**	**PDM (cd^{-1})**	**Scargle (LS) (cd^{-1})**	**Period04 (cd^{-1})**	**4σ (mmag)**	**z (mmag)**
Case 1	**0.0**	1.0 ± 3.0E-5	1.0 ± 1.0E-8	0.99 ± 2.0E-9		
	0.3	0.99 ± 3.0E-5	1.0 ± 3.3E-4	0.99 ± 3.4E-4	0.08	0.07
	0.6	1.0 ± 2.9E-3	1.0 ± 6.9E-4	0.99 ± 7.9E-4	0.16	0.13

many aliases due to its fitting procedure. Unlike PDM, LS found only one strong peak at the correct frequency; no other signal appeared in the periodogram. The error value of LS was better than that of PDM (Table 4.1). To check the effects of noise level on the results, the noise was gradually increased. As shown in Fig. 4.4 (on page 75), the frequency intensity in the PDM periodogram was inversely correlated with noise, although the amplitudes in LS slightly increased from 1.20 to 1.21 mmag for noise levels of 0.3 and 0.6. Further, the LS error was ten times more sensitive than the one found by PDM in the noisiest case, whereas PDM gave a better error value for noise level of 0.3.

The four-sigma and z significance values are also presented in Fig. 4.4. They were quite close to each other in noise level of 0.3 ($4\sigma = 0.08$ mmag; $z = 0.07$ mmag). On the other hand, the difference grew with increasing noise as the 4σ value went up to 0.16 mmag in noise level of 0.6, whereas the z value became 0.13 mmag. All these results are given in Table 4.1.

4.5.2 Case 2

The shape of the LC was changed in order to produce a slightly more complicated time series. To do this, a phase of $\phi = \pi/2$ was applied to the *cosine* in the Eqn. 4.3, and thus the equation was transformed into a *sine* function, which was derived as:

$$\begin{aligned} m(t) = & \sum_{i=1}^{n} A_i \cos\Big\{2\pi(t-t_i)/P - \phi_i\Big\} \\ = & \sum_{i=1}^{n} \Big\{A_i \cos\phi \ \cos\big(2\pi(t-t_i)/P\big) + A_i \sin\phi \ \sin\big(2\pi(t-t_i)/P\big)\Big\} \\ = & \sum_{i=1}^{n} \Big\{\alpha_i \cos\big(2\pi(t-t_i)/P\big) + \beta_i \sin\big(2\pi(t-t_i)/P\big)\Big\} \ , \end{aligned} \tag{4.6}$$

where α and β are amplitudes.

In this way, a curve with two nearly-equal minima was produced. For the noiseless data, only PDM found the correct period with high precision. LS detected a value of around 2.0 cd^{-1}

Table 4.2: Analysis results of the period determination methods for Case 2.

LC	**Noise Level**	**PDM ($\mathbf{cd}^{-1}$)**	**Scargle (LS) ($\mathbf{cd}^{-1}$)**	**Period04 ($\mathbf{cd}^{-1}$)**	**4σ (mmag)**	**z (mmag)**
Case 2	**0.0**	1.0 ± 3.5E-5	1.0 ± 7.8E-8	0.99 ± 1.6E-8		
	0.3	1.0 ± 3.9E-4	1.0 ± 2.2E-4	0.99 ± 2.1E-3	0.09	0.07
	0.6	0.99 ± 3.3E-4	1.01 ± 3.9E-4	0.99 ± 4.3E-3	0.16	0.13

since it could not distinguish the difference between the minima. Similarly, both methods found twice the actual value in the noisy LCs instead of determining the correct period. However, as seen in Fig. 4.5 (on page 76), the periodograms had a peak at the accurate frequency, although the LS periodogram showed a quite weak signal. To obtain the expected value, the frequency range was restricted around 1.0 cd^{-1} and the data was re-analysed (Table 4.2). In addition, the four-sigma was almost same with the z value for the noise level of 0.3. However, it indicated a higher significance level than the z value for the most noisy LC, similar to Case 1.

4.5.3 Case 3

The investigation was carried a step further, and another simulated LC model was obtained by using the Eqn. 4.6. In this case, equation coefficients were changed, and a curve with unequal minima was generated. During the analyses, only PDM managed to find the correct period for the noiseless data set. PDM also detected a weak frequency at 2.0 cd^{-1}, compared to the dominant one. On the other hand, the most dominant peak was at 2.0 cd^{-1} in the LS periodogram, and the peak at the correct period was almost as strong as the main peak.

Table 4.3: Analysis results of the period determination methods for Case 3.

LC	**Noise Level**	**PDM (cd^{-1})**	**Scargle (LS) (cd^{-1})**	**Period04 (cd^{-1})**	**4σ (mmag)**	**z (mmag)**
Case 3	**0.0**	1.0 ± 3.0E-5	0.99 ± 1.0E-7	0.99 ± 4.8E-9		
	0.3	1.0 ± 1.2E-4	0.99 ± 1.6E-4	0.99 ± 4.8E-4	0.08	0.07
	0.6	0.99 ± 1.2E-4	0.99 ± 4.5E-4	0.99 ± 9.6E-4	0.16	0.13

The same situations were also seen in the noisy LCs (Fig. 4.6; on page 77). To determine the expected value in LS periodograms, frequency interval was restricted around 1.0 cd^{-1}, and calculations were re-performed. As a result, the accurate periods were obtained. In terms of the period errors, PDM gave comparably better values for the noisy curves (Table 4.3). The four-sigma and z significance levels were also calculated. It was found that both values were quite close to each other for the LCs with 0.3 noise level whereas the difference increased with increasing noise, as seen in Table 4.3 and Fig. 4.6.

4.5.4 Case 4

Following the latest case, much more realistic LCs began to be generated. For this, the writing of a new Fourier series, which would easily represent harmonics in the LC, was attempted, instead of using previous simple equations. Some other terms were therefore added to the series, and

the new equation was derived as:

$$m(t) = \sum_{i=1}^{n} \Big\{ \alpha_i \sin\big(2\pi(t-t_i)/P\big) + \beta_i \cos\big(2\pi(t-t_i)/P\big) + \gamma_i \sin\big(4\pi(t-t_i)/P\big) + \delta_i \cos\big(4\pi(t-t_i)/P\big) \Big\} , \tag{4.7}$$

where γ and δ are also amplitudes. The LC produced by the new Fourier series was comprised of a primary maximum and a hump superimposed on its descending branch. As seen in Fig. 4.7 (on page 78), this extra structure was also detectable in the noisy curves.

Similar to Case 3, the PDM periodogram gave the correct period in the first trial, and weak effects of the hump appeared at the frequency of 2.0 cd^{-1} (Fig. 4.7). In addition, LS was also able to determine the accurate frequency. However, unlike PDM, the strength of the additional peak was significantly high in the LS periodogram. Although the additional structure in the LC affected the main frequency, particularly in the most noisy situation, both LS and PDM found the expected result easily. In addition, it would be useful to note that the error value of the LS period was greater than that of PDM for the noise level of 0.3, even though it was smaller for the noiseless time series. In the noisiest situation, both methods generated quite close error values (Table 4.4). Comparing the significance levels, the four-sigma and z values were similar to the previous cases.

Table 4.4: Analysis results of the period determination methods for Case 4.

LC	**Noise Level**	**PDM ($\mathbf{cd}^{-1}$)**	**Scargle (LS) ($\mathbf{cd}^{-1}$)**	**Period04 ($\mathbf{cd}^{-1}$)**	**4σ (mmag)**	**z (mmag)**
Case 4	**0.0**	1.0 ± 1.0E-4	1.0 ± 8.6E-5	1.0 ± 6.0E-9		
	0.3	1.0 ± 9.0E-5	1.0 ± 1.3E-4	1.0 ± 5.2E-4	0.08	0.07
	0.6	1.0 ± 1.2E-4	1.0 ± 1.8E-4	1.0 ± 1.0E-3	0.16	0.13

4.5.5 Case 5

Two different levels of random (white) noise were used for generating LCs until this case. However, as previously mentioned, not only uncorrelated noise but also red noise collectively constituted the main problem in the astronomical time series. To examine the effects of this component on data, Eqn. 4.5 given in Case 1 was combined with the red noise model ($x(t)$) produced by Eqn. 4.1. In this equation, $\epsilon(t)$ was the white noise multiplied by $\sigma = 0.3$ mmag. In Fig. 4.8 (on page 79), the simple sinusoidal with $\epsilon(t)$, and the one with the red noise component are presented in the first and second columns.

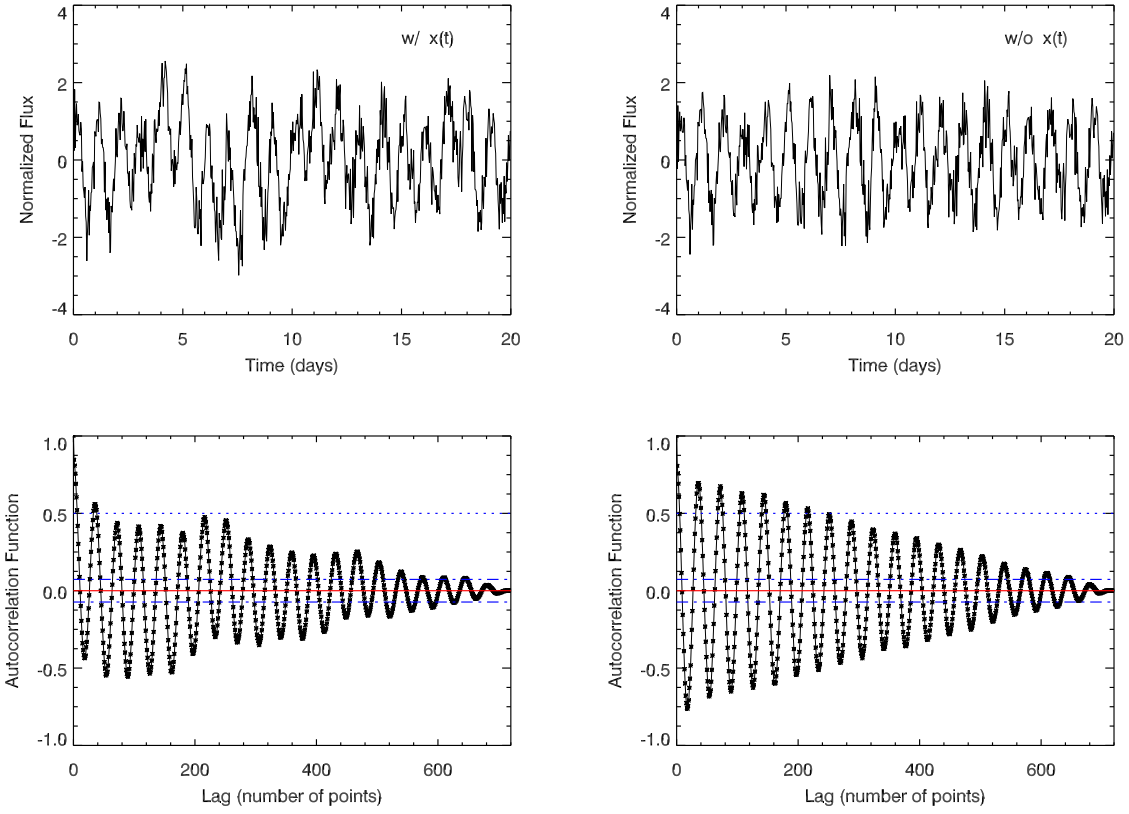

Figure 4.2: Auto-correlation functions of contaminated (the first column) and clean (the second column) LCs are presented in the figure. The imaginary line of the contaminated correlogram exhibits an exponential decrement. This structure rapidly falls below the half-life, which means white noise predominated over red noise. The recurrent variation in every 200 lags and 1-day cycles ($\sim$ 36 lags) is also observable. On the right side, the LC cleaned from the long-term variations is given. Its auto-correlation function displays a steeper slope.

As seen from the figure, the red noise component slightly distorted the simple sinusoidal LC. Even though the 1-day period was explicit, the additional long-term variations attracted attention. These structures were detected by both PDM and LS methods at around 0.15 and 0.30 cd^{-1}. These peaks were detectable but weak in the LS amplitude spectrum compared to the main frequency. However, they were still above both four-sigma and z significance levels. On the other hand, PDM was more sensitive to long-term variations rather than the expected frequency, and the peak at 0.30 cd^{-1} was dominant in its periodogram.

Such a noise type was detected with the help of the autocorrelation method. The contaminated LC and its correlogram are given in Fig. 4.2 (the first column). As seen in figure, the imaginary line exhibited an exponential decline. However, this structure rapidly decreased the half-life, meaning that white noise predominated over red noise. Also, it was possible to observe

recurrent variation in every 200 lags (~ 0.30 cd^{-1}) in addition to the 1-day cycles (~ 36 lags).

Since these low-frequencies that were detected were spurious, they must be removed in order to generate better results. To this end, the time series were fitted by a low-order polynomial as discussed in Section 4.2, and a curve without or with a reduced red noise component was derived. As presented in the last column of Fig. 4.8, PDM and LS were also cleaned from the artificial structures, and both techniques identified the expected frequency. Their error values of around 10^{-3} cd^{-1} were quite comparable.

Furthermore, comparison of the significance levels in the periodograms showed that the simple sinusoidal LC with $\epsilon(t)$ had quite close levels ($z = 0.07$ mmag, $4\sigma = 0.08$ mmag). However, these levels increased with the increasing noise values. Even though the four-sigma and z were around 0.09 mmag for the contaminated LC, they became 0.12 mmag for the cleaned curve. This indicated that the additional noise component within red noise was added to the LC. Thus, the overall white noise level increased and led to an increment in significance levels.

4.5.6 Case 6

In this case, red noise and synthetic LC models were slightly improved. To mimic a time series observed by the *STEREO*, a different data set was generated by using several sinusoidal variations consisting of randomly chosen frequencies and amplitudes. This simulation was comprised of ten frequencies that were also randomly distributed between 0 and 12 cd^{-1} on the periodogram, which was roughly the period interval of B-type or δ Scuti-type stars (Fig. 4.9; on page 80). The main frequency was at 6.93 cd^{-1} with an amplitude of 1.73 mmag, and the less intense peak was at 3.80 cd^{-1} (A = 0.34 mmag). Five frequencies were between 4 and 12 cd^{-1}, four of which had an amplitude value greater than 1.0 mmag. The lowest frequency was located at 0.32 cd^{-1}. The chosen frequency values and their amplitudes are given in Table 4.5.

Frequency analyses of the original curve revealed that the LS method was more successful compared to PDM, since PDM failed to detect the expected frequencies even though there was no noise component in the time series. Accordingly, PDM determined the most dominant peak at 16.85 cd^{-1}, whereas it was at 6.93 cd^{-1} in the LS periodogram. The other intense peaks were at 1.80, 8.60, 11.35, and 13.00 cd^{-1} in the PDM power spectrum. However, three of them were spurious signals. These findings therefore provided an idea about PDM's reliability in multi-frequency analyses. On the other hand, the original time series was pre-whitened to determine the most significant frequencies by using the LS method. This process was repeated until the

highest amplitude was no longer significant ($z = 0.24$ mmag). As a result, two alias frequencies at around 6.89 ($f_1 - 0.027$) and 6.95 ($f_1 + 0.027$) cd^{-1}, which were most probably a consequence of the data sampling, were observed. This pre-whitening process was also repeated with the help of Period04. Due to its multiple fitting ability, Period04 did not produce any artificial peaks on the periodogram.

The effects of both white and red noise components were also investigated as in Case 5. Firstly, a random noise component with a Gaussian distribution ($\epsilon(t)$) was generated. It was then multiplied by $\sigma = 0.3$ mmag, and added to the data (Fig. 4.9, second column). Based on this noise and other parameters, 4σ and z significance levels were calculated as 0.23 and 0.24 mmag, respectively. During the frequency analysis, it was observed that the frequencies obtained by the LS method were above the significance levels, but that the peaks at 0.32, 0.93, 2.22, and 3.80 cd^{-1} were quite close to these levels. Moreover, recurring pre-whitening procedures displayed the alias frequencies at 6.89 and 6.95 cd^{-1}. However, these peaks were not seen among the Period04 results as previously mentioned. The PDM method could not succeed in finding the correct period again by detecting the main frequency at 16.85 cd^{-1}.

In the final and most important test, a red noise component ($x(t)$) was added to the original LC by making use of the power law. LS frequency analysis showed that the known frequencies at the low-frequency region were significantly affected by the noise, and that some spurious peaks, such as the ones at 0.08, 0.15, and 0.52 cd^{-1}, developed in the same region. Among them, the amplitude of the peak at 0.15 cd^{-1} was far above the significance levels (marked in Table 4.5), while intensities of 0.08 and 0.52 cd^{-1} were slightly significant. In addition to this, the real peak at 0.93 cd^{-1} was above the z level, but remained below the 4σ. The frequency at 0.32 cd^{-1} was lost within the noise.

As discussed in Section 4.2, it may not be possible to properly distinguish red noise from the data, but its effects can be reduced using certain functions. Given this, some trials were performed in order to correct this component. At first, the long-term variations were fitted with a smoothing function, and the removal of the red noise effect was attempted. However, this resulted in losing the real frequencies at 0.32 and 0.93 cd^{-1}. Thus, another method, which was a least-squares fit to a logarithmic periodogram, was used (Vaughan, 2005).

If it is suspected that there is a power law in the power spectrum, then the parameters of interest are the slope of the spectrum (α) and the normalization coefficient (β). One of the simplest ways to estimate these parameters is to fit the raw periodogram with a model in the form

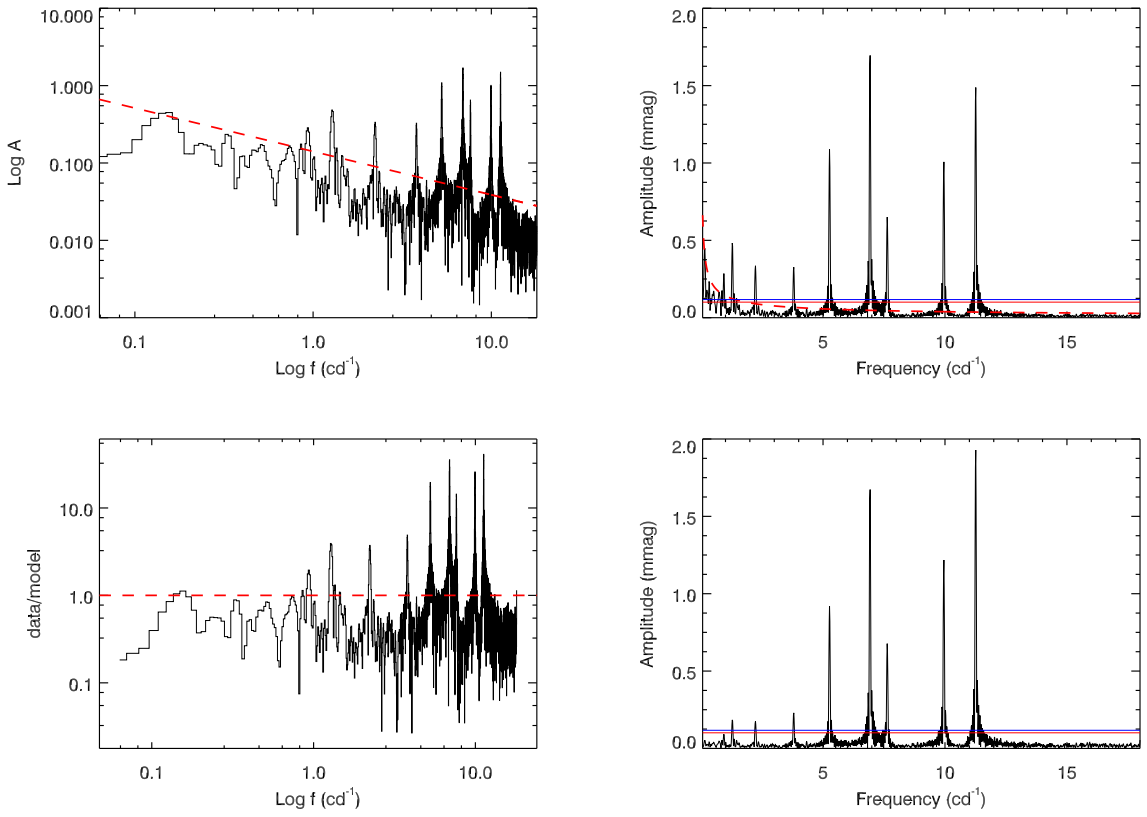

Figure 4.3: Raw and cleaned logarithmic spectra and related periodograms are presented in the figures. On the top row, the slope of the spectrum indicates that there is a red noise component in the LC. So, a least-squares method is applied by fitting a linear function to the $log - log$ data (red dashed line) (top left). This fit is also shown in the normal periodogram by an exponential red line (top right). On the bottom, the logarithmic spectrum is divided by the fit, and the red noise component is removed or at least reduced (bottom left). As seen in the normal periodogram, the effect of red noise on the low frequencies is fixed (bottom right).

of $P(f) = \beta\ f^{-\alpha}$ using the least-squares method. However, the problem is that the periodogram exhibits non-Gaussian distribution around the true underlying spectrum. For this reason, the logarithm of the periodogram is fitted to deal with this problem. The great benefit of working on a logarithmic scale is that the power law becomes a linear function ($logP(f) = log(\beta) - \alpha log(f)$). Therefore, a least-squares fitting procedure was used for calculating the parameters by fitting a linear function to the $log - log$ plot. This plot and the best fit are presented in Fig. 4.3.

The $log - log$ plot of the raw periodogram is given in the upper-left section of the figure. The least-squares fit is represented by the red dashed line. The same line is also displayed in the original periodogram on the upper right. The effect of the correlated noise on the data can be clearly observed in this figure. In the bottom row, the logarithmic periodogram was divided by the linear fit, and the noise effect was removed or at least reduced. Thus, it was expected

Table 4.5: Randomly produced frequencies and their amplitudes (original), along with the analysis results of the contaminated and corrected LCs are given in the table.

	original		**original** + $\epsilon(t)$		**original** + $x(t)$		**corrected**	
	F (cd^{-1})	A (mmag)	F (cd^{-1})	A (mmag)	F (cd^{-1})	A (mmag)	F (cd^{-1})	A (mmag)
f_1	6.9253	1.73	6.9236(2)	1.73(2)	6.9238(5)	1.73(3)	11.2600	1.93
f_2	11.2580	1.50	11.2548(3)	1.50(2)	11.2549(6)	1.50(3)	6.9200	1.61
f_3	5.2668	1.10	5.2653(4)	1.12(2)	5.2648(8)	1.12(3)	9.9500	1.22
f_4	9.9527	1.02	9.9499(4)	0.99(2)	9.9500(9)	0.98(3)	5.2700	0.82
f_5	7.6351	0.66	7.6330(6)	0.67(2)	7.6329(13)	0.67(3)	7.6300	0.68
f_6	1.2807	0.51	1.2815(8)	0.51(2)	1.2819(17)	0.50(3)	1.2800	0.18
f_7	0.3214	0.42	0.3217(11)	0.38(2)	0.1495(17)*	0.55(3)	3.8000	0.23
f_8	0.9323	0.37	0.9312(12)	0.36(2)	2.2239(25)	0.34(3)	2.2200	0.18
f_9	2.2229	0.35	2.2215(12)	0.35(2)	3.7966(27)	0.32(3)	0.9300	0.09
f_{10}	3.7957	0.34	3.7960(14)	0.32(2)	0.9333(30)	0.29(3)	0.3200	–

*: This is a spurious frequency that arises from the addition of red noise.

that the amplitude spectrum desired would be obtained (Fig. 4.3, bottom right).

However, this removal caused different effects on low and high frequencies, which prevented the derivation of the original LC. For instance, the intensities of the frequencies at 9.95 and 11.26 cd^{-1} increased around 20% whereas the other peaks lost power, and the peak at 11.26 cd^{-1} became the main frequency after the amplitude increments. Due to the fact that the red noise was more dominant in the low frequencies, its removal also led the amplitude of 0.93 cd^{-1} to fall below the significance levels, and the amplitudes of 2.20, and 3.80 cd^{-1} to be closer to the levels. Additionally, the real frequency at 0.32 cd^{-1} still could not be obtained. The overall changes in frequencies and their intensities are given in Table 4.5. According to these results, it was considered that even if the procedure applied to the time series was simple, it left significant impacts on the real periodogram and substantially changed the original results.

4.6 Discussion

In this chapter, some noise types seen in time series, their characteristics and detection methods were introduced. Further, their effects on real data were investigated by generating several synthetic LCs. Finally, the positive and negative features of PDM and LS were probed.

Firstly, the properties of time series derived from the *STEREO* were replicated to mimic real LCs during the production of simulated data. Accordingly, the observation duration and cadence were adjusted as 20 days and 40 minutes, respectively, which resulted in a data set with 720 data points and a Nyquist frequency of around 18 cd^{-1}. With the help of these parameters and various Fourier series, six different LCs, five of which were mono-periodic and one of which was multi-periodic, were created.

In the later stages, two different levels of white noise were added to these data. Taking

Table 4.6: Overall results of PDM and LS methods for all six cases are presented in the table. The frequencies correctly found (c.f.) and the smallest sigma values (s.s.) are shown with bold check marks. The PDM method was unsuccessful at Case 2 with noise levels of 0.3 and 0.6 as well as at Cases 5 and 6. On the other hand, LS could not find the true frequency for Cases 2 and 3.

Method		**Case 1**			**Case 2**			**Case 3**			**Case 4**			**Case 5**	**Case 6**		
		0.0	0.3	0.6	0.0	0.3	0.6	0.0	0.3	0.6	0.0	0.3	0.6	red	0.0	0.3	red
LS	c.f.	✓	✓	✓	–	–	–	–	–	–	✓	✓	✓	✓	✓	✓	✓
	s.s.	✓	–	✓	✓	✓	–	✓	–	–	✓	–	–	–			
PDM	c.f.	✓	✓	✓	✓	–	–	✓	✓	✓	✓	✓	✓	–	–	–	–
	s.s.	–	✓	–	–	–	✓	–	✓	✓	–	✓	✓	✓			

advantage of the noise values and LC parameters, the significance levels (z and 4σ) of the signals were estimated, and their variations were examined for six cases. Additionally, a red noise component was derived based on the power law, and its effects on simulated LCs were studied.

The overall results obtained from PDM and LS analyses are presented in Table 4.6. In the table, the ability to find the correct frequency (c.f.) and to calculate the smallest sigma value (s.s.) in different cases is given by bold check marks for both methods. According to this, both methods detected an equal number of true periods in total. However, the results varied depending on different cases and noise levels. For instance, the PDM method was unsuccessful at correctly analysing LCs with nearly-equal minima in the noise levels of 0.3 and 0.6 as well as LCs with red noise – Case 5 and Case 6. On the other hand, LS could not find the true frequency for LCs with nearly-equal and unequal minima, which meant that the LS method could not exactly detect the differences in minima. However, it was seen that LS was suitable for determining multi-frequencies. The only problem here was that LS produced alias frequencies as a result of a pre-whitening procedure in the periodogram. Therefore, it was considered that Period04 was more appropriate for such analyses, since it could perform multi-fitting to a complex amplitude spectrum such as that of δ Scuti stars.

Furthermore, PDM dominated slightly over LS in estimating the error values. Based on Table 4.6, PDM gave the smallest error values for seven cases. The most notable situation was that PDM generally detected the closest values to the correct frequency in noisy LCs. Additionally, although both methods had unique features, it was clear that they also displayed some deficiencies for different LCs and noise levels. Since they were seen to be complementary to each other, it would be better to use both methods in further analyses.

Comparing z and 4σ significance levels, it was observed that both levels were mostly close to each other, even for the noisy time series. However, 4σ values were slightly greater than those of the z for all cases. They rose with increasing noise levels, and showed that there was a possibility to fail in picking up real low-amplitude frequencies. On the other hand, it was known that the number of frequencies increased with decreasing amplitude. Among low-amplitude peaks, it was possible to observe alias frequencies being produced as a result of Fourier fitting, as expressed in Balona (2014). These residuals had significant amplitudes, which might be considered as real, in high SNR space missions, and led to the observance of more frequencies than the expected number (Poretti et al., 2009). Therefore, in addition to the four-sigma, z significance level was also considered for deciding whether a signal was real or not during the analyses.

Finally, the effects of red noise on mono- and multi-frequencies were investigated. According to Blomme et al. (2011), the existence of red noise in stellar signals indicated stochastic, chaotic, or quasi-periodic effects. The physical source of red noise in early-type stars was not clear, but it was suggested that the red noise could come from either a sub-surface convection layer, granulation, or non-homogeneities in the stellar wind. Based on these speculations, it is possible to encounter such a noise component in analyses of Be- or δ Scuti type stars. However, the purpose of this study is to investigate pulsational properties of these stars rather than study long-term variations. As discussed in Case 6, it is not easy to completely remove red noise from periodogram. The real frequencies in both low- and high-frequency regions are negatively affected during the removal. Therefore, long-term variations can be cleaned by using a smoothing function instead of working on $log - log$ periodograms in further analyses. In this case, an additional important point should be considered: if the spectrum is smoothed, this will change the statistics, and, in turn, the required false-alarm threshold level. If a running-mean smoothing function is performed, the appearance of the data is improved; however the number of independent data points is reduced (each smoothed value depends on the original values in adjacent points in the time series). This then reduces the number of independent frequencies in the periodogram. For this reason, as discussed in section 4.2, the *poly_fit* function can be taken into account for further analyses.

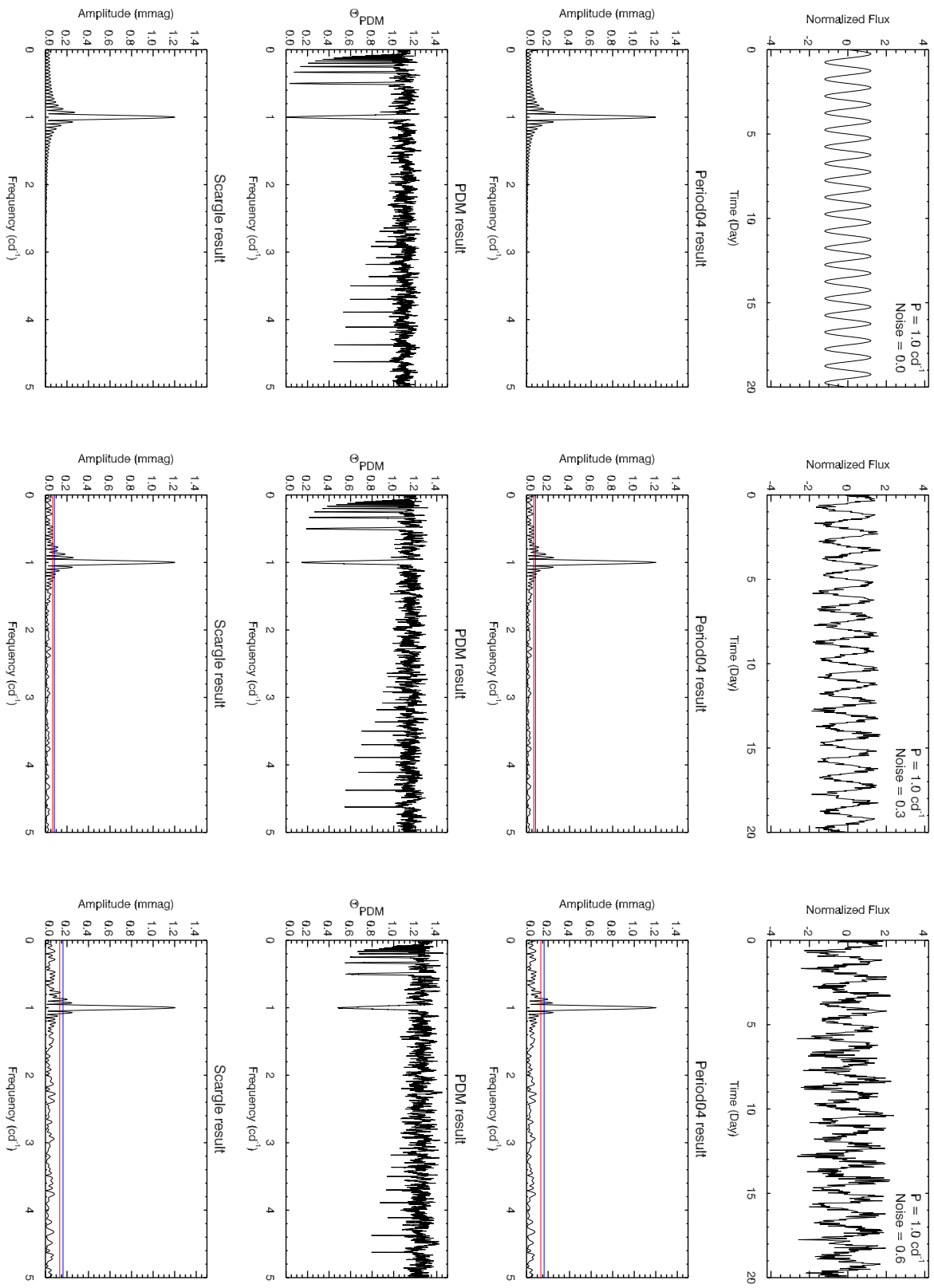

Figure 4.4: Case 1: Clear and noisy synthetic LCs of a simple sinusoidal and related period analysis results.

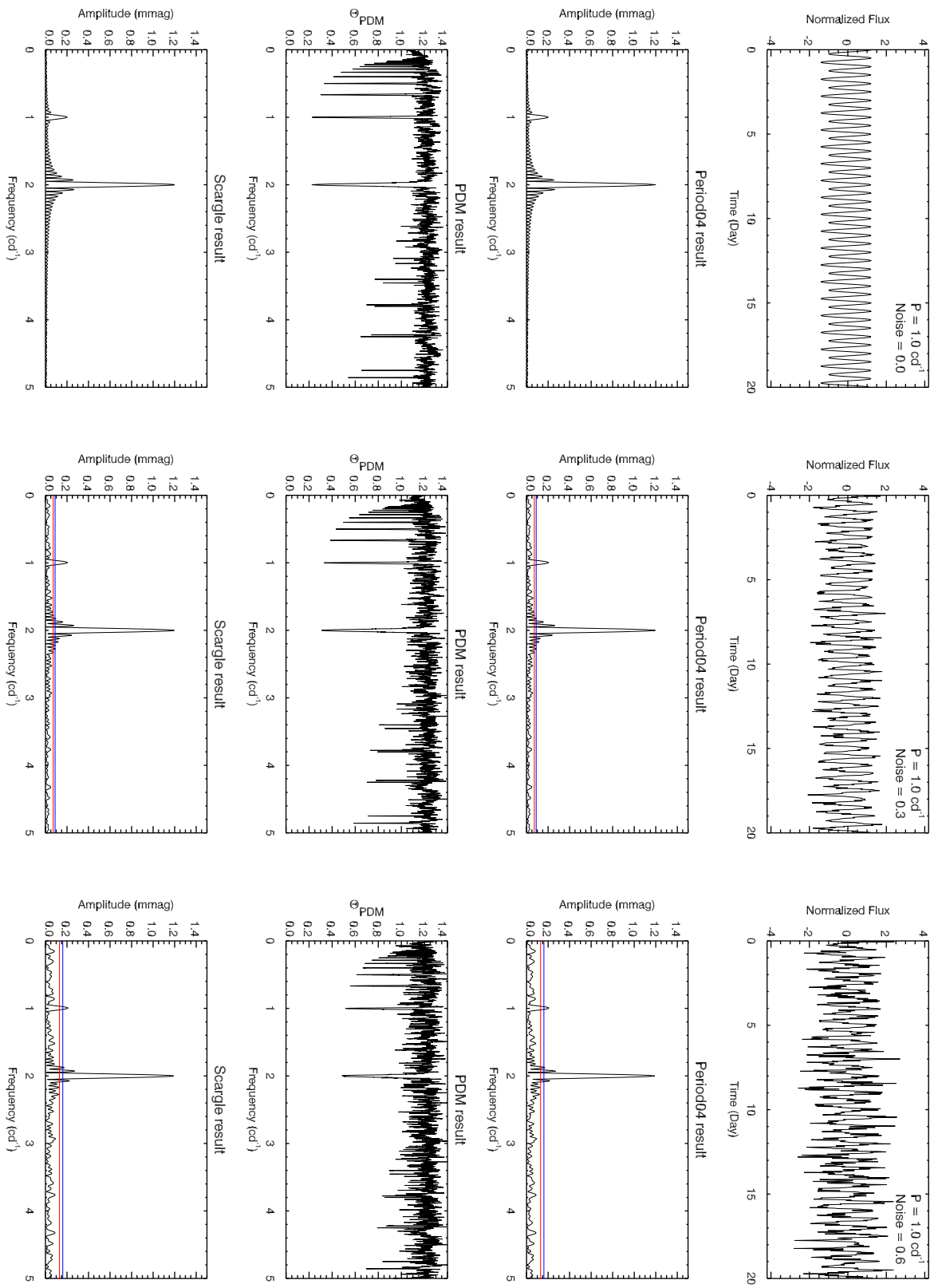

Figure 4.5: Case 2: Clear and noisy synthetic LCs with nearly-equal minima and related period analysis results.

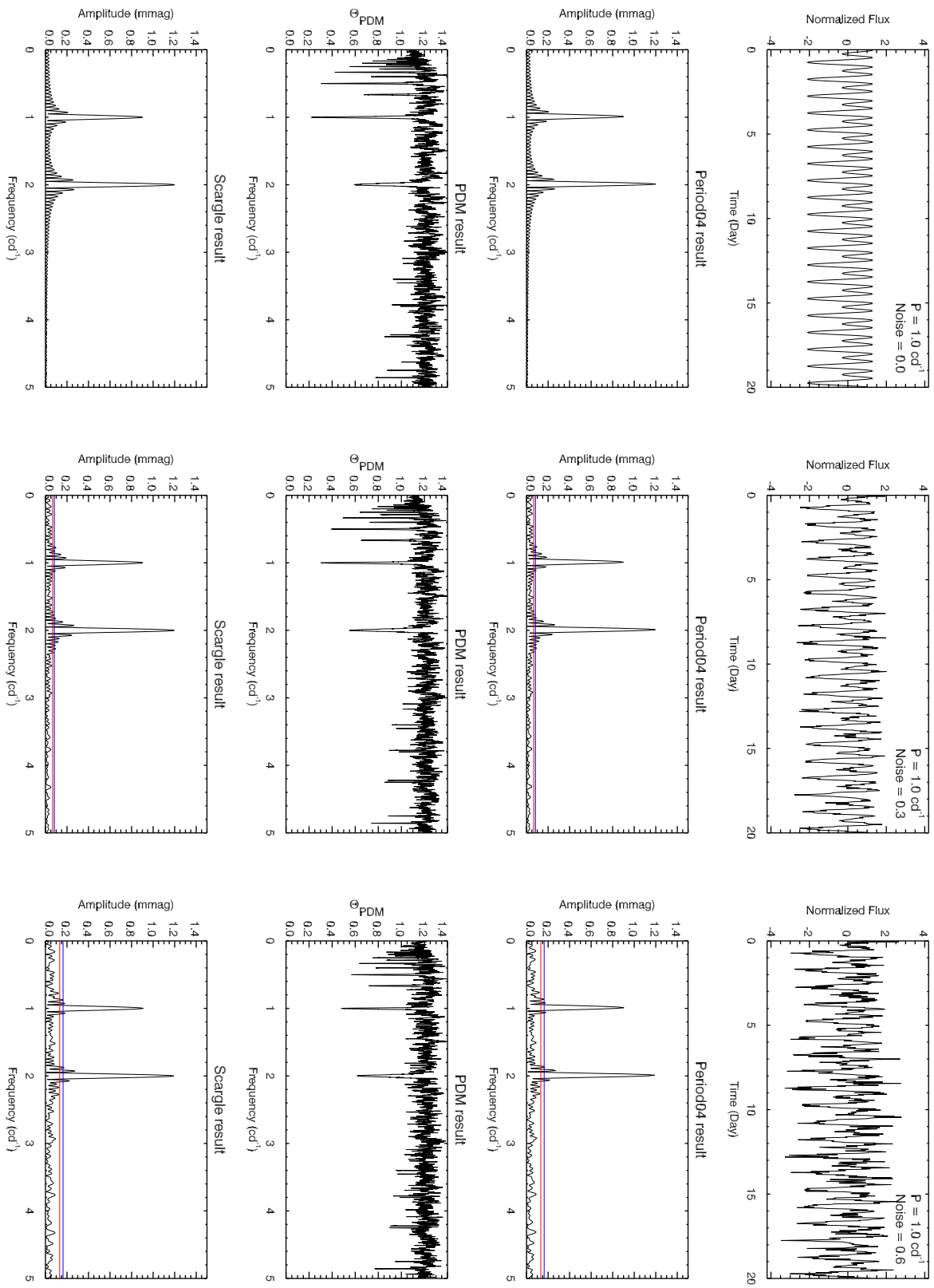

Figure 4.6: Case 3: Clear and noisy synthetic LCs with unequal minima and related period analysis results.

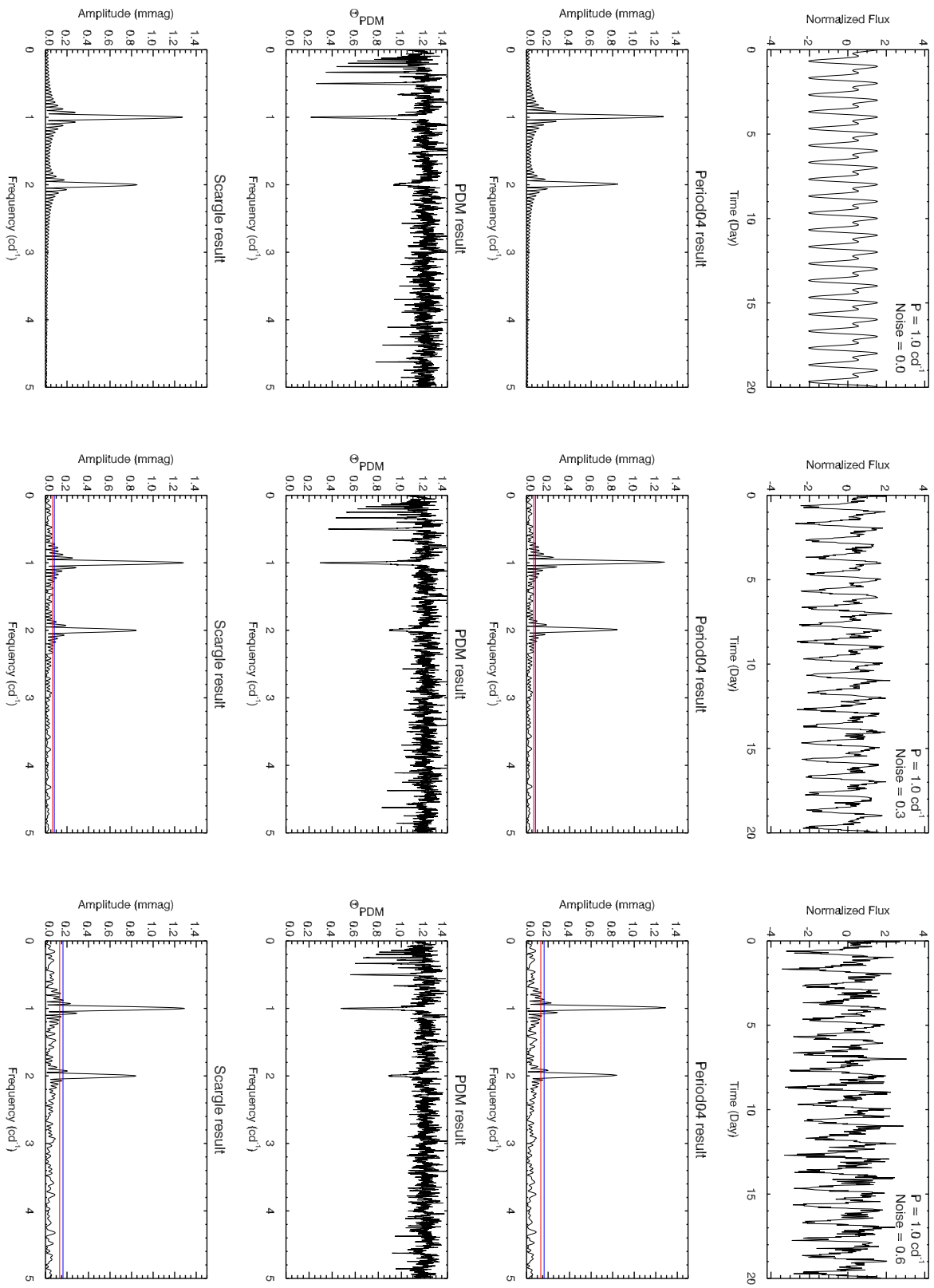

Figure 4.7: Case 4: Clear and noisy synthetic LCs with a hump superimposed on the descending branch and related period analysis results.

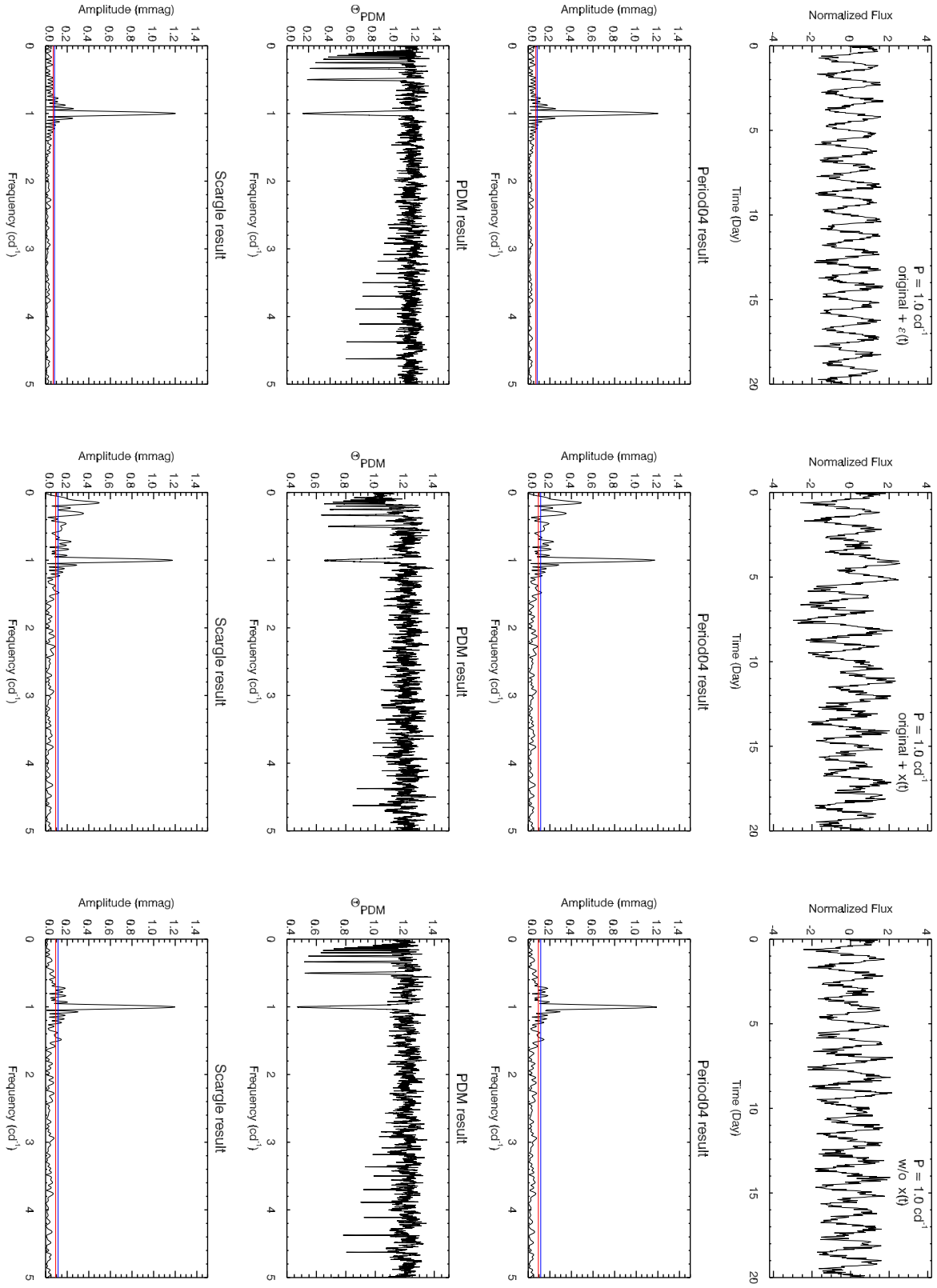

Figure 4.8: Case 5: The LC showing simple sinusoidal variation with a white noise level of 0.3, its combination of a red noise component, and the cleaned LC are shown in the figure. Related periodograms are also given under each LC.

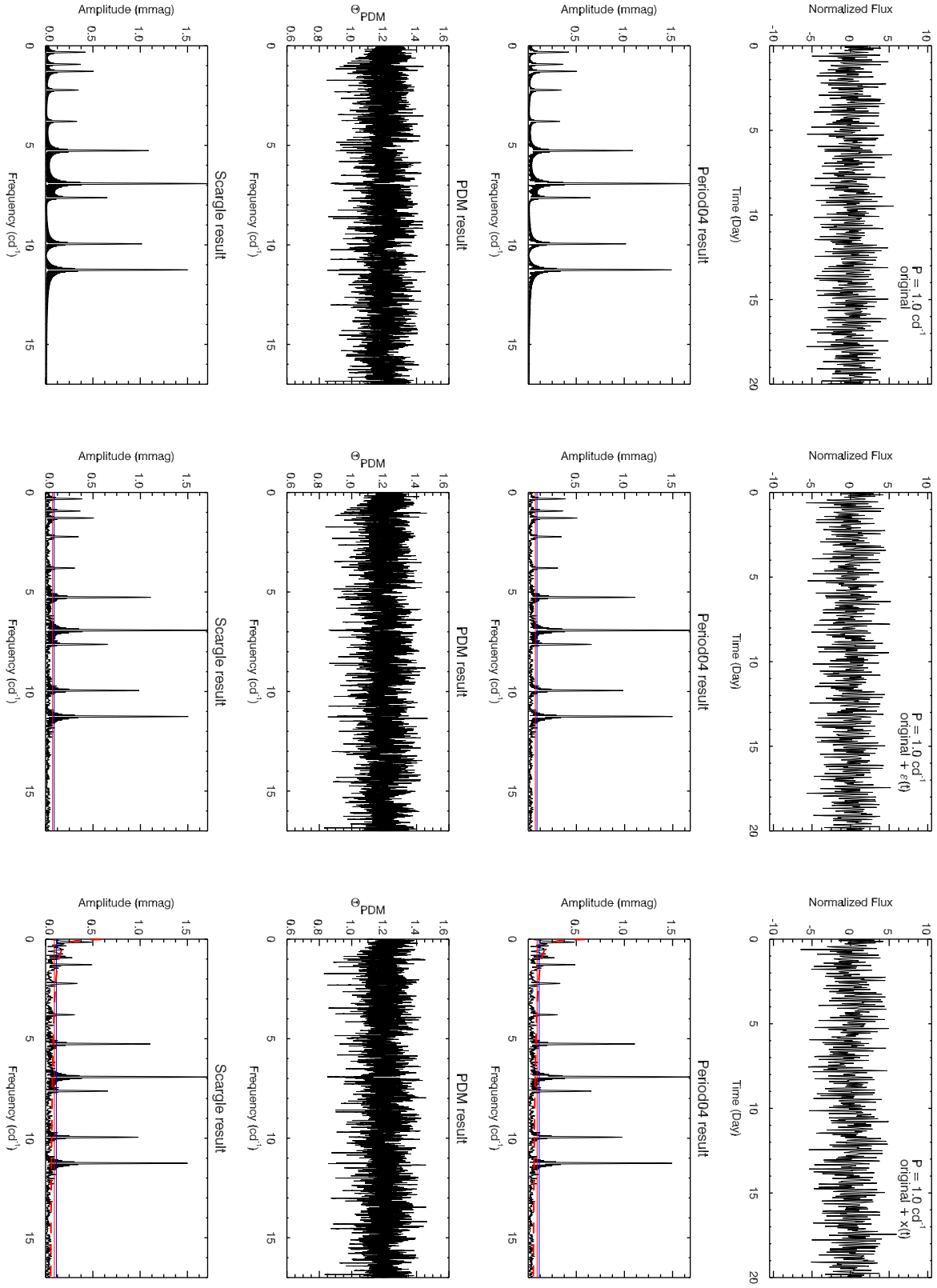

Figure 4.9: Case 6: The LC showing pure multi-periodic variations, and its combinations with white noise and with red noise components are shown in the figure. Related periodograms are also given under each LC.

Chapter 5

Period Evolution of Some Chemically Peculiar Stars

5.1 Introduction

Chemically peculiar variables are spread between late-B and early-F spectral types, and thus contain various stars with effective temperatures greater than 6,500 K (Hubrig et al., 2005). These rotating variables are comprised mostly of Ap and Bp stars, which differ from other types having the same effective temperature by their abnormal chemical compositions and slow rotations.

The reason for the peculiarity is an under-abundance of solar-like elements, as well as an over-abundance of both metal and rare-earth elements across their surfaces (Mikulášek et al., 2009). Magnetic fields, radiative acceleration, and atomic diffusion determine the surface distribution of elements (Kochukhov, 2011), and lead them to be present in the form of spots and rings on the surface. Along with rotation, these non-uniformly distributed regions cause periodic variations in magnetic fields, line profile, and energy distribution, as well as in photometric brightness (oblique-rotator model). The periods of these variations are generally between a day and a week.

Depending on the slow rotation, surface spot regions can remain stable for decades. Such a situation enables remarkably accurate calculations of surface distribution, rotation period, and rotational breaking mechanisms. However, only very few of the CP stars discovered in our galaxy and others exhibit periodic variations, and less than one-tenth of these have been observed for scientific investigation.

To study these types of stars, accurate observations are needed (accuracy $>$ 0.005 mag; Mikulášek et al. (2009)). For this reason, the high-precision instruments of the *STEREO* satellite are quite a suitable, space-based source, since seasonal and four-year *STEREO* observations provide a precision of 2.0×10^{-4} and 7.0×10^{-5} mmag, respectively. In this chapter, several CP stars presenting periodic light variations will be introduced by making use of four-year observations obtained between 2007 and 2011. Their rotation periods will be calculated with the help of a LC refinement pipeline, and long-term period changes will be investigated.

5.2 Analysis of STEREO data

For the analyses presented here, we used LCs obtained from the *STEREO* between 2007 and 2011 for the chosen CP samples. Since observation data were taken from the *HI-1A* instrument, each light set was formed of approximately 20-day data chunks with a 40-minute sampling. In order to prepare L2 data for analysis, a pipeline comprised of a series of procedures, functions, and loops written in IDL was developed and scrutinized in several segments as follows:

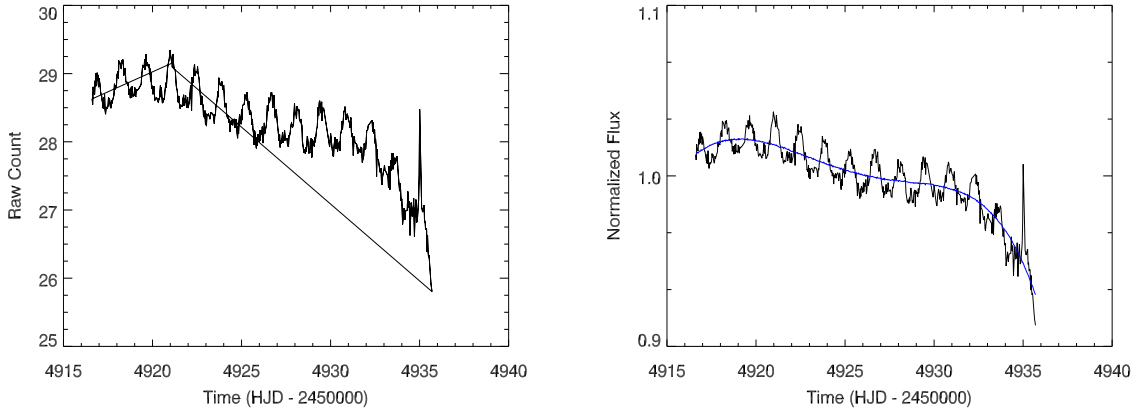

Figure 5.1: 20-day pre-processed data of HD 30466 observed in 2009 is shown on the left. It has some bad observation points and long-term variation as well as repetitive values. On the right, the LC cleaned from bad data points is fitted by a 3^{rd} order polynomial (blue line) as the first step.

5.2.1 Cleaning Pre-processed Data

Pre-processed data can still have some poor observation points in time series. These are basically "NAN" and "0" values that originate due to various spacecraft and instrumental effects such as connection loss with telemetry, blooming, or corrupted data (Sangaralingam and Stevens, 2011). In such a case, original measurements are replaced by "NAN" or "0" values. To be able

to continue on to other steps and avoid errors, these values were removed from the time series. Further, some data sets have repetitive values that affect observation weight and cause false frequency computation (Fig. 5.1, left). In order to eliminate these values, data sets were put in a time order. The same time values and corresponding photon counts were then deleted. Lastly, the rest of data was normalized to 1.0 for the unification of all 20-day data sets.

5.2.2 The First De-trending

After the removal of poor observation points, we obtained the LC that showed both long-term trends and some unusual, sudden fluctuations. There is more than one factor that causes long-term variations. The most penetrating ones are solar-wind events or CMEs. Also, end-of-frame and flat-field effects can distort an LC. Therefore, a short loop containing a polynomial fit was written. This loop automatically fits the LC with polynomials having an order from 1 to 9; the sigma values of each fit are then compared with each other in this loop. From this comparison, the polynomial with the lowest sigma value was taken. Thus, any trend that occurred due to different deforming effects was removed. The 3^{rd} or 4^{th} order polynomial, which is the CCD response function of *HI-1A*, was most frequently used during this procedure (Fig. 5.1, right).

5.2.3 The First Sigma Clipping

The next problem that needed to be corrected is the unexpected transient fluctuations on the LC. These structures are thought to have been generated by a solar streamer or a bright object in the same frame with the target star (Fig. 5.2, left). For this situation, a sigma clipping was utilized in the pipeline. In order to remove abnormal data points and avoid damaging any important variation, the sigma value was calculated according to the LC scatter, and outliers were removed.

5.2.4 The Second De-trending

The intensity of sudden fluctuations mentioned above is sometimes dozens of magnitudes greater than that of stellar variation. In this case, it may not be possible to conclude if there is any other trend on the LC. Therefore, the LC was checked for the last time by performing another automatic polynomial fit. In this way, any potential trend was extracted before moving to first frequency analysis. Thus, an LC that was purified from all distorted effects was obtained for further analyses. This extraction is given in Fig. 5.2 (right): as the curve did not show any significant change, the fit was a straight line, and thus was not plotted in the figure.

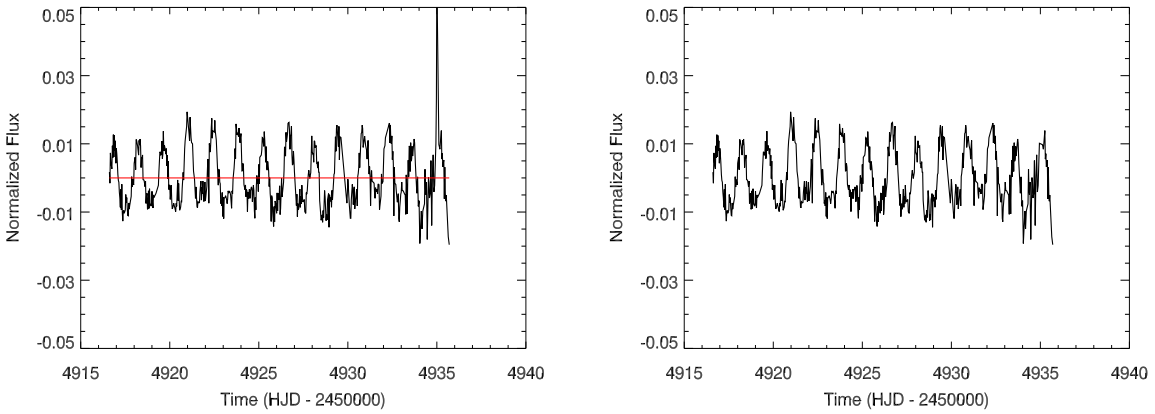

Figure 5.2: Residuals after the first de-trending are seen on the left. The LC has still some fluctuations due to solar streamer or a bright object in the same frame with target star. As a result of sigma clipping, a LC cleaned from distorted effects is obtained (right).

5.2.5 The First Lomb-Scargle

The main purpose of this analysis is to detect hidden signals in noisy time series. In order to detect a signal, Fourier techniques are generally used. However, due to the reasons mentioned in Section 3.1, astronomical time series include gaps and non-uniformly spaced data. For this reason, classical techniques cannot be implemented in these cases.

The LC of a rotating CP variable shows a sinusoidal variation through spot modulation on stellar surfaces. The LS algorithm is more sensitive to such variations, since Eqn. 3.3 becomes identical to the equation for obtaining frequency harmonics by a linear least-squares fitting of *sine* waves to the data ($h(t) = Acos\omega t + Bsin\omega t$) with the specific selection of τ in Eqn. 3.4. All analyses were therefore performed using this method (Fig. 5.4, left). During the analyses, the number of independent frequencies (N_{id} = 268 for LC of HD 30466 taken in 2009) was calculated with $N_{raw}/2$, where N_{raw} is the number of observation points in the raw data, in order to derive reliable results, and FAP was assumed to be 99% ($P_0 = 0.01$). Apart from these, signals were sought between the frequency range of 0.05 – 18 cd^{-1} (Nyquist frequency), and variabilities greater than the Nyquist frequency were not taken into account. The z (Eqn. 4.4) and four-sigma significance levels were also estimated (for 2009 LC of HD 30466, z and 4σ levels were around 1.09 and 1.36 mmag). These levels are shown with red and blue straight lines in Fig. 5.4.

Up to this point, a classical frequency detection method for a single and simple peak is used. However, the main frequency can sometimes be formed of multiple peaks, and a peak point may

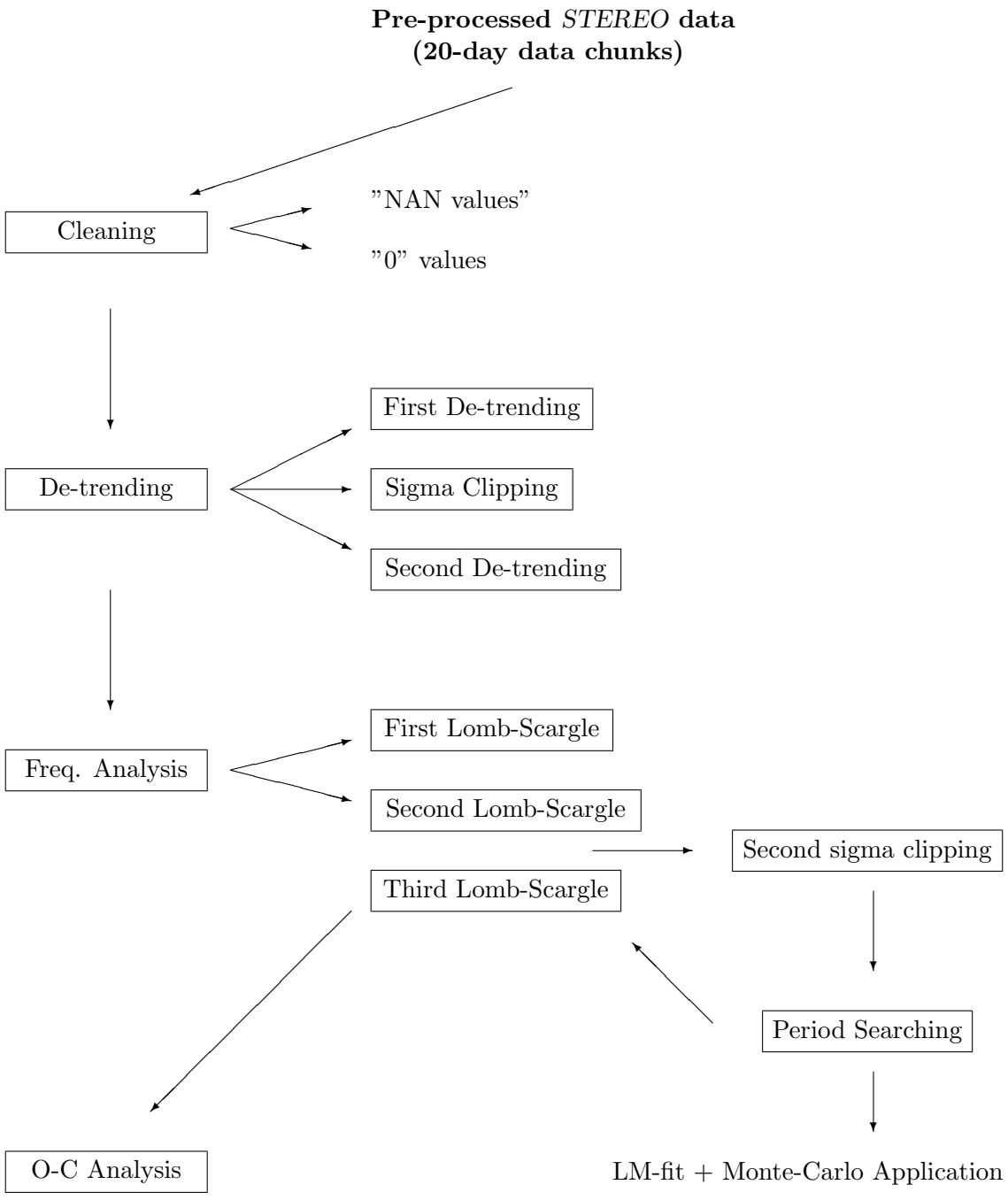

Figure 5.3: The pipeline schema for period refinement of *STEREO* time series.

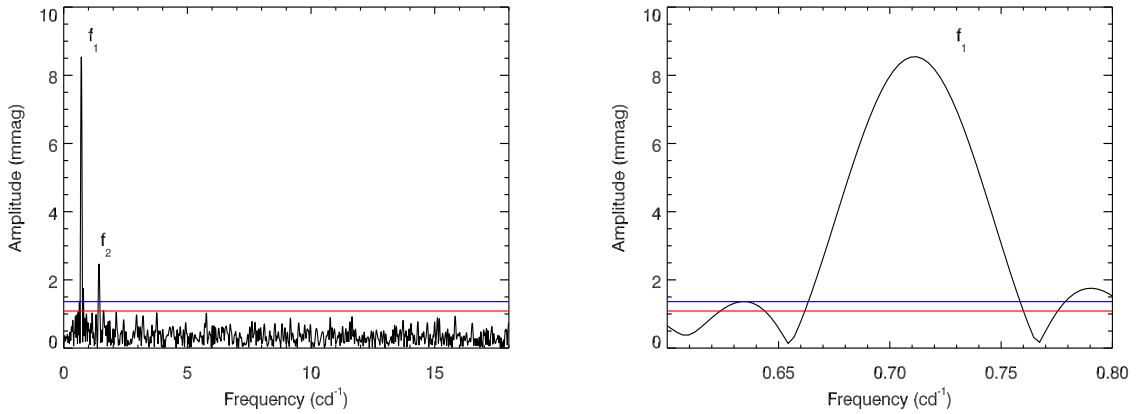

Figure 5.4: The LS periodogram of HD 30466 is seen on the left. The number of independent frequencies (N_{id}) is taken as 268. The Nyquist frequency of the *STEREO* (18 cd^{-1}) is used for the upper limit of the periodogram, and the FAP is also assumed to be 0.01 (99% significance). The main and the second frequencies are shown with f_1 and f_2, respectively. On the right, the zoomed-in periodogram is given. In order to save time, to get rid of other effects, and to derive an accurate value, the main frequency is zoomed-in by $\pm$0.1 cd^{-1}. z and four-sigma significance levels are also estimated as around 1.09 and 1.36 mmag, and shown with red and blue straight lines, respectively.

shift away from the expected value. To prevent any miscalculation, a simple routine was also written. The main purpose of the routine was essentially to populate arrays with maximum value as well as one point on either side, and to make an analytic parabolic fit to these three data points. Thus, more accurate frequency and error values were determined by making an analytic estimation of the revised frequency rather than a polynomial fit.

5.2.6 The Second Lomb-Scargle

Apart from the accuracies of results, rapid analyses are also crucial in order to save time. However, the processing time required for period analysis takes longer since the frequency range (0.05 to 18 cd^{-1}) is quite large, and obtaining reliable results in a short period may become difficult. To solve this problem, the initial LS frequency was restricted by $\pm$0.1 cd^{-1} from both sides of the peak point (Fig. 5.4, right). Thus, the region that contains only the main frequency was focused on, and rest of the data was removed from the periodogram. The same routine defined in Section 5.2.5 was then carried out. Consequently, we managed to save time and obtain the most accurate frequency value.

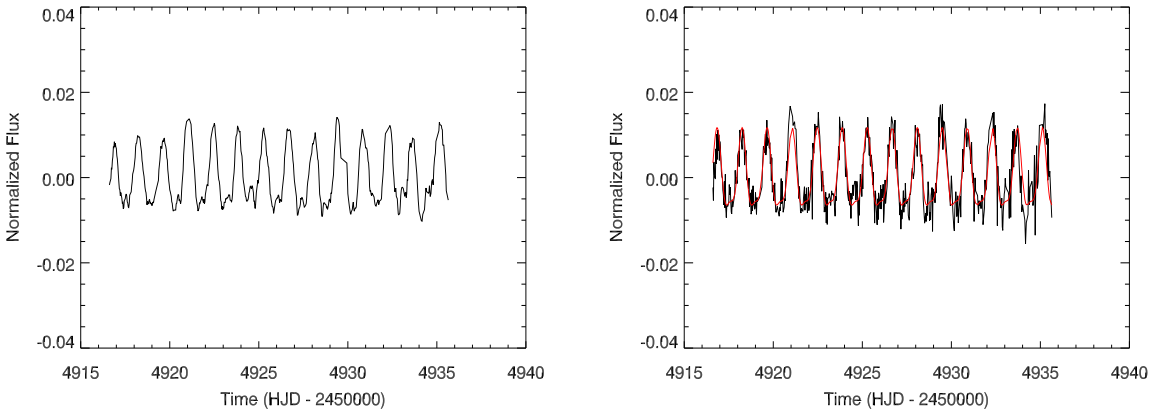

Figure 5.5: The average LC is shown on the left figure. On the right, the cleaned curve fitted by the LM-fit method (red curve) is given. The red simulated curve is then used in the Monte-Carlo method.

5.2.7 The Second Sigma-Clipping

To work on a cleaner LC, we applied another sigma-clipping to the original curve. The sigma value for specifying upper and lower clipping levels was calculated from the difference of the original LC and an average curve, which was produced by averaging five consecutive data points of the original curve (Fig. 5.5, left). All outliers were subsequently removed from the data according to these levels. Therefore, the LC was completely cleaned from all distorted effects and ready to be used in the LM-fit procedure.

5.2.8 The Levenberg-Marquardt Optimisation (LM-fit) Method

The LM-fit routine is a non-linear least-squares method to fit a function with an arbitrary number of parameters. It can be performed on a time series formed of any non-linear function. Before fitting, an initial guess of the parameter values is required, and these estimations should be close to the actual values. The routine performs consecutive iterations to approximate the solution. The set of parameters that gives the smallest chi-square is the best-fitting set. During the process, if the chi-square value does not change after three iterations, the routine stops and the parameters found are accepted as the expected results. If this does not happen, the maximum number of iterations is 50, unless otherwise specified by the user.

In order to determine a model of the LC examined, the LM-fit procedure was applied to the curve by defining a simple Fourier series. In the case of any other harmonics in the LC, more than one Fourier series with different coefficients and their derivatives were defined. As initial

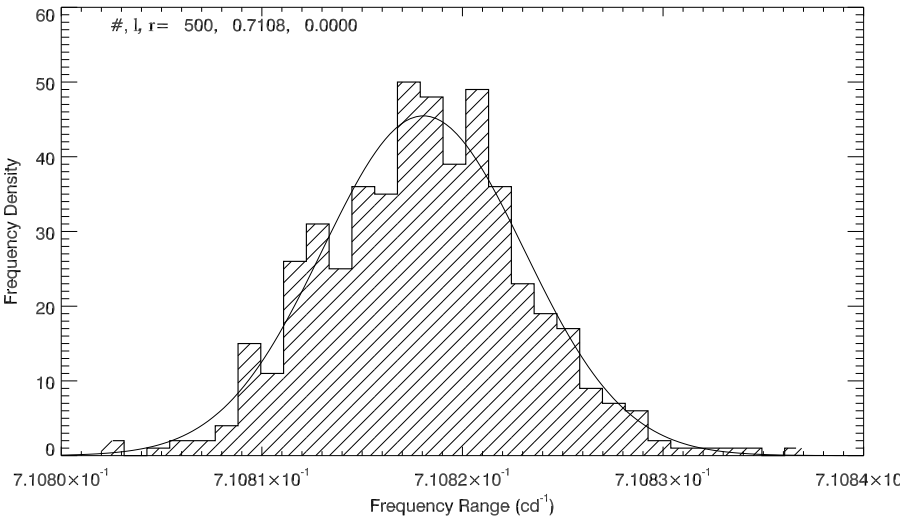

Figure 5.6: Monte-Carlo distribution for the combined data of HD 30466 is shown in the figure. The most accurate frequency and its sigma value are found to be 0.710818(7) cd^{-1} after 500 iterations.

parameters, the frequency value obtained from the second LS and the amplitude value of the average LC were used. The most accurate fit was obtained after 5,000 iterations. The cleaned LC and the fit (model curve) that resulted from the LM-fit procedure are presented in Fig. 5.5 (right).

5.2.9 The Monte-Carlo Method and The Third Lomb-Scargle

The Monte-Carlo method is mostly used to model a data set distribution with significant ambiguity, and requires repeated random sampling. The only criterion needed in order to have a good approach is to be able to produce a uniformly distributed and sufficient number of elements.

Once a model LC was derived from the cleaned data with the help of the LM-fit procedure, the most accurate frequency and its uncertainty were assessed using the Monte-Carlo simulation algorithm. To do this, random Gaussian noise with the mean of zero and the sigma value, which was determined from the cleaned curve, was produced. This noise component was then added to the model fit.

Following this, another LS procedure was implemented to this noisy curve. Instead of analysing all data, the frequency value obtained from the second LS was zoomed-in upon. However, unlike the previous application, its sensitivity was increased, and the main frequency was evaluated with a sigma value of ± 0.01 cd^{-1}. Once a frequency value was identified, all these processes were repeated by adding another noise component to the model curve. After 500

repetitions, 500 random frequencies around the actual one were produced. When a probability distribution was performed by a histogram, a well-defined peak, close to the expected value, was plotted on the diagram, and the most accurate frequency was calculated using a simple Gaussian fit (Fig. 5.6). Moreover, the final frequency error was found from the standard deviation of these 500 frequencies.

5.3 Other Procedures

Considering the inconsistencies between the results found by the PDM and LS methods during the synthetic LC analyses outlined in Chapter 4, all processes taking part in the pipeline were repeated by using the PDM technique, and another group of periods was derived. Frequency searching with PDM revealed that the LS method detected different period results for a number of stars such as HD 24769 and HD 125248, similar to the case of some synthetic LCs. In such situations, period accuracies were confirmed either with results in the literature if available, or with data derived by the *Hipparcos* satellite. The frequency analyses were then re-performed by restricting frequency ranges. On the other hand, it was learned that PDM sigma values were greater than that of the LS, and its Monte-Carlo distributions were not sufficiently uniform to obtain precise frequencies. Due to these reasons, LS periods were used for analyses. LC profiles of the sample stars were generated based on periods derived from combination of all annual LCs. In addition, Period04 results were provided for comparison. All of these results are given in the second, third, and fourth columns of the relevant tables in each result section. Other properties such as amplitude of the variation (Amp), number of data points (N), number of independent frequencies (N_{id}), mean level of noise in the periodogram where there was no significant peak (A_m), and significance levels (z and 4σ) estimated with an FAP of 0.01 are also presented in the same tables.

To perform O-C calculations and to investigate period variabilities over years, the best extremum times (either minimum or maximum) were obtained from LCs, and were put together with data from the literature. Light elements of the stars were presented in the form of $HJD_{(max)} = T_0 + PE\ (\pm\ \frac{1}{2}\frac{dP}{dt}\overline{P}E^2)$, where T_0 was the zero epoch, P was the rotational period in days, E was the number of cycles and $\frac{1}{2}\frac{dP}{dt}\overline{P}$ represented the long-term variation in period due to a possible magnetic braking. Archival time values given as JD were converted to Heliocentric JD using RA and DEC values, and in cases in which epochs corresponded to minimum times, phase corrections were applied. Further, if we were unable to reach any standard deviation value

for the literature's data, we assumed that they deviated ± 1 day from the expected epochs.

If the sample stars displayed any variation in period, the parameters that might be affected by this change were roughly estimated with basic equations given as:

1. Kinetic energy of star: $E = \frac{1}{2} I \omega^2$, where I is the moment of inertia and is found by $I = \frac{2}{5} M R^2$, where M is the mass and R is the radius of the star. Also, ω is the angular frequency calculated from $\omega = 2\pi/P$, where P is the rotational period,

2. Change rate of the kinetic energy and also the luminosity:

$$L = \frac{dE}{dt} = -\frac{2E}{P}\frac{dP}{dt} \ ,$$

3. Angular momentum of the star:

$$J = I\omega \ ,$$

4. Change rate of the angular momentum:

$$\frac{\dot{P}}{P} = -\frac{\dot{J}}{J} \ ,$$

5. Change rate of the mass (Nieuwenhuijzen and de Jager, 1990):

$$log(-\dot{M}) = -14.02 + 1.24 \ log(L/L_{\odot}) + 0.16 \ log(M/M_{\odot}) + 0.81 \ log(R/R_{\odot}) \ ,$$

6. Spin-down, mass loss and energy loss time-scales:

$$\tau_{SD} = \frac{P}{\dot{P}}; \qquad \tau_{ML} = -\frac{M}{\dot{M}}; \qquad \tau_{EL} = -\frac{E}{\dot{E}} \ ,$$

7. Main sequence time-scale of the star:

$$\tau_{MS} = \tau_{\odot} \ (\frac{M}{M_{\odot}})^{-2.5} \ ,$$

where $\tau_{\odot}$ is the MS time-scale of the Sun: $\tau_{\odot} = 10^{10}$ year.

5.4 Target Selection

The basis of our CP samples was mostly constituted by α^2 CVn type rotating variable stars obtained from the *Simbad* Database. To increase the number of these samples, many different catalogues such as Dubath et al. (2011), Wraight et al. (2012), Renson and Manfroid (2009), Renson and Catalano (2001), and Catalano and Renson (1997) were also probed. 8,040 CP stars were processed during this investigation. For target selection, rather than chemical or magnetic properties of the selected stars, four essential points were considered; brightness, galactic coordinates, LC and periodogram purity, and aperture photometry.

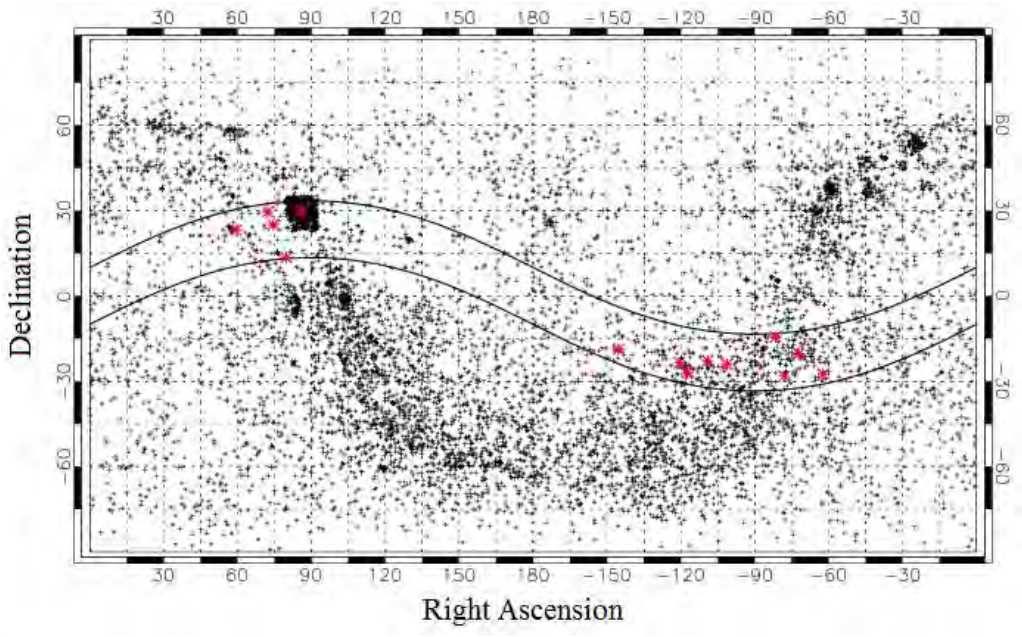

Figure 5.7: The diagram shows all 8,040 CP stars taken from different databases. The FOV of the *STEREO/HI-1A* is represented by the path between the black strips and the red plus symbols are the targets that meet the selection criteria.

As the first criterion, as many bright stars as possible were selected. Although the *STEREO* satellite can observe $11^{th} - 12^{th}$ mag targets, only 10^{th} mag or brighter stars were preferred. Thus, those data sets that were contaminated from background effects such as coronal activities were eliminated. For the other criterion, whether or not the catalogue stars were within the FOV of the *STEREO* was ascertained. Those targets that did not have an appropriate right ascension value and a declination between $\approx \pm 30^{\circ}$ were removed from the list. As a result, 413 candidates in suitable locations and brightness intervals were detected.

Following this, the LCs and periodograms of the selected stars were controlled. Those

Table 5.1: The sample stars and their characteristics in the literature.

Star	**Ra. (°)**	**Dec. (°)**	***V*-Mag. (^{m})**	**Sp. Type**	**Variable Type**
HD 24769	59.26586	23.17555	6.06	B9III	α^2 CVn
HD 30466	72.31668	29.57136	7.26	A0Si	α^2 CVn
HD 31592	74.53914	25.05041	5.79	A0V	CP1
HD 34547	79.72053	13.56718	7.43	A0pSrCr	?
HD 125248	214.65940	-18.71597	5.86	A9SrEuCr	α^2 CVn
HD 142884	239.45334	-23.52730	6.78	B8/9IIISi	α^2 CVn
HD 145102	242.56634	-26.90912	6.59	B9VSi	α^2 CVn
HD 150714	250.91538	-22.73648	7.57	A0Si	?
HD 155804	258.69752	-24.06028	8.23	A3m	?
HD 171184	278.46166	-14.42579	7.89	A0Si	α^2 CVn
HD 173657	281.90479	-28.27973	7.41	B9SiCr	?
HD 178929	287.83022	-20.34725	7.72	B7II/III	?
HD 187473	297.79266	-27.47196	7.32	B9SiSrCrEu	α^2 CVn
HD 246706	85.90343	29.75279	9.13	B8SiSr	?

showing less noise and high sinusoidal signals during the four-year mission of the *STEREO* were determined. According to these criteria, only 19 objects having quite good LCs and clear amplitude spectra were obtained. Finally, those targets having a neighbouring star in the same aperture were searched. As discussed in Section 2.1.3, if there is a neighbour within a radius of 6 pixels ($\sim$ 6 arcmin) centred on the target star, and magnitudes of both stars differ by less than a factor of 1.5, then it is most likely to get caught up in the aperture. Such a star would therefore contribute at least some flux to the final LC. Based on these restrictions, five of the selected targets were not included in the final sample stars, due to the high probability of having contaminated data resulting from neighbouring stars. In the end, 14 stars were selected.

The visual brightness values of these stars ranged between 5.79 and 9.13 mag. The great majority of these 14 samples was within the spectral type of B9 and A0 (5 B9-type and 5 A0-type) as discussed by Kochukhov (2011), and consisted of α^2 CVn type variables. There was also a CP1 type rotating variable and six unclassified samples. Coverage of the *HI-1A* instrument and 8,040 magnetic stars collected from catalogues are shown in Fig. 5.7. The FOV of the *STEREO*/*HI-1A* is represented by the path between the black strips. Moreover, all 14 CP samples are also presented with asterisk symbol, and their characteristics are listed in order of HD catalogue names in Table 5.1.

5.5 Results

5.5.1 HD 24769 (33 Tau; HIP 18485; HR 1221)

HD 24769 (B9III, $V = 6.06$ mag) has been the subject of numerous investigations for 40 years. The purpose of some of these studies was to obtain the period of the star. At first, Winzer (1974) suggested a photometric period of around 1.48 days, and Pearce and Hill (1975) found a period of 1.5919(2) days. However, detailed spectroscopic research performed by Hube (1981) revealed that the period was twice these results (2.975272(4) days), and that it fulfilled all radial velocities. Based on spectroscopic orbital solutions, Hube (1981) also considered that the star was an ellipsoidal variable.

This finding was supported by Morris (1985), who classified HD 24769 as a single-lined ellipsoidal variable. Accordingly, it was a component of a non-eclipsing close binary system, and its shape was distorted due to mutual gravitation. Its light variation was also explained by cross sectional regions changing in different phases on its surface. Later, Gulliver et al. (1985) derived LCs having two unequal minima, and confirmed that the period was around 2.975 days. Different from the previous results, Adelman et al. (1998) reported that their y photometry and Gulliver et al.'s (1985) V-data corresponded with period value of 3.0266 days (0.3305 cd^{-1}) and its alias of 1.4936 days (0.6695 cd^{-1}). However, the radial curve of this study affirmed Hube's (1981) result.

The most recent study was conducted by Dimitrov and Panov (2006), who obtained 787 photometric data points and 36 spectra. Combining their radial velocity and photometric data with the literature results, they improved the light elements as $HJD_{minI} = 2451884.366 + 2.9752350(8) \times E$.

Table 5.2: Frequency analysis results of HD 24769.

HD 24769	**LS** (cd^{-1})	**Period04** (cd^{-1})	**PDM** (cd^{-1})	**Amp** (mmag)	N (#)	N_{id} (#)	A_m (mmag)	z (mmag)	4σ (mmag)
2007	0.3360(3)	0.6720(6)	0.3348(9)	16.48(13)	595	298	0.44	1.41	1.75
2008	0.3359(2)	0.6717(4)	0.3362(6)	16.01(31)	612	306	0.33	1.06	1.31
2009	0.3365(2)	0.6729(3)	0.3362(6)	16.54(21)	595	298	0.38	1.20	1.50
2010	0.3369(2)	0.6738(4)	0.3355(7)	16.77(22)	602	301	0.38	1.21	1.51
Comb	0.336112(2)	0.672224(4)	0.3350(10)	16.43(28)	2404	1202	0.19	0.65	0.76

In our study, we obtained four consecutive years of LCs covering the period between 2007 and 2010 (Fig. A.1; on page 286). Similar to earlier studies, we observed an LC with double maxima and minima. Since the depths of the minima were nearly equal, neither of our frequency

analysis methods detected the expected period. Instead, both found a frequency value of around 0.67 cd^{-1} in the seasonal LCs (twice of the literature period). Since we also derived the same result from *Hipparcos* data, four-year *STEREO* observations were combined to calculate a more precise period. Indeed, a frequency value of 0.34 cd^{-1} was determined in this way (Fig. A.2, mid-right; on page 287). Thus, the frequency interval of the individual curves was restricted, and the analyses were repeated. Although the expected period value was found using PDM, there was no variation at around 0.34 cd^{-1} on the LS periodogram. Therefore, the LS period could not be calculated (Fig. A.2, mid-left; on page 287).

Table 5.3: Available period values and extremum times for HD 24769.

Time (year)	**Period (day)**	**References**	**Extremum Times (HJD)**	**References**
1970-1980	2.975272(4)	Hube (1981)	2448266.4561(108)	Perryman et al. (1997)
1981	2.975272	Gulliver et al. (1985)	2448269.4111(103)	
1991-1993	2.975290	Dubath et al. (2011)	2451884.3660(50)	Dimitrov & Panov (2006)
1995-1997	2.975272	Adelman et al. (1998)	2454230.3288(119)	This study
2000-2005	2.975235(8)	Dimitrov & Panov (2006)	2454569.5009(64)	
2007	2.9752(10)	Wraight et al. (2012)	2454914.6217(148)	
2007-2010	2.975198(17)	This study	2455265.6960(126)	

Following this, the PDM period was tested to produce a folded LC. The aim here was to understand the general characteristics of light variation, but we were unable to obtain a curve having the desired quality with this period value. Therefore, half of the combined LS frequency was used (Table 5.2), and a considerably good LC was generated (Fig. A.2, upper-left; on page 287). z and 4σ significance levels given in Table 5.2 were also plotted in LS periodograms with red and blue straight lines, respectively.

Apart from these calculations, a possible long-term period variation in the star was investigated. To do this, all available periods (Table 5.3) were collected from the literature and joined with the *STEREO* period (a red diamond symbol) in Fig. A.2 (lower left; on page 287). Since some archival periods were calculated from a combination of multiple observations, we deemed it suitable to use a combined *STEREO* period instead of individual values derived from seasonal LCs. Additionally, the mean period value and its standard deviations ($\pm 1\sigma$) are depicted using dotted lines. As seen in the figure, the period of the star shows a significant change over 40 years. Whereas stellar rotation decelerates between 1970 and 1990, the period begins to decrease after 1990. We found ratios for these changes to be 1.20×10^{-6} and -5.50×10^{-6} days yr^{-1}, respectively.

On the other hand, we also performed an O-C analysis of the star to check this period variation. Initially, all minimum times of the individual LCs were calculated. Secondary minimum times having the least standard deviations were selected for each year. By doing so, four epoch values were derived to represent annual variations. In addition to the *STEREO* data, we also searched literature data and found five reference epochs. Since three of them were primary minima, we applied phase corrections to these epochs (Table 5.3). Other values calculated by Pearce and Hill (1975) and Hube (1981) were obtained from radial velocity curves; we therefore did not include them in the analysis. In the Fig. A.2 (lower right; on page 287), all data are presented with black (literature) and red (*STEREO*) diamond symbols. To be able to construct an O-C diagram, the best minimum time and *STEREO* period were used. Accordingly, we computed the ephemeris elements to be:

$$HJD_{(minII)} = 2454914.6217(148) + 2.975198(17)E - 2.32(56) \times 10^{-8}E^2 \ .$$

Based on these results, we detected a long-term period decrease beginning in the 1990s in the O-C diagram, and derived the variation rate as $dP/dt = -5.69(1.37) \times 10^{-6}$ days yr^{-1} or $-0.49(12)$ s yr^{-1}. Such a change in the period indicated an increase in the kinetic energy of the star. Using the physical parameters given by Wraight et al. (2012) (T = 9,617(159) K, M = 3.14(21) M$_\odot$, $log(L/L_\odot)$ = 2.24(16) and R = 4.76(89) R$_\odot$, which was calculated from temperature and luminosity values provided), we roughly calculated this energy and the rate at which the energy increased as $E = 8.20(3.10) \times 10^{46}$ erg and $dE/dt = 9.94(4.48) \times 10^{33}$ erg s^{-1}. We also found the corresponding angular momentum and its variation rate to be around $J = 6.71(2.55) \times 10^{51}$ erg s and $dJ/dt = 4.07(1.83) \times 10^{38}$ erg. According to period and angular momentum variations, the acceleration time-scale of the star was approximately $\tau_{AC} = 5.23(3.08) \times 10^5$ yr, which was compatible with the duration derived from the variation rate of the kinetic energy ($\Delta\tau = E/(dE/dt) = 2.61(1.54) \times 10^5$ yr). However, these results were three orders of magnitude smaller than the MS lifetime of the star; $\tau_{MS} = 5.72(96) \times 10^8$ yr.

If such a period variation occurred due to a mass transfer between the components, at least one of the components had to fill the Roche lobe. With the help of the physical parameters M_1 = 2.79 M$_\odot$ and M_2 = 1.085 M$_\odot$, provided by Dimitrov and Panov (2006), we discovered that the Roche lobe radii of the components were 4.10 and 6.30 R$_\odot$, respectively. In other words, the primary star was near the mass transfer phase, and the shape of the parabola in

the O-C diagram confirmed that transfer direction was from the more massive star to the less massive one. According to this assumption, the transfer rate between the components would be around $dM/dt = -1.13 \times 10^{-6}$ $M_{\odot}yr^{-1}$.

As a result of a mass transfer, the donor star would lose some of its mass, which would cause a decrease in period and also radius of the star. We estimated the change in radius as approximately $dR = -4.55(1.39) \times 10^{-6}$ $R_{\odot}yr^{-1}$ for a given change of period. Finally, we found the rotational velocity of the star to be $Vsini = 74(14)$ $km\,s^{-1}$ using radius ($R = 4.76(89)$ $R_{\odot}$) calculated from temperature and luminosity values, and inclination angle ($i = 66°$) given by Dimitrov and Panov (2006), as well as our period value. This finding was quite close to the one obtained by Wraight et al. (2012) ($Vsini = 70(6.4)$ $km\,s^{-1}$).

5.5.2 HD 30466 (V473 Tau; HIP 22402)

The photometric variability of HD 30466 (A0Si, $V = 7.26$ mag) was first detected by Burke et al. (1970). They calculated the period of this variation as around 1.39(2) days, but this period value produced an LC with a scattered maximum. Hence, Rakosch and Fiedler (1978) noted that their observations were more adaptable with a double period.

Subsequently, Maitzen (1977) derived a rotation period of 2.7795(1) days, which was indeed twice that of previous values. As a result of the double period, two minima and maxima having different levels were formed in the LC; this situation was explained in terms of the different chemical regions on the surface. Most importantly, this was a significant case since a double-wave structure was not a common condition among Si stars. In a recent study, Jerzykiewicz (2009) investigated rotation periods and found a value of 1.4068541(29) days in U, B, and V-bands. However, he could not completely determine the origin of the variabilities, as he was unable to conclude whether the star was an oblique rotator or a g-mode pulsator.

Table 5.4: Frequency analysis results of HD 30466.

HD 30466	**LS** ($\mathbf{cd^{-1}}$)	**Period04** ($\mathbf{cd^{-1}}$)	**PDM** ($\mathbf{cd^{-1}}$)	**Amp** (**mmag**)	N (#)	N_{id} (#)	A_m	z (**mmag**)	4σ
2007	0.7104(8)	0.7101(8)	0.7120(16)	8.63(25)	524	262	0.33	1.04	1.30
2008	0.7101(6)	0.7101(6)	0.7118(15)	10.93(24)	552	276	0.38	1.22	1.52
2009	0.7116(7)	0.7116(8)	0.7157(15)	8.62(24)	535	268	0.34	1.09	1.36
2010	0.7128(7)	0.7128(8)	0.7123(20)	9.20(25)	563	282	0.34	1.10	1.38
Comb	0.710818(5)	0.710818(7)	0.711164(5)	9.33(13)	2174	1087	0.18	0.60	0.70

In this research, we obtained four consecutive years of data between 2007 and 2010. As reported by other researchers, all the LCs had explicit periodicity. Individual PDM and LS analyses of annual curves showed a frequency at around 0.71 cd^{-1} (Table 5.4), but this result was slightly longer than the literature periods. Furthermore, we detected the existence of another strong peak at approximately 1.40 cd^{-1} (0.71 days) on the LS periodogram, whereas the PDM method did not find any indication regarding this structure (Fig. A.3; on page 288). On the other hand, the period value of 4.0779 days given in the *Hipparcos* catalogue did not appear on the periodograms.

Combining the four-year data, the precise rotation period of the star was determined with the help of the PDM and LS methods. Since the LS technique gave a better period, the main LC was plotted based on this value, and its accuracies as well as its shape were confirmed with the *Hipparcos* data. Accordingly, the folded LC was clearly formed by a maximum and a

Table 5.5: Available period values and extremum times for HD 30466.

Time (year)	**Period (day)**	**References**	**Extremum Times (HJD)**	**References**
1963-1993	1.4068541(29)	Jerzykiewicz (2009)	2438451.1380(100)	Jerzykiewicz (2009)
1967-1968	1.39(02)	Burke et al. (1970)	2438451.1540(220)	
1963-1964	1.39	Rakosch & Fiedler (1978)	2438750.7800(190)	
1974	1.38975(5)	Maitzen (1977) (P/2)	2439860.8060(230)	
1990-1993	1.4066952	Dubath et al. (2011)	2448480.6010(190)	
1990-1993	1.407020(39)	Rimoldini et al. (2012)	2439870.6300(500)	Burke et al. (1970)
2007	1.4069(6)	Wraight et al. (2012)	2438466.7297	Rakosch & Fiedler (1978)
2007-2010	1.406829(10)	This study	2438466.3665(1300)	Maitzen (1977)
			2454241.5599(125)	This study
			2454583.4049(129)	
			2454922.4465(133)	
			2455274.1565(135)	

broad minimum (Fig. A.4, upper left; on page 289). The maximum was quite strong and had a flat top, indicating a cooler chemical structure on the surface. Moreover, there was a barely detectable bump in the middle of the minimum. This might be an indication of a hot spot affecting minimum light of the star, and is probably the cause of the peak at 1.40 cd^{-1} on the LS periodogram.

Also, we produced a folded LC using the double *STEREO* period since Maitzen (1977) noted that his observations were compatible with the period value of 2.7795 days. As shown in Fig. A.4 (upper right; on page 289), we derived a relatively clean LC with two minima and maxima. Even though the minimum at $\phi \approx 0.3$ was slightly more scattered than the other one, the consecutive structures appeared similar to each other. Therefore, we assumed that the period value of 1.41 days was the full rotation period.

To investigate a possible period variation, we collected all literature values given in Table 5.5, and present them in Fig. A.4 (bottom left; on page 289) using black diamond symbols. Since some of them were the results of multi-observations, we used the combined *STEREO* period instead of seasonal periods (a red diamond symbol). As seen in the figure, we found two different period paths ($\approx$1.390 and $\approx$1.408 days) since the quality and number of observation data differed from one study to another. Therefore, it was not possible to calculate any period variation using these values. However, when only the values given in Jerzykiewicz (2009) (10-year observations), Wraight et al. (2012), and this study (*STEREO* observations) were considered based on their reliabilities, the change in period suggested a possible period increase with a rate of 0.03 $\mathrm{s\,yr}^{-1}$ in the star over 45 years.

In order to confirm such a variation, we analysed variabilities in the O-C diagram. For

the calculation, the maximum times of the individual LCs were derived, and these values were combined with the epochs from the literature, given in Table 5.5. The epochs provided by Rakosch and Fiedler (1978), and Maitzen (1977) were converted from JD to HJD. Based on Fig. A.4 (right bottom; on page 289), we found out that the O-C diagram of the star exhibited a period decrease with the variation rate of around $-1.27(30)\times10^{-6}$ days yr^{-1} or $-0.11(3)$ s yr^{-1} (blue straight line). With the help of the LS period and using the best *STEREO* maximum time, we determined the light elements as:

$$HJD_{max} = 2454583.4049(129) + 1.406829(10)E - 2.44(58) \times 10^{-9}E^2 \ .$$

Since this star was a single rotating variable, such a period decrease might most likely be explained by an acceleration in rotation after a magnetic braking, and might affect the dynamic structure of the star. Using the physical parameters T = 11,081(280) K, M = 2.59(14) $M_\odot$, $log(L/L_\odot)$ = 1.64(15), and R = 1.80(32) $R_\odot$, which was calculated from temperature and luminosity values provided, as given by Wraight et al. (2012), we roughly calculated the kinetic energy of the star and the rate at which energy increased as $E = 4.31(1.57) \times 10^{46}$ erg and $dE/dt = 2.46(1.07) \times 10^{33}$ erg s^{-1}. We also found the corresponding angular momentum and its variation rate to be around $J = 1.67(61) \times 10^{51}$ erg s and $dJ/dt = 4.77(2.07) \times 10^{37}$ erg. According to period and angular momentum variations, the acceleration time-scale of the star was approximately $\tau_{AC} = 1.11(63)\times10^6$ yr, which was slightly higher than the duration derived from the variation rate of the kinetic energy ($\Delta\tau = E/(dE/dt) = 5.55(3.15) \times 10^5$ yr). We also found the MS lifetime of the star as $\tau_{MS} = 9.28(1.25) \times 10^8$ yr.

In addition to these, such a period decrease might be a result of a change in stellar mass with a rate of around $dM/dt = -1.92(88) \times 10^{-12}$ $M_\odot$yr^{-1}, or a consequent of a change in radius with a rate of around $dR = -8.10(2.42)\times10^{-7}$ $R_\odot$yr^{-1}. Finally, we found the rotational velocity of the star to be V_{eq} = 65(12) km s^{-1} with the help of our combined LS period and radius value ($R = 1.80(32)$ $R_\odot$), estimated from the parameters given above.

5.5.3 HD 31592 (k Tau; 98 Tau; HIP 23088; HR 1590)

HD 31592 (A0V, $V = 5.79$ mag) is one of the brightest objects among the program stars. Unfortunately, there is not yet enough information about its structure and evolution in the literature. Paunzen et al. (2013) is the only researcher who performed a photometric study and determined a rotation period of 0.8679(2) days (1.15 cd^{-1}).

In the most detailed investigation, we extracted four-year LCs from the *STEREO* database. Even though the LCs obtained in 2007, 2008, and 2010 were clear, we had to remove some data points from the LC taken in 2011 due to excessive scattering, and thus we lost half of the observation points. As seen in Fig. A.5 (on page 290), all LCs displayed clear sinusoidal variations. However, depths of consecutive minima seemed to be unequal, and their shapes resembled an eclipse-like structure.

Table 5.6: Frequency analysis results of HD 31592.

HD 31592	**LS** (cd^{-1})	**Period04** (cd^{-1})	**PDM** (cd^{-1})	**Amp** (mmag)	N (#)	N_{id} (#)	A_m (mmag)	z (mmag)	4σ (mmag)
2007	0.5743(7)	1.1494(12)	0.5762(13)	6.39(19)	626	313	0.16	0.52	0.65
2008	0.5758(5)	1.1516(8)	0.5723(12)	6.40(16)	687	344	0.12	0.40	0.50
2010	0.5774(5)	1.1549(8)	0.5763(9)	6.73(18)	683	342	0.18	0.58	0.72
2011	0.5763(20)	1.1575(30)	0.5784(32)	6.82(27)	252	126	0.40	1.22	1.59
Comb	0.576088(3)	1.152187(6)	0.5762(47)	6.51(10)	2248	1124	0.09	0.30	0.36

Due to these nearly-equal minimum levels, we derived different results from PDM and LS analyses. For all cases, PDM considered LCs as double-waved and calculated period values of around 0.57 cd^{-1}. Unlike PDM, LS found the rotational period to be around 1.15 cd^{-1}. This conflicting result was not seen in the four-year combined periodograms (Fig. A.6, middle; on page 291). Although Paunzen et al. (2013) gave a period quite close to our LS value, we could not confirm it with *Hipparcos* data, since its LS analysis resulted in an irrelevant frequency: $P_{Hip} = 1.60$ cd^{-1}. On the other hand, PDM analysis of *Hipparcos* data found a period of 0.58 cd^{-1}, but we could not produce a clean folded curve using either *Hipparcos* or combined PDM periods. For these reasons, we generated two folded LCs: one with the four-year LS period and one with half of this period to compare the results and determine the actual period of the star (Fig. A.6, top; on page 291).

According to the figures, the curve produced with the LS period had a single-waved structure that was quite similar to that of Paunzen et al. (2013). Moreover, although we derived a smooth maximum, the data points of the minimum and the ascending branch were slightly scattered.

Further, the folded LC plotted using half of the LS period (~ 0.57 cd^{-1}) was formed of double maxima and minima. Characteristically, the maxima were rather good and had equal heights. In contrast, one of the minima was explicitly deeper and smoother than the other one. This brightness difference in the folded LC confirmed typical structures in the seasonal observations. Considering these observational facts, we presumed that the period of 0.57 cd^{-1} was the full rotational period of the HD 31592. The overall results obtained from the frequency analyses and other properties of the LCs are presented in Table 5.6. z and 4σ significance levels are shown with red and blue straight lines in the relevant figures.

Table 5.7: Maximum times of HD 31592.

Time (HJD)	**References**
2454235.9048(31)	This study
2454583.0812(95)	
2455277.4228(43)	
2455615.9201(137)	

Since no archival light elements were given to examine a long-term period change, we benefited from period values of *STEREO* LCs, and the data provided by Paunzen et al. (2013). Assuming the period to be around 0.57 cd^{-1}, we multiplied Paunzen et al.'s (2013) result by two for analysis. This value is shown along with combined LS and annual periods by using black diamond, red diamond, and asterisk symbols, respectively, in Fig. A.6 (left bottom; on page 291). As seen in the figure, although the period seems to decrease between 2007 and 2011, the four-year combined period is in accordance with Paunzen et al.'s (2013) finding, and there is no significant variation between the two data results.

For the O-C variation of the star, we used only the maximum times of *STEREO* LCs shown in Table 5.7. As shown in Fig. A.6 (right bottom; on page 291), we detected a moderate increase in the period. However, this variation was within the error limits of the data points (blue line). Using the best maximum time and LS period obtained from the folded LC with double maxima and minima, we determined the light elements as $HJD_{(maxI)} = 2454235.9048(31) + 1.735850(9)E$. The radius of the star was calculated as 2.05(15) $R_\odot$ with the help of the physical parameters ($log(L/L_\odot) = 1.56(6)$, T= 9,907(105) K, $M/M_\odot = 2.37(5)$) given by Paunzen et al. (2013). Finally, rotation velocity was estimated to be around $V = 60(4)$ km s^{-1}. This value was half that of Paunzen et al. (2013)'s result, since we used the period value of 0.57 cd^{-1}, instead of 1.15 cd^{-1}.

5.5.4 HD 34547 (HIP 24789)

HD 34547 (A0SrCr, $V = 7.43$ mag) is one of the most under-researched CPs. The only study was performed by Wraight et al. (2012), who determined a photometric rotation period of 1.7145(10) days (0.58326 cd^{-1}).

In this investigation, we probed seasonal LCs of HD 34547 taken from the *STEREO* satellite between 2007 and 2011. As shown in Fig. A.7 (on page 292), LC structures were clearly sinusoidal. However, the shape of some curves such as the one observed in 2011 was distorted by a probable surface spot. Therefore, we obtained inconsistent frequency results with the PDM method during analyses ($P_{2007} \approx 0.14$ cd^{-1}, $P_{2008} \approx 0.29$ cd^{-1}, $P_{2010} \approx 0.19$ cd^{-1}, $P_{2011} \approx 0.19$ cd^{-1}). Despite this, we found a frequency value of about 0.58 cd^{-1}, which was compatible with Wraight et al.'s (2012) finding, for the four-year combined data. Hence, we restricted PDM to around 0.58 cd^{-1}, and determined the actual periods for the seasonal LCs. Apart from this, we encountered no problems regarding LS analyses and derived the expected frequency value.

Table 5.8: Frequency analysis results of HD 34547.

HD 34547	**LS** (cd^{-1})	**Period04** (cd^{-1})	**PDM** (cd^{-1})	**Amp** (mmag)	N (#)	N_{id} (#)	A_m (mmag)	z (mmag)	4σ (mmag)
2007	0.2913(9)	0.5829(18)	0.5816(52)	15.11(60)	517	259	0.60	1.90	2.39
2008	0.2913(7)	0.5826(14)	0.5853(39)	18.88(52)	596	298	0.46	1.47	1.83
2010	0.2920(7)	0.5842(14)	0.5881(32)	18.27(60)	447	224	0.41	1.31	1.66
2011	0.2900(8)	0.5799(16)	0.5765(42)	16.03(57)	435	218	0.28	0.89	1.12
Comb	0.291649(3)	0.583298(7)	0.5814(38)	17.06(29)	1995	998	0.22	0.73	0.87

To test the accuracies of the combined periods and their compliance with the data, we attempted to produce folded LCs. Consequently, we realized that the LS period gave a preferable curve (Fig. A.8, upper left; on page 293). As seen in the figure, the main light variation was clearly a sinusoid with a single-waved structure. This structure and the period of 0.58 cd^{-1} were also confirmed by analysing *Hipparcos* data with the LS method. However, a discrepancy between analysis techniques reappeared, since PDM determined a period value of around 0.28 cd^{-1} for the *Hipparcos* data. Considering these results, along with the geometrical irregularity in the minimum and the descending branch of the curve, we suspected that there might be double minima, similar to that in HD 31592. To resolve this suspicion, we plotted a folded LC using half of the combined LS period (~ 0.29 cd^{-1}), and present the result in Fig. A.8 (upper right; on page 293). Accordingly, we derived a less scattered, quite good curve with double maxima and minima. However, the shapes of the maxima were slightly different; in particular,

the primary maximum had a sharper top and its ascending branch was comparably more oblique than the other. Further, the minima also seemed to be different: although the first minimum could not be folded perfectly, it was clear that the second minimum was deeper. Based on these findings, we concluded that the full rotation period of the star may be around 0.29 cd^{-1}. These results are given in Table 5.8. LC properties such as mean noise levels (A_m) and significance levels are also presented in the table. z and 4σ levels were plotted in LS periodograms for all LCs.

Due to a lack of historical records, it was not possible to search for a long-term period variation. However, with the help of the period value obtained from *Hipparcos* data (1.71467(19) days; Perryman et al. (1997)), we attempted to generate a rough idea about change between 1990 and 2011. Assuming the period was to be around 3.429 days, we combined twice the *Hipparcos* and Wraight et al.'s (2012) results with our *STEREO* period (shown with red asterisk) (Fig. A.8, left bottom; on page 293). However, we could not compute any change in the data due to large error values.

Table 5.9: Maximum times of HD 34547.

Time (HJD)	**References**
2454237.7823(111)	This study
2454587.5169(118)	
2455273.2574(175)	
2455619.5776(172)	

To check for a possible period change, we also investigated the O-C variation of HD 34547. Since there was not a retrospective extremum time in the literature, we could only examine variation that occurred between 2007 and 2011. As shown in Fig. A.8 (bottom right; on page 293), we detected a slight increase in the period. However, the change was within error limits and thus ignored. Using the best maximum time and half of the combined period value, we determined the light elements as $HJD_{(max)} = 2454237.7823(115) + 3.428779(39)E$.

Finally, with the help of the physical parameters provided by Wraight et al. (2012) ($log(L/\mathrm{L}_\odot)$ = 1.22(17), T=10,077 K), we calculated the radius and rotational velocity of the star as $R/\mathrm{R}_\odot = 1.34(26)$ and $V_{eq} = 20(4)$ $\mathrm{km\,s^{-1}}$.

5.5.5 HD 125248 (CS Vir; HIP 69929; HR 5355)

HD 125248 (A9SrEuCr, $V = 5.86$ mag) is a well-known, bright CP star that has attracted the attention of many researchers due to its variabilities over more than 80 years. Morgan (1931) was the first investigator who detected variable line intensities similar to those in α^2 CVn. In a spectroscopic observation, Hockey (1969) stated that the star was a spectroscopic binary with a period of 4.4 years by using radial velocity data and previous findings. On the basis of magnetic field observations, he showed that HD 125248 also had a 9.2954-day rotational period. Unlike other authors, Blanco et al. (1978) found a slightly shorter period value of 9.29477 days after a three-year observation. Additionally, Catalano et al. (1992) obtained some variabilities in infra-red region and derived the best period to be 9.29571(18) days, compatible with visible light, spectrum, and magnetic field variations. Leone and Catanzaro (2001) combined their observations with previous ones as well as *Hipparcos* data, and identified a single-waved LC in U and B filters. They also observed a double-waved curve having different maximum levels in the V filter. Recently, Mikulášek et al. (2004) concluded that light variations could be represented by a linear combination of two mutually orthogonal normalized LCs, and improved the period as 9.295450(30) days by combining all the literature data (592 observations over 43 years).

Table 5.10: Frequency analysis results of HD 125248.

HD 125248	**LS (cd^{-1})**	**Period04 (cd^{-1})**	**PDM (cd^{-1})**	**Amp (mmag)**	N (#)	N_{id} (#)	A_m (mmag)	z (mmag)	4σ (mmag)
2007	0.1068(2)	0.2137(5)	0.1067(8)	11.13(19)	650	325	0.19	0.60	0.74
2008	0.1056(2)	0.2110(3)	0.1062(6)	15.09(16)	656	328	0.18	0.58	0.72
2009	0.1075(5)	0.2155(11)	0.1096(10)	12.05(46)	252	126	0.84	2.59	3.38
2010	0.1092(3)	0.2181(6)	0.1109(8)	12.46(22)	605	303	0.23	0.75	0.93
2011	0.1094(2)	0.2195(4)	0.1090(7)	16.04(21)	673	337	0.24	0.76	0.95
Comb	0.107580(1)	0.215153(3)	0.1070(9)	13.33(11)	2836	1418	0.12	0.42	0.49

In this study, we analysed five-year LCs of HD 125248 taken between 2007 and 2011. Unlike other samples, we obtained photometric data, which displayed only 1.5 light cycles since the rotation period was relatively longer. As given in Fig. A.9 (on page 294), LC variations were sinusoidal, and levels of extremum points were nearly equal. For this reason, we had some problems similar to those experienced with HD 24769 during the detection of the correct period. Also, LC data taken in 2009 was quite poor; due to the small number of data, its noise level and hence significance levels were noticeably higher (Table 5.10).

We initially applied the LS method to seasonal data and acquired a frequency value of around 0.21 cd^{-1} (4.76 days), which was half of the literature period, as expected. Since there was no

Table 5.11: Available period values and extremum times for HD 125248.

Time (year)	Period (day)	References	Extremum Times (HJD)	References
1944-1945	9.295	Deutsch (1947)	2433103.9516(1500)	Stibbs (1950)
1947-1950	9.2954	Babcock (1951)	2440284.6869(100)	Blanco et al. (1978)
1949	9.295(3)	Stibbs (1950)	2440698.3180(120)	Mikulášek et al. (2004)
1953-1957	9.2954	Babcock (1960)	2440373.0000(454)	mCPod*
1964	9.2957(2)	Adam (1965)	2440391.6420(522)	
1964-1965	9.2954	Hockey (1969)	2440405.4504(482)	
1969	9.2954	Maitzen and Rakosch (1970)	2440614.6464(590)	
1970	9.2954	Wolff and Wolff (1971)	2440679.7024(528)	
1969-1971	9.29477(5)	Blanco et al. (1978)	2454372.0510(182)	This study
1970-1971	9.2954	Maitzen and Moffat (1972)	2454715.9750(114)	
1972-1974	9.2954	Pyper and Adelman (1985)	2455069.2099(341)	
1974	9.29541(7)	Renson (1975)	2455403.8410(231)	
1950-2000	9.29545(3)	Mikulášek et al. (2004)	2455757.0882(199)	
1989-1991	9.29571(18)	Catalano et al. (1992)		
1999	9.29545	Leone and Catanzaro (2001)		
2007-2011	9.29541(12)	This study		
1972-1973	9.3	Pilachowski and Bonsack (1975)		
1990-1993	9.2918	Dubath et al. (2011)		
1990-1993	9.287	Perryman et al. (1997)		
2007	9.3105(13)	Wraight et al. (2012)		

* http://astro.physics.muni.cz/mcpod/
Note : The extremum time given by Blanco et al. (1978) represents U_{min}, and $U_{max} \sim U_{min} - 0.5$.

peak around the actual frequency, we could not restrict the LS periodogram, and calculated halves of the LS frequencies. Similar results were also derived from Period04. Following this, the same analyses were performed with the PDM technique. As there was a limited number of light cycles, it also failed to find the desired frequency, but could be restricted to around 0.10 cd^{-1}. Thus, we derived the literature period for individual and combined LCs.

The PDM and LS periods of the five-year data combination were then used to check general LC characteristics of HD 125248. Since the LS period provided a more suitable folded curve, it was chosen for further calculations. As shown in Fig. A.10 (upper left; on page 295), the main LC exhibited a double-waved structure that was not observed in most studies, and one of the minima was slightly shallower than the other. Moreover, we added *Hipparcos* data to the study, and its frequency analysis gave a similar period (0.10763 cd^{-1}) with the *STEREO* value (Fig. A.10, upper right; on page 295). However, the shape of the folded curve was different since observation filters were not the same. Even though it had double maxima and minima, the secondary maximum was considerably fainter than the primary one.

Apart from this, we investigated a possible long-term period variation by collecting all available literature data, even though a period constancy was reported by several authors. Since many studies about the star existed, we found 20 period values as seen in Table 5.11. Of these values, 16 were around a mean period of 9.295375 days, whereas the last four data in

the table excessively deviated from this value and did not fit our LCs very well. Therefore, we did not use them during calculations. In Fig. A.10 (left bottom; on page 295), literature and combined *STEREO* data are shown with black and red diamond symbols, respectively. From the graphic, it was not easy to deduce any period change in the star over 70 years because the vast majority of the data was gathered around the mean value. However, our five-year data suggested a small increase in the period, and we calculated the overall variation to be around 0.69 $\mathrm{s\,yr^{-1}}$.

Hoping to substantiate this period change, we put literature epochs and the *STEREO* maximum times together (Table 5.11). Before analysis, we applied phase corrections to some data since they were minimum times, and converted some of them to HJD. Accordingly, the values exhibit upward curving parabola since 1950, as seen in Fig. A.10 (lower right; on page 295). We derived the rate of this parabolic change to be around $3.40(1.60) \times 10^{-6}$ $\mathrm{days\,yr^{-1}}$ or 0.35(14) $\mathrm{s\,yr^{-1}}$. The error of the quadratic term of the least-squares fit was quite high due to the precisions of literature data, and this may have affected the result. Based on our findings, we computed the light elements as: $HJD_{(max)} = 2454715.9750(114) + 9.2954(1)E + 5.09(2.04) \times 10^{-8}E^2$.

Such an increase in the period indicated a possible decrease in the kinetic energy of the star. Using the physical parameters T= 9,817(1.03) K, $M = 2.27(7)$ $\mathrm{M_\odot}$, $log(L/\mathrm{L_\odot}) = 1.50(8)$, and $R = 1.95(18)$ $\mathrm{R_\odot}$ (calculated from temperature and luminosity values provided), given by Kochukhov and Bagnulo (2006), we roughly calculated this energy and the rate at which the energy decreased as $E = 1.02(19) \times 10^{45}$ erg and $dE/dt = -2.77(1.23) \times 10^{31}$ $\mathrm{erg\,s^{-1}}$. We also found the corresponding angular momentum and its variation rate to be around $J = 2.60(49) \times 10^{50}$ $\mathrm{erg\,s}$ and $dJ/dt = -3.54(1.57) \times 10^{36}$ erg. According to period and angular momentum variations, the spin-down time-scale of the star was approximately $\tau_{SD} = 2.33(1.12) \times 10^6$ yr, which was compatible with the duration derived from the variation rate of the kinetic energy ($\Delta\tau = E/(dE/dt) = 1.16(56) \times 10^6$ yr). We also found the MS lifetime of the star as $\tau_{MS} = 1.29(10) \times 10^9$ yr.

In addition to these, such a period increase might be a result of a change in stellar mass with a rate of around $dM/dt = 1.35(32) \times 10^{-12}$ $\mathrm{M_\odot yr^{-1}}$, or a consequent of a change in radius with a rate of around $dR = 4.19(1.72) \times 10^{-7}$ $\mathrm{R_\odot yr^{-1}}$. Finally, we found the rotational velocity of the star to be $V_{eq} = 11(1)$ $\mathrm{km\,s^{-1}}$ with the help of our combined LS period and radius value ($R = 1.95(18)$ $\mathrm{R_\odot}$) estimated from the parameters given above. This velocity value was comparable with the finding of Wraight et al. (2012) ($V sini = 12.5(5.7)$ $\mathrm{km\,s^{-1}}$).

5.5.6 HD 142884 (V928 Sco; HIP 78183)

HD 142884 (B8/9Si, $V = 6.78$ mag) is a giant star whose LC peculiarity was discovered by Garrison (1967). The periodicity of this variability was calculated as 0.80302 days by North and Waelkens (1983). Due to long observation intervals, North (1987) reported some difficulties regarding choosing the correct period among multiple results, and gave a rotation period value of 0.80299(2) days. Subsequently, North (1998) determined a reliable period of 0.80302 days in an investigation involving the rotational braking of Si stars.

Table 5.12: Frequency analysis results of HD 142884.

HD 142884	**LS** ($\mathbf{cd^{-1}}$)	**Period04** ($\mathbf{cd^{-1}}$)	**PDM** ($\mathbf{cd^{-1}}$)	**Amp** (**mmag**)	N (#)	N_{id} (#)	A_m (**mmag**)	z (**mmag**)	4σ (**mmag**)
2007	1.2430(13)	1.2430(16)	1.2471(31)	6.70(30)	598	299	0.30	0.96	1.20
2008	1.2426(11)	1.2426(13)	1.2466(21)	6.45(27)	677	339	0.20	0.66	0.82
2010	1.2475(13)	1.2475(14)	1.2484(32)	6.70(27)	675	338	0.26	0.85	1.05
2011	1.2439(11)	1.2439(13)	1.2395(20)	6.48(25)	684	342	0.21	0.69	0.86
Comb	1.245381(6)	1.245381(8)	1.2427(29)	6.56(14)	2634	1317	0.12	0.41	0.48

Following these research developments, we obtained four-year LCs of HD 142884 in this study. Although a small number of observation points was removed from the data observed in 2007, all curves showed clear periodicities. This star was one of the rare samples for which the LS and PDM methods found very close period results during frequency analyses (≈ 1.24 cd^{-1}). For the four-year combined data, both techniques displayed quite strong peaks at 1.2454 cd^{-1} and 1.2427 cd^{-1}, respectively. However, since the PDM period did not provide a clean curve, a folded LC was produced with the LS period. As seen in Fig. A.12 (upper left; on page 297), it had a single-waved sinusoid as well as an additional structure superimposed on the descending branch. *Hipparcos* data (Perryman et al., 1997) also exhibited a similar hump around the minimum, but it was slightly shifted towards the ascending branch.

To investigate the period variation of the star, we collected all available literature data (Table 5.13). As shown in Fig. A.12 (bottom left; on page 297), they are represented with black diamond symbols and the combined *STEREO* period is given with red symbol. According to the figure, the period showed a slight increase from 0.8029 to 0.8031 days between 1980 and 1990, but following that it decreased down to 0.8029 days in 20 years.

This decrease can be also seen in the O-C diagram, where a black data point was provided from North (1987) and but was corrected since it represented a minimum time. Red diamonds also indicate the maximum times derived from *STEREO* LCs (Table 5.13). In the figure, the

Table 5.13: Available period values and extremum times for HD 142884.

Time (year)	**Period (day)**	**References**	**Extremum Times (HJD)**	**References**
1983	0.80302	North and Waelkens (1983)	2445349.9220	North (1987)
1983	0.80299(2)	North (1987)	2454402.5644(85)	This study
1990-1993	0.80318(7)	Perryman et al. (1997)	2454740.6068(82)	
2007	0.8030(2)	Wraight et al. (2012)	2455424.7400(88)	
2007-2011	0.802967(4)	This study	2455780.4551(67)	

data suggested an upward-curving parabola, but the variation was within error limits. Using the best maximum time and the combined LS period, we calculated the light elements of the star to be:

$$HJD_{(max)} = 2455780.4551(67) + 0.802967(4)E \ .$$

Finally, we found the radius and rotational velocity of the star as $R/\mathrm{R}_{\odot} = 2.01(33)$ and $V_{eq} \approx 127(21)$ km s^{-1} with the help of the physical parameters $log(L/\mathrm{L}_{\odot}) = 2.17(14)$, T=14,223(270) K, provided by Wraight et al. (2012). This rotational velocity was slightly lower than Wraight et al.'s (2012) finding ($Vsini = 155(18.4)$ km s^{-1}).

5.5.7 HD 145102 (V952 Sco; HIP 79235)

The first photometric measurements of HD 145102 (B9VSi, $V = 6.59$ mag) were performed by Vanbeveren and Hensberge (1978), who detected marginal variabilities in v, b, and y bands. Due to a small variation amplitude, they could not find an exact rotation period, but suggested some possibilities such as 0.539(50), 0.584(10), 0.772(10), 0.873(10), 1.17(2), 1.41(2), 3.44(15), and 7.00(30) days. Afterwards, Cernicharo et al. (1985) and Borra et al. (1985) gave a period of around 1.693 days for stellar rotation. However, it was realized that the comparison star was a variable, and results were thought to be affected by this variability. Indeed, North (1987) found three possible periods – 1.4233, 1.4207, and 1.4179 days – consistent with the 1.41-day period given by Vanbeveren and Hensberge (1978). Unfortunately, he was unable to produce previous LCs with his own periods.

Table 5.14: Frequency analysis results of HD 145102.

HD 145102	**LS (cd^{-1})**	**Period04 (cd^{-1})**	**PDM (cd^{-1})**	**Amp (mmag)**	N (#)	N_{id} (#)	A_m (mmag)	z (mmag)	4σ (mmag)
2007	0.7051(12)	0.7050(14)	0.7058(19)	3.36(16)	614	307	0.16	0.51	0.63
2008	0.7017(15)	0.7018(13)	0.7103(20)	3.33(15)	675	338	0.16	0.53	0.65
2010	0.7058(19)	0.7059(19)	0.6956(39)	3.42(19)	587	294	0.19	0.61	0.75
2011	0.7048(12)	0.7053(13)	0.7067(44)	3.86(17)	685	343	0.18	0.57	0.70
Comb	0.705301(9)	0.702400(10)	0.7091(36)	3.49(8)	2561	1281	0.09	0.29	0.34

In this study, we obtained four-year data of HD 145102. Unlike in previous studies, the LC amplitudes were good enough to compute variability periods for each year. Even in 2007, the LC gave the expected period although some data points were taken out due to bad observations. The LS and PDM algorithms were in good agreement with each other and found similar results (LS $\approx$ PDM ≈ 0.71 cd^{-1}). In addition to the main frequency, both methods detected another structure at around 0.35 cd^{-1} in the data observed in 2008, and this period was stronger than the primary one in the PDM periodogram. For this reason, we restricted the frequency range and derived a frequency close to 0.70 cd^{-1}. This structure was also quite strong in the LS periodogram in 2008 compared to the other years. Moreover, all annual LS amplitude spectra had an additional peak at approximately 1.40 cd^{-1}, and it was powerful enough to be detected in the four-year combined LS periodogram (Fig. A.13; on page 298 and Fig. A.14; on page 299).

A folded LC was produced with the LS period. It had a sinusoidal shape with a single maximum and a wide minimum, as well as an additional structure around the minimum. Such a curve was also obtained by using *Hipparcos* data (Perryman et al., 1997), and its period was

Table 5.15: Available period values and extremum times for HD 145102.

Time (year)	**Period (day)**	**References**	**Extremum Times (HJD)**	**References**
1978	1.41(2)	Vanbeveren and Hensberge (1978)	2445831.5880	North (1987)
1984	1.41795(7)	North (1987)	2454393.8366(126)	This study
1990-1993	1.4177(2)	Perryman et al. (1997)	2454746.8845(127)	
2007	1.4178(6)	Wraight et al. (2012)	2455433.1092(94)	
2007-2011	1.41784(2)	This study	2455771.9757(148)	

compatible with our result ($P_{Hip} \approx 0.70$ cd^{-1}). To search for a possible period variation, we brought all available literature data together (Table 5.15). In Fig. A.14 (bottom left; on page 299), these values and the combined LS period are shown with black and red diamond symbols, respectively. Since the period found by Vanbeveren and Hensberge (1978) had a large error, we did not take it into account for our calculations. Accordingly, the rest of the data exhibited a small decrease in the period of about -3.11×10^{-6} days yr^{-1}.

In the O-C graphic given in Fig. A.14 (bottom right; on page 299), we combined the extremum times provided by North (1987) and derived from *STEREO* LCs (Table 5.15). Since the archival data included a minimum time, we applied a phase correction. However, the overall data did not exhibit any period variation. The light elements were computed as:

$$HJD_{(max)} = 2454393.8366(126) + 1.417835(19)E \ .$$

Finally, we calculated the radius and rotational velocity of the star as $R/\mathrm{R}_{\odot} = 2.90(51)$ and $V_{eq} \approx 104(18)$ km s^{-1} with the help of the physical parameters $log(L/\mathrm{L}_{\odot}) = 2.03(15)$, T=10,919(182) K, provided by Wraight et al. (2012). Our rotational velocity was much higher than Wraight et al.'s (2012) result ($Vsini = 71.3(1.5)$ km s^{-1}).

5.5.8 HD 150714 (V2353 Oph; HIP 81893)

HD 150714 (A0Si, $V = 7.57$ mag) is one of the unknown stars in the literature since there has not yet been any study focused on the star and its characteristics.

In this research, we initially obtained four-year LCs of HD 150714. Due to bad observations, a number of data points that composed a whole maximum was removed from the LC observed in 2008. In contrast, other curves were clear and continuous. As shown in Fig. A.15 (on page 300), seasonal data showed cyclic modulations, as well as a secondary structure in the middle of each minimum.

The PDM and LS methods found accurate frequencies for the main variability (PDM $\approx$ LS ≈ 0.61 cd^{-1}). Additionally, both techniques detected the secondary periodicity at around 1.22 cd^{-1}. Whereas it was noticeably weaker in PDM periodograms, LS produced two peaks with nearly the same intensity in 2008 and 2011. Frequency analyses of the combined data also detected two quite powerful peaks at around 0.61 and 1.22 cd^{-1}(Fig. A.16, mid-left; on page 301). Moreover, a folded LC was generated using the combined LS period. The main curve produced was formed of a double-waved sinusoid whose secondary maximum was remarkably fainter than the primary one, and perfectly represented the annual variations.

Table 5.16: Frequency analysis results of HD 150714.

HD 150714	**LS (cd^{-1})**	**Period04 (cd^{-1})**	**PDM (cd^{-1})**	**Amp (mmag)**	N (#)	N_{id} (#)	A_m (mmag)	z (mmag)	4σ (mmag)
2007	0.6157(9)	0.6148(13)	0.6151(13)	19.10(74)	619	310	0.66	2.12	2.64
2008	0.6157(10)	0.6159(19)	0.6150(14)	14.11(76)	681	341	0.51	1.65	2.04
2010	0.6140(12)	0.6140(15)	0.6128(28)	19.44(78)	677	339	0.63	2.04	2.53
2011	0.6130(11)	0.6132(17)	0.6139(13)	13.60(72)	693	347	0.57	1.85	2.29
Comb	0.613851(4)	0.613851(9)	0.6142(16)	16.48(38)	2670	1335	0.30	1.02	1.19

In order to investigate a possible period variability, we put all available period values together with our data (Table 5.17). As seen in Fig. A.16 (bottom-left; on page 301), the overall data suggested an increase in period, but several conflicting period results were given between 1990 and 1993. We calculated the variation rate of this increase to be around 3.60×10^{-5} days yr^{-1}.

On the other hand, we also analysed O-C data to confirm the variability seen in the period. Hence, we collected published maximum times in the literature and combined them with our results (Table 5.17). We found that the data showed an upward-curving parabolic variation (Fig. A.16, bottom-right; on page 301). From the data, the stellar period increased since the 1990s even though it appeared to be stable between 2007 and 2011. We derived the rate of this

change to be $2.15(1.37) \times 10^{-6}$ days yr^{-1} or $0.19(11)$ s yr^{-1}. Accordingly, the light elements of the star were:

$$HJD_{(max)} = 2454406.3093(69) + 1.629060(12)E + 4.80(3.05) \times 10^{-9}E^2 \ .$$

The error of the quadratic term of the least-squares fit was quite high due to the precisions of literature data. Therefore, it might not be possible to interpret such a variation as an indicator of a magnetic deceleration. However, if this change was indeed real, it might have affected the dynamic elements of the stars. Based on these results and using the physical parameters given by Wraight et al. (2012) (T = 10,547(60) K, M = 2.58(18) $M_\odot$, $log(L/L_\odot)$ = 1.71(19) and R = 2.15(47) $R_\odot$, which was calculated from L and T values), kinetic energy and its variation rate were estimated at around $E = 4.59(2.04) \times 10^{46}$ erg and $dE/dt = -3.84(2.98) \times 10^{33}$ erg s^{-1}. We also found the corresponding angular momentum and its variation rate to be around $J = 2.05(91) \times 10^{51}$ erg s and $dJ/dt = -8.59(6.67) \times 10^{37}$ erg. According to period and angular momentum changes, the spin-down time-scale of the star was approximately τ_{SD} = $7.58(6.77) \times 10^5$ yr, which was compatible with duration derived from the energy and its variation rate ($\Delta\tau = E/(dE/dt) = 3.79(3.39) \times 10^5$ yr). Also, we found the MS lifetime of the star to be around $\tau_{MS} = 9.35(1.63) \times 10^8$ yr.

Table 5.17: Available period values and extremum times for HD 150714.

Time (year)	**Period (day)**	**References**	**Extremum Times (HJD)**	**References**
1990-1993	1.62817	Dubath et al. (2011)	2448095.3849(200)	Perryman et al. (1997)
1990-1993	1.62829	Perryman et al. (1997)	2448098.6733(156)	
1991	1.62880(11)	Watson (2006)	2448501.0020(100)	Watson (2006)
2007	1.6290(8)	Wraight et al. (2012)	2454406.3093(69)	This study
2007-2011	1.629060(12)	This study	2454750.0396(111)	
			2455440.7629(101)	
			2455786.1238(98)	

In addition to these, such a period increase might be a result of a change in stellar mass with a rate of around $dM/dt = 2.73(1.56) \times 10^{-12}$ $M_\odot$yr^{-1}, or a consequent of a change in radius with a rate of around $dR = 1.42(96) \times 10^{-6}$ $R_\odot$yr^{-1}. Finally, we found the rotational velocity of the star to be $V_{eq} = 67(15)$ km s^{-1} with the help of our combined LS period and radius value (R = 2.15(47) $R_\odot$) estimated from the parameters given above.

5.5.9 HD 155804

HD 155804 (A3, $V = 8.23$ mag) has not previously been studied in the literature. We monitored this star between 2007 and 2011 and derived good periodic variations during a four-year time interval. Due to bad observations, some data points were removed from the LC taken in 2008, but this did not cause any significant change in period. Following frequency analyses, we obtained similar period results with both PDM and LS methods for each year.

Table 5.18: Frequency analysis results of HD 155804.

HD 155804	**LS** ($\mathbf{cd^{-1}}$)	**Period04** ($\mathbf{cd^{-1}}$)	**PDM** ($\mathbf{cd^{-1}}$)	**Amp** **(mmag)**	N (#)	N_{id} (#)	A_m	z **(mmag)**	4σ
2007	0.9371(28)	0.9370(29)	0.9319(62)	14.29(88)	684	342	0.81	2.62	3.25
2008	0.9220(37)	0.9219(40)	0.9157(120)	12.09(1.00)	667	334	1.00	3.23	4.01
2010	0.8770(34)	0.8769(36)	0.8705(111)	15.49(91)	676	338	0.86	2.76	3.42
2011	0.9147(37)	0.9147(38)	0.9144(88)	12.75(96)	640	320	0.86	2.76	4.37
Comb	0.917374(17)	0.917374(17)	0.9249(117)	11.91(51)	2667	1334	0.47	1.63	1.89

For the four-year combined LC, the algorithms determined slightly different frequency values (PDM = 0.92493 cd^{-1}, LS = 0.91737 cd^{-1}). The best folded LC, consisting of a smooth single-waved sinusoid, was produced with only the LS period. However, the accuracy of curve shape and LS period could not be checked since there was no *Hipparcos* data for this star. The overall results of the frequency analyses and LC properties are given in Table 5.18. The significance levels of the frequencies detected are plotted in the relevant periodograms in Fig. A.17 on page 302 and Fig. A.18 on page 303.

Since there was no archival information, we could not search for a long-term period variation, but we attempted to interpret short-term changes using only seasonal *STEREO* results. According to these, the data indicated a period increase with a variation ratio of around 0.01 days yr^{-1} between 2007 and 2011, as seen in Fig. A.18 (bottom left; on page 303).

To support such a variation, we also investigated the changes in the O-C diagram with the help of the best maximum times (HJD-2400000) obtained from annual *STEREO* LCs (54405.3693(122), 54756.3740(204), 55445.3048(316), 55783.2138(178)). As shown in Fig. A.18 (on page 303), the variation was within the error limits of the data points. Additionally, we calculated the light elements of the star as:

$$HJD_{(max)} = 2454405.3693(122) + 1.090068(20)E \ .$$

5.5.10 HD 171184 (V451 Sct; HIP 91001)

There have been few studies regarding HD 171184 (A0Si, $V = 7.89$ mag) and its period evolution in the literature. The first study was performed by *Hipparcos* team, which calculated a rotation period of around 2.79926(8) days (Perryman et al., 1997). Later, Dubath et al. (2011) determined a similar period using *Hipparcos* data (Table 5.20).

Table 5.19: Frequency analysis results of HD 171184.

HD 171184	**LS (cd^{-1})**	**Period04 (cd^{-1})**	**PDM (cd^{-1})**	**Amp (mmag)**	N (#)	N_{id} (#)	A_m (mmag)	z (mmag)	4σ (mmag)
2007	0.3571(10)	0.3572(12)	0.3564(19)	22.81(90)	697	349	0.83	2.70	3.34
2008	0.3571(10)	0.3571(11)	0.3614(21)	21.92(82)	671	336	0.77	2.48	3.08
2010	0.3528(7)	0.3527(8)	0.3529(15)	23.93(93)	701	351	0.71	2.29	2.83
2011	0.3527(11)	0.3525(12)	0.3536(30)	23.31(86)	624	312	0.93	2.99	3.72
Comb	0.354403(5)	0.354414(7)	0.3600(34)	26.27(46)	2693	1347	0.40	1.38	1.60

In our investigation, we probed four-year LCs observed by the *STEREO* satellite between 2007 and 2011. As seen in Fig. A.19 (on page 304), seasonal data displayed good periodic cycles as well as secondary structures that were close to the ascending branches at the minimum phases. PDM and LS results were in agreement, and both techniques found the frequency value at around 0.35 cd^{-1}. The overall results and LC properties are presented in Table 5.19. Significance levels that were calculated based on noise values (A_m) of the periodograms were also plotted in relevant figures.

Additionally, we detected clear frequencies for the four-year combined data (Fig. A.20, middle; on page 305), but the period of the main peak detected with PDM (0.36 cd^{-1}) was slightly greater than the LS result. To produce a folded LC, we preferred to use the LS period since the *Hipparcos* data were compatible with this value. The folded curve was formed of a single-waved sinusoid, and the distorted effect of the additional structure was clearly observed.

Table 5.20: Available period values and extremum times for HD 171184.

Time (year)	**Period (day)**	**References**	**Extremum Times (HJD)**	**References**
1990-1993	2.79926(8)	Perryman et al. (1997)	2454433.7754(179)	This study
1990-1993	2.79963	Dubath et al. (2011)	2454775.1980(146)	
2007-2011	2.821646(38)	This study	2455466.4986(129)	
			2455807.9257(223)	

Apart from this, we also inspected a possible period variation in the star by combining all available periods in the literature and our *STEREO* results (Table 5.20). As shown in Fig. A.20

(on page 305), the period of the star increased from 2.80 to 2.82 days over two decades, and we derived its variation ratio to be approximately 7.34×10^{-3} days yr^{-1}.

To gain insight regarding this change in the O-C diagram, we used maximum times obtained from *STEREO* LCs. However, we could detect no variation in the diagram. Using the LS period and the best maximum time, we determined the ephemeris elements as:

$$HJD_{(max)} = 2454775.1980(146) + 2.821646(38)E \ .$$

Finally, we calculated the radius and rotational velocity of the star as $R/\mathrm{R}_{\odot} = 2.30(45)$ and $V_{eq} \approx 41(8)$ km s^{-1} with the help of the physical parameters, $log(L/\mathrm{L}_{\odot}) = 2.00(17)$, T=12,050(1.03) K, provided by Kochukhov and Bagnulo (2006).

5.5.11 HD 173657 (HIP 92215)

HD 173657 (B9SiCr, $V = 7.41$ mag) is another rarely studied peculiar star. The only scientific research on it was performed by Koen and Eyer (2002), who found its rotation period as 1.93720 days.

We analysed four-year data covering the period between 2007 and 2011. Although the LCs were noisy, main variability and additional structure in the descending branch were still distinguishable. The PDM and LS techniques determined a similar frequency at around 0.52 cd^{-1}. Furthermore, PDM detected another frequency at 1.00 cd^{-1} in the LCs observed in 2007 and 2008, but this frequency was not apparent in the 2010 and 2011 data. In contrast, the same structure appeared in all LS periodograms, and its strength varied year by year. The overall results of the frequency analyses and LC properties are presented in Table 5.21.

Table 5.21: Frequency analysis results of HD 173657.

HD 173657	**LS (cd^{-1})**	**Period04 (cd^{-1})**	**PDM (cd^{-1})**	**Amp (mmag)**	N (#)	N_{id} (#)	A_m (mmag)	z (mmag)	4σ (mmag)
2007	0.5208(21)	0.5208(23)	0.5151(28)	8.73(60)	696	348	0.48	1.54	1.90
2008	0.5200(22)	0.5200(26)	0.5165(15)	5.68(51)	686	343	0.47	1.53	1.90
2010	0.5127(17)	0.5127(19)	0.5196(36)	11.37(62)	584	292	0.47	1.50	1.87
2011	0.5212(19)	0.5210(21)	0.5182(60)	8.26(51)	699	350	0.48	1.54	1.91
Comb	0.518919(13)	0.518919(13)	0.5155(42)	8.47(29)	2665	1333	0.24	0.82	0.95

We produced a folded LC by using the combined LS period. The curve was sinusoidal, but its shape was different than those of the other CP samples. It had two maxima with quite different heights. The primary maximum showed a narrow and sharp peak compared to the other (Fig. A.22, top left; on page 307). We were unable to obtain a comparable *Hipparcos* LC, since its period value was different from the LS period. With the help of the literature data and combined LS periods, we also searched for a possible variation in stellar rotation. As seen in Fig. A.22 (bottom left; on page 307), we detected a decrease in the period between 1990 and 2011, and its variation rate was around -5.78×10^{-4} days yr^{-1}.

To confirm such a change, we analysed the maximum times (HJD - 2400000) derived from *STEREO* LCs: 54438.7152(114), 54781.7320(159), 55461.9760(151), 55812.7244(187). However, the data points exhibited no change between 2007 and 2011. Lastly, using the improved rotation period and the best maximum time, we obtained the light elements as:

$$HJD_{(max)} = 2454781.7320(159) + 1.927083(50)E \ .$$

5.5.12 HD 178929 (HIP 94274)

HD 178929 (B7II/III, $V = 7.72$ mag) is a CP star that had yet not been studied. Our observations covered a four-year time interval between 2007 and 2011. Individual LCs displayed at least four light cycles for each season, but we removed most of the points from the data observed in 2010 due to intensive scatter (Fig. A.23; on page 308). The LCs had clear, single-waved sinusoidal modulations as well as bulges superimposed on both ascending and descending branches. Because of small cycle numbers, we had difficulties performing analyses with PDM. For all LCs, PDM failed in finding the expected result and gave a frequency value of around 0.15 cd^{-1}. LS, in contrast, detected the variation at 0.30 cd^{-1}.

Table 5.22: Frequency analysis results of HD 178929.

HD 178929	**LS (cd^{-1})**	**Period04 (cd^{-1})**	**PDM (cd^{-1})**	**Amp (mmag)**	N (#)	N_{id} (#)	A_m	z (mmag)	4σ
2007	0.2923(9)	0.2923(9)	0.2901(32)	24.1(7)	700	350	0.66	2.14	2.64
2008	0.2975(8)	0.2976(8)	0.2991(26)	25.2(6)	690	345	0.66	2.14	2.64
2010	0.2947(12)	0.2941(12)	0.2947(34)	26.8(8)	686	343	0.66	2.15	2.66
2011	0.3004(16)	0.3002(17)	0.3000(48)	22.5(1.1)	700	350	1.20	3.87	4.78
Comb	0.296045(5)	0.296048(7)	0.2949(36)	24.4(4)	2776	1388	0.40	1.39	1.61

Since frequency analyses of the four-year combined data found the most powerful peak at approximately 0.30 cd^{-1}, this value was assumed to be the most accurate period. The overall results derived from the LCs are given in Table 5.22. Also, the significance levels of the periodograms are presented in Fig. A.23 (on page 308) and Fig. A.24 (on page 309).

By using the combined LS period, we produced a folded LC that excellently demonstrated all characteristics of annual curves. To prove the accuracy of our period, we also extracted *Hipparcos* data (Perryman et al., 1997), and found a frequency value of around 0.29904(6) cd^{-1}. This value was quite compatible with our results, and the shape of the folded *Hipparcos* curve was analogous to our LC. Apart from this, since the PDM method detected a period of 0.15 cd^{-1}, we also attempted to generate a folded curve with this value, and derived a good double-waved variation. However, the shapes of consecutive structures were similar to each other, and hence we did not take this period into account.

In order to check a possible period variation, we used *Hipparcos* and combined *STEREO* periods. As shown in Fig. A.24 (bottom left; on page 309), we determined a period increase between 1990 and 2011, and calculated its variation rate to be around 1.94×10^{-3} days yr^{-1}. However, such a change did not exist in the O-C graphic that consisted of the best maximum

times – 54439.0536(138), 54776.8298(167), 55465.9132(146), 55820.6049(167) – calculated from annual LCs. Accordingly, we computed the light elements as:

$$HJD_{(max)} = 2454435.6355(110) + 3.377868(56)E \ .$$

5.5.13 HD 187473 (V4064 Sgr; HIP 97684)

HD 187473 (B9SiSrCrEu, $V = 7.32$ mag) is an α^2 CVn type variable star, and is the most attractive sample due to its outstanding light variations. Its photometric period was first determined by Hensberge et al. (1977) as 4.75(4) days. They stated that this variability had an outstanding amplitude of 0.1 mag in y and in b, 0.07 mag in v, and greater than 0.2 mag in u bands. They also detected a secondary maximum. Later, Hensberge et al. (1978) improved upon earlier findings to determine the period to be 4.718(1) days. Apart from these investigations, Catalano et al. (1998) searched the near-infrared variability of the star and derived a double-wave behaviour with an extraordinary amplitude of 0.1 mag. This was the largest observed variation among CP stars. To the present day, many other studies have attempted to find a period value and generally obtained close results (Table 5.24).

Table 5.23: Frequency analysis results of HD 187473.

HD 187473	**LS (cd^{-1})**	**Period04 (cd^{-1})**	**PDM (cd^{-1})**	**Amp (mmag)**	N (#)	N_{id} (#)	A_m (mmag)	z (mmag)	4σ (mmag)
2007	0.2142(3)	0.2143(5)	0.2126(5)	50.52(96)	697	349	0.52	1.67	2.06
2008	0.2142(3)	0.2148(6)	0.2126(5)	49.96(1.03)	670	335	0.55	1.77	2.19
2010	0.2105(15)	0.2097(18)	0.2111(32)	48.20(1.99)	533	267	2.59	8.25	10.34
2011	0.2130(3)	0.2134(6)	0.2119(7)	48.88(98)	702	351	0.48	1.54	1.90
Comb	0.214863(2)	0.214863(5)	0.21203(3)	49.27(59)	2602	1301	0.51	1.74	2.03

In this investigation, we used four-year LCs, three of which (2007, 2008, and 2011) showed excellent and clear variations. Similar to previous observations, the secondary structure was detectable around the minimum phase in each year (Fig. A.25; on page 310). In contrast, the LC of 2010 was quite noisy and had a smaller number of cycles. As shown in Table 5.23, in which the LC properties are presented, the number of data points and noise level of the data taken in 2010 were not comparable to those of other years.

The PDM and LS techniques detected two significant frequencies at around 0.21 cd^{-1} for the primary change and 0.40 cd^{-1} for the other structure. However, whereas the latter one was almost invisible in PDM periodograms, LS displayed powerful peaks. Additionally, PDM had another variability at 0.10 cd^{-1}, which might be an alias of the main frequency. This was slightly more powerful than the primary peak in 2010 due to the problem previously mentioned. A folded LC was generated by the LS period since it provided a very good curve with no dispersion. As described by Hensberge et al. (1978), it exhibited spectacular variations with a double-wave.

Table 5.24: Available period values and extremum times for HD 187473.

Time (year)	**Period (day)**	**References**	**Extremum Times (HJD)**	**References**
1975	4.75(4)	Hensberge et al. (1977)	2442619.5839	Hensberge et al. (1978)
1977	4.718(1)	Hensberge et al. (1978)	2454449.5216(67)	This study
1993	4.718(1)	Catalano et al. (1998)	2454793.9276(87)	
1990-1993	4.71303	Dubath et al. (2011)	2455822.4961(88)	
1990-1993	4.71810(19)	Perryman et al. (1997)		
2007-2011	4.6541347(1)	This study		

To search for a long-period variation, we collected all available literature data (Table 5.24). According to the period trend graphic in Fig. A.26 (on page 311), the period given by Hensberge et al. (1977) was greater than the other values. Even though the data between 1975 and 1995 showed no change over 20 years, our four-year combined period (red diamond) was 0.063 days shorter than the average period value ($\overline{P}$= 4.7168 days). Considering these circumstances, it was clear from the figure that the period decreased since the 1970s; we calculated the variation ratio for this change to be around -2.24×10^{-3} days yr^{-1}.

Moreover, we also followed the trail of such a change in the O-C diagram (Fig. A.26, bottom right; on page 311). To do this, we put the extremum times directly taken from the literature and the *STEREO* together (Table 5.24). Since the LC data of 2010 was not usable, we did not calculate a maximum time for this year. Also, the epoch given by Hensberge et al. (1978) was converted to HJD, but this value was somewhat controversial. Whereas this epoch was given as a reference of a zero phase, which coincided with the light minimum by Hensberge et al. (1978), it corresponded to the light maximum in the observation of Catalano et al. (1998).

For the latter case, which is presented in Fig. A.26 (bottom right; on page 311), we could not determine any period variation. For the former case, we applied a phase correction, and consequently the overall data displayed a period decrease with a variation rate of around $-2.78(1.84)$ s yr^{-1}. Such a decrease and also its error were quite extreme and not persuasive. As a result, we determined the light elements as:

$$HJD_{(max)} = 2454449.5216(67) + 4.6541347(1)E \ .$$

5.5.14 HD 246706 (HIP 26993)

HD 246706 (B8SiSr, $V = 9.13$ mag) is one of the faintest samples and had not been studied in detail since its discovery. We obtained four-year photometric data of HD 246706 between 2007 and 2011. All LCs showed an explicit modulation with the frequency value of around 0.68 cd^{-1}. The periods found by the PDM and LS algorithms were in good agreement with each other, except for the data taken in 2007. Unlike the LS method, PDM found a frequency of around 0.25 cd^{-1} due to high noise in this data.

Table 5.25: Frequency analysis results of HD 246706.

HD 246706	**LS (cd^{-1})**	**Period04 (cd^{-1})**	**PDM (cd^{-1})**	**Amp (mmag)**	N (#)	N_{id} (#)	A_m	z (mmag)	4σ
2007	0.6807(17)	0.6807(17)	0.6991(65)	20.27(1.21)	613	307	1.43	4.59	5.71
2008	0.6848(17)	0.6848(18)	0.6752(48)	20.30(1.03)	668	334	1.31	4.23	5.25
2010	0.6792(17)	0.6792(17)	0.6815(39)	19.79(1.08)	688	344	1.28	4.13	5.12
2011	0.6799(19)	0.6799(21)	0.6772(61)	23.29(1.30)	501	251	1.55	4.93	6.20
Comb	0.680448(8)	0.680448(11)	0.6859(47)	20.66(58)	2470	1235	0.69	2.37	2.77

In order to fold the phases of four-year LCs, we used the LS period since it produced unscattered data points. The folded LC was formed of a single-waved sinusoidal whose maximum was wider than the minimum, and whose ascending branch was slightly steeper. This structure was also the characteristic of the annual curves. A similar period and LC were also derived with *Hipparcos* data (Perryman et al., 1997). However, due to the quality of observations, the data were scattered. From the period trend graphic in Fig. A.28 (bottom left; on page 313), we attempted to discern a possible change in the period. To do this, we used values given by Wraight et al. (2012) (1.4697(6) days) and derived from *Hipparcos* data (1.4696(2) days), as well as our combined LS period. However, we could not determine any variation since the sigma values of literature data were quite large. Nevertheless, we were able to construct an O-C diagram by combining the best maximum times (54250.8920(105), 54590.3658(222), 55281.0897(159), and 55622.0439(229)). Similar to the period-trend graphic, the change was within the error limits of the data points. Accordingly, we obtained the light elements as $HJD_{(max)} = 2454590.3658(222) + 1.469621(18)E$.

We also calculated the radius and rotational velocity of the star as $R/\mathrm{R}_{\odot} = 1.32(56)$ and $V_{eq} \approx 45(19)$ $\mathrm{km\,s^{-1}}$ with the help of the physical parameters $log(L/\mathrm{L}_{\odot}) = 1.59(37)$, T=12,561(3) K, provided by Wraight et al. (2012). Our rotational velocity was comparable with that of Wraight et al. (2012) ($Vsini = 35(5.3)$ $\mathrm{km\,s^{-1}}$).

5.6 Discussion

In this study, photometric data of selected CP stars were derived from the *STEREO* satellite between 2007 and 2011 for the purpose of investigating their period evolution. A total of 8,040 CP variables were initially collected from various catalogues, and LCs of 3,473 observable candidates were screened. Of these, only 14 targets were chosen for detailed period analysis, as they met our selection criteria: brightness with $V \leq 10^m$, position within the FOV of the *STEREO*, clean variations in LC and amplitude spectrum, and being unaffected by the light of a neighbouring star.

During the analyses, four years of seasonal LCs and a compilation of these data were examined with two widely-used frequency detection methods: LS and PDM. Their results were compared to each other and those of Period04. With the help of the refinement pipeline coded, the best periods and their sigma values (mostly $\sigma_P \approx 10^{-5}$ days) were obtained. These were then used to investigate short-term (between 2007 and 2011) variations in period. In addition, epoch values representing maximum times of *STEREO* LCs were calculated and supplemented with all those relevant archived observations that were available to study the period evolution seen in the O-C diagram.

Accordingly, all samples showed quite significant light changes, which could be fitted well by a *sine* function and its first harmonic. Their period distribution was exactly within the range given as $1 < P_{CP}$ (days) < 10 for CP variables (in extreme cases the periods can be around 0.5 days or as long as several decades; Mikulášek et al. (2011)). These values were quite consistent with archival records. In contrast, the photometric periods of some samples, such as HD 31592 and HD 34547, were different from those in the literature since their rotation periods were twice the photometric periods. This result was reached by checking folded LCs produced with four-year combined data. The period values of all sample stars can be found in the last column of Table 5.27.

Ten of the samples did not display a significant change in their O-C graphics between 2007 and 2011. All variations were within the error limits of data points. This finding was not surprising, since strict periodicity due to slow rotation is a common property of the majority of these stars, as stated by several researchers such as Mikulášek et al. (2009). However, it should be considered that the four-year time interval was quite short to observe a potential period variation, meaning that this interval might constitute a small fraction of a significant change.

Table 5.26: Periods and their variation rates as well as spin-down and MS lifetimes of four CP stars are presented in table.

HD	P (day)	dP/dt (s yr^{-1})	$\dot{P}/P$ (s^{-1})	$\tau_{SD/ACC}$ (yr)	τ_{MS} (yr)
24769	2.975197(16)	-0.49(12)	-6.06(1.46)$\times10^{-14}$	-5.23(3.08)$\times10^{5}$	5.72(96)$\times10^{8}$
30466	1.406830(10)	-0.11(3)	-2.86(68)$\times10^{-14}$	-1.11(63)$\times10^{6}$	9.26(1.25)$\times10^{8}$
125248	9.29541(12)	0.35(14)	1.36(55)$\times10^{-14}$	2.33(1.12)$\times10^{6}$	1.29(10)$\times10^{9}$
150714	1.629060(12)	0.19(12)	4.18(2.66)$\times10^{-14}$	7.58(6.77)$\times10^{5}$	9.35(1.63)$\times10^{8}$

In contrast, it is reported in the literature that a small number of CP stars show notable period changes within several years. CU Vir and V901 Ori, which have alternating period increases and decreases, and BS Cir, which has a moderate rotation deceleration, are some of the most important samples among these stars (Mikulášek et al., 2014). The variation rates of their periods are given as $\dot{P}/P = 5.28 \times 10^{-14}$ s^{-1} for Cu Vir, $\dot{P}/P = 1.33 \times 10^{-13}$ s^{-1} for V901 Ori, and $\dot{P}/P = 3.02 \times 10^{-14}$ s^{-1} for BS Cir.

Meynet and Maeder (2006) suggest that the moment of inertia and rotation period should change in mildly rotating stars showing no substantial angular momentum loss, and that evolution models in fact predict a slowing in their stellar rotation. Mikulášek et al. (2014) then points out that the fastest change in period is seen in the most massive stars ($\tau_{MS} \approx 30$ Myr), and is roughly $\dot{P}/P = 1.04 \times 10^{-15}$ s^{-1}. However, change rates given for CU Vir, V901 Ori, and BS Cir and even their errors are several times greater than evolutionary changes. Such a result was also confirmed in this study. Based on our examination of *STEREO* and archival data, it was detected that HD 24769, HD 30466, HD 125248, and HD 150714 had explicit period variations in their O-C diagrams (Table 5.26). Of these stars, HD 125248 and HD 150714 showed period increases while the periods of HD 24769 and HD 30466 decreased. Further, rotations of HD 125248 and HD 150714 have slowed down 0.35(14) and 0.19(13) s yr^{-1}, respectively. However, their error values were quite high due to the data provided in the literature. On the other hand, it was revealed that HD 30466 has been rotating 0.11(3) seconds faster per year. As seen from Table 5.26, the variation in periods of these stars ($\dot{P}/P = 10^{-14}$ s^{-1}) was 10 times greater than that of the most massive CP stars, and quite compatible with the findings of Mikulášek et al. (2014). In addition, their spin-down and acceleration time-scales were around $\tau_{MS} \sim 10^5 - 10^6$ yr. These values were nearly three orders of magnitude shorter than the MS lifetimes of these stars ($\tau_{MS} = 10^8 - 10^9$ yr). This, in turn, suggested that processes of increase or decrease in

the periods of the samples might be reversible. If so, the length of these cycles can be roughly estimated by $T_{cyc} \sim P \sqrt{2/\dot{P}}$ (Mikulášek et al., 2010). Accordingly, these produced estimates of 92(11) yr, 92(11) yr, 344(69) yr, and 82(26) yr for HD 24769, HD 30466, HD 125248, and HD 150714, respectively.

It is not possible to measure rotational slowing caused by stellar evolution of MS stars with current methods, since variation rates are quite small. Also, if rotational evolution is a consequence only of evolutionary changes, the rotational periods of CP stars would be relatively constant (Mikulášek et al., 2014). In spite of this, observational facts indicate that the periods of some CPs vary. As a result, numerous hypotheses related to the origin of these changes have been offered. These hypotheses, all of which assume that these stars rotate as a solid body (Stibbs, 1950), can be delineated as:

- mass and radius variations during MS evolution,
- angular momentum loss because of standard and magnetized stellar winds,
- precession of rotation axis,
- light-time effect occurring due to an additional component.

The reason for the period decrease in CP stars can be explained by the first two options. However, it was already mentioned that detection of rotational slowing due to evolutionary reasons is not possible since variation is at least three times larger than observational limits (Mikulášek et al., 2014). Also, the spin-down time-scale caused by standard stellar winds can not be measured, because it is much larger than the evolutionary time-scale. Further, angular momentum loss that occurs due to magnetic winds can only be calculated for extremely hot CP stars with strong magnetic fields (Mikulášek et al., 2014). However, the temperature of our three stars is around 10,000 K. For the third explanation, the effects of precession in rotation axis should be seen as cyclic changes in LCs. Yet, there is no peculiarity observed in our LCs, and no archival records found related to such changes. Also, Mikulášek et al. (2011) indicate that the amplitude of these variations originating from precession can be ignored. Finally, the last mechanism is a light-time effect, which causes a cyclic variation in the O-C diagram. This case is not appropriate for our samples, as their O-C variations are parabolic and there are no archival reports indicating that HD 30466, HD 125248, and HD 150714 have a companion star. Therefore, this final explanation is also ruled out.

Considering the options outlined above and the fact that period variation processes might be reversible due to shorter spin-down time-scales than those of MS lifetimes, the rigid rotation hypothesis should be discarded and the differential rotation model should alternatively be discussed in detail as expressed by Stępień (1998). In this model, the outer layers of stars differentially rotate with respect to denser interiors, and they are affected by global magnetic fields; an interaction between meridional circulations and magnetic fields takes place in a region within a star. This region is an interface between inner layers where circulation is dominant and the outer envelope is influenced by magnetism. As a result of differential rotation, a toroidal component of the internal magnetic field is produced, and it increases until the outer magnetically-confined envelope is forced to co-rotate with the interior. Hence, a cyclic increase and decrease in the moment of inertia occurs (Stępień, 1998). This means that an unexpected alternating variability of rotation periods can be observed, and this may be the explanation of the spin-down time paradox of these stars (Mikulášek et al., 2010). In this case, rotation acceleration in HD 30466 and deceleration in HD 125248 and HD 150714 may be interpreted as a consequence of torsional oscillations produced by meridional circulations being in interaction with a magnetic field, and of rotational braking in outer layers caused by angular momentum loss via magnetically-confined stellar wind.

Among these stars, the most significant change is detected in the period of HD 24769 ($\dot{P} \sim 0.49(12)\ \mathrm{s\,yr^{-1}}$). Unlike the other three samples, the reason for such a variation is binarity. This star has been reported to be a single-lined spectroscopic binary in the literature and an ellipsoidal, α^2 CVn type variable in the *Simbad* Database. In addition to its notable period change, this binary is important for another reason. According to Sion (1999), binaries with magnetic CP components are progenitors of cataclysmic variables, particularly of those having strong magnetic properties. It is speculated that the progenitor of the white dwarf component in cataclysmic systems is a $1.5 - 3.0\ \mathrm{M_\odot}$, A-type star located within the CP region on the H-R diagram. Furthermore, the mass transfer rate of such stars is given as $10^{-7}\ \mathrm{M_\odot yr^{-1}}$ (Chen and Han, 2002), which is consistent with the calculated rate of mass transfer for HD 24769. For these features, of interest, this star deserves detailed individual study.

The evolution state of CP stars is a controversial issue that has been discussed for decades. According to Oetken (1985), the magnetism in CP stars (CP2) developed in the final stages of MS evolution. This suggestion was supported by researchers such as Hubrig and Mathys (1994), who investigated peculiar stars in various clusters. Hubrig et al. (2000) revealed that

Table 5.27: Physical parameters of the sample stars are given in the table. Temperature, luminosity and mass values were adopted from the literature (references are in the relevant result sections). Radius and rotational velocities were estimated from period, temperature, and luminosity values. The parameters marked with asterisks were calculated from spectral types and parallax values in the *Simbad* Database.

HD	$Log(L/L_\odot)$	$Log(T)$	M ($M_\odot$)	R ($R_\odot$)	V_{eq} ($km\,s^{-1}$)	P (day)
24769	2.24(16)	3.983(7)	3.14(21)	4.76(89)	81(15)	2.975197(16)
30466	1.64(15)	4.045(11)	2.59(14)	1.80(32)	65(12)	1.406830(10)
31592	1.56(6)	3.996(5)	2.37(5)	2.05(15)	60(4)	1.735847(10)
34547	1.22(17)	4.003	2.16(13)	1.34(26)	20(4)	3.428779(40)
125248	1.50(8)	3.992(1)	2.27(7)	1.95(18)	11(1)	9.295413(115)
142884	2.17(14)	4.153(8)	3.63(19)	2.01(33)	127(21)	0.802967(4)
145102	2.03(15)	4.038(7)	2.95(18)	2.90(51)	104(18)	1.417835(19)
150714	1.71(19)	4.023(3)	2.58(18)	2.15(47)	67(15)	1.629060(12)
155804	0.67(43)*	3.941*		0.95(75)*	44(34)*	1.090068(20)
171184	2.00(17)	4.081(14)	3.03(18)	2.30(45)	41(8)	2.821647(40)
173657	1.99(13)*	4.053*		2.58(78)*	68(21)*	1.927083(50)
178929	2.53(21)*	4.121*		3.53(1.67)*	53(25)*	3.377868(57)
187473	1.64(8)*	4.053*		1.72(32)*	19(3)*	4.654135(49)
246706	1.59(37)	4.099(1)	2.81(27)	1.32(56)	45(19)	1.469621(18)

the H-R distribution of CP stars with $M < 3\ M_\odot$ differed from that of normal stars having the same temperature; the population of magnetic stars increased toward the centre of the MS band. In particular, Hubrig et al. (2000) discovered that magnetic fields showed up only in stars that had completed at least 30% of their MS lifetimes. However, there has been no definitive explanation for the evolution of magnetic fields in the MS. On the other hand, there have been some clues that stars with short-periods, high temperatures, and high mass showed stronger magnetic fields. Yet, there was no relation found between rotational period and the amount of MS lifetime completed for these stars. This situation indicated that CP stars must already have slowed down before they became magnetic (Pöhnl et al., 2003). In contrast, Gomez et al. (1998) discovered that CP stars spread to all MS bands, just like the distribution of normal stars in the same spectral type, and North et al. (1997) reported that CP stars displayed strong magnetic fields in every evolution stage. Stepien (1998) then showed that these stars did not have significant angular momentum loss during their MS lifetimes.

From the explanations above, it is clear that each researcher found different results about the evolution status of CP stars based on the amount and variety of data available. To contribute to these investigations, the temperature and luminosity values of 14 sample stars were derived from the literature, and the distribution of these stars on the H-R diagram was examined. By using these values, the radius and rotational velocity of these stars were also calculated

(Table 5.27). Since there are no archival studies related to HD 155804, HD 173657, HD 178929, and HD 187473, their physical parameters were computed with the help of their spectral types and parallax values provided in the *Simbad* database, and marked with asterisk symbols in Table 5.27. Their temperatures and bolometric corrections were estimated from Flower (1977). Interstellar extinction, A_ν, was found by the relation: $A_\nu = 3.1\ E(B-V)$, and $E(B-V) = (B-V) - (B-V)_0$, where $(B-V)_0$ is the intrinsic colour index approximated from Fitzgerald (1970). Additionally, although there was no error value for temperatures in Flower (1977), luminosity errors were calculated based on the error propagation method.

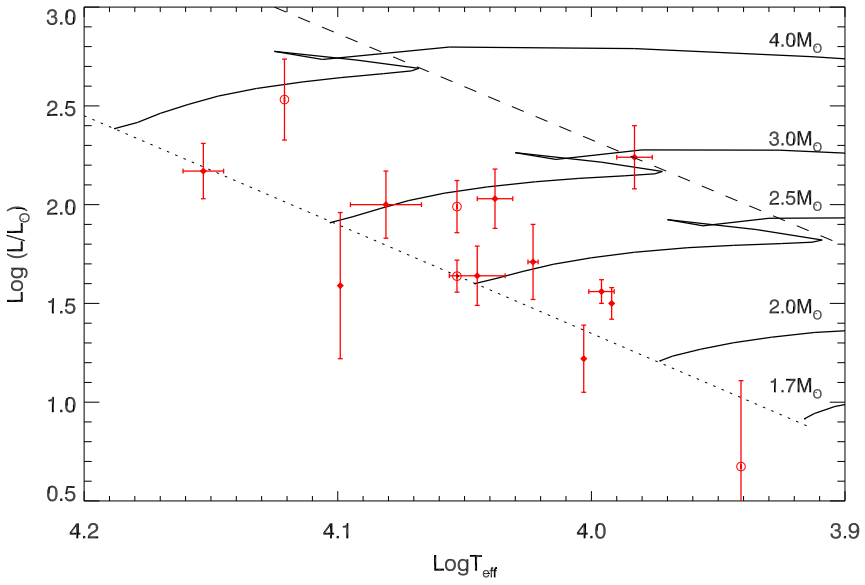

Figure 5.8: Positions of the samples on the H-R diagram are given in figure. Open circles and solid diamonds represent the four stars whose parameters were estimated from parallax values and spectral types, and the samples that have archival records, respectively. Also, evolution paths for intermediate mass stars (continuous lines), zero age MS (dotted line), and terminal age MS lines (dashed line) are from Schaller et al. (1992).

Accordingly, the positions of the sample stars on the H-R diagram are given in Fig. 5.8. Open circles and solid diamonds represent the four stars whose parameters were estimated from parallax values and spectral types, and the samples that have archival records, respectively. Also, evolution paths for intermediate mass stars (continuous lines), zero age MS (dotted line), and terminal age MS lines (dashed line) are from Schaller et al. (1992). As seen in the figure, only a single star, HD 24769, is on the terminal age MS. However, as previously discussed, this location is most likely a result of its binary nature. Similarly, HD 34547, HD 155804, and HD 246706 remain well below the zero age MS line. Among them, the parallax value of

HD 155804 and its error were quite high compared to other samples ($\pi = 14(9)$ mas; Kharchenko (2001)). For the other two stars, either temperature or luminosity is clearly miscalculated in the literature. Apart from those, the rest of the stars are located close to the zero age MS rather than concentrating towards the centre of the MS band or being uniformly distributed. Based on this, our finding corresponds neither to the results of Hubrig et al. (2000) nor to those of Gomez et al. (1998).

Also, 90% of our sample has been determined as an α^2 CVn type variable which shows strong magnetic fields. The distribution of the sample stars close to the zero age MS indicates that they do not need to complete 30% of their lifetimes for magnetic field formation to occur, i.e., it may be assumed that these stars achieve their magnetic properties before they reach the zero age MS. However, it should also be considered that we have a small number of sample stars and that literature data contain great error values.

As reported in the literature, there are numerous compiled catalogues with hundreds of CP stars, including Paunzen et al. (2013) and Wraight et al. (2012) (*STEREO*), Niemczura et al. (2009) (CoRoT), and Romanyuk and Kudryavtsev (2008) (ground-based). There are also several studies related to surface structures (Paunzen et al. (2015) and Lüftinger et al. (2010); surface structures of CoRoT stars HD 49310 and HD 50773), and pulsational behaviours of CP stars (Morel et al. (2014); CoRoT object HD 45975). However, few studies have been performed to achieve a better understanding of the period changes of these variables (Mikulášek et al. (2010), Mikulášek et al. (2014), etc.), and almost none of them are based on space-based missions. Therefore, our investigation is quite important in terms of contributing to studies on the period evolution of CP stars.

To conduct valuable research on the CP phenomenon, reliable observations, a high level of precision, and long-term follow-ups are required. In this stage, the *HI-1A* proves itself suited to this particular objective by facilitating high-quality analyses of the CP stars selected. To increase the accuracy and precision of our results, the amount of data collected between 2007 and 2011 can be increased. To do this, observation data of the *HI-1A* obtained after 2011 can be collected, or LCs observed by the *HI-1B* and the *HI-2* can be made compatible with *HI-1A* data. Additionally, the FOV of SMEI overlaps the outer portion of the *HI-1* imager, even if KEPLER and CoRoT do not. Thus, if there is any available data provided by SMEI, our current data can be combined with those. As a result, further information about the evolutionary stages of our sample stars can be obtained.

Chapter 6

Photometric and Spectroscopic Evolution of Some Bright Be-Stars: The Relationship Between Non-Radial Pulsations and Disk Structures

6.1 Introduction

Be-type variables are defined as non-supergiant B-stars exhibiting spectral line emissions in the hydrogen Balmer series, particularly in the Hα line (Jaschek et al., 1980). Despite sharing the same region with β Cephei and SPB stars on the H-R diagram, classical Be-stars have higher rotational velocities ($250 - 500\ \mathrm{km\,s^{-1}}$; Struve (1931)). They demonstrate periodic modulations in their LCs and have line profiles changing on time-scales from minutes to decades. Long-term variations are attributed to a dense circumstellar disk ejected from the star (Porter and Rivinius (2003), Carciofi et al. (2009), Cranmer (2009)); the emission lines observed are thought to be connected with this equatorial disk. Also, short-term changes are ascribed to NRPs, which might be responsible for the formation of the circumstellar disk.

Disk structure seems to be a persistent feature in some Be-stars whereas it is much more sporadic in others. Its formation and dissipation stand out as a transformation from a normal B-star to a B-emission or a Be-shell star in the spectrum (Sigut and Patel, 2013). Although it

is not clear why only some B-stars turn into Be-variables, the evolutionary stage of the central star and its rapid rotation are considered to be the keystones for this phenomenon (Porter and Rivinius, 2003). However, the actual rotational velocity of the star cannot be easily calculated due to gravity darkening (Townsend et al., 2004). Further, the rotation might not be the main reason for mass ejections since most of the Be-stars rotate below the critical break-up velocity.

To gain a better understanding of all these properties, it is important to observe several Be-stars both photometrically and spectroscopically. This chapter presents five years of photometric and spectroscopic data of nine bright Be-star samples, collected from the *STEREO* satellite and archival sources, respectively. The pulsational characteristics, particularly variations in both frequency and amplitude, of the samples are revealed and compared to the spectroscopic results. Following this, the connection between the circumstellar disk structure and NRPs is discussed.

6.2 Selection of Be-Star Samples

In order to determine the candidates for study, all objects listed as a Be-variable in the *Simbad* Database were searched, and 1,638 stars were initially collected. For the target selection, four important criteria were taken into account: brightness, galactic coordinates, LC and periodogram purity, and aperture photometry.

Table 6.1: Be-star samples and their properties given in the *Simbad* Database.

Star	**Ra. (°)**	**Dec. (°)**	**V Mag. (^{m})**	**Type**
HD 23016	55.57895	19.70026	5.68	B9Vn
HD 23630	56.87115	24.10514	2.87	B7III
HD 26398	62.76415	16.64698	7.10	B7III
HD 36576	83.38180	18.54023	5.67	B2IV-V
HD 37318	84.74173	28.46014	8.66	B1V
HD 37967	85.83126	23.20437	6.16	B2.5V
HD 142983	239.54737	–14.27936	4.94	B3V
HD 147196	245.32996	–23.70799	7.05	B6/B7Vn
HD 178175	287.06959	–19.29029	5.57	B2V

As the first criterion, the brightness of the stars was checked and those with $V > 10^m$ were eliminated from the list, due to possible contamination from coronal activities. Thus, 322 bright stars remained to be investigated. Secondly, the targets within the FOV of the *STEREO* were detected, and those that did not have an appropriate right ascension and declination (between $\pm 30°$) were removed from the list. As a result, the number of candidates was reduced to 101.

Given the nature of Be-stars, many objects selected in this way did not have good LCs

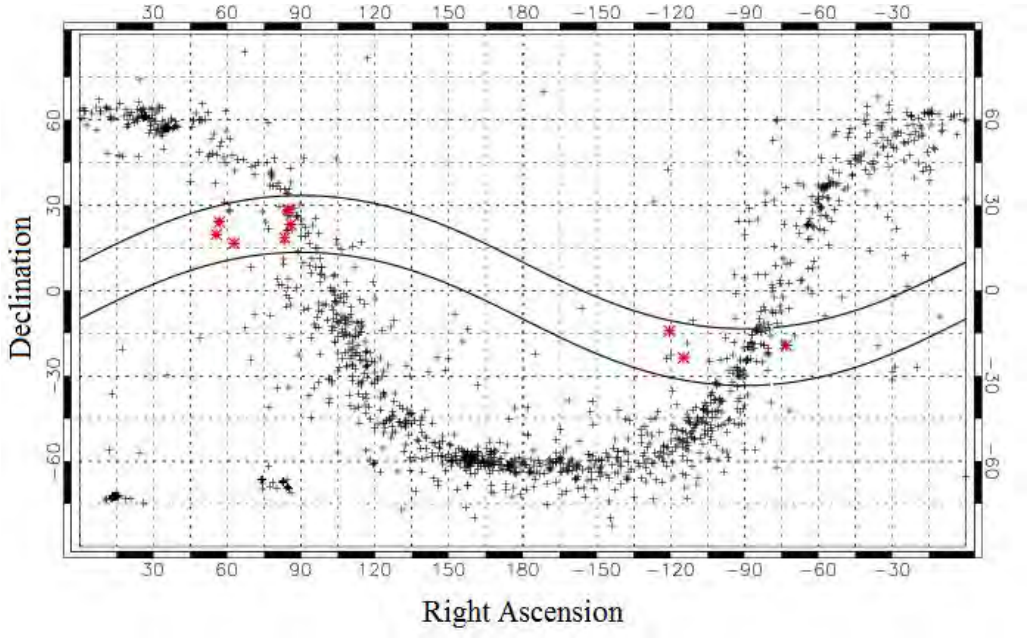

Figure 6.1: Distribution of Be-stars listed in the *Simbad* Database. The *STEREO* FOV is the region within the black strips and red asterisk symbols are the positions of the sample Be-stars.

due to general crowding in the Galactic Plane or the presence of bright neighbours (Fig. 6.1). Therefore, the LCs and periodograms of the selected stars were scrutinised. Those showing less noise and high signals during the four-year mission of the *STEREO* were determined to be those fitting the third criterion. Among them, the targets without a neighbouring star in the same aperture (within a radius of 6 pixels) or those with a neighbour having brightness greater than 1.5 times the target star were finally chosen. This process yielded nine bright Be-stars with good LCs, and these formed the samples studied in the chapter.

Although Be-stars have a spectral type range from O to early-A, our samples were spread throughout only B-type stars. The majority was comprised of MS stars, four of which were early-B type variables. Together with 1,638 target stars (represented with black plus symbols), our samples are shown (with red asterisk symbols) in Fig. 6.1, and listed in Table 6.1 according to their HD catalogue numbers.

6.3 Data Analysis

6.3.1 Time Series Analysis

To conduct the analyses presented in this chapter, LCs obtained from the *STEREO* between 2007 and 2011 were used for the chosen Be-star samples. Since observation data were taken from the *HI-1A* instrument, each light set was formed of approximately 20-day data chunks with a 40-minute cadence. The Nyquist frequency of the sets was around ~ 18 cd^{-1}.

The main goal here was to identify as many oscillations as possible in the photometric data and to catch potential correlations with spectroscopic observations. For this reason, the LCs that were obtained needed to be decontaminated from internal and external effects caused by the circumstances outlined in Chapter 2. Therefore, long-term variations were removed from the LCs by using a 3^{rd} order polynomial fit, and observation points greater than 3σ were clipped. Subsequently, all seasonal data and five years of combined time series were analysed with the LS algorithm for each star. During the analyses, the number of independent frequencies was calculated with $N_{raw}/2$, where N_{raw} is the number of raw observation points, in order to derive reliable results, and FAP was assumed to be 99% ($P_0 = 0.01$). Signals were sought between the frequency range of 0.03 - 10 cd^{-1}.

To detect significant frequencies in the amplitude spectra, a recursive method was applied to the time series: once the frequency with the highest amplitude was identified, it was subtracted from the data by using the least-squares fit if the amplitude was higher than a specific significance level. This procedure was then performed on the pre-whitened data. At this point, the next frequency with the highest amplitude was removed, and this routine proceeded until the last significant frequency was found. The specific significance level was calculated with the help of the Eqn. 4.4, and the corresponding amplitude was derived from $A_z = 2\sqrt{z/N}$ (Balona, 2014). Also, the noise profile of the periodogram was determined for every 0.5 cd^{-1} frequency interval, to use in the equation. The significance levels are presented with red dashed lines in the periodograms. Additionally, mid-observation times of the data sets, the extracted frequencies, their amplitudes, SNR and noise values (A_m) are given in the related tables.

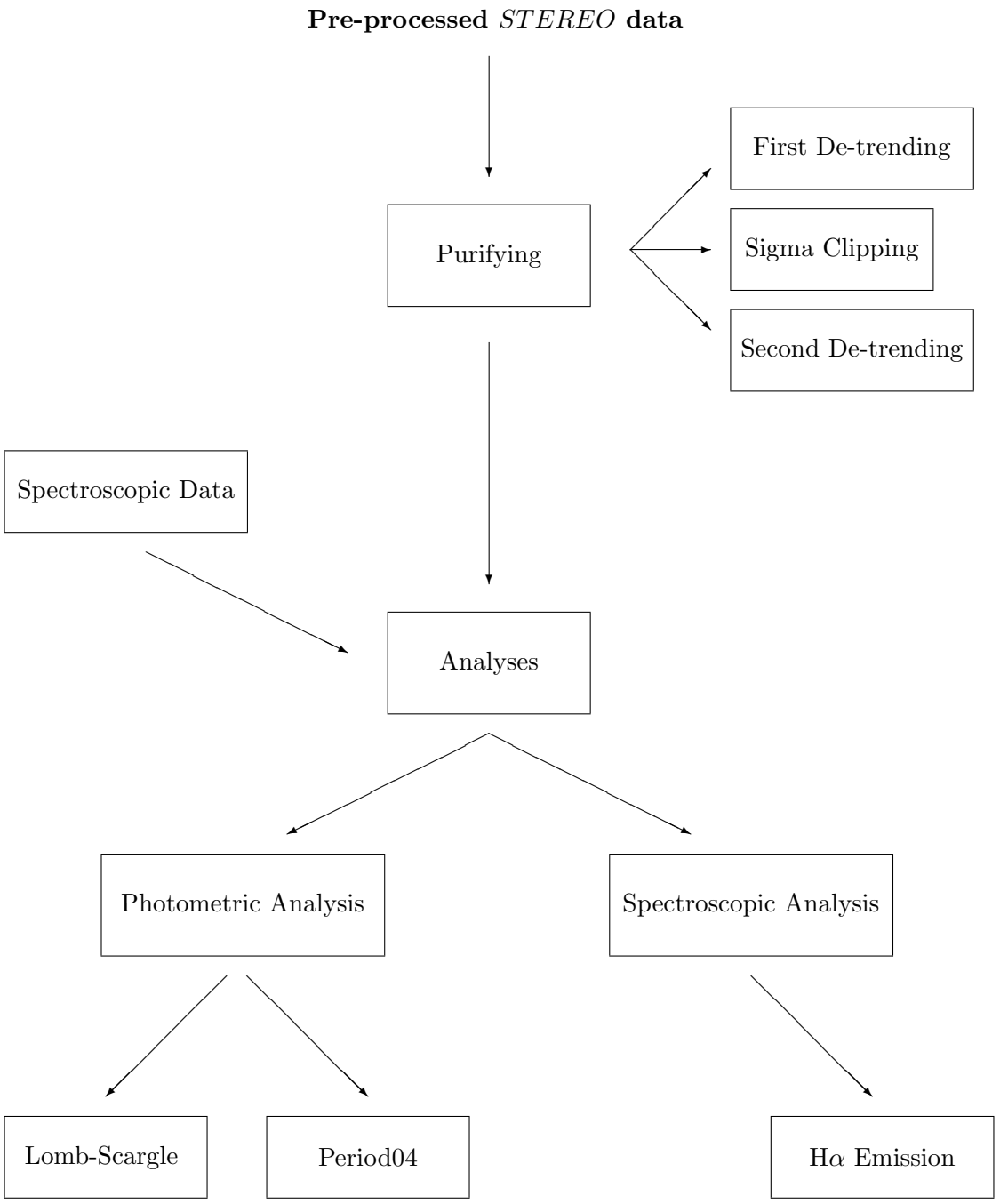

Figure 6.2: Refinement and analysis process of a photometric LC supported by spectroscopic data.

6.3.2 Analysis of the Hα Line Profiles

In order to investigate the relationship between pulsations and disk properties, spectroscopic observations in the *BeSS*[8] Database were included. A number of spectra taken from several telescopes with different equipment were examined for each sample star. Optical spectra were mainly focused on, rather than IUE, in order to make sensitive measurements. Even if some spectra were in the visible region, only high-resolution Hα observations were considered and irrelevant spectral parts were not taken into account during the research. The numbers of available spectra for the samples, mostly obtained between 2006 and 2011, are shown in Table 6.2. Among these, only high-resolution Hα observations were considered. Heliocentric velocity corrections caused by the orbital motion of the Earth were applied to all spectra by using the following equation:

$$\lambda_c = \lambda(1 + \frac{V_s}{c}) \tag{6.1}$$

where λ_c is the true wavelength, λ is the observed wavelength, V_s is the radial velocity in $\mathrm{km\,s^{-1}}$, and c is the speed of the light.

Table 6.2: Time interval of the spectroscopic observations for the target stars and the numbers of the spectra taken during these periods.

Star	**Time Interval (year)**	**Number of Spectrum**
HD 23016	2006 - 2012	13
HD 23630	1995, 2006 - 2011	28
HD 26398	2006 - 2011	7
HD 36576	2007 - 2011	10
HD 37318	2009 - 2012	3
HD 37967	2006-2012	4
HD 142983	1993, 2007 - 2011	21
HD 147196	2008 - 2010	3
HD 178175	2008 - 2011	6

Equivalent widths (EWs) of the Hα lines were measured with the help of the *SPLOT* package of the *IRAF* (noao – onedspec – splot) and *IDL* (continuum-line equivalent width procedure). For the continuum normalization, we followed Jones et al. (2011) and assumed that the error of the normalization was 3%. In order to investigate the degree of variability in EWs, we applied a statistical analysis method called *F-test* (F), based on an *F-distribution* under the null hypothesis ($H_0 : \sigma_1^2 = \sigma_2^2$; Fisher et al. (1987)). This method tests the variation of external and internal errors based on the number of degrees of freedom. These errors can be calculated

[8]http://basebe.obspm.fr/basebe/

with the equations given by Jones et al. (2011). Accordingly, if the variances of the uncertainties are equal, then their ratio equals to 1.0. Adapting the hypothesis to this chapter, if the ratio of the variance and the sigma values of a sample is different than 1.0 ($H_0 : var^2 = \sigma^2$), this means that the system is variable.

In addition to the *F-test*, corresponding confidence coefficients (C) were also derived. This is a numerical value pointing out the degree of variability between the variance of the entire spectrum set of a star and the mean uncertainty. The coefficient values from zero to one indicate an improvement in the relationship whereas zero shows an invariability in the system.

To calculate the intensities of the EWs, two different paths were followed. If line profiles were formed of single-peaked structures, a simple procedure was used to determine peak points. This routine basically populated array with maximum value and one point on either side, and made a parabolic fit to these three data points. Thus, the maximum level was easily derived. However, some emission lines were affected by adjacent telluric lines and showed extra structures near the main peak (Nemravová et al., 2012). In these cases, intensity values were obtained by Gaussian fits. Further, if the Hα profiles were double-peaked, the intensities of V and R components were measured separately by subtracting each maximum intensity from the continuum line, and the V/R ratios were found using the following formulation:

$$V/R = \big[F(V) - F_c\big] / \big[F(R) - F_c\big] \tag{6.2}$$

where $F(V)$ and $F(R)$ are the raw intensities of V and R components, F_c is the level of the continuum line.

6.4 Results

6.4.1 HD 23016 (13 Tau; HIP 17309; HR 1126)

Hα emissions of HD 23016 (B9V, $V = 5.68$ mag) were first suspected by Osawa (1959), and confirmed by Hirata and Asada (1976). The results obtained by Slettebak (1982) showed an absorption profile, flanked by a weak, double-peaked emission line. Ghosh et al. (1999) noted a similar but shallower line at the centre of the Hα profile with the EW of 5.74 Å. Based on these studies, it was concluded that the absorption line was not produced by a shell structure, and that HD 23016 was not a Be-shell star.

We analysed the seasonal and combined LCs taken between 2007 and 2011, and detected that the star exhibited mono-periodic variations over five years. The main frequency in the combined data was calculated to be ~ 1.80 cd^{-1} with the amplitude of 2.76 mmag. The periodograms are presented in Fig. 6.4a (on page 139). The significance levels are shown with red dashed lines in the same figure. The mid-observation times of the data sets, SNR, and noise values at the given frequencies (A_m) can also be found in Table 6.3.

Table 6.3: Frequency analysis results of HD 23016.

HD 23016 Frequencies					
Mid-Obs.Time (HJD)	**No #**	**Frequency (cd^{-1})**	**Amplitude (mmag)**	**SNR**	A_m **(mmag)**
Combined	f_1	1.80487(1)	2.76(8)	13.40	0.21
2007 Frequencies					
2454221	f_1	1.7943(24)	2.24(17)	5.91	0.38
2008 Frequencies					
2454566	f_1	1.803(2)	2.67(15)	6.50	0.41
2009 Frequencies					
2454910	f_1	1.809(2)	2.72(16)	6.77	0.40
2010 Frequencies					
2455255	f_1	1.808(2)	2.81(18)	6.88	0.41
2011 Frequencies					
2455599	f_1	1.806(2)	3.55(25)	6.48	0.55

Frequency analyses of the seasonal LCs indicated that the main frequency and its amplitude varied over five years. As seen in Fig. 6.4c (on page 139), the variation can be represented by a downward-curving parabola, where the frequency rapidly shifted from 1.794 to 1.809 cd^{-1} between HJD2454221 and HJD2454910, and then moderately decreased to 1.806 cd^{-1} on HJD2455599. In addition, the intensity of the main frequency also displayed variability over time. Although the amplitude appeared to be constant ($A \sim 2.73$ mmag) between HJD2454566

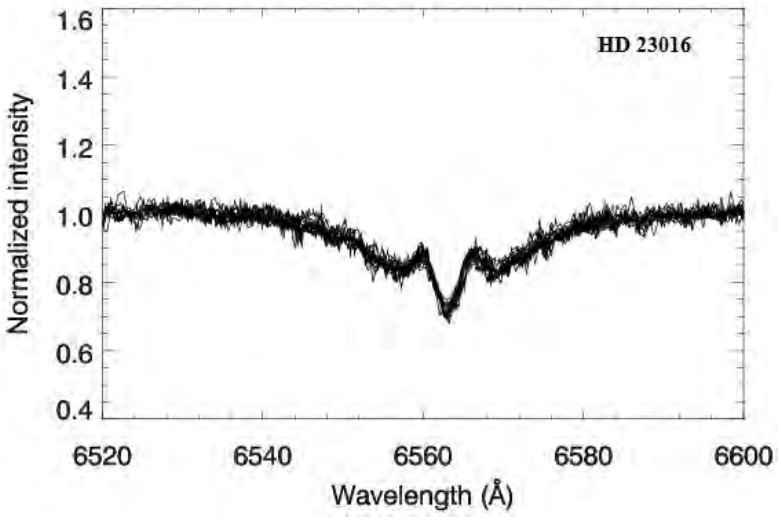

Figure 6.3: 13 spectra of HD 23016 taken between 2006 and 2012 are over-plotted. The broad absorption structure is shown in the figure.

and HJD2455255, five years of data showed an increase from 2.24 to 3.55 mmag.

In order to capture evidence of the relationship between these photometric variations and EW changes of the Hα lines, we examined spectra of HD 23016 obtained between 2006 and 2012. During the six-year observations, individual spectra displayed deeper central absorption lines with an average EW of 5.25 Å at the full width; these lines were surrounded by a double-peaked emission profile as well as shallower broad absorption lines (Fig. 6.3). To obtain more accurate EW measurements, we removed these broad absorptions from the spectra (Fig. 6.4b). In Fig. 6.4d, dotted and straight lines indicate the mean value of all EWs and their standard deviations ($\pm 1\sigma$), respectively. As can be seen from the figure, the data exhibit a decrease of about 0.6 Å in the EW. With the help of the *F-test*, we calculated the degree of this variability as $F = 623.68$ with the confidence level of 0.999 ($C > 99\%$).

Furthermore, EW variations seemed to be inversely proportional to those observed in both frequency and amplitude. In contrast to these changes, the EWs of the Hα line decreased between HJD2454000 and HJD2454700. It was also revealed that EW values remained constant from HJD2454700 to HJD2455800, but then began to decrease after this date. Even though a lack of the photometric data did not permit a detailed interpretation on the relation between spectroscopic and photometric findings, it may be concluded that there was a relation between the disk structure and the oscillation produced by HD 23016.

Finally, for the given physical parameters of T_{eff} = 11,508(106) K and $Log(L/\mathrm{L}_{\odot})$ = 2.428(59) (Zorec and Royer, 2012), the radius of the star was estimated as R = 4.13(32)

$R_{\odot}$. Additionally, the rotational period was calculated to be around 1.15(35) cd^{-1} by using the rotational velocity of $Vsini$ = 240(70) $km\,s^{-1}$ (Clark and Steele, 2000). This value was consistent with 1.08 and 1.21 cd^{-1}, which were well below the significance level in the combined periodogram.

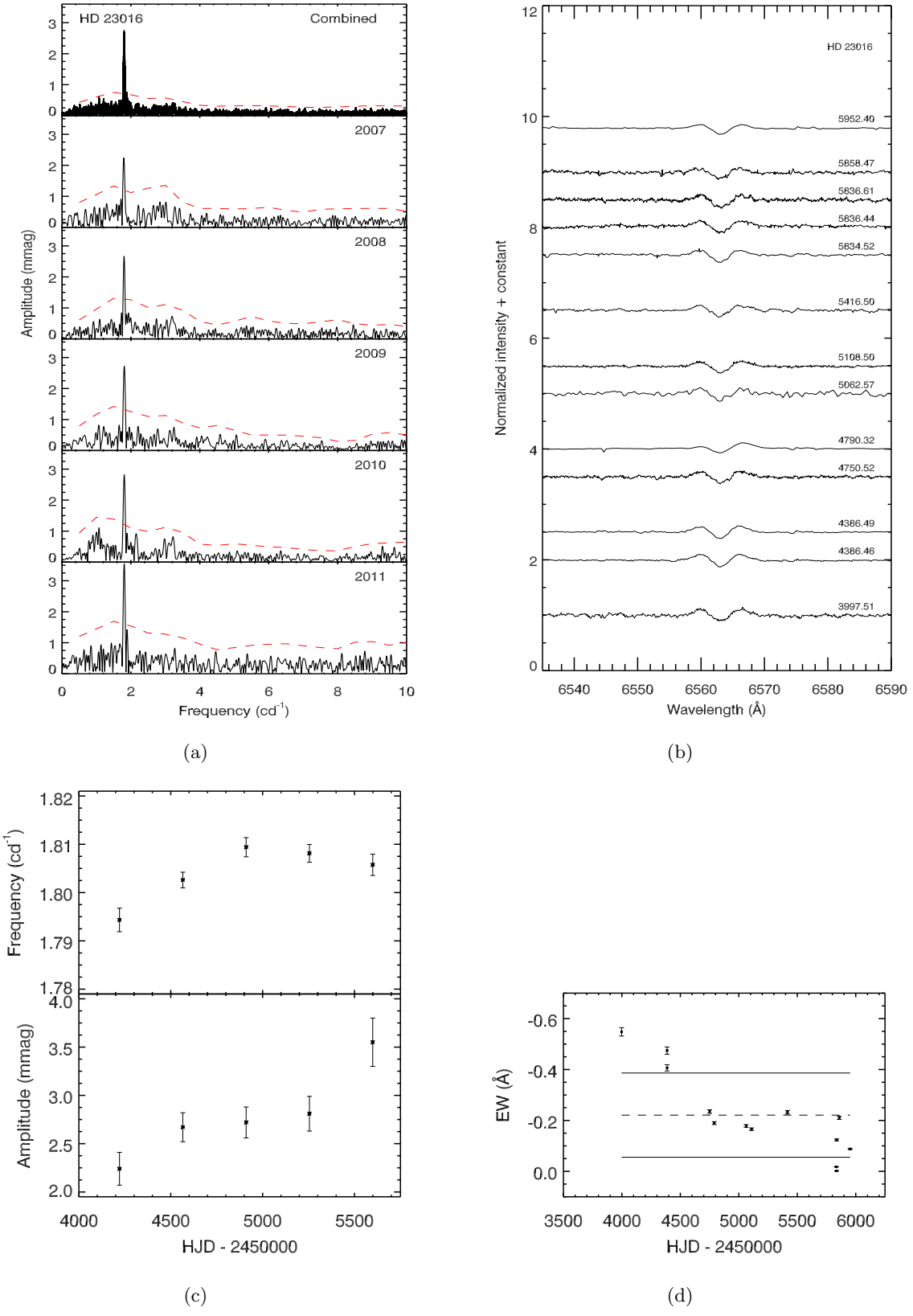

Figure 6.4: (a) Five-year combined and individual power spectra of HD 23016, (b) the Hα observations obtained between 2006 and 2012, (c) seasonal frequency and amplitude variations, and (d) EW variations of the Hα profiles.

6.4.2 HD 23630 (Alcyone; η Tau; 25 Tau; HIP 17702; HR 1165)

HD 23630 (B7III, $V = 2.87$ mag) is a well-studied bright emission star and the primary component of a binary system (Abt and Cardona, 1984). The first important spectroscopic research on this star was performed by Hubert-Delplace and Hubert (1979), who stated that there was no significant variation in the Hα emission profile from 1953 to 1976. Slettebak and Reynolds (1978) confirmed this constancy between 1975 and 1977, and reported a single-peaked structure. Unlike these studies, Andrillat and Fehrenbach (1982) observed a double-peaked and broad Hα emission showing no EW variation.

The spectral analysis performed by Jarad et al. (1989) exhibited no change in emission line. However, they detected three significant frequencies at 0.2419, 1.2416, and 2.2439 cd^{-1} in the power spectrum. After the first EW value was given by Apparao et al. (1993) as $-6.90(5)$ Å, Banerjee et al. (2000) determined the Hα line parameters to be: separation of V and R components ($\Delta\nu$) = 1.543 Å, FWZI = 12.73 Å, FWHM = 5.08 Å, EW = -8.62 Å and $V/R = 1.02$. They described the line feature as symmetrical with regards to V and R components. Their study also pointed out that emission strength was 30% higher than the continuum level. Since the profile had remained constant for many years, Tycner et al. (2005) considered this situation as an incorrect continuum normalization, which resulted in a miscalculation of peak intensity. For this reason, they made corrections for the filling-in effects of absorption profile based on the procedure suggested by Cote and Waters (1987), and gave the net EW to be $-10.2(3)$ Å. Goraya et al. (2009) reported a symmetrical, sharp, and single-peaked emission profile with an EW of -3.61 Å, and stated that emission line was associated with a disk-shaped absorption line, so violet and red edges remained under the continuum level. Recently, the mean EW value was calculated as -3.1 Å by Jones et al. (2011). Their *F-test* ($F = 12.24$) also showed that the Hα line profile was variable at a $> 99\%$ confidence level.

In our study, we analysed combined and seasonal LCs of HD 23630. As seen in Fig. 6.5a, each periodogram displayed a complicated frequency spectrum, which prevented the detection of significant peaks in time series analysis. However, we were able to determine 10 frequencies in the five-year (2007-2011) combined data. These frequencies were obtained based on a specific significance threshold, shown with a dashed line in the figure. From the three periods given by Jarad et al. (1989), we found only the frequency at 2.2413 cd^{-1}; it was not possible to identify either 0.24 cd^{-1} or 1.24 cd^{-1} in the combined periodogram. Further, we determined

Table 6.4: Frequency analysis results of HD 23630.

HD 23630 Frequencies						
Mid-Obs.Time (HJD)	**No #**	**Freq. (cd^{-1})**	**Amp. (mmag)**	**SNR**	A_m **(mmag)**	**Comments**
Combined	f_1	2.41217(4)	0.79(09)	4.43	0.18	
	f_2	2.71428(4)	0.80(09)	4.31	0.19	
	f_3	2.66768(6)	0.62(09)	3.38	0.18	
	f_4	2.33646(5)	0.67(09)	3.75	0.18	
	f_5	2.24125(5)	0.65(09)	3.61	0.18	
	f_6	2.57472(6)	0.62(09)	3.44	0.18	$3f_3 - 2f_2$
	f_7	2.80538(6)	0.60(09)	3.19	0.19	
	f_8	2.48498(6)	0.59(09)	3.32	0.18	$f_3 + 2f_2 - 2f_7$
	f_9	1.43392(6)	0.56(09)	3.65	0.15	
	f_{10}	1.95915(6)	0.54(09)	3.33	0.16	$2f_4 - f_2$
2007 Frequencies						
2454223	f_1	2.255(3)	1.59(16)	4.95	0.32	
	f_2	2.104(3)	1.85(16)	6.48	0.29	
	f_3	2.185(3)	1.37(16)	4.30	0.31	
	f_4	2.327(5)	1.02(16)	3.28	0.31	
	f_5	4.291(6)	0.79(16)	3.90	0.20	$2f_3$
	f_6	4.197(7)	0.68(16)	3.29	0.21	$2f_2$
2008 Frequencies						
2454568	f_1	2.801(4)	1.28(18)	4.03	0.32	
	f_2	2.756(4)	1.32(18)	3.93	0.34	
	f_3	1.606(6)	0.95(18)	3.69	0.26	
	f_4	2.582(5)	1.03(18)	3.22	0.32	$3f_2 - 2f_1$
	f_5	2.707(5)	1.01(18)	3.02	0.34	
	f_6	2.425(6)	0.95(18)	3.22	0.29	$2f_4 - f_2$
	f_7	0.884(7)	0.80(18)	3.31	0.24	$f_6 - f_3$
	f_8	3.335(7)	0.75(18)	3.44	0.22	$f_6 + f_7$
2009 Frequencies						
2454912	f_1	2.952(5)	1.11(17)	4.67	0.25	
	f_2	1.580(5)	1.10(17)	4.64	0.23	
	f_3	3.052(6)	0.89(17)	3.55	0.25	
	f_4	1.202(7)	0.77(17)	4.24	0.18	$2f_1 - f_2 - f_3$
	f_5	2.242(7)	0.77(17)	3.45	0.23	$f_1 + 2f_4 - f_3$
2010 Frequencies						
2455257	f_1	3.000(5)	1.26(21)	5.07	0.25	
	f_2	2.564(5)	1.13(21)	4.32	0.26	
	f_3	2.427(5)	1.34(21)	4.92	0.27	
	f_4	2.343(5)	1.23(21)	4.62	0.27	$2f_3 - f_2$
	f_5	1.439(7)	0.95(21)	3.24	0.29	$f_2 + 2f_3 - 2f_1$
	f_6	3.046(6)	0.98(21)	3.69	0.27	
	f_7	1.103(7)	0.87(21)	3.17	0.28	$f_2 - f_5$
	f_8	2.656(6)	0.98(21)	4.16	0.24	$2f_2 - f_3$
	f_9	2.179(7)	0.93(21)	3.88	0.24	$2f_7$
	f_{10}	5.478(9)	0.73(21)	3.66	0.20	$f_1 + f_3$
2011 Frequencies						
2455601	f_1	2.723(4)	1.41(18)	4.09	0.34	
	f_2	2.929(4)	1.22(18)	4.29	0.28	
	f_3	2.586(4)	1.32(18)	4.77	0.28	$2f_1 - f_2$
	f_4	2.672(4)	1.21(18)	3.71	0.33	
	f_5	2.875(5)	1.06(18)	3.36	0.32	
	f_6	2.447(6)	0.86(18)	3.51	0.25	$2f_1 - f_2$
	f_7	3.575(9)	0.59(18)	3.64	0.16	

that the seasonal amplitude spectra contained a few, relatively distinctive peak regions around 1.55 and 2.51 cd^{-1}, and other frequencies were gathered around these groups. The details of these findings are presented in Table 6.4.

As shown in Fig. 6.6 (the second row on page 144), the seasonal main frequencies appeared to be considerably variable. Accordingly, the frequency increased from 2.25 cd^{-1} on HJD2454223

to 2.99 cd^{-1} on HJD2455257, and dropped down to 2.72 cd^{-1} on HJD2455601. In addition, the frequency at around 2.96 cd^{-1} had a similar decreasing parabolic change, whereas the variations in 2.43, 2.58 and 2.68 cd^{-1} exhibited an increasing trend over time. Compared to the amplitudes of these frequencies, the only significant change was seen in the amplitudes of the f_1 values. Contrary to the change in the main frequencies, their amplitudes showed an upward-curving parabolic variation between HJD2454223 and HJD2455601. However, it should be considered that none of the amplitude spectra showed clear peaks, and that these variabilities might not be real, due to miscalculations. Furthermore, we detected reflections of a δ Scuti type variation at 16.4484 cd^{-1} in the periodograms. Thus, this variation might be responsible for the complexity of the amplitude spectra, and hence for the inconsistency in the frequencies.

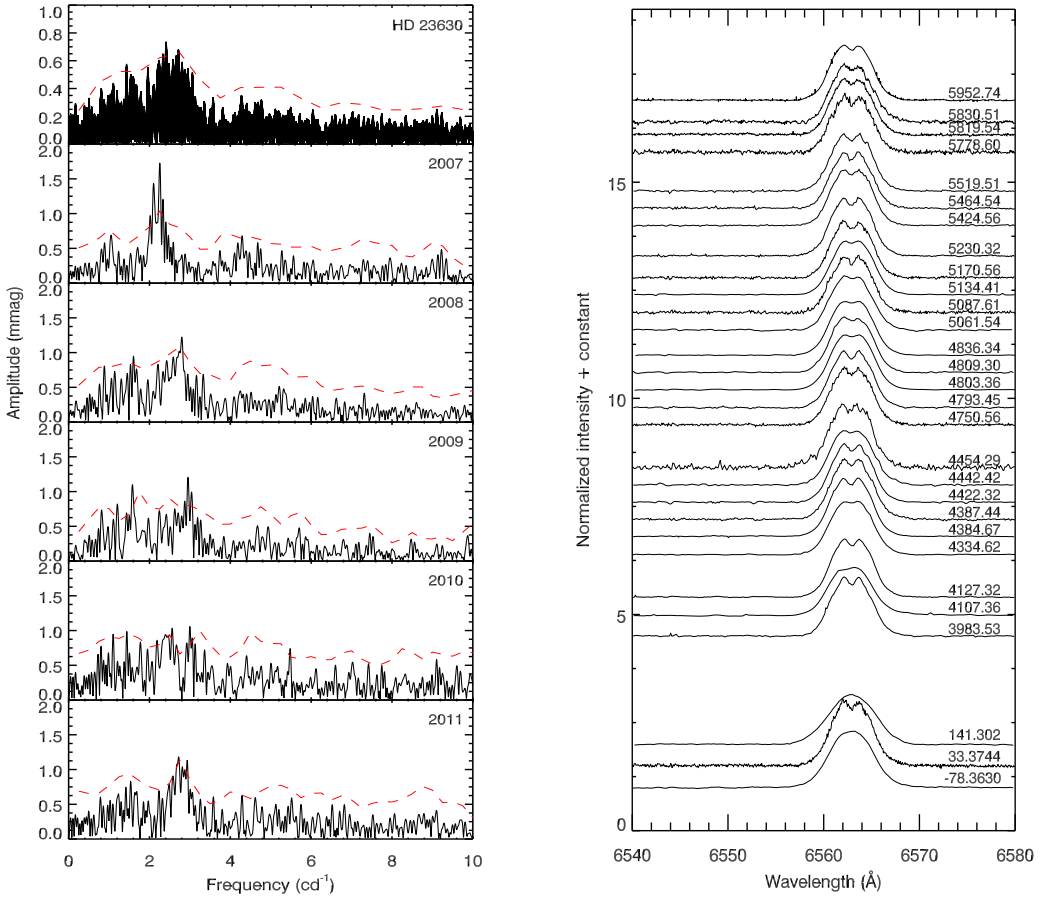

(a) (b)

Figure 6.5: (a) Five years of combined and seasonal amplitude spectra of HD 23630, (b) the Hα emission profiles obtained between 2006 and 2012. The numbers given on the right-hand side are the mid-observation times in Heliocentric JD (HJD-2450000).

Apart from these, 29 spectra of the star covering the period between 1995 and 2012 were examined in detail (Fig. 6.5b). However, only the results between 2006 and 2012 are given in Fig. 6.6 (the first row on page 144) in order to compare them with the photometric findings obtained in the same time period. Accordingly, it was confirmed that a great number of the Hα lines was formed of double-peaked structures, as reported by Andrillat and Fehrenbach (1982) and Slettebak (1986). The rest of the spectra showed single-peak profiles as mentioned by Slettebak and Reynolds (1978), but we determined that these single peaks occurred due to low spectrometer resolutions (6,000 $\leq R \leq$ 8,000) instead of emission variations. We also found that V/R ratios were almost constant between 2006 and 2012. We calculated the mean ratio of this variation to be $\overline{V/R} = 1.012$. Moreover, we detected that the separation of V and R peaks varied from 1.24 Å to 1.61 Å (mean separation $\overline{\Delta\nu} = 1.52$ Å) over six years.

As shown in Fig. 6.6, the EWs of the Hα profile decreased from -7.07 Å on HJD2454454 to -6.23 Å on HJD2455464. We calculated the degree of the variation to be $F = 0.987$ with the confidence level of $C = 49\%$ by using the *F-test*. Since the F value was quite close to 1.0, this variation might be considered as insignificant. However, by fitting the EWs with the least-squares method, we revealed that the variation showed a sinusoidal structure with extramum points on HJD2454379 and HJD2455601. The half-period of this structure was estimated to be around 3.62(12) years.

A comparison of the photometric and spectroscopic data indicated no specific correlation between frequency and EW variations. However, the change in the main frequencies seemed to be inversely correlated with the EW variations, whereas the amplitudes of these frequencies showed a similar change with EWs.

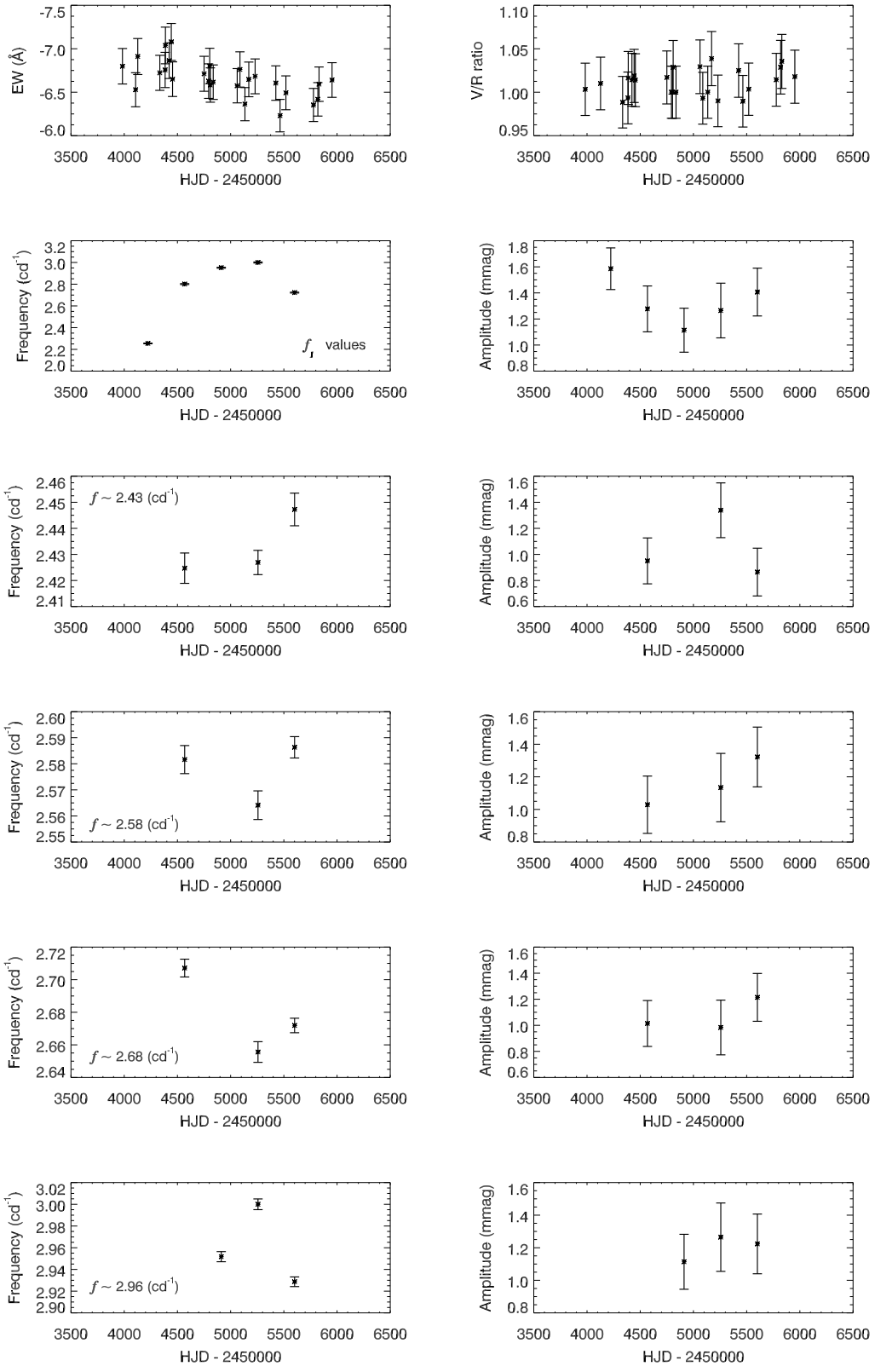

Figure 6.6: A comparison of photometric and spectroscopic results is given in the figure. The variations in the Hα line are given in the first row and the potential changes in both frequencies and amplitudes derived from *STEREO* LCs are presented in the following rows.

6.4.3 HD 26398 (HIP 19529)

The most detailed study regarding HD 26398 (B7III, $V = 7.10$ mag) was performed by Heard (1939), who discovered a quite strong Hα, moderately strong H$_\beta$, weak H$_\gamma$, and tentative H$_\delta$ profile in the spectrum. Heard (1939) also reported that there were uncertainties in determining the spectral type of the stars in the literature (B8 or B6e), and that this could be an indicator of a variable spectrum.

We obtained five consecutive years of LCs taken between 2007 and 2011. The analyses of the time series showed that the frequencies detected in the seasonal and combined periodograms were clustered around 1.17 and 3.09 cd^{-1} (Fig. 6.7a). Although there was a great number of peaks in the low-frequency region, we were able to determine only two dominant frequencies at

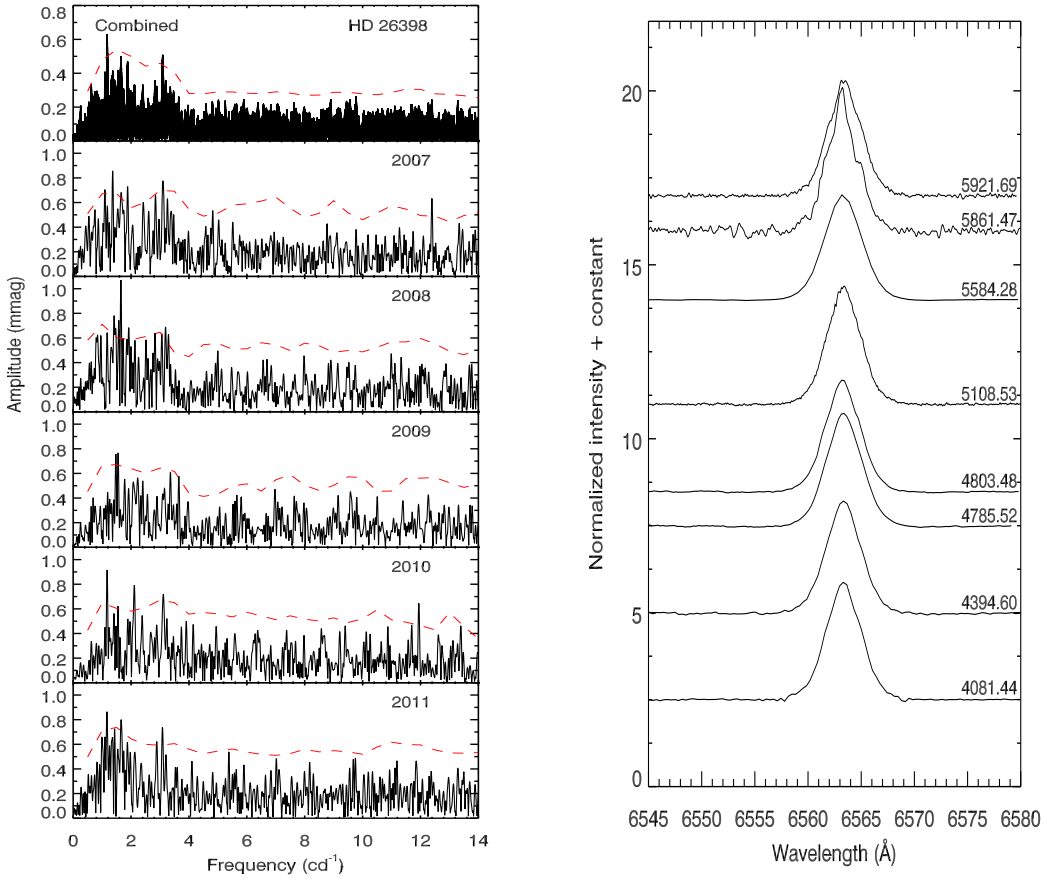

(a) (b)

Figure 6.7: (a) Five years of combined and seasonal amplitude spectra of HD 26398, (b) the Hα emission profiles obtained between 2006 and 2012. The numbers given on the right-hand side are the mid-observation times in Heliocentric JD (HJD-2450000).

1.1754 and 3.0944 cd^{-1}, due to high noise in the combined data (Table 6.5). These frequencies were specified according to the significance level (presented with a red dashed line in Fig. 6.7a) that was produced based on the noise profile of the periodogram. As seen in Table 6.5, some of the frequencies had an SNR smaller than 3.5 in the seasonal data sets. Although this value was the limit frequently used for period detection (Breger et al., 1993), the frequencies we found were over our significance levels, and hence were assumed to be the real oscillations. In addition to the low frequencies, we observed a strong peak at 12.395 cd^{-1} ($A = 0.61$ mmag) in the time series of 2007. Even though the LCs obtained in 2008, 2009, and 2011 did not exhibit such a variation, it appeared at 11.943 cd^{-1} ($A = 0.65$ mmag) in 2010. The reason for the formation of this peak was not clear, but it most likely occurred due to surface granulations.

As presented in Table 6.5, the frequencies found in the seasonal periodograms varied year by year, and this variation was best seen in the most dominant seasonal peaks (Fig. 6.8; the second row on page 148). From the figure, the change in the frequency showed a parabola-like structure where it shifted from 1.37 cd^{-1} to 1.65 cd^{-1} between HJD2454227 - HJD2454571 and decreased down to 1.17 cd^{-1} on HJD2455260. Apart from the main frequencies, we determined five different frequency groups at around 1.17, 1.45, 1.64, 2.86, and 3.10 cd^{-1} having visible changes. Although the ones at 1.17, 1.45, and 3.10 cd^{-1} exhibited descending trends between HJD2454500 and HJD2455600, the rest had an increasing variation in the same time interval. Unlike the frequencies, the changes in the amplitudes were within the error limits, except for that of 1.64 cd^{-1}.

In addition to the photometric data, we also obtained eight spectra covered between 2006 and 2011. As shown in Fig. 6.7b, all data, except for that taken on HJD2455921.69, displayed a single-peaked structure. To find out whether the single-peaked profiles were real or whether they occurred due to low-resolution observations, as in the case of HD 23630, we reviewed the spectrometers that were used to acquire these spectra, and learned that three data (observed on HJD2455921.69, HJD2455861.47, and HJD2455108.53) had been derived from high-resolution spectrometers. Among them, only one spectrum had a double-peaked profile, which might suggest that the star was in a transition phase. Moreover, we investigated the possible changes in the physical properties of the Hα line profile to compare with the photometric results (Fig. 6.8; the first row on page 148). Measurements showed that EW values varied slightly over five years, and that this variation could be represented by a downward-curving parabola. We calculated the degree of this variability to be around $F = 0.90$ with the confidence level of

Table 6.5: Frequency analysis results of HD 26398.

HD 26398 Frequencies						
Mid-Obs.Time (HJD)	**No #**	**Freq. (cd^{-1})**	**Amp. (mmag)**	**SNR**	A_m **(mmag)**	**Comments**
Combined	f_1	1.17538(5)	0.64(7)	4.52	0.14	
	f_2	3.09435(6)	0.51(7)	4.01	0.13	
2007 Frequencies						
2454227	f_1	1.367(5)	0.85(15)	4.62	0.18	
	f_2	3.099(5)	0.79(15)	3.87	0.21	
	f_3	1.883(5)	0.78(15)	4.52	0.17	
	f_4	1.097(6)	0.67(15)	3.61	0.18	$2f_3 - 2f_1$
	f_5	1.691(5)	0.82(15)	4.72	0.17	$f_2 - f_1$
	f_6	1.624(6)	0.71(15)	3.97	0.18	
	f_7	2.840(7)	0.64(15)	3.37	0.19	$f_4 + f_5$
	f_8	12.395(7)	0.61(15)	4.17	0.15	$4f_2$
	f_9	2.428(7)	0.58(15)	3.34	0.17	$f_1 + f_4$
	f_{10}	4.822(8)	0.56(15)	3.91	0.14	$2f_9$
2008 Frequencies						
2454571	f_1	1.649(4)	1.01(15)	5.83	0.17	
	f_2	1.416(6)	0.78(15)	4.32	0.18	
	f_3	3.192(6)	0.77(15)	4.82	0.16	
	f_4	3.283(6)	0.70(15)	4.60	0.15	$2f_1$
	f_5	1.922(6)	0.73(15)	4.33	0.17	$f_4 - f_2$
	f_6	1.177(6)	0.69(15)	3.49	0.20	$2f_2 - f_1$
	f_7	1.465(6)	0.72(15)	4.02	0.18	
	f_8	2.829(7)	0.63(15)	3.57	0.18	$2f_2$
	f_9	1.870(7)	0.62(15)	3.64	0.17	
2009 Frequencies						
2454916	f_1	1.551(6)	0.66(14)	3.50	0.19	
	f_2	1.475(6)	0.64(14)	3.42	0.19	
	f_3	3.361(7)	0.57(14)	3.25	0.18	
	f_4	3.649(7)	0.55(14)	3.48	0.16	$f_1 + f_4$
2010 Frequencies						
2455260	f_1	1.174(5)	0.94(15)	5.38	0.17	
	f_2	2.113(6)	0.79(15)	4.95	0.17	
	f_3	3.112(6)	0.71(15)	3.72	0.19	$2f_2 - f_1$
	f_4	11.943(7)	0.65(15)	4.70	0.14	
	f_5	1.550(7)	0.63(15)	3.87	0.16	$f_4 - 2f_2 - 2f_3$
2011 Frequencies						
2455605	f_1	1.165(5)	0.92(16)	4.76	0.19	
	f_2	1.657(6)	0.80(16)	4.20	0.19	
	f_3	3.085(6)	0.72(16)	4.15	0.17	
	f_4	1.431(7)	0.63(16)	3.27	0.19	$f_3 - f_2$
	f_5	1.001(7)	0.69(16)	3.48	0.20	$f_1 + f_4 - f_2$
	f_6	1.555(7)	0.65(16)	3.43	0.19	
	f_7	2.882(8)	0.57(16)	3.25	0.17	$2f_4$

$C = 45\%$ by using the *F-test*, and this confirmed that there was not a strong variability in EW of the Hα line. This change could be described as an increase from -13.8 to -14.4 Å between HJD2454100 – HJD2454780, and a decrease to -13.2 Å on HJD2455800.

A comparison of variations in photometric and spectroscopic properties indicated that EW values and frequencies at 1.17, 1.45, and 3.10 cd^{-1} exhibited similar changes. This similarity was also seen between EW values and the amplitude of 1.64 cd^{-1}. In contrast, the variation at 2.86 cd^{-1} appeared to be inversely correlated with Hα line widths. Although there was no significant variability in emission line strength, it should be noted that intensity fluctuated between HJD2455500 and HJD2456000, which might be a result of incorrect measurements.

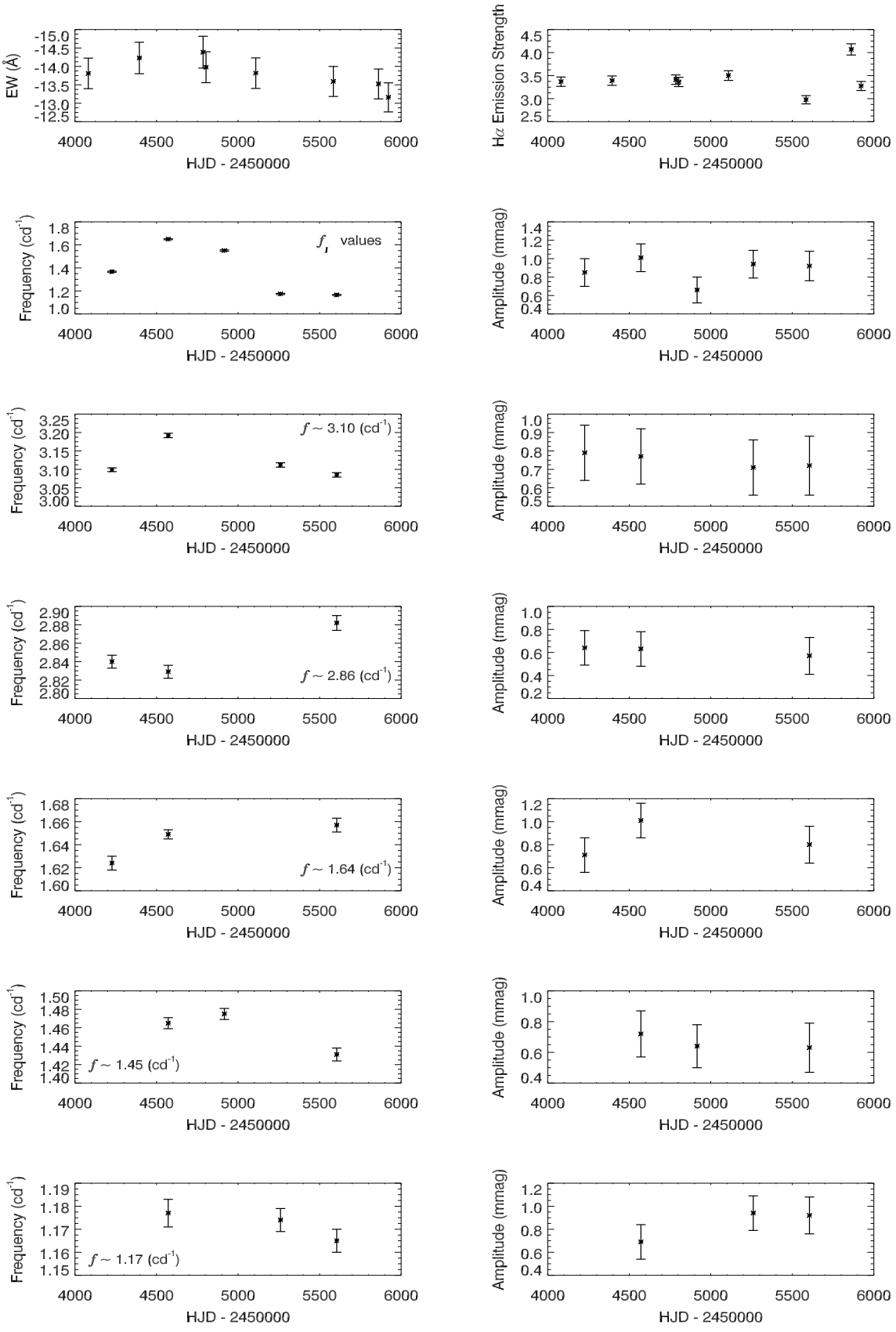

Figure 6.8: A comparison of photometric and spectroscopic results is given in the figure. The variations in the Hα line are given in the first row and the potential changes in both frequencies and amplitudes derived from *STEREO* LCs are presented in the following rows.

6.4.4 HD 36576 (120 Tau; V960 Tau; HIP 26064; HR 1858)

The LC variability of HD 36576 (B2IV/V, $V = 5.67$ mag) was investigated by Bossi et al. (1989), who detected five peaks in y and β filters. These frequencies were given to be 1.085, 0.093, 2.156, 3.131, and 0.775 cd^{-1} in y-filter and 1.094, 0.104, 2.143, 3.122, and 0.772 cd^{-1} in β-filter.

We obtained five years of LCs of this star, collected between 2007 and 2011. Frequency analysis revealed that the combined LC was formed of at least 14 frequencies. Since we removed long-term variations from the data, we could not detect any frequency smaller than 0.9 cd^{-1} (Table 6.6). However, we were able to determine some frequencies quite close to the archival results, given as 1.09 and 2.15 cd^{-1} (Bossi et al., 1989). The combined periodogram had two distinct frequency groups at around 1.01 and 1.95 cd^{-1} (Fig. 6.9a). Similar configurations were

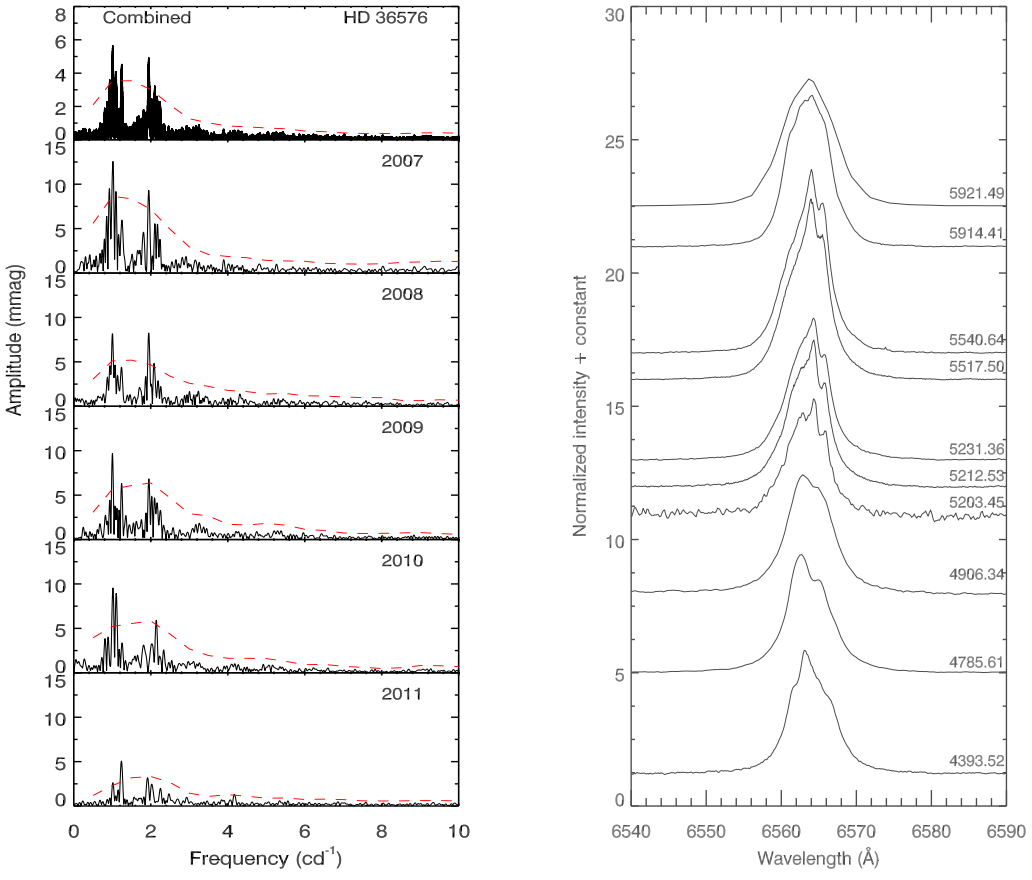

(a) (b)

Figure 6.9: (a) Five years of combined and seasonal amplitude spectra of HD 36576, (b) the Hα emission profiles obtained between 2006 and 2012. The numbers given on the right-hand side are the mid-observation times in Heliocentric JD (HJD-2450000).

also seen in the seasonal spectra. Even though the most dominant peak was the one at around 1.01 cd^{-1} during the five-year time period, its intensity decreased and 1.95 cd^{-1} became the strongest frequency in 2008 (Fig. 6.10; the second row on page 152). These rapid amplitude changes were also observed in other peaks below or above the significance levels (Fig. 6.9a), and might be a result of the interactions between surface granulations and stellar oscillations.

The variations in the two dominant frequencies and their amplitudes are presented in Fig. 6.10. Based on the figure, the frequency at 1.01 cd^{-1} exhibited a sinusoidal variation over five years. It decreased from 1.017 to 1.003 cd^{-1} between HJD2454246 and HJD2354935. Subsequently, it shifted to around 1.016 cd^{-1} in the following years and decreased to 1.012 cd^{-1} on HJD2455624. The intensity of its amplitude dropped from 14 to 2 mmag. Similar to the amplitude change of the main frequencies, it showed an abnormal increase between HJD2454590 and HJD2455279. On the other hand, the frequencies detected at 1.95 cd^{-1} displayed an increasing trend while its amplitude decreased from 9.5 mmag on HJD2454246 to 7.1 mmag on

Table 6.6: Frequency analysis results of HD 36576.

HD 36576 Frequencies						
Mid-Obs.Time (HJD)	**No #**	**Freq. (cd^{-1})**	**Amp. (mmag)**	**SNR**	A_m **(mmag)**	**Comments**
Combined	f_1	1.01200(1)	5.78(19)	6.14	0.94	
	f_2	1.01002(1)	6.26(19)	6.65	0.94	
	f_3	1.94472(2)	5.02(19)	6.20	0.81	
	f_4	1.24230(2)	4.57(19)	4.66	0.98	
	f_5	1.09791(2)	3.63(19)	3.80	0.96	
	f_6	0.93157(2)	3.67(19)	3.97	0.92	$f_2 + f_3 - 2f_1$
	f_7	2.10983(2)	3.61(19)	4.59	0.78	$f_1 + f_5$
	f_8	1.01357(2)	3.23(19)	3.43	0.94	$f_3 - f_6$
	f_9	1.94712(2)	3.06(19)	3.78	0.81	$f_1 + f_3 - f_2$
	f_{10}	0.93107(3)	2.94(19)	3.18	0.92	f_6
	f_{11}	2.15476(3)	2.86(19)	3.71	0.77	$2f_3 + 2f_4 - 2f_7$
	f_{12}	1.10755(3)	2.85(19)	2.98	0.96	$f_4 + 2f_2 - f_{11}$
	f_{13}	2.24956(3)	2.53(19)	3.42	0.74	$f_{11} + f_{12} - f_1$
	f_{14}	1.00551(3)	2.28(19)	2.43	0.94	$2f_2 - f_8$
2007 Frequencies						
2454246	f_1	1.017(1)	13.59(58)	5.33	2.55	
	f_2	0.929(2)	10.92(58)	4.33	2.52	
	f_3	1.946(2)	9.53(58)	4.47	2.13	$f_1 + f_2$
2008 Frequencies						
2454590	f_1	1.949(1)	8.06(38)	5.86	1.38	
	f_2	1.004(1)	8.22(38)	5.48	1.50	
	f_3	2.092(3)	3.80(38)	2.87	1.33	
2009 Frequencies						
2454935	f_1	1.003(1)	9.58(46)	5.76	1.66	
	f_2	1.951(2)	7.15(46)	3.76	1.90	$2f_1$
	f_3	1.245(2)	6.08(46)	3.34	1.82	
2010 Frequencies						
2455279	f_1	1.016(1)	9.43(45)	6.15	1.53	
	f_2	1.112(2)	8.14(45)	4.96	1.64	
	f_3	2.141(2)	6.48(45)	4.06	1.60	$f_1 + f_2$
2011 Frequencies						
2455624	f_1	1.236(1)	5.01(21)	7.13	0.70	
	f_2	1.917(2)	3.30(21)	3.81	0.87	
	f_3	1.012(3)	2.30(21)	3.63	0.63	

HJD2455624 (Fig. 6.10).

We also analysed spectroscopic data of HD 36576 taken between 2007 and 2011. From the Fig. 6.9b, the Hα line was formed of a single-peaked profile with an extra emission, which moved around the line and caused distorting effects on the wings. To have a better understanding of the possible changes in the emission profile, we measured the EW values of the Hα at the full width. During the calculations, the spectrum obtained on HJD2455921.49 was not used, since its resolution was quite low ($R = 800$).

Based on nine measurements, we detected a clear increasing trend with a variation degree of $F = 23.13$ and a confidence level of $C > 99\%$ in EWs values (Fig. 6.10; the first row on page 152). This change was correlated with the increase in the frequency at 1.95 cd^{-1}, and inversely proportional to its amplitude variation. Moreover, emission strength had one of the most spectacular changes, as seen in Fig. 6.10. The intensity decreased slightly between HJD2454400 – HJD2455200 and became considerably stronger in the following years. This decrease observed in emission strength showed similarity with the peculiar amplitude changes of the main frequencies and the 1.01 cd^{-1} in the same time period.

Finally, the radius and the rotational period of HD 36576 were estimated by using the relations $M/\mathrm{M}_{\odot} = (V_{cr}^2 \times R_{\star} \times 6.96 \times 10^8)/(G \times 1.99 \times 10^{30})$ and $P_{rot} = 50.6 \times R_{\star}/V_{eq}$. For these equations, the mass ($M = 10.1(7)$ M$_{\odot}$), the rotational velocity ($V sini = 266(13)$ km s^{-1}), and the critical velocity ($V_{cr} = 487$ km s^{-1}) were obtained from Frémat et al. (2005). Accordingly, the radius and rotational frequency of the star were calculated to be around $R = 8.12(61)$ R$_{\odot}$ and $f_{rot} = 0.65(6)$ cd^{-1}, respectively. This frequency could not be observed in the periodograms, because we removed long-term variations from the data sets.

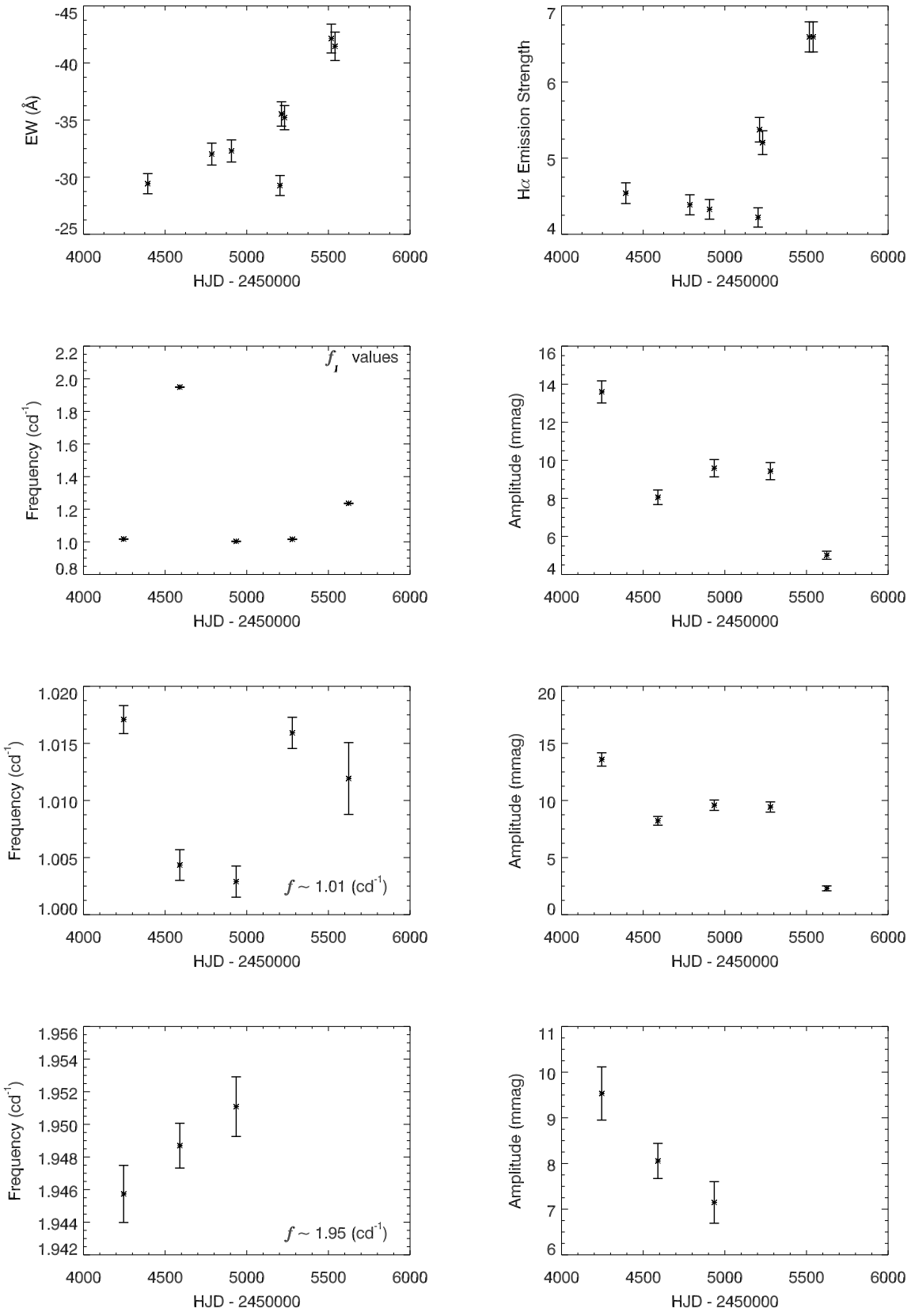

Figure 6.10: A comparison of photometric and spectroscopic results is given in the figure. The variations in the Hα line are given in the first row and the potential changes in both frequencies and amplitudes derived from *STEREO* LCs are presented in the following rows.

6.4.5 HD 37318 (HIP 26574; V1163 Tau)

HD 37318 (B1V, $V = 8.66$ mag) was one of the important subjects for spectroscopic studies of the supernova S147 in the literature. The star was known to be a photometrically constant object before the investigation of Vogt et al. (2004), who found erratic variabilities having a period range between 20−6,000 days in its LC ($A = 0.5$ mag). To understand expanding remnants in a non-homogeneous interstellar medium and interstellar absorption lines of the supernova S147, Sallmen and Welsh (2004) obtained high-resolution spectra of HD 37318, which was located at the distance of 1,380 pc and was in the same direction with the supernova. As a result of their analysis, Sallmen and Welsh (2004) revealed that intermediate velocity absorption structures and other lower-velocity cloud components existed towards HD 37318 and that the star interacted with them.

We obtained five-year photometric data of the star covering the period between 2007 and 2011. The amplitude spectra of HD 37318 were less noisy than those of other Be-samples in this study, and the frequency determination was comparatively easier. Accordingly, we detected 12 frequencies higher than the estimated significance threshold in the combined time series (Table 6.7). Similar to HD 26398 and HD 36576, frequencies were accumulated around two dominant values of 1.2386 cd^{-1} and 2.2195 cd^{-1}. Although the primary peak was 1.23864 cd^{-1} in the combined data, the most dominant peaks appeared at the lower frequencies in the seasonal periodograms, except for the data taken in 2011 ($f_1 = 1.2522$ cd^{-1}; Fig. 6.11a).

The variation in the main frequencies obtained in each year is shown in Fig. 6.12 (the second row on page 156). The configuration of the change resembled a sinusoid reaching its extremum points on HJD2454592 and HJD2455281. Between these dates, the frequency varied from 1.11 to 0.91 cd^{-1}, and jumped to 1.25 cd^{-1} in the following year. Further, we found specific frequency groups near 0.95, 1.23, and 2.22 cd^{-1}. Among them, the frequencies at around 0.95 cd^{-1} and 1.23 cd^{-1} showed a beating-like variation as seen in Fig. 6.12. In addition to these oscillating changes, 1.23 cd^{-1} also displayed an increasing profile over five years. Similarly, the frequency at around 2.22 cd^{-1} shifted slightly from 2.20 cd^{-1} on HJD2454247 to 2.24 cd^{-1} on HJD2455626. From the figure, it was seen that the amplitudes of these frequencies were also variable. While the amplitudes of the main frequencies as well as the ones at 0.95 and 2.22 cd^{-1} decreased, the amplitude of 1.23 cd^{-1} showed an increasing trend during the five-year time period.

We also obtained three high-resolution spectra of HD 37318 taken between 2009 and 2012

(Fig. 6.11b). The Hα lines had a strong double-peaked emission profile, which was a common characteristic of Be-stars observed under a moderate inclination. As shown in Fig. 6.12 (the first row on page 156), the V/R ratio varied over time due to the variabilities in the disk structure. The peaks were nearly equal ($V/R = 1.1$) on HJD2454887. However, the ratio drastically increased to $V/R = 1.45$, as the V component became quite dominant on HJD2455660. Subsequently, the V peak lost its strength and the emission profile regained its symmetrical shape. In addition, EW values of the Hα profile fluctuated analogous to the V/R evolution; this might be evidence of an alteration in the disk.

Since we did not have enough spectroscopic data, it was not possible to understand whether

Table 6.7: Frequency analysis results of HD 37318.

HD 37318 Frequencies						
Mid-Obs.Time (HJD)	**No #**	**Freq. (cd^{-1})**	**Amp. (mmag)**	**SNR**	A_m **(mmag)**	**Comments**
Combined	f_1	1.23864(2)	5.52(28)	6.36	0.87	
	f_2	1.02936(3)	3.64(28)	4.19	0.87	
	f_3	0.98077(4)	2.99(28)	3.63	0.82	
	f_4	0.92628(3)	3.40(28)	4.21	0.81	
	f_5	2.21945(3)	3.21(28)	4.55	0.71	$f_1 + f_3$
	f_6	0.90653(4)	2.72(28)	3.44	0.79	
	f_7	1.12629(4)	3.00(28)	3.51	0.85	$3f_2 + 2f_3$
	f_8	2.10675(4)	2.73(28)	3.41	0.80	$f_3 + f_7$
	f_9	0.96292(4)	2.74(28)	3.37	0.82	
	f_{10}	0.88714(4)	2.53(28)	3.23	0.78	$2f_6 - f_4$
	f_{11}	2.21305(5)	2.28(28)	3.19	0.71	$f_{10} + 2f_7 - f_4$
	f_{12}	2.48570(5)	2.07(28)	4.32	0.48	
2007 Frequencies						
2454247	f_1	0.965(2)	8.83(68)	5.13	1.72	
	f_2	2.199(4)	5.13(68)	3.38	1.52	
2008 Frequencies						
2454592	f_1	1.109(3)	6.44(59)	4.08	1.58	
	f_2	2.220(3)	5.99(59)	5.55	1.08	$2f_1$
	f_3	0.895(3)	5.36(59)	3.92	1.37	
	f_4	1.226(3)	4.89(59)	3.05	1.60	
	f_5	2.095(4)	4.73(59)	4.01	1.18	$f_3 + f_4$
2009 Frequencies						
2454936	f_1	1.004(2)	8.35(60)	5.63	1.48	
	f_2	1.242(2)	7.00(60)	4.86	1.44	
	f_3	1.046(3)	5.20(60)	3.50	1.49	
	f_4	2.108(3)	5.04(60)	3.90	1.29	$2f_4$
	f_5	1.109(4)	4.70(60)	3.23	1.46	
2010 Frequencies						
2455281	f_1	0.912(3)	7.31(67)	5.03	1.45	
	f_2	1.230(3)	6.03(67)	3.70	1.63	
2011 Frequencies						
2455626	f_1	1.252(3)	6.87(67)	4.37	1.57	
	f_2	2.236(5)	3.91(67)	3.49	1.12	

variations in the EWs and V/R values were real, or a part of a long-term structure. Moreover, it was not feasible to establish a connection with photometric results. However, when the frequency at 1.23 cd^{-1} and the f_1 frequencies were considered, the change between HJD2454900 and HJD2456000 seemed to be inversely proportional to the variation in the EW and V/R.

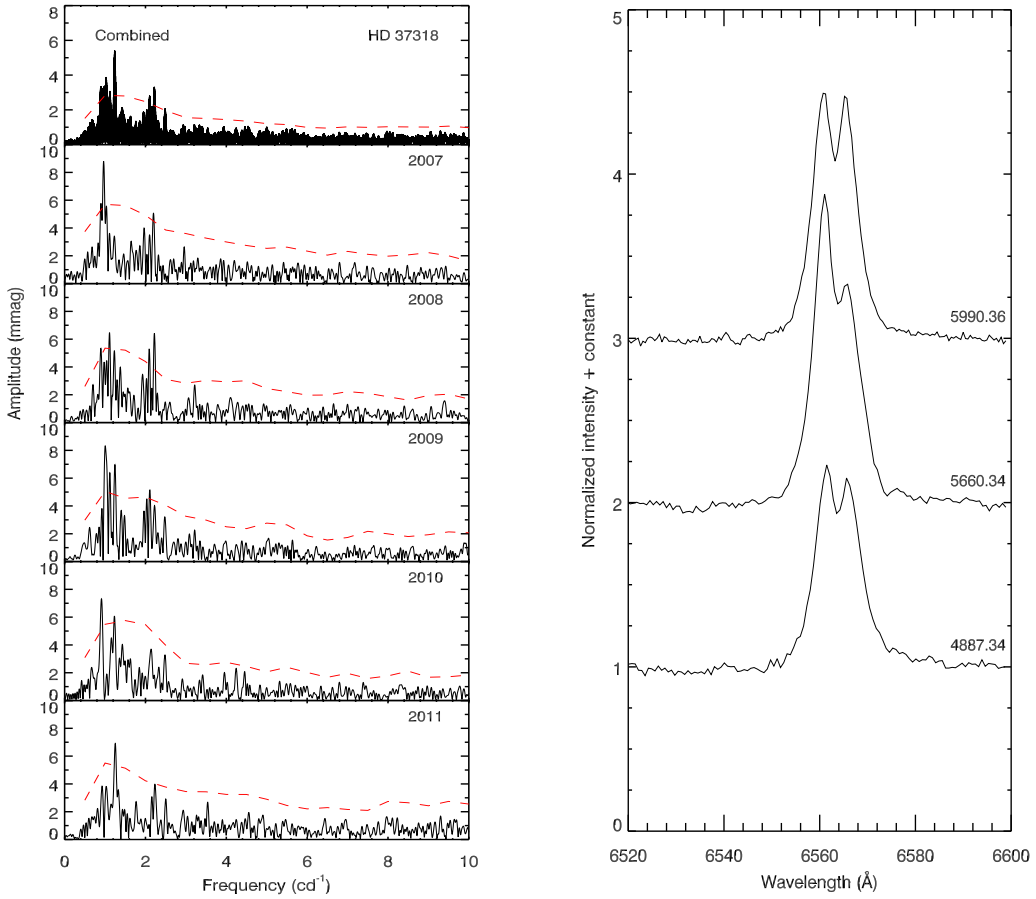

(a) (b)

Figure 6.11: (a) Five years of combined and seasonal amplitude spectra of HD 37318, (b) the Hα emission profiles obtained between 2009 and 2012. The numbers given on the right-hand side are the mid-observation times in Heliocentric JD (HJD-2450000).

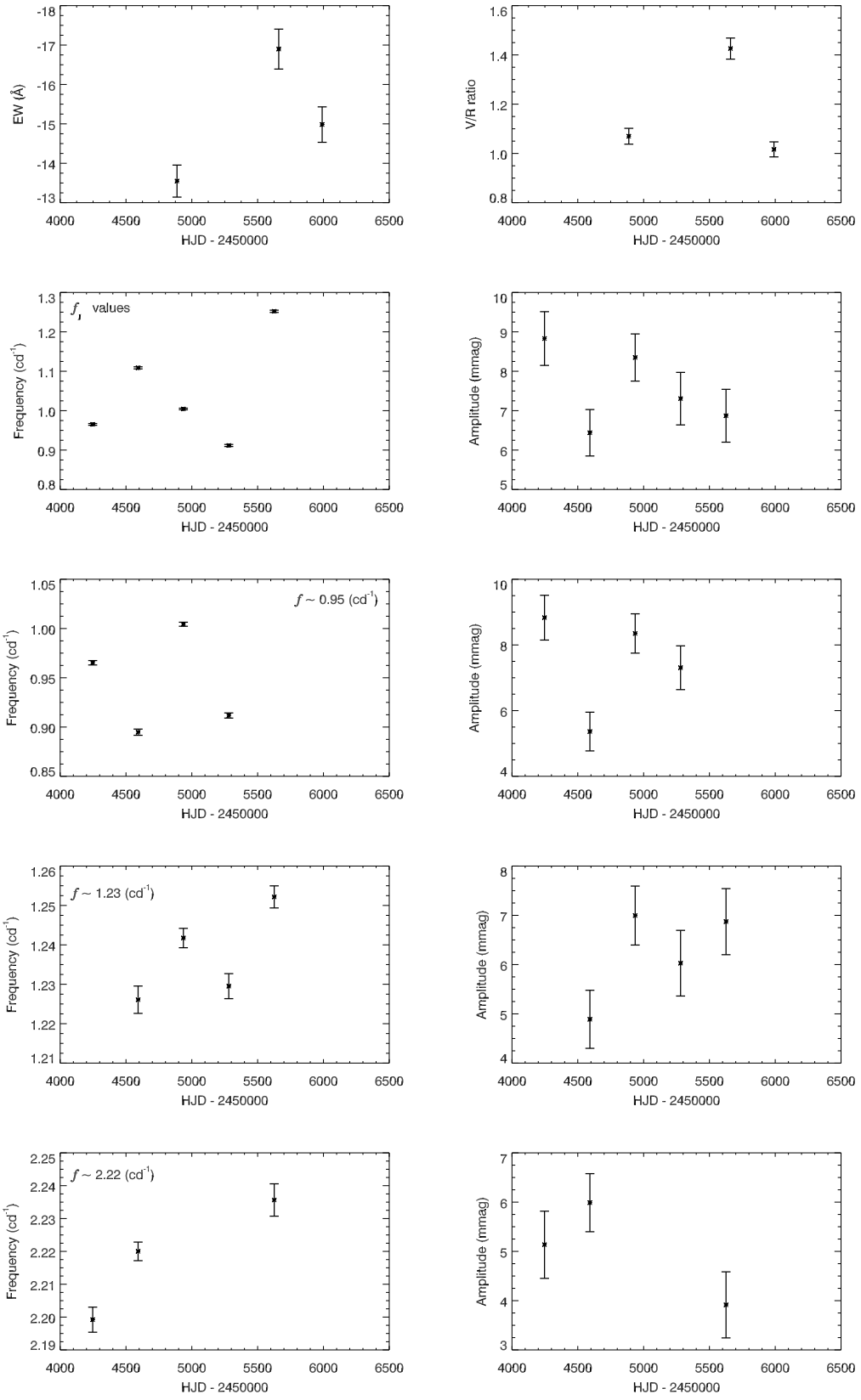

Figure 6.12: A comparison of photometric and spectroscopic results is given in the figure. The variations in the Hα line are given in the first row and the potential changes in both frequencies and amplitudes derived from *STEREO* LCs are presented in the following rows.

6.4.6 HD 37967 (V731 Tau; HIP 26964)

HD 37967 (B2.5V, $V = 6.16$ mag) was classified as a pole-on star having a strong H_β emission superimposed on a broad absorption line, and a strong, single-peaked Hα emission profile in spectra (Burbidge and Burbidge, 1954). Its photometric variabilities ($A = 0.04$ mag) were discovered by Pavlovski and Bozic (1982).

We found seven peaks gathered around three main frequencies at 1.0751, 2.1521, and 4.4399 cd^{-1} in the five years of combined time series. These frequencies were determined according to the specific significance level, which was calculated based on the regional noise characteristic of the periodogram. The significance levels are presented with red dashed lines in Fig. 6.13a and the overall results are given in Table 6.8.

Among the frequencies found, 1.0236 and 1.0751 cd^{-1} were most likely produced by the rotation of the star, since they were quite consistent with the rotational period of 1.18(19) cd^{-1}. This value was found from the archival parameters: the radius of the star was estimated to be

Table 6.8: Frequency analysis results of HD 37967.

HD 37967 Frequencies						
Mid-Obs.Time (HJD)	**No #**	**Freq. (cd^{-1})**	**Amp. (mmag)**	**SNR**	A_m **(mmag)**	**Comments**
Combined	f_1	2.15205(3)	1.67(11)	6.17	0.27	$2f_3$
	f_2	2.13023(3)	1.40(11)	5.16	0.27	
	f_3	1.07509(3)	1.27(11)	4.65	0.27	
	f_4	1.02364(4)	1.17(11)	4.32	0.27	$f_3 + 2f_2 - 2f_1$
	f_5	4.43992(4)	1.06(11)	4.83	0.22	
	f_6	2.14700(4)	1.10(11)	4.05	0.27	$2f_3$
	f_7	2.14245(4)	1.05(11)	3.88	0.27	$2f_3$
2007 Frequencies						
2454248	f_1	4.428(4)	2.41(26)	4.94	0.49	
2008 Frequencies						
2454593	f_1	2.146(2)	5.31(32)	8.22	0.65	
	f_2	1.881(3)	3.05(32)	4.06	0.75	
2009 Frequencies						
2454937	f_1	1.012(2)	2.24(18)	4.92	0.46	
	f_2	2.042(3)	1.73(18)	4.34	0.40	$2f_1$
	f_3	1.078(4)	1.44(18)	3.23	0.45	
	f_4	2.131(4)	1.28(18)	3.19	0.40	$2f_3$
	f_5	4.463(6)	0.91(18)	3.77	0.24	
2010 Frequencies						
2455282	f_1	1.055(2)	2.51(19)	7.35	0.34	
	f_2	1.241(5)	1.25(19)	3.46	0.36	
2011 Frequencies						
2455626	f_1	1.086(3)	1.86(18)	3.77	0.49	
	f_2	1.143(5)	1.28(18)	2.56	0.50	
	f_3	2.146(5)	1.23(18)	3.26	0.38	$2f_1$

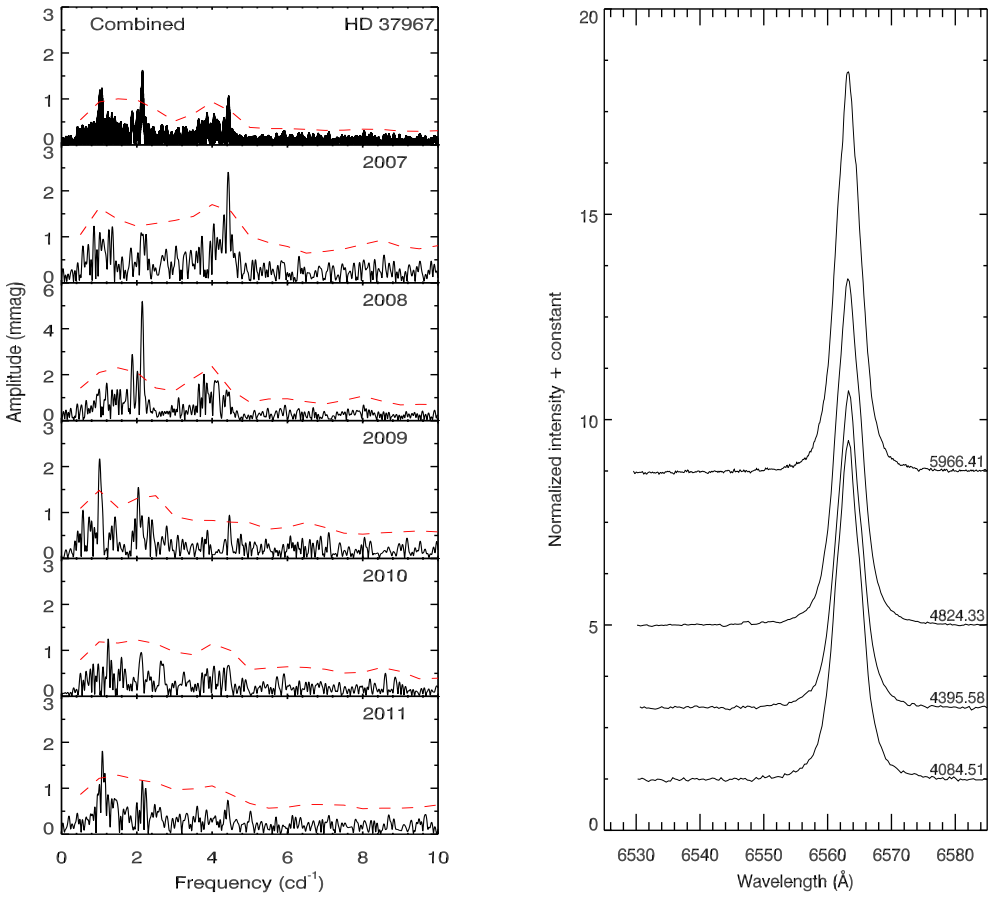

(a) (b)

Figure 6.13: (a) Five years of combined and seasonal amplitude spectra of HD 37967, (b) the Hα emission profiles obtained between 2006 and 2012. The numbers given on the right-hand side are the mid-observation times in Heliocentric JD (HJD-2450000).

around $R = 3.82(56)$ $R_\odot$ by using the angular diameter of $\theta = 1.40 \times 10^{-4}$ arcsec (Pasinetti Fracassini et al., 2001) and the parallax of $\pi = 3.94(58)$ mas (the *Simbad* Database). The rotational velocity ($V sini = 228(16)$ km s^{-1}) was also adopted from Frémat et al. (2005).

As seen in Fig. 6.13a, none of the detected frequencies in the combined data appeared in a seasonal periodogram at the same time. For instance, although there is no frequency at around 4.40 cd^{-1} in 2008, 2010, or 2011, the data taken in 2007 and 2009 displayed such a variability. Also, the peaks at around 1.00 cd^{-1} only came out in the amplitude spectra of 2009, 2010, and 2011. If this situation was not a result of our refinement pipeline, it could be that the pulsation characteristic of the star changed over years. Further, the most remarkable change was observed at 2.146 cd^{-1} in 2008. Despite remaining well below the significance level in 2007 and 2010, the

amplitude of this frequency rapidly increased to 5.38 mmag in 2008, and lost its strength up to 1.23 mmag in the following year.

The variations in the main frequencies (f_1) that were observed in each season are presented in Fig. 6.14 (the second row; on page 160). Accordingly, the frequency at 4.428 cd^{-1} dramatically shifted to the lower values over five years. The most significant change occurred between HJD2454248 – HJD2454937, and the frequency dropped to 1.012 cd^{-1}. The decrease was reversed after HJD2454937 and an increase in the frequency was observed. This variation seemed to be negligible compared to the enormous decrease. However, detailed examination of the change between HJD2454937 and HJD2455626 revealed that the frequency at around 1.05 cd^{-1} actually increased rapidly from 1.012 cd^{-1} to 1.086 cd^{-1} (Fig. 6.14; the last row on page 160).

Apart from these photometric findings, we obtained four spectroscopic data between 2006 and 2012. As reported by Burbidge and Burbidge (1954), the Hα profile was still extremely strong and had a single-peaked structure with a mean intensity of around 8.45 (Fig. 6.13b). However, the emission strengths and the EW values were not stable. As seen in Fig. 6.14 (the first row on page 160), EWs had an increasing profile from HJD2454400 up to HJD2456000, but the width of the Hα profile was narrowed before this time interval. Further, the emission strength also exhibited a proportional change with the EW variation. To check the accuracy of this variability, we used the *F-test* and found $F = 9.24$ with the confidence level of $C \approx 95\%$. Based on these results, we confirmed the change in the properties of the Hα profile, and probably captured a matter ejection phase towards the circumstellar disk.

As previously mentioned, there was an abnormal increase in the amplitude of the f_1 values on HJD2454592, and we realized that this variation nearly coincided with the beginning of the long-term rise in both the EW and emission strengths. The rapid increase at 1.05 cd^{-1} was also quite consistent with the variations of the Hα line. On the other hand, the parabolic changes in the frequencies at 2.14 and 1.07 cd^{-1}, as well as in the amplitudes of 1.07 and 1.05 cd^{-1}, seemed to be connected with the emission profile. Although it is not possible to make clear connections between photometric and spectroscopic results by using these comparisons, the coincidences prompted us to think about the effects of frequency and amplitude variations on disk structure.

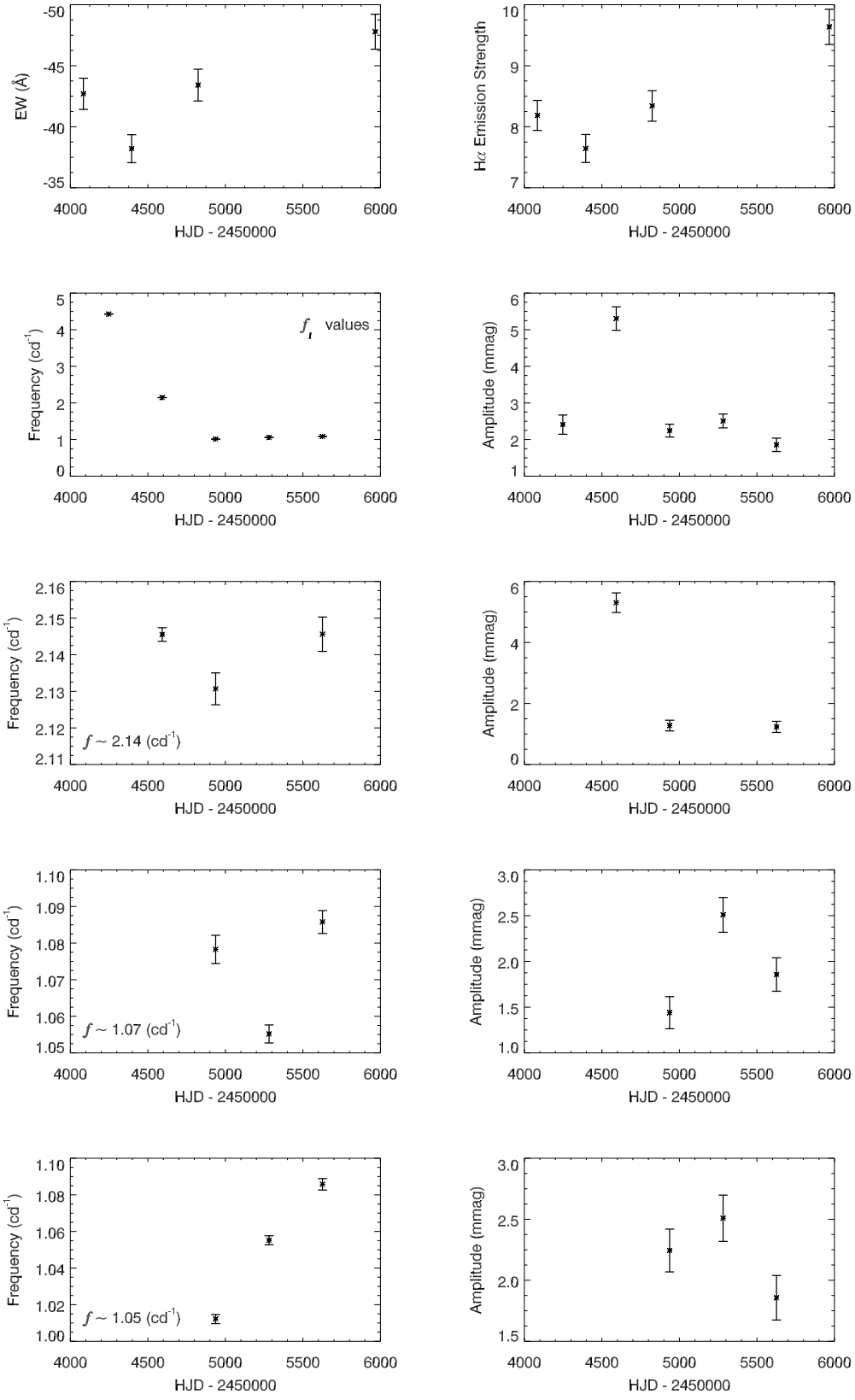

Figure 6.14: A comparison of photometric and spectroscopic results is given in the figure. The variations in the Hα line are given in the first row and the potential changes in both frequencies and amplitudes derived from *STEREO* LCs are presented in the following rows.

6.4.7 HD 142983 (48 Lib; HIP 78207; HR 5941)

HD 142983 (V = 4.94 mag) is a well-researched Be-shell star whose spectroscopic structures and photometric variabilities have been investigated in numerous studies. Although HD 142983 is classified as a B8Ia/Iab-type supergiant (Catanzaro (2013); Lafrenière et al. (2014); Peña-Guerrero and Leitherer (2013)), many researchers consider the star to be an early-type sub-giant, giant, or MS object (B3III to V) (Hanuschik and Vrancken (1996); Draper et al. (2014); Štefl et al. (2012); Touhami et al. (2013)). Similar to most Be-stars, it is a rapid rotator with a projected rotational velocity ($Vsini$) of around 400 km s^{-1} (Štefl et al. (2012); Touhami et al. (2013)).

Using various observational techniques, several periodicities of the star have been reported in the literature (Table 6.9). Among them, two frequencies – 0.227 and 0.551 cd^{-1}, detected by Bossi et al. (1994) – were associated with the changes in the whole spectral line and the shell core, respectively.

Table 6.9: Archival frequency values of HD 142983.

Frequency (cd^{-1})	**Type**	**Reference**
8.70	RV var.	Ringuelet-Kaswalder (1963)
1.52, 2.49	Photometric	McDavid (1988)
2.49	Photometric	Cuypers et al. (1989)
1.25, 1.36, 3.10	LPV	Floquet et al. (1996)
3.70, 7.50, 10.60		
0.227, 0.551	Spectroscopic	Bossi et al. (1994)

Hanuschik and Vrancken (1996) observed a double-peaked Hα profile with asymmetric V and R components ($V/R < 1$). Okazaki (1997) suggested that V/R ratios showed four different periodicities of around 7.5, 10, 12, and 13.5 years between 1950 and 1994. However, Štefl et al. (2012) detected only two of the cycles having lengths of about 11 and 15 years. Gunasekera et al. (2008) also examined the Hα profile, and calculated an EW value of around –16.64 Å. Unlike previous studies, they found a V/R ratio of 2.12. Under the assumption of a constant orbital angular momentum (rotational parameter, j = 1) and Keplerian rotation (j = 1/2), they calculated the radii of the disk to be 2.64 and 6.98 R$_\star$, respectively. However, Štefl et al. (2012) suggested a dense inner disk quite close to or contacting to the star. Accordingly, they obtained the outer radius as 15 R$_\star$ for the H continuum disk and $30 - 50$ R$_\star$ for the diameter of Br$_\gamma$ region, assuming that the star was a B3V-type MS object with a stellar radius of 3.56 R$_\odot$. This result became one of the largest angular diameters among Be-stars.

Table 6.10: Frequencies derived from the combined data of HD 142983.

HD 142983 Frequencies						
Mid-Obs.Time (HJD)	**No #**	**Freq. (cd^{-1})**	**Amp. (mmag)**	**SNR**	A_m **(mmag)**	**Comments**
Combined	f_1	2.48896(1)	9.34(16)	17.92	0.52	
	f_2	2.58671(1)	4.82(16)	10.58	0.46	
	f_3	2.35790(2)	3.72(16)	6.80	0.55	
	f_4	2.46924(2)	2.77(16)	5.14	0.54	
	f_5	5.08150(2)	2.54(16)	7.21	0.35	
	f_6	2.34749(3)	2.27(16)	4.16	0.55	
	f_7	4.84811(3)	2.25(16)	5.01	0.45	
	f_8	4.82110(3)	2.24(16)	5.00	0.45	$3f_4 - f_2$
	f_9	2.40191(2)	2.69(16)	4.87	0.55	$2f_5 - 3f_2$
	f_{10}	2.21153(3)	2.19(16)	4.41	0.50	$f_1 + 2f_9 - f_5$
	f_{11}	2.27600(4)	1.65(16)	3.04	0.54	$f_9 + 2f_6 - f_8$
	f_{12}	4.92142(3)	1.93(16)	4.38	0.44	$f_2 + 2f_9 - f_4$
	f_{13}	2.41783(4)	1.72(16)	3.16	0.55	$f_1 + f_{11} - f_6$
	f_{14}	2.32073(3)	2.15(16)	3.92	0.55	$f_1 + f_{13} - f_2$
	f_{15}	2.16956(3)	2.09(16)	4.24	0.49	$f_7 + f_9 - f_5$
	f_{16}	2.15367(4)	1.63(16)	3.34	0.49	$f_{11} + f_6 - f_4$
	f_{17}	2.05289(4)	1.70(16)	3.92	0.43	$f_{15} + f_4 - f_2$
	f_{18}	4.98940(4)	1.65(16)	3.91	0.42	$f_2 + f_9$
	f_{19}	4.75355(4)	1.51(16)	3.37	0.45	$f_{12} + f_{14} - f_1$
	f_{20}	2.35436(3)	2.00(16)	3.66	0.55	$f_2 + f_7 - f_5$
	f_{21}	2.49647(3)	1.81(16)	3.52	0.51	$f_1 + f_{20} - f_6$
	f_{22}	2.51769(4)	1.71(16)	3.38	0.51	$f_1 + f_{15} - f_{10}$
	f_{23}	0.10927(5)	1.34(16)	4.06	0.33	$f_{14} - f_{10}$
	f_{24}	0.19915(4)	1.41(16)	4.10	0.34	$f_8 - f_{16} - f_4$

In our investigation, we detected 24 frequencies that were above the significance threshold in the combined periodogram (Table 6.10). Similar to the other samples, the power spectra consisted of two dominant frequencies at 2.4889 and 5.0815 cd^{-1}, and most of the peaks were gathered around these frequencies. As seen in Fig. 6.15a, the former was the main frequency ($A = 9.34$ mmag) and was accordant with the findings of McDavid (1988) and Cuypers et al. (1989). In addition, we found two low frequencies at around 0.1 and 0.2 cd^{-1}. To compare these frequencies with the rotational period, we initially adopted the angular diameter ($\theta_s = 0.172(4)$ mas) from Touhami et al. (2013), the parallax ($\pi = 6.97(24)$ mas) from the *Simbad* Database, and the projected rotational velocity ($Vsini = 407(22)$ $km\,s^{-1}$) as well as the inclination angle ($i = 67.4°(3.7°)$) from Frémat et al. (2005). Based on these values, we estimated the radius and the rotational period of HD 142983 as around $R_\star = 2.65(11)$ $R_\odot$ and 3.28(24) cd^{-1}, respectively. From these frequency values, it was obvious that the low frequencies of 0.1 and 0.2 cd^{-1} were not associated with the rotational period.

The primary frequency generally appeared at around 2.49 cd^{-1} during the five-year time interval (Fig. 6.15a). However, this frequency showed an unusual change on HJD2454739 by

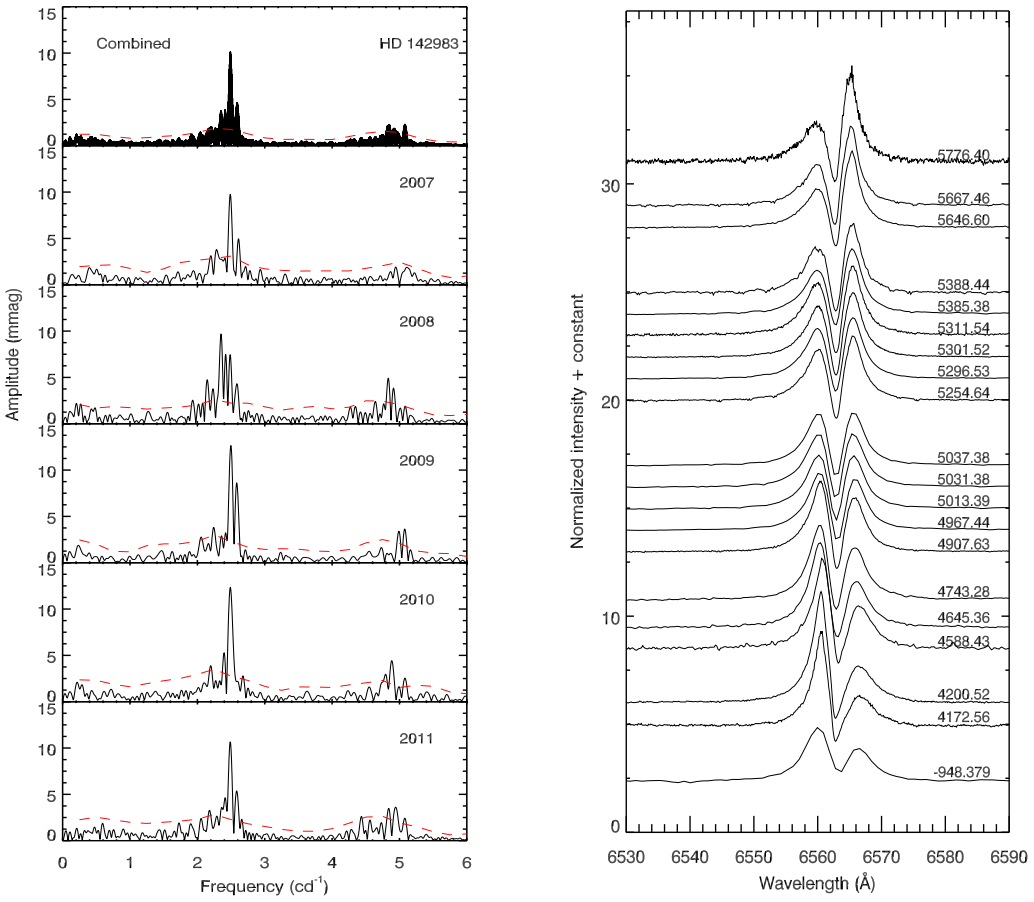

(a) (b)

Figure 6.15: (a) Five years of combined and seasonal amplitude spectra of HD 142983, (b) the Hα emission profiles obtained between 1993 and 2011. The numbers given on the right-hand side are the mid-observation times in Heliocentric JD (HJD-2450000).

decreasing to 2.35 cd^{-1} (Fig. 6.17; f_1 values on page 167). Considering only those changes at around 2.49 cd^{-1}, we realized that it exhibited a beat-like variation in 2007, 2008, 2010, and 2011, but we also observed an abnormal increase of about 0.01 cd^{-1} on HJD2455084 (Fig. 6.17). Analogous with this variability, the frequencies at around 2.17 and 4.95 cd^{-1} had the same beat-like change over five years. Apart from these, we detected seven more groups at around 2.20, 2.24, 2.32, 2.37, 2.42, 2.59, and 5.08 cd^{-1} in the seasonal periodograms. The variations in 2.42 and 2.59 cd^{-1} were quite similar. They both exponentially decreased and showed an unusual drop on around HJD2455428. Also, the frequencies at 2.20 and 2.32 cd^{-1} demonstrated a decreasing parabolic change between 2007 and 2011. Besides, 2.24 cd^{-1} displayed an increasing frequency profile.

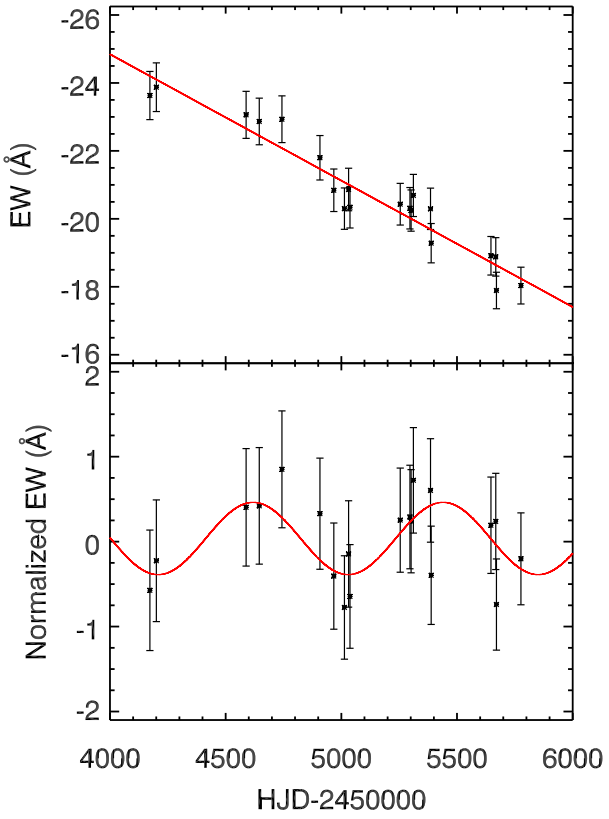

Figure 6.16: EW values of the Hα emission profile between 2007 and 2011 (top). The data have a clear quasi-periodic cycle apart from the long-term decrease. The period of this change is around 2.25(3) years (bottom).

The amplitudes of these frequencies were also variable, as presented in Fig. 6.18 (on page 168). The most remarkable changes occurred in the amplitudes of 2.49 cd^{-1} and the f_1 values. They showed a sinusoidal variation with the minimum on HJD2454739 and the maximum on HJD2455428. In addition, the amplitude of 2.20 cd^{-1} had a parabolic change, whereas the amplitudes of 2.17, 2.32, 2.37, and 2.42 exhibited a similar variation with an abnormal increase on HJD2454739.

For a better understanding of disk structure's effects, 20 spectra taken between 2007-2011 and a spectrum obtained in 1993 were examined. Only the results covering the period between 2007 and 2011 were presented, in order to compare them with the photometric findings derived in the same time interval. The evolution of the emission components and the EW of the Hα profile were monitored. As seen in Fig. 6.15b, the spectra basically showed a strong and narrow absorption line surrounded by violet and red emission components, indicating the existence of a circumstellar disk sector in the sight of line. As shown in the figure, the peak intensities varied

in time. Although the V component was dominant until HJD2454967.44, the intensity of R component started to increase after HJD2455037.38. Further, we noticed that they remained almost symmetrical between these dates. To measure V/R ratio, we calculated peak heights above the zero flux level, and presented a powerful V/R variation that was likely caused by a one-armed density wave of the disk in Fig. 6.17 (the first row on page 167). Accordingly, we discovered that we observed a decreasing branch of long-term disk variability. We determined the degree of this change to be around $F = 7.67$ with $C > 99\%$ by using the *F-test*.

In addition, we derived EW values of the Hα profiles, and found that these values had a variable structure similar to those of the V/R ratios. To be able to calculate the period of the quasi-periodic cycles discussed in the literature, we initially removed the long-term variation in the EW values by performing a linear fit in the form of $ax + b$ to the data (Fig. 6.16, top). We then fit the residuals with a *sine* function and estimated the period of this sinusoidal change to be around 2.25(3) years (Fig. 6.16, bottom).

Comparing the spectroscopic and photometric results, we could not determine a clear connection between the NRPs and the properties of the Hα profile. However, the decreasing trends of both EW and V/R ratio were inversely proportional to the change in 2.24 cd^{-1}. Additionally, the minimum phase of the sinusoidal variation occurred on around HJD2455031; this date coincided with the maximum points of the variations seen at 2.20, 2.42, 2.49, and 4.95 cd^{-1} as well as those seen in the amplitudes of 2.20 and 2.59 cd^{-1}. Furthermore, the maximum of the sinusoidal change on around HJD2454600 showed inverse proportion to the changes at 2.17, 2.37 cd^{-1}, and the unusual drop in the f_1 values. Also, it varied inversely according to the amplitudes of 2.49 cd^{-1} and f_1 values in the same date, whereas the jumps in the amplitudes of 2.17, 2.32, 2.37, and 2.42 cd^{-1} had a similar variation. Finally, an inverse correlation was observed between the frequencies at 2.42, 2.59 cd^{-1}, and the other maximum of the sinusoidal structure occurred on HJD2455450.

Table 6.11: Frequency analysis results of HD 142983.

Mid-Obs.Time (HJD)	**No #**	**Freq. (cd^{-1})**	**Amp. (mmag)**	**SNR**	A_m **(mmag)**	**Comments**
2007 Frequencies						
2454395	f_1	2.490(1)	10.46(32)	11.06	0.95	
	f_2	2.296(2)	4.63(32)	5.21	0.89	
	f_3	2.580(2)	3.86(32)	4.49	0.86	
	f_4	2.381(3)	3.20(32)	3.52	0.91	$2f_1 - f_3$
	f_5	2.169(3)	2.92(32)	3.37	0.87	$2f_2 - f_1$
2008 Frequencies						
2454739	f_1	2.351(1)	8.76(33)	11.33	0.77	
	f_2	2.488(1)	5.60(33)	7.85	0.71	$f_1 + f_2$
	f_3	4.834(2)	4.43(33)	6.25	0.71	
	f_4	2.586(2)	4.85(33)	7.02	0.69	$2f_2 - f_1$
	f_5	2.418(1)	4.78(33)	6.51	0.74	
	f_6	2.149(2)	4.79(33)	6.65	0.72	$2f_1 - f_2$
	f_7	2.229(3)	3.61(33)	4.64	0.78	$f_3 - f_4$
	f_8	4.914(3)	2.99(33)	4.17	0.72	$2f_2$
	f_9	4.637(4)	2.50(33)	3.25	0.77	$2f_1$
	f_{10}	1.927(4)	2.54(33)	4.20	0.60	$f_1 + f_6 - f_4$
	f_{11}	4.345(5)	2.05(33)	3.27	0.63	$2f_6$
2009 Frequencies						
2455084	f_1	2.498(1)	10.83(29)	15.02	0.72	
	f_2	2.587(2)	5.79(29)	9.36	0.62	
	f_3	5.079(3)	3.16(29)	5.88	0.54	$2f_1$
	f_4	2.245(2)	3.91(29)	4.27	0.92	$3f_1 - 2f_2$
	f_5	2.442(3)	3.07(29)	4.16	0.74	
	f_6	2.339(3)	2.93(29)	3.28	0.89	$2f_1 - f_2$
	f_7	4.988(4)	2.62(29)	3.91	0.67	
2010 Frequencies						
2455428	f_1	2.489(1)	13.08(34)	15.13	0.86	
	f_2	2.575(2)	4.78(34)	5.79	0.82	
	f_3	4.883(2)	4.59(34)	7.69	0.60	$3f_1 - f_2$
	f_4	2.194(3)	3.79(34)	3.66	1.04	$f_1 + f_3 - 2f_2$
	f_5	2.382(4)	3.18(34)	3.19	1.00	$f_3 - f_1$
	f_6	5.074(4)	2.55(34)	5.07	0.50	$2f_2$
	f_7	4.766(5)	2.50(34)	3.67	0.68	$2f_5$
	f_8	2.658(5)	2.52(34)	3.22	0.78	
2011 Frequencies						
2455773	f_1	2.488(1)	10.96(32)	15.56	0.70	
	f_2	2.589(2)	5.10(32)	7.56	0.67	
	f_3	2.372(2)	4.15(32)	5.19	0.80	$2f_1 - f_2$
	f_4	4.942(2)	3.76(32)	5.86	0.64	$2f_1$
	f_5	4.841(3)	3.39(32)	4.67	0.73	$f_1 + f_3$
	f_6	2.175(3)	3.38(32)	4.05	0.83	$2f_3 - f_2$
	f_7	2.273(3)	3.08(32)	3.57	0.86	$f_5 - f_2$
	f_8	2.431(3)	2.80(32)	3.75	0.75	
	f_9	4.433(4)	2.59(32)	3.53	0.73	$f_6 + f_7$
	f_{10}	5.084(4)	2.48(32)	4.65	0.53	$f_1 + f_2$
	f_{11}	2.066(4)	2.40(32)	3.16	0.76	$f_9 - f_3$

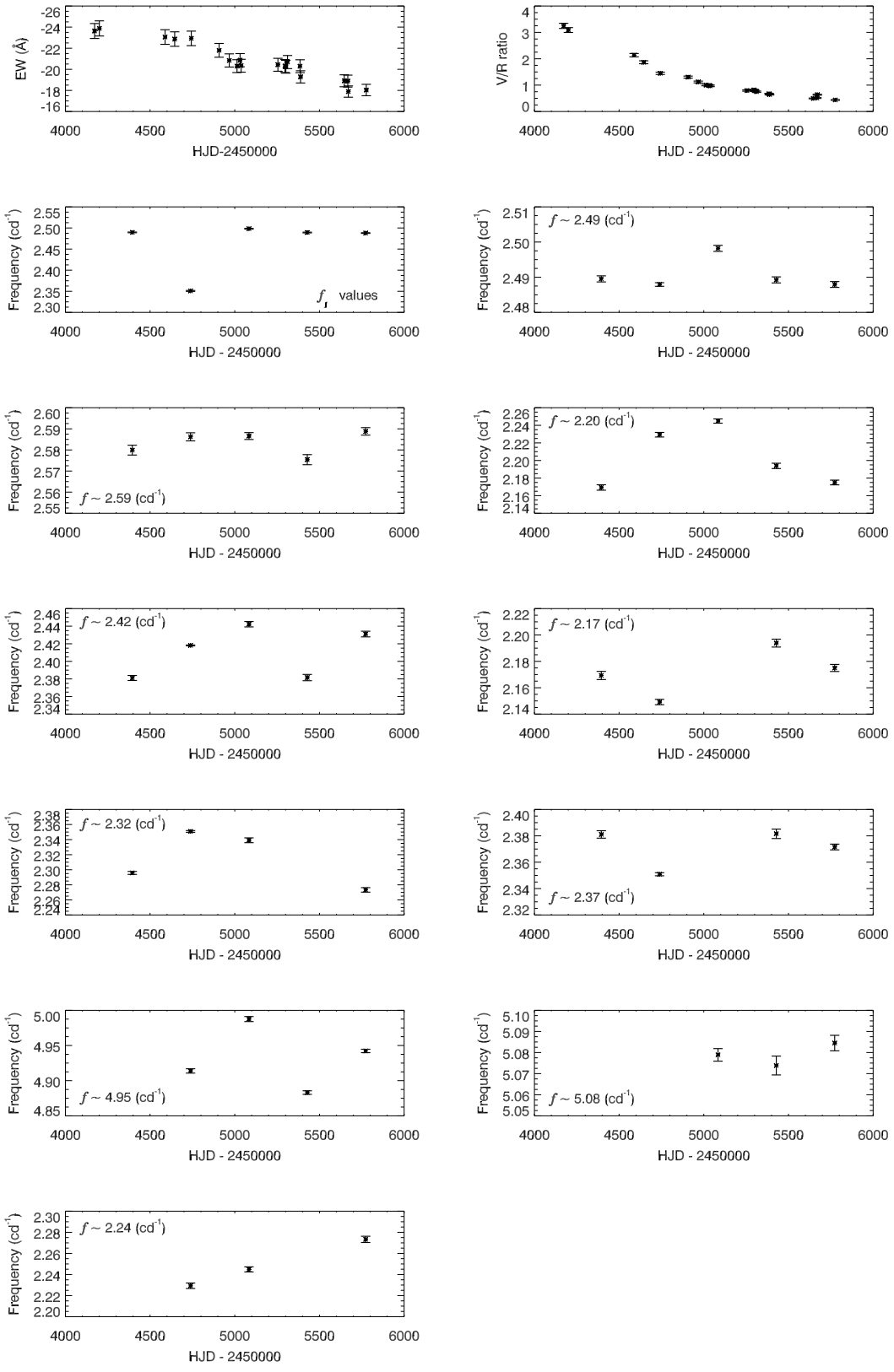

Figure 6.17: A comparison of photometric and spectroscopic results is given in the figure. The variations in the Hα line are given in the first row and the potential changes in frequencies derived from *STEREO* LCs are presented in the following rows.

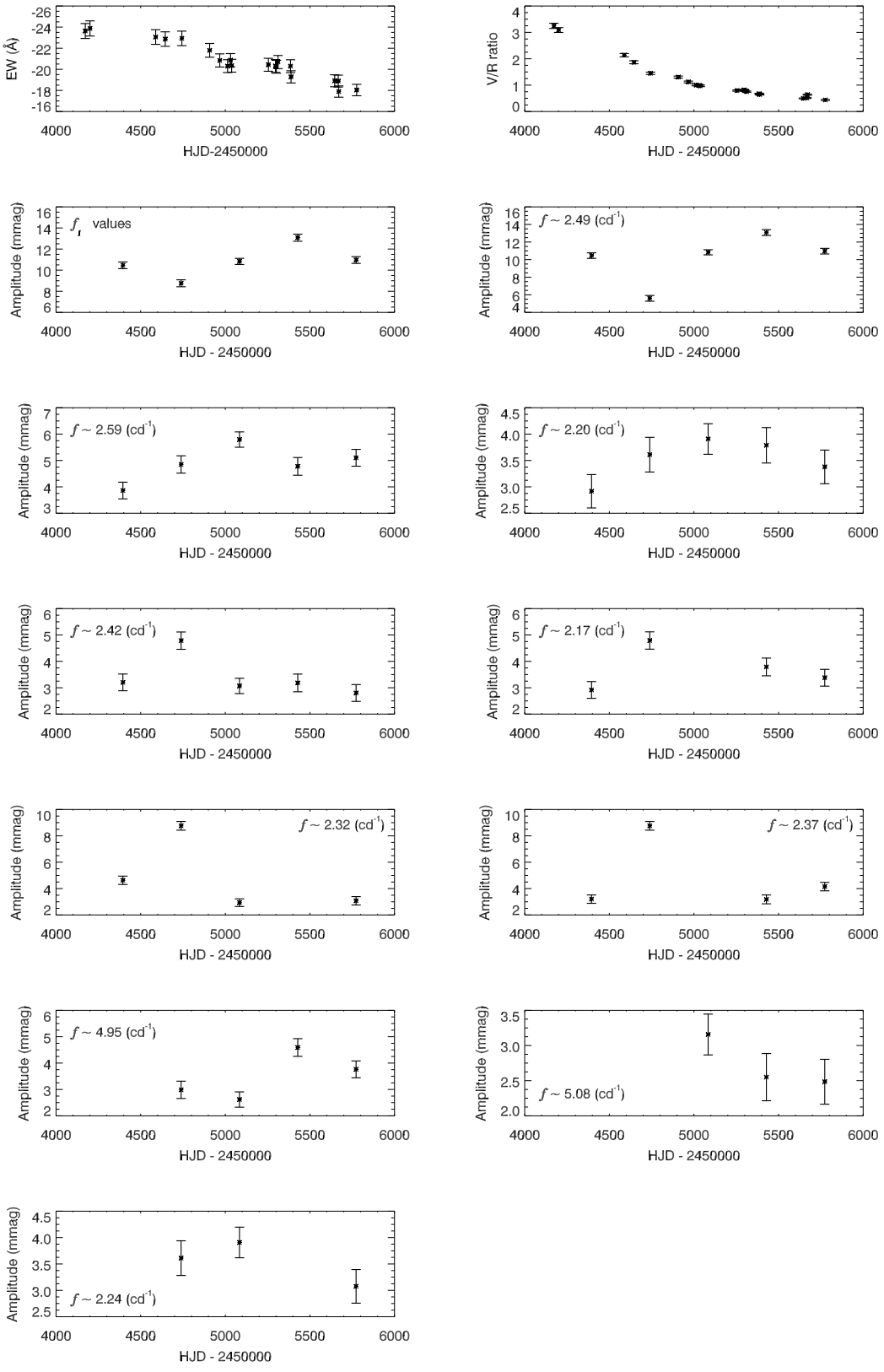

Figure 6.18: A comparison of photometric and spectroscopic results is given in the figure. The variations in the Hα line are given in the first row and the potential changes in frequency amplitudes derived from *STEREO* LCs are presented in the following rows.

6.4.8 HD 147196 (HIP 80126)

HD 147196 (B6/7V, $V = 7.05$ mag) was reported to show a range of excitation from B5 to B9 and quite broad hydrogen lines in its spectrum (Garrison, 1967). Irvine (1990) observed a strong single-peaked Hα profile with the EW value of ~ 15 Å, and The et al. (1993) confirmed this strong Hα emission. Unlike Irvine's (1990) finding, they found a double-peaked profile within a broad photospheric absorption located at 6,562.4 Å. V and R emission components also appeared at 6,561.1 Å and 6,565.1 Å, respectively. According to this wavelength difference, they mentioned that the peaks were quite close to each other to have been detected in low-resolution observations of Irvine (1990). Based on the comparison of their results and those from the archives, The et al. (1993) suggested that HD 147196 recently became active and probably transformed from a B-type star in a shell phase to a Be-phase, which was a typical characteristic of the classical Be-stars.

In our recent investigation, we obtained five-year photometric LCs of the star taken between 2007 and 2011. In contrast with the other samples, the curves were quite noisy. We thus hardly detected signals during the frequency analyses of the seasonal and combined data. We were able to extract eight significant frequencies in the combined periodogram (Table 6.12). The peaks were accumulated around 1.5 and 3.5 cd^{-1}. The most dominant signal was at 0.9780 cd^{-1}, which was considerably below the significance level in the seasonal data.

The main frequency observed in the seasonal data was at around 1.55 cd^{-1}. It was relatively strong over four years, but shifted to a lower frequency value of 0.9574 cd^{-1} on HJD2455779. Between HJD2454401 and HJD2455435, the frequency decreased from 1.57 cd^{-1} to 1.52 cd^{-1}. However, it showed an abnormal jump to 1.60 cd^{-1} on HJD2455090. Unlike the frequency, the amplitudes were constant in the five-year time interval (Fig. 6.19c; on page 172).

Apart from the photometric LCs, we also obtained three spectra of HD 147196 taken in 2008, 2009, and 2010. As mentioned by The et al. (1993), Hα emissions were in a broad photospheric absorption. This structure was therefore removed by a Gaussian fit to derive emission profiles (Fig. 6.19(b); on page 172). As seen in the figure, V components were at around 6,560 Å, although R peaks were located at 6,565.2 Å. Moreover, it is clear from Fig. 6.19(d) that the V/R ratio showed a rapid transformation. Whereas the rate was slightly over 1.0 on HJD2454672, the R component became dominant in the following year ($V/R < 1.0$), after which the ratio reversed on HJD2455359 ($V/R > 1.0$). However, unlike V/R variation,

the EW evolution of the emission profile had a different pattern that continuously decreased over three years. We calculated the degree of this variation to be around $F = 7.74$ with the confidence level of $C > 88\%$ by using the *F-test*.

As previously mentioned, LCs acquired between 2007 and 2011 were quite noisy, and did not allow for determining accurate frequency values. Further, we had a limited number of spectroscopic observations. For these reasons, it was not possible to find a clear relation between photometric and spectroscopic data. However, it should be noted that the decreases in the frequency and EW values over the same time interval were similar. Also, the frequency jump on HJD2455090 might trigger a mass ejection towards the disk, since the V/R ratio changed in this date. However, this change might also be an indication of a one-armed spiral structure in the disk rather than a mass ejection.

Table 6.12: Frequency analysis results of HD 147196.

HD 147196 Frequencies						
Mid-Obs.Time (HJD)	**No #**	**Freq. (cd^{-1})**	**Amp. (mmag)**	**SNR**	A_m **(mmag)**	**Comments**
Combined	f_1	0.97801(6)	0.78(11)	4.65	0.17	
	f_2	3.19038(6)	0.70(11)	4.64	0.15	
	f_3	1.53005(6)	0.73(11)	4.04	0.18	
	f_4	3.63450(7)	0.67(11)	4.53	0.15	
	f_5	1.58204(7)	0.66(11)	3.70	0.18	
	f_6	1.19586(7)	0.66(11)	3.68	0.18	
	f_7	1.33334(7)	0.60(11)	3.34	0.18	$3f_4 - 3f_2$
	f_8	3.43718(8)	0.57(11)	3.92	0.15	$f_4 + f_7 - f_3$
2007 Frequencies						
2454401	f_1	1.570(5)	1.58(22)	5.00	0.32	
	f_2	1.456(6)	1.37(22)	4.34	0.32	
	f_3	1.314(6)	1.27(22)	3.83	0.33	$2f_2 - f_1$
2008 Frequencies						
2454746	f_1	1.552(5)	1.45(24)	3.99	0.36	
	f_2	0.993(5)	1.25(24)	3.63	0.34	
	f_3	2.796(6)	1.06(24)	3.37	0.31	
	f_4	0.734(7)	1.02(24)	3.61	0.28	$f_3 - 2f_2$
	f_5	3.628(7)	0.97(24)	3.29	0.29	$f_1 + f_3 - f_4$
2009 Frequencies						
2455090	f_1	1.597(6)	1.40(23)	4.85	0.29	
	f_2	3.187(7)	1.14(23)	3.39	0.34	$2f_1$
	f_3	1.328(8)	1.01(23)	3.77	0.27	
2010 Frequencies						
2455435	f_1	1.524(6)	1.35(26)	4.26	0.32	
	f_2	3.647(7)	1.17(26)	3.56	0.33	
	f_3	1.773(7)	1.14(26)	3.59	0.32	
	f_4	0.465(8)	0.83(22)	3.82	0.22	
2011 Frequencies						
2455779	f_1	0.957(4)	1.65(26)	4.77	0.35	
	f_2	1.724(6)	1.27(26)	3.93	0.32	

Finally, the rotational velocity of HD 147196 was estimated by using the relation $V_{eq} \sim 0.7V_{cr}$, where V_{eq} and V_{cr} are the equatorial and the critical velocities of the star, respectively (Townsend et al., 2004). The critical velocity was found from $V_{cr} = \sqrt{GM/R_{eq}}$, where G is the gravitational constant, M is the mass of the star given by Hohle et al. (2010) to be $M/\mathrm{M}_{\odot} = 3.8(1)$, and R is the radius of the star ($R/\mathrm{R}_{\odot} = 3.4$) adopted from Pasinetti Fracassini et al. (2001). Based on these equation and parameters, the critical and equatorial velocities were found to be 462(21) $\mathrm{km\,s^{-1}}$ and 323(16) $\mathrm{km\,s^{-1}}$, respectively. This equatorial velocity value gave a rotation frequency of 1.88(19) $\mathrm{cd^{-1}}$, which was not clearly seen in the periodograms.

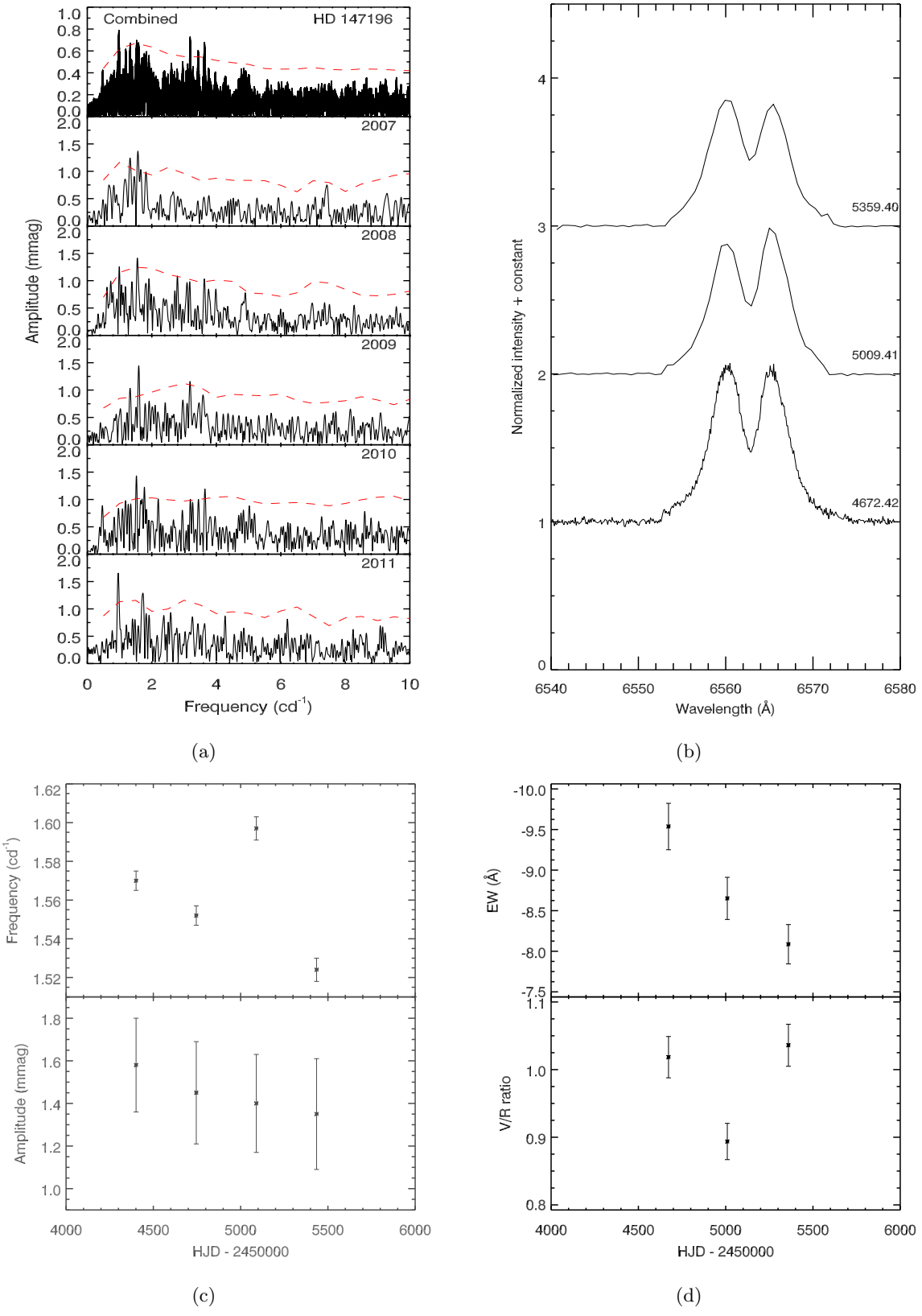

Figure 6.19: (a) Five-year combined and individual power spectra of HD 147196, (b) spectroscopic observations obtained between 2008 and 2010, (c) seasonal frequency and amplitude variations, and (d) EW and V/R variations of the Hα profile.

6.4.9 HD 178175 (V4024 Sgr; HIP 93996)

The emission lines of HD 178175 (B2V, $V = 5.57$ mag) were discovered by Merrill and Burwell (1933), and its LC variability was detected by Walraven et al. (1964). Feinstein and Marraco (1979) found irregular photometric variations ($A = 0.25$ mag) on large time-scales, while Renson (1978) obtained short time-scaled oscillations having a period of 1.37 days ($A = 0.04$ mag). Mathys et al. (1986) confirmed these short-term changes and derived a frequency value of 0.54 days, which was more comparable with NRPs of Be-type stars.

Additionally, Barker and Anderson (1982) observed a weak Hα emission line with a narrow core absorption in a wide photospheric absorption. In the following year, they observed a double-peaked emission showing a weak central reversal. They also reported that the photospheric

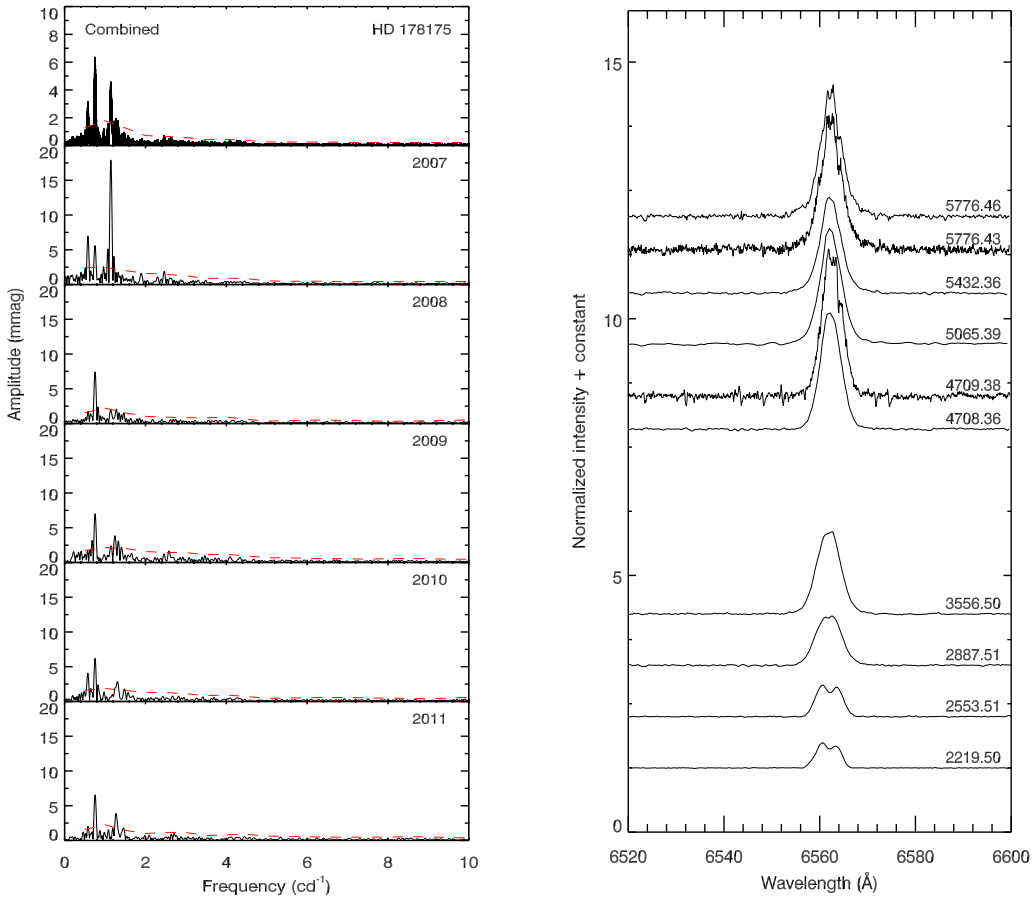

(a) (b)

Figure 6.20: (a) Five years of combined and seasonal amplitude spectra of HD 178175, (b) the Hα emission profiles obtained between 2001 and 2011. The numbers given on the right-hand side are the mid-observation times in Heliocentric JD (HJD-2450000).

structure disappeared and the profile displayed a flat continuum. Later, Jaschek and Jaschek (1992) determined a similar double-peaked, strong line profile with $R > V$.

In the recent photometric and spectroscopic investigations, we found 10 frequencies having an SNR greater than the specific significance threshold in the combined power spectrum. These are listed in Table 6.13. We realized that the periodogram consisted of three main frequencies at 0.57611, 0.75321, and 1.14246 cd^{-1} (Fig. 6.20a). However, the last two were relatively more powerful than the first peak, and the remaining frequencies were mostly accumulated around these two frequencies. The peak at around 0.75 cd^{-1} was explicitly dominant between 2008 and 2011. It exhibited an increasing profile over five years, as seen in Fig. 6.21 (on page 176). It should also be noted that the frequency shifted to a lower value on around HJD2455472. Further, its amplitude was also variable: although it had a parabolic variation changing from 7.5 to 6.0 mmag between HJD2454783 and HJD2455817, it was about 2.0 mmag weaker on HJD2454439. The frequency at 1.14 cd^{-1} was quite strong on this date, but its dominance was temporary and the peak became insignificant after HJD2455128 in the seasonal data.

The frequency discussed by Mathys et al. (1986) was determined to be around 0.57 cd^{-1}. The analyses showed that both frequency and its amplitude changed over time. The amplitude exhibited an inverse proportion to the frequency, decreasing from 6.5 mmag to 1.6 mmag. Apart from these, we detected two varying frequency sets at around 1.26 and 1.30 cd^{-1} in the seasonal data. The variation at 1.26 cd^{-1} had an increasing trend, whereas the other frequency showed an opposite change in the same time period. Their amplitudes displayed an increasing parabolic variation.

Moreover, we obtained three high-resolution and three low-resolution spectra taken between 2001 and 2011. As described by Jaschek and Jaschek (1992) and Barker and Anderson (1982), we found double-peaked Hα profiles in the high-resolution spectra, and determined the variation in the V/R ratios of the emission components. Even though the V component was dominant on around HJD2454700, the R peak became stronger on HJD2455800 (Fig. 6.21; the first row on page 176). Also as shown in the figure, we observed that the EW values exhibited an abnormal variation. However, once we eliminated the low-resolution data (taken on HJD2454708.36, HJD2455065.39, and HJD2455432.36), the remaining data points produced a variation similar to that seen in the V/R ratio ($F = 13.87$, $C \approx 99\%$).

It was not possible to make a connection between photometric and spectroscopic results, since some of the spectra were observed at a low-resolution. However, the increasing variation

Table 6.13: Frequency analysis results of HD 178175.

HD 178175 Frequencies						
Mid-Obs.Time (HJD)	**No #**	**Freq. (cd^{-1})**	**Amp. (mmag)**	**SNR**	A_m **(mmag)**	**Comments**
Combined	f_1	0.75321(1)	6.29(10)	12.98	0.48	
	f_2	1.14246(1)	5.21(10)	10.05	0.52	
	f_3	1.14496(1)	5.83(10)	11.23	0.52	
	f_4	1.14443(1)	4.30(10)	8.27	0.52	
	f_5	1.14389(1)	3.06(10)	5.89	0.52	
	f_6	0.57611(2)	2.48(10)	5.64	0.44	
	f_7	1.26761(2)	2.14(10)	3.95	0.54	
	f_8	1.32070(2)	1.86(10)	3.85	0.48	$f_1 + f_4 - f_6$
	f_9	0.57994(2)	1.90(10)	4.32	0.44	$f_6 + 2f_4 - 2f_2$
	f_{10}	1.14611(2)	1.78(10)	3.43	0.52	$2f_3 - f_4$
2007 Frequencies						
2454439	f_1	1.145(3)	17.85(20)	23.36	0.76	
	f_2	0.575(1)	6.46(20)	8.26	0.78	
	f_3	0.750(1)	5.19(20)	6.59	0.79	
	f_4	2.465(3)	1.92(20)	3.39	0.57	$f_1 + f_2 + f_3$
	f_5	1.892(4)	1.53(20)	3.62	0.42	$f_1 + f_3$
2008 Frequencies						
2454783	f_1	0.752(1)	7.48(16)	10.36	0.72	
	f_2	1.138(2)	2.27(16)	3.45	0.66	
	f_3	1.276(2)	2.17(16)	3.53	0.62	
2009 Frequencies						
2455128	f_1	0.754(1)	6.80(22)	10.12	0.67	
	f_2	1.249(2)	3.34(22)	4.34	0.77	
	f_3	1.334(2)	2.88(22)	3.79	0.76	
	f_4	1.139(3)	2.34(22)	3.25	0.72	$2f_2 - f_3$
	f_5	2.583(4)	1.57(22)	3.02	0.52	$f_2 + f_3$
2010 Frequencies						
2455472	f_1	0.752(1)	5.93(19)	9.65	0.61	
	f_2	0.575(1)	3.79(19)	5.86	0.65	
	f_3	1.310(2)	2.92(19)	5.01	0.58	$f_1 + f_2$
	f_4	1.268(3)	2.08(19)	3.64	0.57	
	f_5	1.479(3)	1.78(19)	3.05	0.59	$2f_1$
2011 Frequencies						
2455817	f_1	0.755(1)	6.45(19)	9.33	0.69	
	f_2	1.274(1)	4.14(19)	6.42	0.64	
	f_3	1.456(3)	2.02(19)	4.30	0.47	$2f_1$
	f_4	0.580(3)	1.62(19)	2.87	0.56	$f_2 - f_1$

trends of the frequencies at 0.75 and 1.26 cd^{-1} were inversely correlated with the decreasing EW and V/R changes, whereas the variation at 1.30 cd^{-1} was correspondent with the spectroscopic changes. Similarly, the amplitudes of 1.26 and 1.30 cd^{-1} showed an opposite change compared to the EW values and V/R ratios.

Finally, the radius and the rotational period of HD 178175 were estimated by using the relation $V_{cr} = \sqrt{GM/R_{eq}}$, where G is the gravitational constant, M is the mass of the star given by Hohle et al. (2010) to be $M/M_\odot = 10.1(1)$, and V_{cr} is the critical rotational velocity calculated as $V_{cr} = 396$ km s^{-1} by Frémat et al. (2005). Accordingly, we found the radius and the rotational period of the star to be $R = 5.54(72)$ $R_\odot$ and 0.40(8) cd^{-1}, respectively. This frequency was roughly half of the f_1 value detected in both seasonal and combined periodograms.

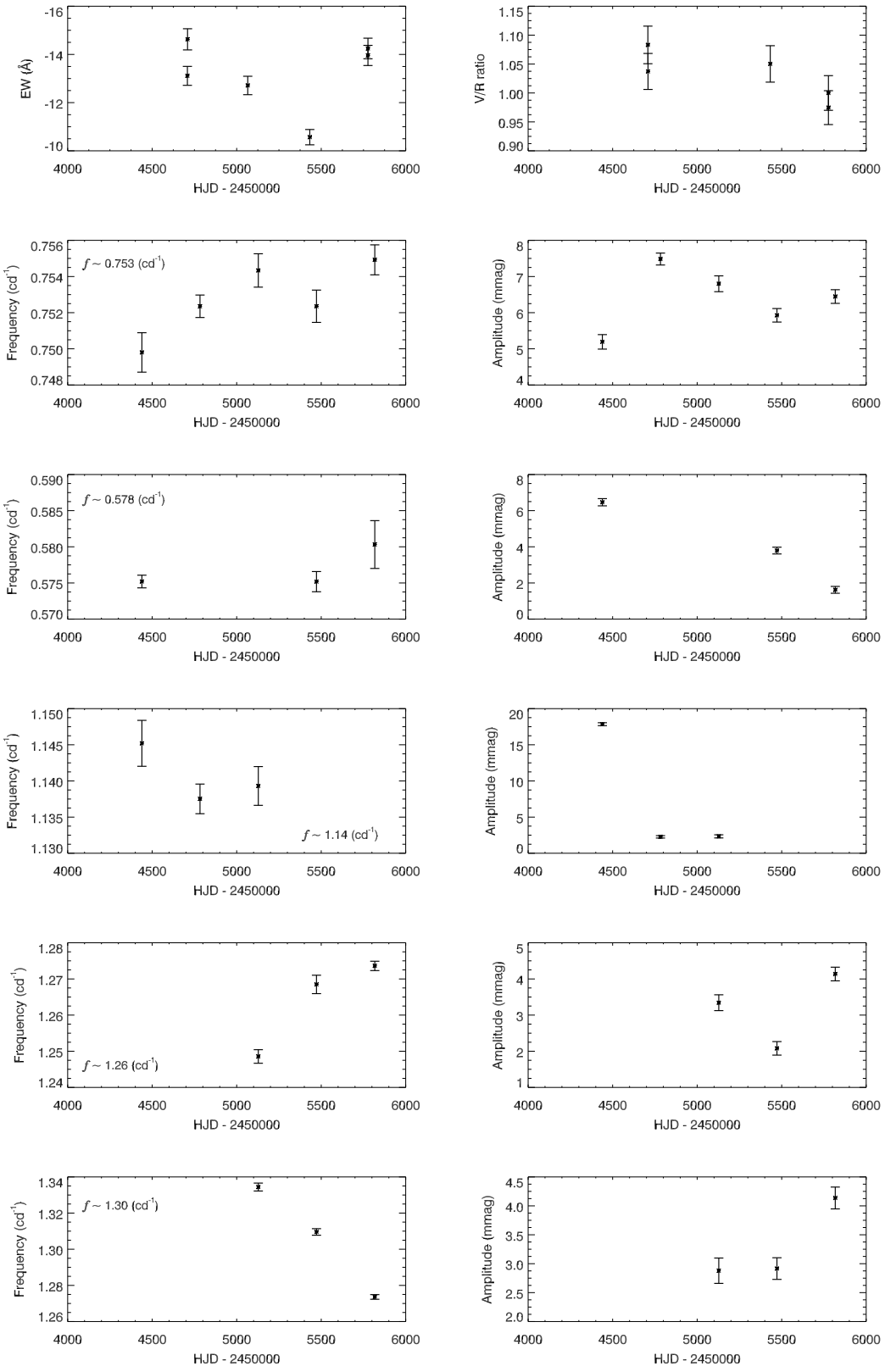

Figure 6.21: A comparison of photometric and spectroscopic results is given in the figure. The variations in the Hα line are given in the first row and the potential changes in both frequencies and amplitudes derived from *STEREO* LCs are presented in the following rows.

6.5 Discussion

In this chapter, five years of consecutive LCs belonging to a sample of bright Be-type stars were obtained from the *HI-1A* instrument of the *STEREO* satellite. The data were collected between 2007 and 2011 to detect a maximum number of periodicities and establish a connection with the archival spectroscopic data taken in the same time interval. A total of 1,638 candidates were initially collected from the *Simbad* Database and nine samples that met our selection criteria were chosen for detailed analyses. Even though Be-type stars range from late-O to early-A spectral type, the group consisted of only B-stars, five of which were early types. Seven of these samples were MS objects, and there were two giant stars in the group.

In order to carry out an effective examination of these stars, the analysis was advanced in two different ways. The refinement pipeline was first used to clean LCs from external and internal effects, and thus the most appropriate data for NRP detection were obtained. The seasonal and combined LCs were examined with the help of the LS method, and the results were compared to those of Period04. For each periodogram, regional noise levels were determined by averaging the noise values in every 0.5 cd^{-1}, and a specific noise characteristic was thus established. Based on this characteristic, the significance level was calculated with 99% probability. Those frequencies whose amplitudes were greater than this level were then detected. The detection precision of five-year combined data was around 10^{-5} cd^{-1} in frequency and 10^{-4} mag in amplitude.

As a result of the Fourier analyses, we not only discovered a great number of frequencies, but also revealed valuable information related to the pulsation characteristics of the sample Be-stars. The most important feature standing out in both seasonal and combined periodograms is that each sample, except for HD 23016, demonstrates explicit frequency groups. These configurations vary from one star to another and form mostly two, in some cases three different groups. For instance, HD 37967 and HD 147196 display three frequency groups while HD 23630, HD 26398, HD 36576, HD 37318, HD 142983, and HD 178175 consist of binary groups in their amplitude spectra. This distribution is displayed clearly in Fig. 6.22. The histogram was produced by using all the frequencies derived from the five-year combined data of the nine sample stars. These frequencies and the most dominant peaks detected in each combined periodogram are shown with grey and red lines, respectively. According to this figure, the majority of the frequencies is accumulated around 1.1 and 2.2 cd^{-1}.

This situation can be summarized as follows: Be-variables share the same region with SPB

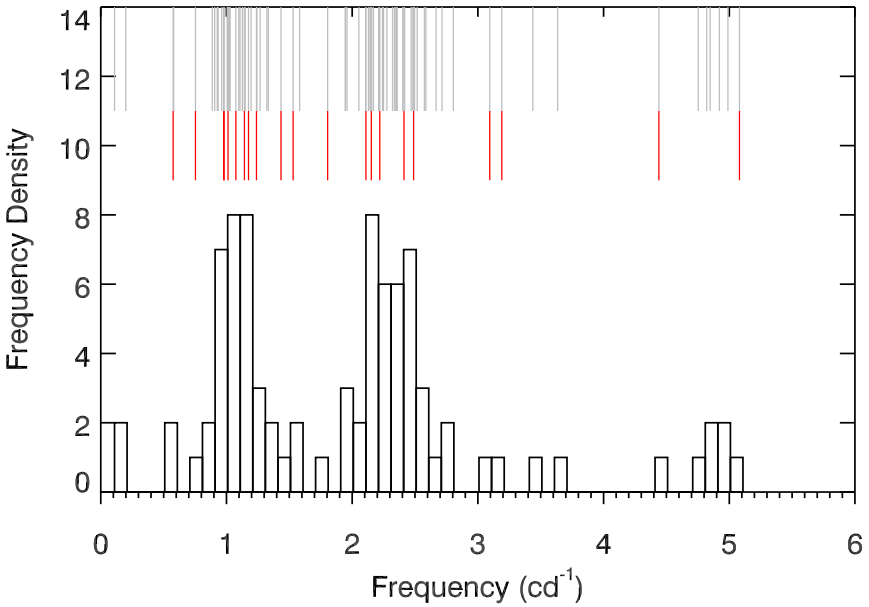

Figure 6.22: Frequency distribution of the selected sample stars shows that the oscillations are mostly accumulated around 1.1 and 2.2 cd^{-1}. All frequencies and the most dominant peaks detected in each combined periodogram are presented with grey and red lines, respectively. The lengths of these lines are not related to the frequency density.

and β Cephei stars on the H-R diagram. It is therefore expected that the κ-mechanism triggers p- and g-modes in Be-stars (Neiner and Hubert, 2009). However, Hubert and Floquet (1998) state that most of the studied early-type Be-stars, as well as 30% of the late types, have a period between 0.5 and 3.5 cd^{-1}, which corresponds to SPB-type oscillations. In SPB stars, the source of the oscillations is the κ-mechanism near the Fe opacity bump, and this mechanism initiates high-order, non-radial g-mode pulsations. Unlike SPB stars, the prograde modes are dominantly excited among the high-order g-modes in Be-types. These modes have frequencies of around $|m|\Omega$ in the observer's frame, where $|m|$ is the azimuthal order and Ω is the rotation frequency (Cameron et al., 2008). In a fast rotator, frequencies in the co-rotating frame (f_g) of intermediate- to high-order g-modes are quite smaller than $|m|\Omega$. In this case, the frequencies in the observer's frame are $f_g - m\Omega \approx -m\Omega$, and they produce a group that is close to $\approx |m|\Omega$ or that is separated from other groups by $\approx |m|\Omega$ (Saio, 2014). The amplitude spectra of SPB stars are characterized with such a grouping. This property makes the periods of light variations close to their rotation periods or half of it (Cameron et al., 2008).

These frequency groupings, which are also observed in the periodograms of our eight Be-

stars, have been reported in several ground- and space-based studies. For instance, Rivinius et al. (1998a) detected two frequency groups at around 1.98 and 3.57 cd^{-1} in μ Cen, and identified these to be retrograde g-modes with $l = |m| = 2$. Similarly, Neiner et al. (2005) determined two significant frequency clusters at 2.6 and 3.0 cd^{-1} in the power spectrum of Be-star HD 202904. These were produced by models of NRPs with a retrograde mode with $l = 3$, $m = 0$ and a zonal mode with $l = 3$, $m = 3$, respectively. For the MOST objects HD 127756 and HD 217543, the frequency peaks were accumulated around $1.0 - 2.0$ cd^{-1} and $2.0 - 4.0$ cd^{-1}, respectively. These groups were modelled as prograde g-modes with $|m| = 1$ and $|m| = 2$ (Cameron et al., 2008). In addition to these, *Hipparcos* data of HD 217675 showed that the star has pulsated around two dominant frequencies, 0.79 and 1.57 cd^{-1} (Hubert and Floquet, 1998). These examples can be extended with KIC 6954726 (Balona et al., 2011a) and several CoRoT stars studied by Huat et al. (2009), Diago et al. (2009), Neiner et al. (2009), and Gutiérrez-Soto et al. (2010).

Cameron et al. (2008) state that this property, seen in the Fourier spectra, can be used to estimate the rotation frequencies of rapidly rotating B-stars by simply looking at the distribution of the pulsation frequencies. As a demonstration, they examined the periodograms of HD 217543 and HD 127756, and indicated that HD 217543 has rotated two times faster than the latter star. A similar situation is also valid for *STEREO* Be-stars. As previously discussed, most of our samples have periods of around 1.0 and 2.0 cd^{-1}. However, the frequencies of HD 142983 are significantly higher than the average (2.49 and 5.08 cd^{-1}) and the frequencies of HD 178175 are grouped at the lower frequency values (0.75 and 1.42 cd^{-1}). Accordingly, it can clearly be suggested that HD 178175 is the most slowly rotating star in the group, while HD 142983 rotates at least two times faster compared to the other samples. This estimation can be confirmed by checking the archival rotational velocities of these stars ($Vsini = 111(71)$ $km\,s^{-1}$ for HD 178175 and $Vsini = 407(22)$ $km\,s^{-1}$ for HD 142983).

The great effect of rotational velocity on the high-order g-mode frequencies is explained by Saio (2013) with a theoretical model. As seen in Fig. 6.23, the variations in the growth rates and the azimuthal order m of the low-degree modes are investigated based on four different rotational velocities. In the figure, the x-axis represents the frequencies in the observer's frame; red solid and blue dotted lines are even and odd modes, respectively. In the bottom graphic, it is shown that the rotation only disperses the frequencies of a star with $Vsini = 36$ $km\,s^{-1}$ as a result of the effect of transformation from co-rotating to inertial frames. For the rotational velocity of 75 $km\,s^{-1}$, r-modes appear, whereas there is no significant change existed in g-modes.

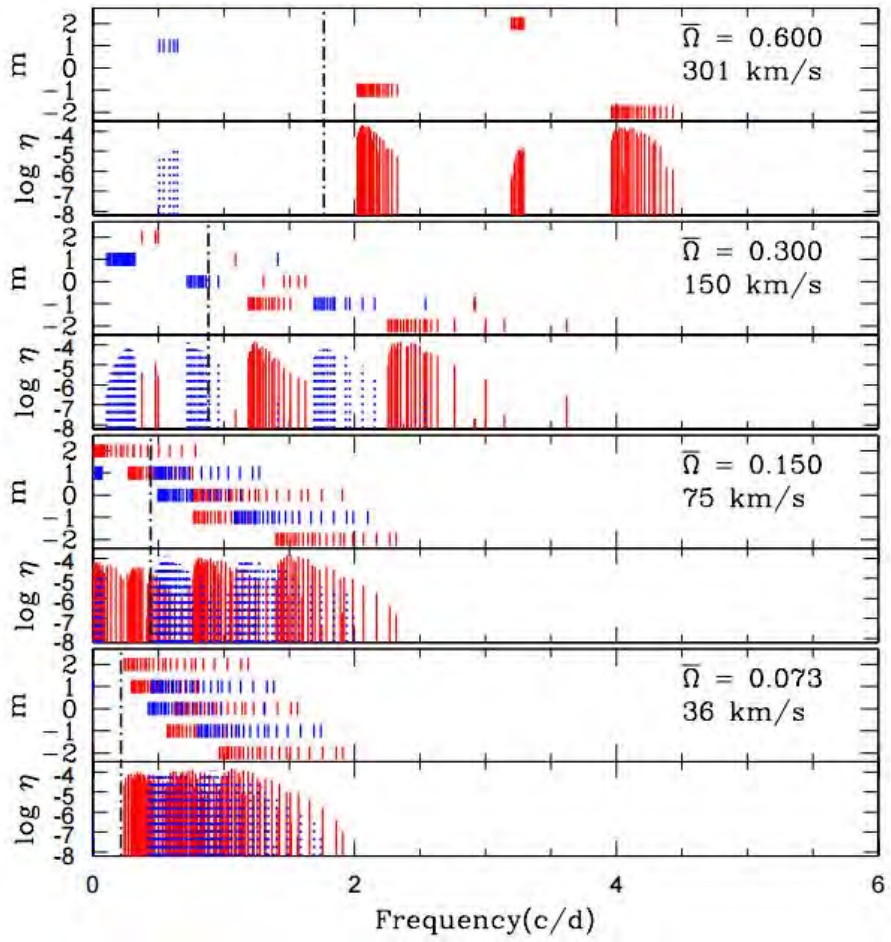

Figure 6.23: The great effect of the rotational velocity on the high-order g-mode frequencies is presented in the figure. The variations in the growth rates and the azimuthal order m of the low-degree modes are investigated based on four different rotational velocities (36, 75, 150, and 300 km s^{-1}). The x-axis is the frequencies in the observer's frame, red solid and blue dotted lines are even and odd modes, respectively (taken from Saio (2013)).

The r-modes are toroidal oscillations occurring as a restoring force for toroidal motions. For a higher rotation ($Vsini = 150$ km s^{-1}), g-modes with $m > 0$ are damped and prograde g-modes remain excited. Due to the damping of retrograde g-modes and the increasing effect of $-m\Omega$, frequency groupings become conspicuous. As presented in Fig. 6.23 (the second graphic from the top), the frequency groups occur at around 1.25 and 2.50 cd^{-1} in this velocity value. This model illustrates the frequency distributions observed in most of our Be-stars quite well. Further, if the rotation velocity is increased to 300 km s^{-1}, well-populated frequency groups are formed around 1.2Ω and 2.3Ω corresponding to $m = -1, -2$ for prograde sectoral g-modes (Fig. 6.23; top). In this case, the frequencies seem to be shifted to around 2.25 and 4.25 cd^{-1}. Considering that HD 142983 rotates at 400 km s^{-1}, it is quite normal to observe frequency groups at 2.50

Table 6.14: Physical parameters of *STEREO* Be-star samples.

Star HD	**Temperature** ($logT$)	**Luminosity** ($log(L/\mathrm{L}_{\odot})$)
23016	4.061(4)[a]	2.428(59)[a]
23630	4.110(10)[b]	3.435(44)*
26398	4.121(20)*	3.291(208)*
36576	4.389(7)[b]	4.102(123)*
37318	4.383(20)*	3.782(354)*
37967	4.244(15)[b]	3.235(119)*
142983	4.303(8)[b]	3.150(29)*
147196	4.096(20)*	2.308(72)*
178175	4.278(13)[b]	3.936(107)*

[a]: Zorec and Royer (2012), [b]: Frémat et al. (2005), *: these parameters are estimated from $B-V$ colour index and *Hipparcos* parallax values.

and 5.00 cd^{-1}.

Apart from these, another significant difference seen in the periodograms of the sample Be-stars is that the amplitude intensities of the late-type Be-stars HD 23630, HD 26398, and HD 147196 are notably lower than those of the other group members. Whereas the amplitudes of these three stars do not exceed 0.8 mmag, the amplitude values detected in other samples are greater than 1.0 mmag. In addition to this, their periodograms do not exhibit notable frequency groups, even though they have high rotational velocities. These stars also display NRPs with similar amplitude intensities instead of one or two dominant peaks. As discussed by Percy (2007), this type of structure is a typical characteristic of late-type SPB stars, and is an indication of a replacement of the convective core with a radiative dense one. In the radiative dense core, the Brunt-Vaisala frequency is quite high. This therefore causes a radiative damping that results in a shortening of the wavelengths of g-modes (Saio, 2013).

In order to confirm whether HD 23630, HD 26398, and HD 147196 are SPB type stars, the positions of the sample Be-stars on the H-R diagram were investigated. Their temperature and luminosity values were obtained from the relevant literature. For those samples with no archival information, the physical parameters were estimated from *Hipparcos* parallaxes and spectral types by following Flower (1977) (Table 6.14). These parameters were then used in the model produced by Saio (2013) for comparison (Fig. 6.24). In Fig. 6.24, the locations of SPB and β Cephei type stars taken from Saio (2013) are shown with triangles and inverted triangles, respectively. Archival Be-stars and the *STEREO* samples are given with red filled circles and black plus symbols, respectively. Large filled circles represent the Be-stars with NRPs found by MOST and CoRoT satellites. Theoretical models are generated based on $X = 0.7$ and $Z = 0.02$.

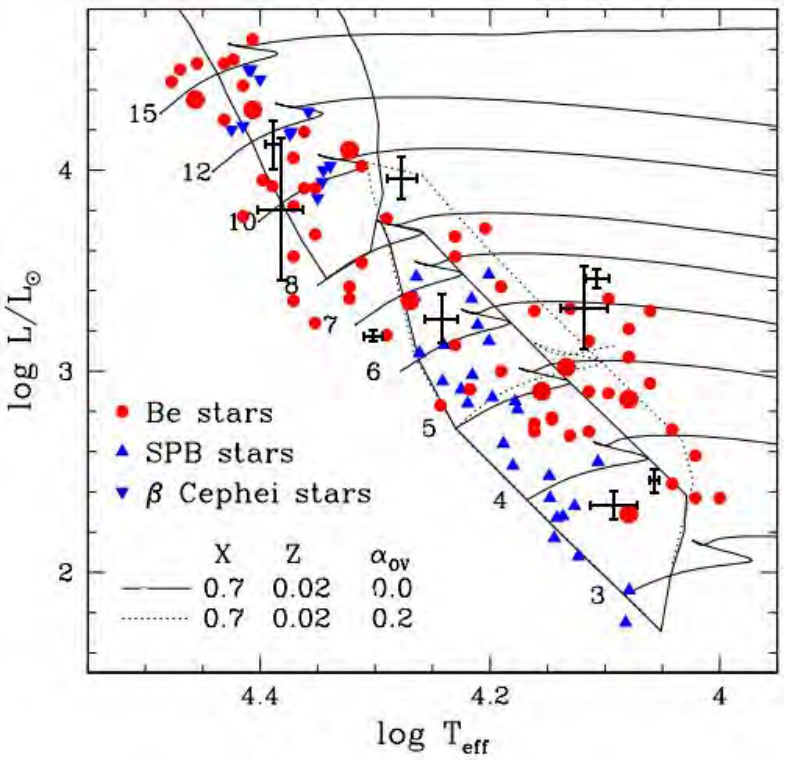

Figure 6.24: Positions of Be-stars on the H-R diagram are presented in the figure. SPB and β Cephei type stars are shown with triangles and inverted triangles, respectively. Archival Be-stars and nine *STEREO* samples in this study are given with red filled circles and black plus symbols, respectively. Big filled circles represent the Be-stars with NRPs found by MOST and CoRoT satellites. Theoretical models are generated based on $X = 0.7$ and $Z = 0.02$. Solid lines are evolutionary tracks and instability boundaries for p- and g-modes produced from models without core overshooting and dotted lines are from models with core overshooting of 0.2 H_p (taken from Saio (2013)).

Solid lines are evolutionary tracks and instability boundaries for p- and g-modes produced from models without core overshooting, and dotted lines are from models with core overshooting of 0.2 H_p. According to this figure, HD 23630, HD 26398, and HD 147196 are indeed located within or close to the SPB instability strip (the ones with $logT < 4.2$ in the figure). This confirms the abnormal oscillation behaviours seen in their periodograms.

Among the samples that demonstrate explicit frequency groups, HD 36576 and HD 37318 are situated in the β Cephei instability strip, although they do not have any high frequencies in their amplitude spectra. HD 37967 lies within the SPB strip but is also quite close to the p/g hybrid region. Moreover, HD 142983 and HD 178175 stand outside the p- and g-mode instability strips, but are close to the hybrid region. Even though all of these stars have a common grouping property and low frequencies in their periodograms, they are located in different parts of the

diagram. Therefore, it is not possible to attribute this property to the positions of the stars on the H-R diagram. However, it is possible that this is related to their being early-type Be-stars (Table 6.1). Also, the inconsistency in the positions of these stars may be explained by the uncertainties of the physical parameters of the sample stars. Balona (1990) states that there are several factors that affect luminosity and temperature of Be-stars. Firstly, they rotate faster than the stars used for calibrations, and thus their radii are systematically greater; using these values cause miscalculations of temperature or luminosity. Further, their spectral types and luminosity classes are poorly defined. The uncertainty in the classification is two or three spectral subtypes and one or two luminosity classes. In addition to these, spectral type depends on the degree of rotation and inclination angle, i.e., a rapidly rotating Be-star with equator-on position can be mistaken for a later type star that has a slow rotation.

Another sample star that falls into the SPB instability strip is HD 23016. Although it has a rotational velocity of 240(70) $\mathrm{km\,s^{-1}}$, its amplitude spectrum shows no particular frequency group. According to the *STEREO* data, this star is a mono-periodic Be-star with the period of 1.80 $\mathrm{cd^{-1}}$. This is not a very common situation in the literature, and there are only a few studies involving mono-periodic Be-stars. Some of them are λ Eri (Balona and James, 2002), ω CMa (Stefl et al., 2010), and 21 Be-stars discovered in the seismology fields of CoRoT (Gutiérrez-Soto et al., 2007). Even though the actual factor that causes this monotonic change is not precisely known, various hypotheses based on rotational modulations, stellar spots, co-rotating clouds, and binarity have been proposed (Sareyan et al. (1998), Balona (1990)). Since there has been no archival study related to HD 23016, it is not possible to make any assumptions. However, it should be noted that the Hα profile of the star is that of a wine bottle, which shows up at $i = 0°$. Consequently, the expected NRPs may not be observed due to this restricted line of sight.

Furthermore, this mono-periodic pulsation brings another important subject into question. While NRPs are known to be effective in the disk formation of many Be-stars (μ Cen; Rivinius et al. (1998a)), there is no interference of such modes in HD 23016 (at least in the *STEREO* photometric observations) and it is traditionally believed that a mono-periodic pulsation does not provide sufficient kinetic energy and angular momentum to form a rotationally-supported circumstellar disk (Owocki, 2004). Since the Hα profile of HD 23016 is significantly variable, it means that there are some other mechanisms in this star that trigger the mass loss. In this context, two studies demonstrating that NRPs are not necessary for disk formation can be given

as examples. 28 CMa is a mono-periodic variable with a period of 0.72 cd^{-1} and having cyclic outbursts. Stefl et al. (2010) examined the variations in its disk structure by using two different models: the steady-state Keplerian and the time-dependent disk models. While the former did not match with the observations, the time-dependent disk models, which considered the clearing of the inner disk expected to occur during the quiescent phase (with no mass loss), gave results that were quite consistent with the real data. As a result, it was revealed that the star had a tenuous inner disk due to the matter re-accreted onto the star, and this was the source of the observed period. In another investigation, Balona and James (2002) stated that periodic light variations of λ Eri ($P = 1.43$ cd^{-1}) were connected with the circumstellar material above its photosphere. As the detected period was indistinguishable from the rotation period, they suggested that the circumstellar material was co-rotating gas clouds, and that the mass loss in the star was caused by centrifugal magnetic acceleration.

Further research is crucial in order to gain a better understanding of the mono-periodic variability of HD 23016 and its source. However, as discussed in Section 6.4.1, this variation is definitely related to the change in the Hα profile. The increase in both frequency and amplitude over five years is clearly inversely proportional to the changes in EW values, which decrease between 2007 and 2011. Also, the quiescence phase seen in the frequency amplitude takes place in the same time interval with that of the EW.

Apart from this, the importance of NRPs for mass loss and disk formation was understood to a large extent in conjunction with the increase of the space missions. For instance, Goss et al. (2011) indicated that the SMEI data of α Eri had two dominant frequencies at 0.775 and 0.725 cd^{-1}, whose amplitudes increased and decreased over five years and caused a stellar outburst or a stellar cycle. Also, Gutiérrez-Soto et al. (2010) discovered that amplitudes of two main frequencies (1.143 and 2.324 cd^{-1}) found in CoRoT 102719279 reached the maximum intensity shortly before the outbursts and suddenly decreased right after the event. A similar situation was reported for the Be-star HD 49330 (Huat et al., 2009).

For the *STEREO* Be-stars, we traced the variations in both light curves and Hα profiles over five years in order to find a connection between NRPs and disk evolution. We found that while some of our samples showed significantly similar variation patterns, some samples did not present any similarities. For HD 26398, the changes in the frequency at around 3.10 cd^{-1} and in the main frequencies (f_1) observed in each season are remarkably in accordance with those in EW values. They all reach the maximum level on around HJD2454600, and decrease

in the same time period. The decrement in the EWs also occurs after the sudden drop in the amplitude of f_1 values on HJD2454900.

Another significant connection is seen in HD 36576: the frequency at 1.95 cd^{-1} linearly increases, as do the EW values. In contrast to this, the amplitude of this frequency exhibits an inversely proportional change compared to EWs. Moreover, the amplitudes of f_1 values and 1.01 cd^{-1} also have a decreasing profile, in contrast to those seen in the EW and the intensity of the Hα line. The abnormal decrease in emission strength between HJD2454400 – HJD2455200 takes place in the same time interval with those detected in the amplitudes of f_1 values and 1.01 cd^{-1}.

The only direct relationship found for HD 142983 is that the frequency at 2.24 cd^{-1} increases, while EW values and V/R ratio decrease. Apart from this, the beat-like structure of the 4.95 cd^{-1} is exactly inversely proportional to the sinusoidal change of EWs. The sudden jump in the frequency at 2.49 cd^{-1} on HJD2455100 also coincides with the minimum phase of the sinusoidal structure of EWs.

For HD 178175, the most notable pattern is that the emission intensity and the frequency at 1.30 cd^{-1} decrease while 1.26 cd^{-1} increase in the same time period. Similarly, the f_1 values of HD 147196 shift to lower frequencies as the EWs of the Hα profile decrease. The frequency at 1.05 cd^{-1} in HD 37967 shows an analogous change to that of the EW values. Finally, there is no specific correlation between the photometric and spectroscopic findings of HD 37318.

From the information presented above and in the relevant result sections, the most common pattern observed in the sample stars appears to be that EWs, V/R ratios, and frequencies and their amplitudes exhibit direct or inverse correlations, i.e., all these parameters increase or decrease at the same time interval in some samples while one or two of these parameters vary in the opposite way in the others. Apart from this significant point, it should be mentioned that sudden frequency or amplitude variations are also a quite common situation. Even though there is a possibility that these short time-scale changes are a consequence of our LC refinement procedure, they coincide with critical variations in EWs and V/R ratios: the jumps and drops in HD 37967 (the amplitudes of 2.14 cd^{-1} and f_1 values), HD 26398 (the amplitude of f_1 values), HD 23630 (the frequencies of 2.58, 2.68, and 2.96 cd^{-1}), HD 142983 (the frequency at 2.49 cd^{-1}, and the amplitudes of 2.32 and 2.42 cd^{-1}), and HD 147196 (the f_1 values) may be connected with the mass loss process as well as disk formation.

Since the Be-variables presented in this chapter are not well-studied stars, it is not possible

to make a final decision related to the connections between NRPs and circumstellar material around these stars; more photometric and spectroscopic observations are needed to confirm such a relationship. However, although *STEREO* has a shorter seasonal observation duration and collects less data points compared to other space missions, its high-precision measurements and uninterrupted monitoring ability enable researchers to measure NRPs with great accuracy and provide hints about the interactions between these pulsations and mass loss, disk formations, and variations in emission lines. In this sense, the *STEREO* satellite is an important resource in terms of analysing the behaviour of Be-stars.

Chapter 7

Pulsational Characteristics of a Sample of δ Scuti Stars and Their Relations Between Stellar Parameters

7.1 Introduction

δ Scuti stars are pulsating variables situated at the intersection between the MS and the classical instability strip in the H-R diagram. Their periods are between 0.02 days and 0.25 days, with a typical variation amplitude of around 0.02 mag: the amplitude in the v-band varies from 0.003 to 0.9 mag (Breger, 1979). These stars are mostly non-radial pulsators, but some Scuties show radial oscillations. The source of their pulsations is believed to be the κ-mechanism excited by the HeII partial ionization zones.

Due to their positions on the H-R diagram, a location where the asymptotic theory of NRPs is not valid because of low-order modes, the identification of their modes is difficult (Paparó et al. (2013), Tassoul (1980)). Although several long-term, ground-based observations such as that of Breger et al. (2009) exist for mode determination, a comparison between theoretical models and observed frequencies allows identification of only a few modes. This situation is mostly a result of observational constraints, e.g., atmospheric effects or duty cycle. Space missions such as CoRoT, Kepler, and MOST provide new insights into frequency and mode detection by eliminating these constraints. For instance, Poretti et al. (2009) have revealed that there

are about 1000 significant frequencies in the power spectrum of the CoRoT object HD 50844. Further, Balona et al. (2012) have shown that KIC 4840675 has a dominant mode and many other modes of lower amplitude, including several low-frequency variations. Monnier et al. (2010) have also detected 57 pulsation modes in the MOST star, α Oph. Apparently, the large number of pulsations is a recently discovered common property for at least some δ Scuties, and its origin is thought to be the interactions between NRPs and granulation noises produced by surface convections (Kallinger and Matthews, 2010).

Furthermore, another remarkable feature of these stars is that they exhibit both period and amplitude changes over time. The variation rates in periods are given as $dP/Pdt \sim 10^{-7}$ yr^{-1} (Breger and Pamyatnykh, 1998b) while the rates in amplitudes vary from a few days to a few hundred days. Theoretical models propose that period increases are more likely to occur in comparison to period decreases. However, an equal distribution has been observed to exist for both period increases and decreases. These models also suggest that the variation rates are ten times smaller than observational results (Kim et al., 2010). In addition to these properties, it is known that δ Scuti stars display regular spacings between NRPs and radial modes (Breger et al., 1999a). This property offers the chance to investigate the interior structures and characteristics of these stars, as well as their evolutionary stages on the H-R diagram. KIC 9700322 ($\Delta\nu \sim$ 2.78 cd^{-1}; Breger et al. (2011)) and the CoRoT object HD 174966 ($\Delta\nu \sim 5.53$ cd^{-1}; García Hernández et al. (2013)) can be given as examples for this frequency spacing property of δ Scuti stars.

In terms of gaining new insights for understanding the seismic behaviour of δ Scuti stars, observations taken from the space missions MOST, CoRoT, and Kepler have been major breakthroughs. These missions provide determination of long-period oscillations and resolution of beat frequencies with the help of long-term continuous monitoring. Also, their high photometric precision from mmag to μmag enables the detection of low-amplitude variations that are not easily observed from the ground. In line with these examples, in this chapter we use high-precision and long-term photometric data (four years of data obtained between 2007 and 2011) of another space mission, the *STEREO* satellite, to investigate and characterize the pulsational behaviour of a sample of δ Scuti stars.

7.2 Analysis of STEREO Data

In this chapter, *STEREO* LCs observed between 2007 and 2011 were used for the chosen δ Scuti samples. Each time series consisted of a maximum of 20-day photometric data chunks, having a 40-minute cadence and around 720 measurements. The Nyquist frequency was approximately 18 cd^{-1} (depending on quality of LCs; 17.972 cd^{-1} $\leq f_{(Nyq)} \leq$ 18.008 cd^{-1}).

As mentioned in Chapter 2 and Chapter 5, these LCs were contaminated by some sources such as spacecraft and instrumental effects, solar winds, CMEs, solar streamers, and bright background objects. In order to make a sensitive detection of δ Scuti type small variations, high-quality LCs cleaned from these internal and external effects were needed. Therefore, LCs were first purified by the basic pipeline, as explained in Section 5.1. Some parts of the pipeline were modified before performing frequency analyses, since the aim of this study was to detect the largest possible number of pulsation frequencies and to specify their relations.

Regardless of stellar type, contamination sources almost equally affected all observations. For this reason, the first four steps of the pipeline were not changed, and thus potential trends and outliers were removed from the LCs. As presented in Zhou (2010), δ Scuti stars are the second most common variable type in binary or multiple systems. Hence, the curves were subsequently fitted with polynomials to eliminate any existing dominant low frequencies (mostly between 0 and 1 cd^{-1}) that occurred due to proximity and orbital effects.

After the LC refinement, we analysed all seasonal and four-year combined time series using the LS method and obtained the most dominant frequencies to gain an idea about variations. During these analyses, the number of independent frequencies was calculated from $N_{raw}/2$, where N_{raw} is the number of observation points in the raw data, in order to derive reliable results, and FAP was assumed to be 99% ($P_0 = 0.01$). Apart from these, signals were sought between the frequency range of 0.05 - 18 cd^{-1} (Nyquist frequency), and variabilities greater than the Nyquist frequency were not taken into account.

As the second part of the frequency analyses, a recursive method was applied to the LCs to detect every significant frequency. To do this, the Fourier spectrum of the original data was initially derived, and the frequency with the highest amplitude was identified. If this peak was higher than a specific significance level, it was subtracted from the time series by using a least-squares fit. In the next step, the same procedure was applied to the pre-whitened data. At this point, the next significant frequency with the highest amplitude was removed: this routine

continued until the last significant frequency was found.

To extract the significant frequencies in seasonal and combined amplitude spectra, the conventional method of SNR ≥ 4.0 (or SNR ≥ 3.5 for combinations and harmonics of frequencies), suggested by Breger et al. (1993), was put aside, and a more specific technique was performed on periodograms. Unlike the procedures detailed in Chapter 4 and Chapter 5, we did not use a constant mean significance level here, since δ Scuti stars have had quite complex and noisy amplitude spectra due to surface convections. Instead, regional noise values were calculated for every 0.5 cd^{-1} frequency interval up to the Nyquist frequency. In this way, a variable noise profile was determined for each periodogram. Based on this noise characteristic, the specific significance level was then found with the help of the Eqn. 4.4 and the corresponding amplitude was derived from $A_z = 2\sqrt{z/N}$ (Balona, 2014). Since the significance level varied according to noise, it allowed us to be more selective and also enabled the detection of frequencies with low SNR. These noise and related significance levels are presented with red dash-dot and red dashed lines in periodograms, respectively. For a comparison, the constant significance level calculated from the mean noise value of the periodogram is shown with a blue dashed line in the same figures. Additionally, the extracted frequencies, their amplitudes, SNR and noise (A_m) values are given in the relevant tables.

With these detected frequencies, pulsation constants were calculated in order to identify the pulsation modes: in particular, radial and non-radial modes were distinguished by using observational and experimental approximations, which are given as: $Q_0 = 0.032 - 0.036$ days, $Q_1 = 0.024 - 0.028$ days, $Q_2 = 0.0195 - 0.0225$ days, and $Q_3 = 0.016 - 0.0185$ for the fundamental mode and its first three overtones (Fitch, 1981). To separate the radial modes, the ratios between the radial frequencies were found by comparing the observed and the calculated period ratios: $P_1/P_0 \sim 0.761$, $P_2/P_1 \sim 0.810$ and $P_3/P_2 \sim 0.845$ (Breger, 1979). In light of these estimations, the relations of the significant frequencies were evaluated; some speculations related to the types of modes observed in each combined periodogram are made in the following section.

Apart from these, the frequency spectrum of δ Scuti stars is not randomly distributed, as discussed in Section 1.2.4 and Section 7.1. Instead, NRPs are accumulated around radial pulsations and produce regular frequency spacings, similar to those in the Sun. However, one of the difficulties is that these stars have rich frequency spectra, which prevent an easy determination of these spacing characteristics. A simple way to designate such features is to use a histogram consisting of frequency differences (Breger et al., 2009). Subtracting each frequency from all

other frequencies, it is possible to find expected spacings between NRPs. In addition to this technique, we believe that statistical tests such as the *Statistical Hypothesis Test, F-Test, Chi Square Test, etc.*, are needed to obtain more realistic results. For this reason, the *Kolmogorov-Smirnov (KS) Test* (Kolmogorov (1933), Smirnov (1948)) was used to calculate the spacing characteristics of our sample δ Scuti stars. This method is a distribution-free test appropriate for every size of the data sample, and it has no restrictions. Detailed information on this can be found in Appendix B on page 314.

In this chapter, both short- and long-term variabilities in frequencies and in amplitudes are also investigated. For the short-term analysis, *STEREO* data covering the time interval between 2007 and 2011 were used. The frequencies regularly seen in all observations were initially chosen and plotted separately with calculated errors. The correlations between frequency and amplitude variations were then examined. For the long-term analysis, all available data from the literature were collected and compared to our *STEREO* results. If there were any coherent frequency values, they were put together and their variation rates were calculated from the overall data. Since most of the literature results were the products of multi-site observations, we deemed it suitable to use frequency values obtained from four-year combined LCs instead of using seasonal frequencies. These combined frequencies and their errors are shown with red crosses in the relevant figures. We sometimes found more than one result in the literature derived by different researchers for the same observation year. A separate variation rate was therefore also computed for each set of data from the literature; all results are given in the relevant tables.

7.3 STEREO Samples of δ Scuti Stars

For the selection of δ Scuti candidates, those samples that are already known were preferred in order to be able to benefit from archival data for the period analyses. The catalogue created by Lampens and Boffin (2000) was thus used as a reference since it provided insight into many types of δ Scuti variables having different origins, e.g., single stars, components of a binary or multiple systems, and cluster members. As a result, 67 stars were taken from the catalogue.

Before conducting the analyses, the specific selection criteria of brightness, position, LC quality, and aperture photometry of the candidates were scrutinised. Even though the *STEREO* satellite can observe 12^{th} magnitude objects, stars fainter than 10^m were subject to a contamination risk due to background effects such as coronal activities. Therefore, Scuties with a brightness of $V > 10^m$ were removed from the list as the first criterion.

Table 7.1: Sample stars and their characteristics in the literature.

Star	**Ra.** (°)	**Dec.** (°)	**Mag.** (^{m})	**Type**
HD 27397	64.99043	14.03520	5.57	F0IV
HD 27628	65.51466	14.07720	5.72	A3m
HD 28024	66.57693	22.81358	4.29	A8Vn
HD 30780	72.84359	18.83986	5.09	A7IV/V
HD 90386	156.53834	3.93253	6.66	A2V
HD 106384	183.56441	–5.71660	6.56	A5

For the second criterion, the locations of the remaining candidates were determined and compared to the FOV of the *HI-1A*. Stars with inappropriate right ascension and declination (DEC $\sim \pm 30°$) were taken out of the list. Based on these restrictions, 14 stars with suitable brightness and position were identified.

Further, the LCs and periodograms of the selected stars were controlled. Those displaying less noise and high signals during the four-year mission were identified. Among them, the targets without a neighbouring star in the same aperture (within a radius of 6 pixels) or those with a neighbour having a brightness greater than 1.5 times the target star were chosen.

Consequently, six stars that met our selection criteria were obtained. Statistically, one of these stars was an F-type and five of them were A-type pulsators. Three of the targets were components of binary systems. There were also four cluster members in the group. Furthermore, the visual brightness of the objects ranged between $V = 4.29$ and 6.66 mag. Coverage of the

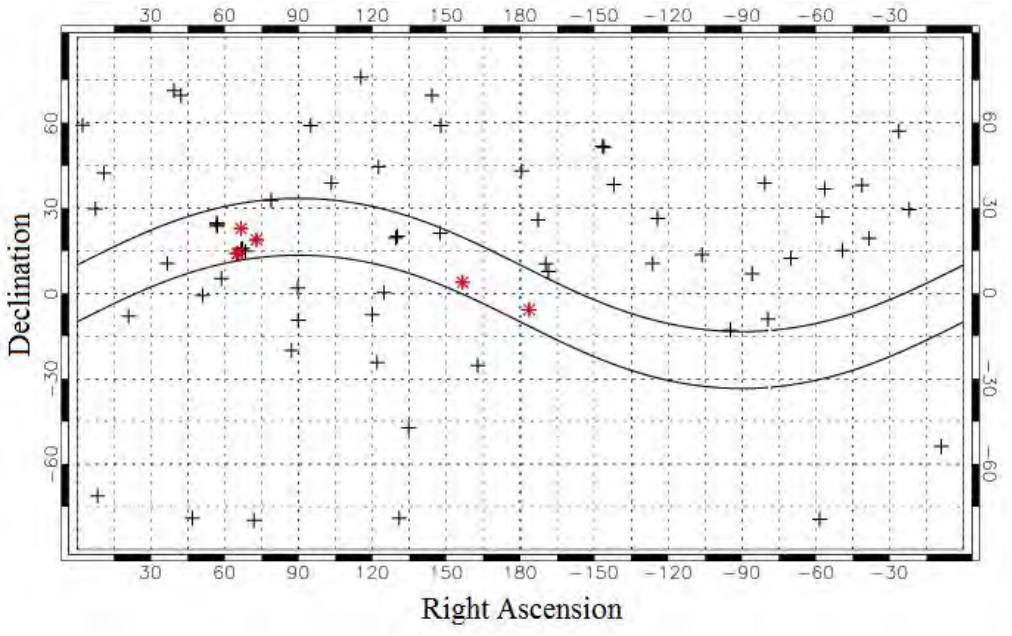

Figure 7.1: Diagram shows all 67 δ Scuti stars taken from Lampens and Boffin (2000) catalogue. The FOV of the *HI-1A* is represented by the path between the black strips, and red asterisk symbols are the targets that meet the selection criteria.

HI-1A instrument and the targets remaining in this region are shown in Fig. 7.1. Chosen δ Scuti stars are designated with a red asterisk sign in the figure, and their characteristics are listed in the order of HD catalogue names in Table 7.1.

7.4 Results

7.4.1 HD 27397 (57 Tau; V483 Tau; HIP 20219; HR 1351)

HD 27397 (F0IV, $V = 5.57$ mag) is a member of the well-populated Hyades open cluster and forms a binary system with another δ Scuti, 58 Tau (Fu et al., 1996). It is located in the red edge of the instability strip in which γ Dor stars exist (Morgan and Hiltner, 1965). Due to being a multi-periodic variable in a cluster and interacting with another pulsator, it is considered to be an asteroseismologically important object. These conditions provide an excellent opportunity to study internal structure and pulsational characteristics of the star, as well as to compare these behaviours with its companion and neighbours.

Table 7.2: All archival frequencies of HD 27397.

Time (year)	**Frequency (cycle per day)**	**Authors**
1981-1995	0.16208, 0.65745, 0.8025, 1.11933, 7.22323, 14.16131, 16.73835, 17.25689, 18.21986, 20.2181, 20.44054, 24.55519	Paparó et al. (2000)
1981	0.654, 0.804, 1.021, 7.232, 14.762, 16.594, 19.048, 18.26, 20.406, 25.556, 29.837	
1986	0.659, 0.845, 6.262, 16.626, 18.202, 20.411, 25.843	
1989	0.626, 0.802, 1.119, 8.002, 16.493, 18.247, 21.434, 29.527	
1995	0.665, 0.813, 7.237, 14.173 16.214, 18.23, 20.446, 29.843	
1967	18.5185	Millis (1967)
1973	18.5185	Fu et al. (1996)
1989	18.221(3), 20.4389(4)	
1978	18.4615	Horan (1979)
1998	0.4022530(2751)	Kaye (1999)

The photometric variability of the star was first discovered by Millis (1967), who gave its period as 0.054 days (18.5185 cd^{-1}, $A = 0.03$ mag). These variations were then confirmed by Horan (1979) by determining a period value of around 1.3 hours (18.4615 cd^{-1}, $A = 0.02$ mag). Later, Lopez de Coca et al. (1990) derived a similar frequency at 18.5185 cd^{-1} with an amplitude of 0.08 mag using the *P-L-C* relation for Scuti stars.

The first, and one of the most detailed, photoelectric photometry of the star was performed by Fu et al. (1996). They obtained 863 measurements after a 10-day observation run, and detected two reliable frequencies with very small amplitudes in time series. With the help of

Table 7.3: Details of the annual observations.

Time (year)	**Observation Points**	**Observation Duration (day)**	**Observation Duration (hour)**	f_{Nyq} **(cd^{-1})**
2007	582	~ 17	~ 412	17.9899
2008	611	~ 17	~ 412	17.9989
2010	676	~ 19	~ 460	17.9938
2011	472	~ 14	~ 340	18.0001
Combined	2341	~ 68	~ 1624	18.0005

rotational velocity, inclination angle and frequency difference ($Vsini$ = 100 km s^{-1}, $i = 90°$, $f_1 - f_2 = 2.217$ cd^{-1}), they assumed that these peaks were a doublet separated due to stellar rotation.

Combining all available data from the literature, Paparó et al. (2000) derived a 54-night observation (232 hours) covering the period between 1981 and 1995. They found many individual frequencies by composing different data sets, and identified 12 modes using the entire set of data. Even though four of these were in the low frequency region, which might be produced by misalignments of different subsets, two peaks were proposed as being generated by binarity or g-modes, as in γ Dor stars. According to Paparó et al. (2000), this result was quite interesting, because if it was true, the star would be the first δ Scuti variable exhibiting both p- and high overtone g-modes. Further, Kaye (1999) obtained a spectroscopic orbital period of around 2.4860(17) days and noted that some of the low frequencies determined by Paparó et al. (2000) were most likely due to duplicity such as geometric or proximity effects.

To analyse the interior structure of 57 Tau, a data set consisting of 68 days from 2007 to 2011 was obtained in this study. This data contained 2,341 photometric measurements equivalent to 1,624 hours of observation (Table 7.3). Frequency analysis of the combined LC showed that there were at least 14 substantial frequencies hidden within the time series (Fig. 7.2). These frequencies were determined according to the specific significance level presented by the dashed red line in Fig. 7.2. Eight of these frequencies had an SNR greater than 4.0, two of which were low frequencies at around ~ 0.7975 and ~ 2.1396 cd^{-1}. Instead of two certain peaks at 0.8025 and 0.6575 cd^{-1} as reported by Paparó et al. (2000), we observed only one strong frequency at 0.7975 cd^{-1}, which was nearly twice the orbital period ($P_{orb} = 0.4023$ cd^{-1}) calculated by Kaye (1999).

Moreover, we detected that main variations started after 15 cd^{-1} as indicated in the literature. Even though the most dominant frequency in the 1980s - 90s data was found at 17.2569

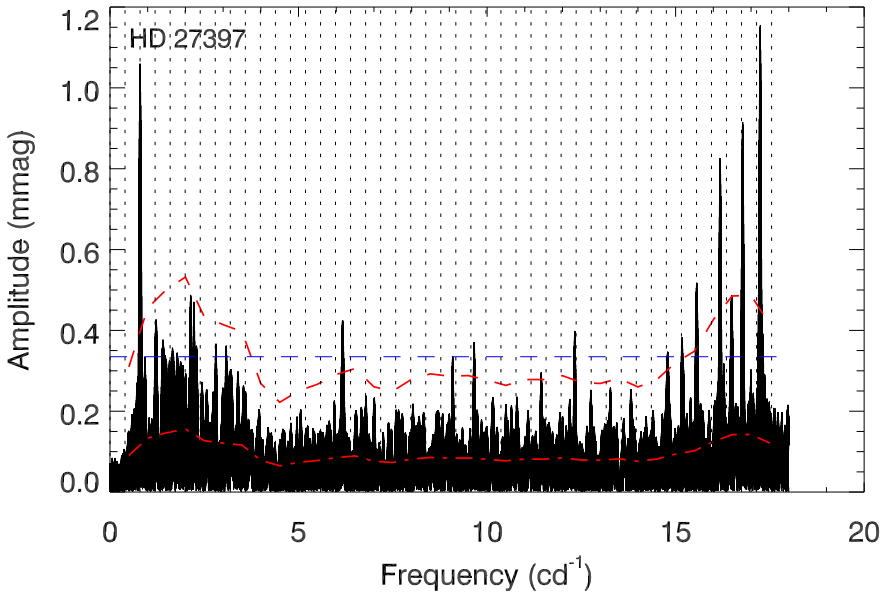

Figure 7.2: The amplitude spectrum of HD 27397 obtained from four-year combined LC. The variable noise level, corresponding significance level and mean significance level are shown with red dash-dot, red dashed and blue dashed lines, respectively. The vertical black dotted lines are the harmonics of the orbital period ($P_{orb} = 0.4023$ cd^{-1}) calculated by Kaye (1999).

cd^{-1} (Paparó et al., 2000), it appeared at around 17.2422 cd^{-1} for the current data. However, it was not possible to identify other variations reported at 18.22, 20.22, 20.44, and 24.56 cd^{-1} since the Nyquist frequency of our combined LC was 18.0005 cd^{-1}. Also, there were distinctive frequencies between 5 and 15 cd^{-1} in the amplitude spectrum (Fig. 7.2). We detected six frequencies in this region, but almost none of them were consistent with previous results. The peaks close to the previous findings were the frequencies at 6.17 and 14.79 cd^{-1}.

As this star was a rapidly rotating δ Scuti ($Vsini = 100$ km s^{-1}), it was possible to observe some split frequencies due to stellar rotation. With the help of the KS test (Appendix B; on page 314), we calculated spacings between frequencies and checked to see whether there was any perturbed peak. Based on the test, we found a regular spacing of around 0.4643 cd^{-1} between frequencies in the combined periodogram. The probability of this result was 0.99, which was greater than the significance level of 95% ($p = 0.05$). However, we could not precisely explain the relation between some of the frequencies detected with this value. For this reason, we computed the harmonics of the orbital period ($\sim$ 0.40 cd^{-1}), and presented them with black vertical dotted lines in Fig. 7.2 as well as in Table 7.4. As seen in the figure, almost all observable peaks

over and under the significance level were in good agreement with the harmonics. Clearly, δ Scuti type variation at around 18.5 cd^{-1} was split as a result of interactions with orbital motion. In contrast, the frequencies at 2.14, 6.17, and 16.18 cd^{-1} seemed to be inconsistent with the harmonics.

Table 7.4: Frequencies derived from the combined data of HD 27397.

HD 27397 Frequencies							
No	**Freq. (cd^{-1})**	**Amp. (mmag)**	**SNR**	A_m **(mmag)**	Q **(days)**	**Comments**	
f_1	17.24223(2)	1.13(07)	8.86	0.13	0.032(1)		$43f_{rot}$
f_2	0.79752(3)	1.06(07)	9.67	0.11		$2f_{rot}$	$2f_{rot}$
f_3	16.77804(3)	0.85(07)	5.91	0.14	0.033(1)		$42f_{rot}$
f_4	16.18343(3)	0.81(07)	6.18	0.13	0.034(1)		
f_5	15.55500(5)	0.51(07)	4.80	0.11	0.036(1)		$39f_{rot}$
f_6	2.13956(6)	0.51(07)	3.51	0.15			
f_7	16.48345(6)	0.50(07)	3.58	0.14	0.034(1)	$f_5 + 2f_1 - 2f_3$	
f_8	6.16719(7)	0.42(07)	4.78	0.09	0.090(4)		
f_9	12.32198(7)	0.39(07)	4.91	0.08	0.045(2)	$f_3 - 2f_6$	$31f_{rot}$
f_{10}	15.17151(7)	0.39(07)	3.88	0.10	0.036(1)		$38f_{rot}$
f_{11}	9.65906(7)	0.38(07)	4.56	0.08	0.057(2)	$f_5 - f_7 - f_{rot}$	
f_{12}	14.79548(8)	0.36(07)	3.98	0.09	0.037(1)	$f_5 + f_7 - f_1$	$37f_{rot}$
f_{13}	9.08919(9)	0.32(07)	3.67	0.09	0.061(2)	$2f_9 - f_5$	$23f_{rot}$
f_{14}	11.43619(9)	0.30(07)	3.88	0.08	0.048(2)	$f_{10} - f_6 - 2f_2$	

Subsequent to these investigations, we also derived pulsation constants of the frequencies within δ Scuti variability region. It was seen that Q constants of 57 Tau were considerably greater than expected values and varied from 0.03 to 0.09 days for frequencies between 5 and 18 cd^{-1}. Considering the frequencies obtained only from the *STEREO* data (up to its Nyquist frequency), we found six frequencies (17.24, 16.78, 16.18, 15.56, 16.48, and 15.17 cd^{-1}) in the fundamental mode interval given by Breger (1979). Among them, only 16.18 cd^{-1} satisfied the relation of $P_1/P_0 = 0.761$, together with the frequency of 12.32 cd^{-1}. However, this relation was reached if 16.18 cd^{-1} was assumed to be the first overtone of the fundamental mode 12.32 cd^{-1}. In this case, the second overtone matched with $\sim 50f_{rot}$ (19.98 cd^{-1}). We were also able to derive the ratio of $P_2/P_1 = 0.810$ by using the frequencies 15.17 and 12.32 cd^{-1}. If 12.32 cd^{-1} was the first overtone, then the fundamental mode and the third overtone would be 9.38 cd^{-1} ($\sim f_{11}$ or f_{13}) and 17.97 cd^{-1} ($\sim 50f_{rot}$). In addition, the ratio between the frequencies of 14.79 and 17.24 cd^{-1} yielded $P_3/P_2 \approx 0.845$. According to this, the fundamental mode and its first overtone were calculated to be around 11.98 cd^{-1} ($30f_{rot}$) and 9.12 cd^{-1} (f_{13}).

Frequency analyses were also performed for individual LCs to study annual frequency and amplitude variations. As shown in Fig. C.2 (on page 319), only four frequencies (0.80, 16.18,

16.78, and 17.24 cd^{-1}) were found to be detectable in each year. However, neither their frequencies nor their amplitudes exhibited significant variation during four years; their changes were within the acceptable error margins.

Table 7.5: Frequencies derived from the individual data of HD 27397.

No	**Freq. (cd^{-1})**	**Amp. (mmag)**	**SNR**	A_m **(mmag)**	**Comments**
			2007 Frequencies		
f_1	17.246(5)	1.09(15)	5.32	0.21	
f_2	0.798(5)	1.04(15)	4.55	0.23	$2f_{rot}$
f_3	16.184(6)	0.84(15)	4.08	0.21	
f_4	16.470(6)	0.85(15)	4.02	0.21	$f_1 - f_2$
f_5	3.079(6)	0.80(15)	3.28	0.24	$2f_1 + 2f_2 - 2f_4$
f_6	16.772(7)	0.77(15)	3.70	0.21	$2f_4 - f_3$
			2008 Frequencies		
f_1	17.240(4)	1.05(12)	5.13	0.21	
f_2	0.794(4)	0.96(12)	5.69	0.17	$2f_{rot}$
f_3	16.178(5)	0.84(12)	3.83	0.22	
f_4	16.780(5)	0.81(12)	3.40	0.24	$f_1 - f_{rot}$
f_5	2.243(6)	0.72(12)	3.68	0.20	$f_4 + 2f_2 - f_3$
f_6	15.560(6)	0.68(12)	3.76	0.18	$f_1 - 2f_2$
f_7	6.177(7)	0.60(12)	3.89	0.15	$f_1 + 2f_5 - f_6$
			2010 Frequencies		
f_1	17.238(3)	1.32(14)	5.22	0.25	
f_2	0.798(4)	1.24(14)	6.03	0.21	$2f_{rot}$
f_3	16.776(5)	0.92(14)	3.54	0.26	$f_1 - f_{rot}$
f_4	16.183(6)	0.79(14)	3.46	0.23	$2f_1 - f_3 - 2f_2$
f_5	9.658(9)	0.50(14)	3.19	0.16	
f_6	9.085(9)	0.48(14)	2.88	0.17	$f_4 + f_5 - f_3$
f_7	6.785(9)	0.47(14)	3.05	0.16	$f_1 - f_2 - f_5$
			2011 Frequencies		
f_1	17.247(7)	1.09(16)	6.35	0.17	
f_2	0.806(7)	0.96(16)	5.54	0.17	2_{frot}
f_3	16.781(8)	0.94(16)	3.88	0.24	$f_1 - f_{rot}$
f_4	1.227(8)	0.93(16)	3.63	0.26	$f_1 + f_2 - f_3$
f_5	16.180(9)	0.83(16)	3.43	0.24	$2f_1 - f_3 - 2f_2$
f_6	6.157(9)	0.79(16)	4.01	0.20	$3f_2 + 3f_4$
f_7	15.559(11)	0.67(16)	3.14	0.21	$f_3 - f_4$
f_8	15.191(11)	0.64(16)	3.10	0.21	$f_1 - f_2 - f_4$
f_9	14.819(12)	0.58(16)	2.89	0.20	$f_7 - f_2$
f_{10}	12.323(13)	0.56(16)	3.22	0.17	$2f_6$

Further, a frequency profile of the star was constructed to search for long-term variations by collecting all available findings from the literature (Table 7.2) and integrating them with *STEREO* data (Table 7.5). Based on this overall profile given in Fig. C.3 (on page 320), three frequencies (16.2140, 17.2569 and 0.8025 cd^{-1}) close to our findings were determined, and their variations carrying on over two decades were examined in detail as shown in Fig. C.4 (on page 321). It was determined that the most dramatic changes occurred in the frequencies at 16.18

and 17.24 cd^{-1}. However, apart from having no error value, the frequency at 16.2140 cd^{-1} found by Paparó et al. (2000) existed only in the data derived in 1995 and was not seen in the combined data taken between 1981-1995. Therefore, its accuracy was suspect. Considering this, the frequency variation at around 16.18 cd^{-1} was calculated to be $dP/Pdt = 1.35(44) \times 10^{-4}$ yr^{-1}. Unlike this, accuracy of the frequency at 17.2569 cd^{-1} was quite high since it was detected in Paparó et al.'s (2000) combined data (shown by a black point with 14-year error bar in Fig. C.4; bottom left on page 321), and its variation ratio was derived as $4.05(28) \times 10^{-5}$ yr^{-1}.

Table 7.6: Frequency variation table of HD 27397.

Frequency ($\mathbf{cd^{-1}}$)	dP/Pdt ($\mathbf{yr^{-1}}$)	dP/Pdt ($\mathbf{yr^{-1}}$)
	1. option	**2. option**
0.80	$2.96(59)\times10^{-4}$	$1.37(1.00)\times10^{-3}$
16.18	$1.35(44)\times10^{-4}$	
17.24	$4.05(28)\times10^{-5}$	

Archival orbital period values of the star were also compared to *STEREO* results. We found four different literature values as seen in Fig. C.4 (top left on page 321). However, two of these frequencies (0.8020 and 0.8040 cd^{-1}) were ignored and the variation ratio was calculated according to the frequency value at 0.8025 cd^{-1} since this one represented 14-year combined data. Moreover, another variation rate was also computed for the data obtained in 1995 due to its being within our error limits. Thus, we found a rate of $2.96(59) \times 10^{-4}$ yr^{-1} for the former and $1.37(1.00) \times 10^{-3}$ yr^{-1} for the latter period.

7.4.2 HD 27628 (60 Tau; V775 Tau; HIP 20400; HR 1368)

60 Tau (A3, $V = 5.72$ mag) is a metallic-lined spectroscopic binary and an important object since it fills an asteroseismologic gap between Am stars and δ Scuti variables on the H-R diagram.

The orbital period of the system was determined by Abt (1961) as 2.14328 days, and Horan (1979) gave a variability period of around 1.5 hours. He also confirmed that the star was located at the red edge of the instability strip. This result was quite remarkable since it was very well known that Am-type variables in both field stars and galactic clusters did not pulsate. Cox et al. (1979) illuminated this situation by suggesting that there might be an instability strip for cool Am stars in the red edge of the normal δ Scuti strip, and that 60 Tau fell in this region.

Zhiping (2000) photoelectrically observed the star for 30 hours and detected two significant frequencies at 13.0364 cd^{-1} and 11.8521 cd^{-1} with the SNR of 10.2 and 5.8, respectively. He calculated the Q values of f_1 and f_2 to be around 0.032 and 0.035 days. He also noted that residuals of the amplitude spectrum still had variability. In addition, it was verified that all Am stars (from evolved and marginal to classical Am stars) could be δ Scuti variables in this study.

Table 7.7: Details of the annual observations.

Time (year)	**Observation Points**	**Observation Duration (day)**	**Observation Duration (hour)**	f_{Nyq} **(cd^{-1})**
2007	583	~ 17	~ 410	17.9979
2008	612	~ 17	~ 414	17.9989
2010	673	~ 19	~ 461	17.9938
2011	483	~ 14	~ 331	18.0001
Combined	2351	~ 67	~ 1615	18.0005

We obtained a four-year time series of the star covering the interval from 2007 to 2011. The overall observations consisted of 2,351 photometric measurements, corresponding to a data of around 1,615 hours. Properties of the combined and individual LCs are given in Table 7.7.

Frequency analysis of the entire set of data showed that there were at least five significant peaks in the combined LC (Fig. 7.3 and Table 7.8). These frequencies were determined based on the significance level of the periodogram calculated according to the regional noise levels. The noise and significance levels are plotted with red dash-dot and red dashed lines in Fig. 7.3, respectively. For the comparison, the significance level computed from a mean noise level is also presented with a blue dashed line in the same figure.

Among the frequencies detected, 11.07 and 14.04 cd^{-1} were at the edge of the significance limit, whereas 0.93, 5.60, and 13.08 cd^{-1} were above this level. All frequencies, except for 0.93

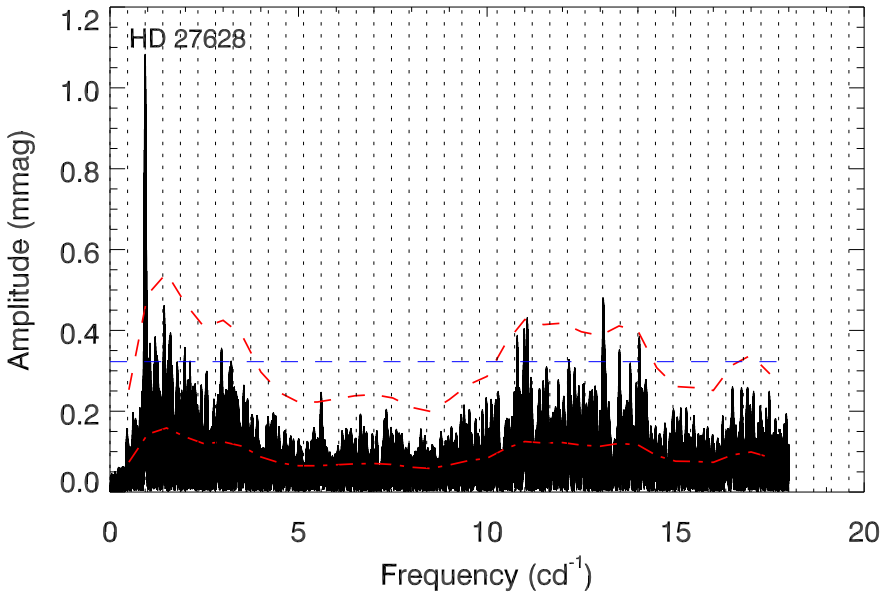

Figure 7.3: The amplitude spectrum of HD 27628 obtained from four-year combined LC. The noise and the significance levels are plotted with red dash-dot and red dashed lines, respectively. For a comparison, the significance level computed from a mean noise level is also presented by a blue dashed line. The harmonics of the orbital period ($\sim$ 0.47 cd^{-1}; Abt (1961)) are shown with black vertical dotted lines.

and 13.08 cd^{-1}, had an SNR between 3.0 and 4.0. The most dominant peak in the periodogram was 0.93 cd^{-1}, which was twice the orbital period given by Abt (1961) as 0.4666 cd^{-1}. Even though one of the two frequencies (13.0364 cd^{-1}) discovered by Zhiping (2000) was confirmed, the one at 11.8521 cd^{-1} was detected neither in the combined nor in the seasonal LCs; the LC taken in 2007, however, exhibited some variabilities between 11 and 12 cd^{-1} (Fig. C.5; on page 322).

Further, we observed that δ Scuti type variations were mostly accumulated between 10 and 15 cd^{-1}. We could extract only three frequencies within this region since the noise level was quite high, but it was clear that residuals of the amplitude spectrum still had other peaks. There were also some activities between 16 and 18 cd^{-1} that were quite below the significance level. Additionally, another variability at around 5 cd^{-1} attracted our attention. The main δ Scuti type frequency (13.08 cd^{-1}) in the combined data set was weaker than many other frequencies in the amplitude spectrum of 2007, 2008, and 2010 although it was quite strong in the 2011 data (Fig. C.5; on page 322). Beside this, we realized that, unlike a typical δ Scuti variable, the dominant pulsation mode of 60 Tau varied year by year. For instance, the main

Table 7.8: Frequencies derived from the combined data of HD 27628.

HD 27628 Frequencies						
No	**Freq. (cd^{-1})**	**Amp. (mmag)**	**SNR**	A_m **(mmag)**	Q **(days)**	**Comments**
f_1	0.93295(3)	1.09(8)	8.14	0.13		$2f_{orb}$
f_2	13.08085(6)	0.47(8)	4.06	0.12	0.033(8)	$28f_{orb}$
f_3	11.06751(7)	0.43(8)	3.37	0.13	0.039(9)	$24f_{orb}$
f_4	14.03945(8)	0.38(8)	3.45	0.11	0.031(7)	$30f_{orb}$
f_5	5.60174(12)	0.25(7)	3.87	0.06	0.078(18)	$12f_{orb}$

peak was 14.12 cd^{-1} in 2007 while it was respectively 13.80, 10.98, and 13.09 cd^{-1} for the time series obtained in 2008, 2010, and 2011. The exact reason for this variability was unclear, but it was suspected that some of these frequencies might be combinations of others. For example, $14.12 \approx f_1 + 1.63 + 11.58$, where 1.63 and 11.58 cd^{-1} were observable but insignificant frequencies in 2007, and $13.80 \approx 3f_1 + 10.98$, where 10.98 cd^{-1} was quite strong but remained under the significance level in 2008 (Table 7.9).

Since we were able to detect only a limited number of frequencies, it was not possible to track spacing patterns between the frequencies determined. However, we attempted to examine the effect of the orbital motion on these frequencies. Thus, we calculated the harmonics of the orbital period value and plotted them with black vertical lines in Fig. 7.3. Similar to those of HD 27397, the observable peaks above and under the significance level were quite consistent

Table 7.9: Frequencies derived from the individual data of HD 27628.

2007 Frequencies					
No	**Freq. (cd^{-1})**	**Amp. (mmag)**	**SNR**	A_m **(mmag)**	**Comments**
f_1	0.928(7)	0.76(15)	4.00	0.19	$2f_{orb}$
f_2	14.124(8)	0.62(15)	3.28	0.19	
f_3	3.372(8)	0.61(15)	3.55	0.17	
2008 Frequencies					
f_1	0.935(4)	1.23(14)	7.52	0.16	$2f_{orb}$
f_2	13.797(8)	0.61(14)	3.32	0.18	
f_3	7.308(13)	0.38(14)	3.05	0.12	
2010 Frequencies					
f_1	0.934(3)	1.35(14)	7.23	0.19	$2f_{orb}$
f_2	1.443(5)	0.86(14)	3.28	0.26	
f_3	10.981(7)	0.64(14)	3.31	0.19	
2011 Frequencies					
f_1	0.949(7)	1.04(16)	7.78	0.13	$2f_{orb}$
f_2	13.091(8)	0.97(16)	5.53	0.18	
f_3	13.522(11)	0.67(16)	3.48	0.19	

with these harmonics. This might be the indication that amplitudes of the most peaks in the periodogram were intensified due to orbital motion.

Moreover, we computed pulsation constants of the δ Scuti type frequencies in the amplitude spectrum. As given in Table 7.8, the Q values of f_2 and f_4 were in agreement with the fundamental mode of a typical δ Scuti star, given by Breger (1979). If the frequency at 13.0837 cd^{-1} was considered to be the fundamental mode, its first overtone was predicted as approximately 16.67 cd^{-1} by using the ratio of $P_1/P_0 = 0.785$ suggested by McNamara (1983) for δ Scuti stars located in the red edge of the instability strip. Further, the error value estimated for the pulsation constant of 13.0837 cd^{-1} was slightly large; this revealed another possibility that 13.0837 cd^{-1} might be the first overtone of the fundamental mode. Based on this, the fundamental mode was found to be around 10.27 cd^{-1}, corresponding to $22f_{rot}$. Its second overtone would be around 16.15 cd^{-1} ($\sim 35f_{rot}$).

In order to see the general frequency profile, we added two frequency values determined by Zhiping (2000) to our *STEREO* data (Fig. C.6; on page 323). As previously mentioned, frequencies were accumulated between 10 and 15 cd^{-1}, but they did not show any regular variation unlike other δ Scuti samples. According to the figure, the most consistent variation was seen in the frequency at 0.93 cd^{-1}. Although there was not a significant change in the stellar orbital period between 2007 and 2011, we determined that it showed a decrease of about $-5.71(2.5)\times10^{-3}$ yr^{-1}. Besides, its amplitude displayed a remarkable inverse parabolic variation.

Moreover, the comparison of the δ Scuti type pulsation at 13.0809 cd^{-1} in our combined periodogram with 13.0364 cd^{-1} given by Zhiping (2000) showed that the pulsation period of the star also decreased between 2000 and 2009 (the mean time value of our four-year mission). The rate of this variation was around $-3.78(54) \times 10^{-4}$ yr^{-1}.

7.4.3 HD 28024 (69 Tau; ups Tau; HIP 20711; HR 1392)

69 Tau (A8V, $V = 4.29$ mag) is a spectroscopic binary in the Hyades cluster (Harper, 1920). Its LC variability was first discovered by Horan (1979), who gave the period of this variation as around 3.2 hours ($A = 0.025$ mag). He also found that 69 Tau was the fastest rotating star ($V_{rot} = 243$ km s^{-1}; Zorec and Royer (2012)) among cluster members.

Bossi et al. (1983) performed the most comprehensive investigation using seven nights of observation (97 points), showing that the LC of the star had a single sinusoidal component with a period of 6.74(8) cd^{-1} ($A = 0.0081$ mag). They also detected a low-amplitude structure at 0.53 cd^{-1} and associated it with the high rotational velocity. Using the main frequency and other parameters in the literature, they calculated a pulsation constant of 0.027 days, which was incompatible with the fundamental mode. With the *P-L-C* relation, Lopez de Coca et al. (1990) improved on the study of pulsation period, giving it as 0.1480 days (6.75676 cd^{-1}) with the amplitude of 0.016 mag.

Unlike other authors, Abt (2008) studied transient hot inner disks around rapidly rotating A-type dwarfs, which occurred due to sporadic mass-loss events. He derived 10 years of spectroscopic data covering 1997 – 2006, and found that mean EW measurements of TiII lines indicated the presence of a variable gaseous material surrounding 69 Tau.

Table 7.10: Details of the annual observations.

Time (year)	**Observation Points**	**Observation Duration (day)**	**Observation Duration (hour)**	f_{Nyq} **(cd^{-1})**
2007	665	$\sim$ 19	$\sim$ 461	17.9988
2008	684	$\sim$ 19	$\sim$ 461	17.9989
2010	684	$\sim$ 19	$\sim$ 461	17.9938
Combined	2033	$\sim$ 58	$\sim$ 1384	18.0005

In this study, we obtained 2,033 photometric data points, corresponding to 1,384 hours of observation, between 2007 and 2010. Details of the LCs are given in Table 7.10. According to frequency analysis of the combined data, we detected the existence of only one significant frequency in the amplitude spectrum. The δ Scuti type variation, which was found at 6.74 and 6.75 cd^{-1} in previous studies, appeared at around 6.81 cd^{-1} with the amplitude of 4.08 mmag (Table 7.11). As seen in Fig. 7.4, there were several other variabilities between 1.00 and 2.5 cd^{-1}, but none of these peaks were above the significance level (indicated by a red dashed line) calculated based on the regional noise characteristic (red dash-dot line) of the periodogram.

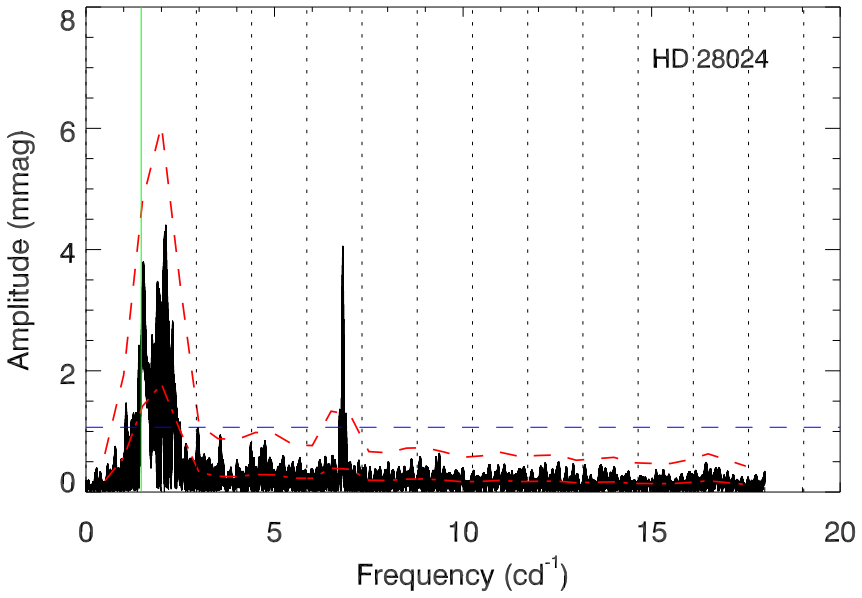

Figure 7.4: The amplitude spectrum of HD 28024 obtained from four-year combined LC. The noise and the significance levels are plotted with red dash-dot and red dashed lines, respectively. For a comparison, the significance level computed from a mean noise level is also presented by a blue dashed line. The rotational period estimated from the rotation velocity of the star is 1.461(31) cd^{-1} and shown with a vertical green line. The black vertical dotted lines are integer multiples of the rotation period.

Our seasonal LCs also seemed to be formed of a single sinusoidal as mentioned by Bossi et al. (1983) (Fig. C.7; on page 324). However, the peaks that appeared between 1.00 and 2.5 cd^{-1} in the combined periodogram were over the significance thresholds in the seasonal amplitude spectra.

Similar to the findings of Bossi et al. (1983), these low frequencies were attributed to rapid stellar rotation. To gain more insight regarding these structures, the rotational period of HD 28024 was estimated from Eqn. 1.10. In this equation, the rotational velocity (243 $km\,s^{-1}$) was taken from Zorec and Royer (2012) and the radius of the star ($R/R_{\odot}$ = 3.28(7)) was calculated from the temperature and luminosity values ($logT$ = 3.8768(29) and $log(L/L_{\odot})$ = 1.491(14)) given by de Bruijne et al. (2001a). Based on these parameters, the rotational period of the star was found to be 1.464(31) cd^{-1}, which was consistent with 1.523719(18) cd^{-1} in the periodogram (indicated by a vertical green dotted line in Fig. 7.4). The peak at around 2.04 cd^{-1} was roughly one-half of the rotational frequency, and it was likely that a split occurred due to the stellar rotation. The aliases of this split were also seen with every integer multiple

Table 7.11: Frequencies derived from the combined and individual data of HD 28024.

HD 28024 Frequencies					
No	**Freq. (cd^{-1})**	**Amp. (mmag)**	**SNR**	A_m **(mmag)**	Q **(days)**
f_1	6.80972(5)	4.08(39)	10.41	0.39	0.036(2)
f_2	3.56185(22)	0.94(38)	3.63	0.26	
2007 Frequencies					
f_1	1.517(2)	8.98(57)	3.72	2.42	
f_2	1.579(2)	9.23(57)	3.88	2.38	
f_3	1.657(3)	7.24(57)	3.05	2.38	
f_4	6.809(4)	4.23(57)	6.04	0.70	
2008 Frequencies					
f_1	2.030(1)	9.41(38)	4.38	2.15	
f_2	2.116(2)	7.82(38	3.62	2.16	
f_3	6.811(3)	4.11(38)	6.48	0.63	
2010 Frequencies					
f_1	2.100(2)	7.84(44)	3.79	2.07	
f_2	2.184(2)	5.97(44)	3.15	1.90	
f_3	6.813(3)	4.63(44)	6.01	0.79	

of the rotational frequency in the periodogram (vertical dotted lines).

In addition, the pulsation constant of the δ Scuti type frequency at 6.81 cd^{-1} was calculated to be around 0.036(1) days (Table 7.11), which was significantly higher than the values given by Bossi et al. (1983) (Q = 0.027 days) and Lopez de Coca et al. (1990) (Q = 0.023 days). However, it was quite close to the Q constant suggested by Breger (1979) for the fundamental mode, and fell in the Q_0 interval ($0.032 \leq Q_0$ (days) ≤ 0.036) of the model developed by Fitch (1981). We therefore considered that 6.81 cd^{-1} might be the fundamental mode of HD 28024. Since there was no other significant variation in the amplitude spectrum, we did not estimate overtones of the fundamental mode.

To track down frequency and amplitude variations in the seasonal LCs, δ Scuti type modulation regularly existing in each year was examined. However, neither the frequency itself nor its amplitude showed any change over three years. Further, two frequency values previously published by Lopez de Coca et al. (1990) and Bossi et al. (1983) were added to *STEREO* frequencies, and variation taking place since the 1980s was investigated. Unfortunately, we were unable to make a comparison and calculate a variation ratio for these frequencies, since the error value given by Bossi et al. (1983) was quite large (σ = 0.08 cd^{-1}), and Lopez de Coca et al. (1990) did not provide an error value for their finding.

7.4.4 HD 30780 (97 Tau; V480 Tau; HIP 22565; HR 1547)

V480 Tau (A7IV/V, $V = 5.09$ mag) is a fast rotating δ Scuti star with the rotational velocity of $Vsini = 180$ km s^{-1} (Royer et al., 2007), and is also a member of the Hyades cluster. It is one of the rare samples that has not been well studied, either photometrically or spectroscopically.

To investigate NRPs in the star, Cao et al. (1998) obtained 740 high-resolution spectra during the MUSICOS project and detected the presence of some moving features in MgII line profile. They determined the frequencies of these variations to be around 16, 29.5, and 39 cd^{-1}. As a continuation of this study, Di Mauro et al. (2002) managed to identify 16 modes between 8 and 30 cd^{-1} using data derived from the MUSICOS campaign, but none of them was published.

Table 7.12: Details of the annual observations.

Time (year)	**Observation Points**	**Observation Duration (day)**	**Observation Duration (hour)**	f_{Nyq} **(cd^{-1})**
2007	639	$\sim$ 19	$\sim$ 461	17.9988
2008	688	$\sim$ 19	$\sim$ 461	18.0009
2010	683	$\sim$ 19	$\sim$ 461	17.9929
2011	556	$\sim$ 16	$\sim$ 387	18.0001
Combined	2566	$\sim$ 74	$\sim$ 1769	17.9988

In our detailed investigation, a total of 2,566 observation points, corresponding to around 1,769 hours of data, were collected during 74 days over four years. The characteristics of the seasonal LCs that constituted the entire set of data are given in Table 7.12. The frequency analysis of the combined time series showed that 97 Tau was a multi-periodic δ Scuti star having at least 40 significant peaks in the amplitude spectrum (Fig. 7.5 and Table 7.14). These frequencies were determined based on the specific significance level, which was calculated from regional noise levels of the periodogram. The significance and noise levels are displayed with red dashed and red dash-dot lines in Fig. 7.5, respectively. This result was a significant discovery in gaining better understanding of the star's interior structure.

Of these 40 frequencies, only four peaks were low frequencies, appearing at 1.0494, 1.3760, 3.0535, and 3.9850 cd^{-1}. According to the relation between period and rotational velocity, given in the Eqn. 1.10, it was revealed that the rotational period of 97 Tau was around 1.35(6) cd^{-1}, which was consistent with f_{16}. In this equation, the radius of the star was calculated to be 2.64(11) R$_\odot$ with the help of the parameters: $logT = 3.886(3)$ and $log(L/\mathrm{L}_\odot) = 1.34(4)$ (Zorec and Royer, 2012). The rotational velocity was also adopted from Royer et al. (2007) ($Vsini =$ 180 km s^{-1}). The δ Scuti type variations were spread between 8 and 18 cd^{-1} in the amplitude

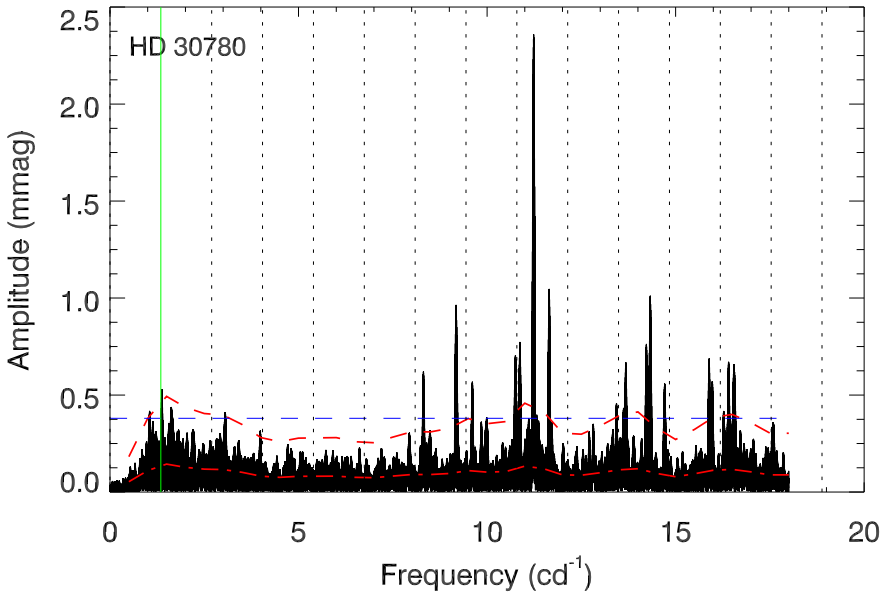

Figure 7.5: The amplitude spectrum of HD 30780 obtained from four-year combined LC. The noise and the significance levels are plotted with red dash-dot and red dashed lines, respectively. For a comparison, the significance level computed from a mean noise level is also presented by a blue dashed line. The rotational period estimated from the rotation velocity of the star is around 1.35(6) cd^{-1} and shown with a vertical green line. The black vertical dotted lines are integer multiples of the rotation period.

spectrum. Unlike Di Mauro et al. (2002), 36 significant peaks were detected within this region. However, the reliability of 16 frequencies, which are marked with asterisk symbols in Table 7.14, was questionable. Although their intensities were greater than the specific significance level, their SNR values were not in agreement with those in Period04, which provided much higher SNR for these frequencies. These were therefore included in our frequency list.

Photometric evidence for regular frequency spacings observed in spectroscopic data was also sought. The Rayleigh frequency of the whole data set (between HJD2454227 and HJD2455620) was computed as around 0.001 cd^{-1}. This meant that any spacing pattern down to 0.001 cd^{-1} could be detectable. For this reason, the differences of all frequencies between 4 and 18 cd^{-1} were calculated, and analysed with the KS test (Appendix B; on page 314). Nine possible spacing patterns with a probability greater than $p = 0.05$ (significance level of 95%) were consequently found, and are presented in Table 7.13. Additionally, some of the irregular small separations in the periodogram were: $\sim$ 0.01 cd^{-1} (16.54-16.55 cd^{-1}, 14.71-14.72 cd^{-1}, 14.22-14.23 cd^{-1}), $\sim$ 0.06 cd^{-1} (13.62-13.68 cd^{-1}, 16.48-16.54 cd^{-1}, 16.55-16.61 cd^{-1}), $\sim$ 0.07 cd^{-1} (16.41-16.48

Table 7.13: The possible spacing patterns in the periodogram of HD 30780.

$\Delta\nu$ ($\mathbf{cd^{-1}}$)	**Prob.**
0.118	0.4
0.133	0.5
0.606	0.4
0.776	0.4
1.670	0.1
1.861	0.2
2.252	0.3
2.389	0.3
2.857	0.2

cd^{-1}, 16.48-16.55 cd^{-1}, 16.54-16.61 cd^{-1}) and ~ 0.08 cd^{-1} (15.89-15.97 cd^{-1}, 13.54-13.62 cd^{-1}).

Further, the pulsation constants of all frequencies were computed to clarify the relation between the frequencies (Table 7.14). According to the calculations, Q values of the δ Scuti type frequencies were in the range of 0.02 and 0.05 days. There were five frequencies (f_1, f_2, f_{18}, f_{33}, and f_{40}) having Q values between 0.032 and 0.036 days, described by Fitch (1981) for the fundamental mode. Among these values, f_{18}, f_{33}, and f_{40} were most probably combination frequencies. Therefore, we assumed that the main frequency was the radial fundamental mode of the star. Based on this assumption, the first overtone was derived as 14.76 cd^{-1} from the period ratio of $P_1/P_0 = 0.761$. This value was consistent with f_{13}, whose Q constant perfectly matched with the estimation of Breger (1979) for the first overtone. Since the second and third estimated overtones (18.23 and 21.44 cd^{-1}) fell beyond the Nyquist frequency, they could not be compared with our results.

Apart from these, seasonal frequency and amplitude variations between 2007 and 2011 were studied. It was noticed that nine frequencies regularly appeared in the individual amplitude spectra. As seen in Fig. C.9 (on page 326), the frequencies at 9.18, 10.74, 10.86, 11.65, 13.67, 14.22, and 14.33 cd^{-1} showed variations over four years. The most conspicuous variability was seen at the frequency of 9.18 cd^{-1}. It could be represented by a parabola having a period increase of $dP/Pdt = 1.22(5) \times 10^{-3}$ yr^{-1} between 2007 - 2009, and a decrease of about $-1.27(7) \times 10^{-3}$ yr^{-1} from 2009 to 2011. The entire variation could also be given as $-1.10(90) \times 10^{-4}$ yr^{-1}. In contrast to these variations, the frequency at 10.86 cd^{-1} displayed an inverse parabolic structure whose period change was found to be $9.54(1.49) \times 10^{-5}$ yr^{-1}. Moreover, compared to other frequencies, a unique increase in period was seen at 14.22 cd^{-1}.

Table 7.14: Frequencies derived from the combined data of HD 30780.

HD 30780 Frequencies						
No	**Freq. (cd^{-1})**	**Amp. (mmag)**	**SNR**	A_m **(mmag)**	Q **(days)**	**Comments**
f_1	11.23570(1)	2.46(7)	18.93	0.13	0.036(1)	
f_2	11.64753(2)	1.09(7)	9.65	0.11	0.035(1)	
f_3	14.32860(2)	1.07(7)	10.06	0.11	0.028(1)	
f_4	9.17809(3)	1.04(7)	10.68	0.10	0.044(2)	
f_5	10.87120(4)	0.70(7)	5.39	0.13	0.037(2)	
f_6	10.74708(4)	0.73(7)	6.06	0.12	0.038(2)	
f_7	14.22174(4)	0.72(7)	6.74	0.10	0.028(1)	
f_8	16.55026(4)	0.74(7)	6.34	0.12	0.024(1)	$2f_4 + 2f_6 - 2f_2$
f_9	15.88994(4)	0.67(7)	6.40	0.11	0.025(1)	$f_3 + f_6 - f_4$
f_{10}	13.68192(4)	0.68(7)	5.81	0.12	0.030(1)	
f_{11}	8.31191(4)	0.70(7)	7.26	0.10	0.049(2)	$f_{10} + 2f_2 - 2f_3$
f_{12}	16.40659(4)	0.65(7)	5.56	0.12	0.025(1)	$2f_{11} + 2f_7 - 2f_3$
f_{13}	14.70720(4)	0.61(7)	6.73	0.09	0.028(1)	$f_1 + f_7 - f_6$
f_{14}	15.97190(5)	0.53(7)	4.83	0.11	0.025(1)	$f_{12} + f_4 - f_{15}$
f_{15}	9.60905(5)	0.56(7)	5.02	0.11	0.042(2)	$2f_2 - f_{10}$
f_{16}	1.37597(5)	0.52(7)	3.69	0.14		
f_{17}	13.43368(6)	0.47(7)	4.20	0.11	0.030(1)	$f_3 + f_6 - f_2$
$^*f_{18}$	11.34884(6)	0.43(7)	3.53	0.12	0.036(1)	$f_1 + f_3 - f_7$
$^*f_{19}$	16.27554(6)	0.44(7)	3.79	0.12	0.025(1)	$f_1 + f_7 - f_4$
f_{20}	3.05350(6)	0.43(7)	3.72	0.12		$f_{10} + 2f_1 - 2f_8$
$^*f_{21}$	10.84859(6)	0.43(7)	3.36	0.13	0.037(2)	$f_1 + f_3 - f_{13}$
f_{22}	9.98532(7)	0.37(7)	3.58	0.10	0.041(2)	$f_1 + f_{15} - f_{21}$
f_{23}	1.04944(7)	0.40(7)	3.42	0.12		
$^*f_{24}$	13.62149(7)	0.39(7)	3.37	0.11	0.030(1)	$f_{11} + f_8 - f_1$
$^*f_{25}$	8.49729(7)	0.39(7)	4.30	0.09	0.048(2)	$2f_{12} - f_{22} - f_3$
f_{26}	17.56335(6)	0.44(7)	4.93	0.09	0.023(1)	$f_2 + f_7 - f_{11}$
f_{27}	17.59432(6)	0.40(7)	4.54	0.09	0.023(1)	$f_1 + f_{16} - f_{15}$
$^*f_{28}$	14.22795(7)	0.38(7)	6.71	0.11	0.028(1)	$f_3 + f_6 - f_{21}$
f_{29}	3.98787(8)	0.35(7)	4.18	0.08		$f_1 + f_4 - f_{12}$
$^*f_{30}$	9.85600(8)	0.34(7)	3.29	0.10	0.041(2)	$2f_2 - f_{17}$
$^*f_{31}$	16.53921(7)	0.36(7)	3.18	0.11	0.024(1)	$f_{18} + f_4 - f_{29}$
$^*f_{32}$	13.54291(8)	0.33(7)	2.95	0.11	0.030(1)	$f_{17} + f_{18} - f_1$
f_{33}	12.81265(9)	0.30(7)	3.24	0.09	0.032(1)	$f_{10} + f_{11} - f_4$
$^*f_{34}$	13.88900(8)	0.31(7)	2.60	0.12	0.029(1)	$f_3 + f_4 - f_{15}$
$^*f_{35}$	16.48259(8)	0.32(7)	2.77	0.11	0.025(1)	$f_{12} + f_{16} - f_9$
$^*f_{36}$	14.72296(9)	0.31(7)	3.41	0.09	0.027(1)	$f_1 + f_3 - f_{21}$
$^*f_{37}$	16.71486(8)	0.32(7)	2.89	0.11	0.024(1)	$f_{26} + f_3 - f_1$
$^*f_{38}$	16.58432(8)	0.32(7)	2.86	0.11	0.024(1)	$f_3 + f_6 - f_{26}$
$^*f_{39}$	7.93733(9)	0.28(7)	3.20	0.09	0.051(2)	$f_{11} + f_5 - f_1$
$^*f_{40}$	12.70970(9)	0.28(7)	3.15	0.09	0.032(1)	$f_{37} - f_{29}$

We found its variation ratio as around $dP/Pdt = 4.89(1.76) \times 10^{-4}$ yr^{-1}. Also, 11.65 and 14.33 cd^{-1} had sinusoidal periodicities. On the other hand, amplitudes of these nine frequencies were mostly stable, except the amplitude of the frequency at 14.22 cd^{-1} (Fig. C.10; on page 327). It showed the most intense variation by decreasing from 1.3 mmag to 0.5 mmag between 2007 and 2010. In contrast, the amplitude intensity of 11.65 cd^{-1} increased from 1.0 to 1.3 mmag over time.

Finally, we investigated long-term frequency variations by collecting all available data from the literature (Fig. C.11; on page 328). However, as previously discussed, neither the frequencies taken from Cao et al. (1998) nor the one given by Breger (Cao et al., 1998) were compatible with our results. Therefore, we could not make a comparison with literature's data.

Table 7.15: Frequencies derived from the individual data of HD 30780.

No	Freq. (cd^{-1})	Amp. (mmag)	SNR	A_m (mmag)	Comments
2007 Frequencies					
f_1	11.234(2)	2.60(14)	11.90	0.22	
f_2	14.229(4)	1.23(14)	6.58	0.19	
f_3	10.859(4)	1.06(14)	4.80	0.22	
f_4	14.329(4)	1.16(14)	6.25	0.19	
f_5	11.650(4)	1.07(14)	5.27	0.20	$2f_1 - f_3$
f_6	14.713(4)	1.00(14)	6.67	0.15	$f_2 + f_5 - f_1$
f_7	9.183(4)	1.01(14)	5.37	0.19	$f_4 + 2f_5 - 2f_2$
f_8	16.404(5)	0.88(14)	4.28	0.21	$f_1 + f_4 - f_7$
f_9	15.970(6)	0.81(14)	4.21	0.19	$f_3 + f_8 - f_1$
f_{10}	1.381(6)	0.79(14)	3.22	0.25	$f_6 + f_7 - 2f_1$
f_{11}	9.983(6)	0.73(14)	4.02	0.18	$f_1 + f_6 - f_9$
f_{12}	13.677(6)	0.76(14)	3.48	0.22	$f_1 + f_5 - f_7$
f_{13}	10.747(6)	0.71(14)	3.27	0.22	$2f_1 - f_5$
f_{14}	1.048(6)	0.74(14)	3.60	0.20	$f_6 - f_{12}$
f_{15}	16.525(6)	0.71(14)	3.51	0.20	$f_1 + f_9 - f_{13}$
f_{16}	16.283(7)	0.67(14)	3.34	0.20	$f_1 + f_2 - f_7$
f_{17}	8.312(7)	0.60(14)	3.36	0.18	$2f_1 - f_2$
f_{18}	17.626(9)	0.48(14)	3.70	0.13	$f_{14} - f_{15}$
2008 Frequencies					
f_1	11.232(2)	2.42(13)	12.31	0.20	
f_2	10.870(3)	1.07(13)	5.63	0.19	
f_3	9.175(4)	0.99(13)	5.97	0.17	
f_4	14.324(4)	0.99(13)	6.00	0.16	$3f_2 - 2f_3$
f_5	14.220(4)	0.83(13)	4.88	0.17	$3f_2 - 2f_3$
f_6	11.652(4)	0.83(13)	4.80	0.17	$2f_1 - f_2$
f_7	10.743(5)	0.76(13)	4.12	0.18	$2f_1 - f_6$
f_8	8.315(6)	0.66(13)	4.28	0.15	$2f_1 - f_5$
f_9	15.893(6)	0.63(13)	3.74	0.17	$f_2 + f_5 - f_3$
f_{10}	17.578(6)	0.59(13)	3.60	0.16	$2f_5 - f_2$
f_{11}	12.827(7)	0.55(13)	3.56	0.16	$f_1 + f_7 - f_3$
f_{12}	13.418(6)	0.59(13)	3.36	0.17	$f_2 + f_6 - f_3$
2010 Frequencies					
f_1	11.233(2)	2.49(14)	11.99	0.21	
f_2	9.176(3)	1.27(14)	7.50	0.17	
f_3	11.645(3)	1.23(14)	6.56	0.19	
f_4	14.334(4)	1.03(14)	6.05	0.17	
f_5	16.552(4)	1.10(14)	5.67	0.19	$f_1 + 2f_4 - 2f_3$
f_6	16.415(4)	0.92(14)	4.92	0.19	$f_1 + f_4 - f_2$
f_7	15.888(5)	0.90(14)	4.61	0.19	$3f_2 - f_3$
f_8	8.313(5)	0.81(14)	4.95	0.16	$f_4 + f_6 - 2f_1$
f_9	10.750(5)	0.80(14)	3.86	0.21	$2f_1 - f_3$
f_{10}	13.684(5)	0.79(14)	3.64	0.22	$f_1 + f_3 - f_2$
f_{11}	9.606(6)	0.70(14)	3.78	0.18	$f_2 + f_3 - f_1$
f_{12}	16.271(6)	0.68(14)	3.58	0.19	$f_3 + f_7 - f_1$
f_{13}	3.054(6)	0.65(14)	3.28	0.20	$f_4 - f_1$
f_{14}	1.044(7)	0.58(14)	3.02	0.19	$f_{13} + f_2 - f_1$
f_{15}	14.211(7)	0.57(14)	3.20	0.18	$f_1 + f_{13}$
2011 Frequencies					
f_1	11.233(2)	2.34(15)	10.31	0.23	
f_2	11.646(4)	1.27(15)	6.31	0.20	
f_3	14.331(5)	1.10(15)	7.04	0.16	
f_4	16.547(5)	1.07(15)	5.80	0.19	$f_1 + 2f_3 - 2f_2$
f_5	10.857(6)	0.96(15)	4.20	0.23	$2f_1 - f_2$
f_6	13.661(7)	0.86(15)	4.42	0.19	$f_3 + 2f_5 - 2f_1$
f_7	9.189(7)	0.82(15)	4.31	0.19	$f_1 + f_2 - f_6$
f_8	9.601(8)	0.73(15)	3.68	0.20	$f_2 + f_7 - f_1$
f_9	1.367(8)	0.73(15)	3.14	0.23	
f_{10}	17.574(7)	0.75(15)	5.28	0.14	$f_2 + 2f_1 - f_4$
f_{11}	10.734(7)	0.76(15)	3.71	0.21	$f_{15} + f_8$
f_{12}	1.149(8)	0.70(15)	3.27	0.21	
f_{13}	14.698(9)	0.62(15)	3.53	0.17	$f_2 + f_3 - f_1$

7.4.5 HD 90386 (RX Sex; HIP 51075)

RX Sex (A2V, $V = 6.66$ mag) is another rarely studied δ Scuti sample. Variability of the star was accidentally discovered by Jerzykiewicz (1972) while it was being used as a comparison star for 23 Sex. He detected short-term variations with the period of 0.0799 days ($A \sim 0.01$ mag), and reported that their origins were due to either a beating phenomenon or a non-periodic variation in LC.

In the most comprehensive investigation regarding its interior structure, we derived 2,673 data points, corresponding to 1,809 hours of observation taken between 2007 and 2011. Compared to the other δ Scuti samples, this star was particularly important since it was successfully tracked by the satellite for 76 days out of an 80-day observation duration over four years. The details of the seasonal and combined LCs are presented in Table 7.16.

Table 7.16: Details of the annual observations.

Time (year)	**Observation Points**	**Observation Duration (day)**	**Observation Duration (hour)**	f_{Nyq} **(cd^{-1})**
2007	684	$\sim$ 19	$\sim$ 457	17.9997
2008	678	$\sim$ 19	$\sim$ 458	18.0001
2010	651	$\sim$ 19	$\sim$ 447	17.9997
2011	660	$\sim$ 19	$\sim$ 447	17.9938
Combined	2673	$\sim$ 76	$\sim$ 1809	17.9999

The frequency analysis of the combined data set showed that there were six frequencies having amplitude greater than the specific significance level in the amplitude spectrum (Table 7.17). As seen in Fig. 7.6, four of these peaks were located in the high-frequency region. Among them, the most dominant frequency was found at around 10.25 cd^{-1} with the amplitude of 1.92 mmag. Also, the second powerful frequency showed up at 12.40 cd^{-1} (0.0806 days) in our amplitude spectrum. This value was quite close to the main frequency (0.0799 days) obtained by Jerzykiewicz (1972). Based on the inconsistencies among the results, it might be suggested that the star gradually switched pulsation modes from 12.50 to 10.25 cd^{-1} over time. Furthermore, the intensity of the 12.40 cd^{-1} in the seasonal LCs seemed to decrease between 2007 and 2011. As a result of this, its amplitude observed in 2010 and 2011 fell below the significance level (Fig. C.12; on page 329). However, their SNR values determined from Period04 were over 4.00, and they were hence included in the analyses.

As seen in Fig. C.12 (on page 329), all seasonal LCs exhibited variabilities around the region of 1.00 cd^{-1}. Since there was not a sufficient number of studies on the physical, chemical, or

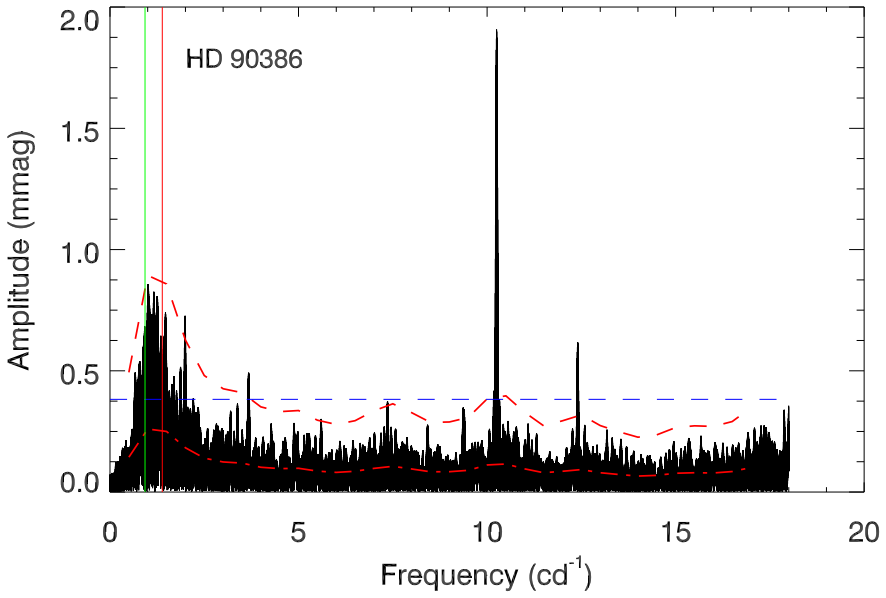

Figure 7.6: The amplitude spectrum of HD 90386 obtained from four-year combined LC. The noise and the significance levels are plotted with red dash-dot and red dashed lines, respectively. For a comparison, the significance level computed from a mean noise level is also presented by a blue dashed line. The rotational periods that are estimated based on rotation velocities of 134 and 200 km s^{-1} are shown with a green line at 0.93(7) cd^{-1} and a red line at 1.39(11) cd^{-1}, respectively.

orbital parameters of the star, interpretation of these variations might not be possible. However, Niemczura et al. (2015) demonstrated that the projected rotational velocities of typical A and F stars ranged from 8 to about 280 km s^{-1}, with a mean of 134 km s^{-1} in the analysis of high-resolution spectroscopic data of A- and F-type stars from the Kepler field, which were obtained with the HERMES spectrograph. Moreover, they found that the maximum of the velocity distribution for A and F stars having an effective temperature between 8,000 and 9,000 K was around 200 km s^{-1}. Since HD 90386 was an A2-type star with an estimated temperature of 8,200 K, its rotational period might be between 0.93(7) and 1.39(11) cd^{-1} for the rotational velocities of 134 and 200 km s^{-1}, respectively. These values were considerably compatible with the frequency accumulation at around 1.00 cd^{-1}, shown between green and red vertical lines in Fig. 7.6.

We also computed the pulsation constants of the δ Scuti type frequencies in the periodogram (Table 7.17). Consequently, Q values of f_1 and f_6 were around 0.031(6) and 0.034(6) days, which were within the theoretical range for the fundamental mode given by Fitch (1981). If the main

Table 7.17: Frequencies derived from the combined and individual data of HD 90386.

HD 90386 Frequencies					
No	**Freq. (cd^{-1})**	**Amp. (mmag)**	**SNR**	A_m **(mmag)**	Q **(days)**
f_1	10.25258(2)	1.92(10)	16.88	0.11	0.031(6)
f_2	1.99122(5)	0.74(10)	4.00	0.19	
f_3	12.40076(6)	0.61(10)	6.76	0.09	0.026(5)
f_4	3.67474(8)	0.50(10)	4.24	0.12	
f_5	7.36338(11)	0.36(10)	3.43	0.10	0.043(8)
f_6	9.36921(11)	0.34(10)	3.92	0.09	0.034(6)
2007 Frequencies					
f_1	10.255(2)	1.94(16)	9.18	0.21	
f_2	12.397(6)	0.77(16)	3.58	0.21	
f_3	9.371(8)	0.59(16)	3.74	0.16	
2008 Frequencies					
f_1	10.254(3)	1.98(17)	8.17	0.24	
f_2	12.413(8)	0.65(17)	3.59	0.18	
2010 Frequencies					
f_1	10.250(3)	1.94(20)	8.34	0.23	
f_2	12.399(1)	0.55(20)	2.93	0.19	
2011 Frequencies					
f_1	10.253(4)	1.77(22)	7.15	0.25	
f_2	3.666(10)	0.69(22)	3.21	0.21	
f_3	12.402(12)	0.55(22)	3.06	0.18	

frequency was the fundamental mode, its first overtone would be around 13.47 cd^{-1}, which was not observed in our amplitude spectrum. In contrast, if 9.37 cd^{-1} was assumed to be the fundamental mode, the first overtone was found as 12.31 cd^{-1} based on the period ratio $P_1/P_0 = 0.761$. This value slightly matched with f_3, and its Q constant was also within the theoretical range given for the first overtone.

Additionally, annual frequency and amplitude variations were investigated to gain better understanding of the short-term pulsation behaviour of RX Sex. To do this, we determined consistently observed frequencies in seasonal LCs (Fig. C.13; on page 330) and surmised that only two frequencies potentially varied. However, all variations were within the error limits, and no significant frequency or amplitude changes were found for both peaks over four years. On the other hand, combining the frequency value (12.5156 cd^{-1}) given by Jerzykiewicz (1972) with our *STEREO* result, a long-term period variation of $2.49(22) \times 10^{-4}$ yr^{-1} was calculated for the frequency at around 12.40 cd^{-1}. It should also be noted that if there was a gradual change between the frequencies (from 12.50 to 10.25 cd^{-1}), the variation rate of the period was obtained as $dP/Pdt = 5.39(2) \times 10^{-3}$ yr^{-1} over 35 years.

7.4.6 HD 106384 (FG Vir; HIP 59676)

FG Vir (A5, $V = 6.56$ mag) is a well-known bright δ Scuti star whose multi-periodicity has been extensively investigated in numerous photometric and spectroscopic campaigns over 40 years (Table 7.23). Its variability was first detected by Eggen (1971), who found a variability period of 0.07 days (14.28 cd^{-1}, $A = 25$ mmag). Carrying out a multi-colour photometry, Lopez de Coca et al. (1984) confirmed this light variation and determined a period of about 0.079 days (12.66 cd^{-1}).

Bossi et al. (1993) showed that there was a dominant mode at 12.7 cd^{-1} ($A = 42.2$ mmag) with six other modes between 8 and 25 cd^{-1} (2.8 mmag $< A <$ 4.8 mmag) in LC of HD 106384. They also noted that the peaks at 9.7, 12.2, 19.9, and 24.2 cd^{-1} were independent from aliasing. Mantegazza et al. (1994) justified this finding by obtaining seven pulsation modes (8.20, 9.66, 12.16, 12.70, 19.86, 21.05, and 24.22 cd^{-1}). They reported that there might be another frequency at around 24.41 cd^{-1}, and also that 12.7 cd^{-1} was the main frequency and the first radial overtone. Subsequently, Breger et al. (1995) acquired 170 hours of data. Apart from the seven conclusive frequencies, they determined three additional modes between 9.19 and 34.12 cd^{-1} (0.8 mmag $< A <$ 22 mmag).

Breger et al. (1998) derived 435 hours of observation after the largest multi-site campaign, and managed to detect 24 peaks. Unlike other studies, they discovered that the pulsation mode at 23.40 cd^{-1} and its amplitude were variable. Relaxing the SNR up to 3.5, they derived nine frequency harmonics and combinations. Further, Breger et al. (2004) carried out another multi-site campaign covering 398 hours and determined six new frequencies. They found that amplitudes and phases of 12.15 and 23.4 cd^{-1} varied year by year. They referred to this phenomenon as the Blazhko effect (Blažko, 1907), and suggested two possibilities as a cause of its origin: two modes beating at close frequencies or a single mode varying in both amplitude and frequency.

To understand amplitude and frequency variations, Breger and Pamyatnykh (2006) examined all available data in the literature. As reported by Breger et al. (2004), they detected two strongly variable frequencies at around 12.15 and 23.40 cd^{-1} as well as the third one at 19.86 cd^{-1}. The results of individual analyses revealed that the frequency at 12.15 cd^{-1} had a beat period of 128 days and that phase variations were coupled to the amplitude changes, which indicated two separate close frequencies beating with each other. Similarly, it was concluded

that the frequency at 23.40 cd^{-1} also consisted of two beating close frequencies, and there might be an additional third component dependent on these frequencies. Unlike 12.15 and 23.40 cd^{-1}, the origin of the last mode at about 19.86 cd^{-1} was not clarified due to a long beating period (> 20 years).

The biggest achievement regarding mode detection was made by Breger et al. (2005) through obtaining 926 hours of observation. They were able to obtain a magnificent frequency resolution and an SNR by combining new data with the earlier projects. In doing so, they detected at least 79 frequencies between 5 and 45 cd^{-1} ($A > 0.2$ mmag) in the amplitude spectrum. Of these, 67 frequencies were determined to be independent pulsation modes.

Table 7.18: Details of the annual observations.

Time (year)	**Observation Points**	**Observation Duration (day)**	**Observation Duration (hour)**	f_{Nyq} **(cd^{-1})**
2007	685	~ 19	~ 459	18.0009
2008	666	~ 19	~ 459	18.0009
2010	679	~ 19	~ 459	17.9956
2011	662	~ 19	~ 459	17.9965
Combined	2692	~ 76	~ 1837	17.9998

In our study, we carried out a photometric investigation of FG Vir using LCs observed between 2007 and 2011. In this four-year time period, 2,692 measurements corresponding to a photometric coverage of 1,837 hours in 76 days were obtained. The properties of the seasonal and combined LCs were given in Table 7.18. As a result of multi-frequency analysis of the combined data, we detected at least 17 frequencies hidden in the time series (Fig. 7.7 and Table 7.19). These frequencies were determined based on a specific significance level calculated from the regional noise level of the periodogram. The significance and noise levels are presented in Fig. 7.7 with red dashed and dash-dot lines, respectively. A significance level, which was calculated from a mean noise level, is also plotted in the same figure with a blue dashed line for comparison.

As seen in Fig. 7.7, the combined LC exhibited variabilities in the low-frequency region. Even though these peaks remained under the significance level, they were attributed to stellar rotation since the relation between period and rotational velocity (Eqn. 1.10) provided a rotational period of around 0.57(3) cd^{-1}. In the Eqn. 1.10, $V_{rot} = 66(16)$ $km\,s^{-1}$ was taken from Zima et al. (2006), and $R = 2.28$ $R_\odot$ was derived from $logT = 3.875(6)$ (Breger et al., 1999b) and $log(L/L_\odot) = 1.170(55)$ (Breger and Pamyatnykh, 2006). This rotational period was not

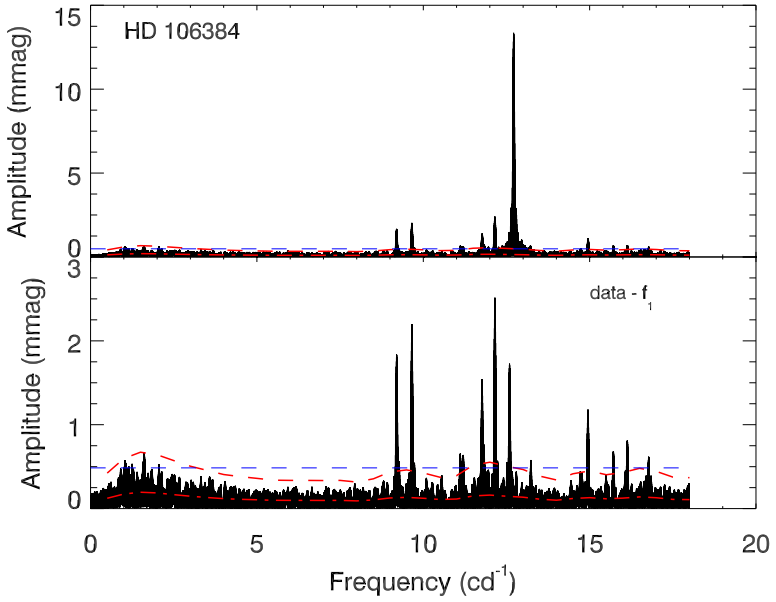

Figure 7.7: The amplitude spectrum of HD 106384 obtained from four-year combined LC. While the top panel shows all frequencies derived from the entire data set, the bottom panel displays peaks after pre-whitening the main frequency at 12.7162 cd^{-1}. The noise and the significance levels are plotted with red dash-dot and red dashed lines, respectively. For a comparison, the significance level computed from a mean noise level is also presented by a blue dashed line. The rotational period estimated from the rotation velocity of the star is around 0.57(3) cd^{-1}, but not observed in the spectrum.

observed in our periodogram, but was considerably compatible with the period of 0.57(14) cd^{-1} calculated by Zima et al. (2006).

Further, all of the 17 frequencies detected were between 9 and 18 cd^{-1} in our amplitude spectrum (f_{Nyq} = 17.9998 cd^{-1}), although Breger et al. (2005) had 20 peaks in the same frequency interval. In this context, it should be noted that we detected 12 more frequencies in this region with Period04, but their amplitudes were not higher than our significance level. These additional frequencies are presented in the sub-section of Table 7.19. Moreover, Breger et al. (2005) mentioned the existence of three additional peaks at 5.75, 7.99, and 8.34 cd^{-1}, which were not seen in our analysis. The most dominant frequency was around 12.7162 cd^{-1} and was quite consistent with the archival results. We also determined that all frequencies were accumulated within three different frequency regions: $9-10$ cd^{-1}, $11-13.5$ cd^{-1}, and $15-17$ cd^{-1}.

Photometric evidence for regular frequency spacings observed in other studies was also stud-

Table 7.19: Frequencies derived from the combined data of HD 106384.

HD 106384 Frequencies						
No	**Freq. (cd^{-1})**	**Amp. (mmag)**	**SNR**	A_m **(mmag)**	Q **(days)**	**Comments**
f_1	12.716218(3)	13.62(9)	60.94	0.22	0.031(4)	
f_2	12.15411(1)	2.59(9)	15.56	0.17	0.032(4)	
f_3	9.65627(2)	2.21(9)	16.32	0.14	0.040(5)	
f_4	9.19911(2)	1.86(9)	13.72	0.14	0.042(5)	
f_5	12.59376(2)	1.75(9)	12.24	0.14	0.031(4)	
f_6	11.76625(2)	1.74(9)	11.22	0.16	0.033(4)	
f_7	14.95133(3)	1.24(9)	9.68	0.13	0.026(3)	
f_8	11.80610(4)	0.90(9)	5.81	0.15	0.033(4)	$f_1 + 2f_4 - 2f_3$
f_9	16.13215(4)	0.85(9)	6.67	0.13	0.024(3)	$f_6 + 2f_3 - f_7$
f_{10}	15.71220(5)	0.70(9)	5.45	0.13	0.025(3)	$f_1 + f_2 - f_4$
f_{11}	11.10914(6)	0.61(9)	5.34	0.11	0.035(4)	$3f_8 - 2f_2$
f_{12}	16.77215(6)	0.61(9)	4.66	0.13	0.023(3)	$f_7 + 2f_1 - 2f_8$
f_{13}	13.23356(7)	0.57(9)	4.80	0.12	0.030(3)	$f_{12} + f_5 - f_9$
f_{14}	11.20688(7)	0.56(9)	4.47	0.13	0.035(4)	$f_2 + f_6 - f_1$
f_{15}	14.76193(8)	0.46(9)	3.66	0.13	0.026(3)	$f_{10} + f_6 - f_1$
f_{16}	15.49461(9)	0.43(9)	3.67	0.12	0.025(3)	$f_2 + f_9 - f_1$
f_{17}	10.55296(9)	0.43(9)	3.95	0.11	0.037(4)	$f_{11} + f_2 - f_1$
f_{18}	12.78846(8)	0.43(9)				
f_{19}	14.71796(8)	0.43(9)				
f_{20}	16.07383(8)	0.43(9)				
f_{21}	11.66610(9)	0.40(9)				
f_{22}	11.80201(9)	0.42(9)				
f_{23}	12.16382(9)	0.39(9)				
f_{24}	11.9578(1)	0.35(9)				
f_{25}	10.0947(1)	0.33(9)				
f_{26}	10.2749(1)	0.30(9)				
f_{27}	11.5398(1)	0.30(9)				
f_{28}	10.4331(1)	0.29(9)				
f_{29}	11.6319(1)	0.29(9)				

ied. The Rayleigh frequency of the whole data set (between HJD2454332 and HJD2455729) was computed as around 0.001 cd^{-1}. This meant that any spacing pattern down to 0.001 cd^{-1} could be detectable. For this reason, the differences of all frequencies between 4 and 18 cd^{-1} were calculated, and analysed with the KS test (Appendix B; on page 314). Based on the test, seven possible spacing patterns with a probability greater than $p = 0.05$ (significance level of 95%) were found, and are presented in Table 7.20.

Apart from these, Breger and Pamyatnykh (2006) reported that there were several close frequencies in their data and some of them exhibited separation of less than 0.01 cd^{-1}. It was not possible to confirm such a finding by using our 17 frequencies. However, when the additional 12 frequencies were included, we derived two frequency pairs at around 11.80 (11.8020 and 11.8061 cd^{-1}) and 12.15 cd^{-1} (12.1541 and 12.1638 cd^{-1}) having spacings of 0.0041 cd^{-1} (244 days)

Table 7.20: The possible spacing patterns in the periodogram of HD 106384.

$\Delta\nu$ ($\mathbf{cd^{-1}}$)	**Prob.**
0.599	0.60
0.704	0.24
0.910	0.93
1.450	0.48
2.008	0.54
2.996	0.97
3.538	0.90

and 0.0097 cd^{-1} (103 days), respectively. Of these pairs, the latter frequency and the Blazhko effect on it are mainly discussed by Breger, who gave the spacing of this frequency (12.15412 and 12.16195 cd^{-1}) as around 0.0078 cd^{-1} (128 days). The discrepancy between our results and theirs may be due to either a decrease of 25 days in the beating period or observational uncertainties.

Subsequently, we calculated Q constants of δ Scuti type frequencies between 9 and 18 cd^{-1} in the periodogram. Accordingly, we obtained a pulsation constant of 0.031(4) days for the main frequency, which matched up with the theoretical Q_0 value given by both Breger (1979) and Fitch (1981) for the fundamental mode. This was also consistent with the results of Breger et al. (1999b) and Daszyńska-Daszkiewicz et al. (2005). If f_1 was assumed to be the fundamental mode, the first overtone was derived theoretically at 16.71 cd^{-1} using the period ratio of $P_1/P_0 = 0.761$. This value was quite close to our observational f_{12}, and its pulsation constant (= 0.023(3) days) was even within the Q_1 range provided by Fitch (1981) for the first overtone. Moreover, the theoretical second and third overtones were calculated to be 20.5 and 24.5 cd^{-1} with the help of period ratios $P_2/P_0 = 0.62$ and $P_3/P_0 = 0.52$. Although we could not observe higher frequencies than the *STEREO* Nyquist frequency, these results were compatible with f_{35} and f_{18} of Breger et al. (2005). On the contrary, Mantegazza et al. (1994) concluded that the main frequency was the first overtone. Based on this approach, the fundamental mode would be around 9.67 cd^{-1} ($P_1/P_0 = 0.761$). Indeed, this value was close to our f_3 frequency, but its Q constant (0.040(5) days) was far beyond the experimental Q_0 interval ($0.032 \leq Q \leq 0.036$). We therefore inferred that the main frequency might be the fundamental mode.

In order to investigate frequency and amplitude variations between 2007 and 2011, all individual amplitude spectra were compared to each other, and the most frequently observed

Table 7.21: Frequency variation table of HD 106384.

Frequency ($\mathbf{cd^{-1}}$)	dP/Pdt ($\mathbf{year^{-1}}$)
9.20	–1.14(44) $\times 10^{-5}$
9.66	–1.05(57) $\times 10^{-6}$
12.15	–4.09(1.89) $\times 10^{-7}$
12.715	–5.62(3.53) $\times 10^{-7}$
12.79	7.91(39) $\times 10^{-6}$
16.07	–4.11(69) $\times 10^{-6}$

frequencies were chosen for the analysis (Table 7.22). As seen in Fig. C.16 (on page 333), eight frequencies showed potential variations during the four-year time period. We found that six of these frequencies varied in time, whereas two were relatively constant. The significant changes were seen at 11.77 and 12.715 cd^{-1}. We observed that the frequencies at 11.77 cd^{-1} showed an inverse parabolic variation increasing between 2007-2008 and regularly decreasing after 2008. The ratios of these changes were found to be $-1.08(34) \times 10^{-3}$ and $8.88(4.88) \times 10^{-4}$ yr^{-1}, respectively. The variation at 12.715 cd^{-1} could most likely be represented by a *sine* function. Whereas it had a descending branch between 2007 and 2008, the variation changed direction around 2009, and the frequency increased from 12.714 cd^{-1} to 12.717 cd^{-1}. Apart from these, the frequencies at 9.20, 12.15, 12.59, and 14.95 cd^{-1} had moderate changes over four years.

Additionally, the frequencies at 11.77 and 12.15 cd^{-1} displayed the most intense amplitude variations (Fig. C.17; on page 334). The amplitude changes at 11.77 cd^{-1} were directly proportional to the changes in frequency, and could be fitted by an inverse parabola. However, change in the intensity of 12.15 cd^{-1} showed a periodic sinusoidal structure with a 0.6 mmag amplitude difference between maximum and minimum points, and with a peak-to-peak period of three years (from 2007 and 2010). As well as being a quite interesting variation, this beating phenomena had already been interpreted as the Blazhko effect by Breger et al. (2004). Furthermore, other frequency amplitudes did not seem to be variable except the ones at 9.66 and 12.59 cd^{-1}. Although the variation was within the error limits between 2007 and 2010, the amplitude of 9.66 cd^{-1} dramatically dropped off in 2011, and analogously the amplitude of 12.59 cd^{-1} decreased from 2.1 mmag to 1.5 mmag in 2008, having remained constant since then.

Following these analyses, we also examined long-term frequency variations by gathering all the data in the literature (Table 7.23) with our *STEREO* results, and found out that there were six frequencies regularly observed since 1980s (Fig. C.18; on page 335). Among them,

12.78 and 16.07 cd^{-1} were taken from the additional frequencies in Table 7.19. Since there were several results in the literature for each frequency value, we calculated period variations according to the best line-fit representing all values. We also used a frequency value (red crosses with error bars) derived from the combined data to represent annual *STEREO* results. As shown in Fig. C.18 (on page 335), the most remarkable period variation was seen at 12.79 cd^{-1} ($dP/Pdt = 7.92(39) \times 10^{-6}$ yr^{-1}). The rest of the frequencies and their variation rates are given in Table 7.21.

Table 7.22: Frequencies derived from the individual data of HD 106384.

No	**Freq. (cd^{-1})**	**Amp. (mmag)**	**SNR**	A_m **(mmag)**	**Comments**
2007 Frequencies					
f_1	12.7161(4)	13.66(18)	28.80	0.47	
f_2	12.156(2)	2.86(18)	9.17	0.31	
f_3	9.658(2)	2.36(18)	8.21	0.29	
f_4	12.591(2)	2.15(18)	7.49	0.29	
f_5	9.198(3)	1.94(18)	6.74	0.29	
f_6	11.765(3)	1.55(18)	5.03	0.31	
f_7	16.136(5)	1.11(18)	4.59	0.24	$f_1 + f_4 - f_5$
f_8	14.948(5)	1.12(18)	5.23	0.21	$3f_5 - f_1$
2008 Frequencies					
f_1	12.7154(4)	13.78(18)	29.32	0.47	
f_2	9.659(2)	2.25(18)	9.09	0.25	
f_3	12.154(2)	2.19(18)	8.04	0.27	
f_4	11.777(3)	1.94(18)	7.02	0.28	
f_5	9.200(3)	1.93(18)	7.99	0.24	$3f_1 - 3f_2$
f_6	12.597(3)	1.59(18)	5.98	0.27	$2f_3 - f_4$
f_7	14.947(5)	1.17(18)	5.02	0.23	$3f_5 - f_1$
f_8	16.137(6)	0.84(18)	3.73	0.23	$f_1 + f_6 - f_5$
f_9	16.771(7)	0.78(18)	3.55	0.22	$f_1 + f_8 - f_3$
f_{10}	15.717(7)	0.75(18)	3.72	0.20	$2f_1 - f_2$
2010 Frequencies					
f_1	12.7162(4)	13.65(19)	29.04	0.47	
f_2	12.150(2)	2.92(19)	8.95	0.33	
f_3	9.656(2)	2.34(19)	9.83	0.24	
f_4	9.197(3)	1.90(19)	8.25	0.23	$3f_1 - 3f_3$
f_5	11.768(0)	1.82(19)	5.99	0.30	$f_2 + f_4 - f_3$
f_6	12.585(3)	1.64(19)	6.49	0.25	$2f_2 - f_5$
f_7	14.954(4)	1.36(19)	6.15	0.22	$3f_4 - f_1$
f_8	11.810(1)	1.08(19)	3.49	0.31	$f_1 + 2f_4 - 2f_3$
f_9	16.130(7)	0.76(19)	3.07	0.25	$f_1 + f_6 - f_5$
f_{10}	14.734(7)	0.76(19)	3.86	0.20	$f_2 + f_5 - f_4$
f_{11}	11.113(7)	0.73(19)	3.55	0.21	$f_3 + f_9 - f_{10}$
2011 Frequencies					
f_1	12.7172(6)	13.40(24)	28.30	0.47	
f_2	12.150(3)	2.32(24)	6.37	0.36	
f_3	9.655(4)	1.87(24)	6.93	0.27	
f_4	9.205(4)	1.72(24)	6.57	0.26	$3f_1 - 3f_3$
f_5	12.597(5)	1.60(24)	4.70	0.34	$f_2 + f_3 - f_4$
f_6	14.950(6)	1.36(24)	4.02	0.34	$3f_4 - f_1$
f_7	11.759(6)	1.32(24)	3.63	0.36	$2f_2 - f_5$

Table 7.23: Archival frequencies of HD 106384.

Time (year)	Frequency (cycle per day)	Authors
2002	9.1990, 9.6560, 12.1540, 12.7160, 12.7940, 16.0710, 19.2280, 19.8680, 20.2880, 21.0520, 23.4030, 24.2280	Daszyńska-Daszkiewicz et al. (2005)
2002	9.1990, 9.6560, 12.1540, 12.7160, 12.7940, 16.0710, 19.2270, 19.8670, 20.2870, 20.8340, 21.0510, 23.4030, 24.2270, 25.4330, 33.5510	Zima et al. (2006)
2002-2004	5.7491, 7.9942, 8.3353, 9.1991, 9.6563, 10.1687, 10.6872, 11.1034, 11.2098, 11.5117, 11.6114, 11.7016, 11.8755, 11.9421, 12.1541, 12.1619, 12.2158, 12.7162, 12.7944, 13.2365, 14.7354, 16.0711, 16.0909, 19.1642, 19.2278, 19.3259, 19.6439, 19.8679, 19.8680, 20.2878, 20.2925, 20.5112, 20.8348, 21.0515, 21.2323, 21.4004, 21.5507, 22.3725, 23.0253, 23.3943, 23.3974, 23.4034, 23.4258, 23.4389, 23.8074, 24.0040, 24.1940, 24.2280, 24.3485, 24.8703, 25.1788, 25.3793, 25.4324, 25.6387, 26.5266, 26.8929, 26.9094, 28.1359, 29.4869, 30.9146, 31.1955, 31.9307, 32.1895, 33.0437, 33.7677, 34.1151, 34.1192, 34.1864, 34.3946, 34.5737, 35.8858, 36.1196, 36.9442, 39.2165, 39.5156, 42.1030, 42.1094, 43.0134, 43.9651, 44.2591	Breger et al. (2005)
2002	9.2000, 9.6600, 10.1700, 11.1000,12.1540, 12.1620, 12.7200, 16.0700, 19.2300, 19.8700, 20.2900, 20.5100, 21.0500, 21.2300, 23.3970, 23.4030, 24.1900, 24.2300, 24.3500, 24.8700, 25.4300, 34.1200, 34.5700	Breger et al. (2004)
1995	9.1990, 9.6560, 12.1540, 12.7160, 16.0740, 19.2280, 19.8680, 20.2880, 21.0520, 21.2320, 23.4030, 24.2000, 24.2280, 34.1190	Mantegazza and Poretti (2002)
1995	9.1990, 9.6560, 10.6870, 11.1100, 11.1950, 11.8700, 12.1540, 12.7160, 16.0740, 19.2280, 19.8680, 20.2880, 21.0520, 21.2320, 21.5510, 22.3720, 23.4030, 24.2000, 24.2280, 24.3540, 25.4320, 28.1400, 33.0560, 34.1190,	Breger et al. (1999b)
1995	12.7900, 18.1600, 19.6500, 20.8300, 25.1800, 25.3700, 29.5000, 31.9200	Breger et al. (1999b) (promising)
1996	9.1990, 9.6560, 12.1540, 12.7160, 19.8680, 21.0520, 23.4030, 24.2280	Viskum et al. (1998)
1995	9.1990, 9.6560, 10.6870, 11.1100, 11.1950, 11.8700, 12.1540, 12.7160, 16.0740, 19.2280, 19.8680, 20.2880, 21.0520, 21.2320, 21.5510, 22.3720, 23.4030, 24.2000, 24.2280, 24.3540, 25.4320, 28.1400, 33.0560, 34.1190	Stankov and Zima (1998)
1995	9.1990, 9.6560, 10.6870, 11.1100, 11.1950, 11.8700, 2.1540, 2.7160, 16.0740, 19.2280, 19.8680, 20.2880, 21.0520, 21.2320, 21.5510, 22.3720, 23.4030, 24.2000, 24.2280, 24.3540, 25.4320, 28.1400, 33.0560, 4.1190	Breger et al. (1998)
1995	12.7900, 18.1600, 19.6500, 20.8300, 25.1800, 25.3700, 29.5000, 31.9200	Breger et al. (1998) (promising)
1993	1.1550, 2.8490, 4.7820, 6.7700, 9.8650	Breger et al. (1996)
1985	9.1970, 9.6560, 12.1540, 12.7160, 19.8680, 20.2880, 21.0570, 23.4060, 24.2310	Dawson et al. (1995)
1993	9.1962, 9.6562, 12.1542, 12.7162, 19.8679, 20.2878, 21.0576, 23.4063, 24.2312, 34.1159	Breger et al. (1995)
1993	11.1900, 19.2300, 21.4800, 24.1900, 26.3300, 40.2900	Breger et al. (1995) (promising)
1992	8.2000, 9.6570, 12.1580, 12.7170 19.8600, 21.0500, 24.2200	Mantegazza et al. (1994)

7.5 Discussion

In this chapter, photometric data of a sample of δ Scuti stars were derived from the *HI-1A* instrument of the *STEREO* satellite. The data were collected between 2007 and 2011 for the purpose of investigating the internal structures and evolution stages of the selected stars. A total of 67 candidates were initially collected from the catalogue created by Lampens and Boffin (2000). Of these, six samples that met our selection criteria of brightness with $V \leq 10^m$, position within the FOV of the *STEREO*, clean variations in LC and amplitude spectrum, and being unaffected by the light of a neighbouring star were chosen for detailed analyses.

This group consisted of one F-type and five A-type δ Scuti variables (4.29 mag $< V <$ 6.66 mag). There were also four cluster members and three binary stars, which allowed the comparison of their amplitude spectra to field and single pulsators in the group. Additionally, we had samples exhibiting metal abundance, large and small amplitude variations, and samples pulsating with one or several modes at the same time among our δ Scuties. Although there was only a few candidates to study, it was a good chance to gain experience in almost all kind of δ Scuti pulsators because of the variety represented.

Four years of seasonal and combined LCs were examined with the help of the LS method, and the results were compared to those of Period04. For each periodogram, regional noise levels were determined by averaging the noise values in every 0.5 cd^{-1}, and a specific noise characteristic was thus established. Based on this characteristic, a significance level was calculated with 99% probability. Frequencies whose amplitudes were greater than this level were then detected. The detection precision in four-year combined data was around 10^{-5} cd^{-1} in frequency and 10^{-5} mag in amplitude.

To identify oscillation modes, the significant *STEREO* frequencies and the relation provided by Breger and Bregman (1975) were used:

$$logQ = -6.456 + 0.5logg + 0.1M_{bol} + logT_{eff} + logP \ ,$$

where $logg$ is the surface gravity, M_{bol} is the bolometric magnitude, $logT_{eff}$ is the logarithm of the effective temperature, and $logP$ is the period. In this equation, temperature and surface gravity, as well as luminosity and mass values of the sample stars, were adopted from the literature. The bolometric magnitude of all samples and the physical parameters of HD 90386

Table 7.24: Selected δ Scuti samples and their physical properties.

Star ID (HD)	**27397**	**27628**	**28024**	**30780**	**90386**	**106384**
$Vsini$ ($\mathrm{km\,s^{-1}}$)	102^{a}	32^{a}	243^{b}	180^{b}	$134-200^{*}$	$21.6(3)^{f}$
$Period$ (day)	0.05799717(9)	0.0764476(4)	0.146849(1)	0.08900196(9)	0.0975364(2)	0.07863973(2)
Q (day)	0.032(1)	0.033(8)	0.036(2)	0.036(1)	0.031(6)	0.031(4)
M_{bol} (mag)	2.37(4)	1.79(5)	0.99(3)	1.60(8)	1.02(18)	1.73(9)
$Logg$	$4.169(33)^{c}$	$4.120(200)^{d}$	$3.742(27)^{c}$	$4.012(31)^{c}$	3.887(159)	$4.000(100)^{f}$
$LogT_{eff}$	$3.878(4)^{c}$	$3.857(4)^{c}$	$3.877(3)^{c}$	$3.897(3)^{c}$	3.914(4)	$3.875(6)^{g}$
$Log(L/\mathrm{L}_{\odot})$	$0.955(14)^{c}$	$0.900(14)^{c}$	$1.491(14)^{c}$	$1.339(35)^{b}$	1.517(67)	$1.170(55)^{h}$
R ($\mathrm{R}_{\odot}$)	1.76(4)	1.82(4)	3.28(7)	2.64(11)	2.85(23)	2.28(16)
M ($\mathrm{M}_{\odot}$)	1.67^{c}	$1.71(12)^{e}$	$2.20(2)^{b}$	$1.98(4)^{b}$	2.28(9)	1.80^{h}
m_1 (mag)	0.194^{i}	0.204^{i}	0.175^{i}	0.207^{i}	0.173^{i}	0.184^{i}

[a]: Tkachenko et al. (2013), [b]: Zorec and Royer (2012), [c]: de Bruijne et al. (2001b), [d]: Soubiran et al. (2010), [e]: Gebran et al. (2010), [f]:Zima et al. (2006), [g]: Breger et al. (1999b), [h]: Breger and Pamyatnykh (2006), [i]: (Rodríguez et al., 2000), [*]: $Vsini$ values estimated from Niemczura et al. (2015).
Note: The estimated errors of the parameters (in particular on the masses and radii) given in the table are statistical errors only. The true errors will be rather larger.

were estimated due to a lack of archival data: temperature and bolometric correction (BC) were approximated from Flower (1996) by using the $B-V$ colour index. Absolute magnitude was found from the distance modulus:

$$M_V = m_V + 5 - 5logd - A_\nu \ ,$$

where m_V and d is the apparent magnitude and the distance values, adopted from the *Simbad* Database. A_ν is the interstellar extinction derived from $A_\nu = 3.1\ E(B-V)$. Here, $E(B-V) = (B-V) - (B-V)_0$ where $(B-V)_0$ is the intrinsic colour index and was taken from Fitzgerald (1970). Further, the luminosity of the star was calculated with the relation:

$$M_{bol} - M_{\odot(bol)} = -2.5log(L/\mathrm{L}_{\odot}) \ ,$$

where $M_{bol} = M_V + BC$ and $M_{\odot(bol)}$ equals to 4.81 mag. Mass value was estimated by means of the equation given by Cox and Pilachowski (2000)

$$log(M/\mathrm{M}_{\odot}) = 0.46 - 0.10M_{bol} \ .$$

Finally, surface gravity (Tsvetkov, 1988) and radius of the star were obtained from the following relations:

$$R/\mathrm{R}_{\odot} = (L/\mathrm{L}_{\odot})^{0.5}\ (\mathrm{T}_{\odot}/T)^2 \ ,$$

$$logg = log(M/\mathrm{M}_{\odot}) - 2log(R/\mathrm{R}_{\odot}) + logg_{\odot} \ ,$$

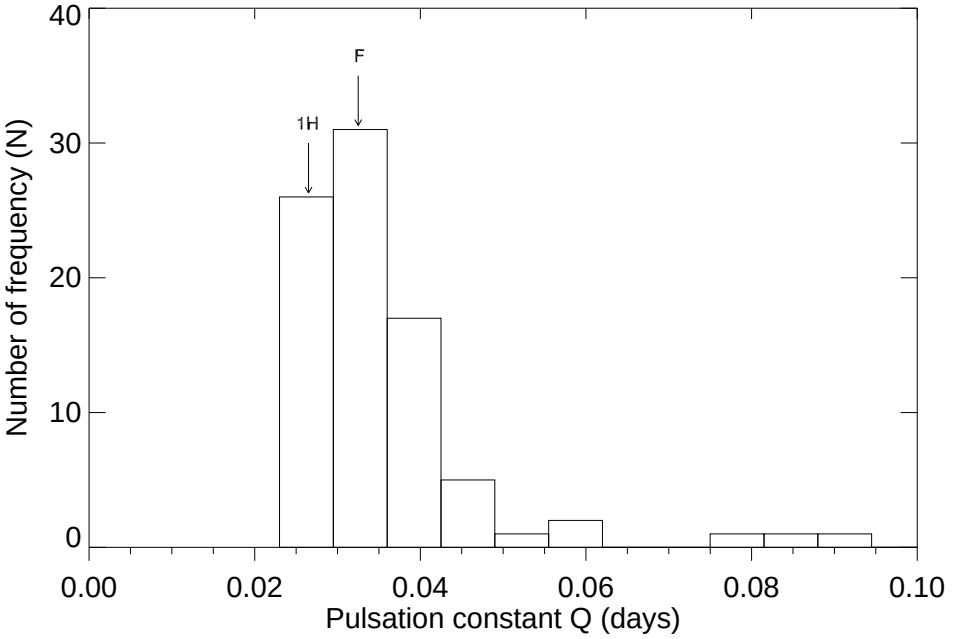

Figure 7.8: Distribution of the pulsation constants for the sample stars. Theoretical Q values for the fundamental mode and its overtone were taken from Breger (1979) and shown with arrows.

where R is the radius and $logg_{\odot}$ equals to 4.437. Error values of all these parameters were computed based on the error propagation method. Estimated and adopted parameters are given with their errors in Table 7.24. Superscript letters indicate the sources from which those parameters were taken, and the parameters with no indices are the estimations made by the relations given above.

The frequency analyses show that the pulsation periods of the sample stars correspond to the lowest radial modes. In particular, they are within the period interval given for the fundamental radial mode ($-1.33 < logP < -0.6$ days; McNamara (2011)). This result can be confirmed with the distribution of the pulsation constants shown in Fig. 7.8. The most dominant two peaks in the figure are quite consistent with $0.032 \leq Q_0 \leq 0.036$ days for the fundamental mode and $0.024 \leq Q_1 \leq 0.028$ days for the first overtone (Fitch, 1981). Based on this distribution, it is possible to conclude that the samples pulsate mostly in the fundamental mode and its first overtone.

Three of the sample δ Scuties, HD 27397, HD 27628, and HD 106384, have shorter period values compared to those of other samples. As discussed by McNamara (2011), these stars also have smaller mass values, varying between 1.60 and 1.80 $M_{\odot}$ (Table 7.24). The projected

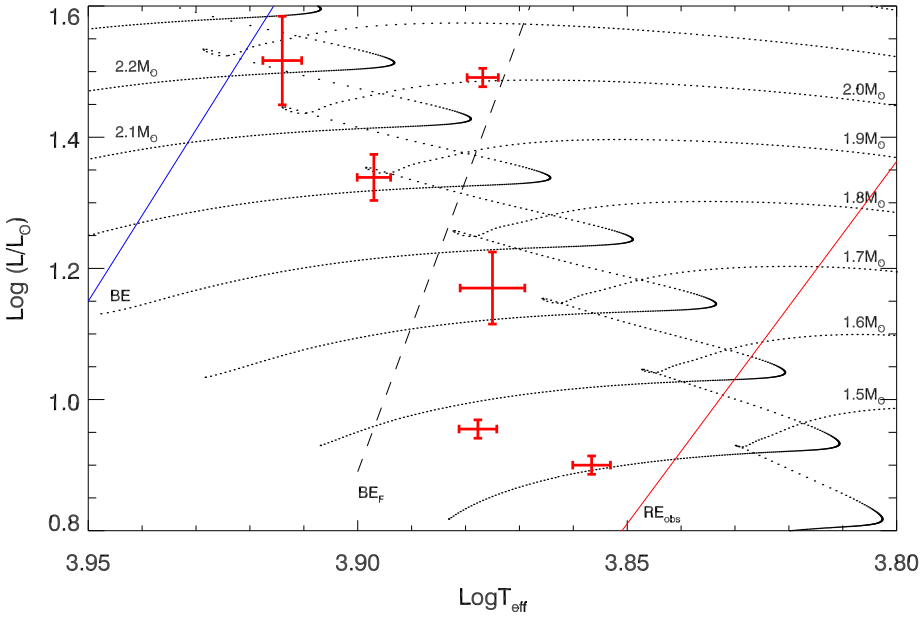

Figure 7.9: The effective temperature ($logT_{eff}$) and luminosity ($log(L/\mathrm{L}_\odot)$) relationship for the sample stars. The evolution tracks start from the homogeneous zero-age MS, and cover the mass range of 1.5 and 2.3 $\mathrm{M}_\odot$. The initial hydrogen and heavy metal abundances are assumed to be $X = 0.70$ and $Z = 0.02$, respectively. The red and blue solid lines are the theoretical blue edge for the radial mode and the empirical red edge of the instability strip. The dashed line marked as BE_F is the theoretical blue edge for the radial fundamental mode (Breger and Pamyatnykh, 1998b). The positions of δ Scuti samples and their errors are also presented with red plus symbols.

velocities of the samples change from 20 $\mathrm{km\,s^{-1}}$ to 250 $\mathrm{km\,s^{-1}}$. While HD 27628 and HD 106384 are slowly rotating stars, the rest of the group has high or moderate rotation velocities. Among them, the rotational velocity of HD 90386 is not conclusive since the physical parameters as well as the inclination angle of the star are not accurately known, i.e., it might be either a slowly or moderately rotating δ Scuti variable depending on these parameters. This variety in rotational velocities of the samples provides a valuable opportunity to understand the effects of rotation on stellar properties.

δ Scuti stars are populated on or near the MS within the instability strip, in which effective temperature and luminosity are between $3.80 < logT_{eff} < 3.95$ and $0.6 < log(L/\mathrm{L}_\odot) < 2.0$, respectively (Milligan and Carson, 1992). From the physical parameters in Table 7.24, it is clearly seen that all the samples fall within these luminosity and temperature intervals. With the help of these parameters, the $logT_{eff}$ - $log(L/\mathrm{L}_\odot)$ model was established in order to determine the positions of these stars on the H-R diagram, investigate their evolution status, and compare

their physical parameters with each other. The theoretical values for stars in the MS and the post-MS phases were provided from Christensen-Dalsgaard (1993)[9] (Fig. 7.9).

In this model, evolution tracks start from the homogeneous zero-age MS, and cover the mass range of 1.5 and 2.3 $M_{\odot}$. Initial hydrogen and heavy metal abundances are assumed to be $X = 0.70$ and $Z = 0.02$, respectively. In the figure, the positions of the δ Scuti samples and their errors are presented with red plus symbols. The red and the blue solid lines are the theoretical blue edge for the radial mode and the empirical red edge of the instability strip. The dashed line marked as BE_F is the theoretical blue edge for the radial fundamental mode (Breger and Pamyatnykh, 1998b). Based on the figure, the majority of the stars are located in the MS. Two stars, HD 27397 and HD 27628, seem to be at the central hydrogen-burning phase in the cool part of the diagram. Also, they are at the earlier stages of their evolution, which indicate that they might be younger than other group members. Further, three samples, HD 30780, HD 90386, and HD 106384, are quite close to the turn-off points at the end of the MS stage where central hydrogen is consumed. Apart from these, HD 28024 appeared to be more evolved than the other samples since it has already passed the turn-off point, and it is most probably at the shell hydrogen-burning stage.

In the region where the Cepheid instability strip intersects with the MS on the H-R diagram, there is a complex relationship between stellar population and atmospheric abundance anomalies. The most stars observed in this intersection are normal abundance δ Scuti variables with relatively high rotational velocities, $Vsini \geq 100$ km s^{-1} (Smalley et al., 2011). δ Scuties overlap with Am stars, as they overlap with many other variables such as Ap, Fp, γ Dor, and δ Boo stars in this region. Am stars mostly exist in short-period binary systems ($P = 1 - 10$ days), and their rotational velocities are lower than 100 km s^{-1} due to a tidal brake between components (Abt, 2009). As discussed in Section 1.3.2 (on page 31), these stars show abnormal metal abundance on their surfaces. The origins of this peculiarity are thought to be atomic diffusion, radiative levitation, and the gravitational settling that occurred depending on slow rotation. Also, the lack of an effective mixing mechanism and turbulence negligible below rotational velocity of 100 km s^{-1} are other factors that cause abnormal metal abundance on the surface (Murphy et al., 2015).

As known, the pulsation source of the δ Scuties is the κ-mechanism driven in the HeII ionization zone, which means helium is the key element in these stars. Yet, δ Scuti type

[9] http://owww.phys.au.dk/ jcd/emdl94/eff_v6/

pulsations are inhibited due to the gravitational settling of helium in slowly rotating stars such as Am types. It was therefore thought that Am stars did not pulsate for many years. However, the detection of the δ Scuti type pulsations in HD 1097 revealed that many Am stars in fact pulsated. These discoveries have been rapidly increasing through space missions such as CoRoT (HD 51844, Hareter et al. (2014)), MOST (HD 114839, King et al. (2006)), and Kepler (KIC 3429637, Murphy et al. (2012)).

In this context, HD 27628 is another example of an Am-δ Scuti type star. We believe that the position of the star between Am and δ Scuti types has been better understood with the help of *STEREO* data. HD 27628 shows all typical properties given for Am stars. It is known that the star is a spectroscopic binary, and its projected rotational velocity is around 32 $\mathrm{km\,s^{-1}}$, which is most probably due to binarity. Its metallicity index m_1 is around 0.204 mag (Rodríguez et al., 2000), and is slightly higher than those of other samples, except for HD 30780 (Table 7.24).

It is stated that pulsating Am stars are cooler than normal δ Scuties and produce lower amplitude compared to δ Scuti stars (Smalley et al., 2011). Referring to the Fig. 7.9, the star is also located quite close to the cool edge of the instability strip on the H-R diagram. Moreover, it can be seen from Fig. 7.3 that indeed the star does not exhibit strong pulsations. This situation indicates that the loss of helium in the partial ionization zone does not suppress pulsations but reduces their intensities. Additionally, the absence of strong pulsations in the amplitude spectrum might be related to the evolutionary status of the star. As shown on the H-R diagram, the star is still on the MS. According to Turcotte et al. (2000), the position of stars on the H-R diagram and their pulsation characteristics are directly related, i.e., it is suggested that pulsation amplitudes intensify as stars evolve or begin to leave the MS.

Further, for the lack of p-modes, energy transferring between modes should also be considered, as speculated by Murphy et al. (2015). Mode coupling is estimated between frequencies in δ Scuti stars. Due to the instability of a linearly driven mode, two other modes grow stronger. This phenomenon is known as the parametric resonance. As a result of these non-linear effects, the amplitude of a linearly-driven p- or g-mode decreases while other g-modes increase (Dziembowski, 1982). These g-modes can be trapped in the deep interior and are not observable on the surface. If this is the case for HD 27628, the abnormal frequency variations seen in its seasonal LCs (on page 322) and the frequency at 11.85 $\mathrm{cd^{-1}}$ observed by Zhiping (2000) but not observable in our data might be explained.

4 CVn (Breger, 2009) and KIC 7106205 (Bowman et al., 2015) can be given as two remarkable

examples of the parametric resonance phenomenon. Their frequency analyses show that the amplitude of a specific frequency decreased over years and the frequency eventually disappeared from the periodogram ($f = 7.375$ cd^{-1} for 4 CVn and $f = 13.394$ cd^{-1} for KIC 7106205). Among our sample δ Scuti stars, HD 30780 is the best example of this situation. The seasonal LCs of this multi-periodic δ Scuti display a significant fall in amplitude of 14.22 cd^{-1}. It appears to decrease from 1.22 mmag in 2007 to 0.56 mmag in 2010, and it vanishes in 2011. The frequency itself also shifts from 14.23 cd^{-1} to 14.21 cd^{-1} over four years. During this process, the amplitude of 11.65 cd^{-1} increases from 0.9 mmag to 1.3 mmag. Such a variation is not seen in KIC 7106205, and might attest to the energy transfer between modes. In addition to these, 9.18, 11.65, and 14.33 cd^{-1} show changes in frequency. While the former has a parabolic change, the latter two exhibit sinusoidal variations.

Amplitude and frequency variations have been detected in almost all pulsating stars, and most of these modulations are periodic. This phenomenon is known as the Blazhko effect in RR Lyrae stars. However, this definition is used for other stars due to the similarities observed (Breger and Pamyatnykh, 2006). Many δ Scuti variables have amplitude variations connected with multi-mode pulsations. The reason for these changes is either two modes beating at close frequencies or a single mode varying in both amplitude and frequency. HD 106384 is the unique example of the Blazhko effect among six sample stars. It was observed several times by Breger (Section 7.4.6; on page 215), and 79 frequencies were detected by using only ground-based data. Of these frequencies, it was revealed that 12.15, 19.86, and 23.40 cd^{-1} were formed of two or three close frequencies that displayed the beating phenomenon. Since the Nyquist frequency of *STEREO* data is around 18 cd^{-1}, we are able to observe only the changes in amplitude of 12.15 cd^{-1}. As discussed in Section 7.4.6, this frequency consists of two modes at 12.1541 and 12.1638 cd^{-1}, and their beating period is around 103 days. Further, we find some hints about energy transfer between other modes: amplitudes of 11.77 and 12.715 cd^{-1} have an inverse parabola, whereas the amplitude of 14.95 cd^{-1} moderately increases. The frequency at 11.77 cd^{-1} also changes in parallel with its amplitude, and a sinusoidal variation is seen at 12.715 and 14.95 cd^{-1}.

As the most slowly rotating star among our samples, HD 106384 is also significant for another aspect of this study. Different from a typical δ Scuti star, it has a rotational velocity of around $Vsini \approx 20$ km s^{-1}. Its periodogram, which keeps both radial and non-radial modes together (the radial fundamental mode = 12.15 cd^{-1}; Breger (2007)), shows higher amplitude variations

(A_{max} = 13.62 mmag) compared to those of the other samples. As discussed in Section 1.2.4 (on page 27), these properties are in accord with those of the HADS that are a sub-type of δ Scuties. For this reason, HD 106384 might be assumed to be a HADS star. However, it is known that the slow rotation produces larger amplitudes up to 1.0 mag, and that the amplitude of a HADS is greater than 0.3 mag. Further, stars with a rotation velocity $Vsini \geq 30$ km s^{-1} have low amplitudes and mostly pulsate with multiple non-radial modes (Breger, 2007). Although these findings clearly contrast with the maximum amplitude intensity and the rotation velocity of HD 106384, this uncertainty might be enlightened with insights from the study of Suárez et al. (2002). They state that there is a strong relation between the estimated inclination angle (i) and oscillation amplitude of a star: in particular, oscillation amplitudes decrease with inclination angle. If the inclination angle of the star is considered to be $i = 15(5)^\circ$ (Zima et al., 2006), this explanation might be reasonable and explain the oscillation characteristic of HD 106384.

Apart from the inclination angle, rotational velocity also has some deforming effects on oscillation frequencies such as departure from equidistant within a given multiplet split and an overall shift of the multiplet itself (Soufi et al., 1995). These effects are shown with a model having $M = 2$ M$_\odot$ and $V_{rot} \approx 200$ km s^{-1} in Fig. 7.10. Accordingly, rapid rotation produces significant shifts in frequencies in the periodogram (top). For instance, the order of occurrence of the frequencies $(n, 2)$ and $(n, 0)$ is clearly changed as seen in the figure. Also, close frequency pairs often show up for the rotating model, and Soufi et al. (1995) gives the separation between these pairs as 0.05 cd^{-1}; in most cases it is larger than 0.09 cd^{-1}. Rotation not only affects p-modes but also affects g-modes, and this parameter is therefore considered for the mode identification of δ Scuti stars.

Among our samples, HD 106384 and HD 30780 are two stars suitable for comparing the effects of rotation on p-modes since HD 30780 is a rapid rotator ($Vsini$ = 180 km s^{-1}), unlike HD 106384 (Table 7.24). The comparison of their periodograms shows that while some frequencies around 9, 11.70, and 16 cd^{-1} remain constant in the amplitude spectrum of HD 30780, the positions of other significant peaks change. Moreover, pairs of close frequencies discussed by Soufi et al. (1995) are observed at around 11, 14, 16, and 17 cd^{-1} in the same periodogram. The smallest separation between the pairs is around 0.006 cd^{-1} (14.2217 − 14.2279 cd^{-1}), but the average value is calculated as 0.05 cd^{-1}.

In addition, mass, element abundance, and convective core overshooting have also important effects on oscillation frequencies. The effects of these parameters have been investigated by

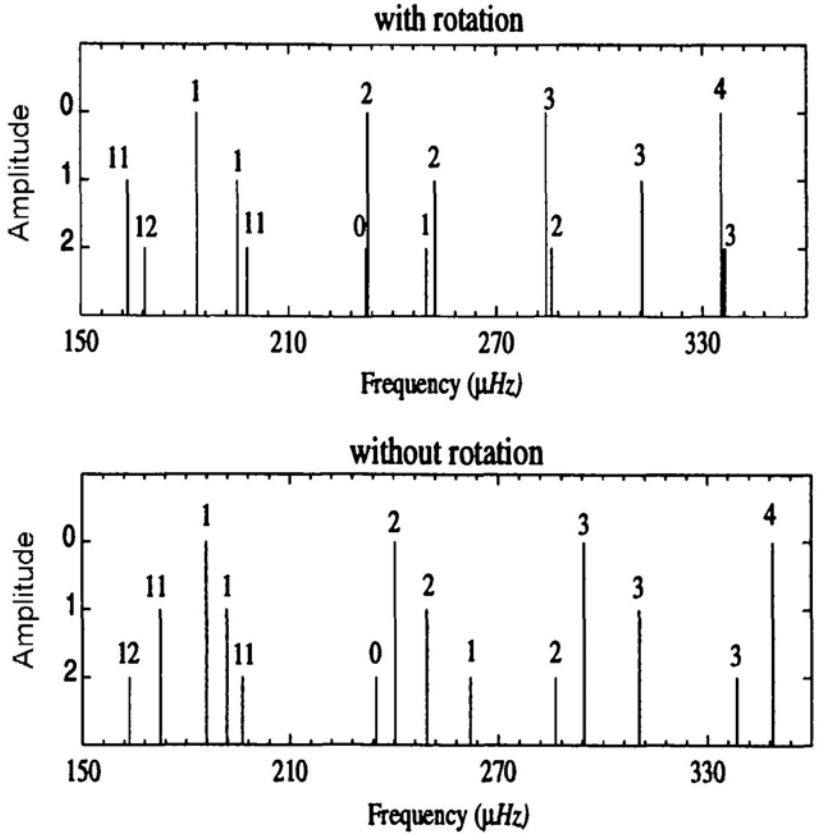

Figure 7.10: Oscillation frequencies of a rotating (top) and a non-rotating (bottom) model. Numbers above the peaks are radial order n, and amplitudes are assigned to modes of different degree that are presented in ordinate. Mass and rotational velocity are assumed to be around $M = 2$ M$_\odot$ and $V_{rot} \approx 200$ km s^{-1} in this model (from Soufi et al. (1995)).

Templeton et al. (2001). In that study, four models are produced using different fundamental parameters, and the changes in frequencies over time are observed. For $l = 0$, these models are presented in Fig. 7.11. Time is referred to as stellar age, which is normalized such that the turn-off point on the early post-MS is equal to 1.0. Based on the study, the common effect seen in the models is that p-mode frequencies decay with increasing age, since an expanding stellar radius leads to an increase in the crossing time of the sound in the star. In contrast, g-modes remain stable over time. The most notable changes in g-modes take place at the end of the MS stage at which the core structure considerably changes. All frequencies have a brief spike at the turn-off point, and the decrease in radial modes continues while g- and mixed-modes increase after this point.

According to Templeton et al. (2001), an alteration in mass has the most considerable impact on pulsation frequencies. In the model with an overshooting of $\alpha = 0.0$, element abundances

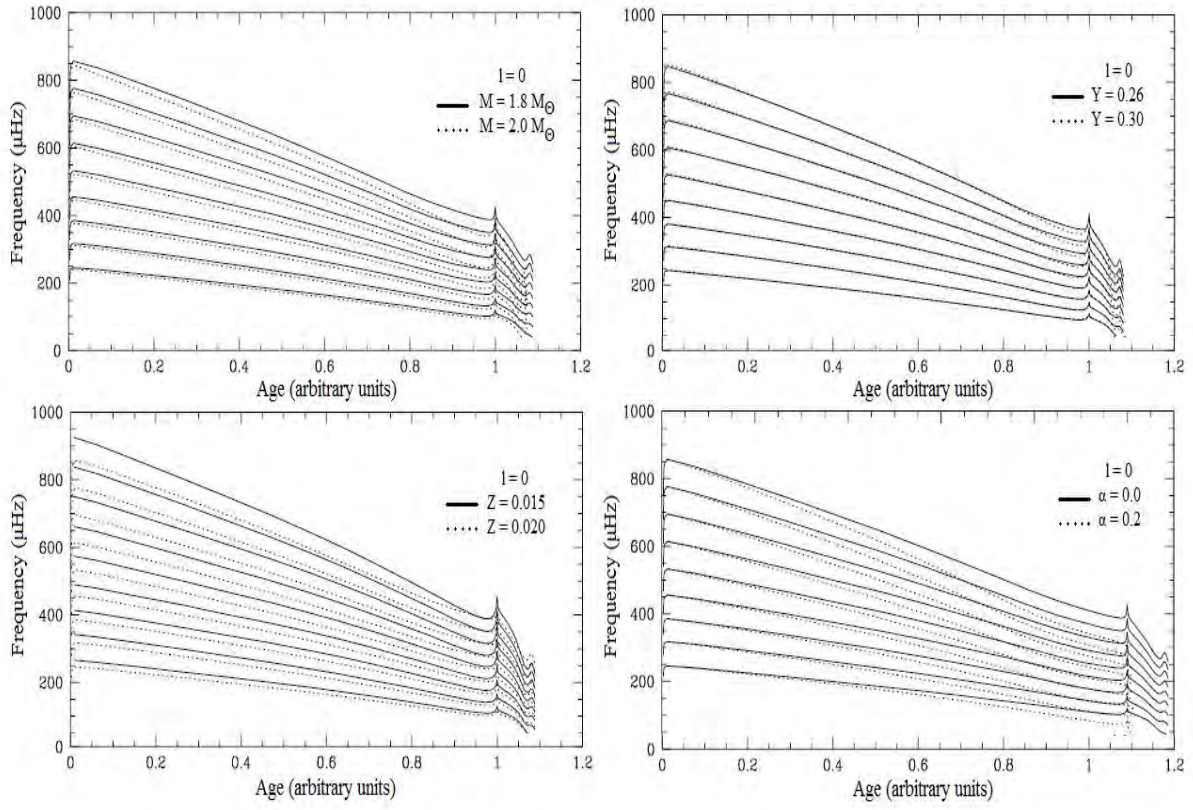

Figure 7.11: Effects of the fundamental parameters on the oscillation frequencies are presented in the figure. Evolution of the pulsation spectra of two models with different masses (top left), different helium abundances (top right), different metal abundances (bottom left) and different convective overshooting parameters (bottom right) are examined in detail for $l = 0$ mode. The x-axis is relative age normalized between 0.0 and 1.2. The point on the early post-MS where the frequencies reach a maximum is equal to 1.0 (from Templeton et al. (2001)).

$Z = 0.02$ and $Y = 0.28$, and having mass values $M = 1.8$ $M_\odot$ and $M = 2.0$ $M_\odot$, the more massive star displays the lower frequencies for both p- and g-modes. The frequency shifts between the models are almost constant for the lower order modes, but the difference increases at higher frequencies over time. Frequency differences are on the order of 0.69 and 1.30 cd^{-1} for $l = 0$ p-modes (Fig. 7.11; top left)

On the top right of the Fig. 7.11, the model with $M = 1.9$ $M_\odot$, $Z = 0.02$ and $\alpha = 0.0$ having initial helium abundances of $Y = 0.26$ and $Y = 0.30$ is shown. The difference between pulsation frequencies is very small until the 80% of the MS lifetime. For low order $l = 0$ modes, this difference is less than 0.09 cd^{-1}. In the other model, while $M = 1.8$ $M_\odot$, $Y = 0.28$ and $\alpha = 0.0$, initial metal abundances are assumed to be $Z = 0.015$ and $Z = 0.020$ (Fig. 7.11; bottom left). The effects produced by this model are between those of the mass and the helium abundance.

The p-modes are mostly affected from the metal abundance. The evolution of $l = 0$ p-modes are close and parallel to each other at lower frequencies. Higher order $l = 0$ modes rapidly decrease over time, and this leads to high frequency ratios between the radial modes. Further, the lower frequency g- and mixed-modes remain constant. The differences between g-modes of two models are small.

In the final model, the convective core overshooting parameter is changed from $\alpha = 0.0$ to $\alpha = 0.2$ while $M = 1.8$ $M_{\odot}$, $Y = 0.28$, and $Z = 0.02$. Based on this, the frequencies are identical at the zero-age MS. The high frequency p-modes exhibit the largest separation over time due to their strong dependence on the radius. All frequencies in the overshooting model are lower. As expected, g-modes are mostly affected because of the larger core (Fig. 7.11; bottom right).

In brief, the change in mass has more influence on pulsation frequencies. It causes significant shifts in p- and g-modes. The change in metal abundance affects p-mode frequencies more than g-modes. Unlike these, while helium abundance produces almost no effect, the effects of the overshooting increase over time even if it causes no variation at the zero-age MS.

As previously discussed, period changes in δ Scuti stars are directly proportional to the changes in the stellar radius, i.e., a period increase is observed with increasing radius for the vast majority of stars in the lower instability strip of the H-R diagram. Breger et al. (1998) gives the variation rates in periods as $dP/Pdt = 10^{-10}$ yr^{-1} and 10^{-7} yr^{-1} for the MS and the longer-period evolved stars, respectively. However, due to the inconsistencies between the theoretical and the observational findings, it is assumed that the period changes observed in population I, δ Scuti stars are not caused by stellar evolutionary changes, but produced by non-linear mode interactions that is explained above. For δ Scuti models in a wide range of oscillation parameters, the rates of these period changes are found to be between 7.00×10^{-4} and 1.00×10^{-3} yr^{-1} (Breger et al., 1998). The latter estimations, which are given for the non-evolutionary period changes, are significantly consistent with the result found in the *STEREO* data. As seen in Section 7.4 (on page 194), the rates calculated for HD 27397, HD 27628, HD 30780, and HD 90386 vary between 10^{-3} and 10^{-4} yr^{-1}. However, in the case of HD 106384, the combination of the archival and *STEREO* data reveals that long-term period changes of the star are around 10^{-6} and 10^{-7} yr^{-1}. This might indicate that the period changes observed in this star are a result of stellar evolutionary changes.

Furthermore, Templeton et al. (2001) mentions that mass, element abundance, and convective core overshooting also have important effects on evolution stages on the H-R diagram

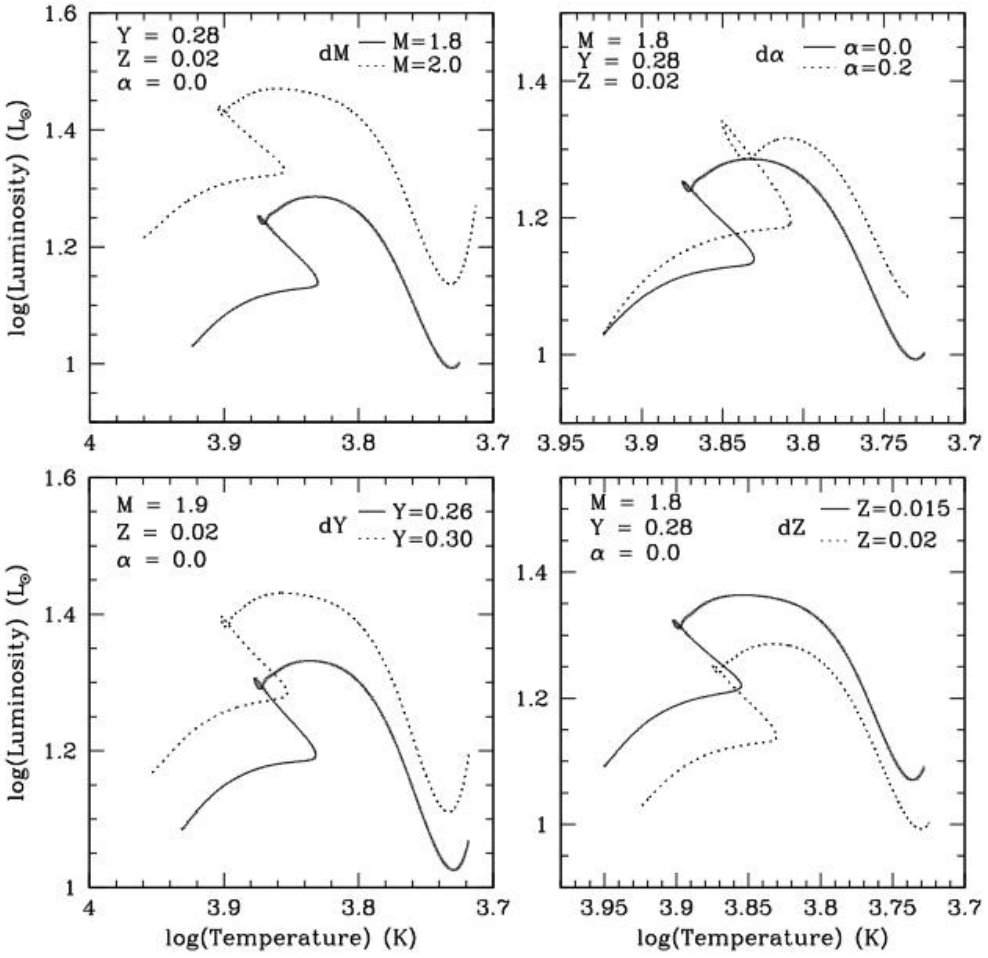

Figure 7.12: Effects of the fundamental parameters on the evolution tracks are shown in the figure. An increase in mass (top left) and helium abundance (bottom left) increases luminosity and temperature while an increase in heavy element abundance (bottom right) produces an opposite effect. Change in overshooting parameter (top right) changes evolution track with time, but the zero-age MS remains unchanged (from Templeton et al. (2001)).

(Fig. 7.12). According to this, the zero-age MS locations of the stars with different masses and initial chemical compositions display considerable differences. In the models in which mass and helium abundance are increased, higher luminosity and temperature values are obtained on the H-R diagram. From the Fig. 7.12 (top left), increasing the stellar mass by 0.2 $M_{\odot}$ results in an increase of about 0.2 dex in luminosity and 0.04 dex in temperature. Similarly, increasing the helium abundance from $Y = 0.26$ to $Y = 0.30$ causes an increase in both luminosity and temperature of about 0.1 and 0.02 dex, respectively (bottom left). The same effect is also derived by decreasing the metal mass fraction from $Z = 0.02$ to $Z = 0.015$ (bottom right).

Separate from these parameters, changing the convective core overshooting produces a completely different effect on the evolution tracks. Breger and Pamyatnykh (1998b) state that an

increase in this parameter leads to an enlargement of the mixed core, and thus more hydrogen becomes available for nuclear burning. As a result of this, the MS stage on the H-R diagram extends. As seen in Fig. 7.12 (top right), the model with overshooting is more luminous than that with no overshooting for a constant temperature. The MS lifetime is 12-14% longer due to the overshooting. However, more hydrogen is consumed at the terminal-age MS in this model and hence the post-MS expansion is faster. Because it causes significant differences in evolution, this parameter is thought to be important for statistical investigations of δ Scuti stars (Breger and Pamyatnykh, 1998b).

Finally, the effects of the rotation on evolution tracks should be briefly discussed. By investigating the models with and without rotation, it is detected that rotation reduces the temperature and the surface gravity of a star. The displacement in the terminal-age MS is similar to that of the model with overshooting. The MS lifetime of the rotating star is 0.5-1.0% longer compared to that of the non-rotating model (Breger and Pamyatnykh, 1998b).

Based on the information given, the comparison of two multi-periodic samples of HD 106384 and HD 30780 indicates that HD 30780 is 0.17 dex more luminous and 0.02 dex hotter than HD 106384 on the H-R diagram. As seen in Table 7.24, the metallicity and the rotational velocity of HD 30780 is greater than that of the other star, which means that the positions of these stars should have been replaced on the H-R diagram. This situation might be explained by the difference between the mass values or helium abundances of the stars, i.e., HD 30780 is hotter and brighter since it has a greater mass value (ΔM = 0.36 $M_{\odot}$), or its initial helium abundance might be higher than that of the other star.

Moreover, HD 28024 has a significantly different location on the H-R diagram compared to the other samples (Fig. 7.9). Based on the diagram, the star completes its evolution in the MS and starts the post-MS stage. For a given luminosity and temperature value (Table 7.24), its mass is quite consistent with the theoretical evolution track. Therefore, it might be thought that the star is indeed at the shell hydrogen-burning phase. In addition, its radius is at least 1.0 $R_{\odot}$ greater than those of the other samples. This might indicate that HD 28024 has a strong convective core overshooting mechanism that consumes more hydrogen at the terminal-age MS, and thus the star rapidly expands at the post-MS stage. HD 28024 is also surrounded by a disk structure (Abt, 2008). According to Abt (2008), the rapidly rotating ($Vsini$ = 200 $\mathrm{km\,s^{-1}}$) A-type stars on or near the MS might have circumstellar dust and/or gas. The observational characteristics of these stars are similar to those of Be-stars. They show small amounts of

changes on time-scales of hours and days, as well as larger amounts with quasi-periodic times of $10-30$ yr^{-1}. The reason for these variations is the amount of material in the disks (Abt, 2008). Since HD 28024 has a rotational velocity greater than 200 km s^{-1}, it is a potential candidate for A-type stars having circumstellar material. Furthermore, its mono-periodic variation with a period of around 6.81 cd^{-1} is slightly lower than the typical oscillation period of a δ Scuti star ($P \approx 10$ cd^{-1}; Oldershaw (2006)). This situation might suggest that the oscillation of the star detected at this frequency is affected by the disk structure, yet neither the frequency itself nor its amplitude presents any variation over four years.

HD 90386, a double-mode pulsator, also has a simple amplitude spectrum. The period ratio between f_1 and f_2 is around 0.827, which is quite consistent with the ratio given by Breger (1979) for the first and the second overtones ($P_2/P_1 = 0.810$). According to Breger and Bregman (1975), it is possible to separate the radial modes from each other since they are temperature dependent. That is, δ Scuties that pulsated with the fundamental mode lie in the cool part of the instability strip whereas the overtone pulsators are found in the hotter part. As seen in Fig. 7.9, HD 90386 is located close to the blue edge of the instability strip and also far from the blue edge for the fundamental mode. Based on this, the star is thought to be an overtone pulsator. Since there is no archival information related to the star, it is not possible to achieve a detailed interpretation. However, its metallicity index m_1 is lower than other samples. So, this might result in higher luminosity and temperature values, which specify its position on the H-R diagram. Its mass value calculated from these parameters is also compatible with the theoretical evolution track. Since the inclination angle is not known, the effects of the rotation on the amplitude spectrum and the evolution status are unclear.

The final sample, HD 27397, forms a binary system with another δ Scuti star, and thus probably has a different amplitude spectrum. Unlike in other samples, the main variations are observed after 15 cd^{-1}, and the maximum pulsation oscillation is at around 18.22 cd^{-1} (Fu et al., 1996), which is beyond the *STEREO* Nyquist frequency. HD 27397 is situated close to the red edge of the instability strip on the H-R diagram. Although the star shares the same location with HD 27628, it is more luminous, hotter, and, above all, its rotational velocity is significantly higher ($Vsini = 100$ km s^{-1}). For these reasons, it is not considered to be an Am-type star as is HD 27628. However, the location of the star exactly overlaps with the γ Dor stars, and it is reported that the star pulsates in g-modes in addition to p-modes (Paparó et al., 2000). These low-frequency structures are also seen in the *STEREO* periodogram. If these have not occurred

due to duplicity such as geometric and proximity effects, HD 27397 might be thought to be a hybrid star.

Further, it should be noted that similar low-frequencies are also detected in the amplitude spectrum of HD 27628. If these oscillations are indeed g-modes, HD 27628 would be one of the rare stars that show all γ Dor, δ Scuti and Am type variations at the same time. The MOST star HD 114839 (T_{eff} = 7,400 K, $logg = 4.20$, $Vsini = 68(2)$ km s^{-1}) can be given as another example for such a type (Hareter et al., 2011). It is the fourth-known such hybrid pulsator that shows both p- and g-modes as well as Am-type properties in the amplitude spectrum (King et al., 2006). Recently, the Am star KIC 11445913 (T_{eff} = 7,250(100) K, $logg = 3.50(20)$, $Vsini = 51(1)$ km s^{-1}) has been also classified as a δ Scuti/γ Dor hybrid with a very rich frequency spectrum (Balona et al., 2011b).

The micro-magnitude precision of the space missions such as KEPLER, CoRoT, and MOST is quite sufficient to detect the δ Scuti type pulsations. For stars of spectral types A-F, these telescopes offer several perspectives: the CoRoT satellite revealed more candidate hybrid δ Scuti/γ Dor stars (Hareter et al., 2010); the KEPLER found that the δ Scuti or γ Dor stars were in fact hybrid pulsators (Grigahcène et al., 2010); the MOST satellite discovered two bright hybrid candidates (King et al., 2006); Balona et al. (2011b) analysed the Kepler data of ten known Am stars and found that six of them exhibit δ Scuti pulsation; and Breger et al. (2012) observed δ Scuti stars in the Praesepe cluster by the MOST satellite and discovered different pulsation behaviours.

As seen from the examples, the space missions provide new insights into behaviours of δ Scuti pulsators and also valuable information about the evolution among δ Scuti, γ Dor and Am type stars. In this context, we believe that the *HI-1A* is also a valuable source for gaining a better understanding of the nature of δ Scuties and their evolution status. Its high-precision and long-term observation capability provided a unique opportunity to detect the smallest variations in δ Scuti LCs and study period changes seen in the selected δ Scuti stars. Further, the differences and common features observed in amplitude frequencies of single and binary samples, multi- and mono-periodic samples, cluster members and field stars, hotter and cooler samples, fast and slow rotators, and high and low amplitude samples were compared. In doing so, we drew attention to several unknown properties of six known δ Scuti stars in this chapter.

Chapter 8

Overview and Future Work

Stars are one of astrophysics' cornerstones, and understanding their structures and evolution plays an essential role in having a solid grasp of the big picture. In this context, variable stars and variability have distinct importance. We can obtain much valuable information (such as radius, mass, etc.), using parameters such as wavelength and frequency intensity of an LC that cannot be derived from non-variable stars. These parameters also enable us to understand physical processes in stars by aiding in our development of theoretical models. Further, since changes can be directly observed, they provide information about all kinds of variations during stellar evolution.

Stars exhibit a wide variety of changes. For instance, they can emerge due to geometric factors such as stellar rotations or eclipses, and they can also arise from physical processes such as oscillations or flares. Even each of these occurrences is unique; it is not possible to investigate all of them at once, since they vary from star to star and from one environment to another. Therefore, as discussed in Chapter 1, this thesis focused on only some early-type variable stars, their variability characteristics, and their connections with evolutionary stages by using photometric data taken from the *STEREO* satellite.

Implementing an effective frequency analysis to the data sets of the selected stars was one of the most important processes and was thus repeatedly emphasized in the thesis. Since there is a direct relation between the method of analysis used and the results, it is crucial to obtain comprehensive knowledge of different types of methods. Therefore, four widely-used frequency analysis techniques were introduced in Chapter 3 to be able to examine astronomical data sets.

Chapter 4 provided an introduction to asteroseismology. In this chapter, a number of synthetic LCs, quite similar to the real curves that were derived from the *STEREO* satellite, were

generated by means of Fourier series. Then, the working principles of the methods outlined in Chapter 3 were tested under different conditions. Throughout the study, LS and PDM were emphasized in particular. Comparing these two techniques, we showed that both methods had advantages and disadvantages: as a result of a series of simulated LC analyses, we observed that both methods detected an equal number of true periods in total. However, the results varied depending on different cases and noise levels. For instance, the PDM method was unsuccessful at correctly analysing LCs with nearly-equal minima in white noise, as well as LCs with red noise. On the other hand, LS could not find the true frequency for LCs with nearly-equal and unequal minima, which meant that the LS method could not exactly detect the depths of minima. It was also seen that LS was suitable for determining multi-frequencies. Furthermore, PDM dominated slightly over LS in estimating error values, and it generally detected the closest values to the correct frequency in noisy LCs.

As described in Chapter 2, the data were obtained from the *STEREO/HI* instruments. Although the primary objective of these instruments was to track CMEs, it was revealed that they could be used as a potential stellar photometer, similar to SMEI. Since then, the *STEREO* has proved to be valuable in terms of asteroseismologic studies, and has been an indispensable data source thanks to its instrumental characteristics. The LCs utilized in the study were derived from *HI-1A*, as its data were of high quality compared to *HI-1B* and *HI-2*. With the cadence of 40 minutes and the observation period of around 20 days, more than 700 observation points were obtained for a target star within a season. This data set, high-precision measurements, and considerable SNR all had great importance with regards to identifying different types of variable star candidates, as well as analysing and modelling their data.

The thesis essentially concentrated upon the frequency analyses of three different variable star groups. In Chapter 5, the most accurate rotational periods of 14 CP stars, most of which had not been studied before, were computed with quite small error values of around $\approx 10^{-5}$ days. These were then used to investigate short-term (between 2007 and 2011) variations in period. Epoch values representing the maximum times of the LCs were calculated and supplemented with all the relevant archived observations that were available to study the period evolution seen in the O-C diagram. In the study, we found that all samples showed quite significant light changes, which could be fitted well by a *sine* function and its first harmonic. Their period distribution was exactly within the range given as $1 < P_{CP}$ (days) < 10 for CP variables. The periods were quite consistent with archival records. In contrast, the photometric periods

of some samples, such as HD 31592 and HD 34547, were different from those in the literature since their rotation periods were twice the photometric periods. The most important results were achieved for HD 30466, HD 125248, and HD 150714, which had explicit period variations in their O-C diagrams. The variation in the periods of these stars was quite compatible with the archival findings obtained for other CP stars. In addition, we discovered that the spin-down and acceleration time-scales of these stars were three orders of magnitude shorter than their MS lifetimes, which was suggestive of reversible period changes. This situation was interpreted as a consequence of torsional oscillations produced by meridional circulations being in interaction with a magnetic field, and of rotational braking in outer layers caused by angular momentum loss via magnetically-confined stellar wind. In the case of HD 24769, we calculated a relatively faster period change that occurred due to binarity. Based on its spectral type, mass value and the mass transfer rate, we speculated that the star might be a possible progenitor of a magnetic cataclysmic variable. Along with the other ten stars that showed no long-term period changes, the locations of all CP samples on the H-R diagram were estimated and their evolution stages were discussed.

In Chapter 6, the collection of five-year photometric data of nine bright Be-star samples from the *STEREO* satellite was analysed in order to gain a better understanding of their pulsational characteristics, as well as the connections of these characteristics with mass loss and circumstellar disk structure. The frequencies were detected with a high precision of around 10^{-5} cd^{-1} in frequency and 10^{-4} mag in amplitude. Thanks to the high-quality data of the *STEREO*, we not only discovered a great number of frequencies that had not previously been observed, but also obtained valuable information related the pulsation characteristics of the sample Be-stars. The most important feature standing out in both seasonal and combined periodograms was that each sample, except for HD 23016, showed explicit frequency distributions that formed mostly two, and in some cases three different groups. The frequencies were generally accumulated around 1.1. and 2.2 cd^{-1}, and this grouping in low-frequencies was one of the characteristics of SPB-type stars. Further, we revealed that the amplitude intensities of the late-type Be-stars HD 23630, HD 26398, and HD 147196 were notably lower than those of the other group members. This situation was also a typical property of late-type SPB stars, and indicated that the Brunt-Vaisala frequency, which was quite high in the radiative core, caused a radiative damping and suppressed the wavelengths of g-modes. In addition to these, the evolution stages of the sample Be-stars were examined and the relation between their positions on the H-R diagram

and the features observed in their amplitude spectra was discussed.

To compare the variations in NRPs detected in the photometric data with spectroscopic changes, high-resolution spectra were accessed from the *BeSS* Database. Parameters such as EW, intensity, and V/R ratios of the Hα lines were then measured, and the variations in emission profile were revealed. All photometric and spectroscopic variations taking place in the same time interval were checked, and possible contributions of NRPs to mass losses and disk formations in these stars were examined. Consequently, the most notable relation between the photometric and spectroscopic changes was that they were directly or inversely correlated with each other in some samples such as HD 26398, HD 36576, and HD 142983, as discussed in Chapter 6. Moreover, we suspected that the sudden jumps and drops in frequencies and their amplitudes might be related to changes in the Hα profile, even though these sudden variations might be a result of the refinement pipeline. Finally, the mono-periodic photometric variation of HD 23016 showed that the NRPs were not the only mechanism to cause changes in the Hα profile. Since a mono-periodic pulsation was not enough to provide sufficient kinetic energy and angular momentum to form a circumstellar disk, it was concluded that this star should be examined by considering other mechanisms.

In Chapter 7, the *STEREO* data collected were presented for the purpose of investigating the internal structures and evolution stages of six selected δ Scuti stars. The frequencies were detected with a precision of 10^{-5} cd^{-1} in frequency and 10^{-5} mag in amplitude. Similar to the findings in Chapter 6, many of these frequencies were new discoveries, and this constitutes a major step toward gaining better understanding of these stars' natures. The distribution of the pulsation constants and dominant periods showed that the sample stars mostly pulsated with the fundamental mode and its first harmonic. Also, by combining the *STEREO* results and the archival findings, we revealed that periods of some samples such as HD 27397, HD 27628, HD 30780, and HD 90386 changed over long time intervals. These variations were significantly consistent with the non-evolutionary period changes given in the literature. In the case of HD 106384, its long-term period changes were much smaller, indicating that the observed variations were a result of evolution. With the help of the physical parameters, we determined the positions of all sample δ Scuties on the H-R diagram and investigated their evolution stages. We found that two stars, HD 27397 and HD 27628, were in the central hydrogen-burning phase in the cool part of the diagram and were in the earlier stages of their evolution. Three samples, HD 30780, HD 90386, and HD 106384, were quite close to the turn-off points at the end of the

MS stage where central hydrogen was consumed. HD 28024 also appeared to be more evolved than the other samples since it had already passed the turn-off point. Further, the effects of rotation, chemical composition, mass, and convective overshooting on the evolution of these stars were scrutinized. As an interesting result, both frequency and evolution analyses suggested that HD 27628 might possibly be an Am, γ Dor, and δ Scuti type hybrid star.

In general, we believe that all the results presented in the thesis will be valuable for further modelling of internal structure and evolution, and that they can serve as the building blocks for more detailed studies. Five years of data sets provided by the *STEREO* are also invaluable in terms of asteroseismology, since long-term consecutive observations are quite difficult to make. The only source that had provided such data sets prior to the launch of the *STEREO* was the SMEI instrument. Since its launch, the *STEREO* has proven itself with its high-quality and long-period observations. For example, the number of target stars in the FOV of *HI-1A* alone is approximately 840,000. As the FOV of *HI-2* instrument is 70°, the number of objects that can be observed will be at least 1,700,000. Moreover, by using the *HI-1* instrument, it is possible to obtain 1,400 data points in a year for just one star, and a total of six billion over five years. If *HI-2* is also taken into consideration, this number reaches 18 billion. It is possible to carry out numerous different asteroseismologic and statistical studies, each making a significant contribution to the study of astrophysics, with such a wealth of data.

As previously mentioned, only *HI-1A* data were used in this thesis. With a five-year observation period, high-precision measurements, and good sky coverage, *HI-1A* alone has already proved that it is sufficient not only for the identification of stellar oscillations but also for monitoring of long-term frequency and amplitude variations. However, as is well known, the accuracy of all research is directly proportional to the number of data used. Therefore, if *HI-1B* and *HI-2* data are added to the current data in future studies, the gaps of approximately 340 days between two observation seasons can be filled and a unique data catalogue can be created.

In addition, the sample stars we studied are or will be located in the FOV of other space tasks. With data taken from these missions, the observation period between 2007 and 2011 can also be extended. SMEI can be given as an example of these space missions. The Solar Mass Ejection Imager was launched in 2003 specifically to detect the arrival of CMEs and other solar structures that propagate towards the Earth. Its detectors are sensitive across the optical wave-band. It contains three identical cameras, each with an FOV of $60° \times 3°$, and a combined FOV of about $170° \times 3°$. This allows SMEI to scan most of the sky every 102 minutes. Its

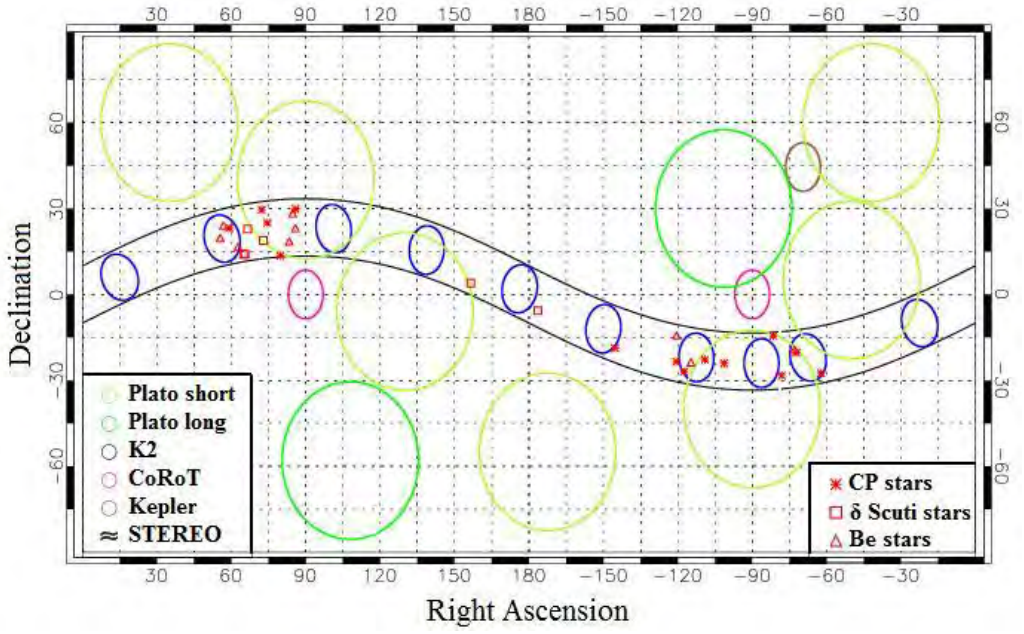

Figure 8.1: The FOVs of the current and next-generation space missions are roughly illustrated in the figure. The FOV of the *STEREO* remains between the black strips, while Kepler, CoRoT, and K2, as well as Plato short- and long-observation fields are shown with brown, pink, blue, yellow-green, and green circles, respectively. TESS and SMEI missions cover almost the entire expanse of the sky. Triangle, square, and asterisk symbols represent Be, δ Scuti, and CP stars studied in this thesis, respectively. As seen in the figure, the sample stars were or will be most likely observed in another mission aside from the *STEREO*.

cameras can detect changes in sky brightness equivalent to a tenth magnitude star in one square degree. Similar to the *STEREO*, SMEI can observe bright background stars with $V \leq 8$ mag as an additional feature. The Nyquist frequency of the data sets is 7.08 cd^{-1}, but it is possible to observe oscillations with a frequency higher than this value, since each camera records an image every four seconds. After obtaining photometric maps of nearly the entire sky for approximately nine years, SMEI was deactivated in 2011 (Eyles et al. (2003), Goss et al. (2011), Hounsell et al. (2012)).

Another important project is the K2 task of NASA, which is a revolutionized version of the Kepler mission. Kepler was launched in 2009 to observe a single FOV located in the constellations of Cygnus and Lyra. However, the loss of two reaction wheels on the Kepler spacecraft terminated the routine data collection process and led to a new era in 2014. Since then, the high-precision, high-cadence, and continuous LCs of the Kepler imager have been released to conduct new research into planet formation processes, young stars, stellar activity, stellar structure and evolution, and extragalactic science. In this mission, the Kepler spacecraft

will be pointed near the ecliptic plane with a new field observed along the ecliptic every three months until 2016. This observation strategy will continuously bring new, well-characterized target regions into view, enabling the capture of images of scientifically important objects across a wide range of galactic latitudes. The observation fields are illustrated with blue circles in Fig. 8.1. These are rough estimations and the original sketch can be found in Howell et al. (2014). In each year of operation, K2 will observe approximately 40,000 targets spread over four FOVs. It will collect data at 30-minute and one-minute cadences and produce 80 ppm photometry for $V \leq 12$ magnitude stars on six-hour time-scales. The former cadence will be used for 10,000–20,000 targets per campaign while the latter will be used for an additional 100 targets per campaign (Howell et al., 2014).

The Transiting Exoplanet Survey Satellite (TESS) will facilitate the next-generation task of searching the newest and brightest stars for transiting planets after Kepler. TESS will be launched in 2017 as an Astrophysics Explorer mission. The main objective of the satellite will be to discover a large number of transiting planets smaller than the Neptune. It will achieve this mission by conducting a two-year, all-sky survey, and focus on MS dwarfs with spectral types F5 to M5. The brightness measurements will be recorded every two minutes, which will enable research of great importance to asteroseismology. According to the ecliptic latitudes, TESS will be capable of observing the targets between a month and a year. The longest observation duration will be for the stars located near the ecliptic poles. Compared to similar stars studied by CoRoT and Kepler, the TESS stars will be more numerous, brighter, and closer to the Earth. Its full-frame images will provide precise photometry ($\sim$ 5 mmag) and allow for the detection of p-mode oscillations of around 6,000 stars with $V \leq 7.5^m$. Stars that are not suitable for searching planets but appropriate for asteroseismology will be added to the input catalogue. Its all-sky coverage and relatively fine time sampling will be the outstanding properties of TESS (Ricker et al. (2014), Stassun et al. (2014)).

PLAnetary Transits and Oscillation of stars (PLATO) will be another next-generation planet finder that will be launched by 2024. It will consist of 34 small aperture telescopes, 32 of which will have a 25-second readout cadence and two with a 2.5-second cadence, providing a wide FOV of 2,232 square degrees and a large photometric magnitude range from 4 to 16 mag. During its six-year-long planned mission, PLATO's main purpose will be to conduct two long-observing runs of three years each, observing at a time resolution of 50 seconds. These runs will be followed by a sequence of shorter runs, in which particularly interesting planetary systems can be re-

observed or additional research can be performed, such as observations of population II stars or open clusters, to improve stellar evolution models. The observation fields of these long and short runs are roughly shown with yellow-green and green circles in Fig. 8.1. The original sketch can be found in Rauer et al. (2014). The targets in these fields will be similar to that of Kepler. However, PLATO will observe a larger number of stars over the mission. It will survey up to 1,000,000 stars, as well as detect and characterize hundreds of small and thousands of giant planets. Asteroseismology will be performed on these bright stars to obtain highly accurate stellar parameters, including masses and ages (Rauer et al., 2014).

As presented in Fig. 8.1, even though Kepler (brown circle) and CoRoT (pink circles) are not able to observe the sample stars studied in this thesis, the FOVs of PLATO and K2 intersect with that of the *STEREO*. In addition, the FOVs of TESS and SMEI missions cover almost the entire expanse of the sky, which also includes the observation path of the *STEREO*. As a consequence, it would not be surprising to find the data of some sample stars in these missions. If the five-year observation duration and the number of current data can be increased in this way, the uncertainties regarding the internal structures of targets and their evolutionary processes can be understood much more clearly.

List of References

AAVSO. American association of variable star observers, June 2010. URL http://www.aavso.org/vsots_delsct.

H. A. Abt. The Frequency of Binaries among Metalmc-Line Stars. *apjs*, 6:37, March 1961. doi: 10.1086/190060.

H. A. Abt. New Data on A-Type Disk Stars. *apjs*, 174:499–503, February 2008. doi: 10.1086/522698.

H. A. Abt. Why are There Normal Slow Rotators Among A-Type Stars? *aj*, 138:28–32, July 2009. doi: 10.1088/0004-6256/138/1/28.

H. A. Abt and O. Cardona. Be stars in binaries. *apj*, 285:190–194, October 1984. doi: 10.1086/162490.

M. G. Adam. The magnetic variable HD 125248. *The Observatory*, 85:204–206, October 1965.

S. J. Adelman, C.-L. M. Pi, and K. E. Rayle. UVBY photometry of 33 Tauri, HD 50169, and HR 7786 and an assessment of FCAPT comparison stars. *aaps*, 133:197–200, December 1998. doi: 10.1051/aas:1998313.

S. J. Adelman, V. Malanushenko, T. A. Ryabchikova, and I. Savanov. On the rotation of the chemically peculiar magnetic star 56 Arietis. *aap*, 375:982–988, September 2001. doi: 10.1051/0004-6361:20010895.

C. Aerts, J. Christensen-Dalsgaard, and D. W. Kurtz. *Asteroseismology*. 2010.

C. Alcock, R. A. Allsman, D. R. Alves, T. S. Axelrod, A. C. Becker, D. P. Bennett, K. H. Cook, K. C. Freeman, M. Geha, K. Griest, M. J. Lehner, S. L. Marshall, B. J. McNamara, D. Minniti, C. Nelson, B. A. Peterson, P. Popowski, M. R. Pratt, P. J. Quinn, A. W. Rodgers,

W. Sutherland, M. R. Templeton, T. Vandehei, and D. L. Welch. The MACHO Project Sample of Galactic Bulge High-Amplitude δ Scuti Stars: Pulsation Behavior and Stellar Properties. *apj*, 536:798–815, June 2000. doi: 10.1086/308979.

E. Alecian. Magnetic fields along the pre-main-sequence phase. In G. Mathys, E. R. Griffin, O. Kochukhov, R. Monier, and G. M. Wahlgren, editors, *Putting A Stars into Context: Evolution, Environment, and Related Stars*, pages 84–92, November 2014.

Y. Andrillat and C. Fehrenbach. Study of H-alpha profile in 72 Be stars. *aaps*, 48:93–136, April 1982.

K. M. V. Apparao, S. P. Tarafdar, R. P. Verma, K. V. K. Iyengar, and K. K. Ghosh. Simultaneous infrared and H-alpha measurements of Be stars. *Journal of Astrophysics and Astronomy*, 14:131–134, December 1993. doi: 10.1007/BF02702362.

J. H. Applegate. A mechanism for orbital period modulation in close binaries. *apj*, 385:621–629, February 1992. doi: 10.1086/170967.

T. Arentoft, C. Sterken, M. R. Knudsen, G. Handler, P. Niarchos, K. Gazeas, V. Manimanis, M. B. Moalusi, F. F. Vuthela, and P. Van Cauteren. Irregular amplitude variations and another abrupt period change in the δ Scuti star V 1162 Ori. *aap*, 378:L33–L36, October 2001. doi: 10.1051/0004-6361:20011248.

H. W. Babcock. The Magnetically Variable Star HD 125248. *apj*, 114:1, July 1951. doi: 10.1086/145448.

H. W. Babcock. Stellar Magnetic Fields. In J. L. Greenstein, editor, *Stellar Atmospheres*, page 282, January 1960.

N. Baker and R. Kippenhahn. The Pulsations of Models of δ Cephei Stars. With 17 Figures in the Text. *zap*, 54:114, 1962.

L. A. Balona. Short-period variability in Be stars. *mnras*, 245:92–100, July 1990.

L. A. Balona. Mode density and frequency extraction in the δ Scuti star HD 50844. *mnras*, 439: 3453–3460, April 2014. doi: 10.1093/mnras/stu193.

L. A. Balona and D. J. James. Short-period line profile and light variations in the Be star λ Eridani. *mnras*, 332:714–722, May 2002. doi: 10.1046/j.1365-8711.2002.05336.x.

L. A. Balona, A. Pigulski, P. D. Cat, G. Handler, J. Gutiérrez-Soto, C. A. Engelbrecht, F. Frescura, M. Briquet, J. Cuypers, J. Daszyńska-Daszkiewicz, P. Degroote, R. J. Dukes, R. A. Garcia, E. M. Green, U. Heber, S. D. Kawaler, H. Lehmann, B. Leroy, J. Molenda-Żaaowicz, C. Neiner, A. Noels, J. Nuspl, R. Østensen, D. Pricopi, I. Roxburgh, S. Salmon, M. A. Smith, J. C. Suárez, M. Suran, R. Szabó, K. Uytterhoeven, J. Christensen-Dalsgaard, H. Kjeldsen, D. A. Caldwell, F. R. Girouard, and D. T. Sanderfer. Kepler observations of the variability in B-type stars. *mnras*, 413:2403–2420, June 2011a. doi: 10.1111/j.1365-2966.2011.18311.x.

L. A. Balona, V. Ripepi, G. Catanzaro, D. W. Kurtz, B. Smalley, P. De Cat, L. Eyer, A. Grigahcène, S. Leccia, J. Southworth, K. Uytterhoeven, H. van Winckel, J. Christensen-Dalsgaard, H. Kjeldsen, D. A. Caldwell, J. van Cleve, and F. R. Girouard. Kepler observations of Am stars. *mnras*, 414:792–800, June 2011b. doi: 10.1111/j.1365-2966.2011.18454.x.

L. A. Balona, M. Breger, G. Catanzaro, M. S. Cunha, G. Handler, Z. Kołaczkowski, D. W. Kurtz, S. Murphy, E. Niemczura, M. Paparó, B. Smalley, R. Szabó, K. Uytterhoeven, J. L. Christiansen, K. Uddin, and M. C. Stumpe. Unusual high-frequency oscillations in the Kepler δ Scuti star KIC 4840675. *mnras*, 424:1187–1196, August 2012. doi: 10.1111/j.1365-2966.2012.21295.x.

D. P. K. Banerjee, S. D. Rawat, and P. Janardhan. Hα observations of Be stars. *aaps*, 147: 229–242, December 2000. doi: 10.1051/aas:2000299.

P. K. Barker. The shell episode of 59 Cygni /1974-1975/. *apjs*, 49:89–109, May 1982. doi: 10.1086/190791.

P. K. Barker and E. R. Anderson. V4024 Sagittarii = MWC 311. *iaucirc*, 3712:2, July 1982.

A. H. Batten. Two Centuries of Study of Algol Systems. *ssr*, 50:1–8, June 1989. doi: 10.1007/BF00215914.

D. Bewsher, D. S. Brown, C. J. Eyles, B. J. Kellett, G. J. White, and B. Swinyard. Determination of the Photometric Calibration and Large-Scale Flatfield of the STEREO Heliospheric Imagers: I. HI-1. *solphys*, 264:433–460, July 2010. doi: 10.1007/s11207-010-9582-8.

C. Blanco, F. A. Catalano, and G. Strazzulla. Photoelectric observations of the Ap stars HD 125248, HD 134798 and HD 184905. *aaps*, 31:205–208, February 1978.

S. Blažko. Mitteilung über veränderliche Sterne. *Astronomische Nachrichten*, 175:325, August 1907. doi: 10.1002/asna.19071752002.

R. Blomme, L. Mahy, C. Catala, J. Cuypers, E. Gosset, M. Godart, J. Montalban, P. Ventura, G. Rauw, T. Morel, P. Degroote, C. Aerts, A. Noels, E. Michel, F. Baudin, A. Baglin, M. Auvergne, and R. Samadi. Variability in the CoRoT photometry of three hot O-type stars. HD 46223, HD 46150, and HD 46966. *aap*, 533:A4, September 2011. doi: 10.1051/0004-6361/201116949.

T. Borkovits and T. Hegedues. On the invisible components of some eclipsing binaries. *aaps*, 120:63–75, November 1996.

E. F. Borra, A. Beaulieu, D. Brousseau, and I. Shelton. The periods of rotation of the magnetic peculiar stars in the Scorpio-Centaurus association - No evidence of braking on the main-sequence. *aap*, 149:266–272, August 1985.

M. Bossi, G. Guerrero, L. Mantegazza, and M. Scardia. Study of the variability of the Delta Scuti stars. VI Pulsational behaviour of HR 1392 (69 Tau). *aaps*, 53:395–397, September 1983.

M. Bossi, G. Guerrero, and G. Bianchini. Photometric Multiperiodicity of the Be Star 120 Tauri. *Information Bulletin on Variable Stars*, 3348:1, July 1989.

M. Bossi, L. Mantegazza, and E. Poretti. Simultaneous photometric and spectroscopic observations of FG VIR (= HD 106384). *Delta Scuti Star Newsletter*, 6:3–4, May 1993.

M. Bossi, G. Guerrero, M. Scardia, and M. Tadini. Rapid spectroscopic variability in the Be star 48 Lib, December 1994. Be Star Newsletter.

D. M. Bowman, D. L. Holdsworth, and D. W. Kurtz. Combining WASP and Kepler data: the case of the δ Sct star KIC 7106205. *mnras*, 449:1004–1010, May 2015. doi: 10.1093/mnras/stv364.

M. Breger. Delta Scuti and related stars. *pasp*, 91:5–26, February 1979. doi: 10.1086/130433.

M. Breger. δ Scuti stars (Review). In M. Breger and M. Montgomery, editors, *Delta Scuti and Related Stars*, volume 210 of *Astronomical Society of the Pacific Conference Series*, page 3, 2000.

M. Breger. Delta Scuti stars: Observational aspects. *Communications in Asteroseismology*, 150: 25, June 2007. doi: 10.1553/cia150s25.

M. Breger. Period Variations of Delta Scuti Stars. In J. A. Guzik and P. A. Bradley, editors, *American Institute of Physics Conference Series*, volume 1170 of *American Institute of Physics Conference Series*, pages 410–414, September 2009. doi: 10.1063/1.3246530.

M. Breger and J. N. Bregman. Period-luminosity-color relations and pulsation modes of pulsating variable stars. *apj*, 200:343–353, September 1975. doi: 10.1086/153794.

M. Breger and A. A. Pamyatnykh. Period changes of Delta Scuti stars and stellar evolution. *Delta Scuti Star Newsletter*, 12:7–7, July 1998a.

M. Breger and A. A. Pamyatnykh. Period changes of delta Scuti stars and stellar evolution. *aap*, 332:958–968, April 1998b.

M. Breger and A. A. Pamyatnykh. Amplitude variability or close frequencies in pulsating stars - the δ Scuti star FG Vir. *mnras*, 368:571–578, May 2006. doi: 10.1111/j.1365-2966.2006.10119.x.

M. Breger, J. Stich, R. Garrido, B. Martin, S. Y. Jiang, Z. P. Li, D. P. Hube, W. Ostermann, M. Paparo, and M. Scheck. Nonradial Pulsation of the Delta-Scuti Star Bu-Cancri in the Praesepe Cluster. *aap*, 271:482, April 1993.

M. Breger, G. Handler, R. E. Nather, D. E. Winget, S. J. Kleinman, D. J. Sullivan, Z.-P. Li, J. E. Solheim, S.-Y. Jiang, Z.-L. Liu, M. A. Wood, T. K. Watson, W. A. Dziembowski, E. Serkowitsch, H. Mendelson, J. C. Clemens, J. Krzesinski, and G. Pajdosz. The δ Scuti star FG Virginis. I. Multiple pulsation frequencies determined with a combined DSN/WET campaign. *aap*, 297:473, May 1995.

M. Breger, G. Handler, E. Serkowitsch, P. Reegen, J. Provencal, M. A. Wood, J. C. Clemens, M. S. O'Brien, D. E. Winget, R. E. Nather, S. J. Kleinman, A. Kanaan, T. K. Watson, M. H. Montgomery, P. A. Bradley, D. J. Sullivan, E. Leibowitz, H. Mendelson, J. Krzesinski, G. Pajdosz, P. Moskalik, and J.-E. Solheim. The δ Scuti star FG Virginis. II. A search for high pulsation frequencies. *aap*, 309:197–202, May 1996.

M. Breger, W. Zima, G. Handler, E. Poretti, R. R. Shobbrook, A. Nitta, O. R. Prouton, R. Garrido, E. Rodriguez, and T. Thomassen. The delta Scuti star FG Vir. III. The 1995

multisite campaign and the detection of 24 pulsation frequencies. *aap*, 331:271–279, March 1998.

M. Breger, G. Handler, R. Garrido, N. Audard, W. Zima, M. Paparó, F. Beichbuchner, Z.-P. Li, S.-Y. Jiang, Z.-L. Liu, A.-Y. Zhou, H. Pikall, A. Stankov, J. A. Guzik, M. Sperl, J. Krzesinski, W. Ogloza, G. Pajdosz, S. Zola, T. Thomassen, J.-E. Solheim, E. Serkowitsch, P. Reegen, T. Rumpf, A. Schmalwieser, and M. H. Montgomery. 30+ frequencies for the delta Scuti variable 4 Canum Venaticorum: results of the 1996 multisite campaign. *aap*, 349:225–235, September 1999a.

M. Breger, A. A. Pamyatnykh, H. Pikall, and R. Garrido. The delta Scuti star FG Virginis. IV. Mode identifications and pulsation modelling. *aap*, 341:151–162, January 1999b.

M. Breger, F. Rodler, M. L. Pretorius, S. Martín-Ruiz, P. J. Amado, V. Costa, R. Garrido, P. López de Coca, I. Olivares, E. Rodríguez, A. Rolland, T. Tshenye, G. Handler, E. Poretti, J. P. Sareyan, M. Alvarez, P. M. Kilmartin, and W. Zima. The δ Scuti star FG Vir. V. The 2002 photometric multisite campaign. *aap*, 419:695–701, May 2004. doi: 10.1051/0004-6361:20035830.

M. Breger, P. Lenz, V. Antoci, E. Guggenberger, R. R. Shobbrook, G. Handler, B. Ngwato, F. Rodler, E. Rodriguez, P. López de Coca, A. Rolland, and V. Costa. Detection of 75+ pulsation frequencies in the δ Scuti star FG Virginis. *aap*, 435:955–965, June 2005. doi: 10.1051/0004-6361:20042480.

M. Breger, P. Lenz, and A. A. Pamyatnykh. Towards mode selection in δ Scuti stars: regularities in observed and theoretical frequency spectra. *mnras*, 396:291–298, June 2009. doi: 10.1111/j.1365-2966.2008.14330.x.

M. Breger, L. Balona, P. Lenz, J. K. Hollek, D. W. Kurtz, G. Catanzaro, M. Marconi, A. A. Pamyatnykh, B. Smalley, J. C. Suárez, R. Szabo, K. Uytterhoeven, V. Ripepi, J. Christensen-Dalsgaard, H. Kjeldsen, M. N. Fanelli, K. A. Ibrahim, and K. Uddin. Regularities in frequency spacings of δ Scuti stars: the Kepler star KIC 9700322. *mnras*, 414:1721–1731, June 2011. doi: 10.1111/j.1365-2966.2011.18508.x.

M. Breger, M. Hareter, M. Endl, R. Kuschnig, W. W. Weiss, J. M. Matthews, D. B. Guenther, A. F. J. Moffat, J. F. Rowe, S. M. Rucinski, and D. Sasselov. Delta Scuti stars in the Praesepe

cluster observed by the MOST satellite. *Astronomische Nachrichten*, 333:131, February 2012. doi: 10.1002/asna.201111640.

D. S. Brown, D. Bewsher, and C. J. Eyles. Calibrating the Pointing and Optical Parameters of the STEREO Heliospheric Imagers. *solphys*, 254:185–225, January 2009. doi: 10.1007/s11207-008-9277-6.

J. C. Brown, J. P. Cassinelli, and M. Maheswaran. Magnetically Fed Hot Star Keplerian Disks with Slow Outflow. *apj*, 688:1320–1325, December 2008. doi: 10.1086/592558.

E. M. Burbidge and G. R. Burbidge. Spectrographic Observations of Emission-Line Stars. *apj*, 119:496, May 1954. doi: 10.1086/145855.

E. W. Burke, Jr., W. W. Rolland, and W. R. Boy. A Photoelectric Study of Magnetic Variable Stars. *jrasc*, 64:353, December 1970.

C. Cameron, H. Saio, R. Kuschnig, G. A. H. Walker, J. M. Matthews, D. B. Guenther, A. F. J. Moffat, S. M. Rucinski, D. Sasselov, and W. W. Weiss. MOST Detects SPBe Pulsations in HD 127756 and HD 217543: Asteroseismic Rotation Rates Independent of vsini. *apj*, 685: 489–507, September 2008. doi: 10.1086/590369.

H. Cao, J. Hao, H. F. Henrichs, E. J. Kennelly, J. E. Neff, A. Hatzes, C. Schrijvers, D. Yang, and L. Huang. NRP observation of the Delta Scuti star V480 Tau. In K. L. Chan, K. S. Cheng, and H. P. Singh, editors, *1997 Pacific Rim Conference on Stellar Astrophysics*, volume 138 of *Astronomical Society of the Pacific Conference Series*, page 33, 1998.

A. C. Carciofi, A. T. Okazaki, J.-B. Le Bouquin, S. Štefl, T. Rivinius, D. Baade, J. E. Bjorkman, and C. A. Hummel. Cyclic variability of the circumstellar disk of the Be star ζ Tauri. II. Testing the 2D global disk oscillation model. *aap*, 504:915–927, September 2009. doi: 10.1051/0004-6361/200810962.

F. A. Catalano and P. Renson. Observed Periods of Ap and Bp stars (Catalano+ 1998). *VizieR Online Data Catalog*, 3199:0, November 1997.

F. A. Catalano, R. Kroll, and F. Leone. The near-infrared variation of the magnetic star HD 125248. *aap*, 263:203–207, September 1992.

F. A. Catalano, F. Leone, and R. Kroll. Near infrared light variations of CP stars. The SiSrCrEu stars. *aaps*, 131:63–72, July 1998. doi: 10.1051/aas:1998423.

G. Catanzaro. Spectroscopic atlas of Hα and Hβ in a sample of northern Be stars. *aap*, 550: A79, February 2013. doi: 10.1051/0004-6361/201220357.

J. Cernicharo, R. Bachiller, and G. Duvert. The Taurus-Auriga-Perseus complex of dark clouds. I - Density structure. *aap*, 149:273–282, August 1985.

X. Chen and Z. Han. Low- and intermediate-mass close binary evolution and the initial-final mass relation - II. Non-conservative case with convective overshooting. *mnras*, 335:948–964, October 2002. doi: 10.1046/j.1365-8711.2002.05680.x.

J. Christensen-Dalsgaard. Pulsation theory and stellar structure. In W. W. Weiss and A. Baglin, editors, *IAU Colloq. 137: Inside the Stars*, volume 40 of *Astronomical Society of the Pacific Conference Series*, pages 483–496, January 1993.

J. Christensen-Dalsgaard. Stellar oscillations, May 2003. URL `http://astro.phys.au.dk/ jcd/oscilnotes/`.

J. Christensen-Dalsgaard. An Overview of Helio- and Asteroseismology. In D. Danesy, editor, *SOHO 14 Helio- and Asteroseismology: Towards a Golden Future*, volume 559 of *ESA Special Publication*, page 1, October 2004.

J. S. Clark and I. A. Steele. A representative sample of Be stars. II. K band spectroscopy. *aaps*, 141:65–77, January 2000. doi: 10.1051/aas:2000310.

G. W. Collins, II. The use of terms and definitions in the study of Be stars. In A. Slettebak and T. P. Snow, editors, *IAU Colloq. 92: Physics of Be Stars*, pages 3–19, 1987.

J. Cote and L. B. F. M. Waters. IRAS observations of Be stars. I - Statistical study of the IR excess of 101 Be stars. *aap*, 176:93–106, April 1987.

A. N. Cox and C. A. Pilachowski. Allen's Astrophysical Quantities. *Physics Today*, 53(10): 100000, October 2000. doi: 10.1063/1.1325201.

A. N. Cox, S. W. Hodson, and D. S. King. Theoretical pulsation of metallic-line stars. *apj*, 231: 798–807, August 1979. doi: 10.1086/157245.

N. Cramer, V. Doazan, B. Nicolet, A. de La Fuente, and M. Barylak. Colour and light variations of PLEIONE between the Be and shell phases. *aap*, 301:811, September 1995.

S. R. Cranmer. A Statistical Study of Threshold Rotation Rates for the Formation of Disks around Be Stars. *apj*, 634:585–601, November 2005. doi: 10.1086/491696.

S. R. Cranmer. A Pulsational Mechanism for Producing Keplerian Disks Around Be Stars. *apj*, 701:396–413, August 2009. doi: 10.1088/0004-637X/701/1/396.

J. Cuypers, L. A. Balona, and F. Marang. Intensive photometry of southern Be variables. I - Winter objects. *aaps*, 81:151–186, December 1989.

J. Daszyńska-Daszkiewicz, W. A. Dziembowski, A. A. Pamyatnykh, M. Breger, W. Zima, and G. Houdek. Inferences from pulsational amplitudes and phases for multimode δ Sct star FG Vir. *aap*, 438:653–660, August 2005. doi: 10.1051/0004-6361:20052902.

J. Daszyńska-Daszkiewicz, W. Szewczuk, and P. Walczak. The β Cep/SPB star 12 Lacertae: extended mode identification and complex seismic modelling. *mnras*, 431:3396–3407, June 2013. doi: 10.1093/mnras/stt418.

C. J. Davis and R. A. Harrison. STEREO/HI from near-Earth objects to 3D comets. *Advances in Space Research*, 36:1524–1529, 2005. doi: 10.1016/j.asr.2005.01.001.

D. W. Dawson, M. Breger, and P. Lopez de Coca. A Photometric Study of the delta Scuti Star FG Virginis Undertaken during 1985/6. *pasp*, 107:517–520, June 1995. doi: 10.1086/133585.

J. H. J. de Bruijne, R. Hoogerwerf, and P. T. de Zeeuw. A Hipparcos study of the Hyades open cluster. Improved colour-absolute magnitude and Hertzsprung-Russell diagrams. *aap*, 367: 111–147, February 2001a. doi: 10.1051/0004-6361:20000410.

J. H. J. de Bruijne, R. Hoogerwerf, and P. T. de Zeeuw. A Hipparcos study of the Hyades open cluster. Improved colour-absolute magnitude and Hertzsprung-Russell diagrams. *aap*, 367: 111–147, February 2001b. doi: 10.1051/0004-6361:20000410.

P. De Cat. *An observational study of bright southern slowly pulsating B stars*. PhD thesis, Institute of Astronomy, Katholieke Universiteit Leuven, Belgium, May 2001.

J. De Ridder. *Contributions to the interpretation of line-profile variations of pulsating B-stars*. PhD thesis, Institute of Astronomy, Katholieke Universiteit Leuven, Belgium, 2001.

P. Degroote, C. Aerts, A. Baglin, A. Miglio, M. Briquet, A. Noels, E. Niemczura, J. Montalban, S. Bloemen, R. Oreiro, M. Vučković, K. Smolders, M. Auvergne, F. Baudin, C. Catala, and E. Michel. Deviations from a uniform period spacing of gravity modes in a massive star. *nat*, 464:259–261, March 2010. doi: 10.1038/nature08864.

A. J. Deutsch. A Study of the Spectrum Variables of Type a. *apj*, 105:283, March 1947. doi: 10.1086/144904.

M. P. Di Mauro, J. Christensen-Dalsgaard, F. Pijpers, and J. Hao. An Attempt at Mode Identification for V480 Tau. In C. Aerts, T. R. Bedding, and J. Christensen-Dalsgaard, editors, *IAU Colloq. 185: Radial and Nonradial Pulsationsn as Probes of Stellar Physics*, volume 259 of *Astronomical Society of the Pacific Conference Series*, pages 336–337, 2002.

P. D. Diago, J. Gutiérrez-Soto, M. Auvergne, J. Fabregat, A.-M. Hubert, M. Floquet, Y. Frémat, R. Garrido, L. Andrade, B. de Batz, M. Emilio, F. Espinosa Lara, A.-L. Huat, E. Janot-Pacheco, B. Leroy, C. Martayan, C. Neiner, T. Semaan, J. Suso, C. Catala, E. Poretti, M. Rainer, K. Uytterhoeven, E. Michel, and R. Samadi. Pulsations in the late-type Be star HD 50 209 detected by CoRoT. *aap*, 506:125–131, October 2009. doi: 10.1051/0004-6361/200911901.

P. D. Diago, J. Gutiérrez-Soto, J. Fabregat, C. Martayan, and J. Suso. Pulsating B and Be Stars in the Magellanic Clouds. In J. M. Diego, L. J. Goicoechea, J. I. González-Serrano, and J. Gorgas, editors, *Highlights of Spanish Astrophysics V*, page 401, 2010. doi: 10.1007/978-3-642-11250-8_99.

D. Dimitrov and K. Panov. Photometric and Spectroscopic Study of the Ellipsoidal Variable 33 Tau. In C. Sterken and C. Aerts, editors, *Astrophysics of Variable Stars*, volume 349, pages 229–232, 2006.

Z. H. Draper, J. P. Wisniewski, K. S. Bjorkman, M. R. Meade, X. Haubois, B. C. Mota, A. C. Carciofi, and J. E. Bjorkman. Disk-loss and Disk-renewal Phases in Classical Be Stars. II. Contrasting with Stable and Variable Disks. *apj*, 786:120, May 2014. doi: 10.1088/0004-637X/786/2/120.

P. Dubath, L. Rimoldini, M. Süveges, J. Blomme, M. López, L. M. Sarro, J. De Ridder, J. Cuypers, L. Guy, I. Lecoeur, K. Nienartowicz, A. Jan, M. Beck, N. Mowlavi, P. De Cat,

T. Lebzelter, and L. Eyer. Random forest automated supervised classification of Hipparcos periodic variable stars. *mnras*, 414:2602–2617, July 2011. doi: 10.1111/j.1365-2966.2011.18575.x.

W. Dziembowski. Nonlinear mode coupling in oscillating stars. I - Second order theory of the coherent mode coupling. *actaa*, 32:147–171, 1982.

A. S. Eddington. Stars, Gaseous, On the pulsations of a gaseous star. *mnras*, 79:2–22, November 1918.

O. J. Eggen. The Nature of the Blue Stragglers in the Old Disk Population. *pasp*, 83:762, December 1971. doi: 10.1086/129212.

C. J. Eyles, G. M. Simnett, M. P. Cooke, B. V. Jackson, A. Buffington, P. P. Hick, N. R. Waltham, J. M. King, P. A. Anderson, and P. E. Holladay. The Solar Mass Ejection Imager (Smei). *solphys*, 217:319–347, November 2003. doi: 10.1023/B:SOLA.0000006903.75671.49.

C. J. Eyles, R. A. Harrison, C. J. Davis, N. R. Waltham, B. M. Shaughnessy, H. C. A. Mapson-Menard, D. Bewsher, S. R. Crothers, J. A. Davies, G. M. Simnett, R. A. Howard, J. D. Moses, J. S. Newmark, D. G. Socker, J.-P. Halain, J.-M. Defise, E. Mazy, and P. Rochus. The Heliospheric Imagers Onboard the STEREO Mission. *solphys*, 254:387–445, February 2009. doi: 10.1007/s11207-008-9299-0.

A. Feinstein and H. G. Marraco. The photometric behavior of Be Stars. *aj*, 84:1713–1725, November 1979. doi: 10.1086/112600.

N. I. Fisher, T. Lewis, and B. J. J. Embleton. *Statistical analysis of spherical data*. 1987.

W. S. Fitch. L O,1,2, and 3 Pulsation Constants for Evolutionary Models of Delta-Scuti Stars. *apj*, 249:218, October 1981. doi: 10.1086/159278.

M. P. Fitzgerald. The Intrinsic Colours of Stars and Two-Colour Reddening Lines. *aap*, 4:234, February 1970.

M. Floquet, A. M. Hubert, H. Hubert, E. Janot-Pacheco, S. Caillet, and N. V. Leister. A search for multiperiodic line profile variations in the Be star 48 Librae. *aap*, 310:849–856, June 1996.

P. J. Flower. Transformations from Theoretical H-R Diagrams to C-M Diagrams. *aap*, 54:31, January 1977.

P. J. Flower. Transformations from Theoretical Hertzsprung-Russell Diagrams to Color-Magnitude Diagrams: Effective Temperatures, B-V Colors, and Bolometric Corrections. *apj*, 469:355, September 1996. doi: 10.1086/177785.

W. A. Fowler, E. M. Burbidge, G. R. Burbidge, and F. Hoyle. The Synthesis and Destruction of Elements in Peculiar Stars of Types a and B. *apj*, 142:423, August 1965. doi: 10.1086/148309.

Y. Frémat, J. Zorec, A.-M. Hubert, and M. Floquet. Effects of gravitational darkening on the determination of fundamental parameters in fast-rotating B-type stars. *aap*, 440:305–320, September 2005. doi: 10.1051/0004-6361:20042229.

J.-N. Fu, S.-Y. Jiang, and Z.-P. Li. Photoelectric photometry of 57 and 58 Tauri, two δ Scuti type stars in the Hyades cluster. *aaps*, 115:469–473, February 1996.

M. Fulle, F. Leblanc, R. A. Harrison, C. J. Davis, C. J. Eyles, J. P. Halain, R. A. Howard, D. Bockelée-Morvan, G. Cremonese, and T. Scarmato. Discovery of the Atomic Iron Tail of Comet MCNaught Using the Heliospheric Imager on STEREO. *apjl*, 661:L93–L96, May 2007. doi: 10.1086/518719.

A. García Hernández, A. Moya, E. Michel, J. C. Suárez, E. Poretti, S. Martín-Ruíz, P. J. Amado, R. Garrido, E. Rodríguez, M. Rainer, K. Uytterhoeven, C. Rodrigo, E. Solano, J. R. Rodón, P. Mathias, A. Rolland, M. Auvergne, A. Baglin, F. Baudin, C. Catala, and R. Samadi. An in-depth study of HD 174966 with CoRoT photometry and HARPS spectroscopy. Large separation as a new observable for δ Scuti stars. *aap*, 559:A63, November 2013. doi: 10.1051/0004-6361/201220256.

R. F. Garrison. Some Characteristics of the B and A Stars in the Upper Scorpius Complex. *apj*, 147:1003, March 1967. doi: 10.1086/149090.

M. Gebran, M. Vick, R. Monier, and L. Fossati. Chemical composition of A and F dwarfs members of the Hyades open cluster. *aap*, 523:A71, November 2010. doi: 10.1051/0004-6361/200913273.

K. Ghosh, K. V. K. Iyengar, B. D. Ramsey, and R. A. Austin. Near-simultaneous Spectroscopic and Broadband Polarimetric Observations ofBE Stars. *aj*, 118:1061–1072, August 1999. doi: 10.1086/300953.

A. E. Gomez, X. Luri, S. Grenier, F. Figueras, P. North, F. Royer, J. Torra, and M. O. Mennessier. The HR-diagram from HIPPARCOS data. Absolute magnitudes and kinematics of BP - AP stars. *aap*, 336:953–959, August 1998.

P. S. Goraya, N. Kumar, B. S. Salaria, and H. S. Ghumman. Spectroscopic Study of Four Members of Balmer Series in Be Stars. *Asian Journal of Chemistry*, 21:184–187, March 2009.

K. J. F. Goss, C. Karoff, W. J. Chaplin, Y. Elsworth, and I. R. Stevens. Variations of the amplitudes of oscillation of the Be star Achernar. *mnras*, 411:162–166, February 2011. doi: 10.1111/j.1365-2966.2010.17665.x.

D. O. Gough. On the rotation of the sun. *Royal Society of London Philosophical Transactions Series A*, 313:27–38, November 1984. doi: 10.1098/rsta.1984.0080.

D. O. Gough. EBK Quantization of Stellar Waves. In Y. Osaki, editor, *Hydrodynamic and Magnetodynamic Problems in the Sun and Stars*, page 117, 1986.

A. Grigahcène, V. Antoci, L. Balona, G. Catanzaro, J. Daszyńska-Daszkiewicz, J. A. Guzik, G. Handler, G. Houdek, D. W. Kurtz, M. Marconi, M. J. P. F. G. Monteiro, A. Moya, V. Ripepi, J.-C. Suárez, K. Uytterhoeven, W. J. Borucki, T. M. Brown, J. Christensen-Dalsgaard, R. L. Gilliland, J. M. Jenkins, H. Kjeldsen, D. Koch, S. Bernabei, P. Bradley, M. Breger, M. Di Criscienzo, M.-A. Dupret, R. A. García, A. García Hernández, J. Jackiewicz, A. Kaiser, H. Lehmann, S. Martín-Ruiz, P. Mathias, J. Molenda-Żakowicz, J. M. Nemec, J. Nuspl, M. Paparó, M. Roth, R. Szabó, M. D. Suran, and R. Ventura. Hybrid γ Doradus-δ Scuti Pulsators: New Insights into the Physics of the Oscillations from Kepler Observations. *apjl*, 713:L192–L197, April 2010. doi: 10.1088/2041-8205/713/2/L192.

H. G. Groth, R. P. Kudritzki, and U. Heber. Photospheric convection zones and evolution of subluminous OB-stars. *aap*, 152:107–116, November 1985.

E. D. Grundstrom, M. V. McSwain, C. Aragona, T. S. Boyajian, A. N. Marsh, and R. M. Roettenbacher. Observations of Be Disk Building: Optical Spectra of NW Serpentis (HD 168797) over 35 days. *Bulletin de la Societe Royale des Sciences de Liege*, 80:371–375, January 2011.

A. F. Gulliver, D. P. Hube, R. W. King, S. L. Morris, and G. Hill. The ellipsoidal variable 33 Tauri. II - Photometry and model. *aj*, 90:1334–1342, July 1985. doi: 10.1086/113839.

S. Gunasekera, J. Adassuriya, and N. I. Medagangoda. Observations of Ha Line Profiles in Be Stars Using 45 cm Cassegrain Telescope at Arthur C Clarke Institute. *Sun and Geosphere*, 3: 67–71, December 2008.

B. N. G. Guthrie. The origin of the peculiar A stars. *Publications of the Royal Observatory of Edinburgh*, 6:145–168, 1967.

J. Gutiérrez-Soto, J. Fabregat, J. Suso, M. Lanzara, R. Garrido, A.-M. Hubert, and M. Floquet. A photometric study of Be stars located in the seismology fields of COROT. *aap*, 476:927–933, December 2007. doi: 10.1051/0004-6361:20078252.

J. Gutiérrez-Soto, T. Semaan, R. Garrido, F. Baudin, A. . Hubert, and C. Neiner. Amplitude variations of the CoRoT Be star 102719279. *ArXiv e-prints*, October 2010.

G. Handler. *Asteroseismology*, page 207. 2013. doi: 10.1007/978-94-007-5615-1_4.

R. W. Hanuschik. On the structure of Be star disks. *aap*, 308:170–179, April 1996.

R. W. Hanuschik and M. Vrancken. Shell lines in 48 Lib: The discovery of narrow optical absorption components (NOACs). *aap*, 312:L17–L20, August 1996.

R. W. Hanuschik, W. Hummel, E. Sutorius, O. Dietle, and G. Thimm. Atlas of high-resolution emission and shell lines in Be stars. Line profiles and short-term variability. *aaps*, 116:309–358, April 1996.

M. Hareter, P. Reegen, A. Miglio, J. Montalban, A. Kaiser, I. Dekany, E. Guenther, E. Poretti, P. Mathias, and W. Weiss. Gamma Dor and Gamma Dor - Delta Sct Hybrid Stars In The CoRoT LRa01. *ArXiv e-prints*, July 2010.

M. Hareter, L. Fossati, W. Weiss, J. C. Suárez, K. Uytterhoeven, M. Rainer, and E. Poretti. Looking for a Connection between the Am Phenomenon and Hybrid δ Sct -γ Dor Pulsation: Determination of the Fundamental Parameters and Abundances of HD 114839 and BD +18 4914. *apj*, 743:153, December 2011. doi: 10.1088/0004-637X/743/2/153.

M. Hareter, M. Paparó, W. Weiss, A. García Hernández, T. Borkovits, P. Lampens, M. Rainer, P. De Cat, P. Marcos-Arenal, J. Vos, E. Poretti, A. Baglin, E. Michel, F. Baudin, and C. Catala. HD 51844: An Am δ Scuti in a binary showing periastron brightening. *aap*, 567: A124, July 2014. doi: 10.1051/0004-6361/201423801.

W. E. Harper. Measures of radial velocity of [kappa] Cassiopeiae, g Persei, 69 Tauri and [epsilon] Cygni. *Publications of the Dominion Observatory Ottawa*, 4:309–330, 1920.

O. Havnes and P. S. Conti. Magnetic accretion processes in peculiar A stars. *aap*, 14:1–11, 1971.

J. F. Heard. Five Newly Discovered Be Stars. *jrasc*, 33:384, November 1939.

H. Hensberge, C. De Loore, E. J. Zuiderwijk, and G. Hammerschlag-Hensberge. Photometry of silicon stars. *aap*, 54:443–449, January 1977.

H. Hensberge, C. Sterken, T. van der Linden, and G. Hammerschlag-Hensberge. Photometry of silicon stars. II. *aaps*, 34:67–71, October 1978.

R. Hirata and Y. Asada. Spectroscopic observations of suspected Be stars. *pasj*, 28:713–716, 1976.

M. S. Hockey. Spectrophotometric observations of the magnetic variable HD 125248. *mnras*, 142:543, 1969.

D. Hoffleit. History of the Discovery of Mira Stars. *Journal of the American Association of Variable Star Observers (JAAVSO)*, 25:115–136, 1997.

M. M. Hohle, R. Neuhäuser, and B. F. Schutz. Masses and luminosities of O- and B-type stars and red supergiants. *Astronomische Nachrichten*, 331:349, April 2010. doi: 10.1002/asna.200911355.

S. Horan. A photometric survey of the Hyades for Delta Scuti variables. *aj*, 84:1770–1774, November 1979. doi: 10.1086/112607.

J. H. Horne and S. L. Baliunas. A prescription for period analysis of unevenly sampled time series. *apj*, 302:757–763, March 1986. doi: 10.1086/164037.

R. A. Hounsell, M. F. Bode, M. J. Darnley, D. J. Harman, P. P. Hick, A. Buffington, B. V. Jackson, J. M. Clover, and A. W. Shafter. Variable Stellar Object Detection and Light Curves from the Solar Mass Ejection Imager (SMEI). In E. Griffin, R. Hanisch, and R. Seaman, editors, *IAU Symposium*, volume 285 of *IAU Symposium*, pages 91–94, April 2012. doi: 10.1017/S1743921312000312.

S. B. Howell, C. Sobeck, M. Haas, M. Still, T. Barclay, F. Mullally, J. Troeltzsch, S. Aigrain, S. T. Bryson, D. Caldwell, W. J. Chaplin, W. D. Cochran, D. Huber, G. W. Marcy, A. Miglio, J. R. Najita, M. Smith, J. D. Twicken, and J. J. Fortney. The K2 Mission: Characterization and Early Results. *pasp*, 126:398–408, April 2014. doi: 10.1086/676406.

A.-L. Huat, A.-M. Hubert, F. Baudin, M. Floquet, C. Neiner, Y. Frémat, J. Gutiérrez-Soto, L. Andrade, B. de Batz, P. D. Diago, M. Emilio, F. Espinosa Lara, J. Fabregat, E. Janot-Pacheco, B. Leroy, C. Martayan, T. Semaan, J. Suso, M. Auvergne, C. Catala, E. Michel, and R. Samadi. The B0.5IVe CoRoT target HD 49330. I. Photometric analysis from CoRoT data. *aap*, 506:95–101, October 2009. doi: 10.1051/0004-6361/200911928.

E. P. Hubble. A spiral nebula as a stellar system, Messier 31. *apj*, 69:103–158, March 1929. doi: 10.1086/143167.

D. P. Hube. The ellipsoidal variable 33 Tauri. I - Spectroscopic orbit. *aj*, 86:1394–1396, September 1981. doi: 10.1086/113020.

A. M. Hubert and M. Floquet. Investigation of the variability of bright Be stars using HIPPARCOS photometry. *aap*, 335:565–572, July 1998.

A.-M. Hubert-Delplace and H. Hubert. *An atlas of Be stars*. 1979.

S. Hubrig and G. Mathys. The evolutionary state of magnetic AP stars. *Astronomische Nachrichten*, 315:343–348, August 1994.

S. Hubrig, P. North, and G. Mathys. Magnetic AP Stars in the Hertzsprung-Russell Diagram. *apj*, 539:352–363, August 2000. doi: 10.1086/309189.

S. Hubrig, N. Nesvacil, M. Schöller, P. North, G. Mathys, D. W. Kurtz, B. Wolff, T. Szeifert, M. S. Cunha, and V. G. Elkin. Detection of an extraordinarily large magnetic field in the unique ultra-cool Ap star HD 154708. *aap*, 440:L37–L40, September 2005. doi: 10.1051/0004-6361:200500164.

S. Hubrig, M. Schöller, I. Savanov, R. V. Yudin, M. A. Pogodin, S. Štefl, T. Rivinius, and M. Curé. Magnetic survey of emission line B-type stars with FORS 1 at the VLT. *Astronomische Nachrichten*, 330:708, July 2009. doi: 10.1002/asna.200911236.

N. J. Irvine. New bright hydrogen emission stars III. *pasp*, 102:669–673, June 1990. doi: 10.1086/132689.

M. M. Jarad, R. W. Hilditch, and I. Skillen. A radial-velocity study of 18 emission-line B stars. *mnras*, 238:1085–1106, June 1989.

T. Jarzębowski. Relation between Light-variation and Magnetic Variation in Magnetic Alpha Variables. *actaa*, 10:31, 1960.

C. Jaschek and M. Jaschek. A southern Be star survey - Spectra and envelope radii. *aaps*, 95: 535–540, November 1992.

M. Jaschek, C. Jaschek, A.-M. Hubert-Delplace, and H. Hubert. A classification of Be stars. *aaps*, 42:103–114, October 1980.

M. Jerzykiewicz. HD 90386: A New Short-Period Variable Star. *pasp*, 84:529, August 1972. doi: 10.1086/129327.

M. Jerzykiewicz. The Period and the Cause of Variability of the Magnetic Ap Star V473 Tauri. *actaa*, 59:307–323, September 2009.

C. Jones and J. R. Percy. Book review: Understanding variable stars (Percy). *Journal of the British Astronomical Association*, 117:281, October 2007.

C. E. Jones, C. Tycner, and A. D. Smith. The Variability of Hα Equivalent Widths in Be Stars. *aj*, 141:150, May 2011. doi: 10.1088/0004-6256/141/5/150.

T. Kallinger and J. M. Matthews. Evidence for Granulation in Early A-Type Stars. *apjl*, 711: L35–L39, March 2010. doi: 10.1088/2041-8205/711/1/L35.

S. D. Kawaler. The Stellar Seismology of the Hot White Dwarf Star PG:1159-035. In J. Christensen-Dalsgaard and S. Frandsen, editors, *Advances in Helio- and Asteroseismology*, volume 123 of *IAU Symposium*, page 329, 1988.

S. M. Kay and S. L. Marple. Spectrum Analysis - A Modern Perspective. *IEEE Proceedings*, 69:1380–1419, 1981.

A. B. Kaye. 57 Tau = HD 27397 - A Spectroscopic Binary. *Information Bulletin on Variable Stars*, 4697:1, April 1999.

E. J. Kennelly, T. M. Brown, R. Kotak, T. A. A. Sigut, S. D. Horner, S. G. Korzennik, P. Nisenson, R. W. Noyes, A. Walker, and S. Yang. The Oscillations of Tau Pegasi. *apj*, 495:440, March 1998. doi: 10.1086/305268.

N. V. Kharchenko. All-sky compiled catalogue of 2.5 million stars. *Kinematika i Fizika Nebesnykh Tel*, 17:409–423, October 2001.

P. Khokhuntod, A.-Y. Zhou, C. Boonyarak, and S.-Y. Jiang. V1162 Orion: Updated Amplitude and Period Variation. *ArXiv e-prints*, September 2011.

P. N. Kholopov, N. N. Samus, M. S. Frolov, V. P. Goranskij, N. A. Gorynya, E. A. Karitskaya, E. V. Kazarovets, N. N. Kireeva, N. P. Kukarkina, N. E. Kurochkin, G. I. Medvedeva, E. N. Pastukhova, N. B. Perova, A. S. Rastorguev, and S. Y. Shugarov. Combined General Catalogue of Variable Stars. In *Combined General Catalogue of Variable Stars, 4.1 Ed (II/214A). (1998)*, page 0, 1998.

D. Kilkenny. Variable stars ii. pulsating stars, August 2013. URL `http://www.star.ac.za/course-resources/local/david-buckley/var2.pdf`.

D.-W. Kim, P. Protopapas, C. Alcock, Y.-I. Byun, J. Kyeong, B.-C. Lee, N. J. Wright, T. Axelrod, F. B. Bianco, W.-P. Chen, N. K. Coehlo, K. H. Cook, R. Dave, S.-K. King, T. Lee, M. J. Lehner, H.-C. Lin, S. L. Marshall, R. Porrata, J. A. Rice, M. E. Schwamb, J.-H. Wang, S.-Y. Wang, C.-Y. Wen, and Z.-W. Zhang. The Taiwan-American Occultation Survey Project Stellar Variability. I. Detection of Low-Amplitude δ Scuti Stars. *aj*, 139:757–764, February 2010. doi: 10.1088/0004-6256/139/2/757.

H. King, J. M. Matthews, J. F. Row, C. Cameron, R. Kuschnig, D. B. Guenther, A. F. J. Moffat, S. M. Rucinski, D. Sasselov, G. A. H. Walker, and W. W. Weiss. HD 114839 - An Am star showing both δ Scuti and γ Dor pulsations discovered through MOST photometry. *Communications in Asteroseismology*, 148:28–33, December 2006. doi: 10.1553/cia148s28.

O. Kochukhov. The spots on Ap stars. In D. Prasad Choudhary and K. G. Strassmeier, editors, *IAU Symposium*, volume 273 of *IAU Symposium*, pages 249–255, August 2011. doi: 10.1017/S1743921311015328.

O. Kochukhov and S. Bagnulo. Evolutionary state of magnetic chemically peculiar stars. *aap*, 450:763–775, May 2006. doi: 10.1051/0004-6361:20054596.

C. Koen. The "four sigma" limit for significant periodicities. *apss*, 329:267–271, October 2010. doi: 10.1007/s10509-009-0199-z.

C. Koen and L. Eyer. New periodic variables from the Hipparcos epoch photometry. *mnras*, 331:45–59, March 2002. doi: 10.1046/j.1365-8711.2002.05150.x.

T. Kogure and K.-C. Leung. A Book on Astrophysics of Emission-Line Stars. In Y. W. Kang, H.-W. Lee, K.-C. Leung, and K.-S. Cheng, editors, *The Seventh Pacific Rim Conference on Stellar Astrophysics*, volume 362 of *Astronomical Society of the Pacific Conference Series*, page 260, June 2007.

A. N. Kolmogorov. Sulla determinazione empirica di una legge di distribuzione (On the empirical determination of a distribution law). 4:83, 1933.

F. Kupka, E. Paunzen, and H. M. Maitzen. The 5200-Å flux depression of chemically peculiar stars - I. Synthetic Δa photometry: the normality line. *mnras*, 341:849–854, May 2003. doi: 10.1046/j.1365-8711.2003.06452.x.

D. W. Kurtz. Pulsation of Chemically Peculiar and Pre-Main Sequence Stars in the δ Scuti Instability Strip. In M. Breger and M. Montgomery, editors, *Delta Scuti and Related Stars*, volume 210 of *Astronomical Society of the Pacific Conference Series*, page 287, 2000.

D. Lafrenière, R. Jayawardhana, M. H. van Kerkwijk, A. Brandeker, and M. Janson. An Adaptive Optics Multiplicity Census of Young Stars in Upper Scorpius. *apj*, 785:47, April 2014. doi: 10.1088/0004-637X/785/1/47.

P. Lampens and H. M. J. Boffin. δ Scuti Stars in Stellar Systems: a Review. In M. Breger and M. Montgomery, editors, *Delta Scuti and Related Stars*, volume 210 of *Astronomical Society of the Pacific Conference Series*, page 309, 2000.

A. F. Lanza and M. Rodonò. Orbital period modulation and quadrupole moment changes in magnetically active close binaries. *aap*, 349:887–897, September 1999.

F. LeBlanc. *An Introduction to Stellar Astrophysics*. 2010.

G. Lenain, R. Scuflaire, M.-A. Dupret, and A. Noels. The epsilon-mechanism in PMS and MS delta Scuti stars. *Communications in Asteroseismology*, 147:93–96, January 2006. doi: 10.1553/cia147s93.

P. Lenz and M. Breger. Period04 User Guide. *Communications in Asteroseismology*, 146:53–136, June 2005. doi: 10.1553/cia146s53.

F. Leone and G. Catanzaro. Spectropolarimetric measurements of the mean longitudinal magnetic field of chemically peculiar stars. II. Phase relating the magnetic and luminosity variabilities. *aap*, 365:118–127, January 2001. doi: 10.1051/0004-6361:20000450.

C. L. Liu. A Tutorial of the Wavelet Transform. NTUEE, Taiwan, 2010.

N. R. Lomb. Least-squares frequency analysis of unequally spaced data. *apss*, 39:447–462, February 1976. doi: 10.1007/BF00648343.

P. Lopez de Coca, R. Garrido, V. Costa, and A. Rolland. Narrow Band Photometry of FG Vir. *Information Bulletin on Variable Stars*, 2465:1, January 1984.

P. Lopez de Coca, A. Rolland, E. Rodriguez, and R. Garrido. Empirical P-L-C relation for Delta Scuti stars - A catalogue. *aaps*, 83:51–69, April 1990.

J.-C. Lu, J.-Y. Wang, T. An, J.-M. Lin, and H.-B. Qiu. Periodic radio variability in NRAO 530: phase dispersion minimization analysis. *Research in Astronomy and Astrophysics*, 12: 643–650, June 2012. doi: 10.1088/1674-4527/12/6/004.

T. Lüftinger, H.-E. Fröhlich, W. W. Weiss, P. Petit, M. Aurière, N. Nesvacil, M. Gruberbauer, D. Shulyak, E. Alecian, A. Baglin, F. Baudin, C. Catala, J.-F. Donati, O. Kochukhov, E. Michel, N. Piskunov, T. Roudier, and R. Samadi. Surface structure of the CoRoT CP2 target star HD 50773. *aap*, 509:A43, January 2010. doi: 10.1051/0004-6361/200912239.

H. M. Maitzen. HD 30466 - A double wave photometric variable silicon star. *aap*, 60:L29, September 1977.

H. M. Maitzen and A. F. J. Moffat. Eleven-band photometry of the magnetic variable HD 125248. *aap*, 16:385–394, February 1972.

H. M. Maitzen and K. D. Rakosch. UBV observations of the magnetic variable HD 125248. *aap*, 7:10–16, July 1970.

L. Mantegazza and E. Poretti. Line profile variations in the delta Scuti star FG Virginis: A high number of axisymmetric modes. *aap*, 396:911–916, December 2002. doi: 10.1051/0004-6361:20021456.

L. Mantegazza, E. Poretti, and M. Bossi. Simultaneous intensive photometry and high resolution spectroscopy of Delta Scuti stars. 1: Mode typing of HD 106384 defined as FG Virginis. *aap*, 287:95–104, July 1994.

G. Mathys, J. Manfroid, and P. Renson. Photometric variability of some early-type stars. *aaps*, 63:403–416, March 1986.

D. McDavid. Optical Variability of 48 Lib. In *Bulletin of the American Astronomical Society*, volume 20 of *Bulletin of the American Astronomical Society*, page 954, September 1988.

D. McDavid, K. S. Bjorkman, J. E. Bjorkman, and A. T. Okazaki. A Connection Between V/R and Polarization in Be Stars. In M. A. Smith, H. F. Henrichs, and J. Fabregat, editors, *IAU Colloq. 175: The Be Phenomenon in Early-Type Stars*, volume 214 of *Astronomical Society of the Pacific Conference Series*, page 460, 2000.

B. J. McNamara. A preliminary multiperiodic light analysis of the star 57 Tau. In P. F. Gott and P. S. Riherd, editors, *Southwest Regional Conference for Astronomy and Astrophysics, 8*, pages 43–45, 1983.

D. H. McNamara. The Identification of Pulsation Modes of High-Amplitude δ Scuti Stars in ω Centauri and the Carina Galaxy. *pasp*, 112:1096–1102, August 2000. doi: 10.1086/316605.

D. H. McNamara. Delta Scuti, SX Phoenicis, and RR Lyrae Stars in Galaxies and Globular Clusters. *aj*, 142:110, October 2011. doi: 10.1088/0004-6256/142/4/110.

A. Meilland, P. Stee, M. Vannier, F. Millour, A. Domiciano de Souza, F. Malbet, C. Martayan, F. Paresce, R. G. Petrov, A. Richichi, and A. Spang. First direct detection of a Keplerian rotating disk around the Be star α Arae using AMBER/VLTI. *aap*, 464:59–71, March 2007. doi: 10.1051/0004-6361:20064848.

P. W. Merrill and C. G. Burwell. No. 471. Catalogue and bibliography of stars of classes B and A whose spectra have bright hydogen lines. *Contributions from the Mount Wilson Observatory / Carnegie Institution of Washington*, 471:1–54, 1933.

G. Meynet and A. Maeder. Single Massive Stars at the Critical Rotational Velocity: Possible Links with Be and B[e] Stars. In M. Kraus and A. S. Miroshnichenko, editors, *Stars with the B[e] Phenomenon*, volume 355 of *Astronomical Society of the Pacific Conference Series*, page 27, December 2006.

G. Michaud. Diffusion Processes in Peculiar a Stars. *apj*, 160:641, May 1970. doi: 10.1086/150459.

G. Michaud. Atomic diffusion in stellar surfaces and interiors. In J. Zverko, J. Ziznovsky, S. J. Adelman, and W. W. Weiss, editors, *The A-Star Puzzle*, volume 224 of *IAU Symposium*, pages 173–183, December 2004. doi: 10.1017/S1743921304004533.

G. Michaud, Y. Charland, and C. Megessier. Diffusion models for magnetic Ap-Bp stars. *aap*, 103:244–262, November 1981.

Z. Mikulášek, J. Zverko, J. Žižnovský, and J. Janík. The analyses of the light curves of magnetic CP stars by advanced PCA methods. In J. Zverko, J. Ziznovsky, S. J. Adelman, and W. W. Weiss, editors, *The A-Star Puzzle*, volume 224 of *IAU Symposium*, pages 657–661, December 2004. doi: 10.1017/S1743921305009531.

Z. Mikulášek, J. Krtička, G. W. Henry, J. Zverko, J. Žižåovský, D. Bohlender, I. I. Romanyuk, J. Janík, H. Božić, D. Korčáková, M. Zejda, I. K. Iliev, P. Škoda, M. Šlechta, T. Gráf, M. Netolický, and M. Ceniga. The extremely rapid rotational braking of the magnetic helium-strong star HD 37776. *aap*, 485:585–597, July 2008. doi: 10.1051/0004-6361:20077794.

Z. Mikulášek, G. Szasz, J. Krticka, J. Zverko, J. Ziznovsky, M. Zejda, and T. Graf. Rotational periods of magnetic chemically peculiar stars. *ArXiv e-prints*, May 2009.

Z. Mikulášek, J. Krtička, G. W. Henry, S. N. de Villiers, E. Paunzen, and M. Zejda. HR 7355 - another rapidly braking He-strong CP star? *aap*, 511:L7, February 2010. doi: 10.1051/0004-6361/200913832.

Z. Mikulášek, J. Krtička, G. W. Henry, J. Janík, J. Zverko, J. Žižňovský, M. Zejda, J. Liška, P. Zvěřina, D. O. Kudrjavtsev, I. I. Romanyuk, N. A. Sokolov, T. Lüftinger, C. Trigilio, C. Neiner, and S. N. de Villiers. Surprising variations in the rotation of the chemically peculiar stars CU Virginis and V901 Orionis. *aap*, 534:L5, October 2011. doi: 10.1051/0004-6361/201117784.

Z. Mikulášek, M. Zejda, and J. Janík. Period Analyses Without O-C Diagrams. In M. T. Richards and I. Hubeny, editors, *IAU Symposium*, volume 282 of *IAU Symposium*, pages 391–394, April 2012. doi: 10.1017/S1743921311027888.

Z. Mikulášek, J. Krtička, J. Janík, M. Zejda, G. W. Henry, E. Paunzen, J. Žižňovský, and J. Zverko. Ap stars with variable periods. In G. Mathys, E. R. Griffin, O. Kochukhov, R. Monier, and G. M. Wahlgren, editors, *Putting A Stars into Context: Evolution, Environment, and Related Stars*, pages 270–278, November 2014.

H. Milligan and T. R. Carson. The pulsation of Delta-Scuti stars. *apss*, 189:181–211, March 1992. doi: 10.1007/BF00643125.

R. L. Millis. *Unpublished PhD thesis*. PhD thesis, University of Wisconsin, 1967.

J. D. Monnier, R. H. D. Townsend, X. Che, M. Zhao, T. Kallinger, J. Matthews, and A. F. J. Moffat. Rotationally Modulated g-modes in the Rapidly Rotating δ Scuti Star Rasalhague (α Ophiuchi). *apj*, 725:1192–1201, December 2010. doi: 10.1088/0004-637X/725/1/1192.

T. Morel, M. Briquet, M. Auvergne, G. Alecian, S. Ghazaryan, E. Niemczura, L. Fossati, H. Lehmann, S. Hubrig, C. Ulusoy, Y. Damerdji, M. Rainer, E. Poretti, F. Borsa, M. Scardia, V. S. Schmid, H. Van Winckel, K. De Smedt, P. I. Pápics, J. F. Gameiro, C. Waelkens, M. Fagas, K. Kamiński, W. Dimitrov, A. Baglin, E. Michel, L. Dumortier, Y. Frémat, H. Hensberge, A. Jorissen, and S. Van Eck. A search for pulsations in the HgMn star HD 45975 with CoRoT photometry and ground-based spectroscopy. *aap*, 561:A35, January 2014. doi: 10.1051/0004-6361/201322289.

W. W. Morgan. Studies in Peculiar Stellar Spectra. II. The Spectrum of B. D. 18deg3789. *apj*, 74:24, July 1931. doi: 10.1086/143322.

W. W. Morgan and W. A. Hiltner. Studies in Spectral Classification. I. The HR Diagram of the Hyades. *apj*, 141:177, January 1965. doi: 10.1086/148099.

S. L. Morris. The ellipsoidal variable stars. *apj*, 295:143–152, August 1985. doi: 10.1086/163359.

S. J. Murphy, A. Grigahcène, E. Niemczura, D. W. Kurtz, and K. Uytterhoeven. Pulsational amplitude growth of the star KIC 3429637 (HD 178875) in the context of Am and ρ Pup stars. *mnras*, 427:1418–1428, December 2012. doi: 10.1111/j.1365-2966.2012.22062.x.

S. J. Murphy, T. R. Bedding, E. Niemczura, D. W. Kurtz, and B. Smalley. A search for non-pulsating, chemically normal stars in the δ Scuti instability strip using Kepler data. *mnras*, 447:3948–3959, March 2015. doi: 10.1093/mnras/stu2749.

C. Neiner and A.-M. Hubert. The pulsations of Be stars. *Communications in Asteroseismology*, 158:194, July 2009.

C. Neiner, M. Floquet, A. M. Hubert, Y. Frémat, R. Hirata, S. Masuda, D. Gies, C. Buil, and C. Martayan. Rotation, pulsations and outbursts in the Be star HD 202904. *aap*, 437:257–272, July 2005. doi: 10.1051/0004-6361:20041901.

C. Neiner, J. Gutiérrez-Soto, F. Baudin, B. de Batz, Y. Frémat, A. L. Huat, M. Floquet, A.-M. Hubert, B. Leroy, P. D. Diago, E. Poretti, F. Carrier, M. Rainer, C. Catala, O. Thizy, C. Buil, J. Ribeiro, L. Andrade, M. Emilio, F. Espinosa Lara, J. Fabregat, E. Janot-Pacheco, C. Martayan, T. Semaan, J. Suso, A. Baglin, E. Michel, and R. Samadi. The pulsations of the B5IVe star HD 181231 observed with CoRoT and ground-based spectroscopy. *aap*, 506: 143–151, October 2009. doi: 10.1051/0004-6361/200911971.

C. Neiner, M. Floquet, R. Samadi, F. Espinosa Lara, Y. Frémat, S. Mathis, B. Leroy, B. de Batz, M. Rainer, E. Poretti, P. Mathias, J. Guarro Fló, C. Buil, J. Ribeiro, E. Alecian, L. Andrade, M. Briquet, P. D. Diago, M. Emilio, J. Fabregat, J. Gutiérrez-Soto, A.-M. Hubert, E. Janot-Pacheco, C. Martayan, T. Semaan, J. Suso, and J. Zorec. Stochastic gravito-inertial modes discovered by CoRoT in the hot Be star HD 51452. *aap*, 546:A47, October 2012. doi: 10.1051/0004-6361/201219820.

J. Nemravová, P. Harmanec, P. Koubský, A. Miroshnichenko, S. Yang, M. Šlechta, C. Buil, D. Korčáková, and V. Votruba. Properties and nature of Be stars. 29. Orbital and long-term spectral variations of γ Cassiopeiae. *aap*, 537:A59, January 2012. doi: 10.1051/0004-6361/201117922.

M. Netopil, E. Paunzen, H. M. Maitzen, O. I Pintado, and I. Kh. Iliev. Chemically peculiar upper main-sequence stars in the Milky Way and beyond. In G. Mathys, E. R. Griffin, O. Kochukhov, R. Monier, and G. M. Wahlgren, editors, *Putting A Stars into Context: Evolution, Environment, and Related Stars*, pages 10–18, November 2014.

E. Niemczura, T. Morel, and C. Aerts. Abundance analysis of prime B-type targets for asteroseismology. II. B6-B9.5 stars in the field of view of the CoRoT satellite. *aap*, 506:213–233, October 2009. doi: 10.1051/0004-6361/200911931.

E. Niemczura, S. J. Murphy, B. Smalley, K. Uytterhoeven, A. Pigulski, H. Lehmann, D. M.

Bowman, G. Catanzaro, E. van Aarle, S. Bloemen, M. Briquet, P. De Cat, D. Drobek, L. Eyer, J. F. S. Gameiro, N. Gorlova, K. Kaminski, P. Lampens, P. Marcos-Arenal, P. I. Papics, B. Vandenbussche, H. Van Winckel, M. Steslicki, and M. Fagas. Spectroscopic survey of Kepler stars. I. HERMES/Mercator observations of A- and F-type stars. *ArXiv e-prints*, March 2015.

H. Nieuwenhuijzen and C. de Jager. Parametrization of stellar rates of mass loss as functions of the fundamental stellar parameters M, L, and R. *aap*, 231:134–136, May 1990.

P. North. Photometric variability of AP and He-weak stars in clusters and associations. II. *aaps*, 69:371–396, June 1987.

P. North. Do SI stars undergo any rotational braking? *aap*, 334:181–187, June 1998.

P. North and C. Waelkens. Photoelectric Photometry of Ap Stars in IC 2602, NGC 6281 and in the Scorpio-Centaurus Group: Preliminary Results. *Information Bulletin on Variable Stars*, 2372:1, July 1983.

P. North, C. Jaschek, B. Hauck, F. Figueras, J. Torra, and M. Kunzli. Absolute Magnitudes of Chemically Peculiar Stars. In R. M. Bonnet, E. Høg, P. L. Bernacca, L. Emiliani, A. Blaauw, C. Turon, J. Kovalevsky, L. Lindegren, H. Hassan, M. Bouffard, B. Strim, D. Heger, M. A. C. Perryman, and L. Woltjer, editors, *Hipparcos - Venice '97*, volume 402 of *ESA Special Publication*, pages 239–244, August 1997.

A. P. Odell. Period variation in BW Vulpeculae redux. *aap*, 544:A28, August 2012. doi: 10.1051/0004-6361/201219418.

L. Oetken. Photometrically determined mean surface magnetic fields of AP stars. *Astronomische Nachrichten*, 306:187, 1985. doi: 10.1002/asna.2113060403.

A. T. Okazaki. Long-term V/R variations of Be stars due to global one-armed oscillations of equatorial disks. *pasj*, 43:75–94, February 1991.

A. T. Okazaki. On the confinement of one-armed oscillations in discs of Be stars. *aap*, 318: 548–560, February 1997.

R. L. Oldershaw. Discrete Cosmological Self-Similarity And Delta Scuti Stars. *ArXiv Astrophysics e-prints*, January 2006.

K. Osawa. Spectral Classification of 533 B8-A2 Stars and the Mean Absolute Magnitude of a0 V Stars. *apj*, 130:159, July 1959. doi: 10.1086/146706.

S. P. Owocki. Rotation and Mass Ejection: the Launching of Be-Star Disks (Invited Review). In A. Maeder and P. Eenens, editors, *Stellar Rotation*, volume 215 of *IAU Symposium*, page 515, June 2004.

A. A. Pamyatnykh, G. Handler, and W. A. Dziembowski. Asteroseismology of the β Cephei star ν Eridani: interpretation and applications of the oscillation spectrum. *mnras*, 350:1022–1028, May 2004. doi: 10.1111/j.1365-2966.2004.07721.x.

M. Paparó, E. Rodriguez, B. J. McNamara, Z. Kolláth, A. Rolland, S. F. Gonzalez-Bedolla, S.-y. Jiang, and Z.-p. Li. A comprehensive study of the delta Scuti star, 57 Tauri (= HR 1351) in the Hyades cluster. *aaps*, 142:1–11, February 2000. doi: 10.1051/aas:2000131.

M. Paparó, Z. Bognár, J. M. Benkő, D. Gandolfi, A. Moya, J. C. Suárez, Á. Sódor, M. Hareter, E. Poretti, E. W. Guenther, M. Auvergne, A. Baglin, and W. W. Weiss. CoRoT 102749568: mode identification in a δ Scuti star based on regular spacings. *aap*, 557:A27, September 2013. doi: 10.1051/0004-6361/201321792.

P. I. Pápics, M. Briquet, A. Baglin, E. Poretti, C. Aerts, P. Degroote, A. Tkachenko, T. Morel, W. Zima, E. Niemczura, M. Rainer, M. Hareter, F. Baudin, C. Catala, E. Michel, R. Samadi, and M. Auvergne. Gravito-inertial and pressure modes detected in the B3 IV CoRoT target HD 43317. *aap*, 542:A55, June 2012. doi: 10.1051/0004-6361/201218809.

L. E. Pasinetti Fracassini, L. Pastori, S. Covino, and A. Pozzi. Catalogue of Apparent Diameters and Absolute Radii of Stars (CADARS) - Third edition - Comments and statistics. *aap*, 367: 521–524, February 2001. doi: 10.1051/0004-6361:20000451.

E. Paunzen, K. T. Wraight, L. Fossati, M. Netopil, G. J. White, and D. Bewsher. A photometric study of chemically peculiar stars with the STEREO satellites - II. Non-magnetic chemically peculiar stars. *mnras*, 429:119–125, February 2013. doi: 10.1093/mnras/sts318.

E. Paunzen, H.-E. Fröhlich, M. Netopil, W. W. Weiss, and T. Lüftinger. The CoRoT chemical peculiar target star HD 49310. *aap*, 574:A57, February 2015. doi: 10.1051/0004-6361/201424511.

K. Pavlovski and H. Bozic. UBV Photometry of some Be stars: progress report. *Hvar Observatory Bulletin*, 6:45, 1982.

M. A. Peña-Guerrero and C. Leitherer. H I Lyman-alpha Equivalent Widths of Stellar Populations. *aj*, 146:158, December 2013. doi: 10.1088/0004-6256/146/6/158.

J. A. Pearce and G. Hill. A spectroscopic investigation of the Pleiades. *Publications of the Dominion Astrophysical Observatory Victoria*, 14:319–343, 1975.

J. R. Percy. *Understanding Variable Stars*. May 2007.

M. A. C. Perryman, L. Lindegren, J. Kovalevsky, E. Hoeg, U. Bastian, P. L. Bernacca, M. Crézé, F. Donati, M. Grenon, M. Grewing, F. van Leeuwen, H. van der Marel, F. Mignard, C. A. Murray, R. S. Le Poole, H. Schrijver, C. Turon, F. Arenou, M. Froeschlé, and C. S. Petersen. The HIPPARCOS Catalogue. *aap*, 323:L49–L52, July 1997.

C. A. Pilachowski and W. K. Bonsack. The effect of line blocking on the light curves of the AP star HR 5355 /HD 125248/. *pasp*, 87:221–229, April 1975. doi: 10.1086/129747.

H. Pöhnl, H. M. Maitzen, and E. Paunzen. On the evolutionary status of chemically peculiar stars of the upper main sequence. *aap*, 402:247–252, April 2003. doi: 10.1051/0004-6361:20030266.

N. Polosukhina, V. Khalak, A. Shavrina, and P. North. A phenomenological picture of the variability of the spotted roAp star HD 83368 (HR 3831). *Astronomy Letters*, 25:608–614, September 1999.

E. Poretti. Asteroseismology of HADS stars: V974 Oph, a radial pulsator flavoured by nonradial components. *aap*, 409:1031–1035, October 2003. doi: 10.1051/0004-6361:20031223.

E. Poretti, E. Michel, R. Garrido, L. Lefèvre, L. Mantegazza, M. Rainer, E. Rodríguez, K. Uytterhoeven, P. J. Amado, S. Martín-Ruiz, A. Moya, E. Niemczura, J. C. Suárez, W. Zima, A. Baglin, M. Auvergne, F. Baudin, C. Catala, R. Samadi, M. Alvarez, P. Mathias, M. Paparò, P. Pápics, and E. Plachy. HD 50844: a new look at δ Scuti stars from CoRoT space photometry. *aap*, 506:85–93, October 2009. doi: 10.1051/0004-6361/200912039.

E. Poretti, M. Rainer, W. W. Weiss, Z. Bognár, A. Moya, E. Niemczura, J. C. Suárez, M. Auvergne, A. Baglin, F. Baudin, J. M. Benkő, J. Debosscher, R. Garrido, L. Mantegazza, and

M. Paparó. Monitoring a high-amplitude δ Scuti star for 152 days: discovery of 12 additional modes and modulation effects in the light curve of CoRoT 101155310. *aap*, 528:A147, April 2011. doi: 10.1051/0004-6361/201016045.

J. M. Porter and T. Rivinius. Classical Be Stars. *pasp*, 115:1153–1170, October 2003. doi: 10.1086/378307.

W. H. Press. Flicker noises in astronomy and elsewhere. *Comments on Astrophysics*, 7:103–119, 1978.

W. H. Press and G. B. Rybicki. Fast algorithm for spectral analysis of unevenly sampled data. *apj*, 338:277–280, March 1989. doi: 10.1086/167197.

G. W. Preston. The chemically peculiar stars of the upper main sequence. *araa*, 12:257–277, 1974. doi: 10.1146/annurev.aa.12.090174.001353.

D. M. Pyper and S. J. Adelman. Spectrophotometry of peculiar B and A stars. XVII - 63 Andromedae, HD 34452, Epsilon Ursae Majoris, CQ Ursae Majoris, CU Virginis, CS Virginis and Beta Coronae Borealis. *aaps*, 59:369–397, March 1985.

D. M. Pyper, I. R. Stevens, and S. J. Adelman. An update on the rotational period of the magnetic chemically peculiar star CU Virginis. *mnras*, 431:2106–2110, May 2013. doi: 10.1093/mnras/stt256.

S. Qian. Orbital period changes of contact binary systems: direct evidence for thermal relaxation oscillation theory. *mnras*, 328:914–924, December 2001. doi: 10.1046/j.1365-8711.2001.04921.x.

I. Radiman, C. Kunjaya, and A. Widjaja. On the Periodical Nature of Annual Variation of the Regressions of the Martian Polar Caps Using the Phase Dispersion Minimization-(PDM) Method. *Jurnal Matematika dan Sains, FMIPA, Institut Teknologi Bandung*, 3:69–78, October 1998.

K. D. Rakosch and W. Fiedler. Photoelectric observations of 14 Ap stars. *aaps*, 31:83–98, January 1978.

H. Rauer, C. Catala, C. Aerts, T. Appourchaux, W. Benz, A. Brandeker, J. Christensen-Dalsgaard, M. Deleuil, L. Gizon, M.-J. Goupil, M. Güdel, E. Janot-Pacheco, M. Mas-Hesse,

I. Pagano, G. Piotto, D. Pollacco, Ċ. Santos, A. Smith, J.-C. Suárez, R. Szabó, S. Udry, V. Adibekyan, Y. Alibert, J.-M. Almenara, P. Amaro-Seoane, M. A.-v. Eiff, M. Asplund, E. Antonello, S. Barnes, F. Baudin, K. Belkacem, M. Bergemann, G. Bihain, A. C. Birch, X. Bonfils, I. Boisse, A. S. Bonomo, F. Borsa, I. M. Brandão, E. Brocato, S. Brun, M. Burleigh, R. Burston, J. Cabrera, S. Cassisi, W. Chaplin, S. Charpinet, C. Chiappini, R. P. Church, S. Csizmadia, M. Cunha, M. Damasso, M. B. Davies, H. J. Deeg, R. F. Díaz, S. Dreizler, C. Dreyer, P. Eggenberger, D. Ehrenreich, P. Eigmüller, A. Erikson, R. Farmer, S. Feltzing, F. de Oliveira Fialho, P. Figueira, T. Forveille, M. Fridlund, R. A. García, P. Giommi, G. Giuffrida, M. Godolt, J. Gomes da Silva, T. Granzer, J. L. Grenfell, A. Grotsch-Noels, E. Günther, C. A. Haswell, A. P. Hatzes, G. Hébrard, S. Hekker, R. Helled, K. Heng, J. M. Jenkins, A. Johansen, M. L. Khodachenko, K. G. Kislyakova, W. Kley, U. Kolb, N. Krivova, F. Kupka, H. Lammer, A. F. Lanza, Y. Lebreton, D. Magrin, P. Marcos-Arenal, P. M. Marrese, J. P. Marques, J. Martins, S. Mathis, S. Mathur, S. Messina, A. Miglio, J. Montalban, M. Montalto, M. J. P. F. G. Monteiro, H. Moradi, E. Moravveji, C. Mordasini, T. Morel, A. Mortier, V. Nascimbeni, R. P. Nelson, M. B. Nielsen, L. Noack, A. J. Norton, A. Ofir, M. Oshagh, R.-M. Ouazzani, P. Pápics, V. C. Parro, P. Petit, B. Plez, E. Poretti, A. Quirrenbach, R. Ragazzoni, G. Raimondo, M. Rainer, D. R. Reese, R. Redmer, S. Reffert, B. Rojas-Ayala, I. W. Roxburgh, S. Salmon, A. Santerne, J. Schneider, J. Schou, S. Schuh, H. Schunker, A. Silva-Valio, R. Silvotti, I. Skillen, I. Snellen, F. Sohl, S. G. Sousa, A. Sozzetti, D. Stello, K. G. Strassmeier, M. Švanda, G. M. Szabó, A. Tkachenko, D. Valencia, V. Van Grootel, S. D. Vauclair, P. Ventura, F. W. Wagner, N. A. Walton, J. Weingrill, S. C. Werner, P. J. Wheatley, and K. Zwintz. The PLATO 2.0 mission. *Experimental Astronomy*, 38:249–330, November 2014. doi: 10.1007/s10686-014-9383-4.

P. Renson. In *F.N.R.S. Bruxelles Gr. de C. Phys. Chim. Geophys. Geol., p. 19*, 1975.

P. Renson. Nouvelle Recherche de Periodes D'etoiles Ap Observees a l'ESO - I. *Information Bulletin on Variable Stars*, 1391:1, March 1978.

P. Renson and F. A. Catalano. Fifth supplement to the catalogue of observed periods of Ap stars. *aap*, 378:113–115, October 2001. doi: 10.1051/0004-6361:20011065.

P. Renson and J. Manfroid. Catalogue of Ap, HgMn and Am stars. *aap*, 498:961–966, May 2009. doi: 10.1051/0004-6361/200810788.

G. R. Ricker, J. N. Winn, R. Vanderspek, D. W. Latham, G. Á. Bakos, J. L. Bean, Z. K. Berta-Thompson, T. M. Brown, L. Buchhave, N. R. Butler, R. P. Butler, W. J. Chaplin, D. Charbonneau, J. Christensen-Dalsgaard, M. Clampin, D. Deming, J. Doty, N. De Lee, C. Dressing, E. W. Dunham, M. Endl, F. Fressin, J. Ge, T. Henning, M. J. Holman, A. W. Howard, S. Ida, J. Jenkins, G. Jernigan, J. A. Johnson, L. Kaltenegger, N. Kawai, H. Kjeldsen, G. Laughlin, A. M. Levine, D. Lin, J. J. Lissauer, P. MacQueen, G. Marcy, P. R. McCullough, T. D. Morton, N. Narita, M. Paegert, E. Palle, F. Pepe, J. Pepper, A. Quirrenbach, S. A. Rinehart, D. Sasselov, B. Sato, S. Seager, A. Sozzetti, K. G. Stassun, P. Sullivan, A. Szentgyorgyi, G. Torres, S. Udry, and J. Villasenor. Transiting Exoplanet Survey Satellite (TESS). In *Society of Photo-Optical Instrumentation Engineers (SPIE) Conference Series*, volume 9143 of *Society of Photo-Optical Instrumentation Engineers (SPIE) Conference Series*, page 20, August 2014. doi: 10.1117/12.2063489.

L. Rimoldini, P. Dubath, M. Süveges, M. López, L. M. Sarro, J. Blomme, J. De Ridder, J. Cuypers, L. Guy, N. Mowlavi, I. Lecoeur-Taïbi, M. Beck, A. Jan, K. Nienartowicz, D. Ordóñez-Blanco, T. Lebzelter, and L. Eyer. Automated classification of Hipparcos unsolved variables. *mnras*, 427:2917–2937, December 2012. doi: 10.1111/j.1365-2966.2012.21752.x.

A. E. Ringuelet-Kaswalder. Short-Period Radial-Velocity Variation of 48 Librae. *apj*, 137:1310, May 1963. doi: 10.1086/147610.

T. Rivinius, D. Baade, S. Stefl, O. Stahl, B. Wolf, and A. Kaufer. Stellar and circumstellar activity of the Be star MU Centauri. II. Multiperiodic low-order line-profile variability. *aap*, 336:177–190, August 1998a.

T. Rivinius, D. Baade, S. Stefl, O. Stahl, B. Wolf, and A. Kaufer. Stellar and circumstellar activity of the Be star MU Centauri. I. Line emission outbursts. *aap*, 333:125–140, May 1998b.

T. Rivinius, D. Baade, and S. Štefl. Non-radially pulsating Be stars. *aap*, 411:229–247, November 2003. doi: 10.1051/0004-6361:20031285.

T. Rivinius, A. C. Carciofi, and C. Martayan. Classical Be stars. Rapidly rotating B stars with viscous Keplerian decretion disks. *aapr*, 21:69, October 2013. doi: 10.1007/s00159-013-0069-0.

E. Rodríguez, M. J. López-González, and P. López de Coca. A revised catalogue of delta Sct stars. *aaps*, 144:469–474, June 2000. doi: 10.1051/aas:2000221.

I. I. Romanyuk and D. O. Kudryavtsev. Magnetic fields of chemically peculiar stars. I. The catalog of magnetic CP stars. *Astrophysical Bulletin*, 63:139–155, June 2008. doi: 10.1134/S1990341308020053.

H. Rovithis-Livaniou. Period changes of close binaries and methods of analysis of the (O-C) diagrams of eclipsing binaries. *Publications de l'Observatoire Astronomique de Beograd*, 80: 107–116, May 2006.

F. Royer, J. Zorec, and A. E. Gómez. Rotational velocities of A-type stars. III. Velocity distributions. *aap*, 463:671–682, February 2007. doi: 10.1051/0004-6361:20065224.

H. Saio. Prospects for Asteroseismology of Rapidly Rotating B-Type Stars. In M. Goupil, K. Belkacem, C. Neiner, F. Lignières, and J. J. Green, editors, *Lecture Notes in Physics, Berlin Springer Verlag*, volume 865 of *Lecture Notes in Physics, Berlin Springer Verlag*, page 159, 2013. doi: 10.1007/978-3-642-33380-4_8.

H. Saio. A- and B-type star pulsations in the Kepler and CoRoT era: theoretical considerations. In G. Mathys, E. R. Griffin, O. Kochukhov, R. Monier, and G. M. Wahlgren, editors, *Putting A Stars into Context: Evolution, Environment, and Related Stars*, pages 305–313, November 2014.

H. Saio, C. Cameron, R. Kuschnig, G. A. H. Walker, J. M. Matthews, J. F. Rowe, U. Lee, D. Huber, W. W. Weiss, D. B. Guenther, A. F. J. Moffat, S. M. Rucinski, and D. Sasselov. MOST Detects g-Modes in the Late-Type Be Star β Canis Minoris (B8 Ve). *apj*, 654:544–550, January 2007. doi: 10.1086/509315.

S. Sallmen and B. Y. Welsh. Intermediate-velocity gas observed towards the Shajn 147 SNR. *aap*, 426:555–565, November 2004. doi: 10.1051/0004-6361:20040093.

V. Sangaralingam. *STRESS - STEREO Transiting Exoplanet and Stellar Survey*. PhD thesis, Astrophysics and Space Research Group, School of Physics and Astronomy, The University of Birmingham, August 2011.

V. Sangaralingam and I. R. Stevens. STEREO TRansiting Exoplanet and Stellar Survey (STRESS) - I. Introduction and data pipeline. *mnras*, 418:1325–1334, December 2011. doi: 10.1111/j.1365-2966.2011.19581.x.

V. Sangaralingam, I. R. Stevens, S. Spreckley, and J. Debosscher. STRESS - STEREO TRansiting Exoplanet and Stellar Survey. In A. G. Kosovichev, A. H. Andrei, and J.-P. Rozelot, editors, *IAU Symposium*, volume 264 of *IAU Symposium*, pages 434–439, February 2010. doi: 10.1017/S174392130999305X.

J. P. Sareyan, S. Gonzalez-Bedolla, G. Guerrero, J. Chauville, L. Huang, J. X. Hao, Z. H. Guo, S. J. Adelman, D. Briot, and M. Alvarez. Rotation modulation or/and pulsation in O Andromedae. I. The photometric results of an international multisite multitechnique campaign. *aap*, 332:155–164, April 1998.

G. J. Savonije. Visibility of unstable oscillation modes in a rapidly rotating B star. *aap*, 559: A25, November 2013. doi: 10.1051/0004-6361/201321961.

J. D. Scargle. Studies in astronomical time series analysis. II - Statistical aspects of spectral analysis of unevenly spaced data. *apj*, 263:835–853, December 1982. doi: 10.1086/160554.

G. Schaller, D. Schaerer, G. Meynet, and A. Maeder. New grids of stellar models from 0.8 to 120 solar masses at Z = 0.020 and Z = 0.001. *aaps*, 96:269–331, December 1992.

M. Schoeller, S. Hubrig, M. Briquet, and I. Ilyin. Magnetic fields in beta Cep, SPB, and Be stars. *ArXiv e-prints*, September 2013.

T. Semaan, C. Martayan, Y. Frémat, A.-M. Hubert, J. G. Soto, C. Neiner, and J. Zorec. Spectral and photometric study of Be Stars in the first exoplanet fields of CoRoT. In C. Neiner, G. Wade, G. Meynet, and G. Peters, editors, *IAU Symposium*, volume 272 of *IAU Symposium*, pages 547–548, July 2011. doi: 10.1017/S1743921311011409.

H. Shapley. On the Nature and Cause of Cepheid Variation. *apj*, 40:448, December 1914. doi: 10.1086/142137.

N. R. Sheeley, Jr., A. D. Herbst, C. A. Palatchi, Y.-M. Wang, R. A. Howard, J. D. Moses, A. Vourlidas, J. S. Newmark, D. G. Socker, S. P. Plunkett, C. M. Korendyke, L. F. Burlaga, J. M. Davila, W. T. Thompson, O. C. St Cyr, R. A. Harrison, C. J. Davis, C. J. Eyles, J. P. Halain, D. Wang, N. B. Rich, K. Battams, E. Esfandiari, and G. Stenborg. Heliospheric Images of the Solar Wind at Earth. *apj*, 675:853–862, March 2008. doi: 10.1086/526422.

M. Sifuzzaman, M.RD. Islam, and M. Z. Ali. Application of Wavelet Transform and its Advantages Compared to Fourier Transform. *Lournal of Physical Sciences*, 13:121–134, October 2009. doi: 10.1086/526422.

T. A. A. Sigut and P. Patel. The Correlation between Hα Emission and Visual Magnitude during Long-term Variations in Classical Be Stars. *apj*, 765:41, March 2013. doi: 10.1088/0004-637X/765/1/41.

C. A. N Silva. Period-Luminosity Relations for delta Scuti Stars, 2011.

E. M. Sion. White Dwarfs in Cataclysmic Variables. *pasp*, 111:532–555, May 1999. doi: 10.1086/316361.

A. Slettebak. Spectral types and rotational velocities of the brighter Be stars and A-F type shell stars. *apjs*, 50:55–83, September 1982. doi: 10.1086/190820.

A. Slettebak. H-alpha and near-infrared spectra of late-type Be and A F-type shell stars. *pasp*, 98:867–871, September 1986. doi: 10.1086/131836.

A. Slettebak. The Be stars. *pasp*, 100:770–784, July 1988. doi: 10.1086/132234.

A. Slettebak and R. C. Reynolds. Halpha variations in spectra of the brighter, northern Be stars. *apjs*, 38:205–228, November 1978. doi: 10.1086/190554.

B. Smalley. Observations of convection in A-type stars. In J. Zverko, J. Ziznovsky, S. J. Adelman, and W. W. Weiss, editors, *The A-Star Puzzle*, volume 224 of *IAU Symposium*, pages 131–138, December 2004. doi: 10.1017/S1743921304004478.

B. Smalley, D. W. Kurtz, A. M. S. Smith, L. Fossati, D. R. Anderson, S. C. C. Barros, O. W. Butters, A. Collier Cameron, D. J. Christian, B. Enoch, F. Faedi, C. A. Haswell, C. Hellier, S. Holmes, K. Horne, S. R. Kane, T. A. Lister, P. F. L. Maxted, A. J. Norton, N. Parley, D. Pollacco, E. K. Simpson, I. Skillen, J. Southworth, R. A. Street, R. G. West, P. J. Wheatley, and P. L. Wood. SuperWASP observations of pulsating Am stars. *aap*, 535:A3, November 2011. doi: 10.1051/0004-6361/201117230.

N. Smirnov. The Annals of Mathematical Statistics. 19:279, 1948.

K. C. Smith. Chemically Peculiar Hot Stars. *apss*, 237:77–105, March 1996. doi: 10.1007/BF02424427.

Á. Sódor, P. De Cat, D. J. Wright, C. Neiner, M. Briquet, P. Lampens, R. J. Dukes, G. W. Henry, M. H. Williamson, E. Brunsden, K. R. Pollard, P. L. Cottrell, F. Maisonneuve, P. M. Kilmartin, J. Matthews, T. Kallinger, P. G. Beck, E. Kambe, C. A. Engelbrecht, R. J. Czanik, S. Yang, O. Hashimoto, S. Honda, J. N. Fu, B. Castanheira, H. Lehmann, Z. Bognár, N. Behara, S. Scaringi, H. Van Winckel, J. Menu, A. Lobel, P. Mathias, S. Saesen, M. Vučković, and MiMeS Collaboration. Extensive study of HD 25558, a long-period double-lined binary with two SPB components. *mnras*, 438:3535–3556, March 2014. doi: 10.1093/mnras/stt2466.

C. Soubiran, J.-F. Le Campion, G. Cayrel de Strobel, and A. Caillo. The PASTEL catalogue of stellar parameters. *aap*, 515:A111, June 2010. doi: 10.1051/0004-6361/201014247.

F. Soufi, M. J. Goupil, W. A. Dziembowski, and H. Sienkiewicz. Consequences of Rapid Rotation on Mode Identification. In R. S. Stobie and P. A. Whitelock, editors, *IAU Colloq. 155: Astrophysical Applications of Stellar Pulsation*, volume 83 of *Astronomical Society of the Pacific Conference Series*, page 321, 1995.

A. Stankov and W. Zima. Photometry of the Delta Scuti Star FG VIR during the 1995 Multi-Site Campaign. *Baltic Astronomy*, 7:243–253, March 1998.

K. G. Stassun, J. A. Pepper, M. Paegert, N. De Lee, and R. Sanchis-Ojeda. The K2-TESS Stellar Properties Catalog. *ArXiv e-prints*, October 2014.

K. Stępień. On a mechanism of an abrupt change of period of CU Virginis. *aap*, 337:754–756, September 1998.

S. Stefl, T. Rivinius, J.-B. Le Bouquin, A. Carciofi, D. Baade, S. Otero, and F. Rantakyrö. The 2008+ outburst of the Be star 28 CMa. In *Revista Mexicana de Astronomia y Astrofisica Conference Series*, volume 38 of *Revista Mexicana de Astronomia y Astrofisica, vol. 27*, pages 89–91, February 2010.

R. F. Stellingwerf. Period determination using phase dispersion minimization. *apj*, 224:953–960, September 1978. doi: 10.1086/156444.

K. Stepien. Why are magnetic AP stars slowly rotating? *Contributions of the Astronomical Observatory Skalnate Pleso*, 27:205–212, April 1998.

C. Sterken and J. Manfroid. The enigmatic flarings of HR2517. *aap*, 305:481, January 1996.

D. W. N. Stibbs. A study of the spectrum and magnetic variable star HD 125248. *mnras*, 110: 395, 1950.

O. Struve. On the Origin of Bright Lines in Spectra of Stars of Class B. *apj*, 73:94, March 1931. doi: 10.1086/143298.

J.-C. Suárez, E. Michel, F. Pérez Hernández, Y. Lebreton, Z. P. Li, and L. Fox Machado. A study of correlation between the oscillation amplitude and stellar parameters of delta Scutis in open clusters. Toward selection rules for delta Scuti star oscillations. *aap*, 390:523–531, August 2002. doi: 10.1051/0004-6361:20020565.

B. Szeidl. Period changes of RR Lyrae stars in globular clusters. In V. E. Sherwood and L. Plaut, editors, *Variable Stars and Stellar Evolution*, volume 67 of *IAU Symposium*, pages 545–552, 1975.

B. Szeidl. Binarity and pulsation: multiplicity through the classical O-C method. In A. Claret, A. Giménez, and J.-P. Zahn, editors, *Tidal Evolution and Oscillations in Binary Stars*, volume 333 of *Astronomical Society of the Pacific Conference Series*, page 183, November 2005.

K. Tanaka, K. Sadakane, S.-Y. Narusawa, H. Naito, E. Kambe, J.-I. Katahira, and R. Hirata. Dramatic Spectral and Photometric Changes of Pleione (28 Tau) between 2005 November and 2007 April. *pasj*, 59:L35, August 2007.

N. J. Tarrant. *Asteroseismology from the Main Sequence to Giant Stars*. PhD thesis, The University of Birmingham, 2010.

M. Tassoul. Asymptotic approximations for stellar nonradial pulsations. *apjs*, 43:469–490, August 1980. doi: 10.1086/190678.

R. J. Tayler. *The stars: Their structure and evolution*. 1970.

M. Templeton, S. Basu, and P. Demarque. Asteroseismology of δ Scuti Stars: A Parameter Study and Application to Seismology of FG Virginis. *apj*, 563:999–1012, December 2001. doi: 10.1086/324041.

P. S. The, M. R. Perez, D. de Winter, and M. E. van den Ancker. The new Be-type star HD 147196 in the Rho Ophiuchi dark cloud region. *aap*, 269:181–186, March 1993.

A. Tkachenko, C. Aerts, A. Yakushechkin, J. Debosscher, P. Degroote, S. Bloemen, P. I. Pápics, B. L. de Vries, R. Lombaert, M. Hrudkova, Y. Frémat, G. Raskin, and H. Van Winckel. Detection of a large sample of γ Doradus stars from Kepler space photometry and high-resolution ground-based spectroscopy. *aap*, 556:A52, August 2013. doi: 10.1051/0004-6361/201220978.

Y. Touhami, D. R. Gies, G. H. Schaefer, H. A. McAlister, S. T. Ridgway, N. D. Richardson, R. Matson, E. D. Grundstrom, T. A. ten Brummelaar, P. J. Goldfinger, L. Sturmann, J. Sturmann, N. H. Turner, and C. Farrington. A CHARA Array Survey of Circumstellar Disks around Nearby Be-type Stars. *apj*, 768:128, May 2013. doi: 10.1088/0004-637X/768/2/128.

R. H. D. Townsend, S. P. Owocki, and I. D. Howarth. Be-star rotation: how close to critical? *mnras*, 350:189–195, May 2004. doi: 10.1111/j.1365-2966.2004.07627.x.

T. G. Tsvetkov. Population I pulsating stars. IV - Period-radius and period-gravity relations. *apss*, 150:357–378, December 1988. doi: 10.1007/BF00641730.

S. Turcotte, J. Richer, G. Michaud, and J. Christensen-Dalsgaard. The effect of diffusion on pulsations of stars on the upper main sequence — δ Scuti and metallic A stars. *aap*, 360: 603–616, August 2000.

C. Tycner, J. B. Lester, A. R. Hajian, J. T. Armstrong, J. A. Benson, G. C. Gilbreath, D. J. Hutter, T. A. Pauls, and N. M. White. Properties of the Hα-emitting Circumstellar Regions of Be Stars. *apj*, 624:359–371, May 2005. doi: 10.1086/429126.

G. Ushomirsky and L. Bildsten. Rapid Rotation and Nonradial Pulsations: κ-Mechanism Excitation of g-Modes in B Stars. *apjl*, 497:L101–L104, April 1998. doi: 10.1086/311282.

S. Štefl, J.-B. Le Bouquin, A. C. Carciofi, T. Rivinius, D. Baade, and F. Rantakyrö. New activity in the large circumstellar disk of the Be-shell star 48 Librae. *aap*, 540:A76, April 2012. doi: 10.1051/0004-6361/201118054.

D. Vanbeveren and H. Hensberge. uvby Photometry of the Ap Star HD 145102. *Information Bulletin on Variable Stars*, 1423:1, May 1978.

S. Vaughan. A simple test for periodic signals in red noise. *aap*, 431:391–403, February 2005. doi: 10.1051/0004-6361:20041453.

S. Vaughan. A Bayesian test for periodic signals in red noise. *mnras*, 402:307–320, February 2010. doi: 10.1111/j.1365-2966.2009.15868.x.

M. Viskum, H. Kjeldsen, T. R. Bedding, T. H. dall, I. K. Baldry, H. Bruntt, and S. Frandsen. Oscillation mode identifications and models for the delta Scuti star FG Virginis. *aap*, 335: 549–560, July 1998.

N. Vogt, P. Kroll, and E. Splittgerber. A photometric pilot study on Sonneberg archival patrol plates. How many "constant" stars are in fact long-term variables? *aap*, 428:925–934, December 2004. doi: 10.1051/0004-6361:20040457.

A. Vourlidas, C. J. Davis, C. J. Eyles, S. R. Crothers, R. A. Harrison, R. A. Howard, J. D. Moses, and D. G. Socker. First Direct Observation of the Interaction between a Comet and a Coronal Mass Ejection Leading to a Complete Plasma Tail Disconnection. *apjl*, 668:L79–L82, October 2007. doi: 10.1086/522587.

G. A. H. Walker, R. Kuschnig, J. M. Matthews, P. Reegen, T. Kallinger, E. Kambe, H. Saio, P. Harmanec, D. B. Guenther, A. F. J. Moffat, S. M. Rucinski, D. Sasselov, W. W. Weiss, D. A. Bohlender, H. Božić, O. Hashimoto, P. Koubský, R. Mann, D. Ružđjak, P. Škoda, M. Šlechta, D. Sudar, M. Wolf, and S. Yang. Pulsations of the Oe Star ζ Ophiuchi from MOST Satellite Photometry and Ground-based Spectroscopy. *apjl*, 623:L145–L148, April 2005. doi: 10.1086/430254.

J. H. Walraven, J. Tinbergen, and T. Walraven. Five-colour observations of 24 classical Cepheids. *bain*, 17:520, June 1964.

T. Walraven, J. Walraven, and L. A. Balona. Discovery of additional pulsation modes in AI Velorum. *mnras*, 254:59–66, January 1992.

J.-Y. Wang, T. An, W. A. Baan, and X.-L. Lu. Periodic radio variabilities of the blazar 1156+295: harmonic oscillations. *mnras*, 443:58–66, September 2014. doi: 10.1093/mnras/stu1135.

C. L. Watson. The International Variable Star Index (VSX). *Society for Astronomical Sciences Annual Symposium*, 25:47, May 2006.

G. Whittaker, V. Sangaralingam, and I. Stevens. New Binary and Exoplanet Candidates from STEREO Light Curves. In M. T. Richards and I. Hubeny, editors, *IAU Symposium*, volume 282 of *IAU Symposium*, pages 143–144, April 2012. doi: 10.1017/S1743921311027232.

G. N. Whittaker. *The Analysis and Removal of Systematic Trends in STEREOs HI-1A Photometry and a Search for Planetary Transits.* PhD thesis, Astrophysics and Space Research Group, School of Physics and Astronomy, The University of Birmingham, December 2013.

J. E. Winzer. *The Photometric Variability of the Peculiar a Stars.* PhD thesis, UNIVERSITY OF TORONTO (CANADA)., 1974.

J. P. Wisniewski, Z. H. Draper, K. S. Bjorkman, M. R. Meade, J. E. Bjorkman, and A. F. Kowalski. Disk-Loss and Disk-Renewal Phases in Classical Be Stars. I. Analysis of Long-Term Spectropolarimetric Data. *apj*, 709:1306–1320, February 2010. doi: 10.1088/0004-637X/709/2/1306.

S. C. Wolff and R. J. Wolff. uvby photometry of Ap stars: The nature of the light variations. *aj*, 76:422–430, June 1971. doi: 10.1086/111138.

K. T. Wraight, L. Fossati, M. Netopil, E. Paunzen, M. Rode-Paunzen, D. Bewsher, A. J. Norton, and G. J. White. A photometric study of chemically peculiar stars with the STEREO satellites - I. Magnetic chemically peculiar stars. *mnras*, 420:757–772, February 2012. doi: 10.1111/j.1365-2966.2011.20090.x.

R. T. Zavala, B. J. McNamara, T. E. Harrison, E. Galvan, J. Galvan, T. Jarvis, G. Killgore, O. R. Mireles, D. Olivares, B. A. Rodriguez, M. Sanchez, A. L. Silva, A. L. Silva, and E. Silva-Velarde. The Origin of Cyclic Period Changes in Close Binaries: The Case of the Algol Binary WW Cygni. *aj*, 123:450–457, January 2002. doi: 10.1086/338084.

L. Zhiping. Pulsation behavior of classical Am star 60 Tauri. *aap*, 360:185–188, August 2000.

A. . Zhou. Pulsating Components in Binary and Multiple Stellar Systems – A Catalog of Oscillating Binaries. *ArXiv e-prints*, February 2010.

A. Zhou. A review of the O-C method and period change. *Astrophysics Reports Publications of the Beijing Astronomical Observatory*, 33:17–33, May 1999.

W. Zima, D. Wright, J. Bentley, P. L. Cottrell, U. Heiter, P. Mathias, E. Poretti, H. Lehmann, T. J. Montemayor, and M. Breger. A new method for the spectroscopic identification of stellar non-radial pulsation modes. II. Mode identification of the δ Scuti star FG Virginis. *aap*, 455: 235–246, August 2006. doi: 10.1051/0004-6361:20064877.

J. Zorec and D. Briot. Critical study of the frequency of Be stars taking into account their outstanding characteristics. *aap*, 318:443–460, February 1997.

J. Zorec and F. Royer. Rotational velocities of A-type stars. IV. Evolution of rotational velocities. *aap*, 537:A120, January 2012. doi: 10.1051/0004-6361/201117691.

Appendix A

Graphical presentations of the results for CP star samples

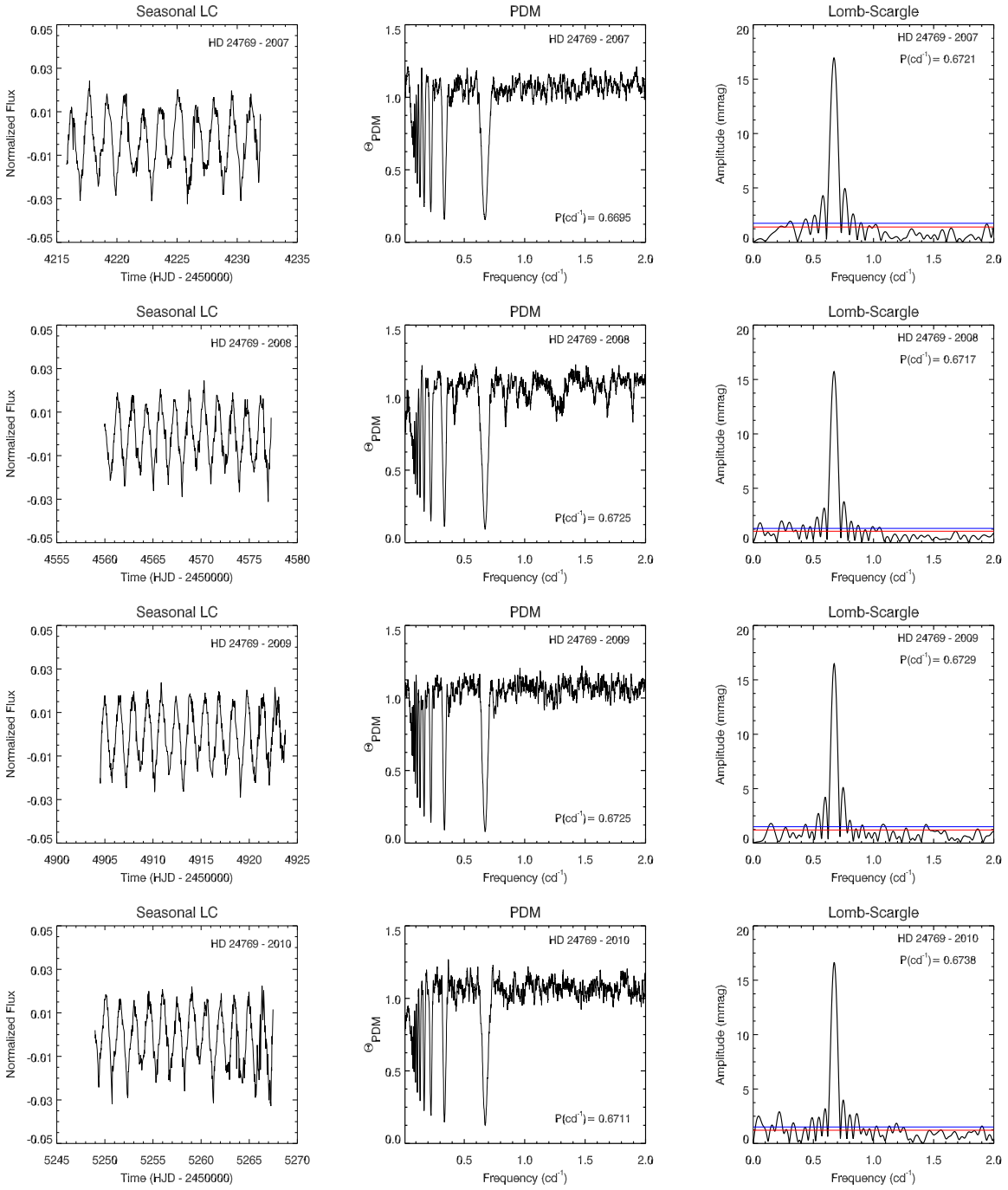

Figure A.1: Annual light curves and related LS and PDM analyses of HD 24769 are shown in the figure.

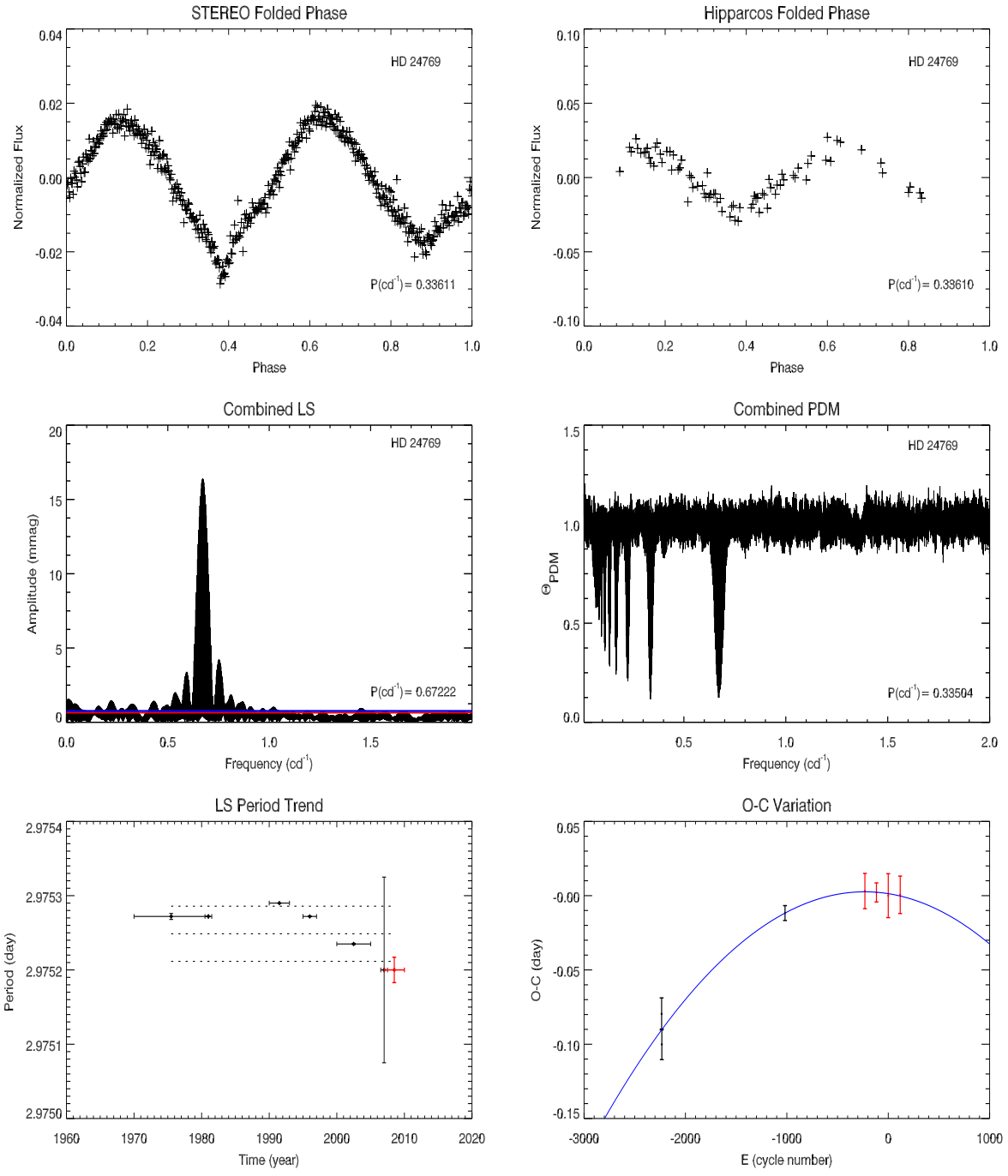

Figure A.2: Folded light curves produced with *STEREO* and *Hipparcos* data, frequency analyses of combined light curves as well as period and O-C graphics of HD 24769.

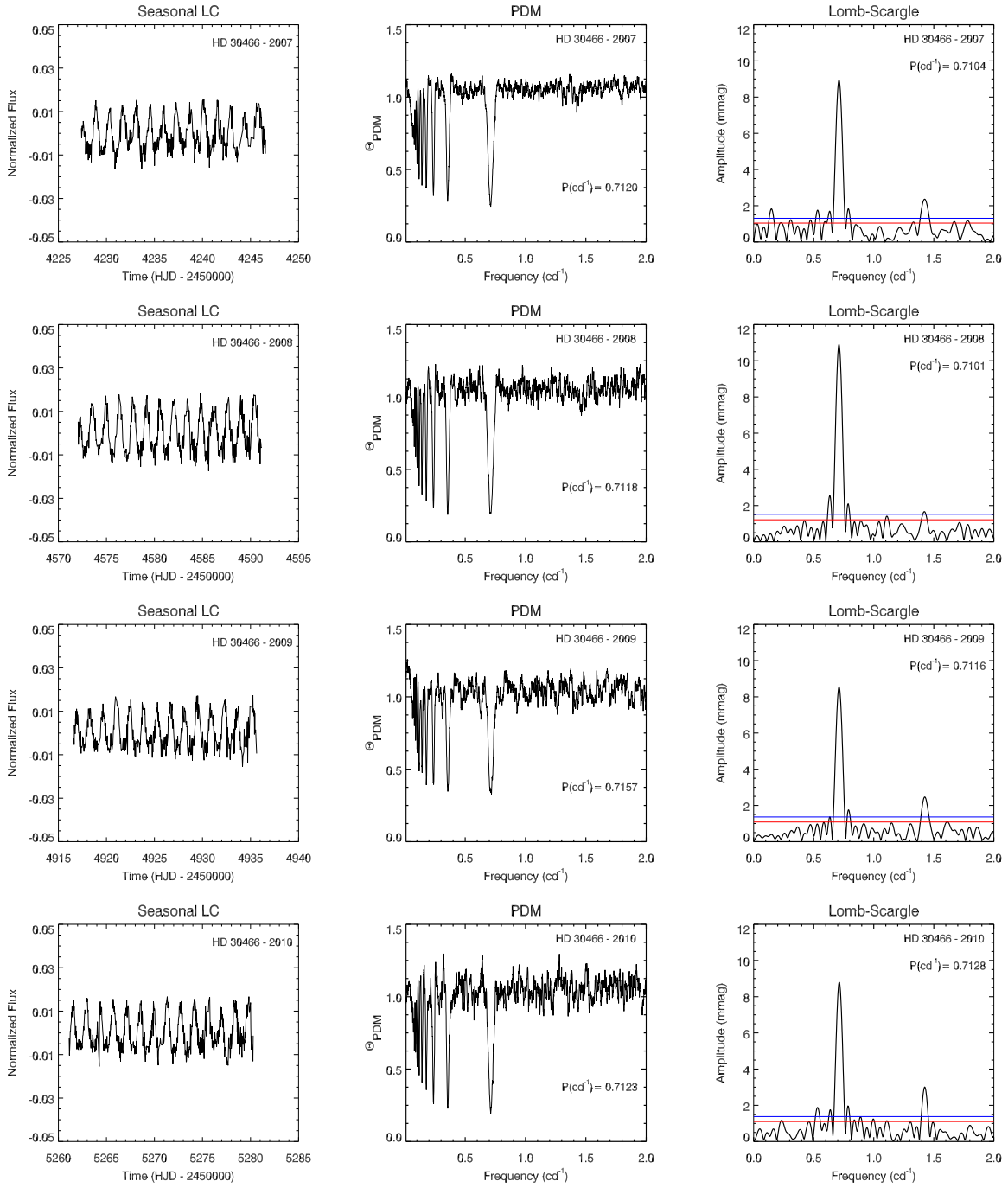

Figure A.3: Annual light curves and related LS and PDM analyses of HD 30466 are shown in the figure.

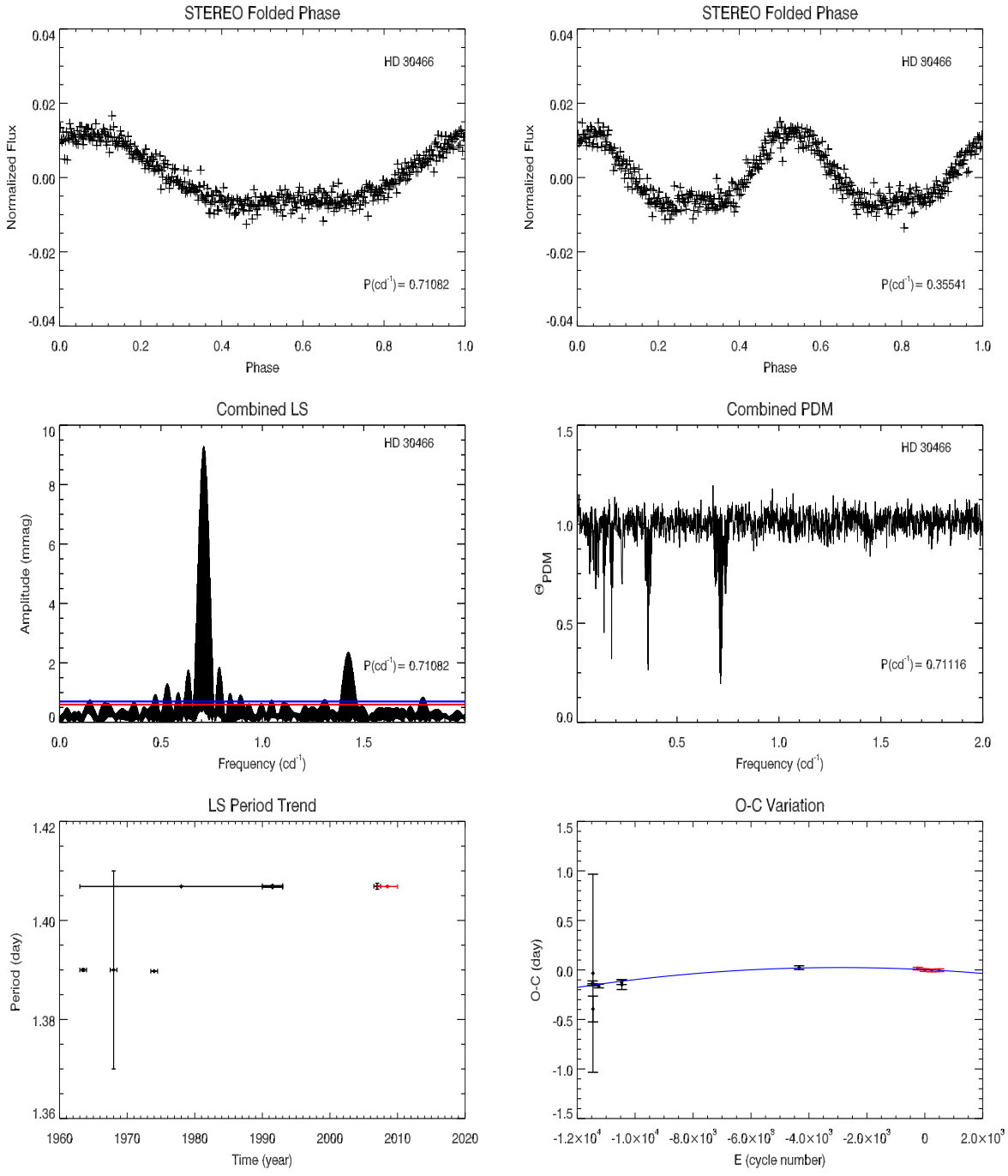

Figure A.4: Folded light curves produced by *STEREO* periods, frequency analyses of combined light curves as well as period and O-C variation graphics HD 30466.

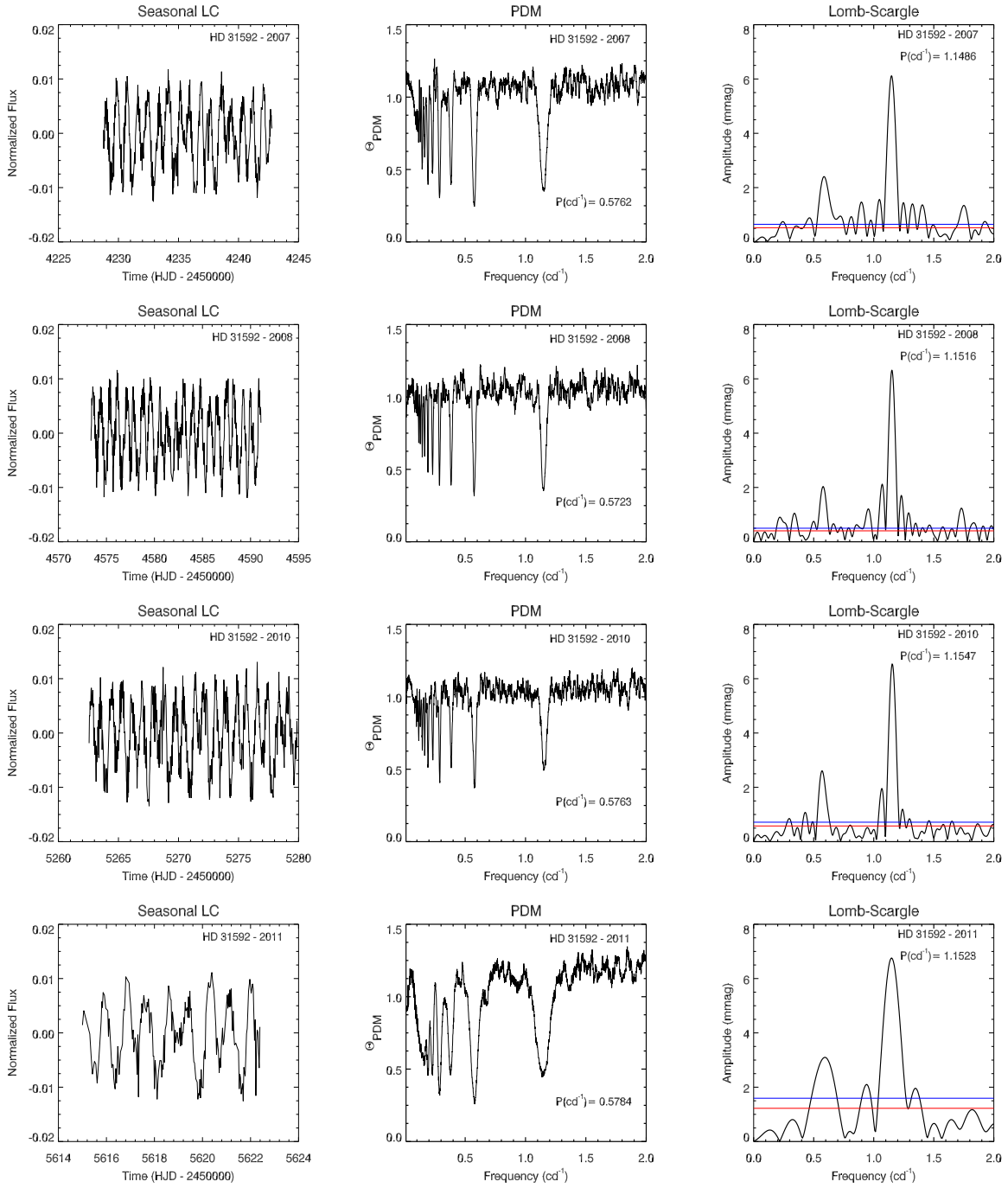

Figure A.5: Annual light curves and related LS and PDM analyses of HD 31592 are shown in the figure.

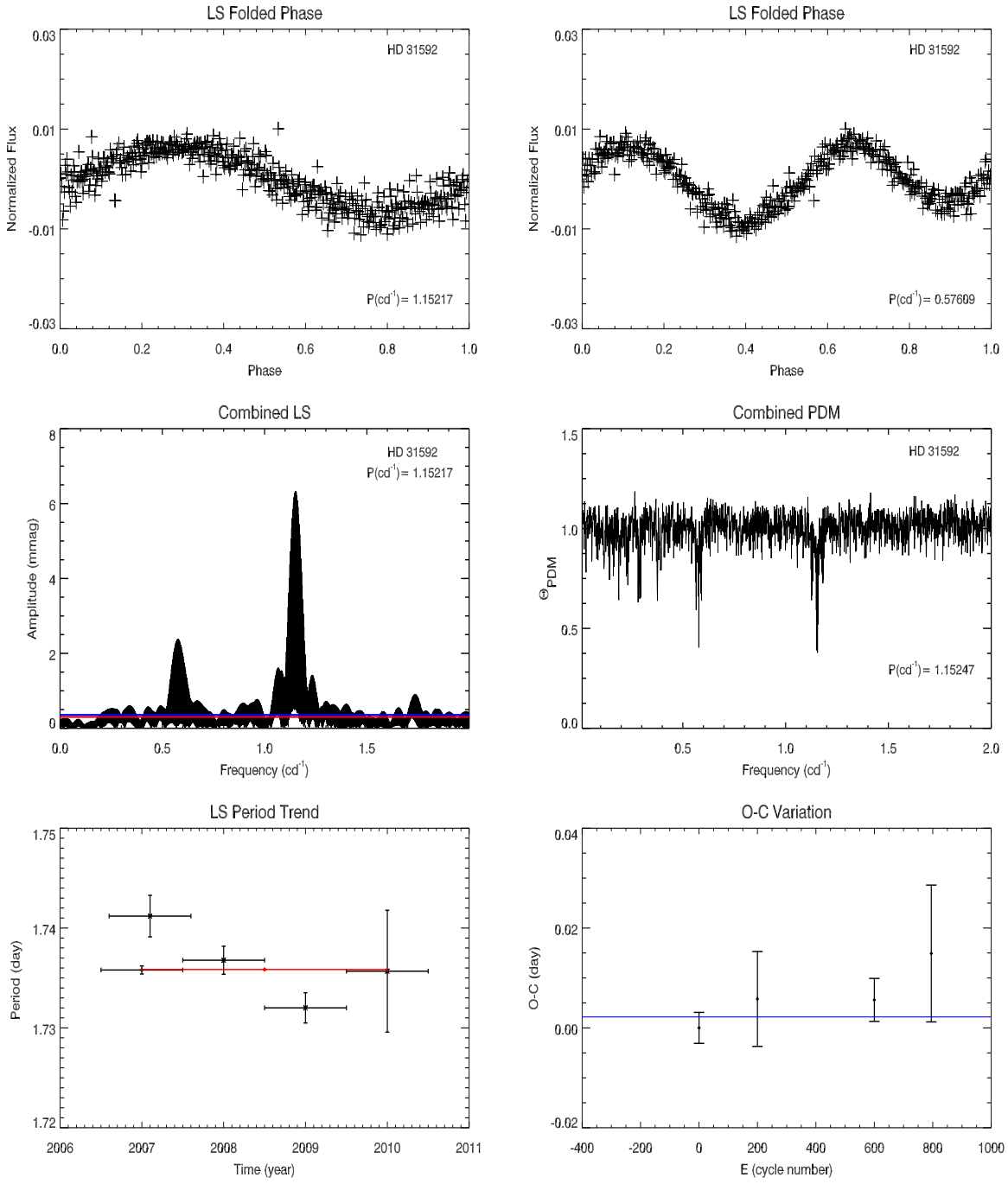

Figure A.6: Folded light curves produced by *STEREO* periods, frequency analyses of combined light curves as well as period and O-C variation graphics of HD 31592.

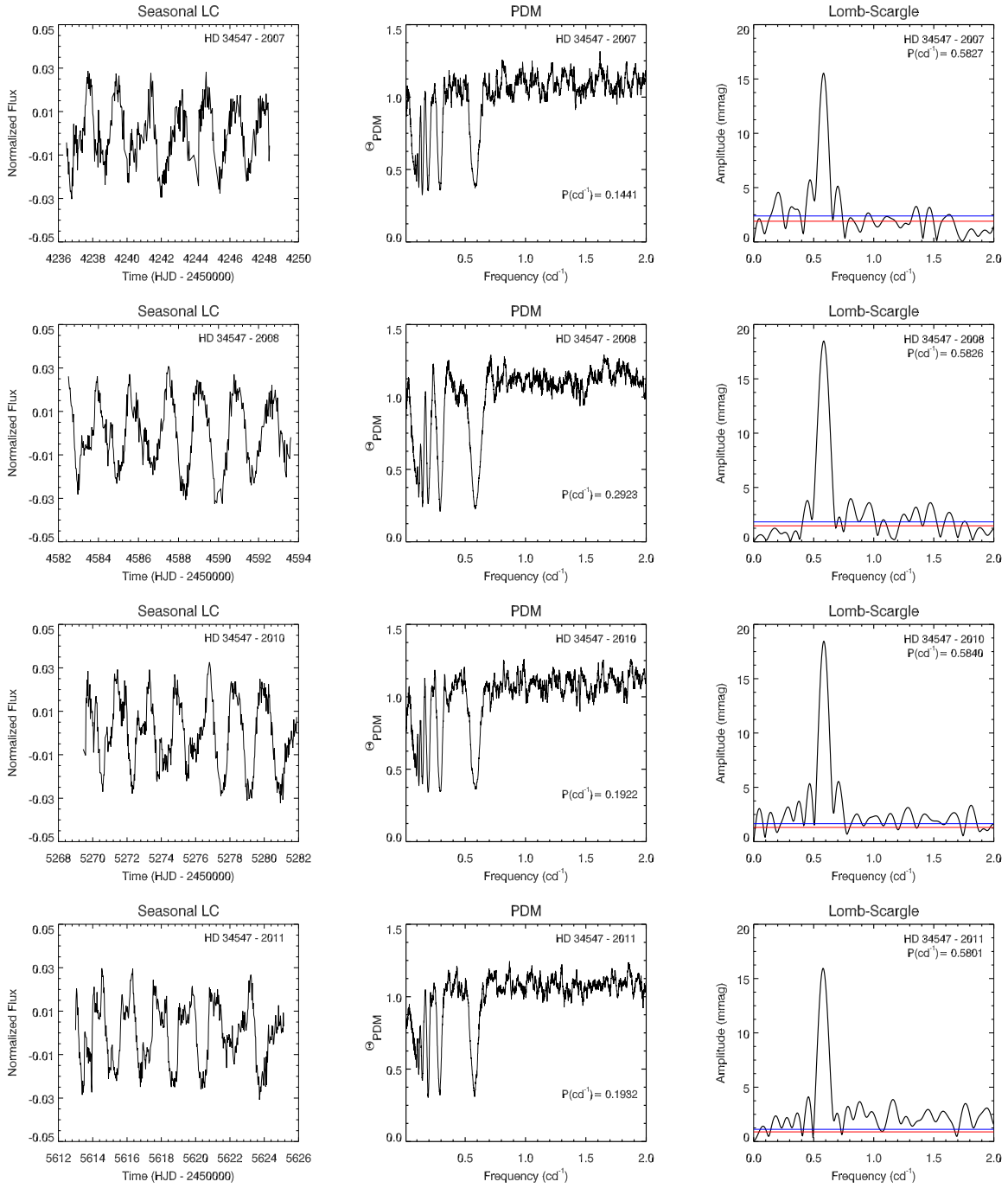

Figure A.7: Annual light curves and related LS and PDM analyses of HD 34547 are shown in the figure.

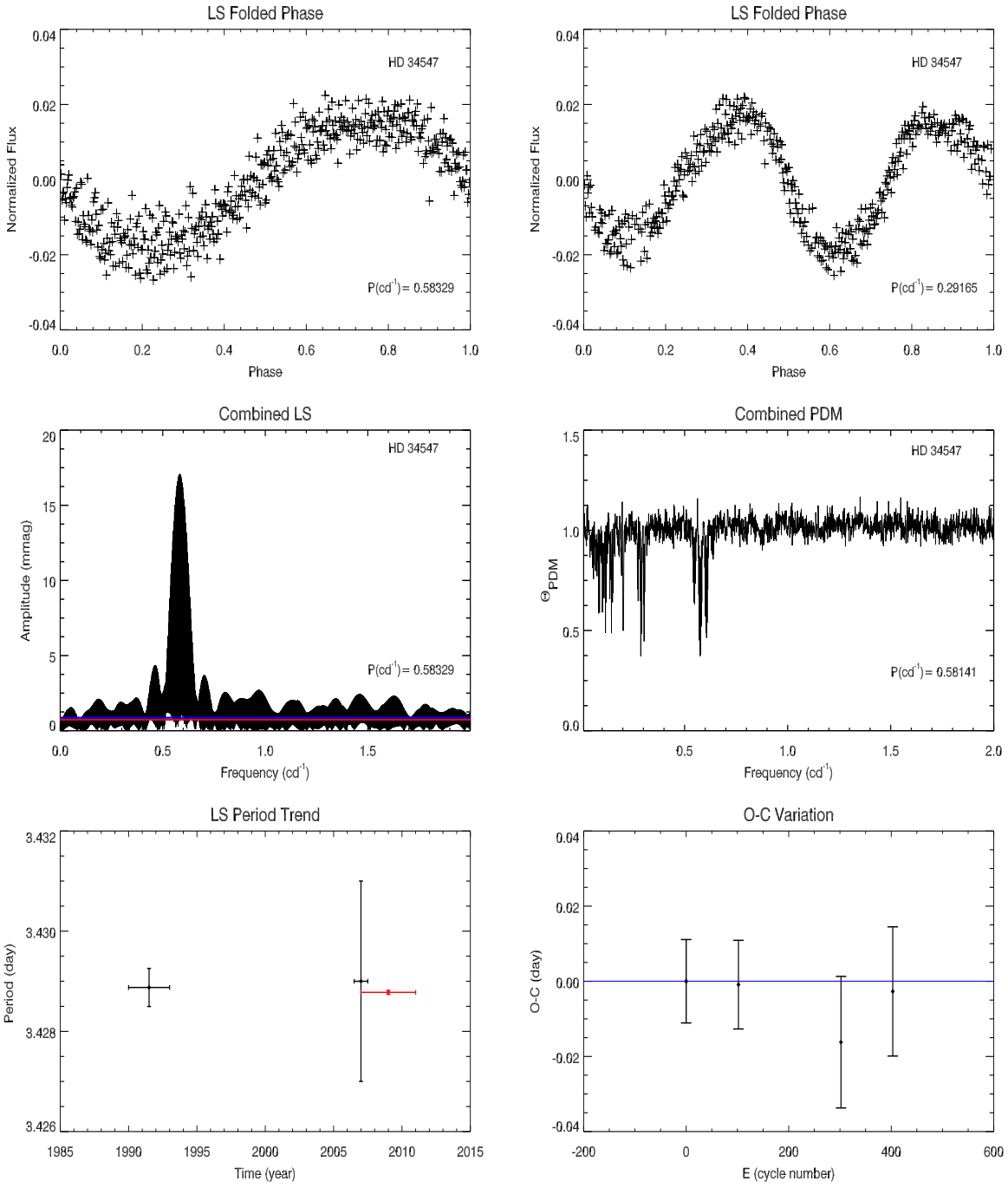

Figure A.8: Folded light curves produced by *STEREO* periods, frequency analyses of combined light curves as well as period and O-C variation graphics of HD 34547.

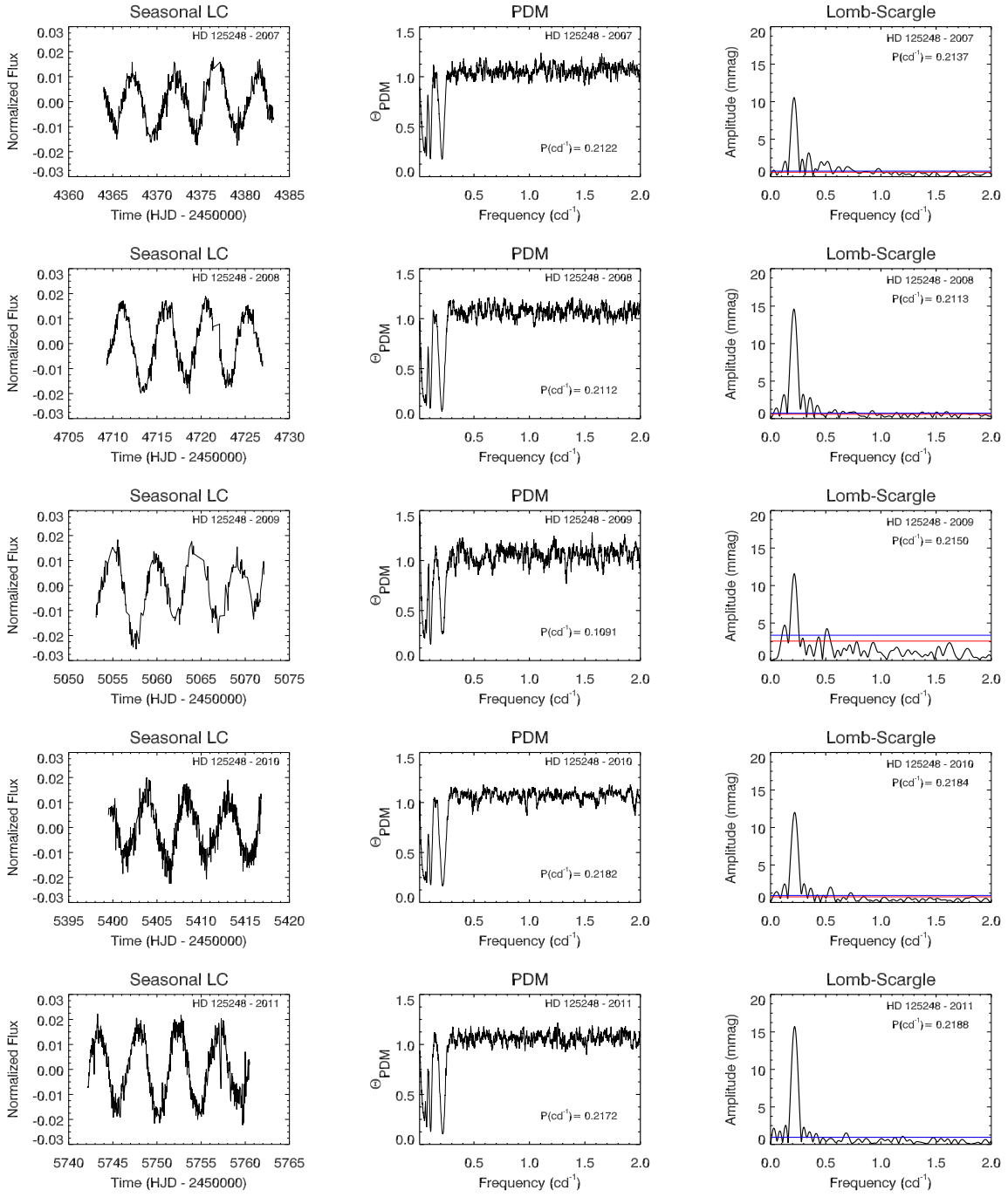

Figure A.9: Annual light curves and related LS and PDM analyses of HD 125248 are shown in the figure.

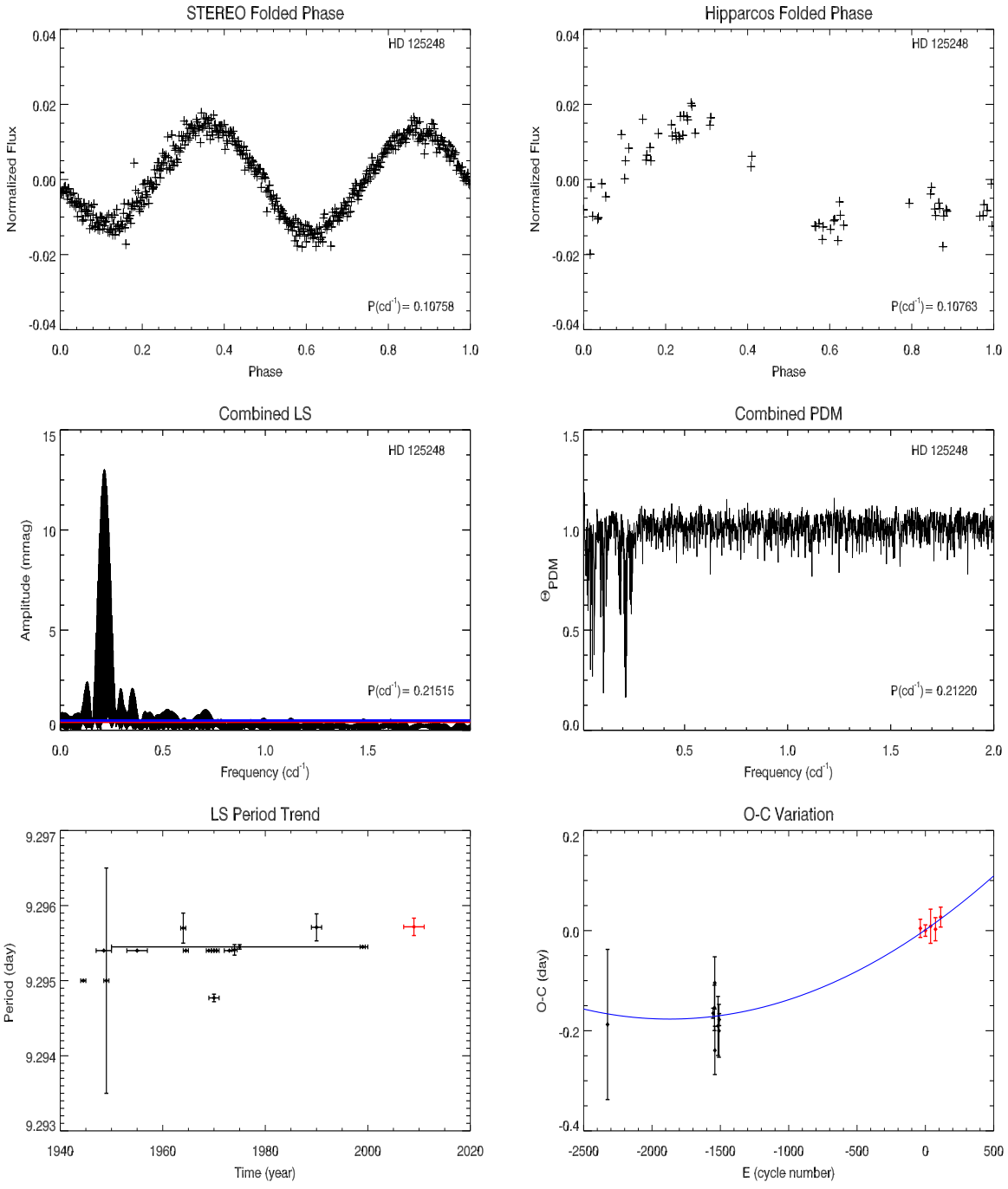

Figure A.10: Folded light curves produced by *STEREO* and *Hipparcos* periods, frequency analyses of combined light curves as well as period and O-C variation graphics of HD 125248.

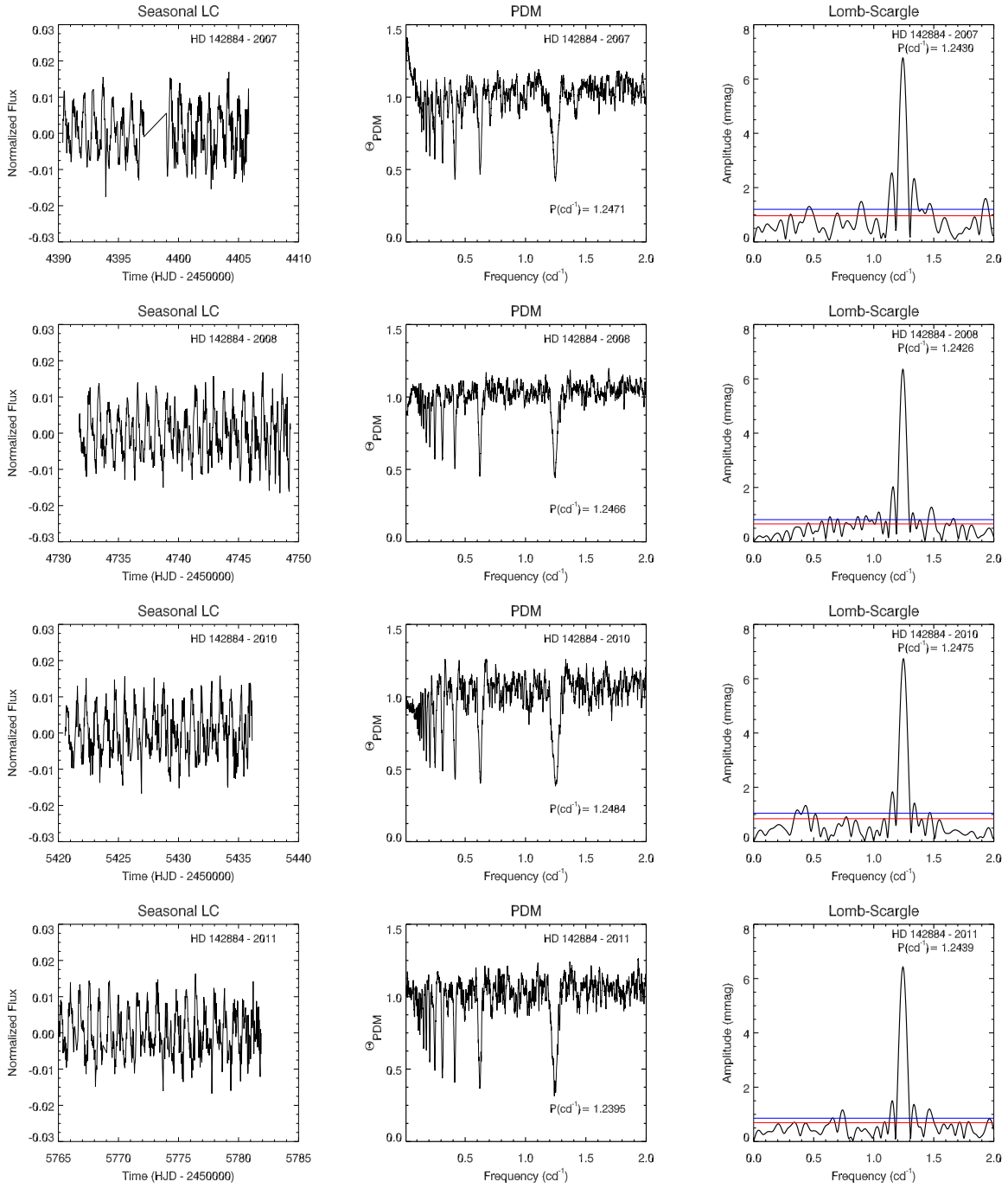

Figure A.11: Annual light curves and related LS and PDM analyses of HD 142884 are shown in the figure.

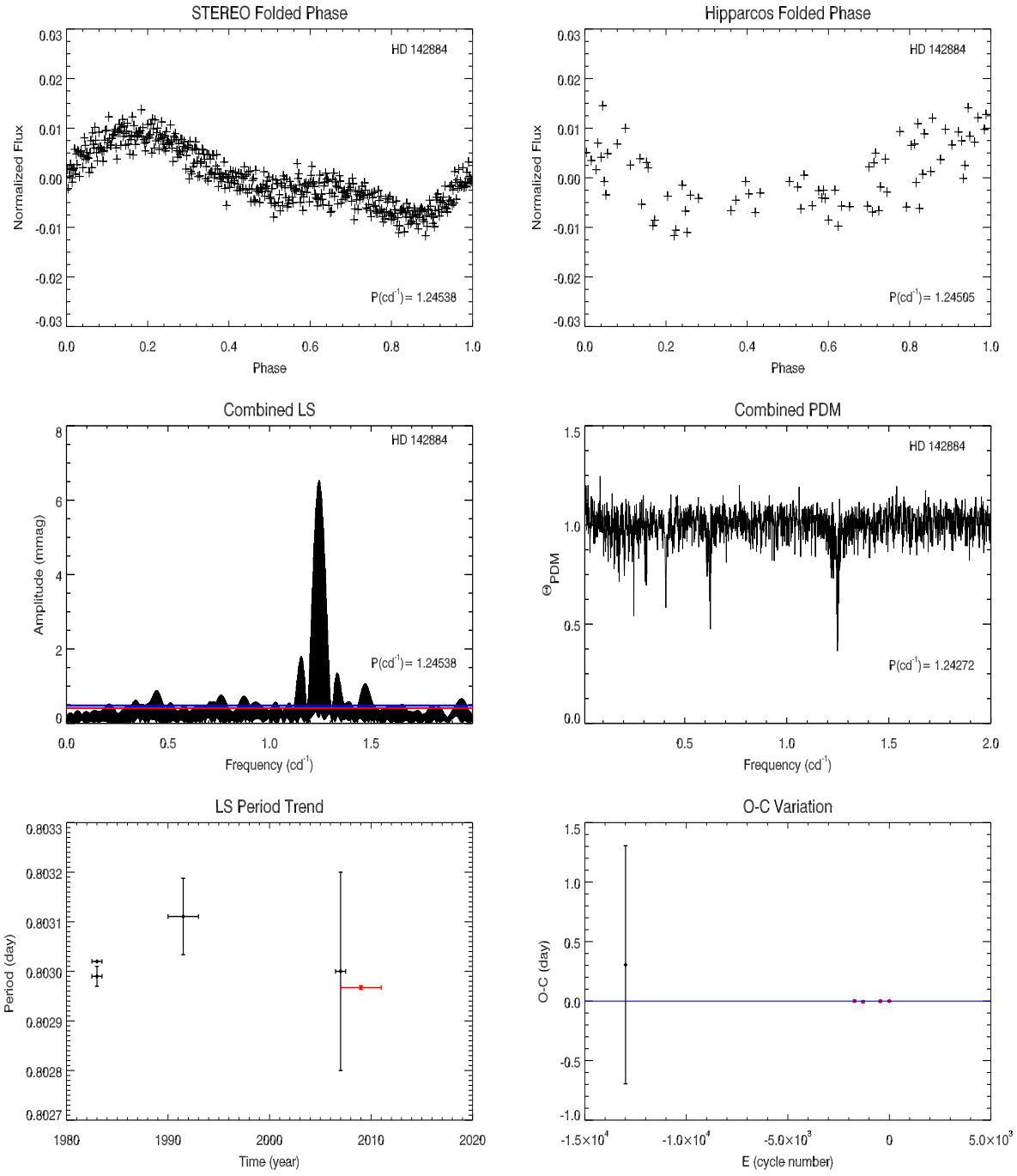

Figure A.12: Folded light curves produced by *STEREO* and *Hipparcos* periods, frequency analyses of combined light curves as well as period and O-C variation graphics of HD 142884.

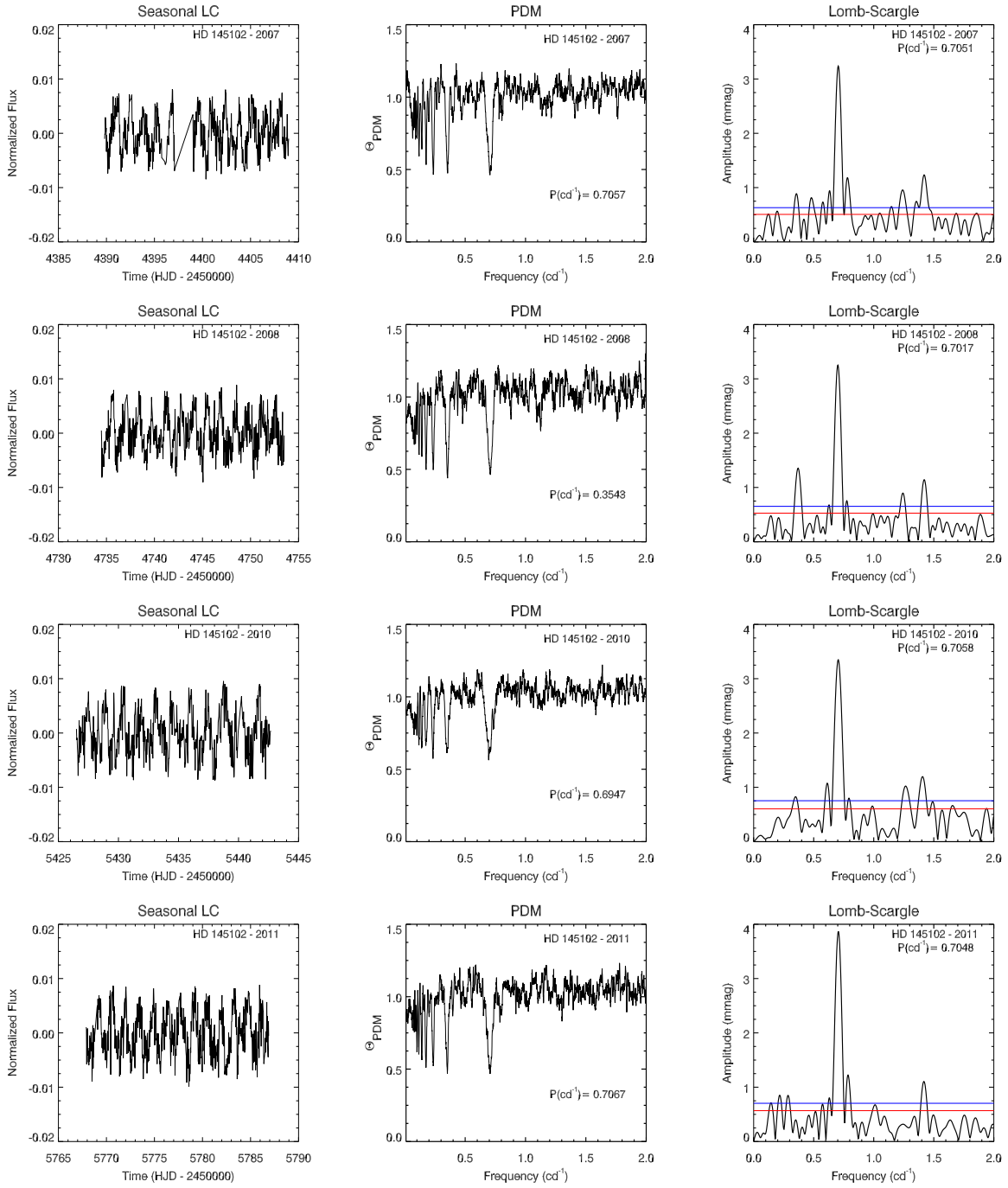

Figure A.13: Annual light curves and related LS and PDM analyses of HD 145102 are shown in the figure.

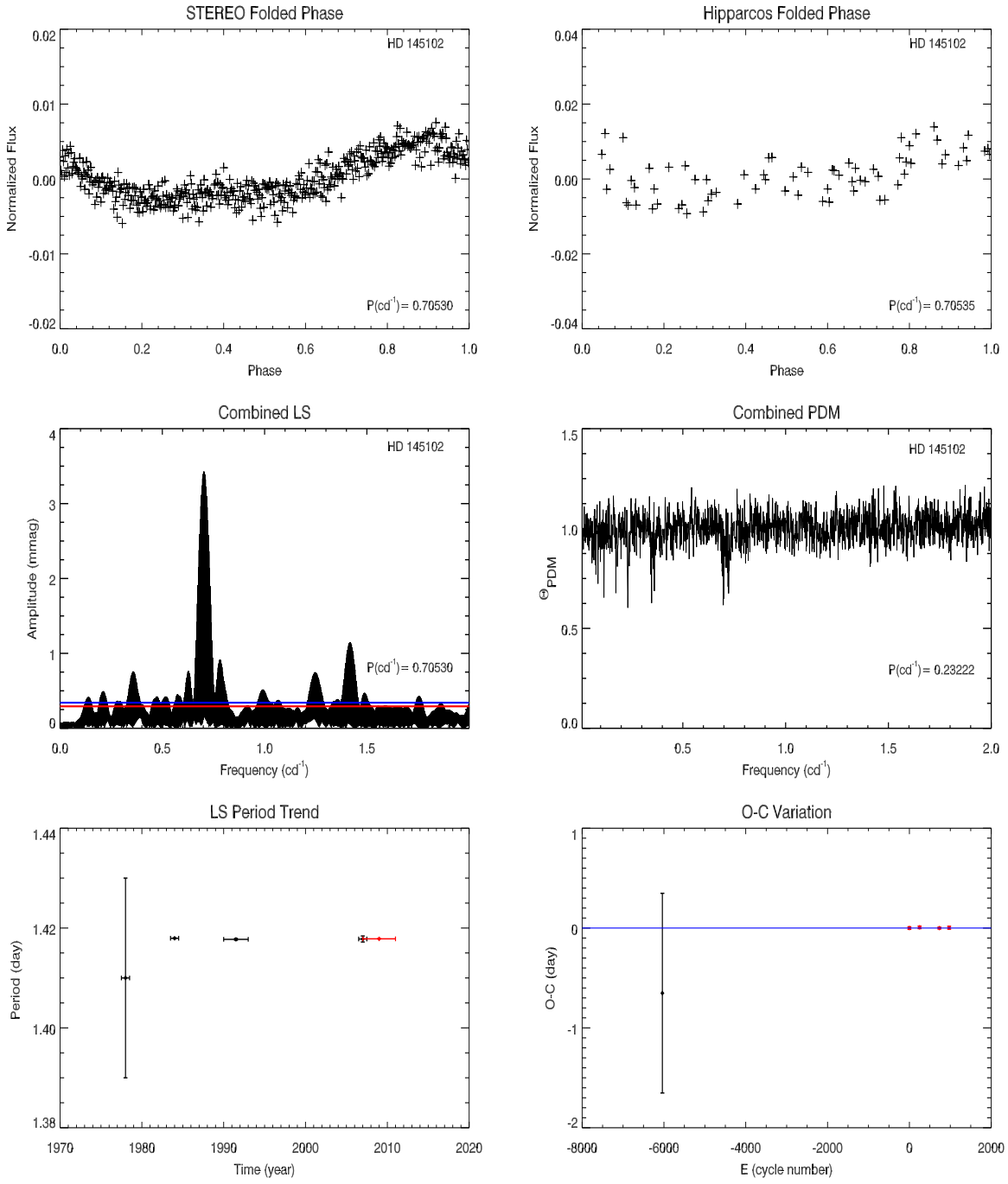

Figure A.14: Folded light curves produced by *STEREO* and *Hipparcos* periods, frequency analyses of combined light curves as well as period and O-C variation graphics of HD 145102.

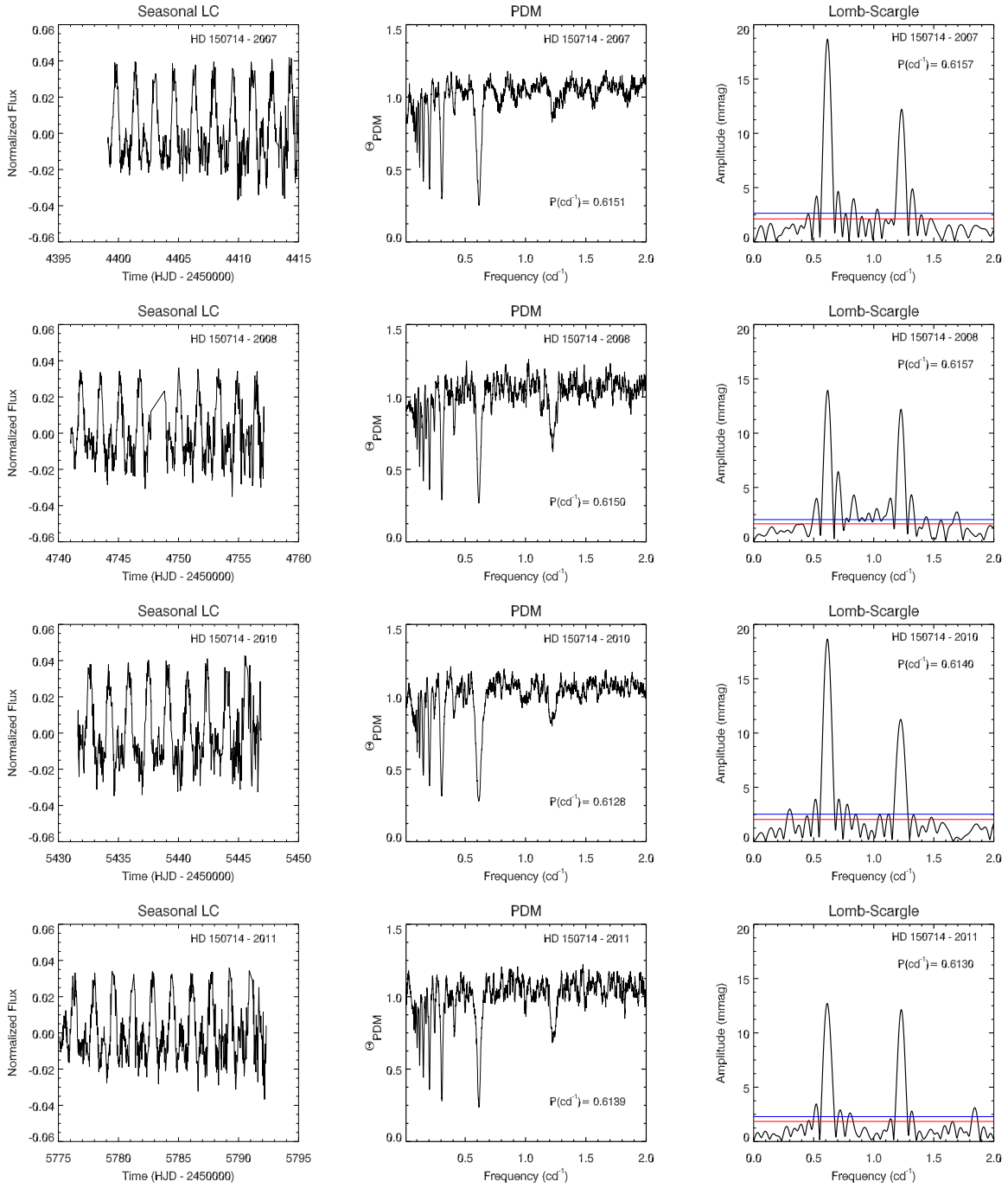

Figure A.15: Annual light curves and related LS and PDM analyses of HD 150714 are shown in the figure.

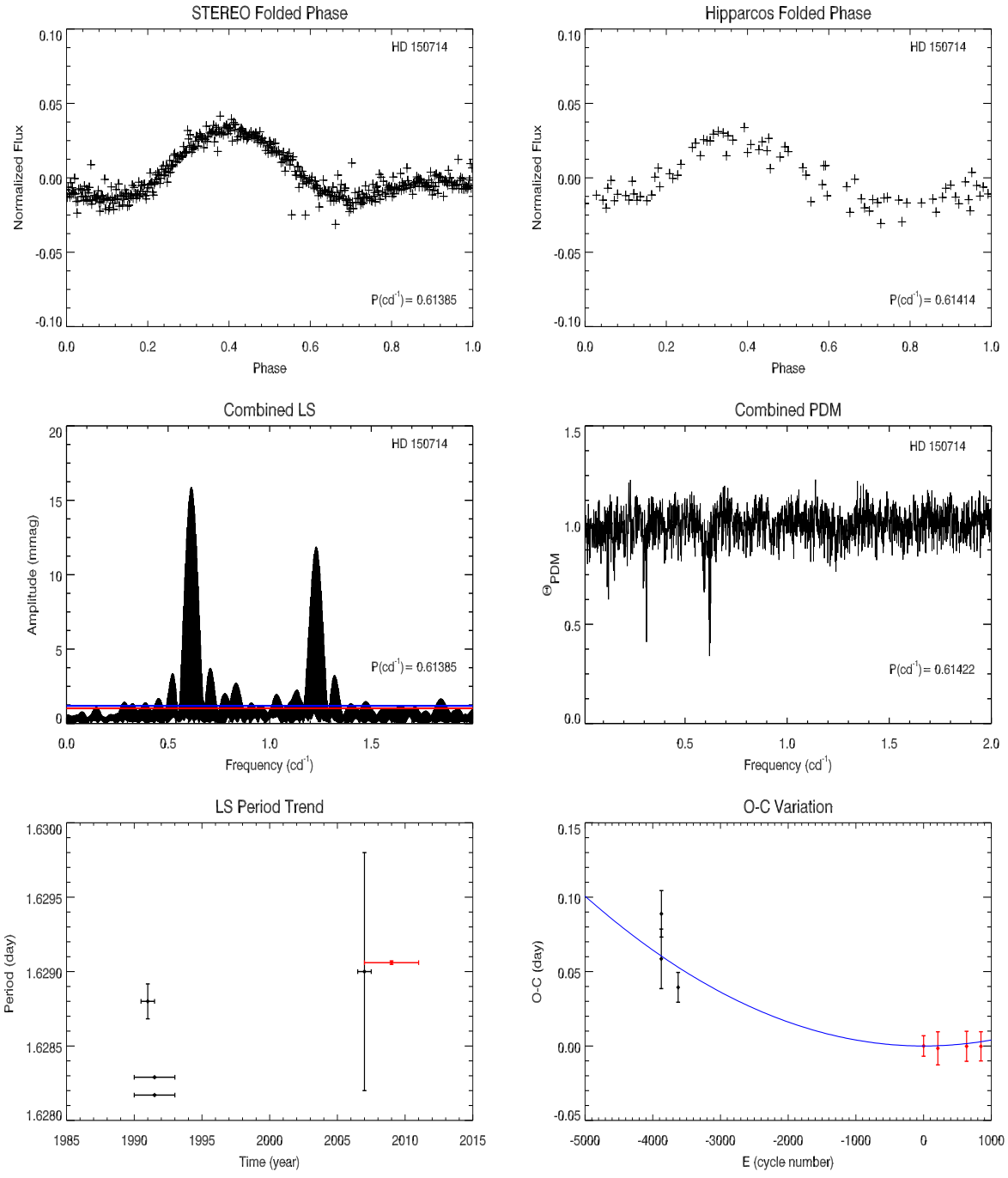

Figure A.16: Folded light curves produced by *STEREO* and *Hipparcos* periods, frequency analyses of combined light curves as well as period and O-C variation graphics of HD 150714.

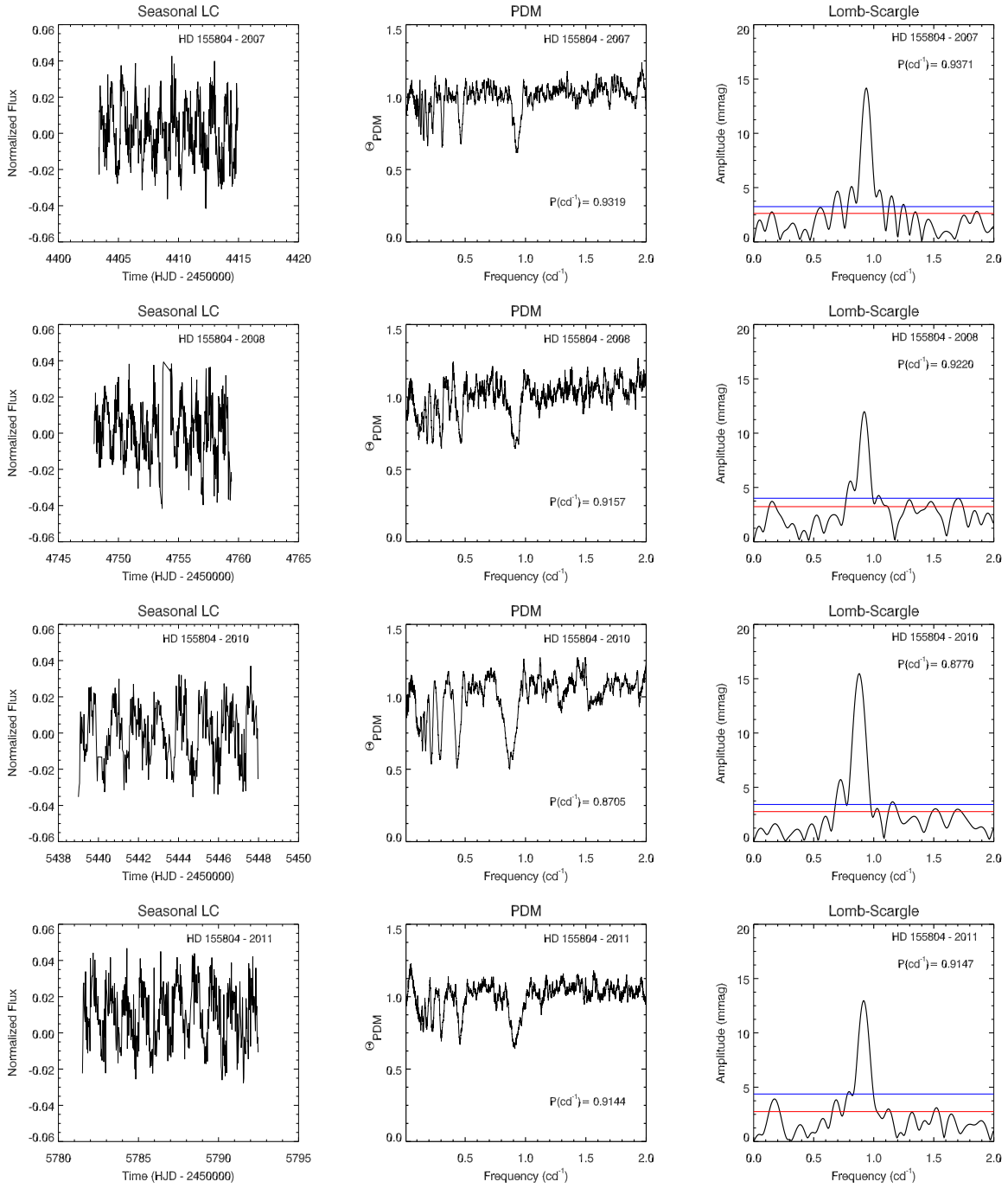

Figure A.17: Annual light curves and related LS and PDM analyses of HD 155804 are shown in the figure.

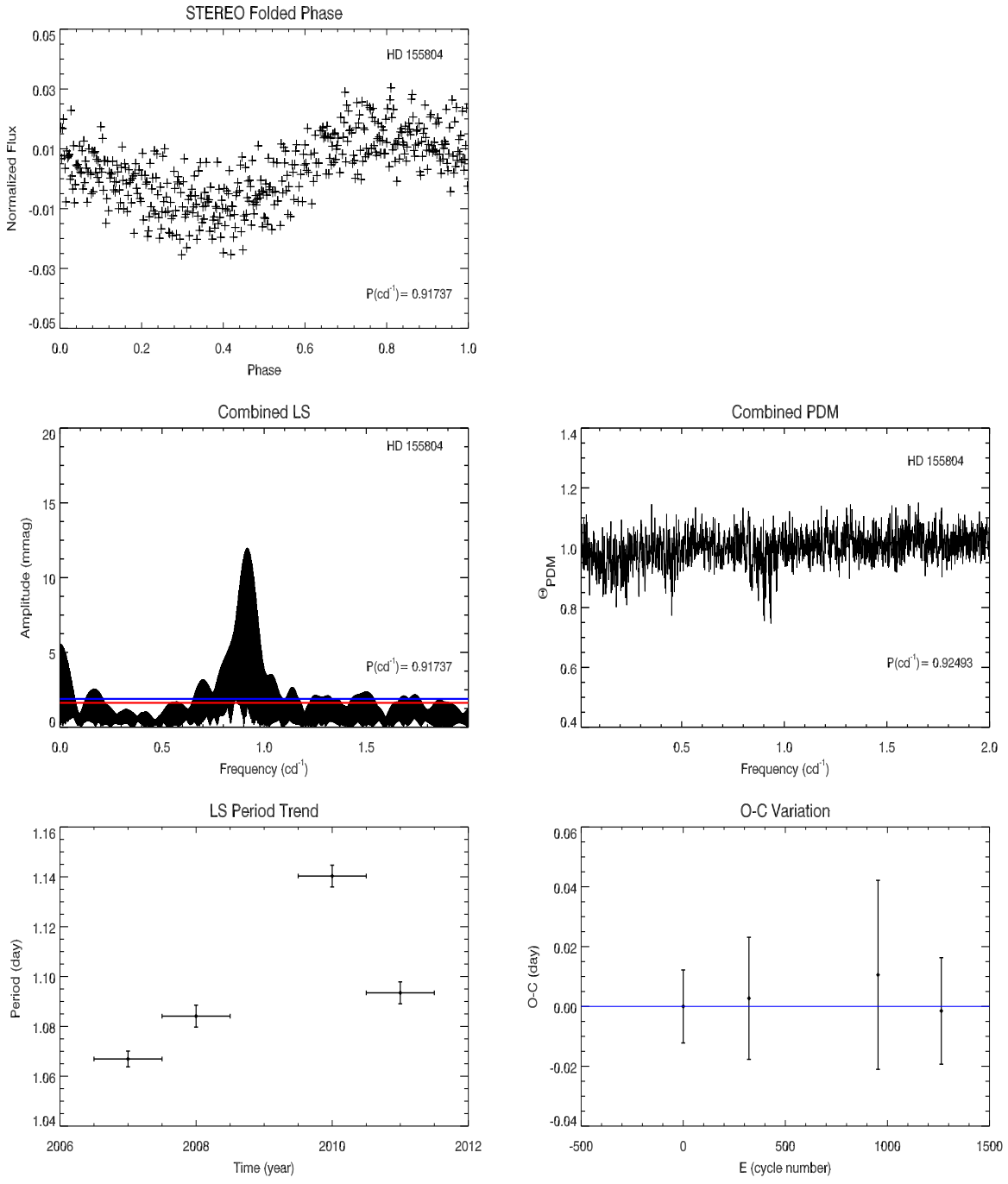

Figure A.18: Folded light curve produced by *STEREO* period, frequency analyses of combined light curves as well as period and O-C variation graphics of HD 155804.

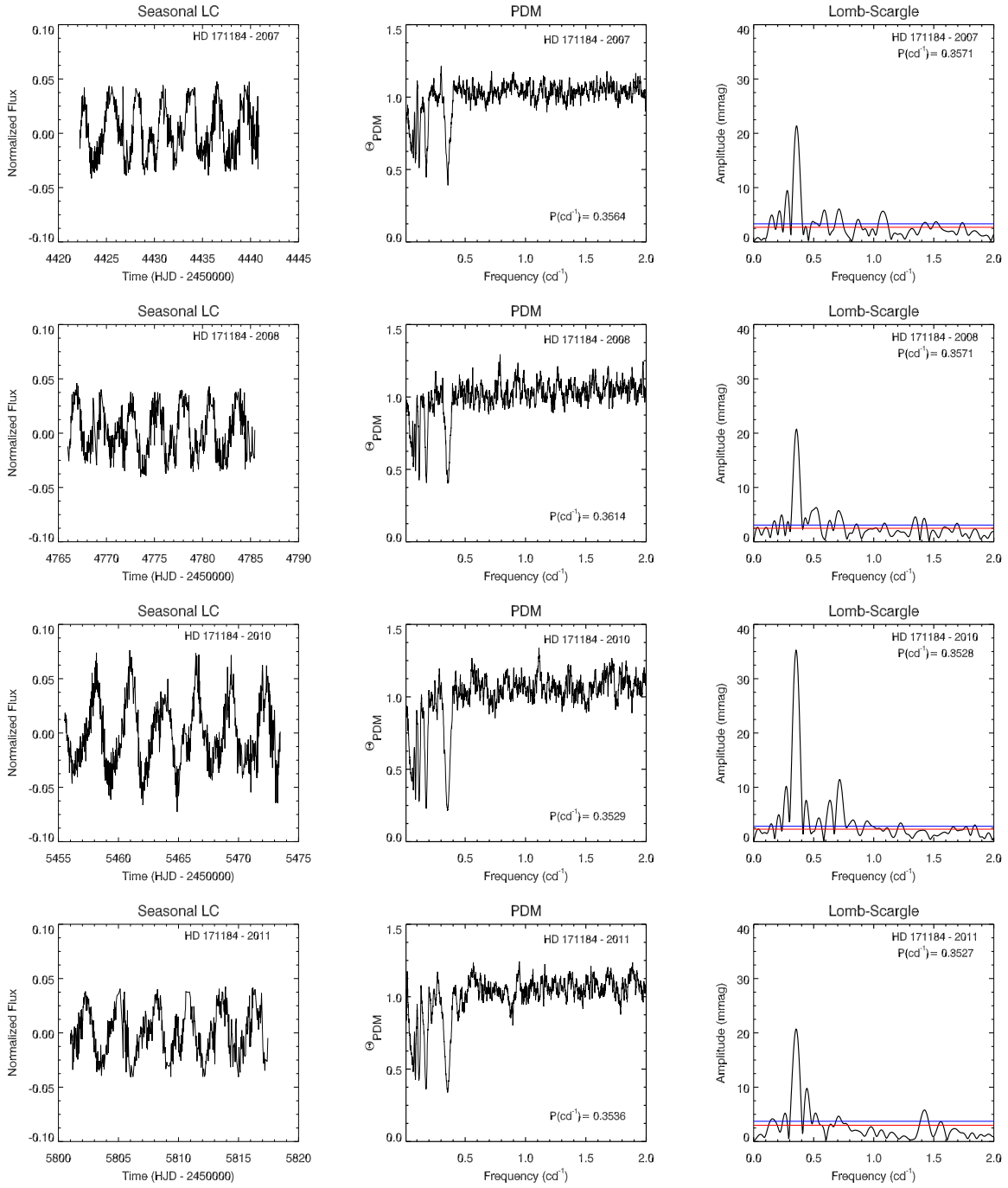

Figure A.19: Annual light curves and related LS and PDM analyses of HD 171184 are shown in the figure.

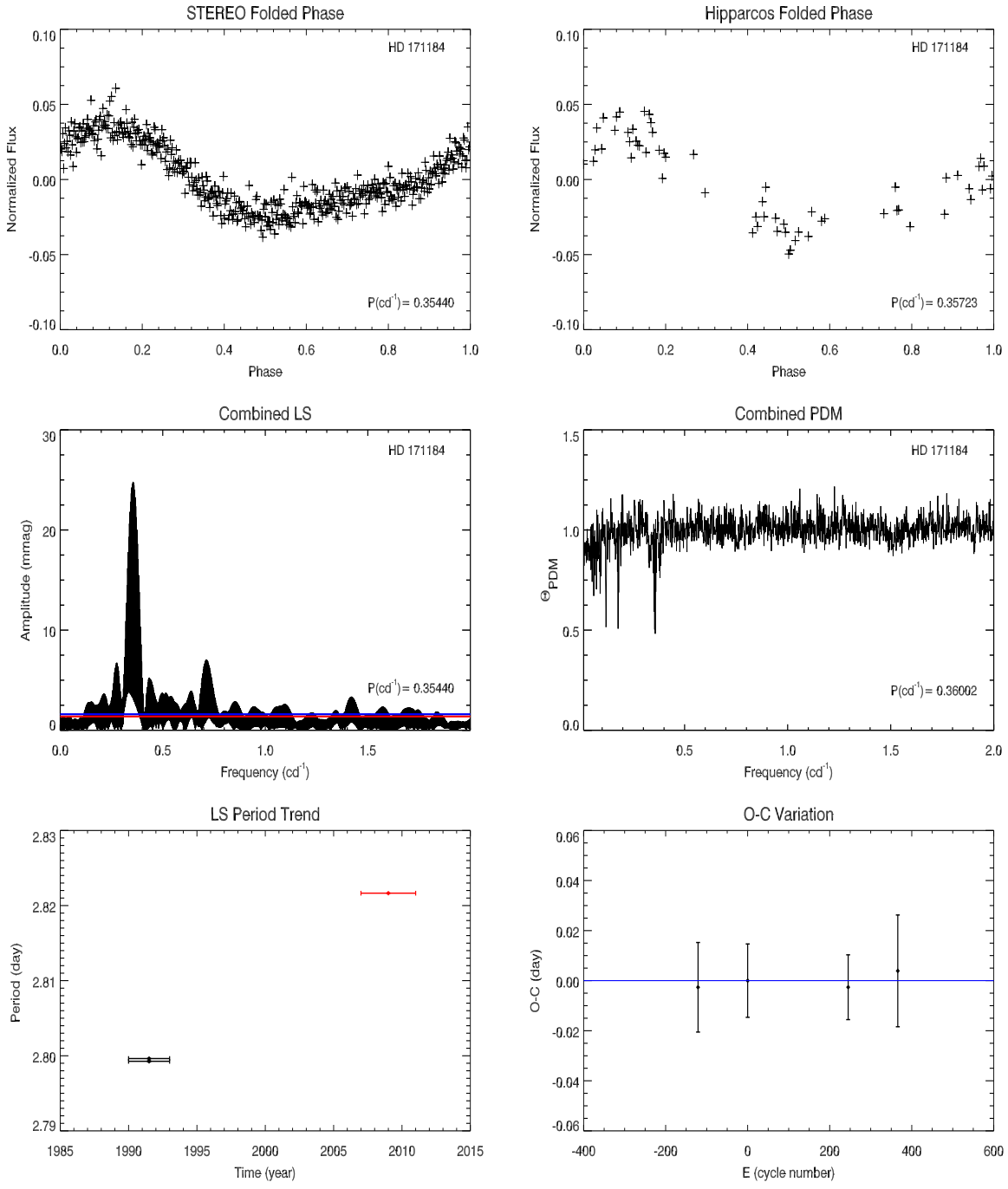

Figure A.20: Folded light curve produced by *STEREO* and *Hipparcos* periods, frequency analyses of combined light curves as well as period and O-C variation graphics of HD 171184.

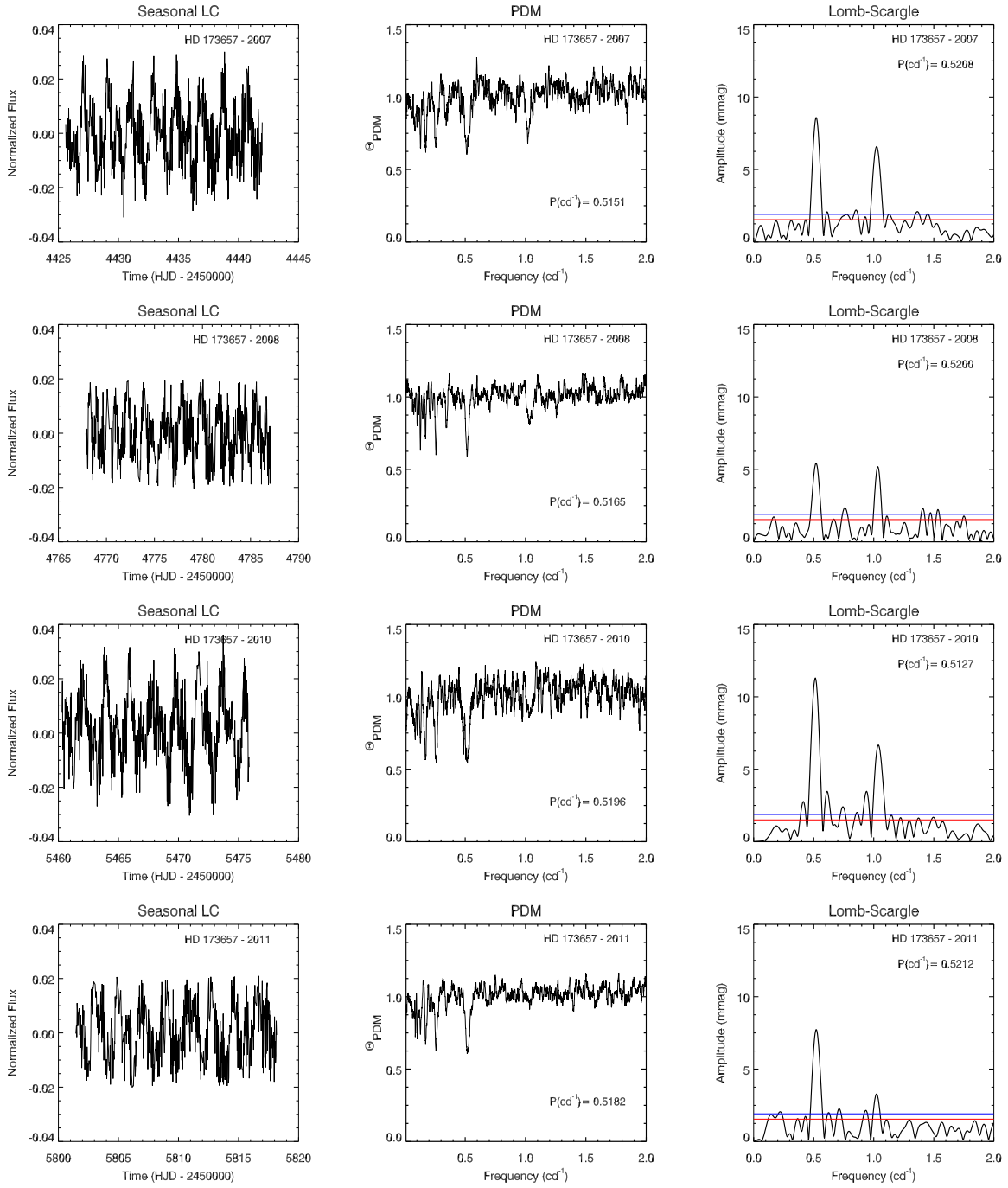

Figure A.21: Annual light curves and related LS and PDM analyses of HD 173657 are shown in the figure.

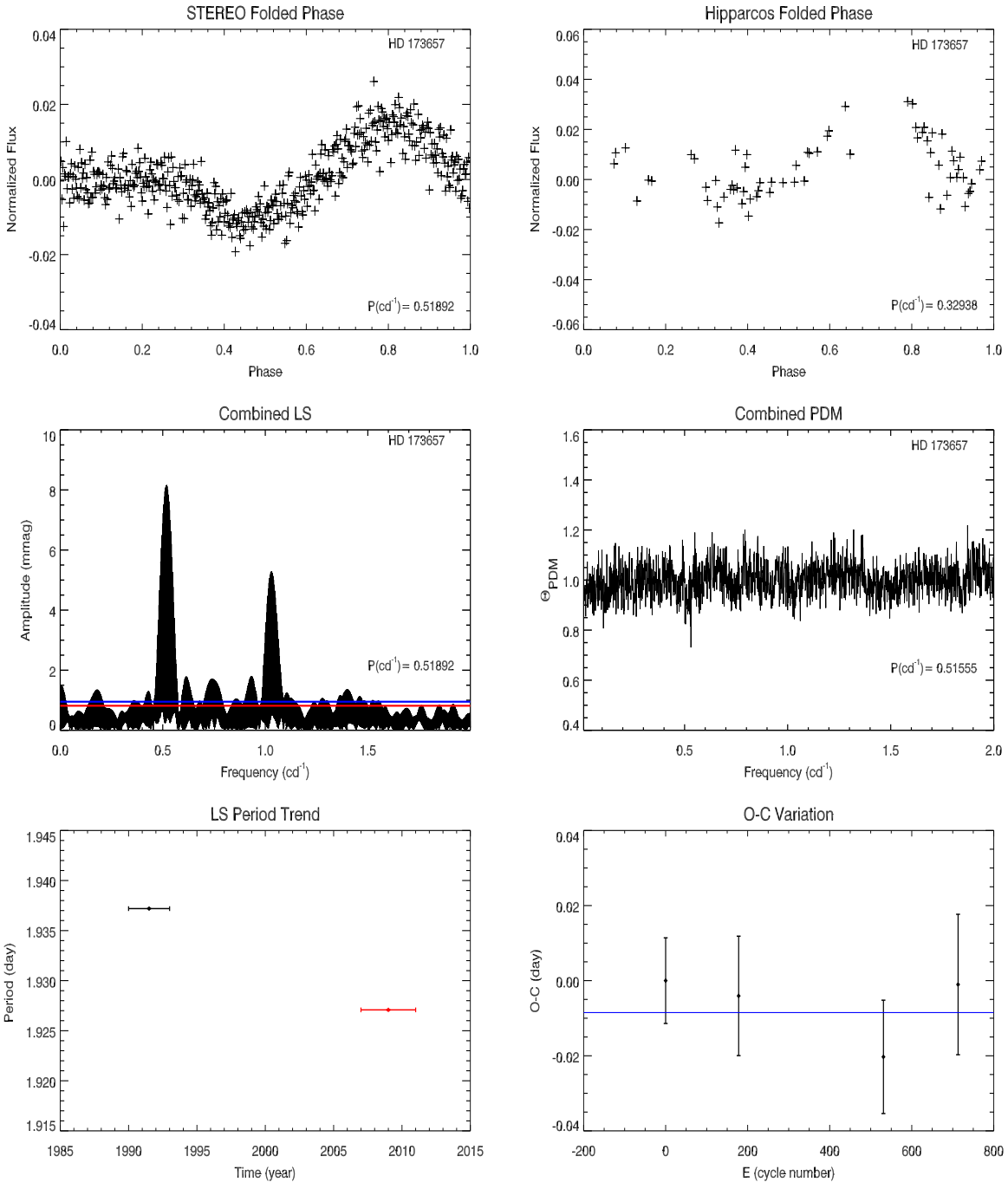

Figure A.22: Folded light curves produced by *STEREO* and *Hipparcos* periods, frequency analyses of combined light curves as well as period and O-C variation graphics of HD 173657.

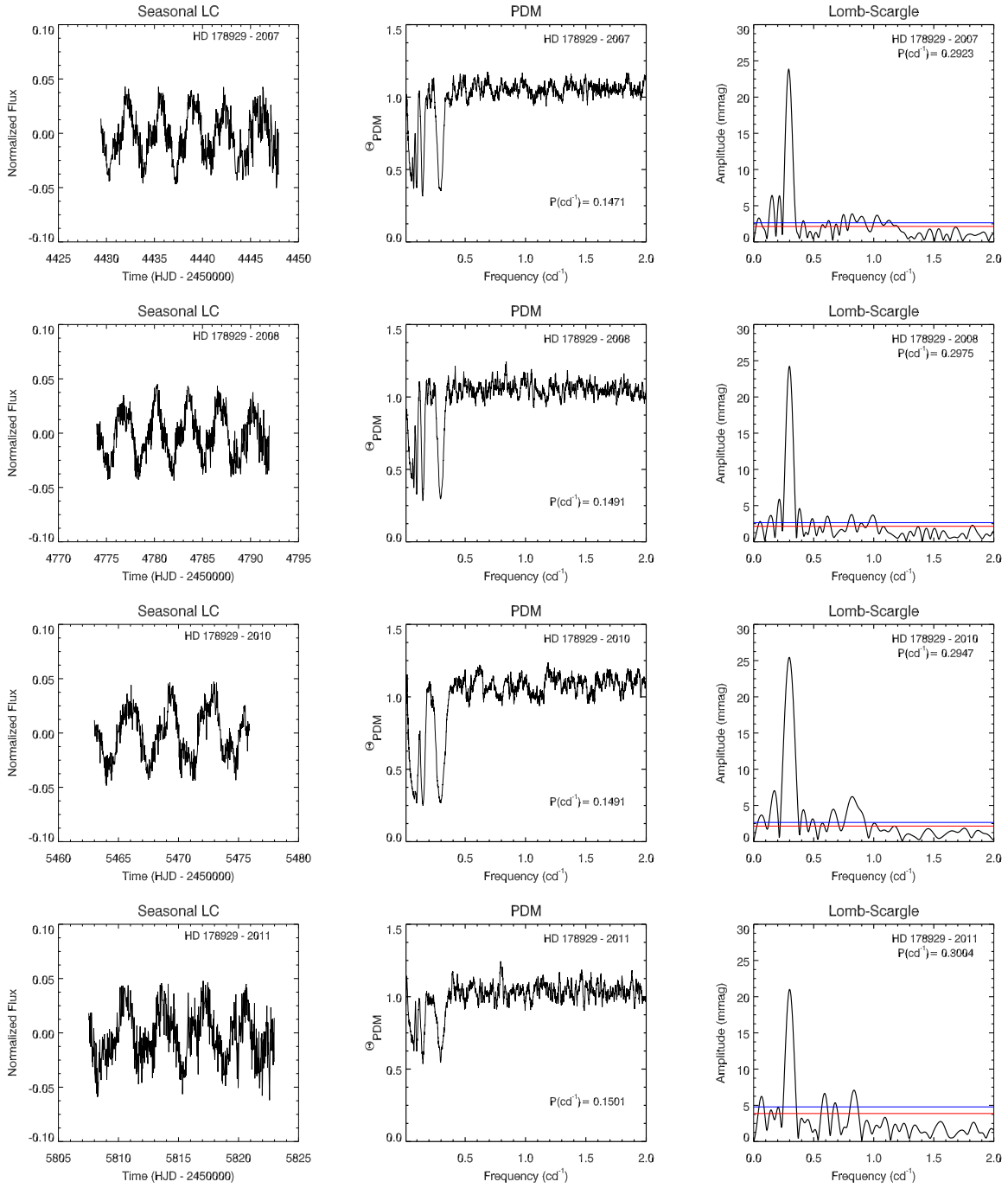

Figure A.23: Annual light curves and related LS and PDM analyses of HD 178929 are shown in the figure.

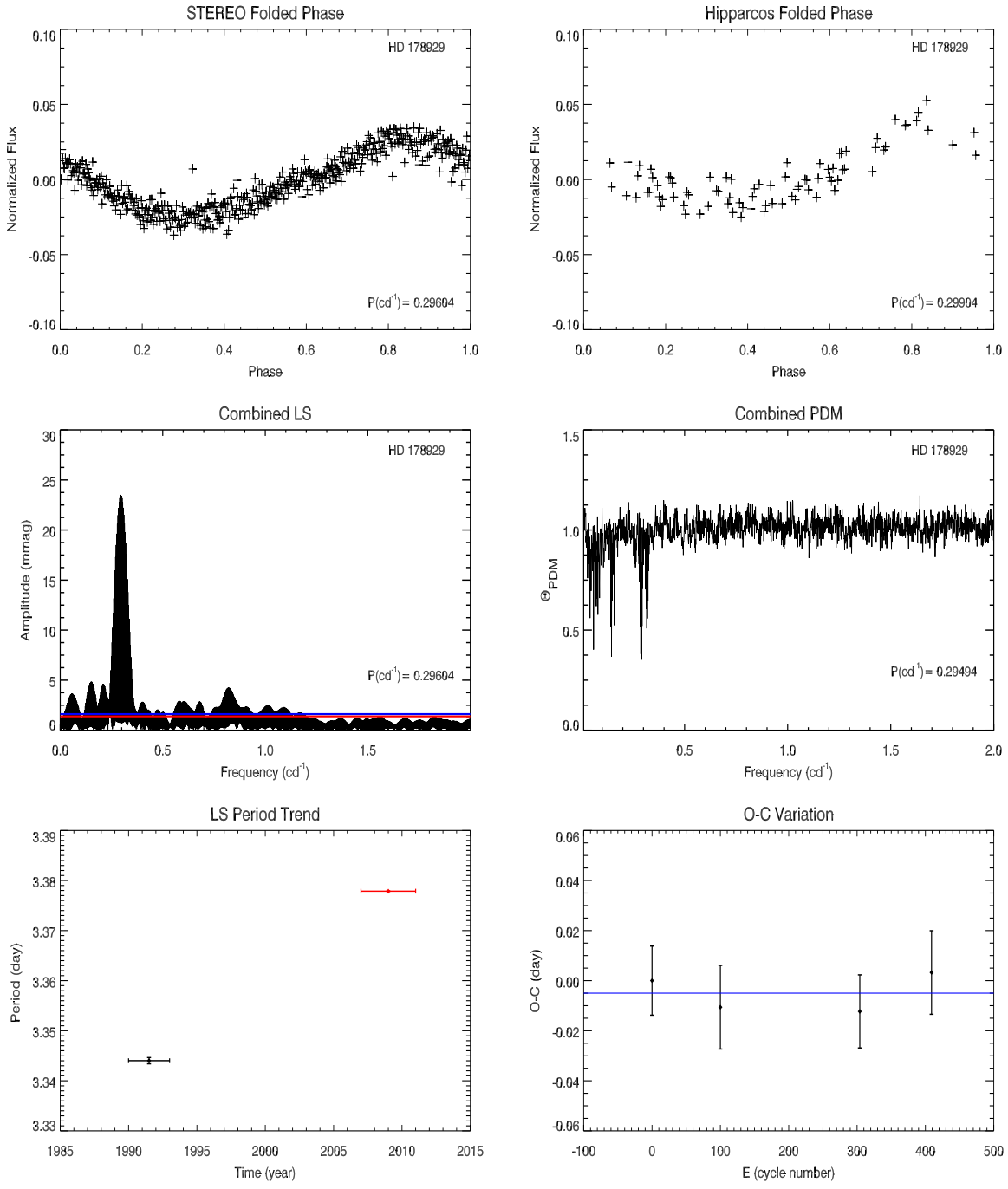

Figure A.24: Folded light curves produced by *STEREO* and *Hipparcos* periods, frequency analyses of combined light curves as well as period and O-C variation graphics of HD 178929.

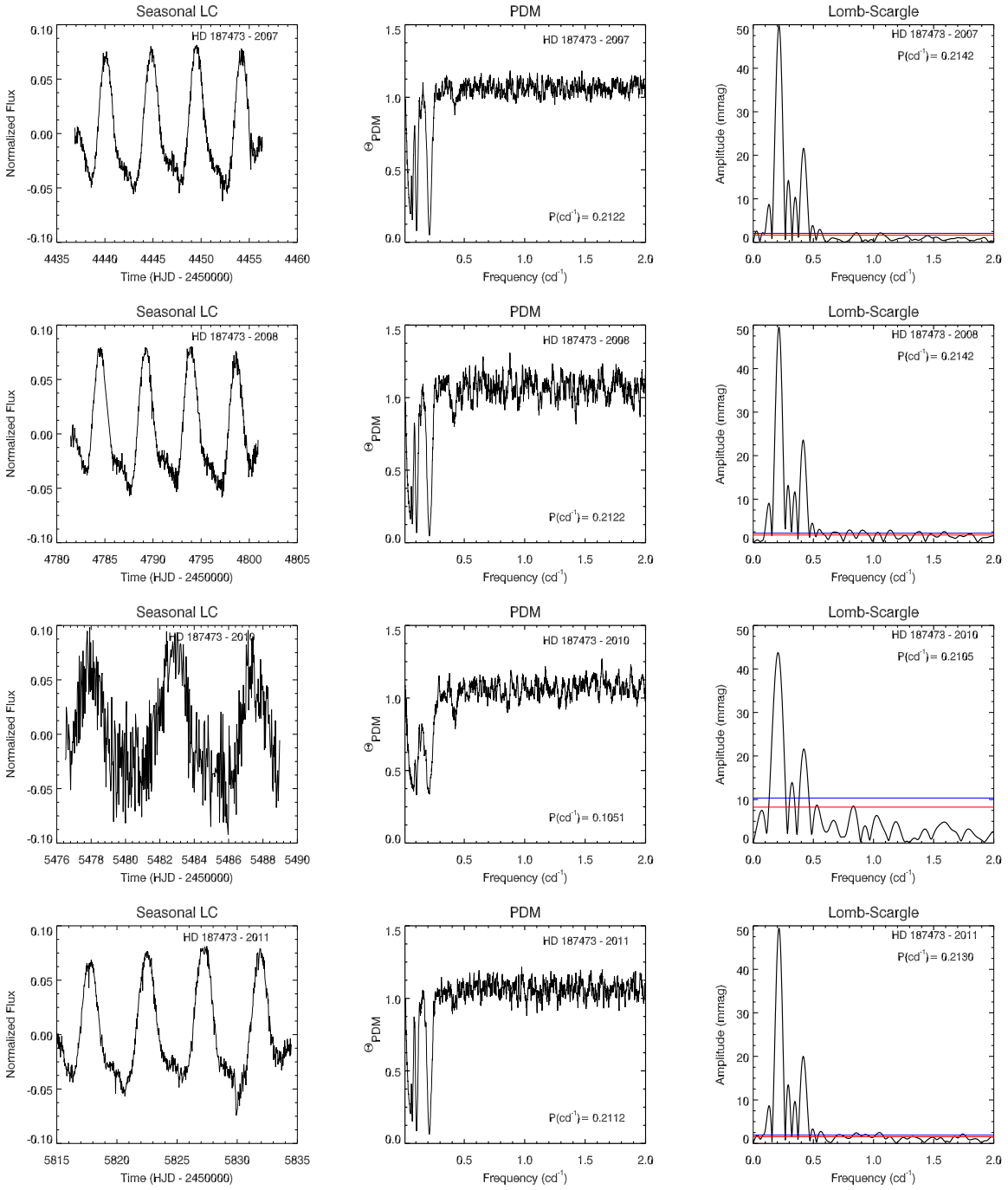

Figure A.25: Annual light curves and related LS and PDM analyses of HD 187473 are shown in the figure.

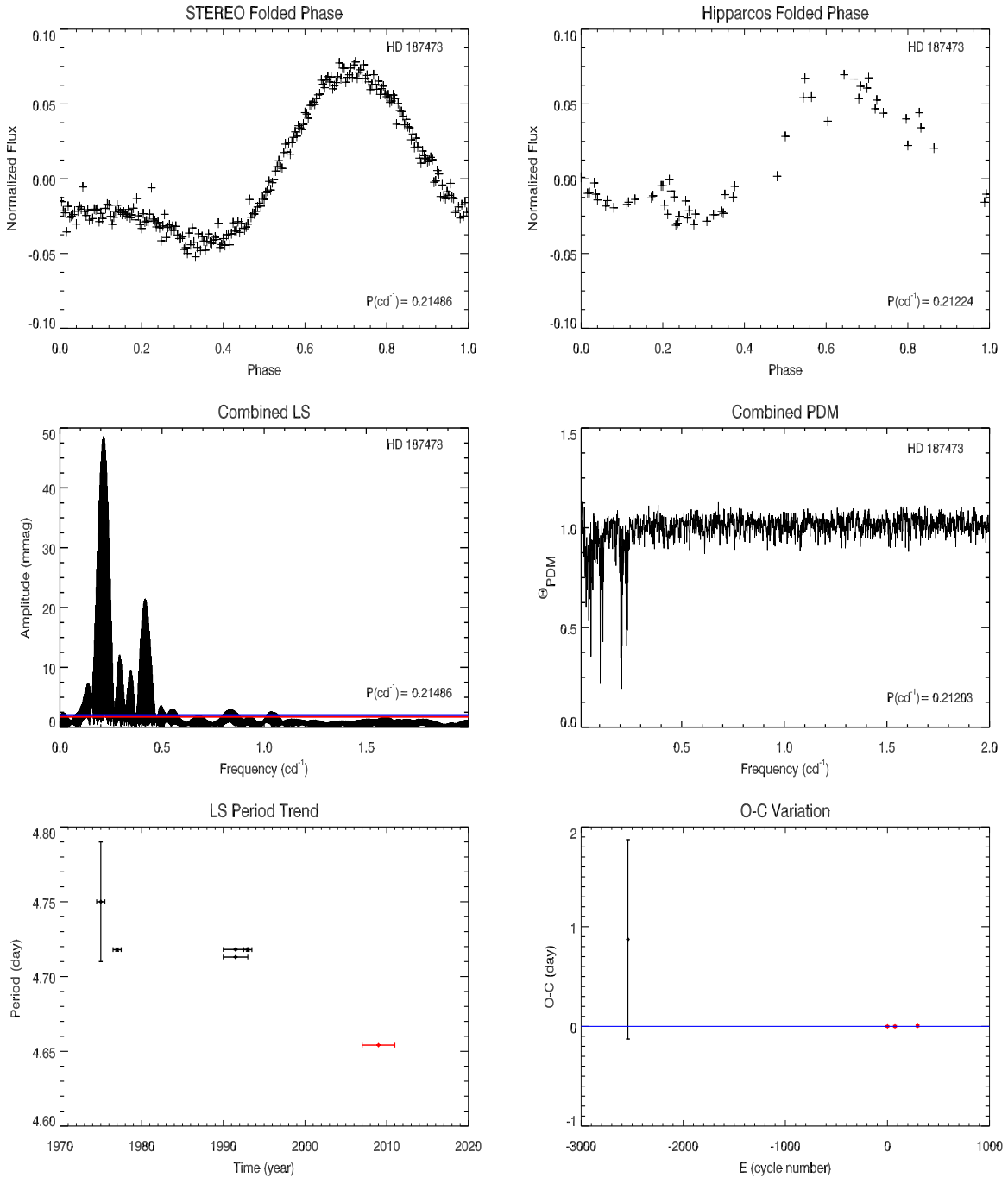

Figure A.26: Folded light curves produced by *STEREO* and *Hipparcos* periods, frequency analyses of combined light curves as well as period and O-C variation graphics of HD 187473.

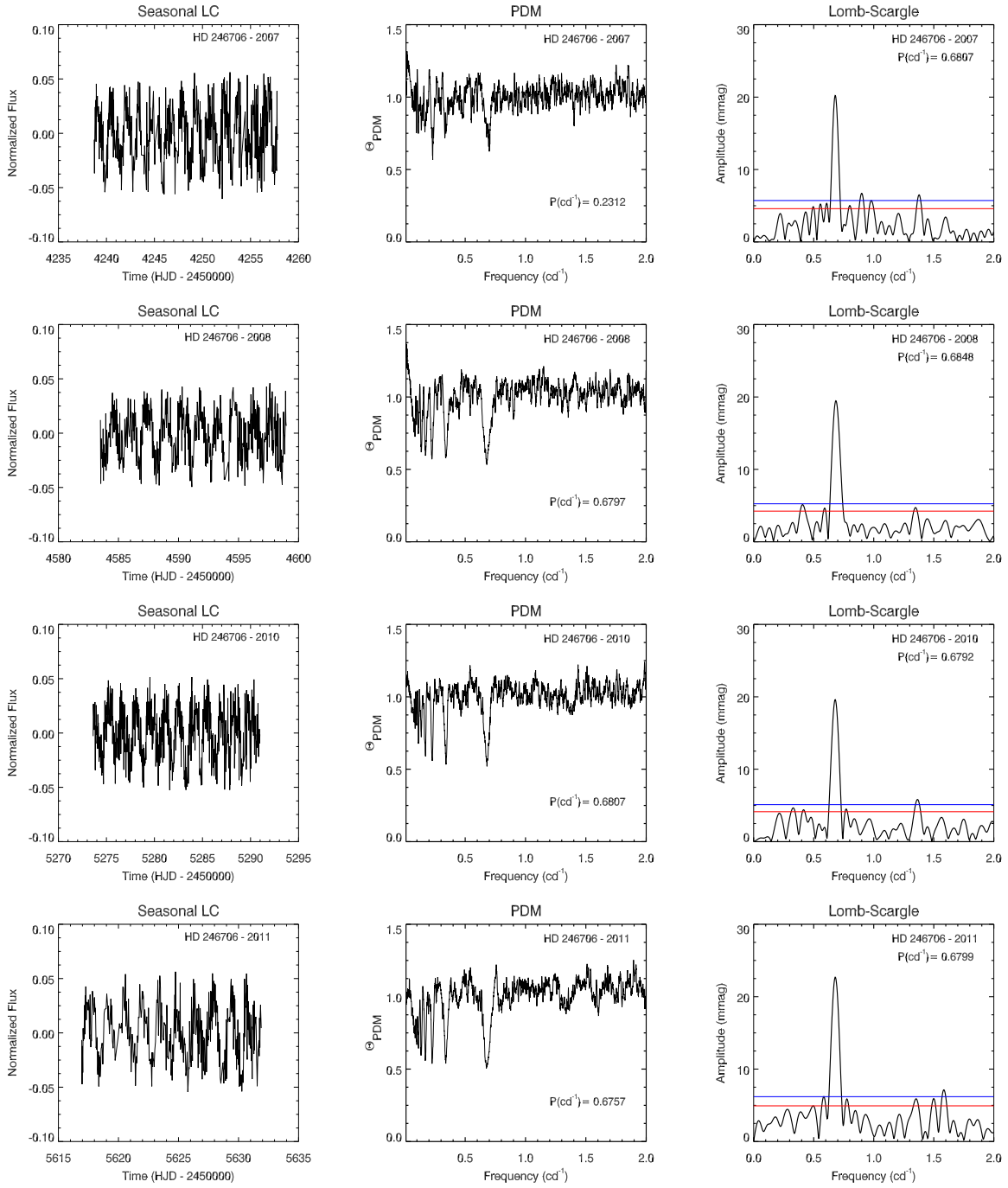

Figure A.27: Annual light curves and related LS and PDM analyses of HD 246706 are shown in the figure.

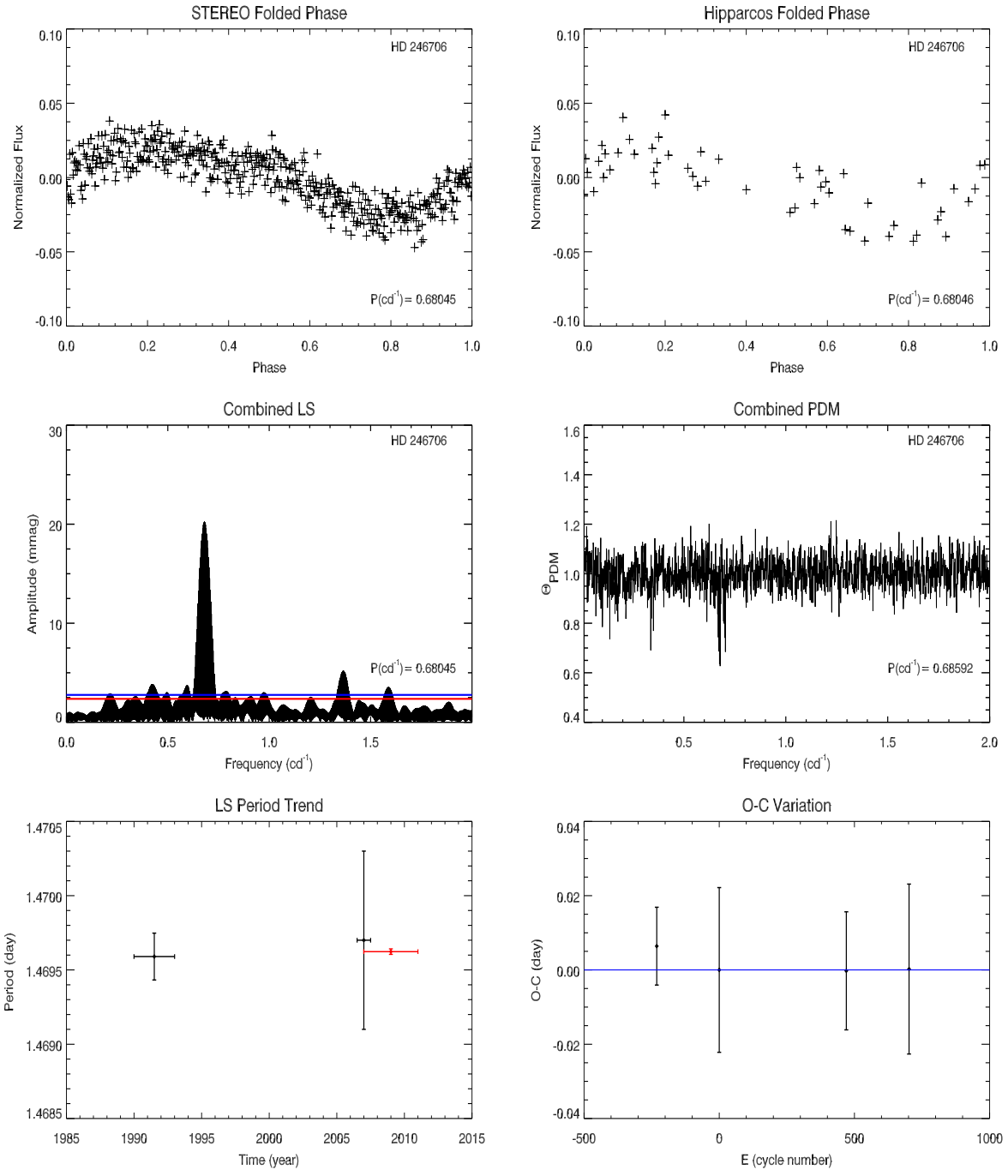

Figure A.28: Folded light curves produced by *STEREO* and *Hipparcos* periods, frequency analyses of combined light curves as well as period and O-C variation graphics of HD 246706.

Appendix B

The Kolmogorov-Smirnov test and its application to δ Scuti stars

The Kolmogorov-Smirnov (KS) test is a widely used non-parametric statistical test to decide the goodness of a fit, which is of vital importance for comparison of theories and observations. It is based on an assumption that two distributions are statistically similar. There are two versions of the KS test, one of which is the one-sample test that compares whether an empirical distribution function is sampled from any specific distribution such as normal, Poisson, uniform or exponential distributions. In the KS test, the main idea is to calculate the maximum vertical deviation (KS statistic, D) between these two data samples. However, unlike chi square test, KS uses proportions rather than frequency counts. Additionally, it works with cumulative relative frequencies, which are increasing proportions of data less or equal to sample size, since cumulative distribution provides better probability estimation due to the fact that data is not indiscriminately divided. To produce these cumulative numbers, data must be sorted in an ascending order.

Moreover, in our study, theoretical data is assumed to show the Poisson cumulative distribution instead of a normal cumulative distribution since events, each of which is not dependent to others, randomly occur at a constant average value (λ). This test utilizes two important hypotheses. The first one is the null hypothesis which assumes that observed and theoretical data are quite similar, and sample follows a specific distribution. Contrarily, the second assumption is that two data sets are significantly different, and there is not any correlation between them.

If the maximum difference D is larger, then the test allows to reject the null hypothesis at a chosen significance level. On the other hand, for small D values, we cannot reject the null

hypothesis. In order to control the greatness of D value, there is a critical limit D_{cr} which is based on a specific significance level (generally $\alpha = 0.05$) and number of degrees of freedom. It can be estimated by $1.36/\sqrt{N}$ if the sample size $N > 35$ and $\alpha = 0.05$. Otherwise, the equation of $1.36/\sqrt{N} - (1/4.5 \times N)$ is used to find the critical limit. According to these, if $D < D_{cr}$, then the KS test decides that distributions are consistent with each other. By using D value, a confidence interval for sample can also be calculated,

$$\begin{aligned} 1-\alpha = \quad & P\Big(D \leq D_{cr}\Big) \\ = \quad & P\Big(\max_x |F(x) - S(x)| \leq D_{cr}\Big) \\ = \quad & P\Big(S(x) - D_{cr} \leq F(x) \leq S(x) + D_{cr} \ ; \ for\ all\ x\Big) \\ = \quad & P\Big(|F(x) - S(x)| \leq D_{cr} \ ; \ for\ all\ x\Big) \ . \end{aligned} \tag{B.1}$$

Thus, $S(x) \pm D_{cr}$ becomes the confidence interval for $F(x)$. To implement the KS test to our δ Scuti samples, there must be some preparations for data samples. Assuming that we have 'n' detected frequencies $(f_1, f_2, ..., f_n)$ in power spectrum, combination number of total spacings between frequencies will be;

$$N = \binom{n}{2} = \frac{n!}{2!(n-2)!} \ , \tag{B.2}$$

and the array which contains these frequency differences will be $\Delta_{ij} = |f_i - f_j|$. For a random frequency spacing ΔF, each element of the Δ_{ij} is calculated by;

$$r(\Delta F) = \Delta_{ij} - \lfloor \frac{\Delta_{ij}}{\Delta F} \rfloor \Delta F \ , \tag{B.3}$$

where $\lfloor x \rfloor$ is the greatest integer smaller than x. The purpose of calculating these $r(\Delta F)$ values is to determine the probability that the $r(\Delta F)$ values are produced from a uniformly distributed function for a selected ΔF (Kawaler, 1988). If so, $r(\Delta F)$ values are expected to be random numbers showing uniform distribution between 0 and 1. Subsequently, 'r' values are divided into bins according to the specified error width 'ϵ'. When division process is applied until the ΔF value is reached, we obtain $B = \Delta F/\epsilon$ bins in total where each bin contains $s \rightarrow \big[0, \epsilon\big] U \big[\Delta F - \epsilon, \Delta F\big]$ elements. If 's' values are randomly distributed in the bins, then we expect on average (N/B) frequency differences in per bin. However, there will be some variations about the mean value. Some bins will randomly have more than others whereas some

of them have less elements, yet all will be distributed around a mean value N/B and a sigma. Such a distribution can be represented by a Poisson distribution given as;

$$PD = e^{-\lambda} \frac{\lambda^s}{s!} \ . \tag{B.4}$$

The bins (b) which have the same amount of elements are counted. Then, a cumulative distribution is produced and divided by the total number of the bins (B). Thus, we obtain normalized cumulative numbers to compare with cumulative 's' values.

$$S(s) = \frac{1}{B} \sum_{i=1}^{s_{max}} b_i \ , \tag{B.5}$$

where s_{max} is the maximum number of 's' elements in all bins. The number of 's' values in each bin 'b' is then counted and a cumulative Poisson distribution is generated by using the function;

$$CPD = F(s) = e^{-\lambda} \sum_{i=1}^{s_{max}} \frac{\lambda^i}{i!} \ . \tag{B.6}$$

Now, we have two cumulative distributions to test their discrepancies with KS test. As previously mentioned, KS test has two important hypotheses, and in this case, they are;

$$\begin{aligned} H_0 : \quad & F(s) = S(s) \quad ; \ for \ all \ s \ , \\ H_1 : \quad & F(s) \neq S(s) \quad ; \ for \ some \ s \ . \end{aligned} \tag{B.7}$$

In order to derive the KS statistic D_s, maximum vertical absolute difference between $S(s)$ and $F(s)$ is computed and compared to D_{cr}.

$$D_s = sup\big[|F(s) - S(s)| \quad ; s \in (-\infty, \infty)\big] \ . \tag{B.8}$$

If $D_s < D_{cr}$, then it is concluded that H_0 cannot be rejected, and that two distributions are in a good agreement. To be able to find if there is unique spacings between detected frequencies, this process is repeated for many ΔF values, and each ΔF is plotted against the logarithm of the probability that the $r(\Delta F)$ values are randomly distributed.

Appendix C

Graphical presentations of the results for δ Scuti star samples

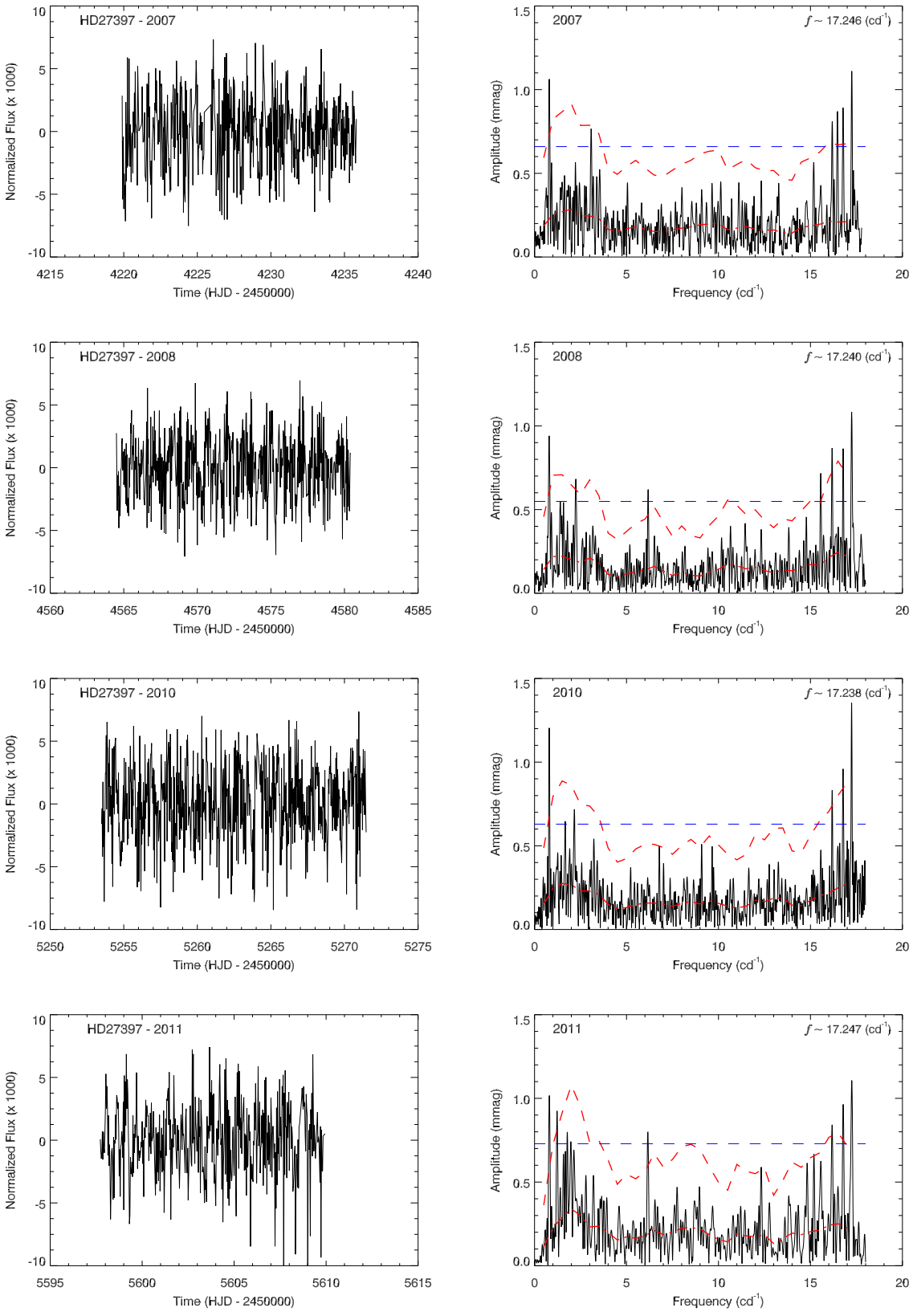

Figure C.1: Annual light curves of HD 27397 and their amplitude spectra.

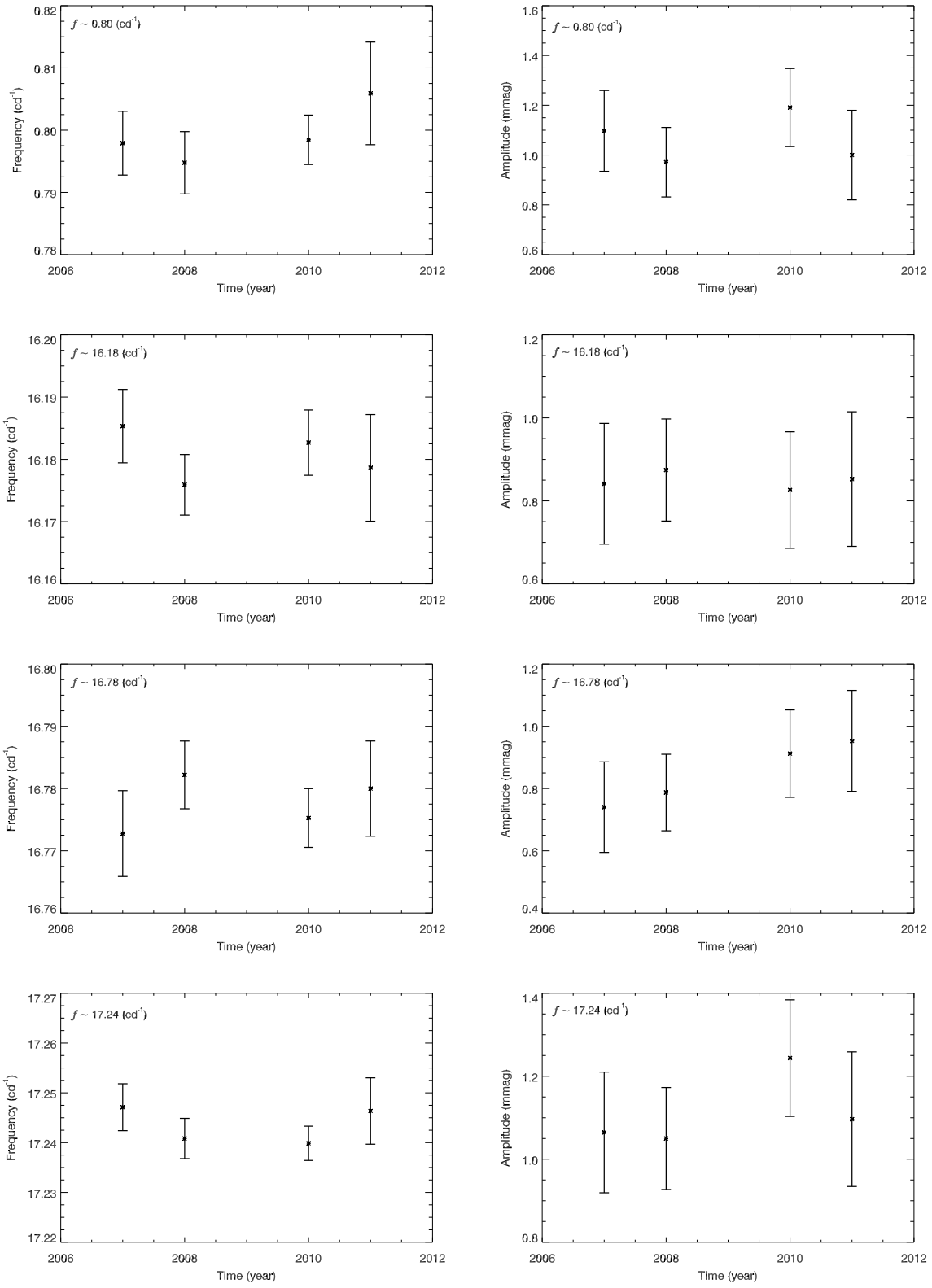

Figure C.2: Four frequencies of HD 27397 and their amplitude variations between 2007 and 2011.

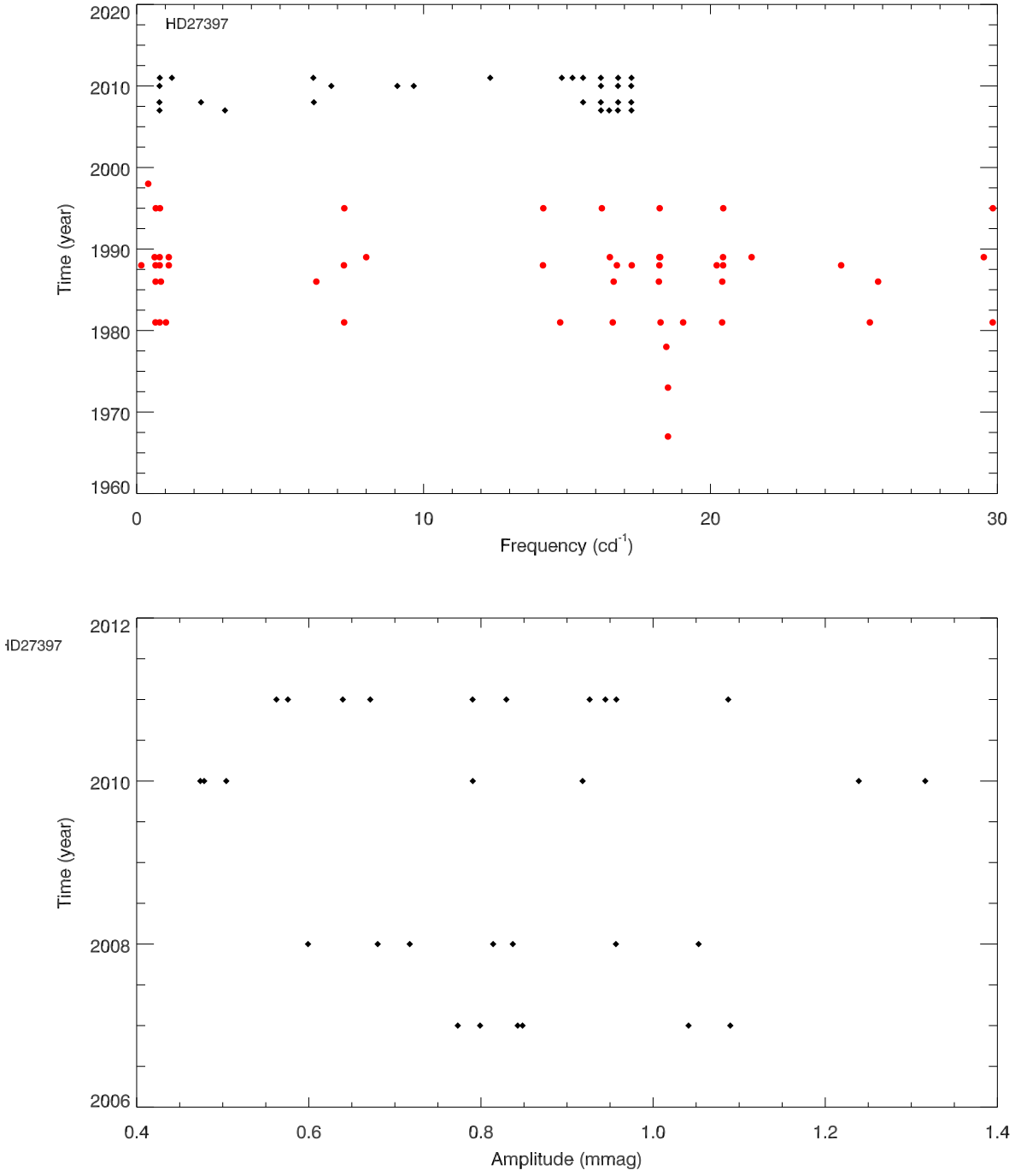

Figure C.3: All available frequencies of HD 27397 and amplitude variations of all *STEREO* frequencies. Black diamonds and red filled circles represent the *STEREO* and literature data, respectively.

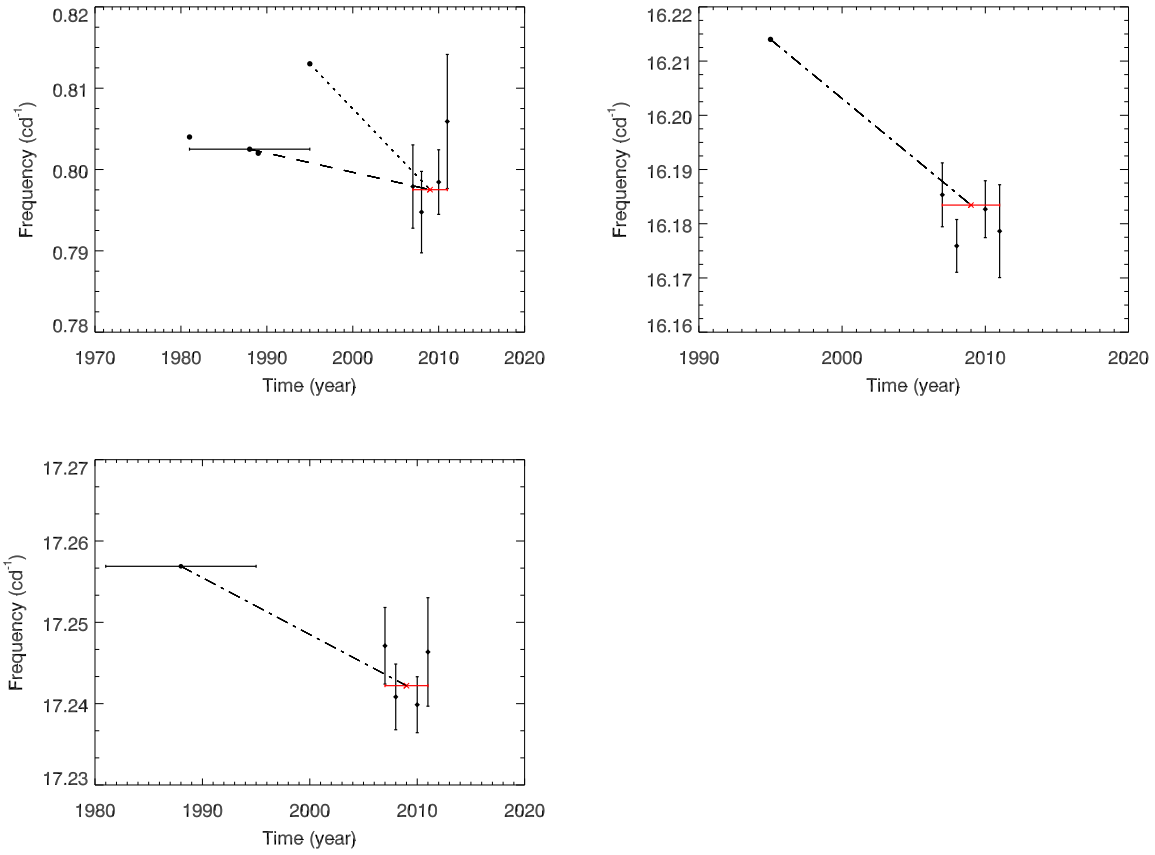

Figure C.4: Variation ratio of three known frequencies.

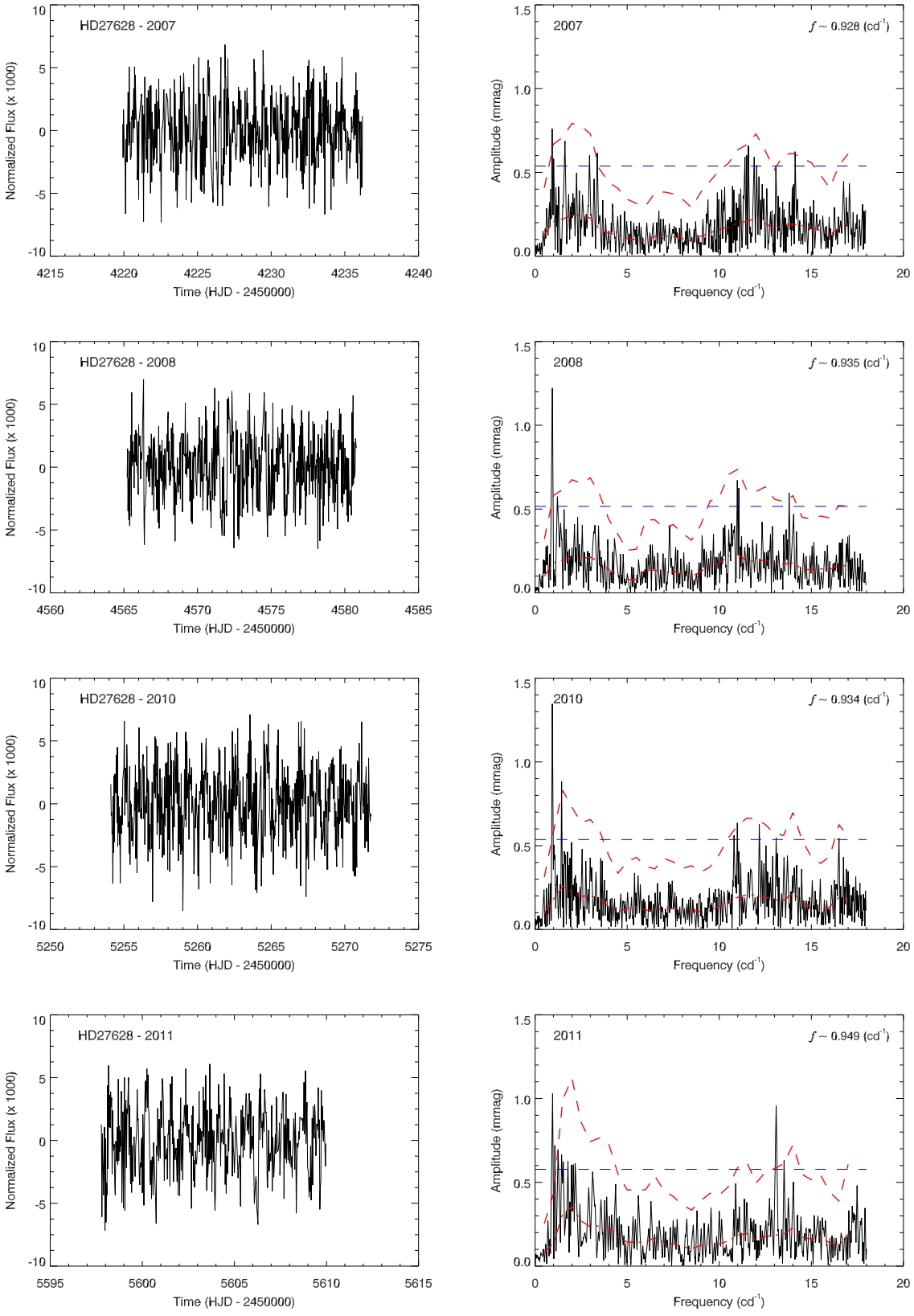

Figure C.5: Annual light curves of HD 27628 and their amplitude spectra.

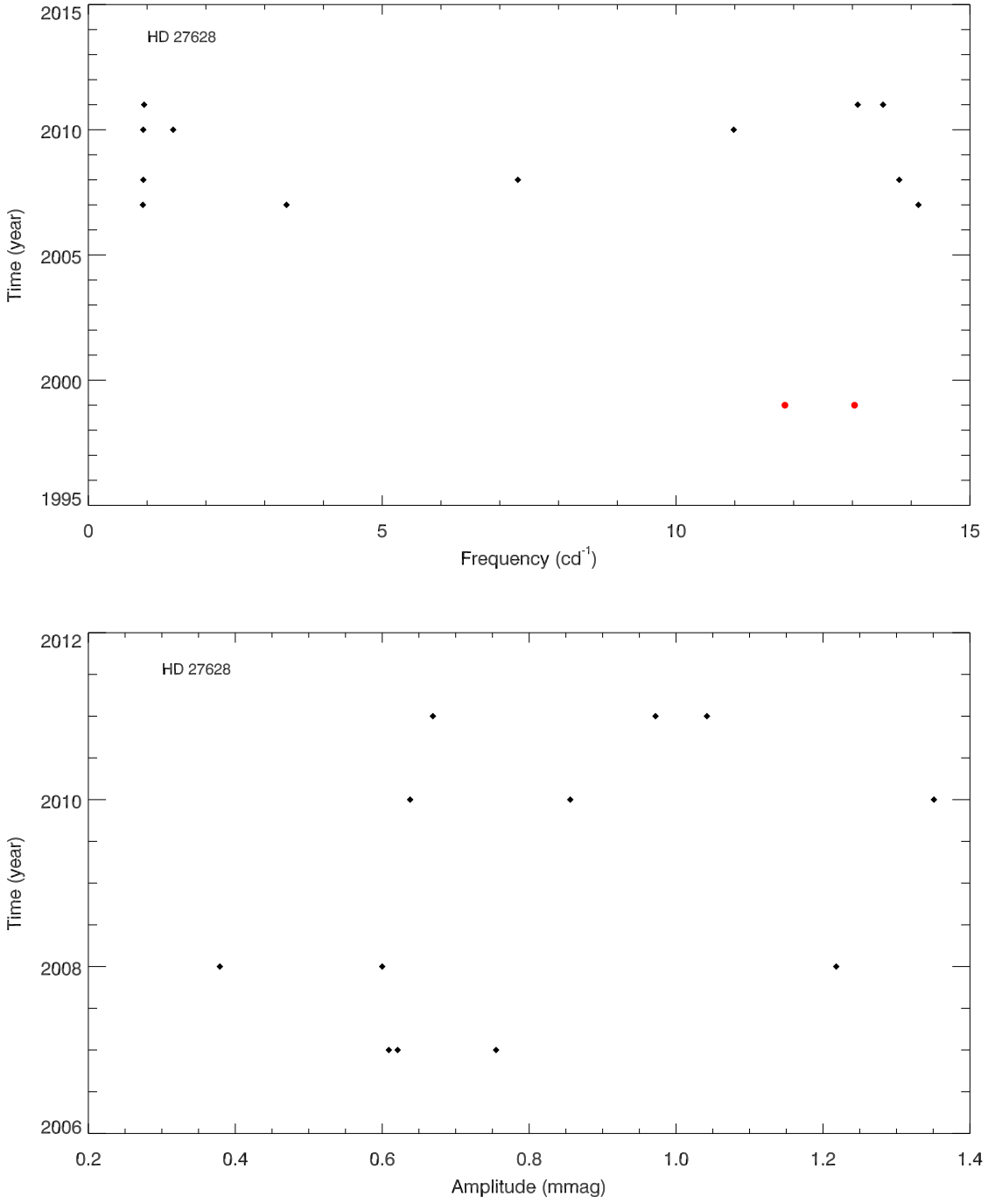

Figure C.6: All available frequencies of HD 27628 and amplitude variations of all *STEREO* frequencies. Black diamonds and red filled circles represent the *STEREO* and literature data, respectively.

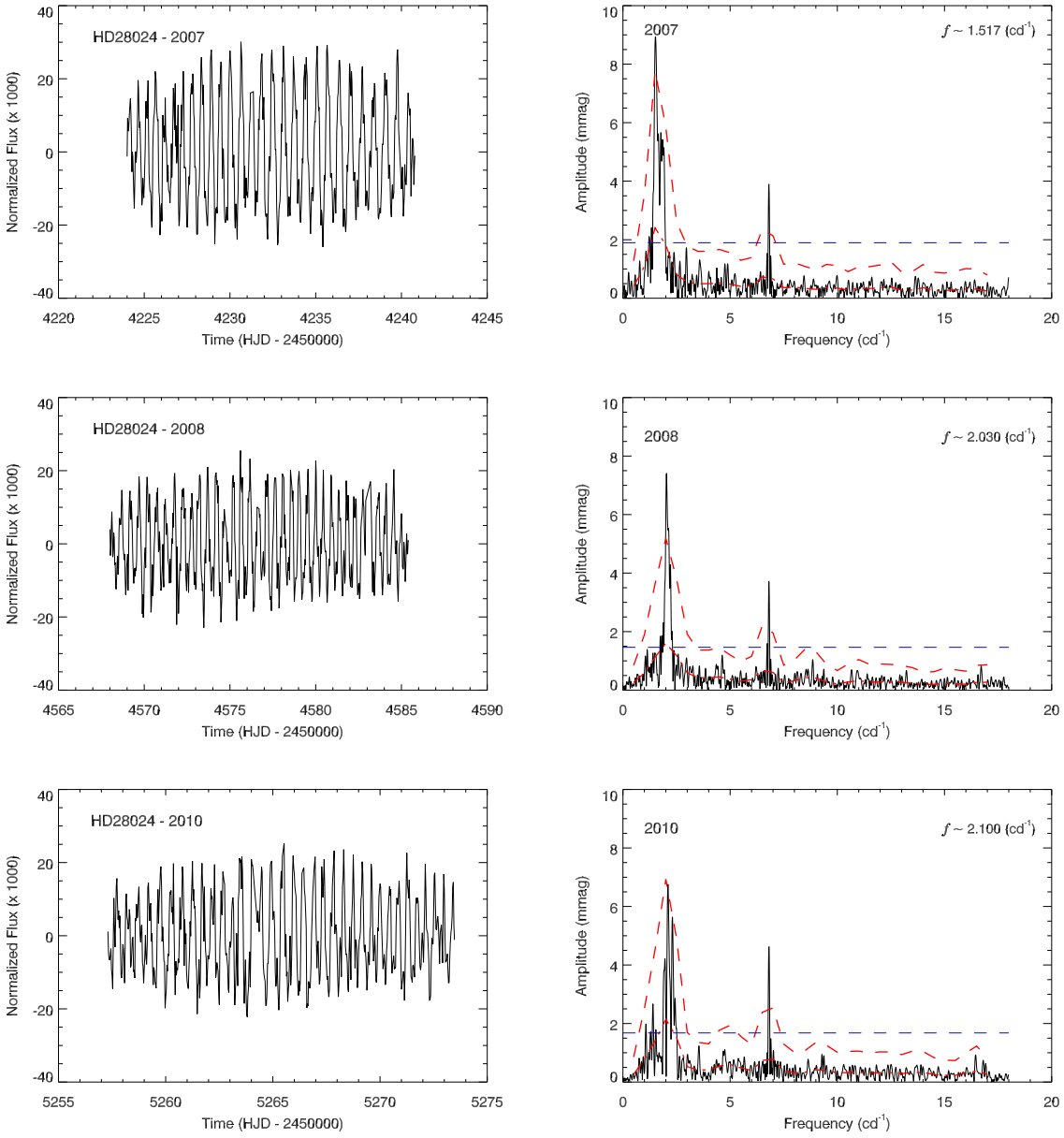

Figure C.7: Annual light curves of HD 28024 and their amplitude spectra.

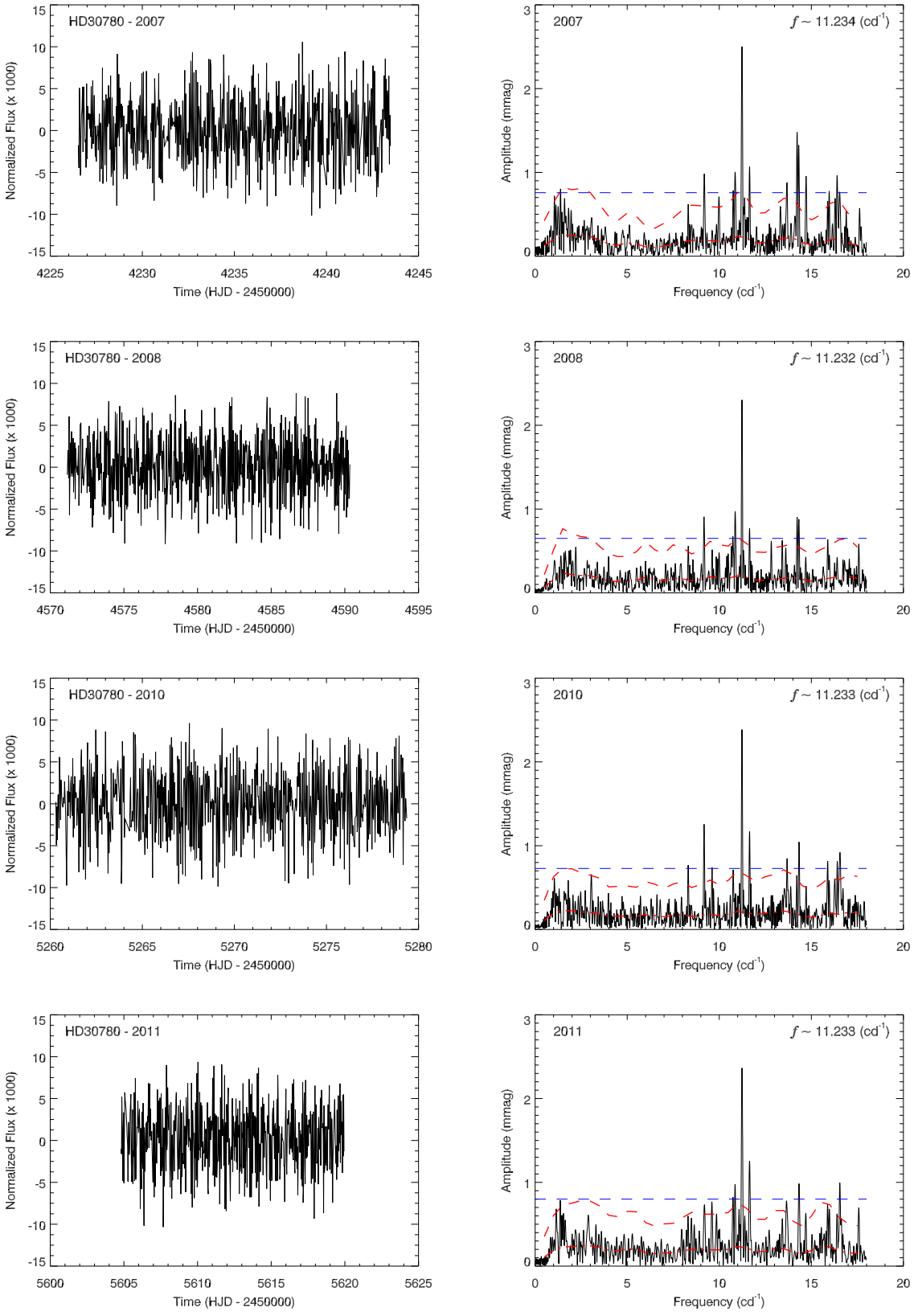

Figure C.8: Annual light curves of HD 30780 and their amplitude spectra.

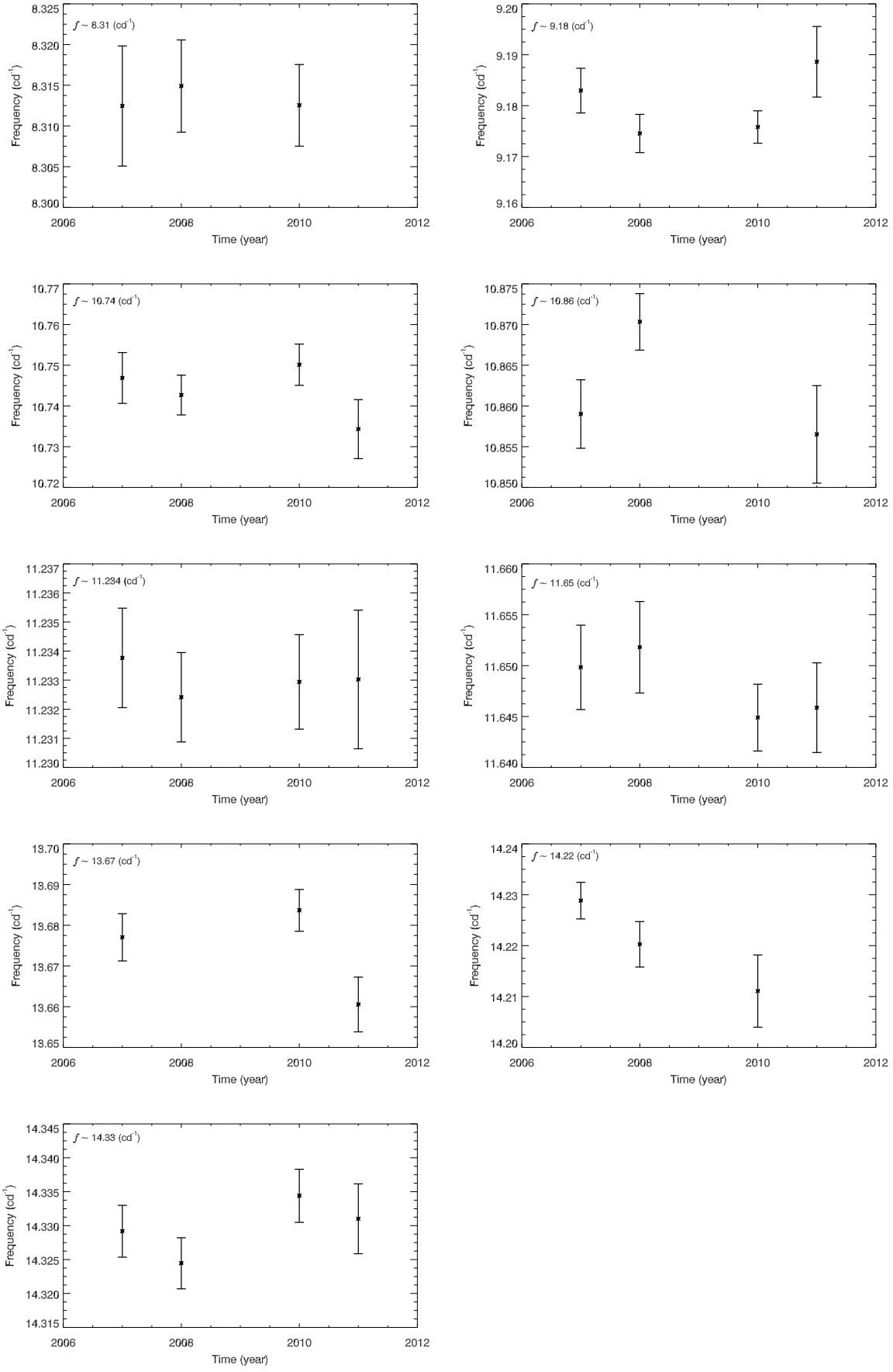

Figure C.9: Nine frequencies of HD 30780 and their variations between 2007 and 2011.

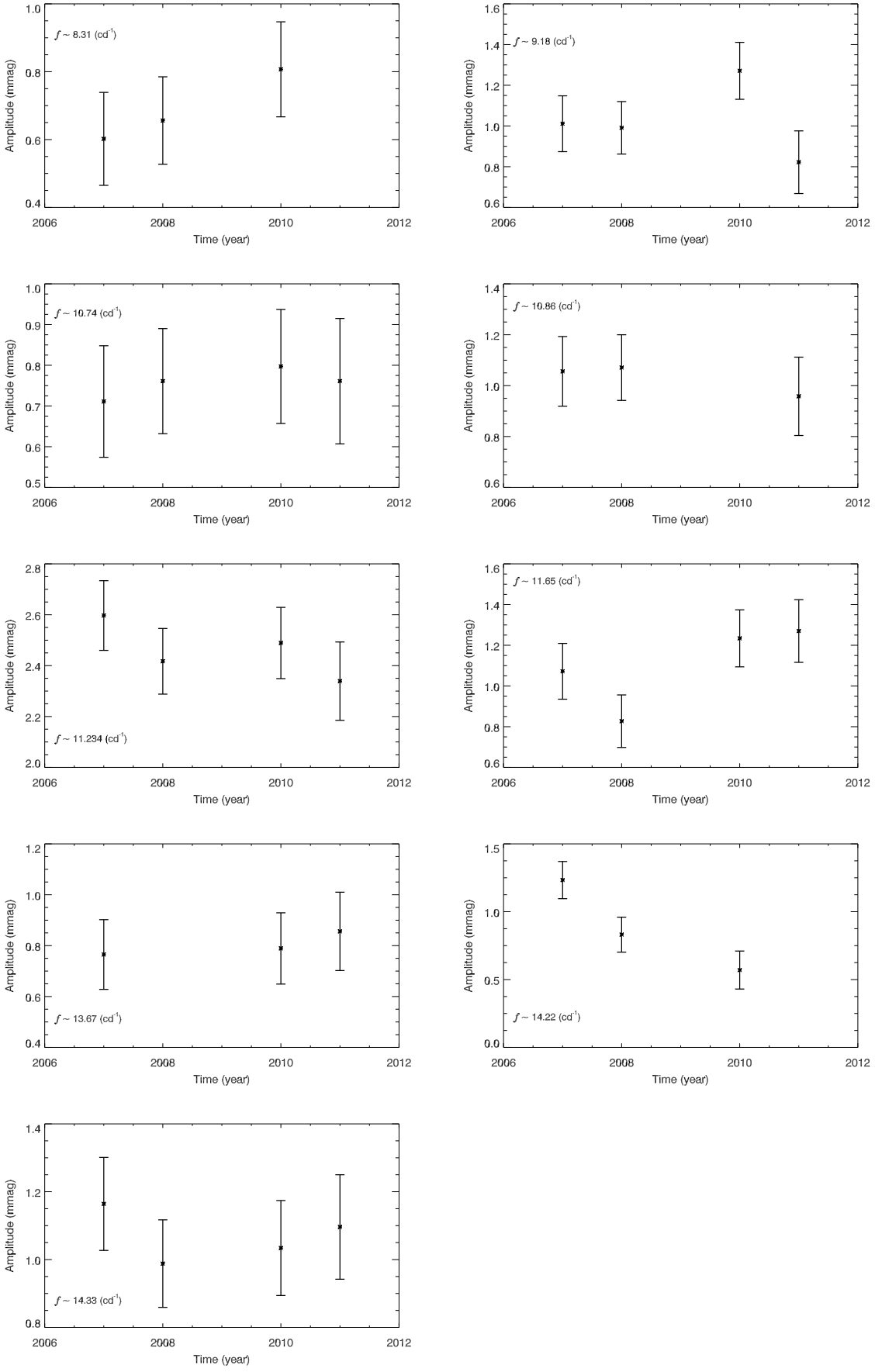

Figure C.10: The amplitude variations of nine frequencies between 2007 and 2011.

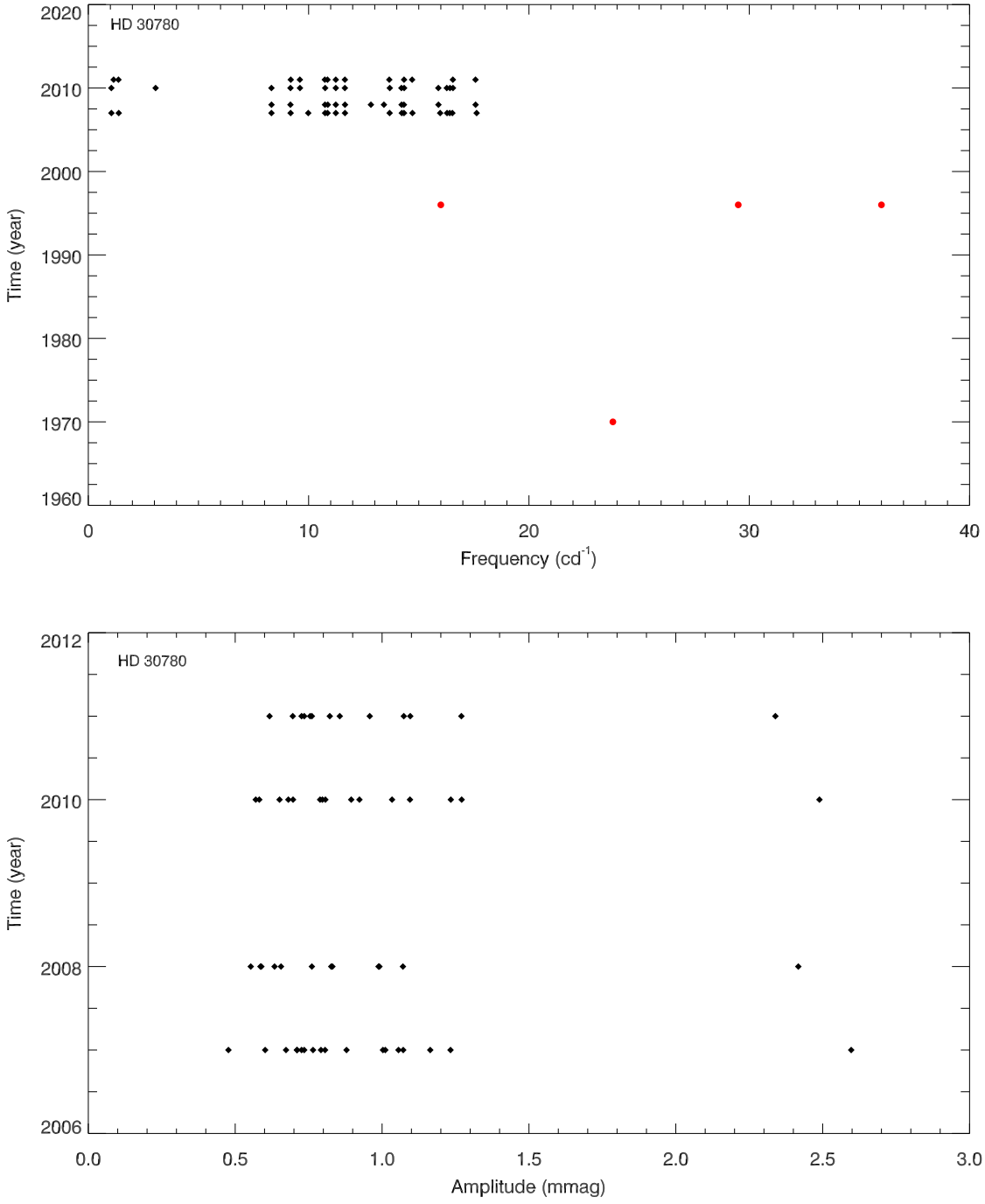

Figure C.11: All available frequencies of HD 30780 and amplitude variations of all *STEREO* frequencies. Black diamonds and red filled circles represent the *STEREO* and literature data, respectively.

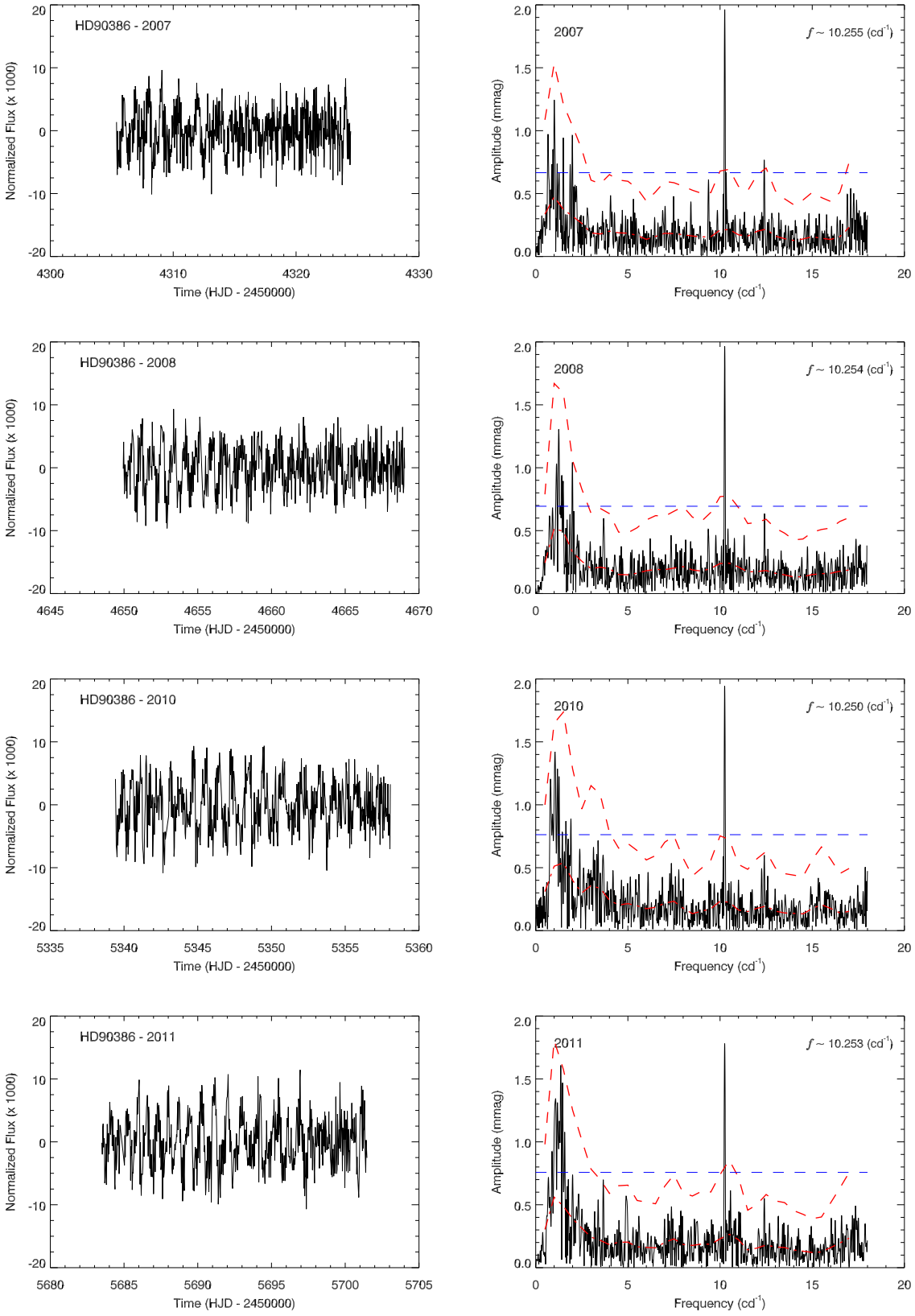

Figure C.12: Annual light curves of HD 90386 and their amplitude spectra.

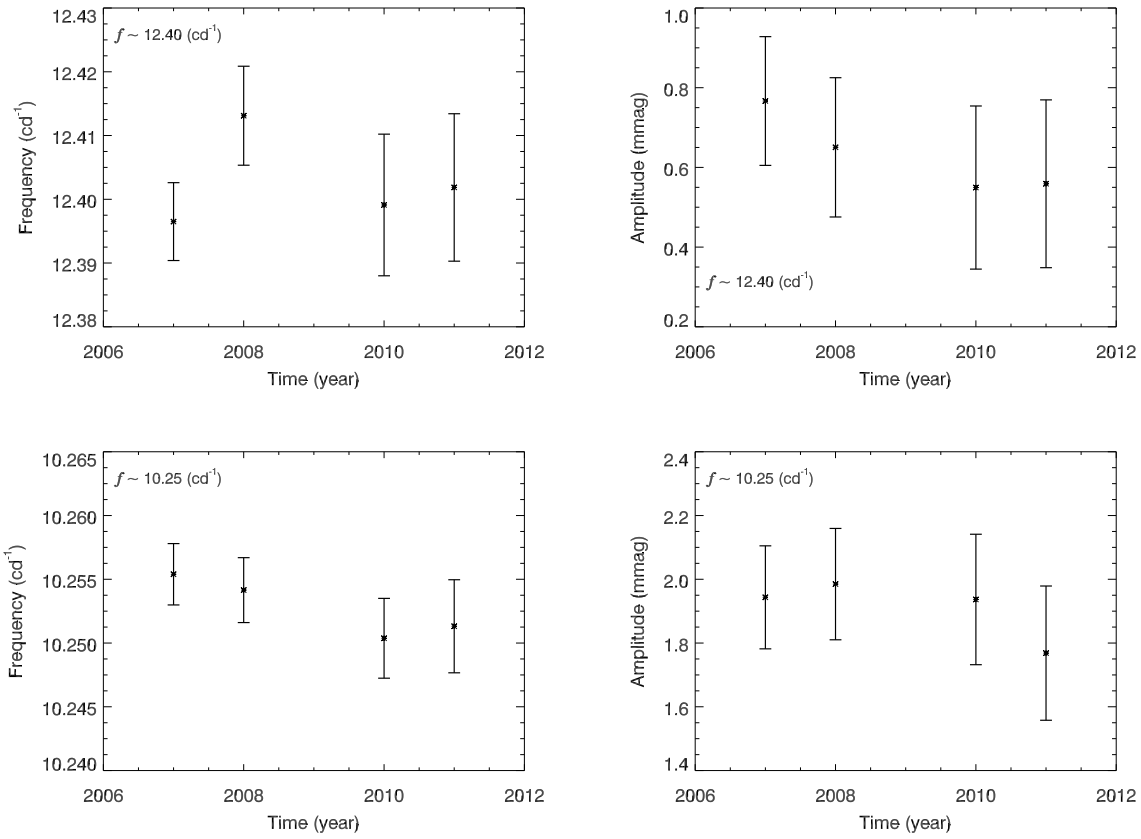

Figure C.13: Two frequencies of HD 90386 and their amplitude variations between 2007 and 2011.

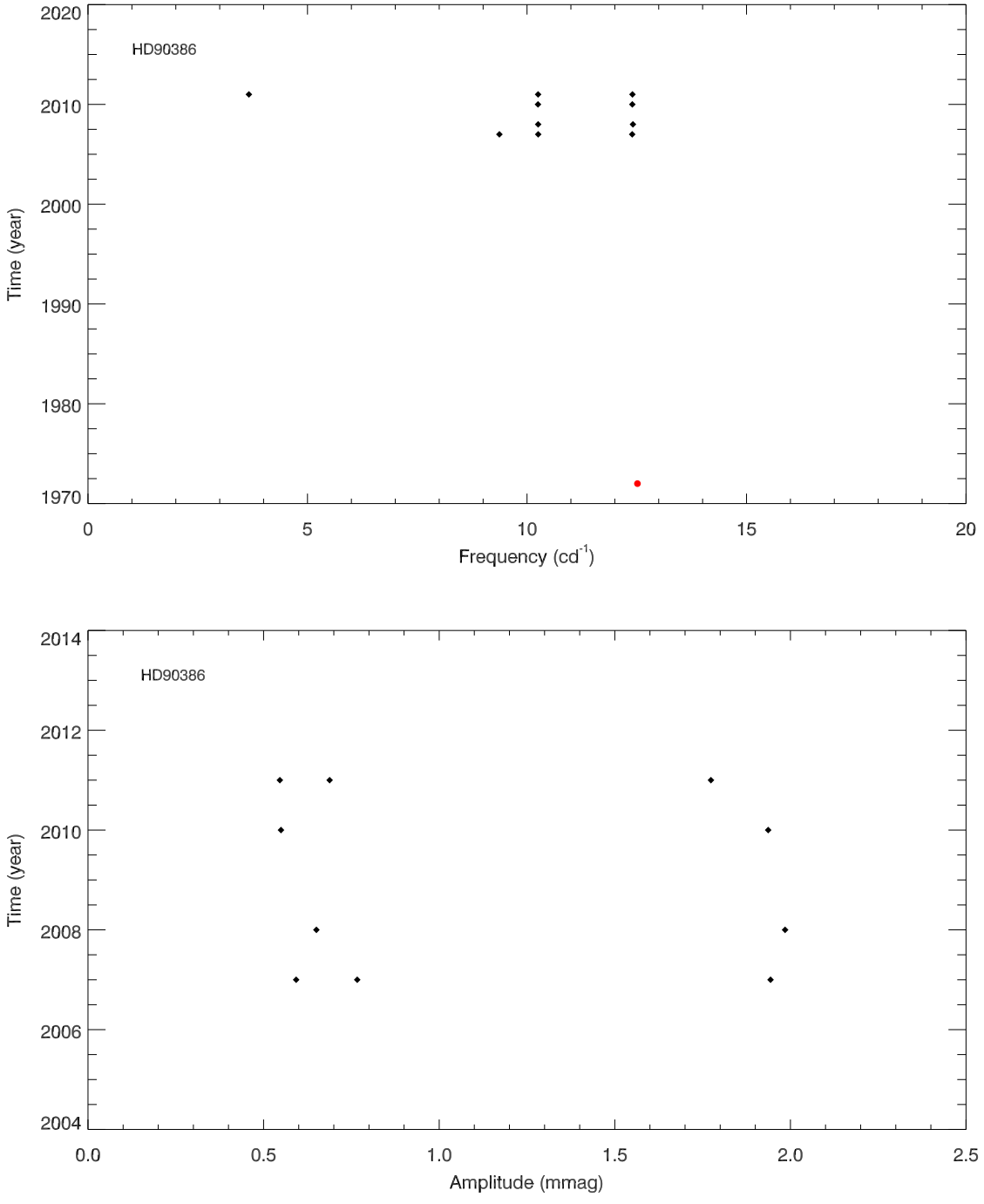

Figure C.14: All available frequencies of HD 90386 and amplitude variations of all *STEREO* frequencies. Black diamonds represent the *STEREO*.

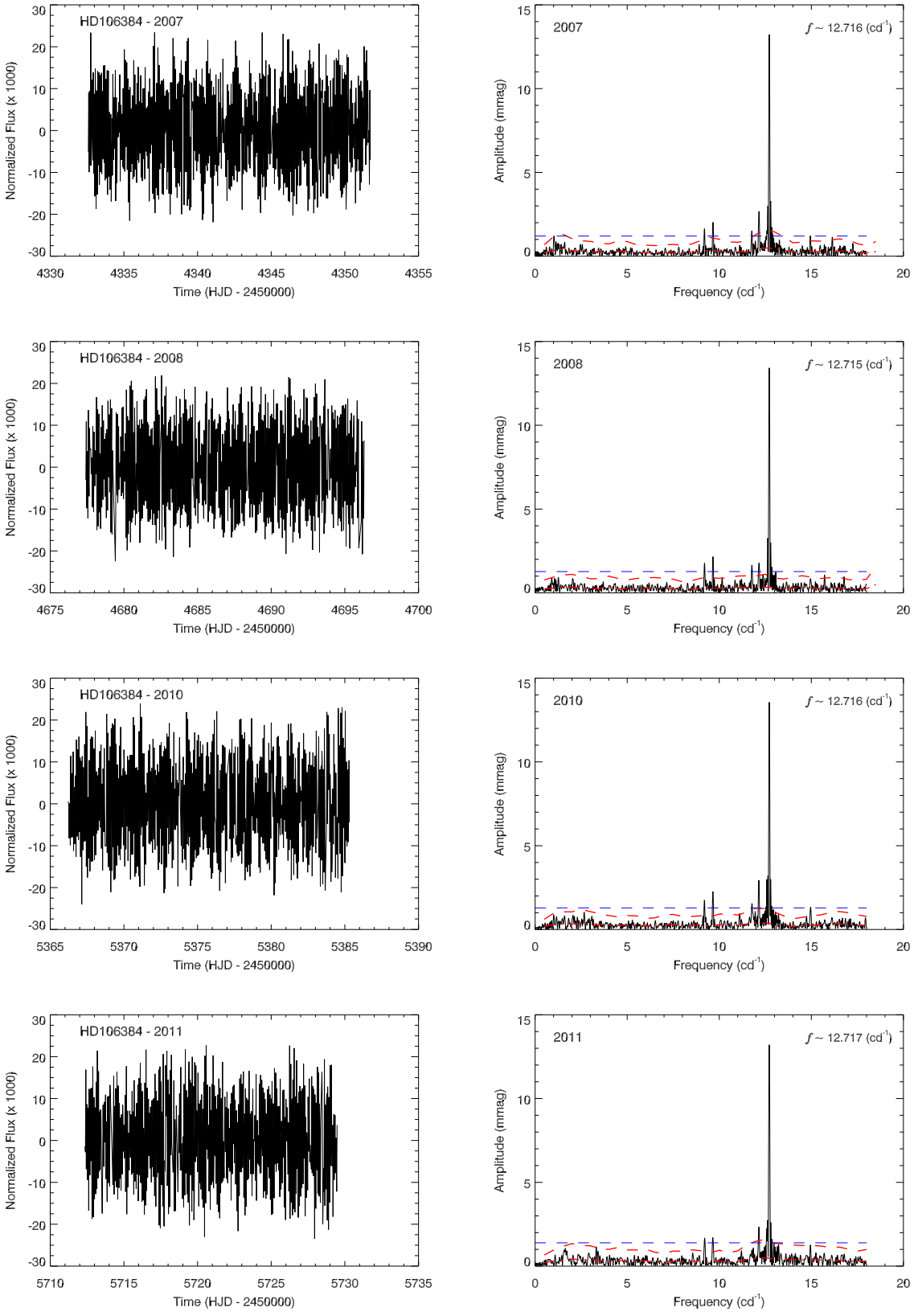

Figure C.15: Annual light curves of HD 106384 and their amplitude spectra.

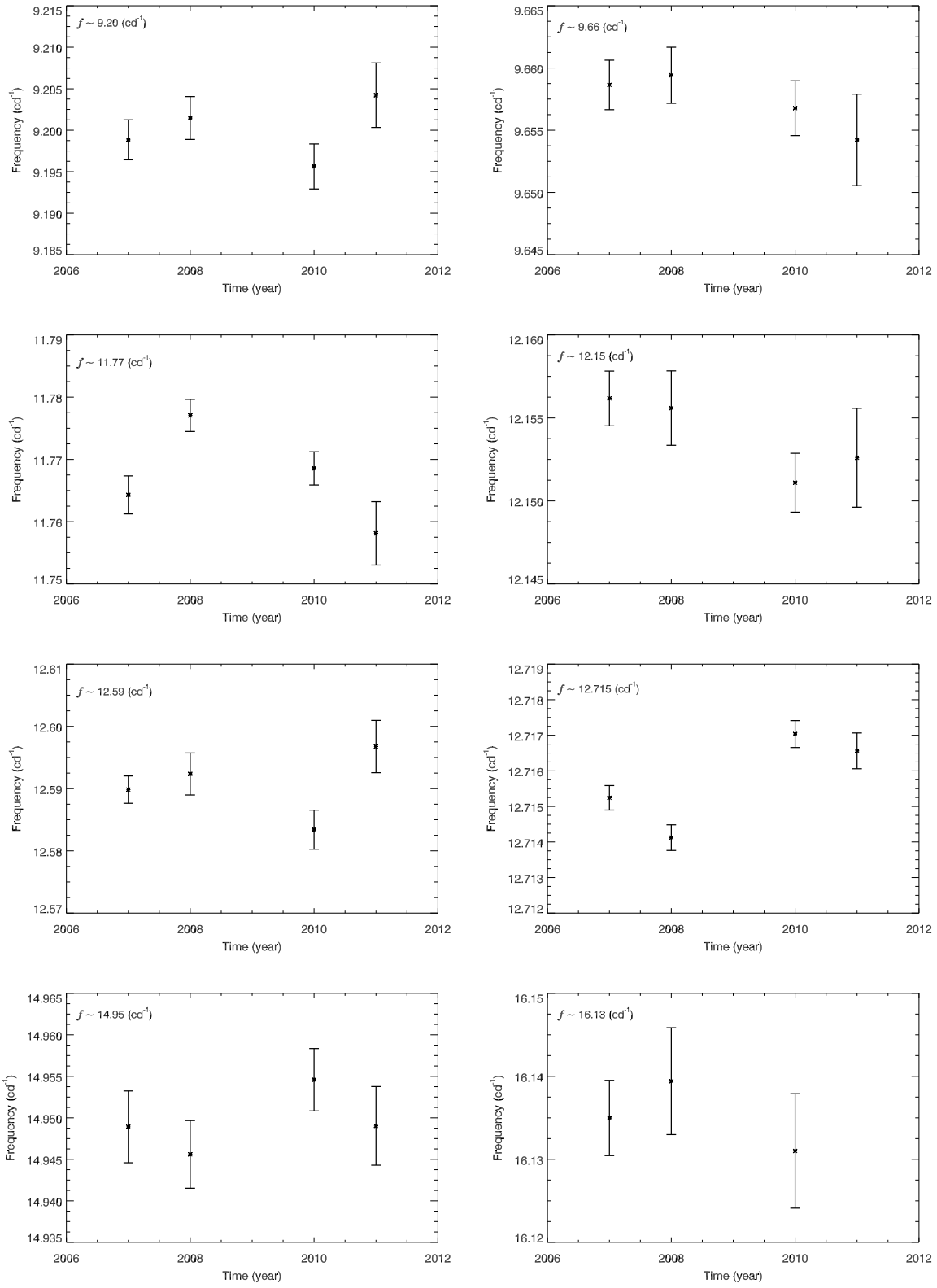

Figure C.16: Eight frequencies of HD 106384 and their variations between 2007 and 2011.

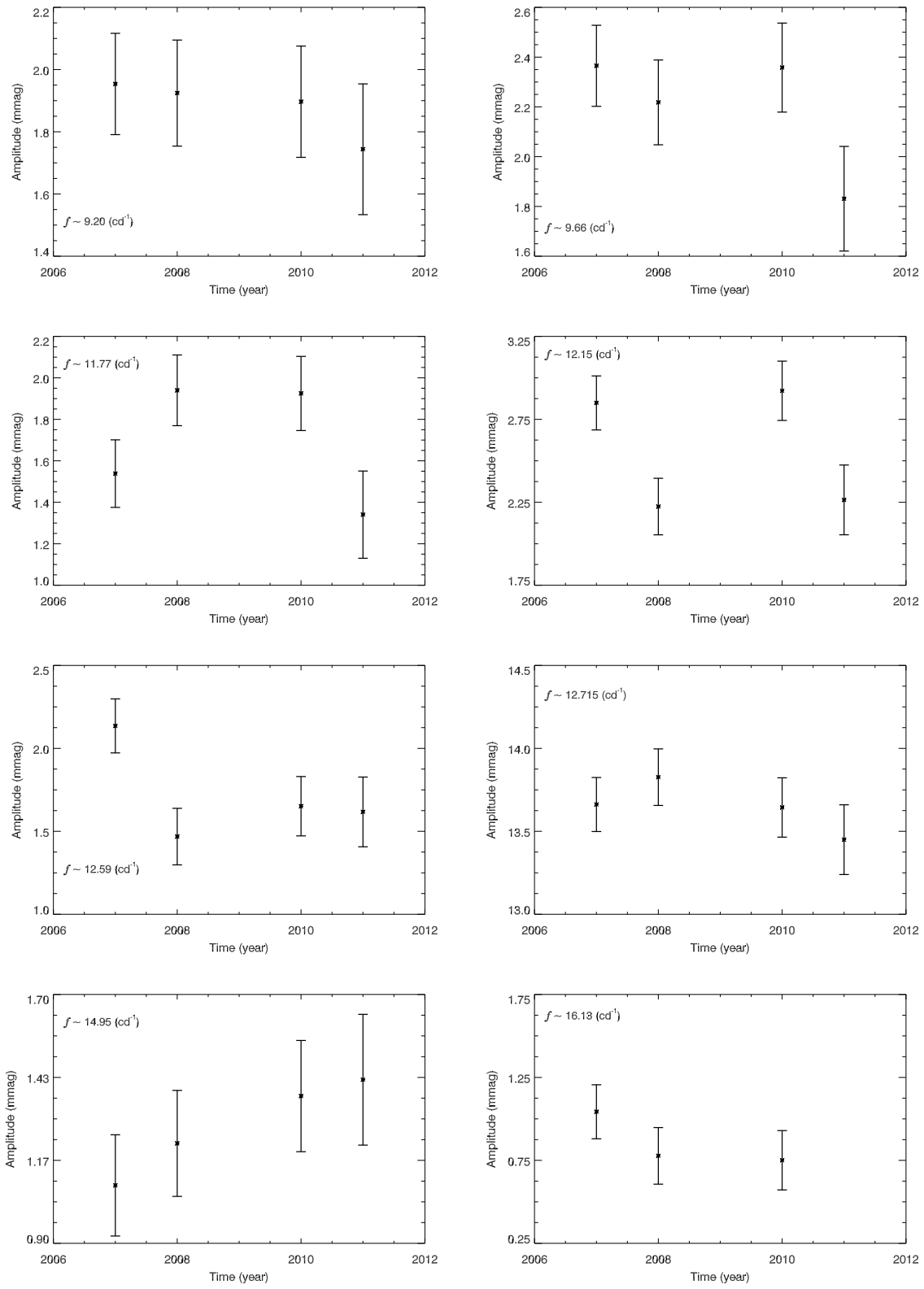

Figure C.17: Amplitude variations of eight frequencies between 2007 and 2011.

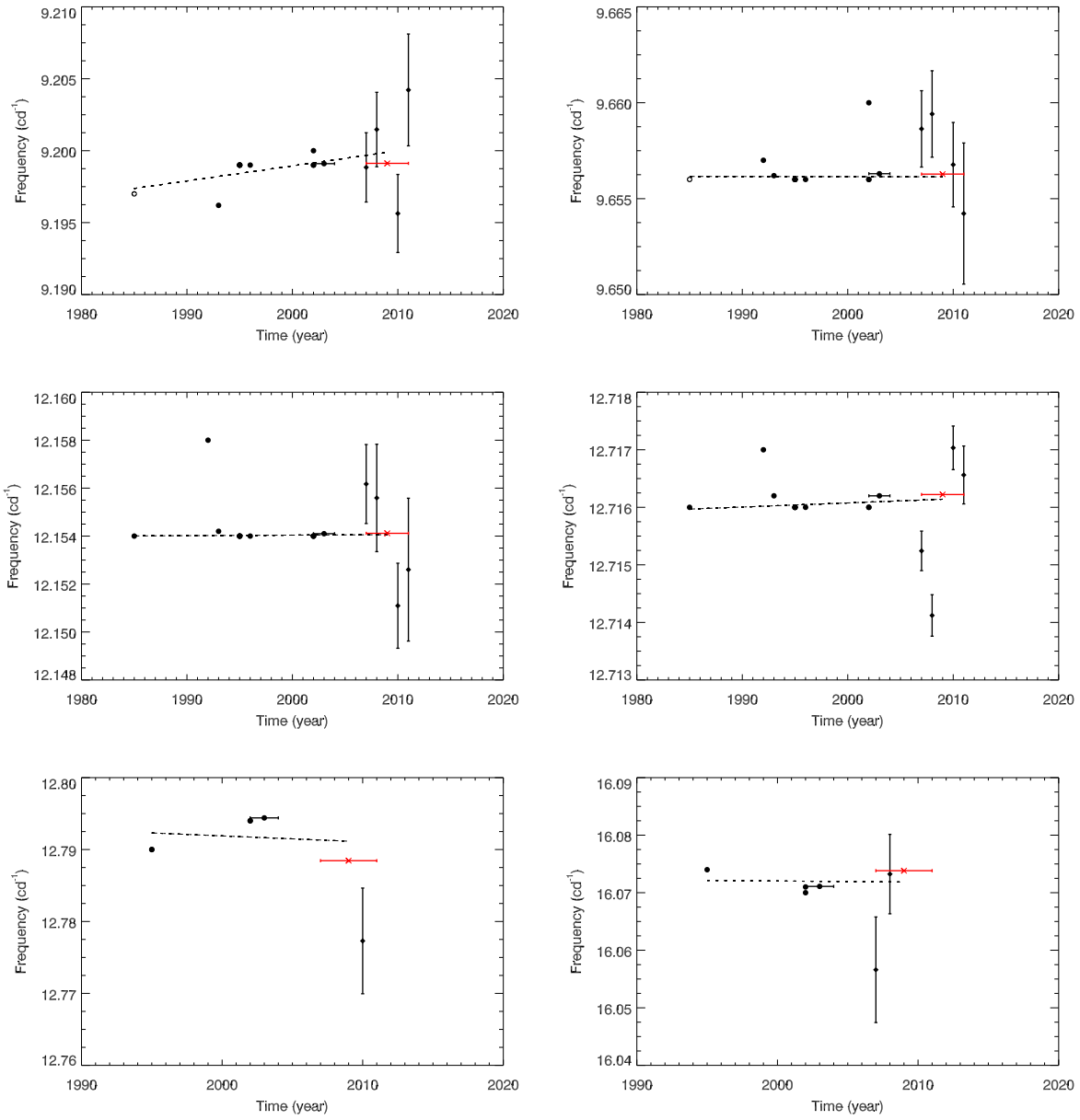

Figure C.18: Variation ratio of six known frequencies.

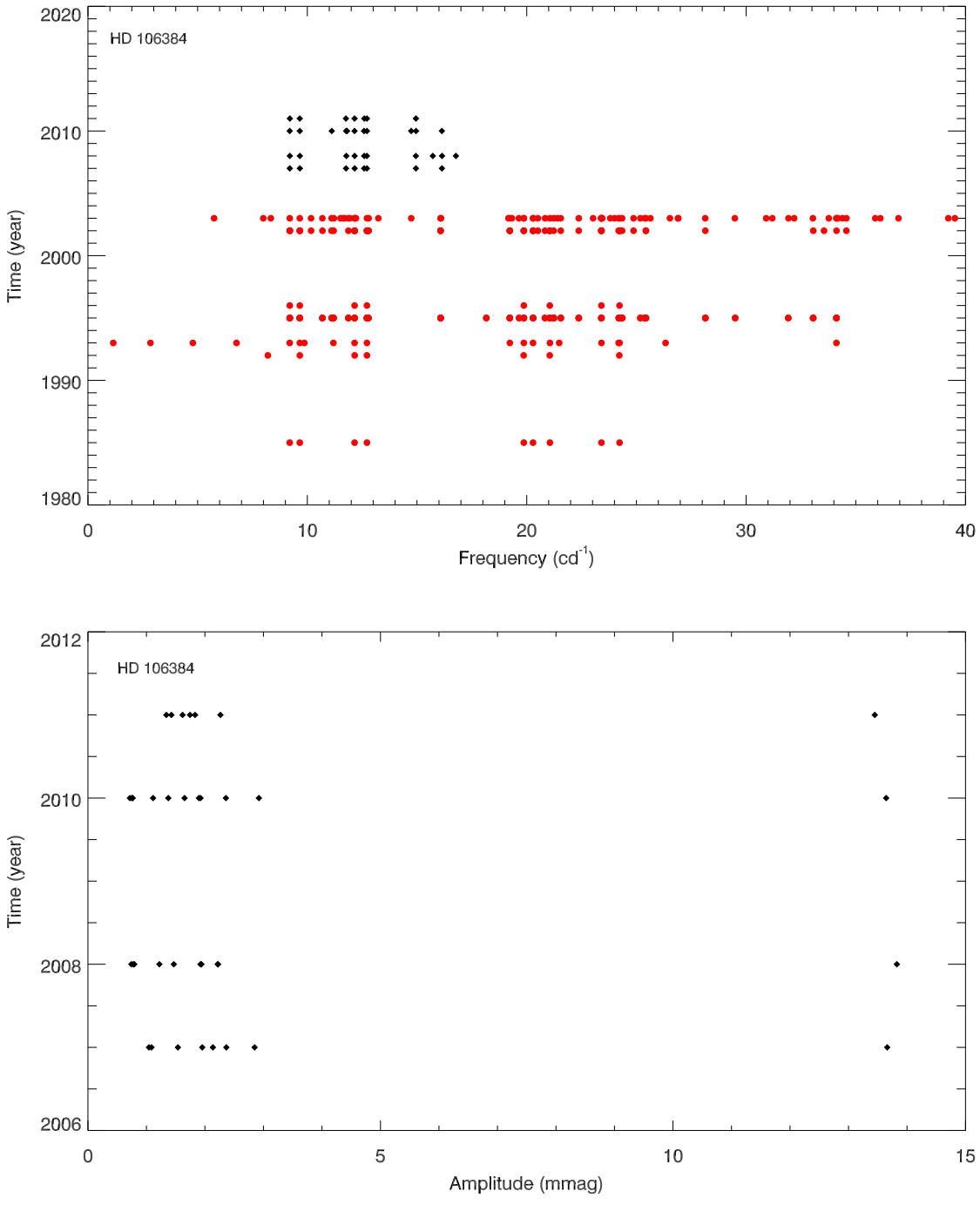

Figure C.19: All available frequencies of HD 106384 and amplitude variations of all *STEREO* frequencies.